UNIVERSITY OF SOUTHAMPTON

FACULTY OF MEDICINE

Human Development and Health

Making Cartilage One Drop at a Time: Harnessing Droplet Microfluidics for Cartilage Tissue Engineering

by

Juan Aviles Milan

Thesis for the degree of Doctor of Philosophy

September 2020

University of Southampton

Abstract

Faculty of Medicine

Human Development and Health

Doctor of Philosophy

Making Cartilage One Drop at a Time:

Harnessing Droplet Microfluidics for Cartilage Tissue Engineering

by

Juan Aviles Milan

Osteoarthritis and other musculoskeletal disorders affect a large proportion of the aged population worldwide. Cartilage tissue engineering approaches have emerged to replace invasive surgical techniques aiming to restore hyaline articular cartilage. Human bone marrow stromal stem cells (HBMSCs) offer the potential as a cell source for differentiation into cartilage tissue. However, their application is hindered by a crucial limitation: subpopulation heterogeneity. The current study provides proof of concept for the implementation of droplet microfluidics for functional assessment of cell aggregates. The goal is to achieve high-throughput cell aggregation simulating early chondrogenic condensation with a view to enriching HBMSC chondroprogenitor subpopulations on the basis of functional, condensation-dependent markers such as SOX9. The *in vitro* characterisation of multicellular spheroids exposed differences in their chondrogenic differentiation outcome linked to cell number. SOX9 expression in large spheroids did not change as a function of time. In contrast, SOX9 expression declined in small spheroids in late chondrogenesis and did not vary significantly during the first week. This indicated that SOX9 could be a potential early marker to predict chondrogenesis in HBMSCs and was further validated by the lack of significant differences in SOX9 mRNA levels during the first week of chondrogenic differentiation. SOX9 heterogeneity was observed on an intra-spheroid level, which highlighted a potential advantage in harnessing even smaller aggregates for enriching stem cells for cartilage tissue engineering. The suitability of *SOX9*-Cy5 nanoflares was assessed for their application for sorting of cell aggregates. The Cy5-positive cell subpopulations corresponded with high *SOX9* mRNA levels only in those instances where there was a clear difference in terms of order of magnitude of Cy5 fluorescence signal between positive and negative gated cells by flow cytometry. Thus, the data suggest that nanoflares were not sufficiently sensitive to dissect HBMSC subpopulations on the basis of biologically relevant differences in *SOX9* expression. The optimisation process of a microfluidic device concluded that soft lithography designs incorporating silanisation and plasma bonding generated highly monodisperse droplet diameters that were promising for cell encapsulation. A functional stability assay demonstrated the higher effectiveness of the Bio-Rad QX200^{TM} droplet generation oil commercial variation compared to the in-house Soton2 surfactant. The droplet microenvironment was suitable for the formation of minimal HBMSC aggregates (comprising only a few cells). HBMSCs aggregates displayed maintained colony formation functionality when re-plated from aggregates incubated in short-term chondrogenic differentiation cultures for up to 3 days. In addition, HBMSC aggregates self-assembled in microdroplets expressed higher levels of *SOX9* than cells cultured in monolayer as early as 24 h of chondrogenic induction. The work presented in this thesis confirms the potential of droplet microfluidics for culturing multicellular spheroids as vehicles for chondrogenesis. The application of this platform for cell aggregation, short-term culture and sorting on the basis of early stage functional markers opens new prospects for harnessing HBMSCs for cartilage tissue engineering.

Table of Contents

List of Tables

List of Figures

List of Figures

List of Figures

Research Thesis: Declaration of Authorship

Print name: Juan Aviles Milan

Title of thesis: Making Cartilage One Drop at a Time: Harnessing Droplet Microfluidics for Cartilage Tissue Engineering

I declare that this thesis and the work presented in it are my own and has been generated by me as the result of my own original research.

I confirm that:

This work was done wholly or mainly while in candidature for a research degree at this University;

Where any part of this thesis has previously been submitted for a degree or any other qualification at this University or any other institution, this has been clearly stated;

Where I have consulted the published work of others, this is always clearly attributed;

Where I have quoted from the work of others, the source is always given. With the exception of such quotations, this thesis is entirely my own work;

I have acknowledged all main sources of help;

Where the thesis is based on work done by myself jointly with others, I have made clear exactly what was done by others and what I have contributed myself;

None of this work has been published before submission

Signature: Date:

Acknowledgements

I would like to express my sincere gratitude to my supervisor, Dr Jonathan Dawson, who saw a suitable candidate to undertake this challenging interdisciplinary project in me. His guidance, his persistent help and the possibility to explore as an independent researcher without censure were instrumental for the successful completion of this work.

I wish to extend my appreciation to the rest of the supervisory team. Prof Xize Niu was essential to introduce me to the field of droplet microfluidics and I thank the entire Niu group for their assistance in training and support through their vast expertise. Also, I thank Dr Rahul Tare for his time and his contribution sharing his knowledge of cartilage tissue engineering and the methodologies developed by his group. Both were crucial to shape my own techniques and provided solid foundations. Lastly, I cannot thank enough Dr Jonathan James West for his kindness in offering his space in the CHB lab and his technical experience to carry out cell encapsulation in microdroplets. Without his collaboration in cooperation with the Hywel group, the goal of this project would not have been realised.

I would like to pay my whole-hearted regard to Versus Arthritis for their financial support throughout this project. The charity has built an enormous link between researchers in the UK. It has been an honour to take part in their goal to fight arthritis.

I wish to acknowledge the assistance and continued support of the Bone and Joint Research group led by Professor Richard Oreffo. He is a true example of how to run an organised yet united group. I would like to thank Ms Julia Wells, Mrs Kate White, Dr Stefanie Inglis and Dr Janos Kanczler for training me and for their work keeping the labs going. In addition, I wish to thank Dr María de Andrés González for introducing me to the world of molecular biology. I would like to say a special thank you to Dr Stuart Lanham for his indispensable assistance making the nanoflare technology available to me, conducting the flow cytometry experiments with me and analysing the results. All in all, I take with me all the memories and the scientific formation acquired during these last four years and I will always cherish them.

It has been a long road and I am truly grateful to my friends that have been there for me in Southampton, inside and outside the University, and from the distance. I can say I have a small group of people that are extremely dear to me. You are all part of the family that I choose. Finally, I lack words to thank my mother Rosa, my grandmother Matilde and my aunt Pilar. You have given me a free hand to choose my own path and trusted my judgement with the utmost affection. Your selfless attention towards my problems and challenges was paramount to keep me on track.

List of Abbreviations

Abbreviation	Description
ACAN	Aggrecan
ACI	Autologous Chondrocyte Implantation
ADAMTS	A Disintegrin And Metalloproteinase with Thrombospondin Motif
ADSC	Adipose-Derived Stem Cell
AF	Alexa Fluor
AFSC	Amniotic Fluid Stem Cell
ALP	Alkaline Phosphatase
A/S	Alcian Blue / Sirius Red
ANOVA	Analysis Of Variances
ASC	Adult Stem Cell
BMP	Bone Morphogenic Protein
BMSC	Bone Marrow Stromal Cell
CAD	Computer-Aided Design
CAM	Cell Adhesion Molecule
CDSC	Cartilage-Derived Stem Cell
CFE	Colony forming efficiency
CFU-F	Colony-Forming Unit-Fibroblast
CHAD	Chondroadherin
CILP	Cartilage Intermediate Layer Protein
COL2	Type II Collagen
COL2A1	Type II Collagen (α_1)
COL10A1	Type X Collagen (α_1)
COMP	Cartilage Oligomeric Protein

CS	Chondroitin Sulphate
CSA	Chondroitin 4-Sulphate Augmented
CTG	Cell Tracker Green
CTO	Cell Tracker Orange
CV	Coefficient of variation
Cy3/Cy5	Cyanine 3/Cyanine 5
DAPI	4',6-Diamidino-2-Phenylindole, Dihydrochloride
DIC	Differential Interference Contrast
DMV	Droplet Morphometry and Velocimetry
DN	Double Network
(c)DNA	(Complementary) Deoxyribonucleic acid
ECM	Extracellular Matrix
ESC	Embryonic Stem Cell
EthD-1	Ethidium homodimer-1
FACIT	Fibril-Associated Collagens with Interrupted Triple helices
FACS	Fluorescence Activated Cell Sorting
FAM	5-carboxyfluorescein
FCM	Flow Cytometry
FF	Flow-focussing
FGF	Fibroblast Growth Factor
FITC	Fluorescein Isothiocyanate
FLM	Fluorescence Light Microscopy
Frz	Frizzled receptor
GADPH	Glyceraldehyde 3-Phosphate Dehydrogenase
GAG	Glycosaminoglycan
GF	Growth Factor

GFP	Green fluorescent protein
HA	Hyaluronic Acid
HAC	Human Articular Chondrocyte
HBMSC	Human Bone Marrow Stromal Cell
H&E	Haematoxylin and Eosin
HIER	Heat-Induced Epitope Retrieval
HFE	Hydrofluoroether
HFPSC	Hoffa's Fat Pad-Derived Stromal cells
HNC	Human Nasal Chondrocyte
HPDSC	Human Periosteum-Derived Stem Cells
HPLC	High Performance Liquid Chromatography
ICAM	Intercellular Adhesion Molecule
IGF-1	Insulin-like Growth Factor 1
IHC	Immunohistochemistry
Ihh	Indian hedgehog
iPSC	Induced Pluripotent Stem Cell
ISCT	International Society for Cellular Therapy
KS	Keratan Sulphate
LEF	Lymphoid Enhancer Factor
LIF	Leukaemia Inhibitory Factor
MACI	Matrix-induced Autologous Chondrocyte Implantation
MACS	Magnetic Activated Cell Sorting
MAT	Matrilin
MDSC	Muscle-Derived Stem Cell
mESC	Mouse Embryonic Stem Cell
MK	Mequaninone

List of Abbreviations

MMP	Matrix Metalloproteinase
mRNA	Messenger Ribonucleic Acid
NCAM	Neural Cell Adhesion Molecule
NF-κB	Nuclear Factor kappa-light-chain-enhancer of activated B cells
NICE	National Institute for Clinical Excellence
OA	Osteoarthritis
PBMSC	Peripheral Blood Mesenchymal Stem Cell
PCM	Pericellular Matrix
PDMS	Polydimethylsiloxane
PDMSC	Placenta-Derived Mesenchymal Stem Cell
PEG	Polyethylene glycol
PFO	1H,1H,2H,2H-Perfluorooctanol
PFPE	Perfluoropolyether
PFAS	Perfluoroalkyl Sulfonate
PG	Proteoglycan
PIER	Protease-Induced Epitope Retrieval
PJR	Partial Joint Replacement
PMMA	Poly(Methyl Methacrylate)
PRELP	Proline/Arginine-Rich End Leucine-Rich Protein
PS	Polystyrene
PTHrP	Parathyroid Hormone-related Protein
PVA	Polyvinyl Alcohol
RT-PCR	Real Time Polymerase Chain Reaction
RT-qPCR	Real Time Quantitative Polymerase Chain Reaction
RGD	Arginylglycilaspartic acid
SAW	Surface Acoustic Wave

SD	Standard Deviation
SDSC	Synovial-Derived Stem Cell
SEM	Standard Error of the Mean
Shh	Sonic hedgehog
SLRP	Small Leucine-Rich Protein
SNA	Spherical Nucleic Acid
SO	Safranin O
SOX	Sex Determining Region Y-Related High Mobility Group-Box
SSC	Skeletal Stem Cell
SSEA	Stage-Specific Embryonic Antigen
TAMRA	5-carboxytetramethylrhodamine
TCF	T Cell Factor
TCP	Tissue Culture Plastic
TE	Tissue Engineering
TGF-β	Transforming Growth Factor β
TJ	T-junction
TJR	Total Joint Replacement
TK1	Thymidine Kinase 1
TLM	Transmitted Light Microscopy
TRA	T-Receptor alpha locus Antigen
TRITC	Tetramethylrhodamine
UCSC	Umbilical Cord-Derived Stem Cell
VEGF	Vascular Endothelial Growth Factor
WJSC	Wharton's Jelly Stem Cell
Wnt	Wingless-related integration site

Chapter 1: Introduction

1.1 Project overview

Musculoskeletal disorders affect people worldwide. The estimated incidence lies between 20–33% representing people who experience pain derived from them. Particularly in the UK, it amounts to 29% of the total population; equivalent to about 18 million people (Briggs et al., 2016, (IHME), 2017, Vos et al., 2017). Among them and linked to cartilage deterioration is osteoarthritis (OA). This degenerative joint desease has emerged as one of the most concerning and prevalent medical conditions. It affects 9.6% of men and 18.0% of women aged above 60 years (Woolf and Pfleger, 2003), with approximately 13.6% prevalence in the UK (UK, 2013) compared to over 8.2% prevalence in the US (Litwic et al., 2013).

Cartilage is avascular and alymphatic and thus exhibits a limited ability for self-regeneration that makes restoring cartilage architecture and functionality a particular challenge. Invasive surgical techniques such as total joint replacement (TJR), mosaicplasty and autologous chondrocyte implantation (ACI) are receiving a lower endorsement in recent years in favour of cartilage tissue engineering-based approaches. As a consequence, an extensive set of cell, biomaterial ("scaffold") and biomolecule combinations constitute a marked rising trend in ongoing research (Hunziker, 2002, Bhosale and Richardson, 2008, Li et al., 2014, Smith and Grande, 2015).

Regarding the cell component of tissue engineering (TE), there exists a series of scaffold-free (i.e. cell-only) techniques developed for physiological-like 3D culture. They rely on cell self-assembly to replicate the early chondrogenic stage of condensation leading to cartilage growth. The three main stem cell sources investigated in the field, with varying degrees of potency, are: embryonic stem cells (ESCs), induced pluripotent stem cells (iPSCs) and adult stem cells (ASCs). The fact that the latter, if autologous, present the lowest risk of immunorejection and an absence of ethical considerations gives them an outstanding position as cells that are readily available avoiding major concerns regarding their application (Levenberg et al., 2009, Medvedev et al., 2010, Wang et al., 2016, Kim and Park, 2017).

The stem cell fraction in bone marrow stromal cells (BMSCs), also known as skeletal stem cells (SSCs), are a plausible cell source for multipotent generation of cartilage amongst the ASC family. Notwithstanding and just like any stem cell type, they pose a serious limitation regarding subpopulation heterogeneity that may have an impact on the quality of engineered cartilage. This explains the need to select from a pool of diverse cell types, even within the mononucleated subset, that present phenotypic variations linked to different musculoskeletal lineages (Bianco et al., 2001).

Isolation attempts have been tackled from a cell surface marker approach, with no predictive and definitive set of markers established to date. The absence of such surface markers for cartilage justifies contemplating a functional approach where a biological phenomenon such as cell condensation triggers the expression of a relevant marker that can be tracked and quantified. One promising candidate that initiates a key transition in phenotype is the master transcription factor SOX9. Unlike a prospective surface marker which would not usually require a biological trigger, a functional marker approach is more complex, in this case requiring a suitable maturation environment to identify the stem cell coupled with an analytical read-out. Added to this, the rarity of SSCs estimated at 1 in 100,000 BMSCs requires sufficient throughput to draw meaningful conclusions (Tew and Hardingham, 2006, Jiang et al., 2018). Microtitre plates fall short for high throughput cell screening approaches. The stem cell rarity example implies the need for a thousand 96-well microplates to identify a single stem cell-driven aggregate. Such costly, laborious and large footprint work stresses the need for more practical and higher throughput techniques for cell compartmentalisation.

Droplet microfluidics enables the high-throughput generation of small volume compartments. Droplets can be generated with volumes from a few femtolitres (and MHz generation frequencies) (Shim et al., 2013) to many nanolitres (Brouzes et al., 2009) offering a million fold dynamic range. Droplet volume is dictated by analytical target, from femtolitres for molecules and bacteria, and picolitres to nanolitres for single cells and nanolitres for accommodating multiple cells. Volume gains are balanced by reduced throughput, with multicellular aggregate environments being in the nanolitre range. Nevertheless and for illustration, droplets can be generated at frequencies of approximately 1 kHz, allowing the generation of over 3 million aggregate-containing droplets in one hour, offering the means to capture more than 30 stem cell containing aggregates. Larger analytical and potentially therapeutic campaigns can be achieved by device parallelisation and extended continuous operation.

Cell encapsulation and passive control operations like droplet splitting, merging, trapping, mixing and sorting have already been described for this purpose (Kintses et al., 2010). As opposed to other techniques that employ continuous flows, droplet microfluidics entails many advantages linked to surface-molecule interactions, cross-contamination, mixing and design opportunities. Surface-molecule interactions are suppressed as the dispersed phase contains all the reagents inside whilst it is the continuous phase that wets the microchannel walls. Individual sample encapsulation in the droplets prevents cross-contamination, which also enables a tight control over the analyte. Despite typical dominant laminar flows in microfluidics, mixing happens rapidly by chaotic advection and can be further accelerated by introducing windings in the channels (Tice et al., 2003). Simultaneously, and more importantly, the platform allows designing for specific kinetics or

reaction times (Niu and deMello, 2012). The fact that these microfluidic devices are able to work with such small volumes has two implications. Firstly, they consume smaller amounts of dynamically controlled reagents and secondly, they can perform as highly sensitive single-cell tailored platforms with biocompatible continuous phases and a potential for extension to culturing cell aggregates in individual droplet microenvironments (Joensson and Andersson Svahn, 2012).

This literature review covers various concepts linked with the project aim of applying a droplet-based microfluidic approach for short-term culture and sorting of HBMSC spheroids for cartilage tissue engineering. The rationale of sorting spheroids formed of HBMSCs with heterogeneous proneness towards cartilage generation reflected on various levels of SOX9 expression lies in predictive SOX9 upregulation upon aggregation down to a scale of tens of cells (Figure 1.1). Hyaline articular cartilage generation and repair necessitates achieving the correct interaction between biomolecules, cell source and environment. Having a clear view of the stages of cartilage development, the role of SOX9 and the composition of cartilage extracellular matrix brings all these elements together and allows to elucidate the structural and functional aspects to imitate. HBMSCs will be defined and evaluated as compatible cell sources with a record of use in the field, focussing on the use of 3D multicellular spheroids and cell sorting strategies with a particular focus on chondrogenesis. Lastly, the advantages of droplet microfluidics as a high-throughput technique for generation and functional assessment will be outlined, covering current advances in the use of HBMSC aggregates in microfluidics.

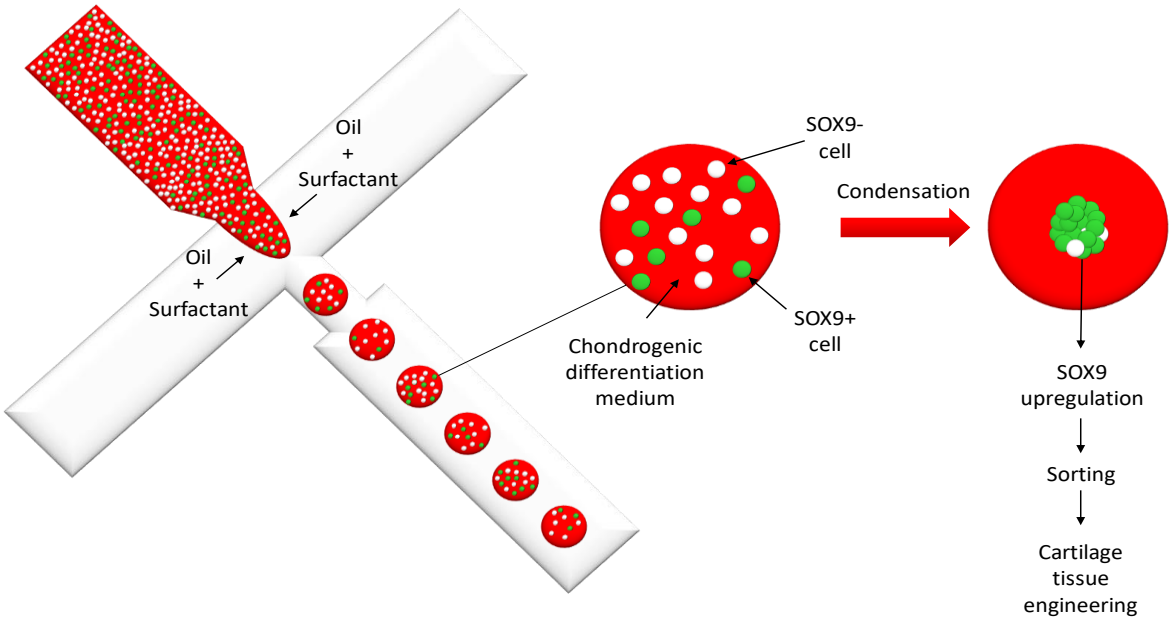

Figure 1.1 Schematic of the rationale of the application of droplet microfluidics for sorting of HBMSC chondroprogenitors for cartilage tissue engineering using SOX9 as a marker.

1.2 Articular cartilage composition and extracellular matrix

Cartilage is a tough but flexible, fibrous and elastic connective tissue with an abundant presence in the human body (e.g. ear, nose, larynx, trachea, ribs, intervertebral discs, joints). It is classified into three types that differ from each other in their extracellular matrix (ECM) composition and, in consequence, their mechanical properties (Temenoff and Mikos, 2000, Carey-Beth and Uhl, 2001, Bhosale and Richardson, 2008):

1. Elastic cartilage: it preserves the shape of the anatomical region that it belongs to and exhibits an ECM where elastin fibres are the predominant component.

2. Fibrocartilage: located in association with tendons and ligaments and adjacent to bone, it displays the highest mechanical strength and load bearing performance due to an ECM that is richer in collagen fibres and their fibre arrangement.

3. Hyaline cartilage: it has an ECM with a moderate amount of type II collagen and chondroitin sulphate. It excels at shock absorption by load distribution; compressive strength through a system of fluid absorption and exudation; and wear resistance by providing a low-friction surface. The hyaline cartilage that is located on joint surfaces is known as articular cartilage.

A key challenge facing articular cartilage tissue engineering is reproducing the correct mechanical function. Cartilage mechanics arise from the balance and interaction of the components of the ECM: (i) the structure and distribution of proteoglycans (PGs, mostly aggrecan) responsible for compressive strength; (ii) type II collagen orientation, i.e. Benninghoff arcade-like structure; lying horizontally and offering wear resistance in the superficial layer and perpendicular to the surface in the transitional and radial zones for tensile strength (Temenoff and Mikos, 2000).

Chondrocytes are the main cell type inhabiting cartilage tissue. These cells are arranged in a low-density profile (constituting 3-10% of the total volume in cartilage) within lacunar enclosed compartments. Chondrocytes play a role in forming, maintaining and repairing cartilage ECM via protein synthesis (e.g. type II collagen, PGs, non-collagenous proteins, matrix-degrading enzymes) (Carey-Beth and Uhl, 2001, Han et al., 2011). In this way, chondrocytes become isolated within their own individual microenvironment which they can modify and respond to, under the influence of mechanical, biochemical and electrical stimuli (Fox et al., 2009). A series of additional characteristics define chondrocytes: no cell-to-cell contact requirement; low cell density in cartilage responsible for an overall low metabolic activity despite a remarkably high individual activity and suitable survivability in hypoxic conditions (Bhosale and Richardson, 2008). A tissue that displays low cell density requirements would suggest that a cartilage environment could be straightforward to engineer. However, cartilage develops from high-density cellular condensations that grow either

interstitially or appositionally (see section 1.3). Common cartilage tissue engineering approaches like static pellet and micromass cultures pay particular attention to the condensation stage during chondrogenesis. They neglect nonetheless the biochemical and biomechanical inputs that stimulate sustained cartilage generation in a three-dimensional scaffold (Mahmoudifar and Doran, 2012).

1.2.1 Extracellular matrix components

The components of cartilage ECM are classified into collagens (60% of dry weight, Figure 1.2), PGs (between 5-10% of dry weight) and non-collagenous proteins. Type II collagen is the most abundant (about 80% of total collagen) and characteristic collagen isoform in cartilage, constituting a specific chondrogenic marker by itself. Type II collagen lies horizontally and offers wear resistance in the superficial layer of articular cartilage and is oriented perpendicular to the surface in the transitional and radial zones for tensile strength (Temenoff and Mikos, 2000, He et al., 2019). It forms fibrous mechanically resistive networks as well as types I, III, V and XI (Gelse et al., 2003, Ross and Pawlina, 2006, Wu et al., 2010). The latter along with type IX collagen represent another significant proportion (15%) (He and Karsdal, 2016), the remaining collagen types being less frequent (up to 5%). Types IX, XII and XIV collagen are grouped into the FACIT (Fibril-Associated Collagens with Interrupted Triple-helices) denomination and have been suggested to act as molecular bridges and matrix stabilisers (Shaw and Olsen, 1991, Chiquet et al., 2014, Chen et al., 2015b). Types VIII and X are known as short chain collagens (Shen, 2005, Knuth et al., 2019), type IV can be located as a part of the basement membrane (Gilbert and Blain, 2018); and the other collagen isoforms are types VI (Cescon et al., 2015), VII and XIII (Siebuhr and Karsdal, 2016) (Figure 1.2) (Van der Kraan et al., 2002, Ricard-Blum, 2011, Demoor et al., 2014, Gao et al., 2014).

Aggrecan is a key PG molecule. It is a chondrogenic marker that is often paired with type II collagen in chondrogenic differentiation experiments to assay the ability of chondrocytes to synthesise hyaline cartilage-like ECM proteins. The specific structure of aggrecan comprises a core protein that is covalently attached to numerous chondroitin sulphate (CS) and keratan sulphate (KS) glycosaminoglycan (GAG) side chains. Aggrecan binds to non-sulphated hyaluronic acid (HA) GAG via link proteins to form large PG aggregates. As a result of these interactions, aggrecan acquires a high polarity given by their negatively charged state that attracts cations (e.g. Na^+) and subsequently water due to osmotic pressures. This phenomenon explains cartilage compression strength upon an external loading balance through exuded fluid by overcoming osmotic pressures and reabsorbing fluid as the stresses recede (i.e. viscoelasticity). It remains a unique feature that neocartilage must secure for a complete functionality and collagen network integrity (Carey-Beth and Uhl, 2001, Bhosale and Richardson, 2008, Fox et al., 2009, García-Carvajal et al., 2013).

Non-collagenous proteins take an active part in cartilage maintenance. Integrins are an excellent example of such owing to their transmembrane receptor nature. It enables the mediation between chondrocytes and the environment surrounding them, whether other chondrocytes or the ECM. In particular, their binding to ECM molecules dictates mechanical and chemical signalling transduction accompanied by cytoskeleton-aided interactions and synergistic actions with other growth factor receptors. Integrins additionally deliver information about the chemical composition and mechanical status of the ECM via signal transduction into the cell. Cells can then respond by modulating their cell cycle, their shape and their migration patterns. A third of the integrins have been discovered to bind the Arg-Gly-Asp (arginylglycylaspartic acid, RGD) motif of some ECM proteins like fibronectin. RGD motifs constitute attachment sites for integrin-mediated cell adhesion and spreading (Barczyk et al., 2010, García-Carvajal et al., 2013). Among the various other binding alternatives available for integrins are collagen Gly-Phe-Hyp-Gly-Glu-Arg or GFOGER sequence, Leu-Asp-Val or LDV sequence present in ICAMs (intercellular adhesion molecules), laminin ligands and basement membrane-specific ligands for heparin sulphate attachment to collagen XVIII (endostatin) and perlecan (endorepellin) (Van der Kraan et al., 2002, Fox et al., 2009, Barczyk et al., 2010, Gao et al., 2014). Other non-collagenous proteins like elastin, the secondary constituent of cartilage fibrils and microfibrils, serve as a biomechanical support to assist in load bearing tasks, maintaining cartilage elasticity and stability by providing flexibility and resilience (He et al., 2013, Royce and Steinmann, 2003).

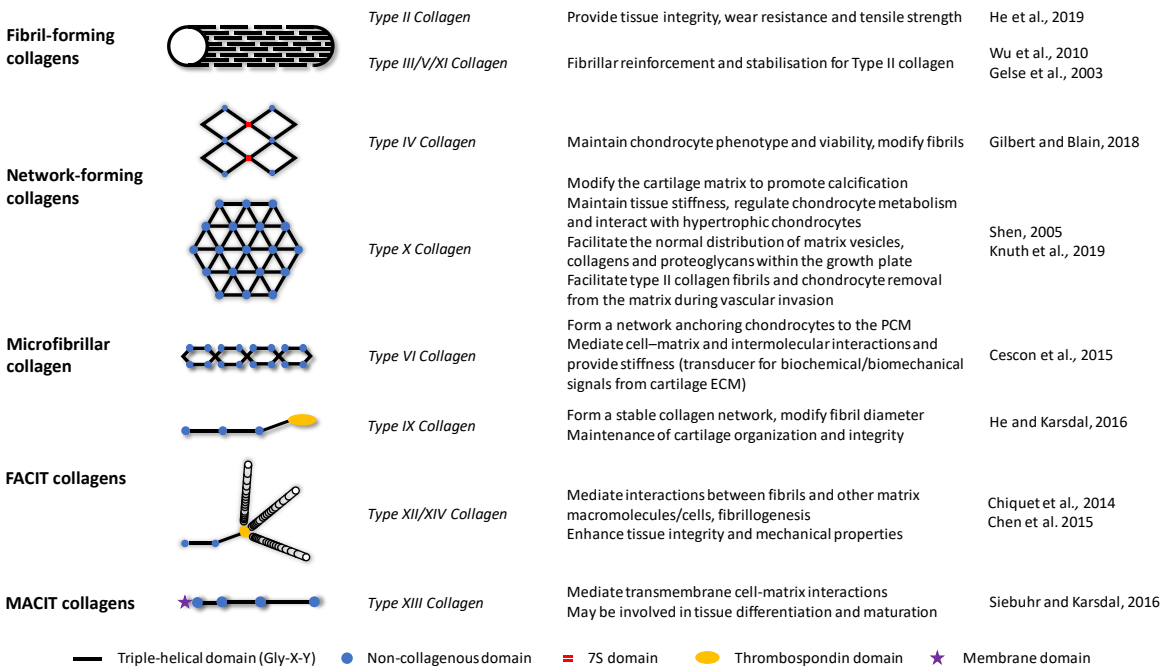

Figure 1.2 Supramolecular assemblies of the different collagen types grouped by geometrical arrangement with their specific roles and references describing them. Modified from Ross and Pawlina (2006), Ricard-Blum (2011), Luo et al. (2017).

Various families of ECM molecules are involved in securing collagen network interconnectivity: matrilins (e.g. MAT1 and MAT3); cartilage oligomeric proteins (COMPs); small leucine-rich proteins (SLRPs) and chondroadherin (CHAD). Matrilins are adaptor proteins associated with PGs and collagen fibres. SRLPs like decorin, biglycan, fibromodulin and asporin are PGs with a common TGF-β bonding characteristic along with COMPs that have been suggested to prompt collagen fibrinogenesis. Other molecules in the SRLP family, the proline/arginine-rich end leucine-rich repeat proteins (PRELPs), mediate type II collagen binding in the cartilage extracellular matrix. CHAD molecules perform as signal transduction enhancers via bonding to chondrocyte cell surface receptors (Seibel et al., 2006, Han et al., 2011, García-Carvajal et al., 2013, Batista et al., 2014).

Cartilage ECM macromolecules degrade over time, which demands a matrix remodelling balance. A normal correct turnover rate is highly dependent on chondrocyte sensitivity to modifications in macromolecular composition or matrix arrangement and the effectivity to enact a successive response directed to replace deteriorated ECM components. This requires a solid chondrocyte-ECM communication that enables chondrocytes to receive instructions in terms of biochemical, electrical and mechanical stimuli (García-Carvajal et al., 2013). Cartilage ECM remodelling is achieved by means of two classes of protease enzymes: matrix metalloproteinases (MMPs) and a disintegrin and metalloproteinase with thrombospondin motif (ADAMTS). For instance, MMP1 and MMP2 are upregulated during early chondrogenesis to reduce protein content of matrix and MMP13 degrades collagen type II in late-stage chondrogenesis. ADAMTS regulate collagen fibril assembly as well as cleavage of PGs (e.g. aggrecan) (Mahmoudifar and Doran, 2012).

1.2.2 Extracellular regions of the cartilage matrix

Cartilage extracellular matrix is divided into three distinct regions where composition and arrangement collagen fibre characteristics vary as a function of the distance from chondrocytes (Figure 1.3). These regions are classified as pericellular, territorial and interterritorial.

The pericellular region (also known as pericellular matrix or PCM) is distributed forming a 2 µm layer around the chondrocyte and is mainly composed of PGs (e.g. aggrecan), GAGs (e.g. HA), glycoproteins (e.g. fibulin) and non-collagenous proteins (e.g. integrins) that respond to external loading by triggering signal transduction via numerous integrin membrane receptors (e.g. CD44, PRELP, CHAD, syndecan, discoidin). Type II, XI and XIII are the most abundant collagens in this region.

The territorial zone surrounds the pericellular matrix. It consists of a thick basket-like network of collagen fibres with a preferential orientation that have been indicated to contribute mechanically to load bearing and energy dissipation.

The interterritorial region is the largest area responsible for cartilage biomechanical properties with randomly oriented large collagen fibrils. The fibrils lie parallel to the surface of the superficial zone, radially in the middle zone and perpendicular to the surface in the deep zone in cartilage. PGs (e.g. decorin, asporin, fibromodulin and a very large concentration of aggrecan) are significantly present in the interterritorial matrix accompanied by matrilin and COMP proteins and glycoproteins like CILP (cartilage intermediate layer protein) (Royce and Steinmann, 2003, Fox et al., 2009, García-Carvajal et al., 2013, Demoor et al., 2014).

Figure 1.3 shows an overview of the articular cartilage ECM regions, which highlights the challenge that reproducing the sophisticated network native to articular cartilage entails. A microenvironment is needed where chondrocytes can synthesise all these molecules and receive exposure to growth factors in a homogeneous manner in order to ensure tissue homeostasis. This prompts stem cell-based cartilage tissue engineering to focus on devising the appropriate strategy to isolate and harness the cells most able to accomplish such robust articular cartilage generation among the entire original mixed population.

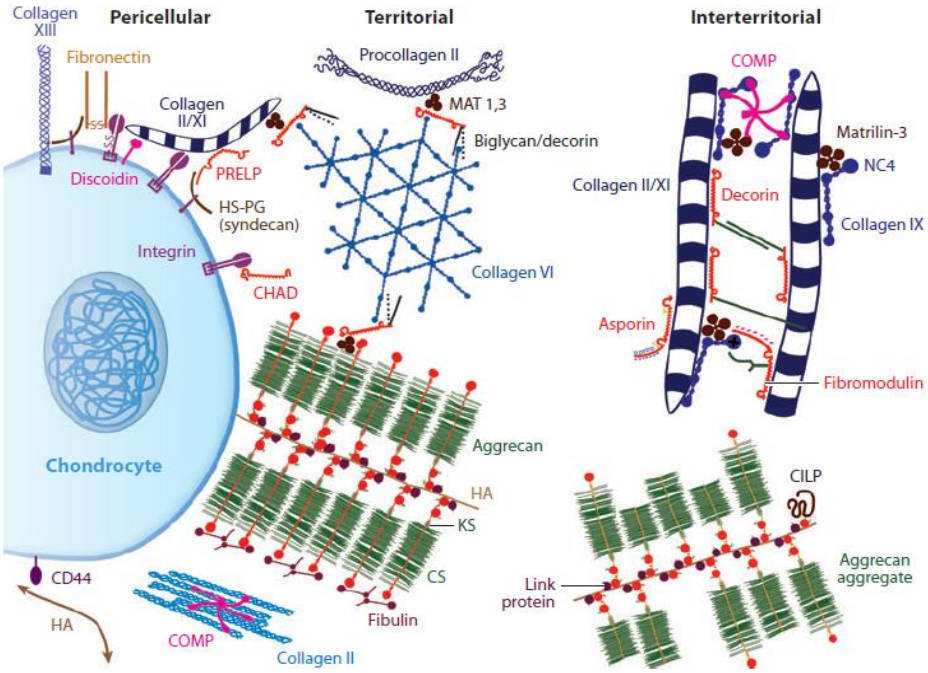

Figure 1.3 Articular cartilage matrix distributed in the different ECM regions. Adapted from Royce and Steinmann (2003).

1.3 Cartilage development and chondrogenesis

Cartilage development through chondrogenesis during endochondral ossification is crucial as an initial cellular-based phenomenon resulting in skeletogenesis in all vertebrates. The stages of endochondral ossification are described below: mesenchymal cell condensation, chondroprogenitor generation and chondrogenesis, terminal differentiation of chondrocytes and ossification (Figure 1.4) (DeLise et al., 2000, Chen et al., 2009).

1.3.1 Condensation

Cartilage formation commences with the occurrence of a pre-cartilage condensation stage where mesenchymal cells migrate from the mesenchyme in the mesoderm and accumulate in the centre of the limb bud due to alterations in the mitotic process that prevent them from dispersing. It is mediated by two main cell adhesion molecules: neural cadherin (N-cadherin) and neural cell adhesion molecules (NCAM) (DeLise et al., 2000, Wang et al., 2014). Pre-chondrocytes at this stage appear as aggregated, which facilitates cell adhesion stemming from strong cell-cell interactions; the synthesis and release of GAGs and growth factors (GFs, see section 1.3.5.3); and the expression of extracellular components such as type I and type IIA collagen and specific cartilage transcription factors SOX9, L-SOX5 and SOX6, which are known as the SOX trio (Figure 1.4) (Demoor et al., 2014). Of these transcription factors, SOX9 is a master regulator for chondrogenesis and the subsequent expression of L-SOX5 and SOX6 enhancers (Akiyama et al., 2002, Liu and Lefebvre, 2015).

1.3.2 Chondrogenic differentiation

The transition into chondrogenesis is dependent on the collaborative interaction of stimuli of a similar nature to those controlling the synthesis of biomolecules by chondrocytes: transcription factors, signalling pathways, metabolites and mechanical stresses, for instance (Chen et al., 2009). Despite having identified some of the agents involved, the exact sequence of molecular events behind chondrogenesis is yet to be determined. The two mechanisms behind chondrogenesis distinguish between inner (interstitial) and superficial (appositional) cartilage growth. Interstitial growth chondrogenesis is characterised by clusters of chondroblasts arranged in lacunae that undergo mitotic division without entering the surrounding extracellular matrix. Subsequently, they differentiate into chondrocytes that are gathered in the so-termed isogenous groups with extracellular matrix around them. Appositional growth stems from a membrane that has an embryonic origin and covers the cartilaginous template: the perichondrium. Following the activation of the gene encoding *SOX9*, the inner cells of that perichondrial chondrogenic layer differentiate into chondroblasts, as opposed to outer cells that advance towards fibroblastic differentiation. Next, chondroblasts, which have preserved their multipotency, further differentiate to become chondrocytes that deposit layers distributed on top of each other (Lawrence et al., 2012, Kierszenbaum and Tres, 2015).

From chondrogenesis to differentiation stage, pre-chondrocytes are gradually converted into mature chondrocytes. The latter possess a greater ability to secrete a more intricate ECM containing a higher proportion of PGs and collagen fibres with a tighter degree of interconnection

compared to the ECM elaborated in early mesenchymal condensation. The synthesis of type II collagen is a distinctive marker for the detection of this differentiation stage (Demoor et al., 2014).

1.3.3 Terminal differentiation and ossification

Lastly, the chondrocytes surrounding the centre of the condensation zone undergo faster proliferation and growth as they progress towards hypertrophy, preceded by a pre-hypertrophic state. Type X collagen then becomes the predominant form that indicates cartilage mineralisation owing to its roles as calcium deposition facilitator within the ECM. An interface appears between cartilage and the ossifying zone, where alkaline phosphatase (ALP), an enzyme that accelerates the creation of bone-like hydroxyapatite crystals from calcium deposits, is expressed in conjunction with vascular endothelial growth factor (VEGF). VEGF is responsible for angiogenesis, the formation of new blood vessels and the extracellular matrix is eventually replaced with osteoclasts and osteoblasts. These occupy vacant spaces left by apoptotic chondrocytes and complete matrix remodelling with the enhanced expression of type I collagen and bone growth factors (Demoor et al., 2014). Anatomically, the tidemark physically separates articular cartilage from calcified cartilage and stabilises the non-mineralised articular cartilage situated above that barrier against hypertrophy and calcification. It delimits a smooth mechanical transition towards subchondral bone, a tissue that is less compliant and resilient, and lowers the risk of fracture caused by crack propagation between two mismatched surfaces (Temenoff and Mikos, 2000, Bhosale and Richardson, 2008, Han et al., 2011, Hoemann et al., 2012, Jayasuriya et al., 2016).

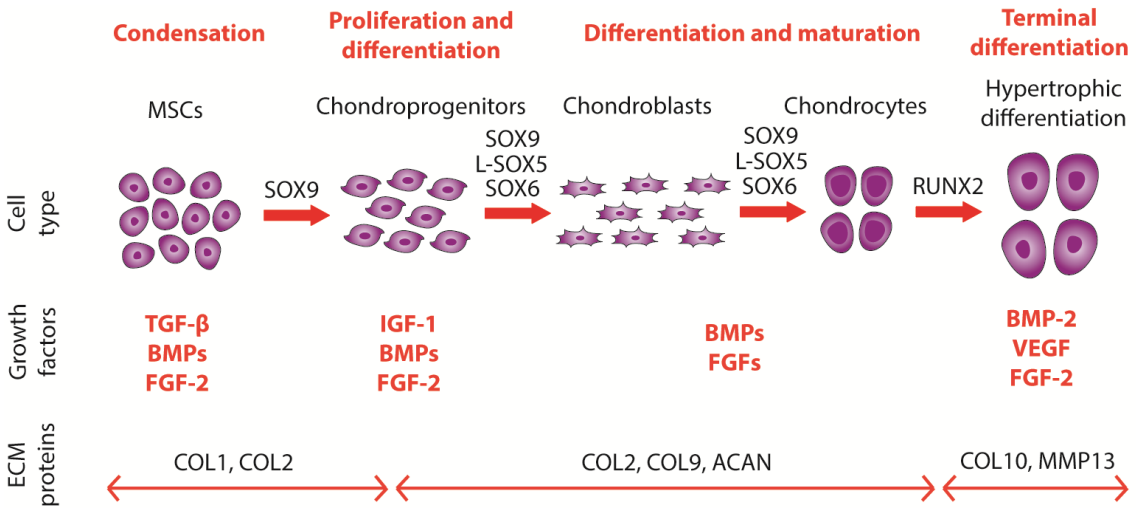

Figure 1.4 Developmental stages of chondrogenesis and sequence of cell types, growth factors (FGF for fibroblast growth factor and IGF for insulin-like growth factor) and ECM proteins involved. Adapted from Akiyama et al. (2002), Ikeda et al., (2005), Kelc et al. (2013).

In addition, chondrocyte-to-osteoblast transdifferentiation has recently emerged as a part of the endochondral ossification process through three different models proposed for chondrocyte-to-osteoblast transdifferentiation (Aghajanian and Mohan, 2018).

1. Chondrocyte to osteogenic precursor: immature chondrocytes differentiate into a transient osteogenic precursor population, which then differentiates into pre-osteoblasts and, ultimately, osteoblasts.

2. Dedifferentiation to redifferentiation: hypertrophic chondrocytes first dedifferentiate into immature chondrocytes, which then directly differentiate into osteoblasts.

3. Direct transdifferentiation: of hypertrophic chondrocytes into osteoblasts.

1.3.4 Articular cartilage morphogenesis

Articular cartilage is distributed across the surface of the bones that constitute synovial joints. Its development is marked by the morphogenesis of the joint and responds to a sequence of two major events. The process starts with a joint determination step, in which the location of the joint is established and articular progenitor cells originating from mesenchymal cells become highly condensed at the joint site and form an interzone. Articular progenitor cells then differentiate into articular chondrocytes at the interzone triggering the second step called joint morphogenesis and leading to the stratified structure of the synovial joint. Chondrocytes eventually arrange in three zones characterised by a distinct morphology and type II collagen fibril orientation. The superficial or tangential zone is composed of small and flat chondrocytes with collagen fibrils aligned to the surface. Chondrocytes acquire a round shape in the thickest intermediate or transitional zone where collagen fibres are distributed at an angle from the surface. The deepest zone is the basal or radial zone, which comprises round-shaped chondrocytes and collagen fibres with a perpendicular orientation relative to the surface. Such varying collagen orientation in zones provides articular cartilage with two unique and pivotal mechanical properties: wear resistance in the superficial layer and tensile strength along the transitional and radial zones (Gadjanski et al., 2012, Decker et al., 2014).

1.3.5 The role of transcription factors, growth factors and signalling pathways in cartilage development

Cartilage development and chondrogenesis are largely driven by the compound effect of transcription factors, growth factors and signalling pathways. Transcription factors and growth factors differ in that the former mainly regulate gene expression at the DNA (deoxyribonucleic acid)

level and the latter induce cellular responses (e.g. migration, proliferation, differentiation, apoptosis) as they bind to cell membrane receptors as well as cell-to-cell communication-derived interactions. Whilst transcription factors have one or multiple DNA binding domains that can attach to specific sequences of the gene that they regulate either directly or indirectly through a nearby sequence, growth factors bind to other cellular molecules. (Schwab, 2008, Hughes, 2011, Zaret and Carroll, 2011, Kelc et al., 2013). Signalling pathways exert influence on both transcription and growth factors, altering gene expression patterns and cellular responses alike. These biochemical signals are of the essence for cells to tailor their metabolic activities to respond to their needs as individual cells and as part of a tissue. The factors mediating signal delivery can be cytokines, growth factors, hormones, morphogens. Wingless-related integration site (Wnt), Indian hedgehog (Ihh) and Sonic hedgehog (Shh) are three morphogen proteins that participate actively in cartilage chondrogenesis (Gao et al., 2014, Matta and Mobasheri, 2014).

1.3.5.1 Transcription factors

1.3.5.1.1 SOX9

SOX9 is a pivotal transcription factor for chondrogenic differentiation. Its expression at the beginning of cartilage development takes place at the early mesenchymal condensation stage. Afterwards, it inhibits premature hypertrophy ending in bone formation. SOX9 is upregulated during certain chondrogenesis stages. For instance, Shh first encourages SOX9 expression along with BMPs to produce more chondrogenic precursors whilst Ihh acts later for chondrocyte proliferation and maturation activating multiple genes for ECM molecules (e.g. *COL2A1* for type II collagen, *COL9A1* for type IX collagen, *ACAN* for aggrecan). Alternatively, Wnt signalling pathway can either upregulate SOX9 at the condensation stage or downregulate it to restrain chondrocyte maturation before hypertrophy begins as SOX9 silences the expression of *COL10A1* gene for type X collagen. SOX9 downregulation upon hypertrophy causes cartilage matrix to be substituted by bone, including the bone marrow perfused with blood vessels (Akiyama et al., 2002, Jo et al., 2014).

1.3.5.1.2 RUNX2

As described above, RUNX2 expression symbolises the last stage of chondrogenic differentiation and the transition towards ossification due to its constant presence since the onset of hypertrophy and throughout the entire hypertrophic differentiation. RUNX2 is a transcriptional factor that activates typical hypertrophic markers such as COL10A1. It propels excess Ihh production that attenuates PTHrP proliferation-inducing ability and its efficiency to delay hypertrophy. Wnt canonical pathway upregulates RUNX2 expression through β-catenin nuclear binding to lymphoid enhancer factor (LEF) and T cell factor (TCF) proteins, forming the RUNX2-expression enhancer

LEF/TCF/β-catenin complex. In contrast, Wnt non-canonical pathway combined with PTHrP and Shh signalling can make a significant contribution to RUNX2 downregulation for hypertrophy detention (Mackie et al., 2008, Mahmoudifar and Doran, 2012, Chen et al., 2015a).

1.3.5.2 Signalling molecules

1.3.5.2.1 Wnt

Wnt signalling can be associated with transcriptional co-activator β-catenin that modulates gene expression in a signalling pathway named 'canonical'. This pathway is triggered when Wnt molecules bind to their Frizzled (Frz) receptors and lipoprotein receptor-related protein (LRP) co-receptors LRP5 or LRP6 and can be counteracted by the 'non-canonical' calcium-dependent kinase C-mediated pathway in which Wnt bind Frz alone and β-catenin is degraded (Mackie et al., 2008, Bianco and Robey, 2015, Chen et al., 2015a).

1.3.5.2.2 Ihh

Ihh is another secreted factor whose signalling pathway in pre-hypertrophic chondrocytes induces parathyroid hormone-related protein (PTHrP) expression. Both proteins are the principal pair of agents regulating chondrocyte maturation and hypertrophy in a negative feedback loop where PTHrP responds by nullifying hypertrophic differentiation. Their synergistic impact fosters chondrocyte proliferation and impedes hypertrophy of any additional chondrocytes, linked to Nkx3.2 homeobox protein upregulation and downregulated transcription factor RUNX2 expression (DeLise et al., 2000, Mackie et al., 2008, Mahmoudifar and Doran, 2012, Chen et al., 2015a).

1.3.5.2.3 Shh

Lastly, Shh signalling upregulates Nkx3.2 and SOX9 expression, so supporting chondrogenesis over hypertrophy (Mahmoudifar and Doran, 2012, Demoor et al., 2014, Chen et al., 2015a). Signalling pathways vastly dictate the equilibrium between chondrogenesis and hypertrophy. Wnt canonical pathway promotes hypertrophy and osteogenesis. In contrast, the cartilage inducer non-canonical Wnt pathway and Shh signalling control hypertrophy progression jointly with Ihh and PTHrP (DeLise et al., 2000, Mackie et al., 2008, Mahmoudifar and Doran, 2012, Demoor et al., 2014, Bianco and Robey, 2015, Chen et al., 2015a).

1.3.5.3 Growth factors

Growth factors (GFs) are essential to regulate cartilage development, maintenance and repair. Chondrogenic differentiation GFs are usually added to enhance cartilage generation and have proved decisive to tailor cell behaviour in TE approaches both during the initial stages of

differentiation and for long-term growth maintenance of the engineered construct. Transforming growth factor-β (TGF-β) family members are the most representative example of a set of soluble proteins that stimulate chondrogenesis by prompting cartilaginous ECM production by BMSCs and the synthetic activity of chondrocytes. Bone morphogenetic proteins (BMPs) influence the entire chondrogenic differentiation process in BMSCs. IGF-1 (insulin-like growth factor 1) is the main growth factor involved in homeostatic synthesis and degradation of PGs. It can play a role in cartilage-like ECM formation in BMSCs and chondrocytes, with likely synergistic interactions occurring when added along with the aforementioned growth factors (Zhang et al., 2009a, Lam et al., 2015).

The TGF-β family (TGF-β1, TGF-β2 and TGF-β3) are also known to induce SOX9 expression mediated by Smad protein transductors within the cells and thus are positioned in favour of chondrogenic commitment. Smad 1/5/8 pathway activation enables the onset of hypertrophy, as opposed to Smad 2/3 (Oshimori and Fuchs, 2012, Demoor et al., 2014). Likewise, the growth factors in this family are believed to promote the synthesis of other adhesion proteins in the matrix (e.g. fibronectin, syndecan, decorin, tenascin, N-cadherin, NCAMs) (Boeuf and Richter, 2010), as well as upregulating the expression of aggrecan and collagen type II cartilage markers (Tuli et al., 2003, Mahmoudifar and Doran, 2012, Lee et al., 2015). Even if TGF- β1 and TGF- β3 have predominantly been added as a part of chondrogenic media in numerous studies, the latter seems to show a slightly quicker differentiation rate, which justifies why it is of major interest for current chondrogenic differentiation assays (Barry et al., 2001, Tare et al., 2005, Boeuf and Richter, 2010, Mueller et al., 2010). Boeuf and Richter also outlined the existing approach to chondrogenic differentiation using pellet culture of 200,000 to 500,000 BMSCs and adding TGF-β3 as a chondrogenic inducer. Cicione *et al*. (2015) compared a list of growth factors observing the most promising chondrogenic differentiation results with higher concentrations of TGF-β3 (Boeuf and Richter, 2010, Cicione et al., 2015).

Transcription factors, growth factors and signalling pathways do not execute their function in an isolated fashion within the cells. Cells secrete a series of molecules that construct the cell environment: the extracellular matrix. It delimits a physical space that mediates cell response to external stimuli and cell-to-cell communication for tissue development via cell surface receptors and adhesion molecules (e.g. integrins, cadherins, cell adhesion molecules or CAMs). The objective of recapitulating the microenvironment and stem cell niche for a certain cell source to differentiate into cartilage can benefit from techniques for high-throughput screening and characterisation. Likewise, it has to consider the distribution and interplay between the components of native cartilage ECM to attain a faithful imitation of the structure of native ECM that brings recreating functionality a step closer (Kim et al., 2011b).

1.4 Cartilage repair and regeneration

Articular cartilage is the target for regeneration in this research work. Despite its unique mechanical properties, articular cartilage can undergo deterioration and injury in joints. Constant exposure to cyclic loading or sudden extreme shocks, among other factors (i.e. diet, physical condition and activity, genetics) are thought to play a role. Additionally, and as aforementioned, articular cartilage lacks the self-repair ability of other vascular, neural and lymphatic tissues such as bone, and can become injured according to three distinct patterns. Matrix disruption is the lowest-impact condition in which the cartilage ECM is damaged in a reversible manner and can be restored. Partial thickness defects are more severe, and the damage affects the cartilage surface without reaching the subchondral bone. The damaged tissue cannot trigger a spontaneous self-repair response at that instance. In full thickness defects, the injury extends through to the underlying subchondral bone and a wound healing mechanism produces a soft fibrocartilaginous callous that is likely to degrade, thus failing to repair the tissue (Temenoff and Mikos, 2000).

1.4.1 Osteoarthritis: current therapies and limitations

Of all the conditions affecting articular cartilage and joints, osteoarthritis (OA) is the most common disorder, especially among elderly people. OA is a debilitating disorder that causes pain, stiffness and disability (Arden and Nevitt, 2006, Glyn-Jones et al., 2015). The stages of OA progression involve biomechanical and biomolecular changes in the entire joint. These include proteolytic degradation of cartilage ECM; subchondral bone remodelling; loss of articular cartilage; growth of bone spurs (also known as osteophytes), synovial and joint capsule inflammation; damage to ligaments, periarticular muscles and menisci (Madry et al., 2012, Man and Mologhianu, 2014).

In a context where OA aetiology is unclear, risk factors (i.e. epidemiology) are the preferred method to address the pathogenesis of the disease. These can be intrinsic factors such as gender, age and genetics that act in favour of increasing the susceptibility of an individual to undergo joint damage and to develop OA. They can interact with other biomechanical external factors related to physical activity, condition or surgical and injury history (Arden and Nevitt, 2006). OA is usually treated by pain relief in early stages through medication (e.g. paracetamol, anti-inflammatory drugs, opioids for severe pain, steroid injections) and supportive treatments (e.g. electric nerve stimulation, physical therapy, assistive devices), although it often culminates in joint replacement in end-stage when these non-surgical methods fail (Gillam et al., 2013).

Total joint replacement (TJR) is the most frequent surgical intervention on people suffering from OA. During the surgery, an artificial prosthesis attempting to replace the native joint (in many cases either hip or knee) is placed to restore the anatomical function of the joint (Zachwieja et al., 2017).

A variety of materials and combinations are available, with ceramic on ceramic (e.g. alumina, zirconia and composites) and ceramic on polymer (e.g. polyethylene-based) being widely used in the clinic (Merola and Affatato, 2019). The procedure may require revision surgery before less than 5 years in the case of implant failure and after 10 to 15 years in patients with a moderate physical activity (Bayliss et al., 2017, Beard et al., 2019). For that reason, partial joint replacement (PJR) offers a less invasive alternative for younger patients or those whose joint is only damaged in certain regions (e.g. femoral head in hips or any of the lateral, medial or patellofemoral compartments of the knee). Its enhanced functionality restoration and the simplicity nevertheless come at the expense of higher rates of revision surgery than TJR interventions (Smith et al., 2019).

The invasiveness and cost of TJR and PJR have encouraged clinicians to explore other minimally disruptive methods that could meet the needs of patients depending on their cartilage defects or the state of the joint. In that regard, bone marrow stimulation techniques (e.g. debridement, drilling, microfracture, spongialisation) pursue cartilage regeneration in full thickness chondral defects by inducing a disruption in the subchondral bone. In consequence, a fibrin clot forms on the surface of the defect and the migration of BMSCs to the site that differentiate into chondrocytes and provides some restoration. However, the fibrocartilage produced is mechanically inferior to articular cartilage and more vulnerable to failure in the short-term (Hunziker, 2002, Bhosale and Richardson, 2008, Glyn-Jones et al., 2015, Makris et al., 2015, Medvedeva et al., 2018). Another surgical strategy for patients with small defects is to concentrate on cartilage replacement via the use of tissue grafts. These implants can be autologous grafts or allogeneic grafts from other human beings that are suitable for larger defects but exhibit immunogenicity risks (Hunziker, 2002, Medvedeva et al., 2018). Unlike allografts, autologous grafts are transplanted from less bearing regions (periosteal, perichondrial, chondrospheres, mosaicplasty) and designed to fit the shape and mechanical loading of the implanted area. Autologous grafts have achieved reduced immunogenicity but with mixed levels of success due to stress shielding at the donor site (Temenoff and Mikos, 2000, Hunziker, 2002, Bhosale and Richardson, 2008, Medvedeva et al., 2018).

1.4.2 Cartilage tissue engineering approaches for regeneration and repair

A shift towards more regeneration-based approaches has become the current trend, offering routes that look into reducing surgical aggressiveness. The concept of tissue engineering coined by Langer in 1993 encompasses those interdisciplinary research lines that unite ‘principles of engineering and the life sciences to develop biological substitutes that restore, maintain, or improve tissue function’ (Langer and Vacanti, 1993, Vacanti and Langer, 1999).

Autologous Chondrocyte Implantation (ACI) is the most recognisable example of tissue engineering brought to the bedside. Peterson first described chondrocyte transplantation in a rabbit model in 1984 but it was not until ten years later that Brittberg reported ACI in humans. Brittberg harvested chondrocytes from a low-weight bearing site at the medial tibia by enzymatic digestion of a periosteal flap biopsy. Following expansion for 11-21 days, they injected the cell suspension into the defect area and sutured the periosteal flap over the lesion (Peterson, 1984, Brittberg et al., 1994).

The cartilage generation response to ACI may vary depending on the patient; either hyaline-like cartilage or rather competent fibrocartilage otherwise may form. Unlike mosaicplasty, ACI only requires a small biopsy from a donor site, which minimises the risk of damage to the donor site in the long-term. First-generation ACI encountered major hurdles in that it consisted in a costly two-step surgical procedure accompanied by *in vitro* cell culture, with long recovery times and the possibility of chondrocyte hypertrophy derived from the periosteal source. Newer generations have incorporated other options to circumvent some of those drawbacks. For instance, third-generation matrix-induced autologous chondrocyte implantation (MACI®, Genzyme Biosurgery, USA) arose from the development of second-generation artificial collagen-based matrices that mimic native cartilage structure to enhance chondrocyte phenotypic stability. Other commercial constructs based on hyaluronic acid, agarose-alginate, fibrin, fibrinogen and scaffold-free therapies continue to be object of trial (Huang et al., 2016).

Clinical debate has been active comparing ACI to the cheaper and simpler microfracture and mosaicplasty. Systematic reviews on randomised patient cohorts have pointed to better clinical outcomes in ACI patients despite lacking statistical significance and long-term follow-ups. Taking cost and clinical effectiveness into account, there is no gold standard as of yet. Microfracture and mosaicplasty would be preferred for small defects prior to case-by-case evaluation and ACI would generally be better suited for larger lesions (Vasiliadis et al., 2010, Mollon et al., 2013, Basad et al., 2015, Makris et al., 2015, Glyn-Jones et al., 2015, Erggelet and Vavken, 2016, Mistry et al., 2017, Medvedeva et al., 2018).

To date, ACI stands as an approved surgical intervention by the National Institute for Clinical Excellence (NICE) in the UK. It is funded by the National Health System (NHS) for the treatment of cartilage defects from 2017 but regulated by strict patient selection criteria. Fourth-generation ACI is still under investigation and envisions the association of some or all of the pillars in the paradigm of cartilage tissue engineering (Figure 1.5). Stem cells (i.e. ESCs, iPSCs and BMSCs) are deemed substitutes for autologous chondrocytes that can differentiate into chondrocytes and retain their phenotype as well as their proliferative capacity. Cells require stimulation from biomolecules like

growth factors and ECM proteins that promote stable chondrogenesis. Moreover, cells can be aided by a scaffold structure although post-implantation complications such as controllable *in vivo* biodegradation, immunological response and biocompatibility have opened the way for the advancement of 3D scaffold-free techniques. BMSCs are the most popular adult stem cell source used in tissue engineering. Its strengths and limitations are further reviewed in the following section (Daher et al., 2009, Mollon et al., 2013, Glyn-Jones et al., 2015, Huang et al., 2016, Goldberg et al., 2017, Medvedeva et al., 2018, Alblawi et al., 2020).

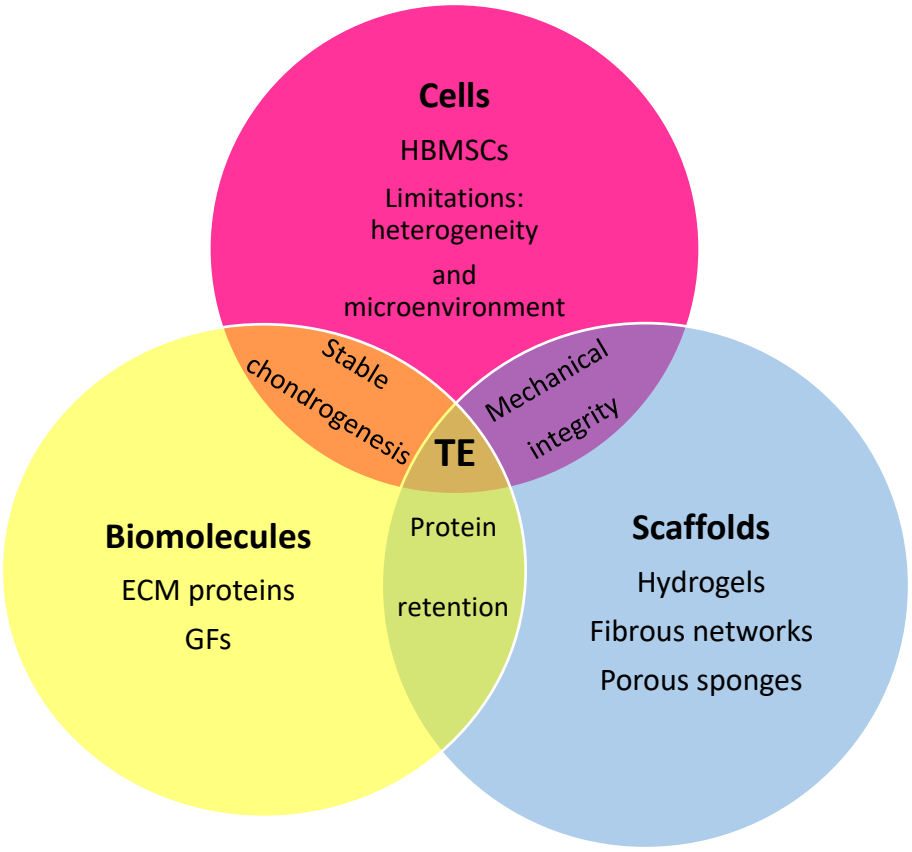

Figure 1.5 Paradigm of cartilage tissue engineering depicted as the interrelationship of three pillars: cell sources (e.g. HBMSCs), scaffolds (e.g. hydrogels, fibrous networks, porous sponges) and bioactive molecules (e.g. ECM proteins, GFs). Cells require the appropriate signals from biomolecules for stable chondrogenesis and scaffolds provide mechanical integrity to their microenvironment as well as protein retention. Daher et al. (2009), Smith and Grande, (2015).

1.5 Bone marrow stromal cells and their potential as cell source for cartilage tissue engineering

Native chondrocytes remain a primary cell source for cartilage tissue engineering as a central element in cartilage repair techniques and surgeries. Chondrocytes may seem the most natural choice, although some critical unresolved issues stand in the way. Examples of these are *in vitro* loss of phenotypic stability and proliferation ability involving de-differentiation upon passaging; downregulation of cartilage-specific extracellular components (e.g. type II and type IX collagen,

aggrecan) together with increased production of type I collagen and generation of mechanically inferior fibrocartilage (Schulze-Tanzil et al., 2004, Darling and Athanasiou, 2005, Otero et al., 2012, Medvedeva et al., 2018). Otherwise, chondrocytes possess the best cartilage-forming prospects even in the first passage with superior mechanical properties and cell viability (Farrell et al., 2014, Danišovič et al., 2016).

Parallel lines of research have also pursued other cell candidates, with stem cells dominating the scope of tissue engineering and regenerative medicine because of their greater maintained proliferative capacity and their ability to differentiate into any or multiple tissues in the human body depending on their potency. In this regard, embryonic stem cells (ESCs) and induced pluripotent stem cells (iPSCs) both fall under the pluripotent category of cells that can achieve indefinite *in vitro* expansion and differentiation into all tissues from the three germ layers: endoderm, mesoderm and ectoderm (Beane and Darling, 2012, Romito and Cobellis, 2016, Medvedeva et al., 2018).

Thomson et al. were the first to isolate from human blastocysts and described as pluripotent cells with specific markers such as stage-specific embryonic antigen 3 and 4 (SSEA-3 and SSEA-4) and the T-receptor alpha locus antigens TRA-1-60 and TRA-1-81 (Thomson et al., 1998, Levenberg et al., 2009, Beane and Darling, 2012). iPSCs were later derived from somatic cells through a cell reprogramming technique pioneered by Takahashi and Yamanaka and involving a cocktail of transcription factors (i.e. the so-called Yamanaka factors: OCT4, SOX2, KLF4 and C-MYC) (Takahashi and Yamanaka, 2006).

Adult stem cells (ASCs) are the last type of stem cells that can regenerate adult tissues. Their inferior multipotency implies a crucial and advantageous restriction on the range of specialised tissue that they can form once they differentiate. Consequently, they are divided into various subsets depending on the tissue source for harvesting; many of which are listed in Table 1.1. ASCs have a lower risk of immunorejection compared to pluripotent stem cells due to the absence of antigens driving lymphocyte activation in spite of their multipotency limitation. It opens at the same time a debate where ESCs, iPSCs and ASCs all have advantages and challenges linked to their application in the clinic (Figure 1.6) (Falanga, 2012, Romito and Cobellis, 2016, Jevons et al., 2018, Medvedeva et al., 2018, Gorecka et al., 2019).

BMSCs are primary cells located within the differentiated stromal system of the bone marrow that contain mixed populations of adult cells and a fraction of fibroblast-like non-hematopoietic stem cells known as skeletal stem cells (SSCs). BMSCs are defined by their multipotent ability to differentiate into tissues originated from the mesodermal germ layer (i.e. giving rise to bone,

cartilage, fat, muscle, tendon, myocardium, bone marrow stroma), accompanied by their potential ability for self-renewal (Bianco et al., 2006, Bianco et al., 2008, Bianco et al., 2013).

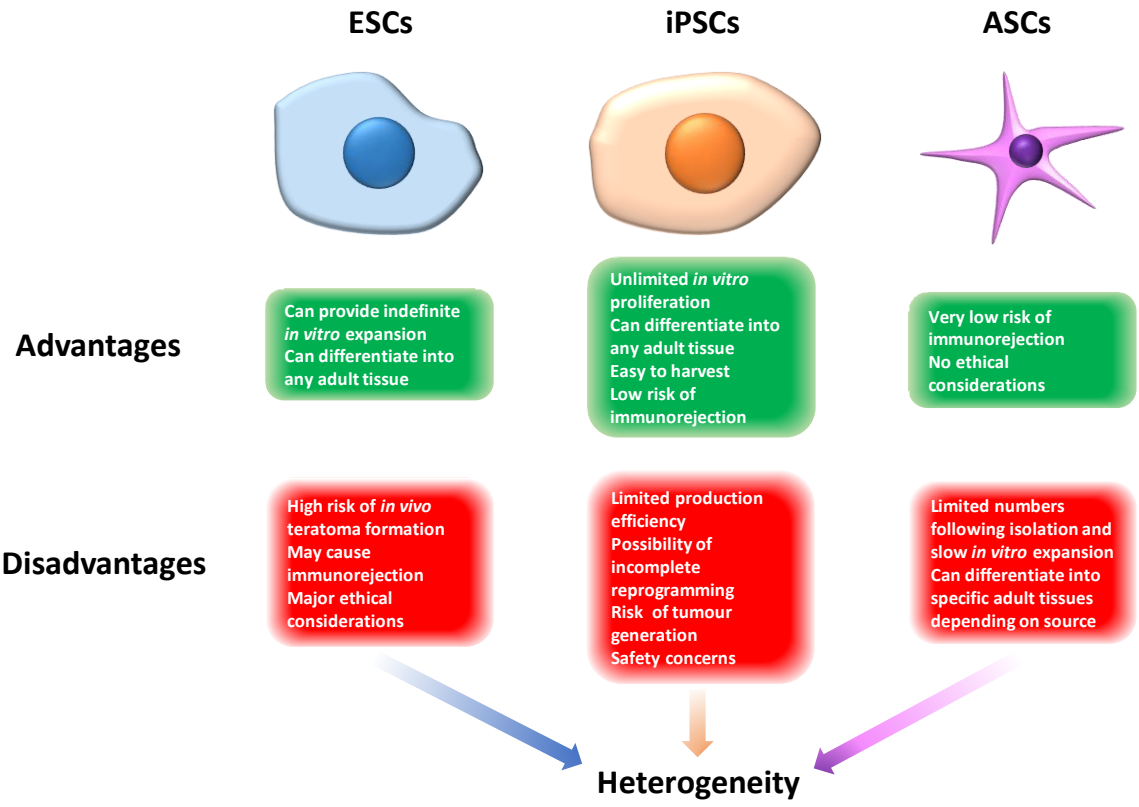

Figure 1.6 Potential stem cell sources for tissue engineering (i.e. ESCs, iPSCs and ASCs) with a comparative schematic of their advantages and disadvantages; ultimately pointing to the common unresolved issue in stem cell therapy: heterogeneity.

However, two factors concerning BMSCs limit the synthesis of high-quality cartilage tissue: heterogeneity and microenvironment. Cartilage microstructure grants a 3D microenvironment that promotes stable chondrogenesis within a specific extracellular matrix (ECM) containing proteins, PGs and cells in a determined density and arrangement that continues to pose problems when it comes to imitating it in a synthetic fashion, as well as reproducing mechanical performance and functionality (O'brien, 2011, Ricard-Blum, 2011, Demoor et al., 2014, Gao et al., 2014). Addressing such a cartilage tissue engineering (TE) challenge calls for careful appreciation of that local tissue microenvironment to succeed in integrating cells into the native extracellular matrix while restoring shape and function of articular cartilage. Current cartilage repair therapies based on mature chondrocytes and BMSCs have a common pitfall: either mechanically poor fibrocartilage or hypertrophic cartilage is formed that is progressively damaged and hampers the ability to withstand everyday loads. It is precisely this setback which reinforces approaches such as microenvironmental stimulation and regulation for cartilage development and acquisition of anatomical functionality over alternative cell sources (Jayasuriya et al., 2016).

It is important to note that the issue of heterogeneity pertains across each of these cell sources. Heterogeneity in ESCs and iPSCs may arise from dynamic transitions between metastable cell states with fluctuating transcription factor expression levels that regulate their response towards differentiation or self-renewal and depend on external environmental stimuli. iPSCs are subject to the additional effect of the somatic source and this is related to some extent to the origin of heterogeneity in ASCs depending on the tissue from which they are harvested (Graf and Stadtfeld, 2008, Krieger and Simons, 2015, Biendarra-Tiegs et al., 2019). The mechanisms behind ASC heterogeneity are not completely understood. Among the possibilities being considered is that heterogeneity may be a residue of morphogenesis during human development, hence explaining the phenotypic and functional differences of subpopulations isolated from different tissues. Other factors that may induce heterogeneity are the long-term in vitro culture conditions that expose cells to external stimuli from an environment that differs from their native in vivo niche and variations in gene expression of individual cells within clonal populations. The latter would account for the inherent stochasticity in the transcription and translation biochemical processes in gene expression (intrinsic noise) and fluctuations originating in the environment (extrinsic noise) that translate into changes in the cell cycle and the presence of cells of different ages (i.e. taken as time from last cell division) (Elowitz et al., 2002, Pevsner-Fischer et al., 2011, Thomas, 2019, Wilson et al., 2019).

Regardless of the origin of heterogeneity, its manifestation within ESC, iPSC and ASC populations interferes with accomplishing phenotypical characterisation, detection of differentiating progenitors and isolation of subpopulations of interest for tissue engineering. These present an enormous challenge for cell transplantation, with cell surface marker-based strategies failing to directly relate stem cell identity to biological function (Gundry et al., 2011).

Heterogeneity amongst BMSC colonies extends to diverse growth rates, cell morphologies and, more significantly, cell phenotypic characteristics that resemble specialised musculoskeletal tissues. In relation to cartilage, BMSC subpopulation heterogeneity often results in the formation of mechanically inferior fibrocartilage, hypertrophic chondrocyte differentiation and a notable tendency for tissue calcification. Bianco postulated the importance of finding a phenotypic trait in a defined subset of BMSCs linked to the intended reproducible differentiation and tissue organisation that it can be traced back to. Specifically for cartilage but also valid for other musculoskeletal tissues, this would be a kind of marker that can serve to isolate the target subpopulations according to the desired phenotypic trait. That same marker would then necessarily correlate with the biological function, morphology and structure characteristic of the musculoskeletal tissue to engineer. Cell surface markers and functional markers are reviewed in section 1.5.4 in this regard as possible cell sorting strategies. This prospect highlights the beneficial

outcome that would come from the isolation of robust cartilage-producing cells from the original heterogeneous BMSC populations (Bianco et al., 2001).

1.5.1 Skeletal stem cells

The bone marrow contains a heterogeneous set of stromal cells, BMSCs. A fraction of them, the so-called SSCs, possesses progenitor characteristics for musculoskeletal lineages. Sacchetti demonstrated evidence of *in vivo* multipotency finding SSC progenitors in bone marrow sinusoids after transplanting BMSCs subcutaneously into immunocompromised mice. Their work served to establish that given the appropriate conditions, the SSC fraction of BMSCs could indeed be guided to produce cartilage (Bianco et al., 2006, Sacchetti et al., 2007, Bianco et al., 2008, Bianco et al., 2013, Dawson et al., 2014, Sheng, 2015, Bianco and Robey, 2015, Danišovič et al., 2016).

Skeletal stem cell-based research in general attempts to evade embryonic stem cell-derived ethical issues and teratoma formation. Additionally, BMSC isolation is strongly driven by their adherent nature. Nevertheless, the yield is limited (Robey reported 10 to 50 per 10^5 nucleated cells) and they form heterogeneous populations distributed in distinct colonies, each of which is originated from a single cell precursor, the colony-forming unit-fibroblast (CFU-F), as named by Friedenstein et al., who first isolated them (Robey, 2011, Friedenstein et al., 1970). Notably, both growth rate (as reflected by their size) and differentiation potential vastly differ among colonies (Bianco et al., 2006, Bianco et al., 2008). These aspects expose the need to develop cell sorting techniques for cells originated from the most promising colonies to generate robust cartilage growth (Bianco and Robey, 2000, Bianco et al., 2001).

1.5.2 BMSCs for cartilage tissue engineering

BMSCs including their stem cell fraction of progenitors towards musculoskeletal lineages referred to as SSCs have been employed for cartilage tissue engineering because of their therapeutic ability, their less invasive cell harvesting method and their chondrogenic success (Bhumiratana and Vunjak-Novakovic, 2015). Beane and Darling conducted an extensive review of the chondrogenic experiments described in the literature assessing chondrogenic success in terms of the pellet mass obtained (mg), glycosaminoglycan secretion (µg GAG/µg DNA) and type II collagen gene expression normalised to *GADPH* (glyceraldehyde 3-phosphate dehydrogenase) housekeeping gene (Table 1.1). All three chondrogenic success indicators considered, they concluded that BMSCs showed hints of greater average chondrogenic induction even if the protocols utilised for isolation, culture and evaluation of chondrogenic differentiation called for optimisation and standardisation to yield more reliable comparisons among cell sources (Beane and Darling, 2012).

Table 1.1 Summary of stem cell types, corresponding purification methods, preferred growth factors and *in vivo* regeneration outcomes as adapted from Beane and Darling (2012). The stem cell types described are: Bone Marrow Stem Cells (BMSCs), Adipose-derived Stem Cells (ADSCs), Synovial-derived Stem Cells (SDSCs), Muscle-derived Stem Cells (MDSCs), Peripheral Blood Mesenchymal Stem Cells (PBMSCs), Wharton's Jelly Stem Cells (WJSCs), Umbilical Cord-derived Stem Cells (UCSCs), Amniotic Fluid Stem Cells (AFSCs), Placenta-derived Mesenchymal Stem Cells (PDMSCs), Embryonic Stem Cells (ESCs), Induced Pluripotent Stem Cells (iPSCs) and Cartilage-derived Stem Cells (CDSCs).

Cell type	Purification method	Chondrogenic potential	Preferred GFs	Description of *in vivo* regenerative success	References
BMSC	FACS Plastic adherence Density gradient	Mass: 0.25 – 9 GAG: 0.8 – 122 Type II collagen: 0.04 – 50	TGF-β3	Scaffolds are generally well-integrated and phenotypically similar to cartilage, although mechanically inferior.	(Barry et al., 2001, Mosna et al., 2010, Li et al., 2011, Ng et al., 2011)
ADSC	FACS Plastic adherence	Mass: 0.1 – 1 GAG: 0.3 – 120 Type II collagen: 0.02 – 3	TGF-β1, TGF-β3	Matrix secretion observed as well as cartilage-like appearance. Nonetheless, inferior degree of integration than that of BMSC scaffolds.	(Estes et al., 2010, Griesche et al., 2010, Li et al., 2011)
SDSC	FACS	Mass: 1 – 4.5 GAG: 2 – 45 Type II collagen: 1 – 2.25	TGF-β3, BMP-2	Successful matrix secretion. Degree of integration similar or inferior to BMSCs.	(Shirasawa et al., 2006, Koga et al., 2008, Han et al., 2010, Pan et al., 2015)
MDSC	Plastic adherence	Mass: 0.1 – 0.5	BMP-4	Appearance similar to native cartilage, though reported inferior integration to BMSCs.	(Kuroda et al., 2006, Gharaibeh et al., 2008, Li et al., 2011)
PBMSC	Plastic adherence Density Gradient	GAG: 3	TGF-β1, TGF- β3	Successful integration and regeneration reported.	(Lund et al., 2008, Chong et al., 2012, Hopper et al., 2015)
WJSC	Plastic adherence	-	TGF-β1, TGF- β3	-	(Wang et al., 2004, Baksh et al., 2007)
UCSC	Density gradient	GAG: 2.5	BMP-2	Cartilage-like matrix secretion and surface architecture reported.	(Zhang et al., 2011)
AFSC	Plastic adherence	GAG: 3.5 – 4	TGF-β1	Inferior matrix secretion to BMSCs.	(Kolambkar et al., 2007, Park et al., 2011)
PDMSC	Plastic adherence	Type II collagen: 0.5 – 15	TGF-β1	-	(Cavallo et al., 2011)
ESC	Mechanical isolation	Mass: 1 – 4.5 GAG: 2 – 45 Type II collagen: 1 – 2.25	TGF-β1, BMP-7	Cartilage-like matrix secretion and surface architecture, as well as successful integration reported.	(Koay et al., 2007, Nakagawa et al., 2009, Gong et al., 2010)
iPSC	-	-	TGF-β1	Matrix secretion reported.	(Wei et al., 2012)
CDSC	Plastic adherence	-	TGF-β1, TGF- β2	Excellent integration in caprine model with no differences observed in repair compared to HACs. Improved type II collagen expression and reduced osteophyte formation in equine model.	(Williams et al., 2010, Frisbie et al., 2015)

Subsequent studies point towards a similar direction highlighting the opportunities of BMSCs for cartilage tissue engineering. Ude et al. designed an *in vivo* OA repair sheep model in which they induced OA in sheep, harvested BMSCs and adipose-derived stem cells (ADSCs) a week after, expanded cells, cultured them in chondrogenic differentiation conditions and reinjected them as a cell therapy. Finally, they evaluated samples from the regenerated patella femoral groove using histological stainings and immunohistochemistry. The comparison between BMSCs and ADSCs showed that the two cell types tended to reach a similar proliferation rate as of passage 2 (P2) despite the initial burst of ADSCs when treated as precursor cells. BMSCs presented a more extensively intense chondrogenic induction, as assayed by gene expression (including *COL2A1, SOX9, ACAN and COL1A2*, the latter being similar for both cell types) measurements using real time quantitative polymerase chain reaction (RT-qPCR) (Ude et al., 2014). Regarding the yield of stromal cells in both tissues, investigations have reported no significant difference with an average figure of 2×10^5 cells/g tissue but a higher number of CFU-Fs in ADSCs that would explain a faster proliferation in early passages yet no robust evidence of more stable chondrogenesis (Boeuf and Richter, 2010).

Danišovič et al. expanded the comparative study with BMSCs and ADSCs adding umbilical cord-derived stem cells (UCSCs) but restricting it to an *in vitro* setting. They confirmed the highest chondrogenic potential of BMSCs by the lowest type I collagen expression and the highest type II collagen expression in passage 3 (P3). Conversely, they failed to cover type X collagen expression as an indicator of apparent hypertrophic tendency (Danišovič et al., 2016).

In vivo studies for cartilage repair reported in the literature have assessed either an individual adult stem cell type or a couple of them (e.g. BMSCs and ADSCs) but a cohesive *in vivo* comparative evaluation of the effect of tissue source on chondrogenic outcome has not been found. More controversial aspects on ASC and, by extension, BMSC application *in vivo* are isolation procedure, expansion culture and chondrogenic differentiation conditions, characterisation and stemness criteria as well as cell therapy administration method (Wyles et al., 2015, Maryam et al., 2019).

1.5.3 Limitations for the use of BMSCs in cartilage tissue engineering

Several challenges facing BMSC-driven chondrogenesis remain to be overcome. During cartilage development, BMSCs do not suppress type I collagen expression leading to fibrocartilage formation that exhibits an incomplete and inferior mechanical performance. Similarly, the upregulation of hypertrophy markers type X collagen, RUNX2, MMP13 (implying that degradation balance is tipped against cartilage ECM generation) and the potentiation of alkaline phosphatase (ALP) activity *in vitro* ultimately reveal a tendency towards osteogenic differentiation and ossification. As a

consequence, the lack of experimental protocols that prevent these alterations from typical native cartilage functions accentuates the deviation from long-term stable chondrogenic phenotypes.

BMSC hypertrophic tendency limitation can be desirable upon implanting into articular cartilage sites in the deep zones of cartilage where the tissue is progressively calcified. Contrarily, superficial zones exhibit completely different needs although the local production of PTHrP can detain calcification by keeping cells in a pre-hypertrophic proliferative state provided that the cartilage surface is healthy (Hollander et al., 2010, Chen et al., 2015a). Other growth factors and transcription factors can be employed together with the already mentioned chondrogenic inducers and signalling pathways. BMP-4 has been reported to enhance BMSC differentiation while preventing hypertrophy. Analogously, MMP13 specific-inhibitor GG86/2 is promising to reduce type II collagen degradation as it increases cartilage ECM regeneration (Chen et al., 2015a).

On the whole, the main challenge could be summarised in maintaining the normal chondrocyte phenotype. The approaches to arrive at the optimum experimental protocol integrate the influence of factors. These include the composition of the chondrogenic medium in terms of concentration and selection of pro-chondrogenic anti-hypertrophic growth factors, the environmental conditions (i.e. mainly the oxygen concentration as chondrocytes need to grow in hypoxic conditions) and the system applied for the construction of the appropriate extracellular matrix from a wide range of biomaterials available (especially hydrogels). Concerning BMSCs, heterogeneity in BMSC cultures represents a crucial limitation to overcome given that it translates into remarkable variations as far as gene expression and its fluctuation over time with respect to more homogeneous chondrocytes (Mahmoudifar and Doran, 2012, Li et al., 2015). The ideal scenario would be to implement a high-throughput technique that recovers robust cartilage-forming cell populations to grow high quality tissue whose chondrogenesis can be coupled with mechanical loading at the right stage (Mahmoudifar and Doran, 2012, Demoor et al., 2014).

1.5.4 Current cell sorting strategies for chondroprogenitors from BMSC fraction

Cell sorting techniques are frequently applied to separate cells according to specific desired properties (e.g. size, density, physical properties, plastic adherence, cell surface markers). With respect to isolating the stem fraction of heterogeneous bone marrow stromal cell population, gradient centrifugation, fluorescence activated cell sorting (FACS) and magnetic activated cell sorting (MACS) constitute the traditional immunoaffinity-based separation methods. Although all of them are high resolution techniques, the rare nature of the stem fraction in BMSCs poses an obstacle to harvesting sufficiently high cell numbers for their use in the clinic (cell therapies can require over 10^6 and up to 10^9 cells) (Sotiropoulou et al., 2007). FACS throughput is restricted to

5000-70000 cells/s at the expense of purity. It has an overall experimental duration of up to 6 hours that may induce shear stress and contamination on cells. MACS is a simpler and cheaper technique reaching similar cell throughputs yet lower purity. Despite their limitations, cell sorting strategies are rather focussing primarily on preserving cell function while ensuring reasonable levels of purity, resolution and yield in a simple and feasible manner (Mattanovich and Borth, 2006, Fernandes et al., 2013).

1.5.4.1 Cell surface markers

Cell surface markers have been explored to extract the chondroprogenitor subset within BMSC heterogeneous populations. As molecules that are attached to cell membranes, cell surface markers are easily accessible to identify subpopulations (Ono and Kronenberg, 2018). *In vitro* studies looking at the expression of surface markers such as CD105 and CD166 motivated by their upregulation observed in the more robust chondrogenic populations have not succeeded in validating their eligibility as a sorting criterion (Pittenger et al., 1999, Zhang et al., 2015b, Narcisi et al., 2015, Cleary et al., 2016). Conversely, $CD271^+$ enriched populations have been shown to enhance repair in articular cartilage defects through structural restoration of cellular morphology and tissue surface properties (Hermida-Gómez et al., 2011). Moreover, $CD271^+$ BMSCs outperform unselected plastic adherent BMSCs through higher expansion ability an upregulation of *SOX9* and *COL2A1* chondrogenic markers *in vitro* along with enhanced *in vivo* regeneration of chondral defects in rat femurs. Further investigation on biomechanical performance of the repaired tissue, and larger animal models that are more representative is still required to substantiate the positive and decisive chondrogenic role of this cell surface marker as well as its interaction with others (Mifune et al., 2013). Low levels detected in other adult stem cell sources and inferior CFU-F and multipotency abilities are other issues to resolve (Watson et al., 2013, Lv et al., 2014).

STRO-1 (mainly) and STRO-4 also belong to the set of stem cell surface markers that have been approached to isolate SSCs. Even if both have shown prospects for the gold standard phenomena for stem cells (i.e. CFU-F formation and trilineage differentiation into bone, cartilage and fat), no conclusive proof of robust chondrogenesis has emerged as yet (Gronthos et al., 2009, Li et al., 2015, Markides et al., 2018).

Cell surface markers are often assessed through their synergistic biological effect rather than their individual action alone. MSCA-1^+CD56^+ pair of cell surface markers is an example of association for chondrogenic enrichment of BMSC subpopulations (Battula et al., 2009, Lv et al., 2014). Chan et al. conducted a comprehensive screening of cell surface markers and established that even more complex combinations of four markers succeeded in inducing cartilage formation *in vivo* following subcutaneous or renal capsule transplantation in mice. They identified $PDPN^+CD146^-CD73^-CD164^+$,

$PDPN^{+}CD146^{-}CD73^{+}CD164^{+}$ and $PDPN^{+}CD146^{-}CD73^{-}CD164^{-}$ as human chondroprogenitors as well as an additional $PDPN^{+}CD146^{-}CD73^{+}CD164^{+}$ subset of multipotent cells that can lead to CFU-Fs *in vitro* from single cells and differentiate into bone and cartilage but do not yield adipose tissue (Chan et al., 2018).

Despite the current progress and efforts driven towards establishing the stem cell surface markers for BMSC chondroprogenitors, the fact that their presence does not necessarily correlate with any biological or functional event occurring at a cellular level is a clear limitation. Neither does flow cytometry achieve a simultaneous measurement and biological characterisation of cell subpopulations (Delmonte and Fleisher, 2019). In addition to this restriction, the experiments aiming to screen cell populations of interest can be remarkably expensive and time-consuming if they seek to comply with the recommendations by the ISCT (International Society for Cellular Therapy) (Dominici et al., 2006). They acknowledged the absence of a universal definition to identify human multipotent stem cells and they proposed the minimal criteria for standardisation:

1. Cells must be plastic-adherent in standard culture medium conditions.
2. Cells must express CD105, CD73 and CD90 and lack expression of CD45, CD34, CD14 or CD11b, CD79alpha or CD19 and HLA-DR exclusion cell surface markers.
3. Cells must be able to differentiate into osteoblasts, adipocytes and chondrocytes *in vitro*.

A recent study by Fabre et al. spanning 31 cell surface markers compared four stem cell types (i.e. BMSCs, ADSCs, dental pulp or DPSCs and WJSCs) to chondrocytes and fibroblasts, all cultured in serum-free conditions. Their results confirmed the expression of ICST recommended markers in all stem cell sources as well as other markers reported in the literature and currently accepted (i.e. CD10, CD13, CD29, CD44, CD166, D7-Fib and HLA-ABC). They concluded the same regarding ICST recommended exclusion markers and the new recognised markers (i.e. CD31, CD33, CD133, CD184 and HLA-G). Interestingly, they found that a significant proportion of the fibroblasts and chondrocytes that they screened followed similar stem cell surface marker expression patterns too (Fabre et al., 2019). This underlines questions also raised by other authors (e.g. Bianco et al.) about the biological basis of the ICST consensus document.

1.5.4.2 Functional markers

The lack of definitive cell surface markers for stemness and chondrogenic potential has driven efforts towards other methods for cell sorting (Gupta et al., 2012). Sorting cells while relying on 'functional markers' differs from cell surface markers, inasmuch as a biological event needs to be activated compared to a static cell morphology status. This concept is strongly connected to the argument by Bianco et al. that isolating subpopulations from the heterogeneous BMSC fraction

requires a phenotypic trait. Such a trait must simultaneously be the sorting criterion and a marker that can be matched to a biological function linked to the intended musculoskeletal tissue to generate (Bianco et al., 2001). That biological event signalling a function could be, for instance, differentiation and the 'functional markers' in this case would be differentiation-specific reporter gene markers. There is evidence of reporter gene markers being used for investigating differentiation in HBMSCs. Lee et al. constructed dual promoter reporter lentiviral gene vectors for live imaging of osteogenic and chondrogenic differentiation in mice. The first common reporter in both cases was a murine leukaemia virus-derived promoter to activate the expression of GFP for cell sorting. The second reporter consisted of a differentiation-specific reporter gene marker (*col1α1* for osteogenesis and *col2α1* for chondrogenesis) driving a luciferase reporter for bioluminescence imaging. For the osteogenesis assay, they transduced HBMSCs, sorted the GFP+ subpopulations by FACS and expanded them for implantation a week after into a segmental bone defect model induced in mice femurs. They loaded the cells in an alginate hydrogel scaffold prior to implantation and performed live animal imaging through bioluminescence followed by haematoxylin and eosin (H&E) histological evaluation of the repaired bone at day 58. For the chondrogenic assay, they acknowledged the impact of the environmental conditions on cartilage generation and took an alternative *in vitro* only approach instead. They installed a live imaging system of chondrogenic differentiation within a bioreactor that monitored the *col2α1* promoter activity by bioluminescence normalised to the signal of a positive chondrosarcoma cell line control. Cells were imaged as pellets made of transduced HBMSCs pre-differentiated towards the cartilage lineage. This work altogether is a proof of principle of techniques for live imaging of osteogenic and chondrogenic differentiation for tissue repair via differentiation-specific 'functional markers'. Interestingly, they outlined that there could be other well-known early chondrogenic differentiation-specific markers such as fibromodulin and COMP that indicate the beginning of cartilage-like ECM formation (Barry et al., 2001, Lee et al., 2012).

SOX9 could be another potential functional candidate that has been discussed in this review. SOX9 is expressed during mesenchymal condensation (i.e. biological phenomenon) and cells that preserve SOX9 expression translate into more stable articular cartilage phenotype (i.e. with the desired tissue 'function') (Williams et al., 2010, Jiang et al., 2020). The challenge associated with SOX9 application is that it is an intracellular nuclear transcription factor and therefore even more challenging to target and to screen than a cell surface marker. Li et al. described a nanoflare technique to quantify its expression in terms of fluorescence emitted when a probe is supplied to the culture medium that fluoresces exclusively as it binds *SOX9* mRNA (messenger ribonucleic acid) transcripts in the cell nucleus. They aimed to validate the use of *RUNX2-Cy3* and *SOX9-Cy5* mRNA probes to quantify the ratio of *RUNX2/SOX9* in live individual HBMSCs after hypothesising that it

was predictive of *in vitro* osteogenic differentiation after a week of culture based on previous results (Loebel et al., 2015). For that purpose, they sorted HBMSCs cultured in basal and osteogenic induction media for 6 days through FACS and quantified *RUNX2* and *SOX9* mRNA expression by RT-PCR. They observed a shift in the FACS fluorescent signal for basal and osteogenic media in cells that had been exposed to the mRNA probes for both markers. *RUNX2* underwent a slight upregulation in osteogenic medium, whereas *SOX9* was downregulated with respect to basal conditions, both of which matching the FACS intensity profiles. When they sorted and quantified cells corresponding to lower and higher intensity peaks of RUNX2 and SOX9, they measured mRNA upregulation in both; but the difference was not statistically significant in any case. They obtained similar results when they sorted cells considering several RUNX2/SOX9 ratios linked to FACS intensities. The highest levels of *RUNX2* and *SOX9* mRNA expression were related to basal conditions for high intensities of *SOX9* and *RUNX2*. Again, they could not conclude any statistical significant difference and their study did not include a group for high *RUNX2*/low *SOX9* FACS intensities. This would have provided relevant information about the high ratio that they had previously hypothesised to be desirable for osteogenesis. Furthermore, their functional assay composed of parallel proliferation assay and Alizarin Red staining after 3 weeks of osteogenic differentiation showed that the low *RUNX2*/low *SOX9* group exhibited the most intense Alizarin Red staining along with the lowest proliferation rate instead. They justified these results by claiming that this group was at a later stage of differentiation given by the highest osteocalcin mRNA levels of all groups, which is a late marker of osteogenic differentiation, and the highest *RUNX2/SOX9* ratio when the average mRNA values were taken. In conclusion, their work set a valuable foundation for the integration of mRNA probes to target live quantification of intracellular markers and to sort cell population using FACS but lacked a robust statistical significance and further functional cell differentiation evidence (Cleary et al., 2016, Li et al., 2016).

Hence, a cell sorting approach relying on a marker that can delve into the functional aspect of heterogeneous cell populations such as BMSCs acquires a significant interest. Even more so if the possibility of extending this principle to processing and sorting small cell aggregates becomes realisable. These aggregates would mimic cell condensation during chondrogenesis. At the same time, they would allow to discriminate whether cell groups in a heterogeneous population of HBMSCs collectively display positive prospects for chondrogenic differentiation on the basis of early SOX9 expression. The benefit of complementing this technology with other techniques such as droplet microfluidics to scale up the production of microaggregates creates new opportunities to isolate small cell populations with enhanced SOX9 expression towards cartilage formation.

1.6 Multicellular spheroids for cartilage tissue engineering

Chondrogenesis-based cell research has engaged actively in a transition from 2D adherent culture to 3D culture pursuing a closer imitation of natural physiological environments with enhanced diffusion of nutrients, gas, growth factors and cellular waste to stimulate cartilage formation. The concept of multicellular spheroids has become more commonplace in the literature to describe spherical-like 3D cell aggregates resulting from a cadherin-mediated cell adhesion phenomenon. The structure of these multicellular spheroids generally comprises (Figure 1.7):

- An external *proliferating zone* that is more exposed to O_2, growth factors and nutrients;
- A *quiescent zone* in the middle characterised by a balance between reduced O_2 and nutrient access and higher CO_2 and metabolite production;
- A deep *necrotic zone* composed of cells that have a very low to inexistent activity due to CO_2 accumulation.

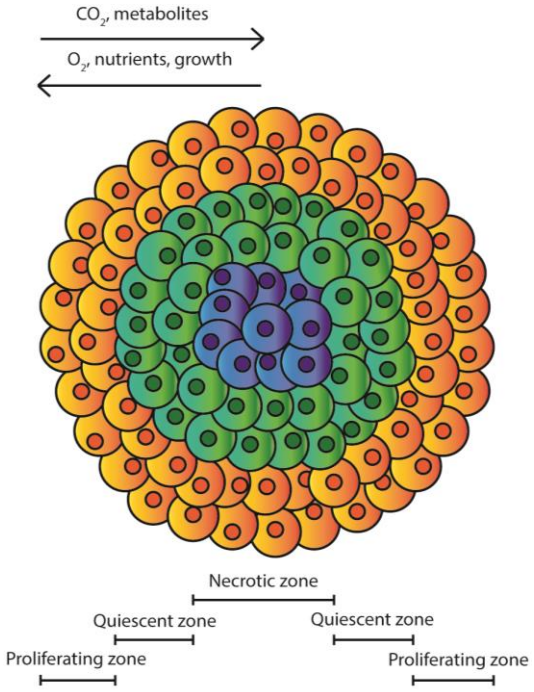

Figure 1.7 General multicellular spheroid structure including separate regions according to cell activity: yellow (proliferative cells), green (quiescent cells) and blue (necrotic core); and flow of substances across the spheroid.

The interest in multicellular spheroids and 3D culture also lies in the enhanced diffusion of nutrients, gas, growth factors and cellular waste up to 150 to 200 µm thickness threshold (once surpassed, diffusion in the cell aggregate starts becomes limited) (Vadivelu et al., 2017). Spheroid dimensions depend entirely on initial pre-set cell-seeding densities. By fixing this variable, finely controlled sizes result for straightforward and automated high-throughput generation of multiple replicates for direct testing of the effect of cell co-cultures, various culture conditions and reagents (Laschke and Menger, 2017).

1.6.1 Spheroid generation: cell culture methods

A series of scaffolds have been developed to host cartilage formation by providing a 3D environment where nutrient diffusion, mechanical properties, pore size, pore interconnectivity, adhesion to the defect site after a minimally invasive implantation procedure and degradability are secured to the extent required for neocartilage growth. Tissue-engineered scaffolds can be classified according to their origin into natural and synthetic; and presented in the shape of porous sponges, fibrous networks or hydrogels (O'brien, 2011, Kim et al., 2011a). Alternatively, scaffold-free techniques have been developed for physiological-like 3D culture relying on cell self-assembly to replicate the early chondrogenic stage of condensation leading to cartilage growth. Several techniques are in use; all considering the advantage of utilising tissue to replace deteriorated tissue (Table 1.2) (Lin and Chang, 2008, Achilli et al., 2012, Cui et al., 2017, Petrenko et al., 2017).

Table 1.2 Strengths and weaknesses of different methods for spheroid formation reported in the literature.

Method for spheroid formation	Strengths	Weaknesses
Pellet culture	Simple, rapid and inexpensive Low oxygen conditions created encourage chondrogenic differentiation	Shear stresses may damage cells Difficult to scale up Aggregation cannot be monitored
Hanging drop	Simple, rapid and inexpensive Co-cultures of different cell types can form heterotypic spheroids Up to 384 spheroids/array	Aggregation cannot be monitored Media changes and addition of reagents are not straightforward
Spinner flask	Fluid movement aids mass transport across the spheroids It enables to scale up	Shear stresses may damage cells Aggregation cannot be monitored Heterogeneity in size and shape It requires specialised equipment
Microfluidics	High-throughput technique, rapid Co-cultures of different cell types can form heterotypic spheroids Shear stresses for aggregation controlled The platform allows for monitoring	It is not straightforward to operate
Cell sheets on thermoresponsive polymers	Co-cultures of different cell types can form heterotypic spheroids	It is time consuming and non-trivial
Liquid Overlay	Simple, rapid and inexpensive It allows for monitoring on well plates	Heterogeneity in size and shape
Rotating wall vessel	Co-cultures of different cell types can form heterotypic spheroids Low shear forces exerted for aggregation It enables to scale up	Heterogeneity may occur in size Difficult to monitor aggregation
External force	Flexibility to reproduce specific patterns Rapid	Cell adhesion is often very non-specific. Heterogeneity in size Unknown side effects on cells It requires specialised equipment
Micro-moulded non-adhesive hydrogels	Over 800 spheroids/mould Easily controllable parameters/patterns The platform allows for monitoring	It is not straightforward to operate It requires specialised equipment
Ultra-low adherence plates	Easy, simple, rapid No centrifuging or shear for aggregation Co-cultures of different cell types can form heterotypic spheroids Up to 384 spheroids/ array The platform allows for monitoring	Heterogeneity may occur in both spheroid size and shape

Pellet culture is one usual scaffold-free technique for chondrogenesis studies that uses centrifugation to induce cell adhesion at the bottom of conical tubes or microwell plates with specific geometries (i.e. U-bottom, V-bottom). Pellet culture relies on the hydrophobic nature of internal surfaces of these tubes and well plates to provide an environment in which the pellet gradually detaches after up to 48 h and enters in suspension under chondrogenic stimulation. Given the resemblance to physiological conditions that take place in embryonic development leading to cartilage and bone growth (e.g. cell-to-cell contact and interaction, nutrient diffusion gradients), pellet culture appears to closely mimic chondrogenic stages (Khang et al., 2014).

1.6.1.1 3D pellet and 2D micromass culture

There is reason to debate the use of micromass culture as opposed to pellet culture. Both high-density culture methods differ in that micromasses are generated by adherence of a small volume of concentrated cell suspension onto a substrate, whereas pellets are non-adherent and remain in suspension. Several studies have quantified larger amounts of extracellular matrix synthesised by micromasses than by pellets, with upregulated *COL2A1* and *ACAN* expression in HBMSCs (Zhang et al., 2010, Mahboudi et al., 2017); as well as reported downregulated *COL1A2* and *COL10A1* hypertrophy markers in micromasses. Nonetheless, reported low levels of *SOX9* expression raise concerns as to whether they are sufficient to sustain cartilage development in the long term. These results contrast with the comparison that Caron made between monolayer 2D and 3D pellet culture in human articular chondrocytes (HACs) (Caron et al., 2012). HACs are known to lose chondrocyte phenotype and dedifferentiate when expanded in vitro in monolayer culture after a few passages, replacing hyaline Type II collagen matrix by Type I Collagen synthesis (von der Mark et al., 1977, Lin et al., 2006, Phull et al., 2016). Their research used mRNA quantification for protein expression, total GAG quantification and RT-qPCR to conclude that 2D culture could lead to hypertrophy in HACs, whereas 3D culture in pellet culture tubes enhanced *COL2A1* and *SOX9*, but also *COL1A1*. Both culture techniques continue to pose similar hypertrophy issues, as supported by the micromass study with co-culture of HACs and HBMSCs conducted by Giovannini et al. Their findings revealed that HBMSCs underwent hypertrophic differentiation on their own regardless of the presence or absence of chondrogenic differentiation growth factors of the TGF-β family. HACs contributed to generate most of the cartilage extracellular matrix but failed to preserve cartilage differentiation in HBMSCs (Giovannini et al., 2010).

1.6.1.2 Pellet culture in microwell plates and conical tubes

Pellet culture in hydrophobic non-adhesive (‘ultra-low attachment’) microwell plates is another alternative method. It avoids artificial mechanical inputs from centrifuging owing to a round-, U- or V-bottom geometry and surface treatment that favour pellet formation by minimising cell adhesion

at the bottom. It also promotes scaling-up the production of spheroids while supplying with smaller amounts of media and reagents. Additionally, while pellet culture in tubes is simple and rapid to perform, it lacks compatibility with mass production of spheroids and renders visualising cells as they aggregate challenging. Microwell plates conversely offer such opportunity for analysis, which is appealing in that it gives an indication of timescales for condensation to occur and a basis for correlation to final chondrogenic differentiation outcomes.

Despite the fact that both culture methods involve laborious manual work, microplates relieve some of the workload by automating cell seeding and optimising characterisation time per aggregate (Achilli et al., 2012, Petrenko et al., 2017). The number of samples and conditions to test is then only limited by the number of wells on the plate. Penick et al. comprehensively explored the practical differences between tubes and microplates for pellet culture applications. HBMSC cell aggregates reached a 3D configuration as a result of the V-bottom shape of the well plates. Fluorescent immunohistochemistry on the cell aggregates after 21 days of culture showed no type I collagen production and positive generalised type II and type X collagen staining, regardless of the pellet culture surface. The pellet formed in a conical tube, however, had a small region in the centre where no type II collagen signal was detected. Quantitative measurements established that pellets grown in microplates were larger and yielded higher DNA and GAG (indicator of ECM synthesis performance) content than those coming from pellet culture in tubes, although the extent of statistical significance was unclear (Penick et al., 2005). The same authors later reported no significant change in cell aggregation (measured in terms of aggregate size) or histological development derived from centrifuging in microplates after 24h of culture. They argued that the centrifuging step was not essential and could hence disappear in favour of avoiding any effects on cellular phenomena (Welter et al., 2007).

Schon et al. addressed the comparison between conical tubes and microplates from a different perspective and drew similar conclusions. After culturing human nasal chondrocytes (HNCs) for up to 4 weeks, Safranin O staining and GAG quantification outputs did not expose major differences regarding PG matrix production. Type I and Type II collagen production on day 7 and day 21 did not differ greatly either, as assessed by Immunohistochemistry and RT-PCR normalised to 18S rRNA. The most favourable differentiation condition was conical tubes supplemented with 1 ml chondrogenic differentiation medium yet it all failed to compensate for the automation, time- and cost-effectiveness that the use of microplates implied (Schon et al., 2012).

Tung et al. built on the concept of high-throughput spheroid generation to implement a 384-well plate powered by liquid handling robotic technology for testing the effect of a set of drugs on cell viability. Cell culture relied on a sophisticated hanging drop system. A small volume of 15 µl cell

suspension was systematically pipetted through each 'access hole' and generated one drop at a time. The drops adhered to a plateau on the bottom surface of the plate due to surface tension: 'hanging drop'. Cells grouped into aggregates in a matter of hours aided by gravity within the drop, forming spheroids after one day of culture. The drops received constant hydration from surrounding water reservoirs to prevent evaporation. The geometry of the cell culture compartment and the adjusted cell-seeding densities provided fine control on drop and spheroid size, respectively (Tung et al., 2011). In contrast, this complex multiplex platform sacrificed spheroid observation during growth, complicated cell media changes and restricted cell-seeding numbers for culture, which may be insufficient for cartilage tissue engineering from a translational point of view (Achilli et al., 2012).

1.6.2 Effect of cell number: microaggregates

Away from conventional cell numbers above 10^5 cells for pellet culture that can self-assemble into large macroaggregates of approximately 200-500 µm diameter, some authors have studied chondrogenic effects for lower cell numbers to avoid necrotic areas at the core. Aggregates below 200 µm are composed of cells that are for the most part in a proliferative state and are considered microaggregates that need fabrication and characterisation techniques in the microscale (Däster et al., 2017, Byun et al., 2019, Hamilton and Rath, 2019). Islam et al. extended the use of 96-well 'ultra-low attachment' plates to several stem cell sources comparing the robustness of the cartilage tissue generated from HACs, UCSCs, HFPSCs (Hoffa's fat pad derived stromal cells) and SDSCs *in vitro*. With an initial seeding density of 5×10^4 cells/well, they characterised their 3D spheroids by means of Alcian blue/Sirius red staining combined with immunohistochemical analysis for Type I and Type II collagen distribution, sulphated glycosaminoglycan (sGAG) quantification and qPCR gene expression. The microplates allowed them to argue that UCSCs underperformed as cell sources for cartilage formation with regard to the other stem cells assessed, which gave rise to tissue resembling that of designated positive controls, HACs (Islam et al., 2016).

Another example of even smaller microaggregates was demonstrated by Moreira Teixeira et al., who described how cell aggregates of 50, 100 and 200 bovine chondrocytes behaved as compared to single cells when seeded into microwells in agarose chips. Microaggregates presented increased *COL2A1*, *SOX9* and *ACAN* mRNA levels, as well as profoundly decreased *COL10A1*, *MMP13*, meaning that a stable cartilage matrix was being formed that was noticeably less hypertrophic. However, their *COL1A1* levels were also higher for microaggregates on day 21, which could suggest fibrocartilage formation, although the difference was not statistically significant. Both human and bovine chondrocytes synthesised a GAG-richer matrix as evaluated by quantification normalised to the amount of DNA and both in vitro and in vivo histological evaluation (Moreira Teixeira et al.,

2012). A later expansion of the study to human periosteum-derived stem cells found downregulation of stemness markers, nuclear *SOX9* translocation and promising expression of articular cartilage-associated genes (i.e. *COL2A1*, *ACAN*, *SOX9*) (Leijten et al., 2016).

1.7 High-throughput cell isolation, culture and sorting techniques

Once the microenvironment for cell proliferation and differentiation has been facilitated, high-throughput techniques come into play for sorting of cell microaggregates to ascertain which populations are positive for the set of markers linked to the tissue to be regenerated. The need for high throughput emanates from the abundance of biomolecular components of cell microenvironments that interplay with cellular functions. The immense volume of interrelationships ensuing simultaneously demands being able to unify responses towards the same direction (Ranga et al., 2014).

1.7.1 High-throughput screening techniques

High-throughput screening research prototypes in association with cell sorting have been reported of late in the literature. Flow cytometry (FCM) is a commonplace high-throughput counting and sorting technique that is applicable to microparticles and entities of similar sizes like cells. FCM can be coupled with FACS technology such that cell sub-populations that come from an originally heterogeneous population can be screened at hundreds or even thousands of cells per second to determine cell viability. This can be achieved by incorporating more complex droplet cell sorters that can reach generation frequencies in the range of 1 kHz for high-speed 70 µm diameter nozzles to determine cell viability (Bergquist et al., 2009).

For the sole purpose of screening, Zhang et al. built a microarray containing over 2000 thermally-responsive polymeric hydrogels that were assessed by quantifying their capacity to uptake, proliferate and release HeLa cells as a function of temperature reduction prior to selecting those with a favourable response (Zhang et al., 2009b). Also concerning HeLa cell sorting but integrating FACS, Nawaz engineered a FACS acoustofluidic sensor used for cell sorting with SAWs (surface acoustic waves). Fluorescein-labelled and unlabelled HeLa cells were assayed by flow cytometry. The sorting purity reached approximately 92.3 ± 3.39% at a total throughput of 1200 cells/s for fluorescently labelled HeLa cells, with 99.18% of the cells maintaining viability. The flow rate sustained on the platform already entailed nearly a ten-fold increase over the figure available a decade earlier of 160 cells/s (Nawaz et al., 2015). Again, combining screening and sorting with physical characterisation of heterogeneous BMSC populations, Xavier et al. applied deformation-based DLD (deterministic lateral displacement) to BMSCs and their STRO-1^+ SSC fraction using flow

rates from 250 to 850 cells/s injected into a PDMS device. This technique enabled size-dependent cell sorting and they recognised two significantly distinct distributions (9.1 ± 1.6 and 18.2 ± 3.1 µm, respective mean sizes and standard deviations) (Xavier et al., 2019).

Along the lines of the challenges described in this review and maintaining the focus on the diversity existing in stem cell populations, Ranga et al. developed the hydrogel microarray technology into a robotic nanolitre liquid-dispensing device to assay over 1000 polymer substrates in cell wells. Their aim was to examine the combined effect of three signalling proteins (i.e. mouse laminin I, type IV collagen and human fibronectin), PEG hydrogel cross-linked with coagulation factor XXIIIa with stiffnesses ranging from 300 to 5400 Pa and peptides with several degrees of sensitivity to MMP degradability on mouse embryonic stem cell (mESC) fate. The cells that emitted a readable signal revealing the expression of pluripotent markers of early differentiation (i.e. NANOG, REX1, OCT4. SSEA1 and inhibition of leukaemia inhibitory factor, LIF, cytokines) in response to modifications in the mechanical properties of the substrate were further characterised by RT-PCR and time-lapse imaging for corroboration (Ranga et al., 2014). In an attempt to replace robotic deposition by more inexpensive techniques, Allazetta and Lutolf pursued the concept of droplet microfluidics. They proposed a system to screen SSCs in an automated fashion and in a wide variety of hydrogel 3D culture microenvironments or niches with volumes as little as a few picolitres and down to single-cell scale resolutions that can fit onto a chip (Allazetta and Lutolf, 2015).

1.7.2 Droplet microfluidics

Droplet microfluidics is a high-throughput technique that adapts the principles of microfluidics for the generation of two-phase droplets that enclose a complete environment with predefined elements and conditions. A series of advantages justify the notable evolution that this approach has seen over the last decade (Brouzes et al., 2009, Stapleton and Swartz, 2010, Gu et al., 2011, Guo et al., 2012, Joensson and Andersson Svahn, 2012, Mazutis et al., 2013, Byun et al., 2014, Niu and deMello, 2012):

- Appropriate droplet size to contain single or a few cells.
- Systematic high-throughput screening given by the automation and parallelisation inserted in the design of a miniaturised microchip.
- Fast operation even in the single-cell scale in timescales as small as tenths of milliseconds. In terms of throughput, kHz generation frequencies are commonplace and small droplets (picolitre volumes) can be formed at MHz ranges. Despite typical dominant laminar flows in microfluidics, mixing happens rapidly by chaotic advection and can be further

accelerated by introducing windings in the channels. Simultaneously, and more importantly, the platform allows designing for specific kinetics or reaction times.

- Higher sensitivities derived from the compartmentalisation of reagents and samples that prevent any risks of cross-contamination. The oil that acts as external inert carrier fluid and coating for the droplets nullifies any interaction between reactants and the surface of the channels.
- Tighter control over the physical and chemical stimuli in microenvironments than conventional 2D cell culture techniques or complex large fluidic systems.
- Very small volumes of samples and reagents (picolitres to microlitres) are required, which helps shortening costs and acquisition times due to augmented surface-to-volume ratios that accelerate interactions.

1.7.2.1 Droplet microfluidic components

Droplet formation relies on a two-phase system where stable droplets are generated as an aqueous reagent is pumped and brought in contact with an immiscible oil carrier fluid inside microchannels. The properties of these droplets vary depending on the application that they are envisioned for: dimensions, shape, monodispersity, droplet generation rate. Cell compartmentalisation has to comply with an additional biocompatibility issue granting the appropriate environment where cell viability is accomplished (Stapleton and Swartz, 2010, Nightingale et al., 2011, Niu et al., 2011, Joensson and Andersson Svahn, 2012, Zhang et al., 2015a).

A droplet-based microfluidic system consists of an aqueous phase (or several of them introduced in several inlets) and an oil phase. Within the aqueous phase, cells/particles are suspended along with fluorescent or magnetic labels and any other macromolecules or hydrogel materials that contribute to the appropriate microenvironment. The oil phase stabilises the water-in-oil or oil-in-water emulsion with a surfactant to elude the coalescence of the droplet. The choice of oil is usually restricted to hydrocarbon and fluorocarbon oils. The latter is preferred in biological contexts because of their inert characteristics (they are immiscible with aqueous and organic solvents and are the only ones where cell survival have been demonstrated) and subsequent stability, in conjunction with their high oxygen retention ability and improved gas exchange. Surfactants containing carboxylic acid head and perfluoropolyether (PFPE) or perfluoroalkyl (PFAS) tail groups are normally employed. Their use is supported by evidence of reduced protein adsorption and cell membrane disruption. As a rule, surfactants are molecules with an amphiphilic behaviour, meaning that individual groups in the molecule will show affinity towards one of two immiscible phases (water and oil in droplet microfluidics). Droplet stabilisation is achieved by means of an event known as Marangoni effect, according to which the droplet interface becomes rigidified as a non-

uniform surfactant distribution appears due to the droplet movement as it forms. The surfactant concentration is comparatively larger at the rear of the bubble and a gradient of surface tension is created that is accompanied by an opposing stress to flow. Thus, when the flow is stopped, forces are removed allowing uniform coating of the droplet with surfactant (Schramm et al., 2003, Baroud et al., 2010, Baret, 2012, Basova and Foret, 2015).

1.7.2.2 Droplet generation

On-chip droplet generation approaches can be divided into active and passive methods. Active approaches take advantage of external stimuli (e.g. electromagnetic fields, pneumatic pressure, optical forces, thermal gradients) to induce time-dependent perturbations in the droplet flow. Droplet size and generation rate is thus kept under control regardless of channel geometry or flow rate at the expense of a lower droplet-generation rate, which essentially explains why passive methods are used more often (simplicity and cost are other key factors). These are strongly affected by fluid dynamics and channel geometries with droplets being generated at frequencies spanning between 10^{-2} and 10^{4} Hz. Fluid dynamic events are vital to understand the forces acting on the droplets as they flow through the channels before being collected. Taking the water-in-oil example, the aqueous phase and the carrier oil would be propelled independently through the channels by the pressure inflicted by the regulating pump connected to the microchip inlets via tubings. The aqueous dispersed phase would meet the continuous oil phase at a junction defined by a special geometrical feature and be exposed to interface instability in a balance between shear stresses attempting to deform the interface and capillary pressure opposing to that source of alteration. Droplet formation as a whole is the result of a balance between diverse forces, each of them having an individual impact that is collected in non-dimensional parameters such as the Reynolds number and the capillary number (Table 1.3).

Table 1.3 Parameters involved in droplet fluid mechanics (Baroud et al., 2010, Gu et al., 2011, Niu and deMello, 2012, Basova and Foret, 2015).

Parameter	Equation	Description
Reynolds number	$Re = \frac{\rho v L}{\mu}$	It displays the ratio of inertial forces represented by the product of density (ρ), mean velocity (v) and channel length (L) to viscous forces, depicted in terms of dynamic viscosity (μ). Values below 2300 indicate laminar flow, which is typically observed in droplet microfluidics except in winding channel geometries where mixing is purposefully prompted via chaotic advection.
Capillary number	$Ca = \frac{\rho v}{\sigma}$	It expresses the relationship between viscous stresses and surface tension (σ). The values of this number reflect the effect of these forces as regards droplet shape. Spherical droplets are prone to form for values below 1 when surface tension exceeds viscous stresses where droplets become increasingly asymmetric as viscous stresses are more dominant.

Droplet size, velocity, frequency control and reagent concentration in passive droplet generation methods is performed taking into consideration the channel dimensions for the design of the device, the flow rates at which the two phases are infused, the specific type of surfactant employed and their concentrations and the different viscosities of the aqueous and oil phase, respectively. Three main strategies concerning geometries stand (Figure 1.8) (Baroud et al., 2010, Gu et al., 2011, Niu and deMello, 2012, Joensson and Andersson Svahn, 2012, Basova and Foret, 2015):

- *Co-flowing streams*: the dispersed and the continuous phase travel through the channel simultaneously (co-flow) in a single liquid stream that breaks off into droplets when the continuous phase velocity exceeds a critical value, v^*, whose magnitude oscillates subject to surface tension at the interface, viscosity relationship of the two phases and the injection flow rate (Figure 1.8A).
- *T-junctions*: the dispersed and the continuous phase are compelled to converge at an orthogonal channel intersection after adjusting the flow rate of both phases. The phase that shows the lowest affinity for the channel walls on the substrate is then dispersed into the continuous carrier fluid of the assembled droplet, which splits into droplets due to the effect of shear stresses on the channel walls (Figure 1.8B).
- *Flow-focussing*: the dispersed phase is injected from a channel in the middle that intersects with two side channels (arranged opposite to each other) containing the continuous phase at a narrow orifice. The continuous phase compresses the dispersed phase through the narrower channel and droplets are created as the destabilisation in the shape of shear stresses incurs segmentation of the two phases. The droplets can concentrate downstream as they flow through an adjacent wider channel for collection (Figure 1.8C).

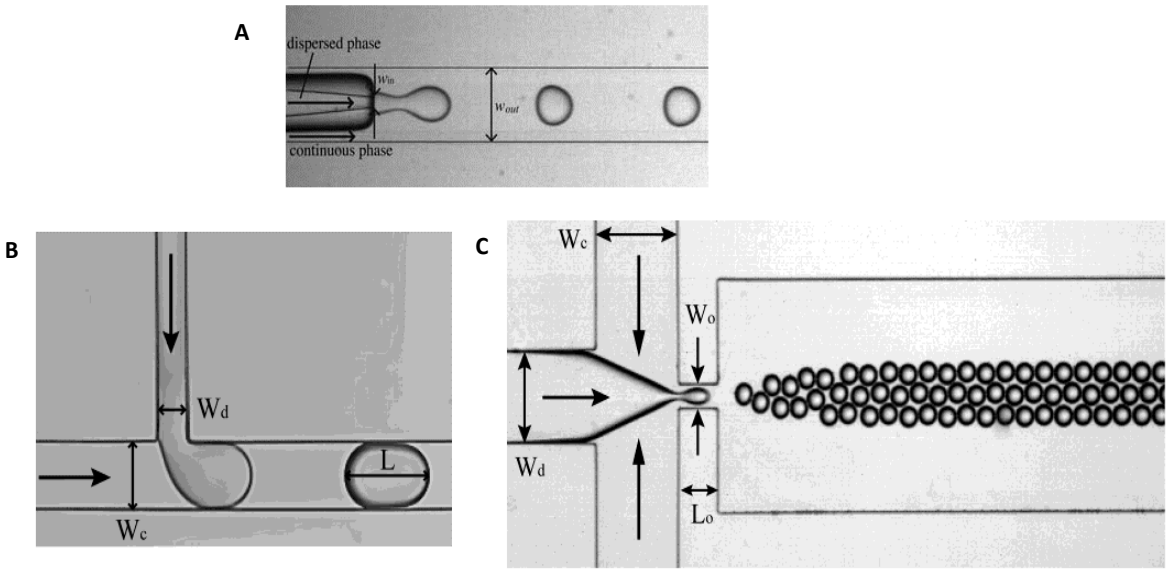

Figure 1.8 Geometry-based strategies for droplet generation: (A) Co-flowing streams, adapted from Baroud et al. (2010); (B) T-junctions; C) Flow-focussing. B) and C) are adapted from Gu et al. (2011).

The possibilities of droplet microfluidics are not limited to the droplet generation stage. Operational units have been optimised to further regulate the droplet behaviour, providing a versatility that is much desired for cell sorting (Figure 1.9D). Passive units are classified into four operations that can or not be part of a sequence (Niu et al., 2011, Gu et al., 2011, Niu and deMello, 2012):

1) *Merging*: it can be carried out by bringing together two separate droplets or by fragmenting a continuous stream with pressure, electrical, optical or thermal stimuli that nullify the stabilising effect of the surfactant. Droplet merging is effective when the time at which droplets simultaneously reach a predefined point in the device is fixed, whilst the continuous stream fragmentation needs a tight control and a uniform spacing between droplets (Figure 1.9A).
2) *Splitting*: this effect is easily reproduced by inserting bifurcations or obstacles (e.g. pillars) in the channels (Figure 1.9B).
3) *Dilution*: it is a core characteristic operation of microfluidic droplets applied to biological systems like cell sorting as it serves as a concentration modulator that operates in an automated and swift manner. The volumetric dilutions can be extended above four orders of magnitude, being these in a scale of three to six orders of magnitude smaller than normal dilutions for *in vitro* activities or other fluidic experimental set-ups (Figure 1.10A).
4) *Trapping*: for storage and incubation or droplet collection, is attained upon the introduction of elements for immobilisation that enclose droplets within a confined region, accumulate them in selected areas or collect them for sorting, screening or recovery (Figure 1.9C).

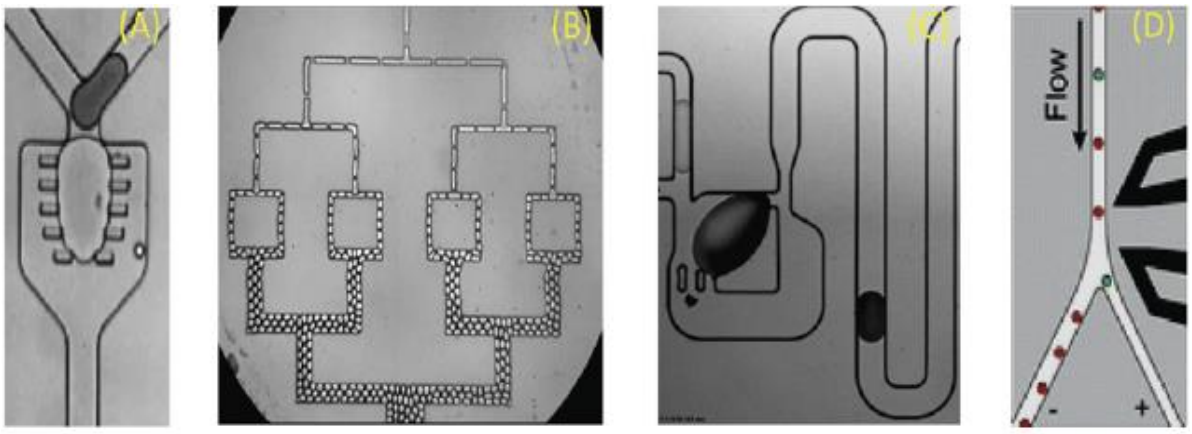

Figure 1.9 Passive operational units inside a microfluidic platform: (A) Droplet merging; (B) Sequential droplet splitting; (C) Droplet trapping; (D) Droplet sorting process. Adapted from Niu and deMello (2012).

In a similar fashion, active operational units consist of elements that integrate the external forces already described for active droplet generation methods: electromagnetic actuators, pressure valves, optical instruments and phenomena, SAW generators and electrophoretic equipment are valid examples of this approach (Gu et al., 2011, Niu et al., 2011, Niu and deMello, 2012).

1.7.2.3 Droplet microfluidic substrate material

The material constituting the microchip substrate has also been a matter of discussion; with the consensus remaining in favour of various aspects that designate the material choice. Cost, fabrication procedure, biocompatibility, degree of chemical interaction between the two phases and thermal stability are decisive altogether. Away from traditional silicon, polymer or glass substrates; materials like fused silica, PMMA (poly (methyl methacrylate)), PS (polystyrene) and more commonly PDMS (polydimethylsiloxane) have been treated as standard for microchip fabrication, either by 3D-printing or soft lithography (for an improved accuracy). Cell-based microfluidic experiments that involve water-in-oil droplets entail carrier oils being in direct contact with channel surfaces that should ideally be hydrophobic enough for uninterrupted stream flow. PDMS substrates are originally hydrophobic and a surface modification must be applied using a coating treatment to increase the affinity of the channel walls with oil and surfactant systems and to eliminate any harmful interaction between the aqueous phase and the channel walls. For that purpose, hydrophobic agents such as Aquapel® and fluorosilanes are made to cover the surface of the channels, rendering them hydrophobic and oleophilic. One further detail has to be contemplated with regard to PDMS inherent porosity: it poses a trade-off between beneficial gas exchange of CO_2 and O_2 for cell culture in the device and detrimental diffusion of small-sized unintended substances that may alter the microenvironment that has been supplied for the biological assay (Niu and deMello, 2012, Joensson and Andersson Svahn, 2012).

1.7.2.4 Microfluidic pumps

Maintaining droplet formation and posterior stream flow for sufficiently long periods of time in view of microfluidic characterisation is a process that comes irremediably assisted by diverse types of pumps. Peristaltic and syringe pumps adjust adequately for cell sorting assays since the samples never come in contact with the pump. This resolves the issue of contamination, especially undesirable in cellular contexts. Peristaltic pumps are constructed according to a mechanism where pressure exerted onto a flexible conduit displaces the fluid carried inside. A rotor that is composed of a certain number of rollers places pressure on localised positions as it rotates both in clockwise and anti-clockwise directions. Liquid is forced through the conduit in an oscillatory pressure. Peristatic pumps are present in open or closed loop variation, depending on whether they allow reservoir refilling or fluid recirculation. The main obstacle existing for these pumps is the pinching phenomenon that tubes may undergo, causing them to occlude, which may transfer harmful pressures onto cells.

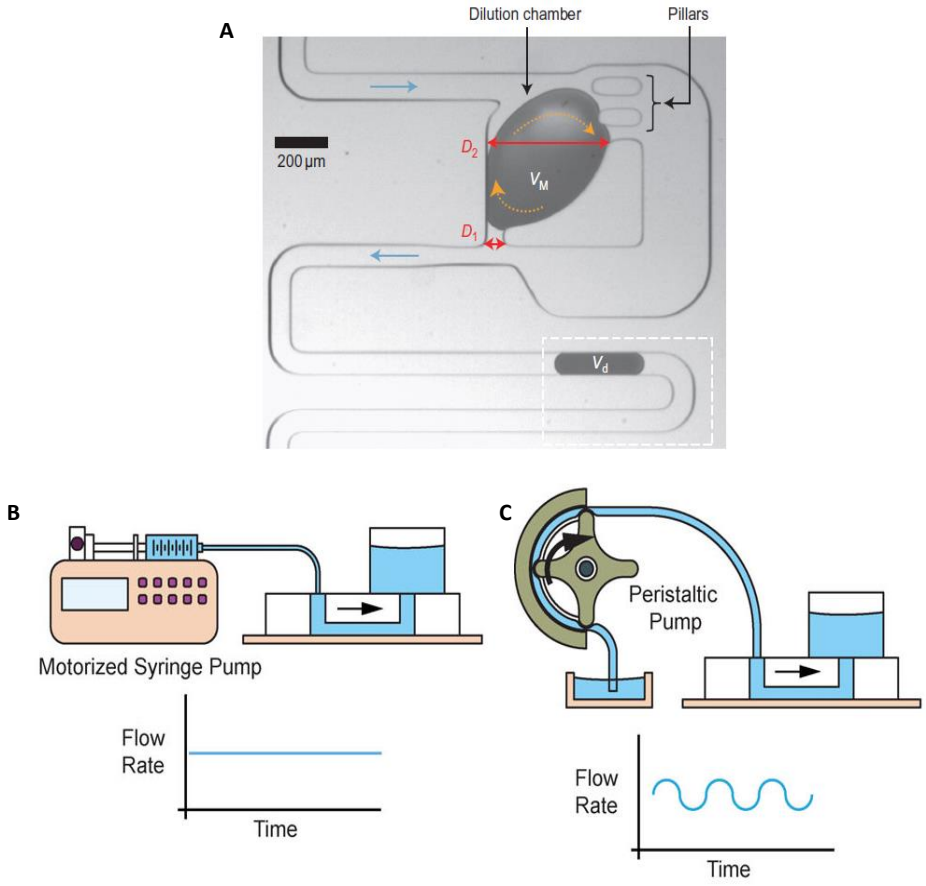

Figure 1.10 Droplet dilution and microfluidic pumps: (A) Schematic of dilution passive operational unit, adapted from Niu et al. (2011). (B) Syringe pump with graphic representation of constant infuse rate and (C) Peristaltic pump with graphic representation of oscillatory flow, both adapted from Byun et al. (2014).

Additionally, some components of peristaltic pumps eventually degrade and wear out over time (Figure 1.10C). Similarly, syringe pumps have received plenty of attention because of their broad range of flow control. Pressure is also employed on a liquid conduit but in this case, is intended to propel fluid out of the syringe tip in a constant flow regime that is connected to the microfluidic chip via tubing. One of the limits that they imply is the fact that they are only able to supply the volume enclosed in the syringe capacity reservoir. This may be a problem for upscaling with larger volumes although it is quite acceptable in droplet microfluidics due to the versatility of dilution operational units and the general purpose of reducing the sample volumes for assays. Alternatively, the pumps and the mechanical parts can contribute to make a costly equipment (Figure 1.10B) (Byun et al., 2014).

1.7.3 Droplet microfluidics for cell sorting

A high-throughput droplet microfluidic technique that systematically manages microdroplets with inner volumes of the order of picolitres to nanolitres defies analyte limits of detection in traditional systems. Optical techniques (e.g. UV-visible absorption, Fourier Transform Infrared spectroscopy or

FTIR, Nuclear Magnetic Resonance or NMR, Raman spectroscopy, phase-contrast for refractive index variations) and analytical chemistry methods (e.g. Liquid Chromatography or LC, Capillary Electrophoresis or CE, Dielectrophoresis or DEP Mass spectroscopy or MS) that have proved successful for droplets in the microlitre scale fall short in the nanolitre scale or subnanolitre scale as the working volumes are above a few microlitres. New detection methods are constantly being optimised to overcome this barrier. Fluorescence assays are of great interest because they represent a way to quantify the concentration of molecules with excellent sensitivity in cell cultures that allow to compare viability and future development prospects. Close monitoring and cell sorting take into account the intensity of the signal emitted by these fluorescent agents that bind to these proteins and sort them accordingly. As previously detailed, FACS has been widely incorporated in FCM experiments for high-throughput sorting and screening of biomolecular events including cell-protein interactions. Indeed, rates of intracellular analysis of about 10^7 cells/h have been reported with parameters such as size, structure and fluorescence emission signals being measured without interfering negatively in cell metabolism (Chan et al., 2011, Niu and deMello, 2012, Xie et al., 2014, Chuang et al., 2014, Liu et al., 2016). Complementarily, further analysis tools can be aggregated to obtain more complete information about the droplet properties in real time as they move inside the microfluidic device. Basu described the MATLAB algorithm released by his group in 2011 under the name Droplet Morphometry and Velocimetry (DMV). DMV is able to interpolate the droplet shape and size from multiple frames captured over a period of time. The only accessory piece of equipment needed is a high-speed camera in brightfield mode recording digital videos with enough resolution to register refraction index differences between the droplet and the environment that serve to delineate the exact boundaries of the droplet and then infer morphology and diameter (Gu et al., 2011, Guo et al., 2012, Basu, 2013, Niu et al., 2013, Lee et al., 2014, Basova and Foret, 2015).

Droplet microfluidics for cell sorting systems appear frequently in the literature. Brouzes et al. first conducted a fluorescence cytotoxicity assay with an encoded drug library on monocytic U937 cells (myeloid lineage) encapsulated within droplets. Cell viability and growth were analysed quantitatively. Cell survival rates surpassed 80% over 4 days of incubation and were maintained at that consistent level from day 1 suggesting that the 13% cell viability loss was induced by the encapsulation process for the most part, likely to cause cell disruption owing to shear stresses or cell interaction with the surfactant at the interface (Brouzes et al., 2009).

Mazutis et al. prepared a 1:10 ratio mixture of two cell types co-encapsulated in 50 pl droplets to detect the concentration of anti-MYC antibody: 9E10 mouse hybridoma cells that secrete the antibody and human leukaemia K562 cells that do not produce it and were stained with orange CMRA dye. Two beads were then introduced for fluorescence-based sorting as a bead suspension with separate detection and capture antibodies that were subsequently brought together with the

cells mixing in the droplet. Cell compartmentalisation is a clear advantage for antibody recognition given that higher concentrations are rapidly attained in such small volume droplets. No appreciable CMRA release was observed, indicating K562 cell viability and cells were efficiently separated on the basis of antibody release into the compartmentalised droplet (Mazutis et al., 2013).

The power and extent of FACS was tested by Liu et al. Their work on mequaninone (MK, a vitamin participating in human metabolic activities) content in mutant cells from a *Flavobacterium sp*. bacterial strain functionalised with rhodamine (Rh123) concluded that there existed a high correlation between the intensity of recorded fluorescent signals and MK concentration as analysed by High Performance Liquid Chromatography (HPLC). Their findings suggested FACS reliability and fluorescence intensity retention with an approximate loss of 13% after 60 min incubation, as well as high-throughput screening of 30 mutant strains (50000 cells/h) cultured for 120 h (Liu et al., 2016).

The high-throughput opportunities from the application of droplet microfluidics have recently reached the study of aggregates and their biological characteristics. Sart et al. designed a microfluidic chamber pattern for real-time imaging of an array of 500 spheroids contained in agarose gels via droplet pinning (Figure 1.11). Their system allowed to characterise in situ aggregation over time (roundness, aggregate area), viability and multiscale flow cytometry as well as off-chip immunocytochemistry, proliferation and RT-qPCR following droplet recovery. It achieved marked improvement of on-chip 3D culture compared to 2D-culture in tissue culture flasks with significant expression of their albumin functional marker (Sart et al., 2017). They later took this microfluidic technology further to induce droplet fusion in anchored droplets within the microfluidic traps for acetaminophen drug screening of hepatocytes. By sequential injection, the large droplets were first made to invade the circular body of the star-shaped anchors and a second population of smaller droplets was then added to fill the remaining triangular regions. Coalescence was promptly triggered by flushing the platform with an emulsion destabilisation agent (i.e. 1H, 1H, 2H, 2H-Perfluoro-1-octanol; known as PFO) (Tomasi et al., 2018). Lastly, they managed to gain new insight into the signalling pathways driving the development of organoids from self-aggregation of WJSCs. They identified two distinct cell populations in their organoid constructs: inner undifferentiated $CD146^{bright}RUNX2^{-}$ WJSCs and outer $CD146^{dim}RUNX2^{+}$ cells differentiating down the osteogenic lineage that were also expressing COX2, regulator angiogenic markers such as VEGF. They hypothesised that the latter populations with upregulated COX2 expression corresponded with a more active NF-κB (nuclear factor kappa-light-chain-enhancer of activated B cells) signalling pathway encouraging cell survival as N-cadherin and F-actin interactions promote cell aggregation (Sart et al., 2020).

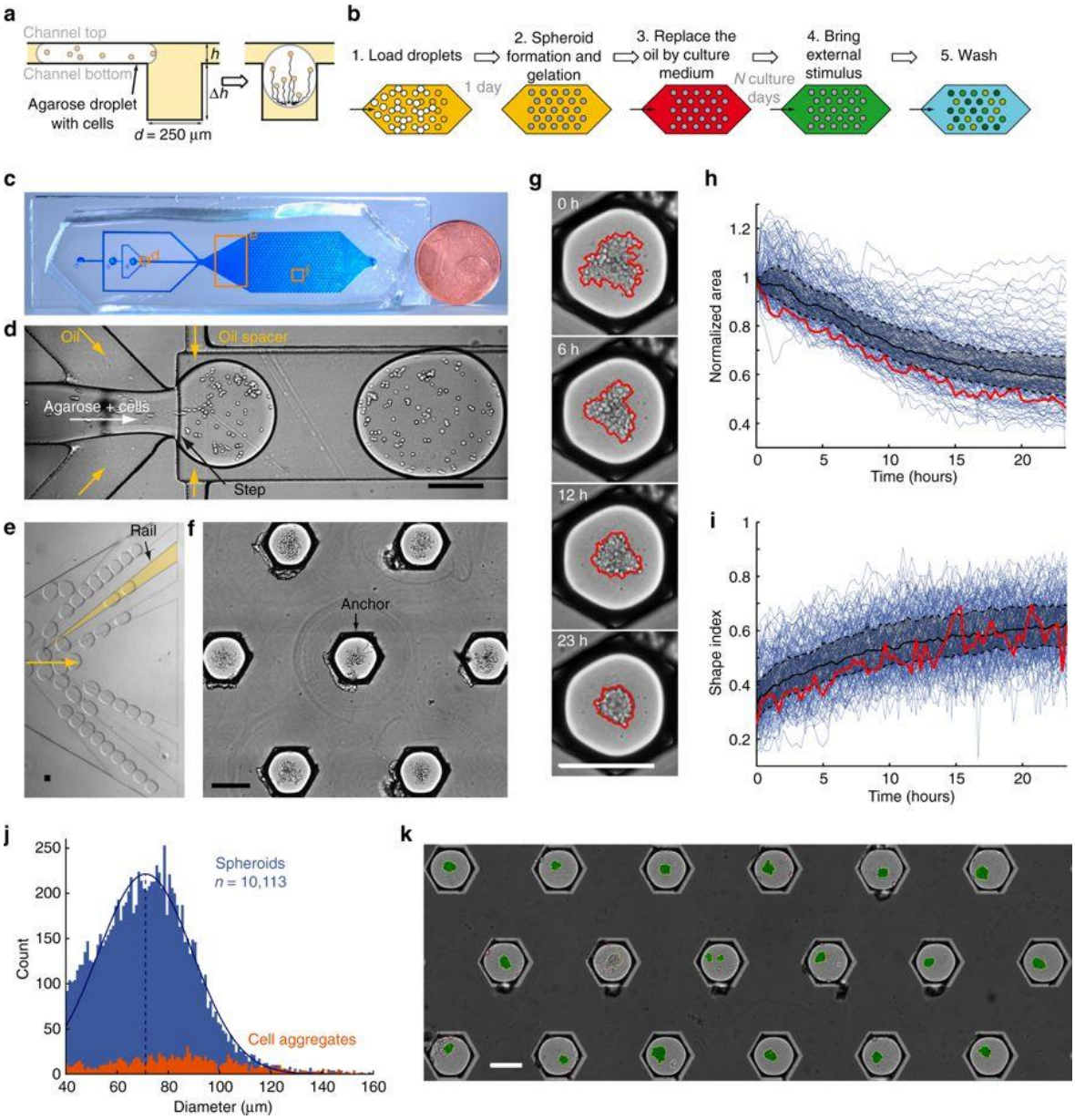

Figure 1.11 Chip design and protocol. **a** Schematic side view of a droplet entering into an anchor that remains trapped due to the reduced surface energy and spheroid formation at the bottom of the droplet after one day of culture (h = 95 µm, Δh = 250 µm, and d = 250 µm). **b** Protocol overview. **c** Photograph of PDMS microfluidic chip. **d** Droplet formation prompted by flow-focussing coupled with a step. **e** Diverging rails distribute the droplets over the width of the culture chamber. **f** Representative anchors with liquid agarose showing the settled cells before spheroid formation. **g** Time lapse of spheroid formation with the red line showing the edge of the detected pattern. **h,i** Kinetics of spheroid formation for n = 152 spheroids. Each blue line represents one spheroid; the red line matches that in g and the black solid and dotted line correspond to the median and first and third quartiles, respectively. **j** Size distribution of all spheroids in 35 chips (blue) and cell aggregates (orange). **k** Image analysis of 18 anchors filled with spheroids stained for LIVE/DEAD. All scale bars are 200 µm. Modified from Sart et al. (2017).

The former studies expose the ambitious projects that can be undertaken through this young droplet microfluidic technique for high-throughput cell monitoring, sorting and screening. If translated to the stem cell field and BMSCs for cartilage tissue regeneration; cell aggregation and its role in enhancing chondrogenesis through an upregulated SOX9 read-out continue to be an

uncharted area to explore. As indicated by Farrell, the problem regarding the low cell viability and inferior mechanical properties of BMSC-derived tissue constructs *in vivo* (e.g. compared to chondrocytes) would be solved if the most robust populations with the set of stimulating conditions could be isolated in order to maximise their potential as articular cartilage tissue producers (Farrell et al., 2014). Droplet microfluidics allows to scale down *in vitro* cartilage differentiation experiments with lower volumes in which there appears a chance to test a large combination of microenvironmental changes in a rapid, automated and less costly manner. Throughout the development of this approach, the question of replicating cartilage native tissue structure and full functionality may be closer to find an answer (Stapleton and Swartz, 2010, Guo et al., 2012).

1.7.4 Human bone marrow cell aggregates in microfluidics

Both 3D spheroid culture and droplet microfluidics are relatively recent disciplines, mostly developed during the last fifteen years. Microfluidic systems for cells focus on assessing the conditions that facilitate physiologically relevant microenvironments for cell proliferation and differentiation (Chou et al., 2015, Zhang et al., 2017b). Furthermore, the advantages of 3D culture have been realised using PDMS extensively as a substrate material to host specific pattern designs and elements that constitute the physical space for seeding, imaging and analysis. The incessant development of microfluidic technologies has thus had a far-reaching effect on the opportunities available that can be translated to tissue engineering and regenerative medicine. For the purpose of this research project, generating droplets to promote cell aggregation entails creating a unique microenvironment for each of the individual spheroids that requires a level of control over cell-seeding density needed, appropriate droplet size and timescale for aggregate formation (Barthes et al., 2014).

Wu discussed the potential of stem cells in microfluidic applications viewed as a representative transitional stage halfway between *in vitro* cell-based assays and *in vivo* animal models (Wu et al., 2011). An example of this concept is the attempt to simulate a model for limb development presented by Occhetta et al. (2015). They assessed chondrogenesis in HBMSC micromasses (77 ± 15 cells) seeded into microwells on a serial dilution generator chip. The aggregates formed within 3 h under continuous flow perfusion. After 7-day culturing in the presence of TGF-β3, they observed on-chip Type II Collagen protein expression indicative of ongoing chondrogenic differentiation (Occhetta et al., 2015). Later, they envisioned the application of their microfluidic tool to find a biochemical treatment for stable chondrogenic commitment of HBMSCs. They established that spheroids subjected to ALK2 and ALK3 receptors targeting BMP signalling inhibition did not affect Type II collagen synthesis but exerted a dose-dependent reduction in *ACAN* and *COL10A1* gene

expression that indicated inferior production of cartilage matrix and a reduction of hypertrophy, respectively (Occhetta et al., 2018).

Other authors have gone one step further to combine microfluidic systems and cell-laden scaffolds. Li et al. synthesised light-cured gelatin norbornene (GelNB) protein microgels cross-linked with poly (ethylene glycol) (PEG) to encapsulate HBMSCs. These microgels were generated by means of a pipette-based microfluidic device consisting two syringes (cell and hydrogel precursor as aqueous phase and 2% Pico-Surf™ in FC40 as carrier oil) attached to needle tips and connected by polytetrafluoroethylene (PTFE) tubes. They cultured the microgels in basal and chondroinductive media, respectively, and assessed them separately. They reported notable type II collagen and aggrecan gene upregulation compared to hydrogel-alone controls and pellet culture, although type I collagen, which is generally predominant in fibrocartilage, was upregulated to a similar extent. This trend was further validated for both collagen types from immunostaining experiments (Li et al., 2017).

The examples above portray the novelty of the droplet microfluidic and spheroids field that are closely intertwined with bioengineering strategies. Various themes have emerged: high-throughput monitoring of on-chip spheroid aggregation over time; biomolecular characterisation of spheroids preceded by aggregate recovery; short-term chondrogenic differentiation of BMSCs on chip; cell-laden hydrogel scaffolds for tissue engineering and biochemical evaluation of the signalling pathway involved in spheroid self-assembly, to name but a few. Nonetheless, there is no evidence of droplet microfluidics being widely used for aggregation from small cell numbers below tens of cells alongside the integration of early functional chondrogenic markers like SOX9 to sort HBMSC chondroprogenitors for cartilage tissue engineering. Bringing both aspects together could contribute to delineating a new practical approach that could be adapted to the clinic.

1.8 Conclusions

To summarise, the prevalence of musculoskeletal diseases that prove damaging to cartilage motivates continuous momentum to place cartilage tissue engineering within the global paradigm of regenerative medicine. Cartilage extracellular matrix (i.e. architecture, structure, biomolecular elements, signalling pathways, biomechanical responses) is a remarkably complex ensemble. An equally complicated chondrogenesis development that is yet to be fully understood raises doubts with respect to the optimal culture conditions that must be supplied for reproducible healthy cartilage regeneration. HBMSCs are a potential stem cell source for cartilage tissue engineering yet subpopulation heterogeneity poses a challenge to isolate chondroprogenitors that the current sorting strategies based on cell surface markers have failed to overcome.

Droplet microfluidics is a novel technique that enables high-throughput generation sorting and functional assessment of cells relying on substrate materials such as biocompatible PDMS chips apt for cell culture. The current research project seeks to potentially scale down 3D scaffold-free pellet culture of HBMSC microaggregates to droplets containing anything from single cells to tens of cells generated on a microfluidic platform and cultured off-chip. There is no definitive set of chondrogenic cell surface markers to isolate the promising HBMSC fraction for articular cartilage tissue engineering from the heterogeneous HBMSC populations as extracted directly from human donors. The strategy proposed consists in harnessing droplet microfluidics to sort early stage HBMSC subpopulations that express a functional marker indicative of chondrogenesis and triggered during cell aggregation in microdroplets, SOX9. The complex issue of regenerating articular cartilage is thus reduced to a drop by drop process on an innovative microfluidic-based system that may well hold the key to finally producing competent native-like tissue.

1.9 Project hypotheses and aims

HBMSCs offer promising self-renewal capacity and hold potential for inducing differentiation into cartilage tissue. However, their application to restore hyaline articular cartilage is hindered by subpopulation heterogeneity and development of mechanically inferior fibrocartilage or the terminal hypertrophic chondrocyte phenotype.

The project stands on the **general hypothesis** that **HBMSC aggregation enhances early *SOX9* expression and that small cell aggregates can be cultured using droplet microfluidics and sorted on the basis of their early *SOX9* expression.** This approach investigates SOX9 as an early functional chondrogenic marker expressed at the condensation stage of cartilage development, which is decisive for chondrogenic differentiation. The current study provides proof of concept for the implementation of droplet microfluidics for functional assessment of small cell aggregates. Small cell aggregates cultured in a 3D environment have been reported to display upregulated expression of chondrogenic genes including *SOX9* compared to single cells, and scaling inversely with cell number (see section 1.6.2). They are thus the focus of this research work seeking to exclude high cell numbers masking the true cell-cell niche optimal for cartilage formation and to increase throughput for analysis. Ultimately, this project envisions the goal of high-throughput screening and sorting of aggregates with high chondrogenic potential for cartilage tissue engineering by means of the functional marker SOX9. This major hypothesis requires previous testing and validation of five other sub-hypotheses:

1) *Multicellular spheroids are an appropriate model to study chondrogenesis in vitro.*

2) *A microfluidic platform can be designed and optimised for high-throughput droplet generation and stability.*

3) *Cells encapsulated in microdroplets form aggregates prompted by gravity in the confinement of a sphere while remaining viable and functional for short-term culture.*

4) *Cell aggregation in microdroplets promotes SOX9 expression in short-term chondrogenic culture conditions compared to standard in vitro cells in monolayer.*

5) *Heterogeneities in SOX9 expression across bone marrow cell subpopulations can be detected and used to harness those that will develop into robust cartilage.*

The first sub-hypothesis involves the harvesting and growth of HBMSCs in conjunction with the appropriate set of growth factors to induce chondrogenic differentiation across various cell numbers, thus bridging the gap between microfluidics and pellet culture.

Optimising the microfluidic chip design and operation is a fundamental step towards achieving a functional device according to the second sub-hypothesis. The cells encapsulated in microdroplets can be monitored, screened and sorted without altering their differentiation outcome. The ability to emit thousands of droplets per second exposes the high-throughput potential of such device. This is reinforced by the joint comparative simplicity and cost reduction coming from using very small volumes of culture media and manufacturing microfluidic chips compared to other techniques, namely robotic assisted dilution and microarrays.

Finally, the crucial point and the uniqueness of this research lies in the translation of *in vitro* chondrogenic differentiation to a microfluidic platform via HBMSC self-assembly into aggregates in microdroplets. With this novel engineering technology, a synergistic effect is desired seeking to address the problem of HBMSC heterogeneity by promoting robust chondrogenesis. Cell aggregates need to form and remain viable long enough to ensure *SOX9* expression, which occurs during the early condensation stage of chondrogenic development.

The ultimate vision beyond this work would be to develop a cell aggregate sorting approach implemented on unselected HBMSC populations. SOX9 would therefore dictate sorting according to varying fluorescence intensity levels. Once sorted, the cell aggregates would merge into macroaggregates that could be characterised after pellet culture to assess the quality of the cartilage tissue generated. The analysis would stand on the assumption that high fluorescent levels indicating abundant SOX9 expression yield robust cartilage, as opposed to poor cartilage stemming from aggregates emitting low levels of fluorescence (Figure 1.12). By perfecting the isolation step,

new prospects of effective stem cell fraction harnessing would arise for their application in cartilage tissue engineering.

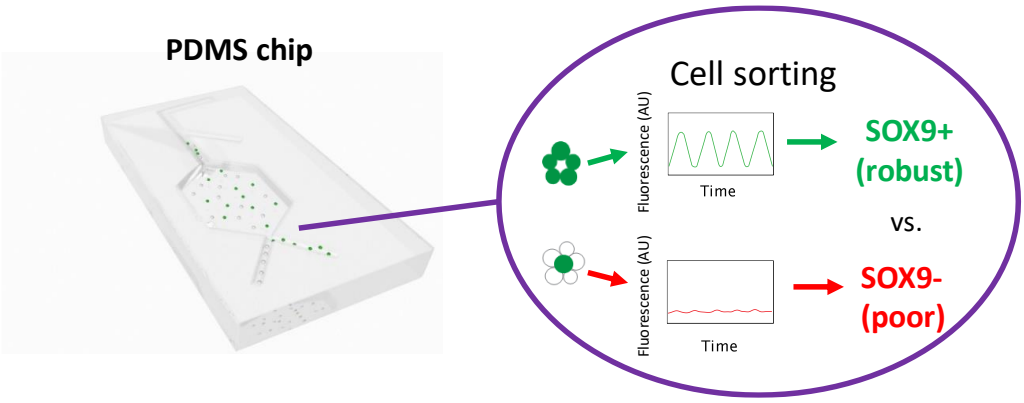

Figure 1.12 Schematic of ultimate project hypothesis: cells forming multicellular spheroids cultured in chambers within PDMS chips can be sorted at one end (cell sorting region) in terms of fluorescent emission from SOX9 mRNA probes binding. High fluorescence intensities (green) would indicate high SOX9 expression and lead to robust cartilage generation, whilst low fluorescence intensities (red) would yield poor cartilage-producing cell populations.

The project aim is to achieve high-throughput cell aggregation simulating early chondrogenic condensation with a view to enriching HBMSC chondroprogenitor subpopulations on the basis of functional, condensation-dependent markers such as SOX9. Droplet microfluidics will be incorporated for high-throughput assembly, monitoring and characterisation of HBMSC aggregates. Three different areas are thus involved in the development of this research work; namely stem cell culture, cartilage tissue engineering and droplet microfluidics.

This research work can be divided into the following objectives:

1. To identify the ability of unselected subpopulations to generate articular cartilage tissue to address relevant aspects for the development of the microfluidic platform for sorting of cell aggregates, i.e. timelines for cell aggregation and SOX9 expression (**Chapter 3**).

    - To study cell aggregation during chondrogenic differentiation focussing on earlier time points and extending over long-term culture to register gradual size changes.

    - To evaluate the chondrogenic potential of HBMSC spheroids across various cell numbers when directed towards chondrogenic differentiation via growth factors.

    - To establish the pattern for SOX9 expression in unselected human bone marrow cell spheroids in relation to the microfluidic cell sorting procedure to be developed.

- To characterise SOX9 heterogeneity in HBMSC spheroids taking into consideration cell number, time, donor, replicates and cell subpopulations within spheroids.

Experimental hypothesis 1: The temporal expression pattern of SOX9 in HBMSC aggregates is compatible with a short period of incubation in microdroplets.

Experimental hypothesis 2: Chondrogenesis in HBMSCs is dependent on cell number down to the scale achievable using droplet microfluidics; i.e. cell aggregation dynamics; histological structure and temporal expression pattern of SOX9.

Experimental hypothesis 3: SOX9 has a heterogeneous expression pattern among HBMSC subpopulations that could be used as a criterion for high-throughput sorting of cell aggregates.

2. To assess the suitability and reliability of a nanoflare strategy for detection and quantification of *SOX9* mRNA transcripts in subpopulations of the live HBMSC population with a view to integrating this strategy for the sorting of small aggregates assembled in droplets generated on a microfluidic platform (**Chapter 4**).

    - To confirm *SOX9*-Cy5 nanoflare uptake by HBMSCs through a quantifiable fluorescent Cy5 signal emitted by targeted cells.

    - To establish a method for *SOX9*-Cy5 nanoflare incubation for specific binding to *SOX9* mRNA transcripts in HBMSCs.

    - To validate that the FACS Cy5-positive fluorescent signal from the cells exposed to *SOX9*-Cy5 nanoflares corresponds to potent chondroprogenitor cells within the HBMSC population

Experimental hypothesis: S*OX9*-Cy5 nanoflares can be used to identify HBMSC populations with high *SOX9* expression.

3. To establish the range of droplet sizes and monodispersity attainable for stable flow in microfluidic devices and encapsulation of cell aggregates in separate compartments as a function of flow rate. The variables delineating the sequence of experiments leading to device optimisation include fabrication method, channel geometry, channel dimensions and channel design (**Chapter 5**).

Experimental hypothesis: Droplet microfluidics can provide stable droplet generation within sizes that are relevant for the formation and culture of cell aggregates within microdroplets.

4. To establish a biocompatible environment by means of a microfluidic device for stabilisation of multiple droplets containing cells. Subsequently, this will allow sufficient culture duration to trigger *SOX9* expression with a view to sorting for the most promising populations with chondrogenic prospects (**Chapter 6**).

    - To confirm the ability of cells to aggregate indicating chondrogenic condensation and to define time and cell density required for viable cell aggregation in microdroplets.
    - To devise a high-throughput droplet microfluidic generation strategy for efficient monitoring, screening and future sorting of aggregates.
    - To characterise aggregate functionality after incubation in microdroplets.
    - To test the main project hypothesis that aggregates formed inside microdroplets experience *SOX9* upregulation compared to monolayer cultures

Experimental hypothesis: HBMSCs self-assemble into aggregates within spherical microdroplets in a PDMS microfluidic device and can be cultured long enough to sort the aggregates on the basis of *SOX9* expression to harness the most robust cartilage-producing populations.

Chapter 2: General methods

In this section, some general techniques are included with the objective of framing the context of this research work by providing a brief background on common methodologies employed. The detailed complementary list of the materials and equipment used in this project is in Appendix A.

2.1 Isolation of unselected human bone marrow stromal cells

HBMSCs were extracted from unscreened human patients undergoing total hip replacement or femoral fracture surgery at Southampton General Hospital and Spire Southampton Hospital. The bone marrow tissue handled for this purpose as approved by the Southampton General Hospital and South West Hants Local Research Ethics Committee would otherwise have been discarded.

The isolation procedure relied on plastic adherence on tissue culture plastic (TCP) of mononucleated cells from the bone marrow that attach preferentially, whereas hematopoietic cells remain in suspension and can be removed after sequential washings during culture expansion.

The tube containing the bone marrow sample was filled with 10 ml αMEM (Lonza, UK) containing 1% Penicillin-Streptomycin (P/S, 100 U/ml potassium penicillin and 100 µg/ml streptomycin sulphate, Lonza, UK) (v/v) and shaken vigorously before pouring its content into another tube to maximise cell yield (Figure 2.1).

The tube containing the cell suspension was centrifuged at 272 g for 4 min, the supernatant carefully discarded, and the cell pellet resuspended in 20 ml αMEM. A Fisherbrand™ 70 µm sterile cell strainer was placed on a new tube to remove any existing blood clots or bone chips.

Cells were counted with 0.1% acetic acid (v/v) (Sigma-Aldrich, UK) and 1:1 Trypan Blue (Sigma-Aldrich, UK) dilution (v/v) by mixing 50 µl cell suspension and the same volume of 0.1% acetic acid for red blood cell lysis and then 100 µl Trypan Blue for contrast. The remaining cell suspension was centrifuged again at 272 g for 5 min and the resuspended cells were aliquotted in flasks for culture and expansion by seeding approximately 2×10^7 cells in T75 flasks or 2×10^8 cells in T175 flasks. The composition of the culture medium was: αMEM + 10% FBS (v/v) (Foetal Bovine Serum, Life Technologies, UK) + 1% P/S (v/v).

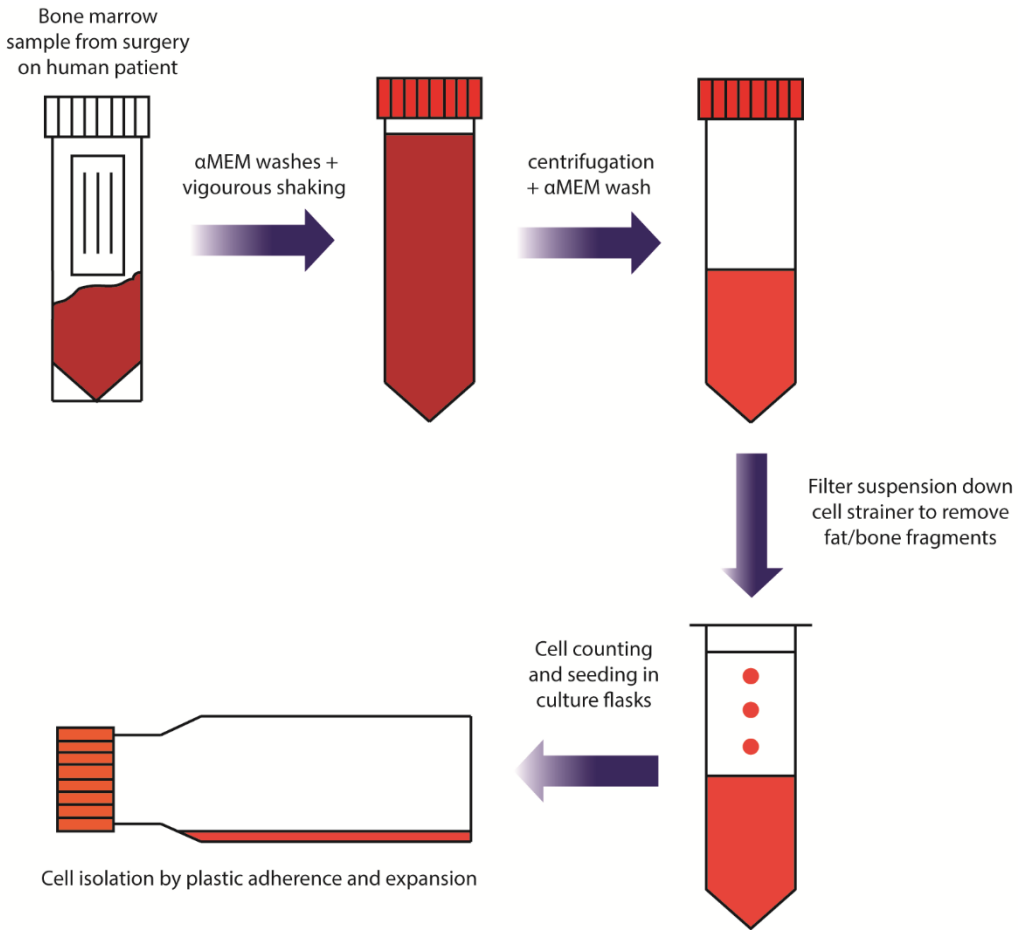

Figure 2.1 Schematic of bone marrow cell isolation protocol from human samples.

2.2 Isolation of human articular chondrocytes from femoral heads

In addition to bone marrow samples, femoral heads were sourced from human patients undergoing similar surgeries at Southampton General Hospital and Spire Southampton Hospital according to availability. Before handling femoral heads, and to assess the degree of osteoarthritis, a visual inspection of the human femoral head was routinely undertaken. Following suitability verification, a Petri dish was prepared with enough sterile DPBS (Dulbecco's Phosphate-Buffered Saline, Lonza) to cover cartilage tissue and to maintain hydration.

a) Using a sterile disposable scalpel (Swann-Morton, UK), articular cartilage strips were cut into 1 mm^2 pieces and placed in a 50 ml conical tube.

b) The cartilage strips were subjected to an enzymatic incubation cycle. Enzymes were prepared before handling tissue and volumes of 2-5 ml were consistently added to the tube containing cartilage strips depending on the amount of tissue collected to ensure that it was fully immersed in the enzymatic solution. The sequence of addition followed this particular order, washing with DPBS between enzymes:

1) T/E (Trypsin-EDTA, 1700000 U/l trypsin, 2 g/l EDTA, Lonza, UK) was diluted to 1X from 10X stock by adding 9 ml sterile DPBS. The samples were incubated for 30 min at 37°C as a pre-digestion step with manual shaking every 10 min.

2) Hyaluronidase (from bovine testes, Sigma-Aldrich, UK) was dissolved at a concentration of 1 mg/ml sterile DPBS and the solution was sterilised using a 0.2 µm sterile syringe filter (Filtropur S 0.2, Sarstedt, Germany). An incubation period of 15 min at 37°C with a manual shaking after 7.5 min enabled PG digestion in the extracellular matrix by hyaluronidase.

3) Collagenase B (from *Clostridium histolyticum*, Sigma-Aldrich, UK) was prepared as 10 mg/ml serum-free αMEM + 1% P/S (v/v). The enzyme suspension was vortexed and left to dissolve on a roller while handling the femoral head to digest the collagen molecules in the extracellular matrix and release chondrocytes from cartilage. An overnight incubation on an orbital shaker at 37 °C or a shaking incubator was applied to enhance digestion, but no longer than 15 h to avoid loss of cell viability.

c) Following overnight incubation, a volume of 5 ml αMEM + 1% P/S (v/v) was added to the digested cell suspension and filter-sterilised through a 70 µm cell strainer into a 50 ml conical tube to separate human articular cells (HACs) from undigested matrix. The cell suspension was centrifuged at 272 g for 10 min and resuspended in 10 ml DMEM-F12 (Life Technologies, UK) + 1% P/S (v/v) for cell counting and then distributed in flasks for expansion in chondrogenic culture medium: DMEM-F12 + 5% FBS (v/v) + 1X ITS (10 µg/ml insulin; 5.5 µg/ml transferrin; and 5 ng/ml selenium; 1:100 volume dilution from 100X stock solution, Sigma-Aldrich, UK) + 100 µM ascorbate-2-phosphate (A2P, Sigma-Aldrich, UK) + 1% P/S (v/v).

2.3 Cell culture

Three different cell types were used: a control chondroprogenitor cell line, ATDC5, and two human primary cell types: HBMSCs and HACs. The cells were expanded in monolayer culture as detailed below.

2.3.1 ATDC5 teratocarcinoma-derived murine cells

The ATDC5 chondroprogenitor murine cell line was purchased from Lonza. These cells were used supplemented with DMEM (Dulbecco's Modified Eagle Medium with 4.5 g/l Glucose with L-

Glutamine, Lonza), 5% FBS (v/v), 1X ITS and 1% P/S (v/v), for culturing (Table 2.1). The cells were consistently expanded and passaged below 70% confluence.

2.3.2 HBMSCs

The resulting human bone marrow cells from direct isolation from human samples were cultured in αMEM +10% FBS (v/v) + 1% P/S (v/v) and washed three days following isolation to remove non-adherent hematopoietic cells, leaving enough time for HBMSCs to adhere (Table 2.1). Subsequent washes and media changes every three days further assisted in enriching the adherent populations expanded from multiple colonies. The cells were harvested or passaged once they became 80-90% confluent.

2.3.3 HACs

Human articular chondrocytes were cultured in DMEM/F-12 (Life Technologies, UK) + 5% FBS (v/v) + 1X ITS + 100 µM A2P + 1% P/S (v/v) chondrogenic medium to promote maintenance of their chondrocyte phenotype against fibroblastic dedifferentiation. Media changes were performed every three days and the cells were used or passaged from multiple colonies at 80-90% confluence.

Table 2.1 Cell types employed in this project with their corresponding media employed for culture and expansion. The concentrations of supplements presented in % refer to volume percents.

ATDC5	hBMMNCs	HACs
DMEM + 5% FBS + 1X ITS + 1% P/S	αMEM + 10% FBS + 1% P/S	DMEM-F12 + 5% FBS + 1X ITS + 100 µM A2P + 1% P/S

2.3.4 Chondrogenic differentiation in 96-well ultra-low adherence microplates

Chondrogenic differentiation studies were systematically carried out using BRAND inertGrade 96-well round-bottom microplates. This culture platform was selected due to its 'ultra-low adherence' treatment that prevents cell aggregates from attaching to the bottom of the well, thus creating a 3D environment for pellet culture. In addition, the small well dimensions allowed for a reduction of the culture volume (200 µl/well as opposed to 1 ml used for pellet culture in tubes) along with in-situ characterisation while culturing and scale-up of the number of samples tested per experiment. Additionally, it was a unique way to address chondrogenesis for small cell numbers to bridge the gap between droplet microfluidics and conventional pellet culture for cartilage tissue engineering applications. The use of these plates presented an extra advantage in terms of testing several cell seeding densities and time points on the same plate; both of great interest for this research project.

All the cell types included in the previous section were trypsinised using 1X T/E and incubated at 37°C and 5% CO_2 for 5 min to detach cell monolayers. For HBMSCs, collagenase type IV (Life Technologies, UK) was added by diluting the 2% (w/v) stock solution in serum-free αMEM at 1% (v/v) to break up the collagen matrix of 80-90% confluent cultures and incubated with cells for 30 min prior to trypsinisation. The cells were then centrifuged at 272 g for 5 min, counted and seeded in the microwells at various cell densities: 500, 5000, 50000 and 500000 cells/well; by aliquoting 200 µl chondrogenic differentiation medium in each of them. The chondrogenic medium for ATDC5 cells comprised DMEM supplemented with 5% FBS (v/v), 1X ITS, 100 µM A2P, 10 nM dexamethasone (Sigma-Aldrich, UK), 10 ng/ml TGF-β3 (Peprotech) and 1% P/S (v/v) (Tare et al., 2005). Alternatively, the chondrogenic differentiation medium was modified for primary HBMSCs and HACs, using higher grade αMEM and removing FBS. The absence of FBS for chondrogenic differentiation has been endorsed as a means to reduce risks of infection and experimental variability given by interactions between the proteins in the serum composition and growth factors (Bilgen et al., 2007, Kamil et al., 2007). The cells were incubated in an incubator at 37°C, 20% O_2 and 5% CO_2 and aggregated forming multicellular spheroids after up to 3 days regardless of cell density. The chondrogenic differentiation medium was replaced every 3 days during the entire period of culture; which was followed by spheroid characterisation (Figure 2.2, e.g. time lapse analysis, histology, molecular biology).

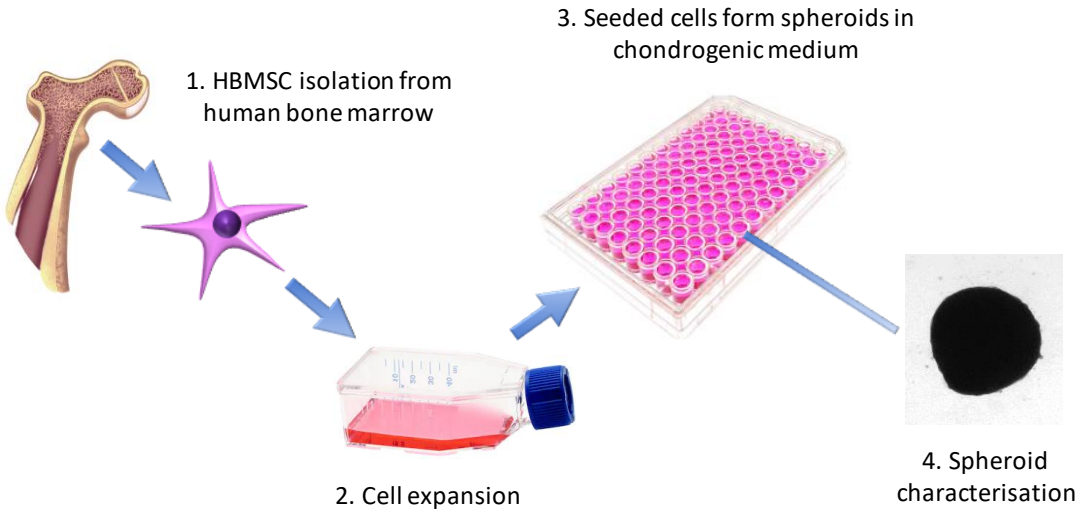

Figure 2.2 Schematic example of chondrogenic differentiation experiment for HBMSCs from isolation to scaffold-free pellet culture of multicellular spheroids in ultra-low adherence multiwell plates.

2.4 Microscopic characterisation of cells and multicellular spheroids

Cells and multicellular spheroids were routinely monitored through a range of microscopy techniques depending on the aspects to assess and the methods used for sample processing (i.e.

characterisation of cells in culture flasks, well plates, sections on slides, encapsulated cells in microdroplets). The below sections cover the most relevant microscopy settings and their applications throughout this research work.

2.4.1 Transmitted light microscopy and fluorescence light microscopy

Two separate pieces of equipment supported transmitted light microscopy (TLM) and fluorescence light microscopy (FLM) imaging: a Carl Zeiss AxioVert 200 Inverted Microscope and a Nikon Eclipse Ti Inverted Microscope. The former ran on the Axiovision Rel. 4.8 software and acquired images with either an AxioCam MR3 (monochromatic) or an AxioCam HR (colour) camera and the following set of objectives and magnifications: A-Plan 2.5x/0.06, A-Plan 5x/0.12, A-Plan 10x/0.20 Ph1Var1 and LD A-Plan 20x/0.30 Ph1Var1. The latter operated on the NIS-Elements software. Images were captured with a Nikon Digital Sight DS-Qi1Mc camera) using CFI Plan Fluor Series for Phase Contrast (DL) objectives (i.e. 4x/0.13 PhL DL, and 10x/0.25 Ph1 DL magnification) and a Plan Fluor ELWD 20x/0.45 magnification objective.

TLM imaging modes on the Carl Zeiss AxioVert 200 microscope included H/DIC (Differential Interference Contrast) and Phase contrast (0,1 and 2). H/DIC and the AxioCam HR were used to image colour stained samples such as cells and colonies on wells and spheroid sections on slides. The Phase Contrast modes and the AxioCam MR3 were optimal to resolve details in cells and spheroids growing in tissue culture plastic flasks or wells, as well as single cells and small aggregates encapsulated in microdroplets. FLM on the Carl Zeiss AxioVert 200 microscope relied on a X-Cite® Series 120 Q fluorescence lamp and a set of three fluorescent filters: DAPI (excitation 365 nm; emission 420 nm), FITC (fluorescein isothiocyanate; excitation 485/20 nm, emission 515 nm) and TRITC (tetramethylrhodamine; excitation 510-560 nm, emission 590 nm) . FITC and TRITC were used for imaging of cells in droplets for viability assays.

Nikon TL mode was best suited for cell imaging of colonies and aggregates on well plates while recording their position for time-dependent studies. FLM on the Nikon functioned through DAPI (excitation 395/25 nm, emission 460/50 nm), GFP (green fluorescent protein; excitation 470/40 nm, emission 525/50 nm), Cy3 (cyanine 3; excitation 535/40 nm, emission 590/40 nm) and Cy5 (cyanine 5; excitation 620/60 nm, emission 460/50 nm), DAPI filters, CoolLED pE-100 Illumination system for fluorescence. FLM was mainly used for observation of immunostained sections emitting with Alexa Fluor 488 and counterstained with DAPI. The Cy5 filter was used detection of Cy5-nanoflares fluorescence signal when cultured with cells.

2.4.2 Time-lapse microscopy

Time-lapse microscopy enabled the study of biological phenomena and changes in cell cultures over time. The Nikon Eclipse Ti microscope incorporated time lapse functionality with optional TLM and FLM additions. TLM was compatible with cell aggregation assays on leading to ATDC5/HBMSC/HAC spheroid formation on ultra-low adherence multiwell plates. FLM-assisted time lapse microscopy served to investigate nanoflare uptake in monolayer cultures.

2.4.3 Confocal microscopy

A Leica TCS SP5 microscope was used to characterise the immunofluorescent staining of whole mount cell aggregates made up of 500 and 5000 cells using similar antibody reagents as the immunofluorescent sections (i.e. Alexa Fluor 488 for the secondary antibody and DAPI as a counterstaining for cell nuclei). The samples were imaged immersed in a wet buffer consisting of 100 µl 80% glycerol (v/v) (Sigma-Aldrich, UK) and 20% 1X PBS (v/v) on glass bottom 8-well microchamber slides (ibidi, Germany). The HCX PL FLUOTAR 10x/0.30 PH dry objective was compatible with small aggregates on well plates that were not compact enough to be transferred to chamber slides, whilst the HC PL APO lambda blue 20x/0.70 IMM UV glycerol objective was the generally preferred option for imaging spheroids on microchamber slides.

The software Leica Application Suite X (LAS X) version 3.7.0 was used for image acquisition and analysis. Sequential scanning between frames was executed at a scan speed of 600 Hz and a step size of 4.99 µm to build the stacked planes of each spheroid taken from the middle section towards the top to avoid accounting for any interference of DAPI signal into the Alexa Fluor 488 (AF488) channel. Table 2.2 below contains a description of the optical hardware settings for the sequential scanning performed.

Table 2.2 General sequential hardware settings for the Leica TCS SP5 confocal microscope.

Sequential scanning 1		**Sequential scanning 2**	
Excitation laser line wavelength		*Excitation laser line wavelength*	
405 nm	Intensity: 30%	405 nm	Intensity: 30%
488 nm	Intensity: 0%	488 nm	Intensity: 0%
Active emission channel bandwiths		*Active emission channel bandwiths*	
DAPI (414 – 475 nm)	Offset: -1%	AF488 (497 – 600 nm)	Offset: -1%
Transmitted light channel	Offset: 0%		

2.5 Statistical analysis

Statistical analysis was carried out using GraphPad Prism version 8.2.1 software. Statistical significance was determined on the basis of the p value computed after completing any given statistical analysis. P values were reported in accordance with the GraphPad style, which defines levels of statistical significance through the number of asterisks assigned to them. Thus, no statistical significance (ns) corresponded to $p > 0.05$ and significance was considered from p values below 0.05 (i.e. less than 5% probability that the results did not provide support for the research hypothesis being tested). Significance was represented using * to refer to p values between 0.05 and 0.01; moderate significance was shown using ** for p values between 0.01 and 0.001; high significance was depicted using *** for p values between 0.001 and 0.0001 and extreme significance was displayed for p values below 0.0001 through ****. A hash (#) symbol was analogously used in time-dependent assays to represent statistical differences between different groups belonging to the same time point.

One-Way ANOVA (analysis of variances) was employed to assess any statistical differences between the means of three or more unpaired groups. Welch and Brown-Forsythe tests were added for sample groups that did not have equal variances. Two-way ANOVA statistical analysis was conducted when the effect of two variables or factors was being examined.

2.6 Histological techniques

The histological characteristics of the tissue generated in chondrogenic differentiation cultures were studied to determine its resemblance to articular cartilage-like tissue generated in the same conditions. For that purpose, unselected HBMSCs sections were compared to a theoretical chondroprogenitor control, ATDC5, and a human positive control cell type, HACs. The spheroid samples from chondrogenic differentiation were fixed in 4% PFA (w/v) (Paraformaldehyde, Thermo Fisher Scientific, UK) overnight. After processing in graded ethanol concentrations (v/v) (50%, 90% and two separate 100%, VWR, UK) for 30 min, once in 50% ethanol/Histo-Clear (v/v) (National Diagnostics™, UK) and twice in 100% Histo-Clear (v/v) for 30 min, the samples were embedded in paraffin (Thermo Fisher Scientific, UK) and sectioned at 5 µm thickness using a HM 325 rotary microtome (Thermo Fisher Scientific, UK).

2.6.1 Alcian Blue/Sirius red (A/S) staining

Alcian blue targets PG-rich regions of cartilage matrix, whereas Sirius red stains preferentially the areas in which collagen is predominant. Pre-warmed slides at 37°C in an IWC 200 insulated drying

cabinet (Thermo Fisher Scientific, UK) were de-waxed and cleared through two 100% (v/v) Histo-Clear baths for 7 min each, rehydrated in a descending series of graded ethanols (v/v) (100%, 100%, 90% and 50%) for 2 min each and a water bath for 10 min. Weigert's Haematoxylin (Clin-Tech Ltd., UK) was employed to stain cell nuclei by applying directly onto samples and covering them for 10 min in the dark. Excess haematoxylin was removed by dipping the slides in acid alcohol (1% HCl (v/v) in 70% ethanol (v/v), HCl supplied by ACROS Organics^{TM}, Thermo Fisher Scientific, UK) 2-4 times depending on staining strength. The samples were subsequently stained with 0.5% Alcian Blue 8GX (w/v) (Sigma-Aldrich, UK) containing 1% acetic acid (v/v) (Sigma-Aldrich, UK) for 10 min, washed, exposed to 1% aqueous phosphomolybdic acid (w/v) (ACROS Organics^{TM}, Thermo Fisher Scientific, UK) to enhance Sirius red staining by improving collagen contrast for 10 min and stained in 0.1% Sirius Red F3B in saturated picric acid (w/v) (Clin-Tech Limited, UK) for 45 min to 1h (Dolber and Spach, 1987). The slides were finally dehydrated in ascending ethanol concentrations (v/v) (50%, 90%, 100% and 100%) and in two Histo-Clear solutions for 30 s each and mounted using DPX in a fumehood (Thermo Fisher Scientific, UK).

2.6.2 Safranin O (SO) staining

Safranin O reveals the presence of cartilaginous matrix, which appears in various shades of red whose intensity scales directly with the sGAG content of the sample of interest. The slides were treated in a similar manner to that described for A/S staining. Once cell nuclei were counterstained with Weigert's Haematoxylin, the slides were rinsed in 1% acetic acid (v/v) for 10-15 s and stained in in 0.1% Safranin O (w/v) (Sigma-Aldrich, UK) for 15 min, followed by dehydration, clearing and mounting (similar procedure to A/S staining).

2.7 Immunohistochemical staining of spheroid sections and whole mount samples

Immunohistochemistry (IHC) is a technique that relies on the specificity of antibody-antigen binding to detect the presence of target proteins (antigens) in the sample tissue as well as localise their distribution at a cellular level. The interaction between antibody-antigen can be visualised via highly sensitive markers or labels such as fluorophores (fluorescent dyes) and enzymes linked to the primary antibody; also known as secondary antibodies. The proteins targeted were nuclear SOX9 as an early chondrogenic marker in cells, type II collagen cartilage-specific collagen type and aggrecan as an indicator of PG synthesis and present in the extracellular matrix. Antigen retrieval methods were applied to counteract any negative effects derived from the exposure to PFA formalin fixative, which may cause alterations in protein conformation rendering the epitopes on

the antigen target protein inaccessible (Ramos-Vara, 2011, Kabiraj et al., 2015, Zhang et al., 2017a). Protease-induced epitope retrieval (PIER) with hyaluronidase was selected to unmask collagen epitopes (Hendrix et al., 1982, Roberts et al., 2009). Alternatively, a more aggressive heat-induced epitope retrieval (HIER) on slides placed in a citrate buffer at 95°C was carried out for detection of nuclear SOX9 and aggrecan in the extracellular matrix (Krahl and Sellheyer, 2010, Ramos-Vara, 2011, Lacerda et al., 2013).

BSA (Bovine Serum Albumin, Thermo Fisher Scientific, UK) was used as a standard protein blocker to minimise non-specific binding by the primary antibody (Xiao and Isaacs, 2012). A permeabilisation buffer containing 1X PBS, 10 mg/ml BSA, 0.3% Triton™ X-100 (v/v) (Sigma-Aldrich, UK) and 5% goat serum (v/v) (Sigma-Aldrich, UK) was employed for SOX9 and aggrecan stainings to enhance antibody access to intracellular structures and to further block any non-specific sites interfering with antibody-antigen binding. Goat serum was added given that the set of antibodies employed were raised in goats.

2.7.1 Fluorescence immunostaining on slides

The 5 µm thick slides to be stained were cleared, dewaxed and rehydrated in a similar way to those prepared for histological stainings (section 3.2.2). Antigen retrieval involving hyaluronidase digestion at 37°C for 20 min was performed on samples stained for anti-type II collagen antibody (0.1 µg/ml working concentration). Hyaluronidase from bovine testes (Sigma-Aldrich, UK) was added at a concentration of 0.8 mg/ml in 10 mg/ml BSA in 1X PBS. For anti-SOX9 and anti-Aggrecan HIER, the slides were submerged in a black box containing a 0.01 M citrate buffer (pH 6.0) and heated in a water bath at 95°C for 20 min. The citrate buffer was made by dissolving 3 g sodium citrate (Sigma-Aldrich, UK) in 1 l distilled water and pipetting 200 µl acetic acid, titrating when necessary. The slides were then rinsed in distilled water and 1X PBS. Circles were drawn around the sections with a hydrophobic barrier pen (Vector Laboratories ImmEDGE™, Cole-Parmer, UK) for better localisation of samples and antibodies covering them during incubation. Permeabilisation buffer was added on slides stained for SOX9 (6.7 µg/ml working concentration) and aggrecan (0.1 µg/ml working concentration) for 5 min and all slides were blocked in 10 mg/ml BSA in 1X PBS for 30 min. Primary antibodies were incubated at 4°C overnight, rinsed briefly in running tap water bath and washed in 0.05% Tween 20 (v/v) (Fisher Scientific, UK) in 1X PBS (referred to as 0.05% PBS Tween (v/v)) for 10 min. Secondary antibodies were incubated for 1 h at room temperature, again rinsed in running tap water bath and washed in 0.05% PBS Tween three times for 5 min each. Antibodies were added onto section using volumes such that the sections were fully covered. Counterstaining in DAPI (4',6-Diamidino-2-Phenylindole, Dihydrochloride; Invitrogen, UK; excitation peak at 358 nm wavelength and emission peak at 461 nm) was carried out at a 1:200 dilution (v/v)

in 1X PBS from 10 mg/ml stock solution and the samples were mounted in Fluoromount (Sigma-Aldrich, UK) solution medium to preserve fluorescence. The samples were covered and imaged on a Nikon Eclipse Ti microscope.

Permeabilisation and blocking times were extended to 30 min and 1h, respectively, for the comprehensive SOX9 characterisation study with three cell types (ATDC5, HACs and HBMSCs) two cell numbers (50000 and 500000) and two time points (day 7 and day 21), and then replicated for type II collagen and aggrecan.

2.7.2 Whole mount fluorescence immunostaining

An initial protocol was tested to stain whole mount spheroids consisting of 500 and 5000 cells. The spheroids were fixed in 4% PFA (w/v) overnight and washed in 1X PBS twice. Antigen retrieval involving hyaluronidase digestion at 37°C for 20 min was performed on samples stained for anti-Type II collagen antibody. Hyaluronidase from bovine testes (Sigma-Aldrich, UK) was diluted from stock concentration (520 U/ml) by dissolving 1.6 mg hyaluronidase in 2 ml of 10 mg/ml BSA in 1X PBS. For anti-SOX9, the spheroids were treated with permeabilisation buffer for 5-10 min. Both hyaluronidase and permeabilisation buffer were washed with 0.05% PBS Tween (v/v) three times prior to blocking in 10 mg/ml BSA in 1X PBS for 5 min. The primary antibody working dilution was added to the 96-well plate at a volume of 25 µl and the samples were left to incubate for 1 h-1 h 30 min at room temperature. After washing three times in 0.05% PBS Tween (v/v) for 5 min each, the samples were incubated with a similar volume of the AF488 secondary antibody (excitation peak at 490 nm wavelength and emission peak at 525 nm) working dilution in the dark for 1 h and washed with 0.05% PBS Tween (v/v) twice for 10 min. All the samples received DAPI nuclear counterstaining (25 µg/ml in 1X PBS) for 5-10 min, followed by two washes in 0.05% PBS-Tween (v/v). The samples were covered and stored in 1X PBS at 4°C before imaging. The samples were observed under a Leica TCS SP5 confocal microscopy on 8-well microchamber slides (ibidi, Germany) and z-stacks taken of each individual spheroid to find the antibody distribution and localisation from the surface to the core.

2.7.2.1 Optimised whole mount fluorescence immunostaining protocol

The samples cultured in chondrogenic differentiation media were transferred to flat-bottom 96-well plates (Corning, Corning, Costar, Sigma-Aldrich, UK) for SOX9 staining and fixed in 4% PFA (w/v) overnight at their corresponding time point. PFA was washed off three times with 1X PBS and the samples were permeabilised using 1% Triton™ X-100 (v/v) in 1X PBS at 4°C. Samples were again washed three times with 1X PBS. The blocking step was performed in 0.1% Triton™ X-100 (v/v), 30 mg/ml BSA and 5% goat serum (v/v) in 1X PBS at 4°C overnight. Samples received two washes with

PBST (0.1% Triton™ X-100 (v/v) in 1X PBS) for 15 min each, after which the SOX9 primary antibody was added as a 6.7 µg/ml (1:150 volume dilution) in PBST and they were incubated on a gentle rocker at 4°C for 48 h. The primary antibody was then washed off four times in PBST for 30 min each. AF488 goat anti-rabbit secondary antibody was diluted at a 1:50 ratio in PBST for a 40 µg/ml working concentration and distributed among the samples. These were incubated on a gentle rocker at 4°C for 24 h and the four 30 min washes in PBST were repeated for all samples. DAPI was diluted to 25 µg/ml (1:200 volume dilution from 14.3 mM stock concentration) in 1X PBS as the counterstain, incubating the small 500 cell spheroids for 30 min and the larger 5000 cell aggregates for 1 h and washing all of them twice in 1X PBS for 15 min. The set-up for sample observation was not altered but the samples were optically cleared in 80% glycerol (v/v) (Sigma-Aldrich, UK)/20% 1X PBS (v/v) overnight on 8-well microchamber slides prior to analysis and sequential scanning was performed to retrieve all the stacks while suppressing any interference of DAPI in the SOX9 AF488 channel.

2.7.3 Colourimetric immunohistochemistry on slides

Colourimetric immunohistochemistry differs from IF immunohistochemistry in that the secondary antibody label binding to the primary antibody is an enzyme. High affinity biotin-streptavidin peroxidase enzyme-substrate combination was the colorimetric method of choice for this staining procedure comprising a sequence of events: (i) biotin attachment to primary antibody, (ii) streptavidin-peroxidase covalent bonding to biotin, (iii) reaction between peroxidase and a chromogen substrate, aminoethyl carbazole (AEC) (Ramos-Vara, 2011, Kabiraj et al., 2015).

The protocol for colourimetric immunohistochemistry coincided exactly with immunofluorescence histochemistry on slides until antigen retrieval and permeabilisation were completed and the sections were marked with a hydrophobic barrier pen. The sections were then covered with 3% H_2O_2 (v/v), diluted in distilled water from 30% H_2O_2 (v/v) (Sigma-Aldrich, UK) stock solution. Its role is to quench any endogenous peroxidase present in cells/tissue that may yield high non-specific background signal as the conjugate secondary antibody is added and in the course of the reaction with the substrate AEC. The samples were blocked with 10 mg/ml BSA in 1X PBS for 5-10 min, followed by overnight incubation at 4°C with primary antibody. The slides were rinsed in running tap water bath and washed in 0.05% PBS Tween (v/v) for 10 min to remove excess primary antibody. The biotinylated secondary antibody, goat anti-rabbit biotin (Dako, Agilent, USA), was diluted 1:100, incubated for 1 h at room temperature, rinsed gently in running water bath and washed in 0.05% PBS Tween (v/v) for 10-15 min. ExtrAvidin®-Peroxidase (Sigma-Aldrich, UK) diluted 1:100 (v/v) with 10 mg/ml BSA in 1X PBS was left to act on the slides for 30 min, rinsed in running water bath and washed in 0.05% PBS Tween (v/v) for 10 min. An AEC substrate mixture was prepared in a glass

beaker by dissolving 0.01 g AEC (Thermo Fisher Scientific, UK) in 1.25 ml dimethylformamide (DMF, Fisher Scientific, UK) solvent. A volume of 500 µl of that AEC substrate mixture was added to 9.5 ml sodium acetate buffer (pH 5.0; BDH® GPR™, UK), along with 5 µl 30% H_2O_2 (v/v) to further inactivate any remaining peroxidase on the sample that may interfere with the colourimetric reaction and leave abundant background noise. This working substrate solution was immediately filtered onto the samples using a glass funnel lined with small filter paper and left to sit for up to 10 min or as long as was needed for the red colour to develop. The reaction was then terminated in a running water bath and the samples were counterstained in Alcian blue for 30-45 s, rinsing in running water bath and mounted with water-based Hydromount (National Diagnostics™, UK) medium. The slides were air-dried overnight before imaging under the Zeiss AxioVert 200 microscope.

2.8 Reverse transcriptase quantitative polymerase chain reaction

Quantitative polymerase chain reaction is a popular technique that serves to quantify gene expression in biological samples through the real-time amplification of target complementary DNA (cDNA) specific sequences related to transcript levels, i.e. referring to chondrogenic markers in multicellular spheroids in this study. SYBR Green dye was the reporter detection method for the reaction quantification binding double-stranded DNA products, as opposed to transcript-specific fluorescent probes such as TaqMan (Ponchel et al., 2003, Graves et al., 2015). For the PCR to occur, two previous steps are required: RNA extraction from samples and reverse transcriptase (RT) reaction to convert the RNA obtained into cDNA.

2.8.1 RNA extraction and isolation using Arcturus® Picopure® RNA Isolation kit

RNA was extracted from multicellular spheroids using the Arcturus® Picopure® RNA Isolation kit (Applied Biosystems, UK) according to the manufacturer's indications. The spheroids were transferred into 1.5 ml Eppendorf tubes using a Pasteur pipette and lysed via incubation in 100 µl extraction buffer (XB) inside a water bath set at 42°C for 30 min, accompanied by an ULTRA-TURREX T8 homogeniser (IKA, UK) when necessary. The resulting lysate was centrifuged at 3000 g for 2 min and the supernatant was carefully pipetted into a new centrifuge tube without disturbing the pellet. That lysate was stored at -80°C until proceeding with the isolation to minimise RNA degradation by inactivating RNases.

The RNA purification column in the kit was pre-conditioned by pipetting 250 µl conditioning buffer (CB) onto the purification column filter membrane and incubating for 5 min at room temperature, after which the purification column was centrifuged at 16000 g for 1 min so as to elute the CB through. A volume of 100 µl 70% ethanol (v/v) was incorporated to the cell extract, mixing well by

pipetting up and down for a combined volume of about 200 µl. The cell extract and ethanol mixture was pipetted into the pre-conditioned purification column and centrifuged at 100 g for 2 min to bind RNA to the column, immediately followed by a centrifugation at 16000 g for 30 s to remove the flow-through. Wash buffer 1 (W1) was added into the purification column at a volume of 100 µl and centrifuged at 8035 g for 1 min. DNase treatment was carried out on the samples at this point to remove genomic DNA that may alter the products from polymerase chain reactions, as described in RNAse-Free DNase set (Qiagen, UK). For the spheroids, 10 µl DNase I stock solution (Bioline, UK) were pipetted into 30 µl RDD buffer per sample. The 40 µl DNase mix was transferred directly onto the purification column membrane and incubated for 15 min at room temperature. Again, W1 was introduced in the purification column at a volume of 40 µl and centrifuged at 8035 g for 15 s. Wash buffer 2 (W2) was first pipetted using a volume of 100 µl and centrifuging at 8035 g for 1 min and then the same volume was added centrifuging at 16000 g for 2 min (repeating this centrifuge cycling if W2 remains on the membrane). The purification column was moved to 0.5 ml microcentrifuge tubes provided in the kit and 11 µl elution buffer (EB) were inserted directly onto the membrane of the purification column by gently bringing the pipette tip in contact with the surface of the membrane to ensure maximum absorption. EB was incubated on the purification column membrane for 1 min, distributed by centrifuging at 1000 g for 1 min and made to flow through with a 16000 g incubation for 1 min. This step was repeated with the same volume of EB to wash the membrane and maximise RNA yield. RNA concentrations were measured using a NanoDrop™ 1000 Spectrophotometer (Thermo Fisher Scientific, UK), deeming RNA purity for an absorbance ratio at 260 to 280 nm wavelengths (A_{260}/A_{280}) of 2.0 (Desjardins and Conklin, 2010).

2.8.2 RNA extraction and isolation using the ReliaPrep RNA Cell MiniPrep system kit

Given the higher purity and yield of the resulting RNA compared to the Arcturus® Picopure® kit mentioned throughout the previous section, the ReliaPrep RNA Cell MiniPrep system kit (Promega, UK) was used to isolate RNA from sorted cells and aggregates formed within microdroplets as specified by the manufacturer. The cell lysis buffer (BL-TG) was prepared fresh for every isolation by diluting 1-Thioglycerol in BL buffer at a 1:100 volume ratio (e.g. 325 µl 1-Thioglycerol in 3.25 ml BL buffer for 30 samples). Given the cell-seeding density of the assay, 100 µl BL-TG buffer was mixed with 35 µl isopropanol for molecular biology (Sigma-Aldrich, UK). The wells were washed with DPBS (Lonza, UK) prior to adding the BL-TG buffer containing isopropanol, mixing well and scraping each well with the end of a pipette tip to harvest the cell lytic material. The lysate solutions were transferred to Minicolumns and collection tubes in the kit and centrifuged at 12000 g for 30 s at 25°C. The liquid deposit at the bottom of the collection tube was discarded and 500 µl RNA Wash solution were added to each column and the same centrifugation cycle was applied. A DNAse I

solution was then prepared to remove genomic DNA composed of 24 µl Yellow Core Buffer, 3 µl 0.09 M $MnCl_2$ and 3 µl DNAse I dilution (DNAse I diluted in nuclease-free water as recommended by the manufacturer) per sample. The solution was mixed by gently pipetting and 30 µl were carefully applied onto each Minicolumn membrane and incubated at room temperature for 15 min. A volume of 200 µl Column Wash solution was then added to the DNAse I solution and the samples were centrifuged at 12000 g for 15 s. The samples were washed again with 500 µl RNA Wash solution, centrifuged at 12000 g for 30 s and all the collection tubes were discarded and replaced. A last wash with 300 µl RNA Wash solution was performed followed by a centrifugation cycle of 12000 g for 2 min. The Minicolumn was finally placed in an Elution tube, a volume of 15 µl nuclease-free water was pipetted and the tube was centrifuged at 12000 g for 1 min. The samples in the Elution tubes were placed in ice and the RNA yield was measured using a Nanodrop™ 1000 Spectrophotometer (Fisher Scientific, UK).

2.8.3 Reverse transcription using the Superscript™ VILO™ cDNA Synthesis Kit

Taking into consideration the expected low RNA yields from extraction of spheroids consisting of hundreds of cells and in order to maximise cDNA synthesis output for accountable qPCR amplification, the Superscript™ VILO™ cDNA Synthesis Kit (Invitrogen, UK) was used to complete the reverse transcription process that generates a single-strand cDNA from an RNA template.

The calculations normalised starting RNA concentrations among samples for cDNA synthesis. Aiming to reach the lower limit recommended as ideal by the manufacturer, 150 ng/µl, the RNA solution was diluted accordingly in nuclease-free water (Promega, UK) where necessary. Samples with very low RNA yields were used at the maximum volume possible. For a target 10 µl cDNA volume per sample, 7 µl RNA sample were gently mixed with 2 µl VILO reaction mix comprised of random primers, deoxynucleotides (dNTPs) and magnesium chloride ($MgCl_2$); and 1 µl SuperScript III Enzyme Blend containing SuperScript III RT, RNaseOUT Recombinant Ribonuclease inhibitor and proprietary helper protein. The samples were exposed to the following thermal cycle in a Veriti™ 96-Well Thermal Cycler (Applied Biosystems, UK): 25°C for 10 min; 42°C for 120 min; 85°C for 5 min and cooling down to 4°C.

2.8.4 RT-qPCR plate preparation

Primer dilutions were prepared from 100 µM stock primers purchased from Sigma-A for each gene quantified by adding nuclease-free water for a final 5 µM working solution (1 ml) composed of 50 µl forward primer, 50 µl reverse primer and 900 µl nuclease-free water. A master mix was made with a combination of nuclease-free water, primer working solution and GoTaq® qPCR Master Mix

(Promega, UK) in that particular sequence and vortexed vigorously. The master mix and the cDNA samples were transferred into semi-skirted 96-well PCR plates with raised rim (Starlab, UK) and sealed with polyolefin film (Starlab, UK). The plates were inserted into a 7500 quantitative RT-PCR system (Applied Biosystems, UK) and the settings were adjusted for detection with ROX™ dye and SYBR Green I reagents on Standard Curve Calibration coupled with melt curve to validate primers by ruling out primer-dimer formation. Non-template controls were added as the master mix from each gene to dismiss primer-dimer interactions or PCR-related contamination.

2.8.5 Statistical analysis of gene expression

The threshold cycle (C_t) values or the cycle number at which gene expression is detected as the fluorescence generated surpasses the fixed fluorescent threshold indicating background signal were examined for analysis (McCall et al., 2014), deeming 'negligible expression' for C_t values within the 35-39 interval. The general C_t threshold for calculations was set at 0.2 to ensure measurements within the linear range of the reaction.

The statistical analysis was based on ΔC_t values computed as:

$$\Delta C_t = Average\ C_t\ (GOI) - \ Average\ C_t\ (HKG) \tag{2.1}$$

where GOI is the gene of interest and HKG stands as housekeeping gene. The average values of the technical replicates employed were the input variables in this expression. The qPCR results were then presented as relative gene expression normalised to the housekeeping gene using the $\Delta\Delta C_t$ method (Livak and Schmittgen, 2001) that references the ΔC_t values of the target samples to a control sample such that:

$$\Delta\Delta C_t = \Delta C_t\ (sample) - \ \Delta C_t\ (control) \tag{2.2}$$

Therefore, the resulting fold changes in gene expression among samples were finally shown as $2^{-\Delta\Delta C_t}$ owing to the nature of polymerase chain reaction, where the products duplicate in each cycle. The statistical method performed on ΔC_t values was Two-way analysis of variances (ANOVA) Tukey's multiple comparisons test on GraphPad Prism 8.2.1. Two-way ANOVA was used to examine the effect of cell number and time (independent variables) on the expression of the genes in question in connection with chondrogenesis. The statistical analysis was conducted on the assumption that the samples were normally distributed after performing a Shapiro-Wilk normality test for the small sample sizes in this research project.

Chapter 3: Study of heterogeneity and the role of SOX9 in chondrogenesis of HBMSC spheroids

3.1 Introduction

In this chapter, the ability of HBMSC spheroids cultured at different cell numbers to stimulate chondrogenesis is addressed to further understand the feasibility of scaling down pellet culture of large spheroids. This assessment is conducted as a proof of principle of chondrogenic differentiation of aggregates in microdroplets and the conditions required for sorting in connection with SOX9 expression.

Pellet culture is the current gold standard for *in vitro* scaffold-free chondrogenic differentiation and can take place in culture vessels such as conical tubes and microwell plates fabricated with precise geometries (e.g. U-bottom, V-bottom) and coating treatments for low adherence (Watts et al., 2013). In contrast to 2D micromasses, pellet culture does not require a substrate and provides a 3D environment conducive for chondrogenesis and representative of cartilage development at embryonic stages (Khang et al., 2014). Microplates offer the advantage of more automated high-throughput seeding, screening and analysis of spheroids. Studies performed to compare both pellet culture approaches have concluded no significant differences concerning the synthesis of extracellular matrix components (e.g. PGs, type II collagen) and only modest differences at the molecular scale. These studies indicate that augmented scalability and ease of handling outweigh the lower COL2A1 and ACAN mRNA levels on cells cultured on plates (Penick et al., 2005, Welter et al., 2007, Schon et al., 2012).

Recent studies have explored the effect of spheroid size on chondrogenesis. From the macroscopic end, Sarem et al. tested several HBMSC aggregate cell numbers from 70000 up to 300000 to ascertain the biomechanical-derived interactions and biomolecules regulating chondrogenesis (Sarem et al., 2019). They encountered more cartilage-like cell morphology and higher type II collagen secretion in the smallest aggregates and attributed it to inhibition in necrosis from the aggregate core and outwards and more efficient matrix deposition (Figure 3.2A). The same tendency was met on the other end for microaggregates. An earlier study with cell microaggregates consisting of a range of numbers from 50 to 250 cells cultured in agarose microwells reported the upregulation of transcriptional markers for chondrogenic differentiation (SOX9, COL2A1 and ACAN) with respect to single-cell controls for bovine articular chondrocytes (Moreira Teixeira et al., 2012).

A similar trend was later observed for human periosteal-derived stem cells (HPDSCs) (Leijten et al., 2016).

In addition, these studies highlighted that the smallest 50 cell aggregates were the most responsive to chondrogenic induction as observed by their upregulated expression of chondrogenic genes. Furthermore, there is evidence that SOX9 upregulation in aggregate compared to monolayer culture also holds for macroaggregates and other pluripotent stem cells (e.g. HESCs) (Wang et al., 2019). All these findings reinforce the hypothesis that SOX9 expression is greater in microaggregates than in single cells, possibly due to the effect of mimicking early cartilage condensation. These observations suggest that sorting more responsive microaggregates on the basis of chondrogenic potential could be more effective than sorting single cells.

As extensively reviewed in the introductory chapter, HBMSCs find a major limitation in that they are a heterogeneous cell population comprising cells with varied differentiation potential in relation to the development of musculoskeletal lineages such as cartilage (Pittenger et al., 1999, Bianco et al., 2001, Baugé and Boumédiene, 2015). The lack of predictive cell surface markers for chondroprogenitors explains the need to investigate other strategies and other markers. In this context, SOX9 is a potential candidate as an early marker and master transcription factor in chondrogenesis and pre-chondrocyte condensation (Liu and Lefebvre, 2015, Liu et al., 2018, Lefebvre et al., 2019).

While the condensation event is clearly important for chondrogenic differentiation, it is not yet clear how it affects the expression of chondrogenic markers on all the scales comprising large and small aggregates. More specifically for SOX9, even if it is widely known that it plays a role in regulating chondrogenesis from an early stage, the exact optimal time point for detection and quantification has not been defined. Neither has the correlation between aggregation across different cell numbers and SOX9 expression been investigated. Thus, the aim of the work presented is to verify whether SOX9 is an appropriate marker to sort chondroprogenitors from heterogeneous unselected HBMSCs. This is addressed by examining how SOX9 expression changes over time and for different cell numbers as well as its heterogeneity in HBMSC spheroids. Throughout this chapter, multicellular spheroids were cultured in chondrogenic differentiation conditions driven by a cocktail of ‘essential’ growth factors. The constructs obtained were assessed at different time points and initial cell-seeding densities to address SOX9 expression patterns. Time-lapse analysis was conducted to define time intervals for cell aggregation down to low cell numbers, as well as changes in spheroid sizes under chondrogenic stimulation. Histological techniques were used to determine an optimum cell number for chondrogenic differentiation of large spheroids. Fluorescent immunohistochemistry targeted SOX9 expression and distribution. It was used to (i) verify that

SOX9 was an early marker indicative of chondrogenesis, (ii) to analyse variations linked to culture time and cell number and (iii) to investigate SOX9 heterogeneity levels for the design of an accurate criterion for sorting of aggregates. RT-qPCR analysis aimed to reveal *SOX9* gene expression patterns in early and late time points for different cell numbers. Lastly, it focussed on the first week of culture to establish if there was any particular time point characterised by higher levels that was preferable for sorting of aggregates formed in microdroplets.

3.1.1 Hypotheses

The work in this chapter seeks to test three hypotheses that underlie the stem cell enrichment strategy being developed in this thesis:

1) 'The temporal expression pattern of SOX9 in HBMSC aggregates is compatible with a short period of incubation in microdroplets'.

2) 'Chondrogenesis in HBMSCs is dependent on cell number down to the scale achievable using droplet microfluidics; i.e. cell aggregation kinetics; histological structure and temporal expression pattern of SOX9'.

3) 'SOX9 has a heterogeneous expression pattern among HBMSC subpopulations that could be used as a criterion for high-throughput sorting of cell aggregates'.

3.1.2 Aims

The *in vitro* studies of HBMSCs in the present chapter aim to identify the ability of unselected subpopulations to generate articular cartilage tissue to address relevant aspects for the development of the microfluidic platform for sorting of cell aggregates, i.e. timelines for cell aggregation and *SOX9* expression. The specific objectives are as follows:

1. To study cell aggregation during chondrogenic differentiation focussing on earlier time points and extending over long-term culture to register gradual size changes.
2. To evaluate the chondrogenic potential of HBMSC spheroids across various cell numbers when directed towards chondrogenic differentiation via growth factors.
3. To establish the pattern for SOX9 expression in unselected human bone marrow cell spheroids in relation to the microfluidic cell sorting procedure to be developed.
4. To characterise SOX9 heterogeneity in HBMSC spheroids taking into consideration cell number, time, donor, replicates and cell subpopulations within spheroids.

3.2 Methods

Unless otherwise stated cell spheroids of different cell numbers: 500, 5000, 50000 and 500000 were cultured in ultra-low adherence 96-well round-bottom in chondrogenic differentiation medium (section 2.3.4). The characterisation techniques included time-lapse microscopy to visualise cell aggregation leading to spheroid formation; histological and immunohistochemistry stainings to measure protein expression of chondrogenic markers and RT-qPCR to quantify expression of chondrogenic genes focussing on SOX9 at an early stage of chondrogenesis.

3.2.1 Cell culture and chondrogenic differentiation of multicellular spheroids

The ATDC5 chondroprogenitor murine cell line was purchased from Lonza. These cells were supplemented with DMEM, 5% FBS, 1X ITS and 1% P/S (v/v) for expansion. Primary cells were isolated from human samples. HBMSCs were cultured in αMEM, 10% FBS (v/v) and 1% P/S (v/v) and HACs were cultured in DMEM-F12, 5% FBS (v/v), 1X ITS, 100 µM A2P and 1% P/S (v/v) (see section 2.3 for more details). Chondrogenic differentiation assays were conducted on BRAND inertGrade 96-well round-bottom microplates. The chondrogenic differentiation medium for ATDC5 cells consisted of DMEM supplemented with 5% FBS (v/v), 1X ITS, 100 µM A2P, 10 nM dexamethasone, 10 ng/ml TGF-β3 and 1% P/S. Serum-free αMEM was used for primary HBMSCs and HACs instead. The chondrogenic differentiation medium was replaced every 3 days.

3.2.2 Study of cell aggregation using time-lapse microscopy

Time-lapse microscopy in a Nikon Eclipse Ti microscope enabled the visualisation of the cell aggregation phenomenon with different cell numbers as a function of culture time. The samples were seeded in ten-fold dilutions from 500000 cells down to 500 cells in 96-well BRAND pellet culture plates containing 200 µl chondrogenic differentiation medium per well and imaged in transmitted light mode (TL) with 4x magnification, capturing images every 3 min for 24 h. The same procedure was performed for ATDC5 cells, HBMSCs and HACs.

The resulting images were acquired and assembled by NIS Element AR software. Image processing and analysis were completed using ImageJ (n = 3, experimental replicates). Subsequently, a series of plots were produced to characterise aggregate evolution over time as a function of cell number by means of cell aggregate cross sectional area, size and roundness (2D equivalent to 3D sphericity). Image J measured cell aggregate cross sectional area and roundness directly. From that given value for area, the aggregate size was computed as the aggregate diameter (double its radius, R) using the following expression:

$$D = 2\sqrt{\frac{A}{\pi C}} \tag{3.1}$$

where D is the aggregate diameter, A is the maximum aggregate cross sectional area and C is the aggregate circularity, a factor that was integrated to account for deviations from ideal circular shapes taking values from 0 to 1. The expression derives from the area of an ideal circle ($A = \pi R^2$) corrected with the circularity factor C.

3.2.3 Descriptive histological analysis using Bern Score

The histological grading system first described by Grogan was applied to examine the quality of A/S and SO stainings performed as described in sections 2.6.1 and 2.6.2 to give a semiqualitative measurement and to extract any differences across cell numbers regarding their ability to yield cartilage-like constructs (Grogan et al., 2006). Hence, a Bern score with values between 0 (minimum) and 9 (maximum) was assigned to ATDC5 (n = 1), HAC (n = 3, biological replicates) and HBMSC (n = 3, biological replicates) sections stained with both dyes. The evaluation was in accordance with the categories and subcategories included in Table 3.1. The scores were plotted and analysed using a Two-way ANOVA Tukey's multiple comparisons test comparing cell rows on GraphPad Prism version 8.2.1 and declaring statistical significance for $p \leq 0.05$.

Table 3.1 Bern score grading system with the categories and subcategories to assess the histological quality of the cartilage pellet produced ranging from 0 for the minimum score to 9 for the maximum score.

Scoring category	Score
A. Uniformity and darkness of Alcian Blue/Sirius Red and Safranin O staining	
No stain	0
Weak staining of poorly formed matrix	1
Moderately even staining	2
Even dark stain	3
B. Distance between cells/amount of matrix secreted	
High cell densities with no matrix in between (no spacing between cells)	0
High cell densities with little matrix in between (cells < 1 cell-size apart)	1
Moderate cell density with little matrix (cells approximately 1 cell-size apart)	2
Low cell density with moderate distance between cells (> 1 cell-size apart) and an extensive matrix	3
C. Cell morphologies represented	
Condensed/necrotic/pycnotic bodies	0

Spindle/fibrous	1
Mixed spindle/fibrous and with rounded chondrogenic morphology	2
Majority rounded/chondrogenic	3

3.2.4 Immunohistochemical staining

3.2.4.1 Fluorescence immunohistochemistry (IF)

The fluorescence signal emitted upon fluorescent dyes linking to primary antibodies was the method of detection selected for antigens of chondrogenic proteins on tissue samples following differentiation culture as it provided a point of reference to establish existing differences in protein expression across the entire range of cell numbers used: 500 to 500000. Hence, the smaller cell numbers (500 and 5000) were stained whole mount due to the complications that their size entailed to process, embed in paraffin and section; and larger cell numbers (50000 and 500000) were stained as paraffin sections on slides with the antibodies contained in Table 3.2. Negative controls were incorporated as part of every fluorescent immunohistochemistry procedure to calibrate imaging and to determine the threshold for positive staining on test samples.

Table 3.2 List of antibodies and dilution factors used for fluorescence immunohistochemistry.

Type of antibody, class and host	Description	Working dilution factor
Primary, polyclonal (rabbit)	Anti-SOX9 (Millipore, UK)	1:150 dilution (6.7 µg/ml) in 10 mg/ml BSA in 1X PBS
Primary, polyclonal (rabbit)	Anti-Type II Collagen (Calbiochem, USA)	1:500 dilution (0.1 µg/ml) in 10 mg/ml BSA in 1X PBS
Primary, monoclonal (goat)	Anti-Aggrecan (R&D Systems, USA)	1:240 dilution (0.1 µg/ml) in 10 mg/ml BSA in 1X PBS
Secondary, polyclonal (goat)	Anti-rabbit IgG (H+L), Alexa Fluor 488 (Invitrogen, UK):	1:50 dilution (40 µg/ml) in 10 mg/ml BSA in 1X PBS
Secondary, polyclonal (rabbit)	Anti-goat IgG (H+L), Alexa Fluor 488 (Invitrogen, UK):	1:50 dilution (40 µg/ml) in 10 mg/ml BSA in 1X PBS

The staining protocols employed for 50000 and 500000 spheroid sections of the three cell types tested is thoroughly detailed in sections 2.7.1 and 2.7.3. Whole mount immunostaining was used

for smaller spheroids for which paraffin embedding was not practical due to their size. Whole mount ATDC5 and HBMSC spheroids of 500 and 5000 cells were initially stained after chondrogenic stimulation for 7 and 21 days according to the method in section 2.7.2.

Enhanced SOX9 nuclear penetration into the core of the spheroids was deemed crucial. A semi-quantitative image analysis method was elaborated to estimate the extent of antibody dye diffusion using the staining mentioned above. Antibody penetration inside each spheroid was analysed using Leica LASX software and contained in a variable designated as 'diffusion pathway length' in µm. The centre of the spheroids was taken to retrieve the region of interest (ROI) to characterise antibody diffusion. The distance from end to end of the intensity peaks associated with the fluorescent signal emitted by the antibody excitation was measured on both sides of the spheroids and their average value assigned to the diffusion pathway length variable. Average values were selected on the assumption that spheroids could be approximated to ideal perfect spheres. The plots were made in GraphPad from such values and cell numbers (500, 5000), days of culture (7,21) and dye molecule of interest (DAPI, type II collagen or COL2 and SOX9).

The staining protocol resulting from the optimisation described in Appendix B.5.1 and included in section 2.7.2.1 for characterisation of SOX9 expression during early time points (days 1, 3 and 7) of culture of 500 and 5000 spheroids in HACs and HBMSCs. The study was conducted to describe any possible heterogeneities due to cell number, day of culture and among replicates. This information was hypothesised to give an indication of levels of expression and heterogeneity that may be translated to the subsequent application to fluorescence-activated cell sorting of small cell aggregates formed after using a droplet microfluidic platform.

3.2.5 Gene expression analysis using RT-qPCR

A time-dependent study of the effect of cells number on chondrogenic differentiation of HBMSC spheroids was carried out to compare the mRNA levels of two genes associated with chondrogenic differentiation (SOX9 and COL2A1) and a gene indicative of hypertrophy (COL10A1) at an early time point (day 7) and a late time point (day 21). Spheroids formed of 500, 5000 and 50000 cells were cultured in chondrogenic differentiation and harvested at set time points for RNA extraction (n =1 biological sample and experimental sample per condition).

With a focus on SOX9 at early time points that were relevant for aggregate culture in microdroplets, HBMSC spheroids were cultured in chondrogenic differentiation conditions for 1, 3 and 7 days and initial cell-seeding densities of 50000 (n = 5 experimental replicates), 5000 (n = 10 experimental replicates) and 500 (n = 15 experimental replicates) cells per aggregate. The number of experimental replicates was increased in order to maximise RNA yield. The experiment was

repeated for three different patients (biological replicates) to account for patient variability effects and using three technical replicates for RT-qPCR.

RNA was extracted from multicellular spheroids using the Arcturus® Picopure® RNA Isolation kit (Applied Biosystems, UK) following the manufacturer's indications (see section 2.8.1). The resulting RNA concentrations were quantified using a NanoDrop™ 1000 Spectrophotometer (Thermo Fisher Scientific, UK). After normalisation of RNA concentrations, the reverse transcriptase reaction was completed for cDNA synthesis using the Superscript™ VILO™ cDNA Synthesis Kit (Invitrogen, UK) in a Veriti™ 96-Well Thermal Cycler (Applied Biosystems, UK) as described in section 2.8.3. The RT-qPCR plates were prepared as specified in section 2.8.4 using the primer sequences in Table 3.3. The cDNA templates were amplified using a 7500 quantitative RT-PCR system (Applied Biosystems, UK) adding non-template controls and the relevant positive controls (e.g. HAC pellets at P0). For the purpose of analysis, fold changes in gene expression among samples were quantified using the $2^{-\Delta\Delta C_t}$ method. Two-way ANOVA Tukey's multiple comparisons test was performed on ΔC_t values on GraphPad Prism 8.2.1. A normal distribution was assumed for the statistical analysis as a result of a Shapiro-Wilk normality test that was applied taking into consideration the small sample sizes, i.e. up to n = 3 (see section 2.8.5).

Table 3.3 List of human PCR primers used and their characteristic sequence and amplicon size in base pairs.

Gene	Primer sequence	Amplicon size (bp)
Human		
β-ACTIN	F: 5' GGCATCCTCACCCTGAAGTA 3'	82
	R: 5' AGGTGTGGTGCCAGATTTTC 3'	
TBP	F: 5' TGCACAGGAGCCAAGAGTGAA 3'	132
	R: 5' CACATCACAGCTCCCCACCA 3'	
RPL13	F: 5' AAAAAGCGGATGGTGGTTC 3'	157
	R: 5' CTTCCGGTAGTGGATCTTGG 3'	
SOX9	F: 5' CCCTTCAACCTCCCACACTA 3'	74
	R: 5' TGGTGGTCGGTGTAGTCGTA 3'	
COL2A1	F: 5' CCTGGTCCCCCTGGTCTTGG 3'	58
	R: 5' CATCAAATCCTCCAGCCATC 3'	
COL10A1	F: 5' CCCACTACCCAACACCAAGA 3'	95
	R: 5' GTGGACCAGGAGTACCTTGC 3'	

3.3 Results

3.3.1 Time-lapse aggregation of multicellular spheroids in chondrogenic culture

In order to assess the ability of low cell numbers to form aggregates in microdroplets, ten-fold decreasing cell numbers from 500000 to 50 cells/well were cultured in chondrogenic medium and imaged over a period of 24 h. ATDC5 chondroprogenitor cells were first used as a proof of principle of cell aggregation due to their chondroprogenitor abilities.

The time-lapse experiment showed that cells started forming an aggregate regardless of the initial cell number after less than 6 h for all the samples examined (Figure 3.1). In some cases, however, the majority of cells gathered in a large aggregate whilst a few isolated cells may simultaneously group into smaller aggregates (see n = 5000 sample for a distinct example of this phenomenon).

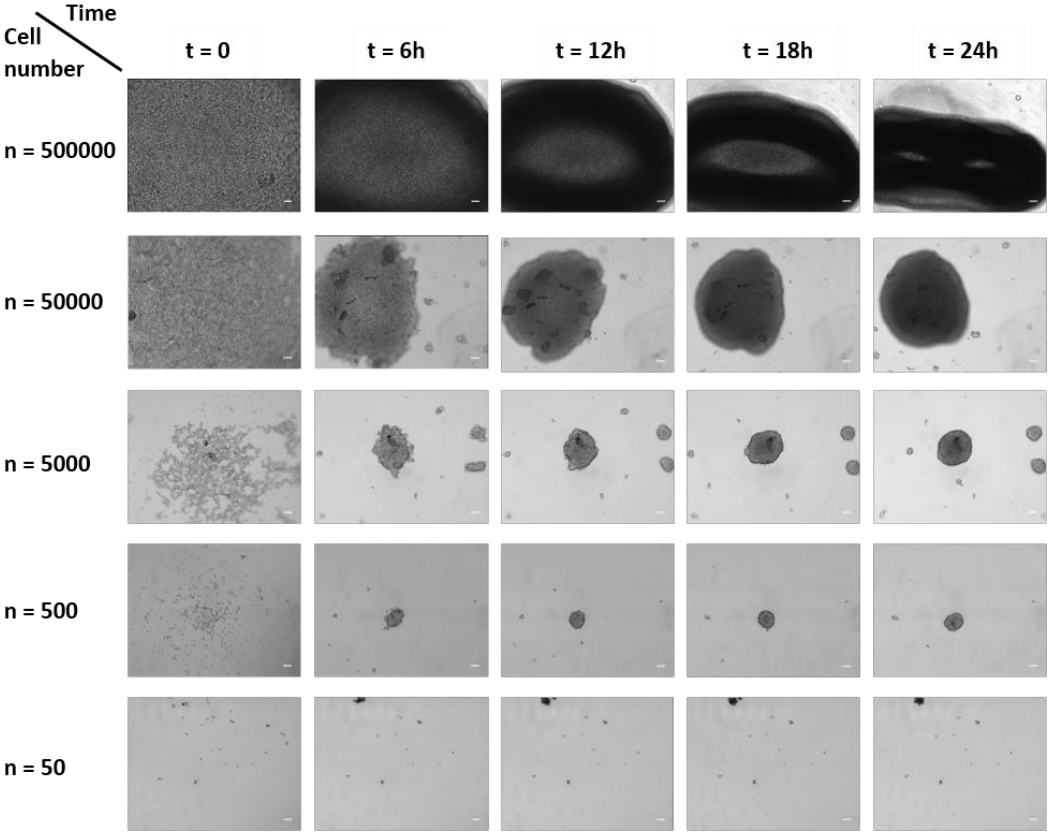

Figure 3.1 Morphological evolution of ATDC5 cell aggregates from different ten-fold cell densities in 96-well microplates over a period of 24 h. Scale bar = 100 µm.

The size of cell aggregates increased with cell number: they doubled in size from 50 to 500 cells; obtained the largest increment, about 2.4 times, from 500 to 5000 cells and finally reached a 1.7-fold increase from 5000 to 50000 cells (Figure 3.2C). Their roundness was close to 0.9 for all cell numbers except for upper and lower limits, where it dropped to less than 0.75 and below 0.6, respectively. In the case of the lower limit, this value was reasonably an underestimation that

stemmed from the inability to predict the exact point in which the cell aggregate would assemble; thus capturing part of the cell aggregate only. As for the upper limit, it exceeded the size of the field of view captured by the microscope at its lowest magnification and by the end of the recording the pellet experienced a strong condensation towards the centre of the microwell and took an oval shape with an inferior value of roundness as a consequence (Figure 3.2B)

Complementary to the size of the cell aggregates, the change in maximum cross sectional area was studied over the same period of time. In general, the maximum cross sectional area decreased significantly with time pointing to cell aggregate formation (Figure 3.2A). Note that the irregular decrease profile of the upper cell number was due to incomplete capture of the aggregate due to size at the early time points. A similar tendency was observed for 50000 and 5000 cells. From 500 cells and downwards, the maximum cross sectional area rose until the aggregate had formed and remained stable afterwards.

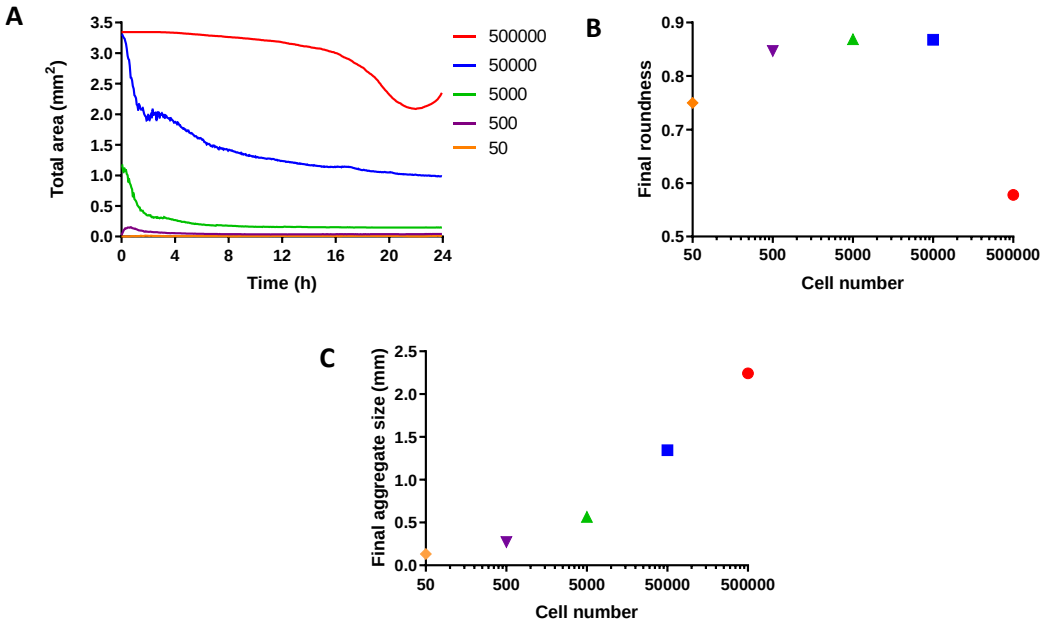

Figure 3.2 Image analysis plots of time-lapse ATDC5 cell aggregation experiment: (A) Maximum aggregate cross sectional area over time-lapse culture; (B) Final roundness for each cell number; (C) final aggregate size for each cell number after 24 h. Error bars are included within data points (n =3 , experimental replicates).

ATDC5 cells were kept in pellet culture for the standard 21 day culture period set for experiments and images were taken of spheroids (n = 2) every 2-3 days with media changes under the Zeiss Axiovert microscope and analysed using ImageJ applying a similar method to time-lapse video analysis for cell aggregate formation. Cell aggregates underwent continuous growth over time (Figure 3.3A and B). The graphs were plotted taking reference total aggregate area at time 0 until the first medium change on day 2 for simplicity reasons, even if the time-lapse evolution in Figure 3.2A is the appropriate starting point until 24 h. Roundness stabilised by the end of culture and became close to 0.9 or above regardless of cell number (Figure 3.3C and D).

The time-lapse cell aggregation experiment was repeated for HBMSCs (F69 P1) cultured in chondrogenic differentiation conditions (serum-free medium containing chondrogenic growth factors) for both the 24 h assay and the entire 21 d culture (n = 2). The results of the former were analysed assigning a value of 0 to cell groups corresponding to unclear or incomplete aggregate formation. The highest two cell-seeding densities succeeded in generating a fairly complete single spheroid after 24 h. 500000 cell samples aggregated almost instantaneously and visible after 6 h, whereas initial 50000 cell samples formed a macroaggregate after 18 h surrounded by multiple microaggregates of various sizes (Figure 3.4). The remaining cell numbers did not self-assemble into one spheroid a day after culture set-up and produced multiple irregular microaggregates whose size diminished as a function of decreasing cell density. 50 cell samples were excluded from the size quantification due to their excessively small size and sparsity that impeded clear localisation when imaging under the Zeiss Axiovert microscope and their characterisation through image analysis.

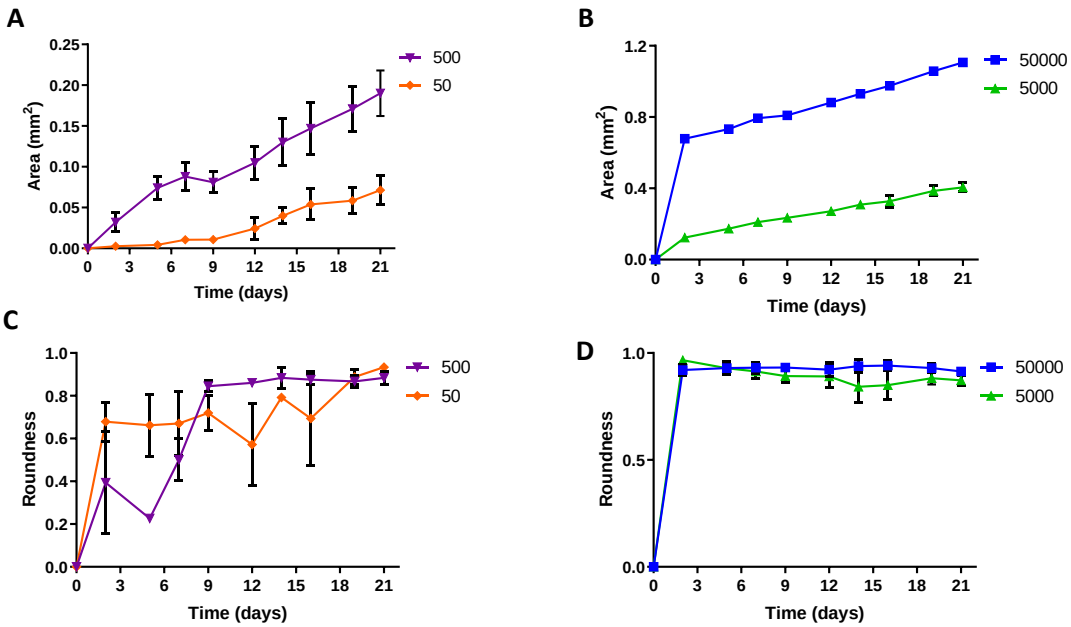

Figure 3.3 Image analysis plots of time-lapse ATDC5 cell condensation over 21 days of chondrogenic differentiation culture: (A) Maximum aggregate cross sectional area over time for 500 and 50 cell spheroids; (B) Maximum aggregate cross sectional area over time for 50000 and 5000 cell spheroids; (C) Roundness for 500 and 50 cell spheroids; (D) Roundness for 500 and 50 cell spheroids. The error bars represent the SD of n = 3 experimental replicates.

Over the 21 day period of chondrogenic differentiation, all the cell samples underwent a sharp area increase (representative of aggregate size) from seeding to day 2, which shifted to a gradual drop during the next two weeks and entered a plateau region until the culture came to an end, where the aggregates only became slightly smaller (Figure 3.5A, B and E). The decline scaled directly with increasing cell numbers. Spheroid roundness fluctuated continuously throughout chondrogenic differentiation time points and values between 0.75 and 0.9 were registered for the cell numbers assessed without noticeable differences between them (Figure 3.5C and D).

HAC aggregation was finally investigated as the clinically relevant human control. The lower end 50 cell spheroid samples were removed from the study based on the quantification challenges found above in HBMSCs. HACs were supplemented with the same chondrogenic differentiation medium as HBMSCs. As described for HBMSCs, HACs experienced slow cell aggregation that did not lead to a compact spheroid over the course of one day. Again, cell aggregation efficiency scaled inversely with cell number (Figure 3.6).

HACs shared a similar behaviour to HBMSCs during chondrogenic differentiation culture: the spheroids gradually became smaller for all cell numbers, with a minor dimensional variation for 500 cell samples where aggregation was not always fully integrated into a single spheroid by day 21 (Figure 3.7A and B). HACs size reduction was comparably less sharp as well, having final aggregate sizes that reached about five times those of HBMSCs spheroids and linked to a lesser extent of cell death as differentiation progressed (Figure 3.7E). Spheroid roundness underwent slight fluctuations (Figure 3.7C and D).

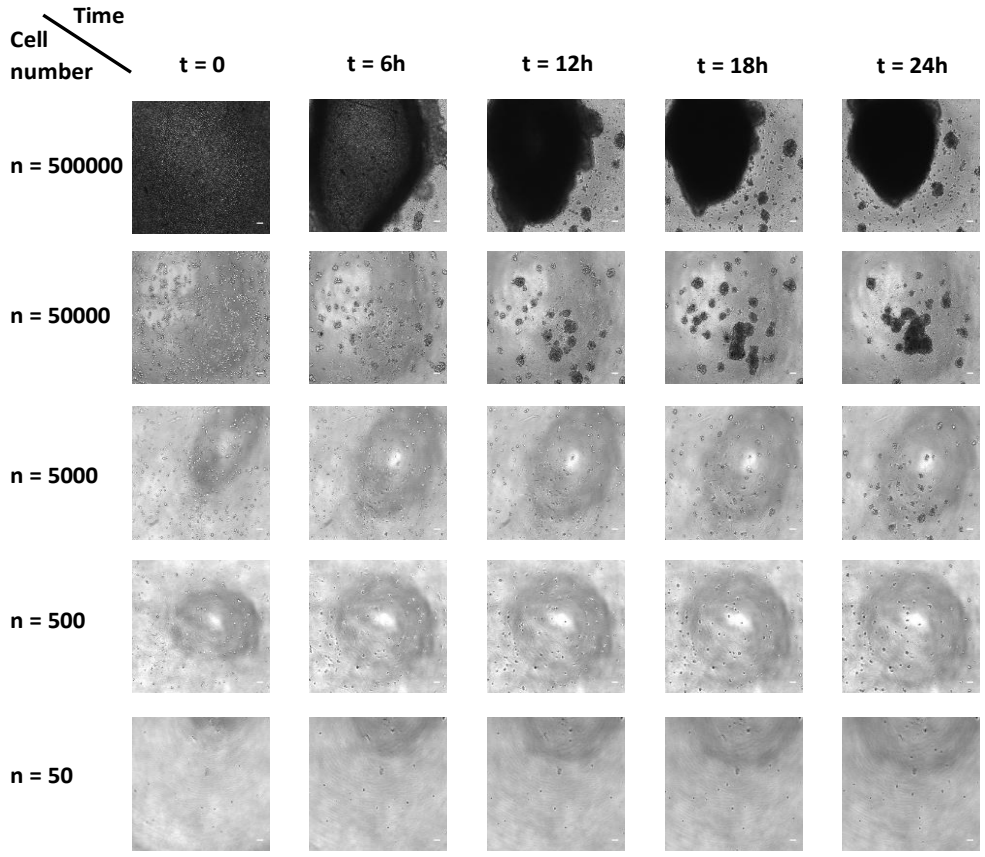

Figure 3.4 Morphological evolution of F69 P1 HBMSC aggregates from different ten-fold cell densities in 96-well microplates over a period of 24 h. Scale bar = 100 µm.

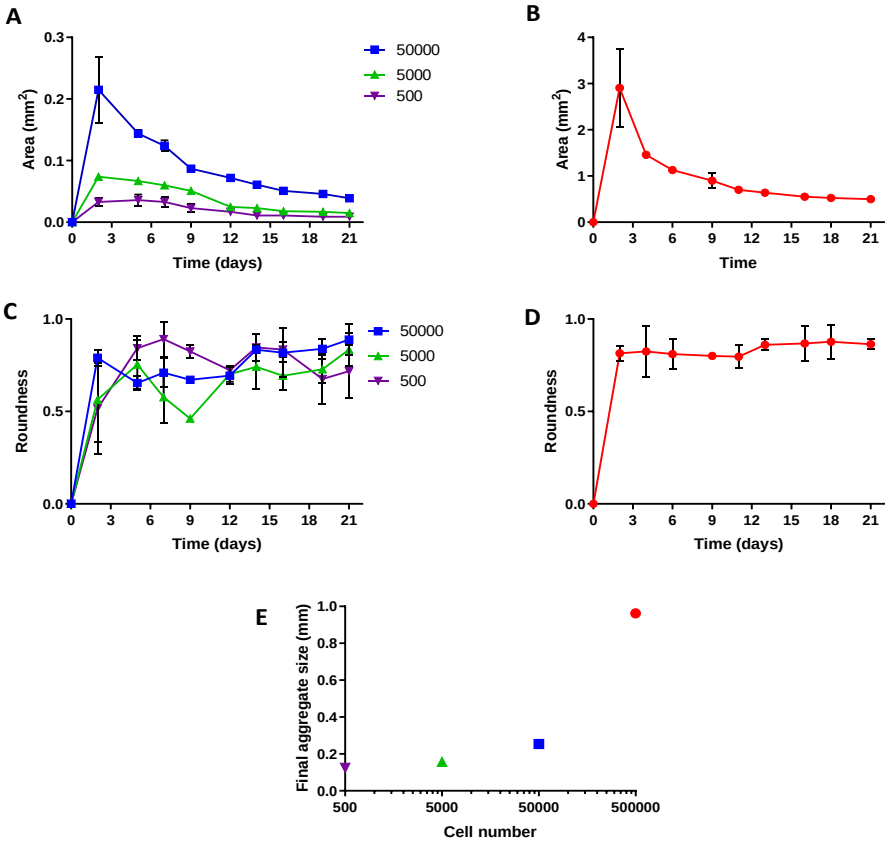

Figure 3.5 Image analysis plots of time-lapse HBMSC condensation over 21 days of chondrogenic differentiation culture: (A) Maximum aggregate cross sectional area over time for 50000, 5000 and 500 cell spheroids; (B) Maximum aggregate cross sectional area over time for 500000 cell spheroids; (C) Roundness for 50000, 5000 and 500 cell spheroids; (D) Roundness for 500000 cell spheroids; (E) Final aggregate size for all cell numbers (error bars are included within the data). The error bars represent the SD of n = 3 experimental replicates.

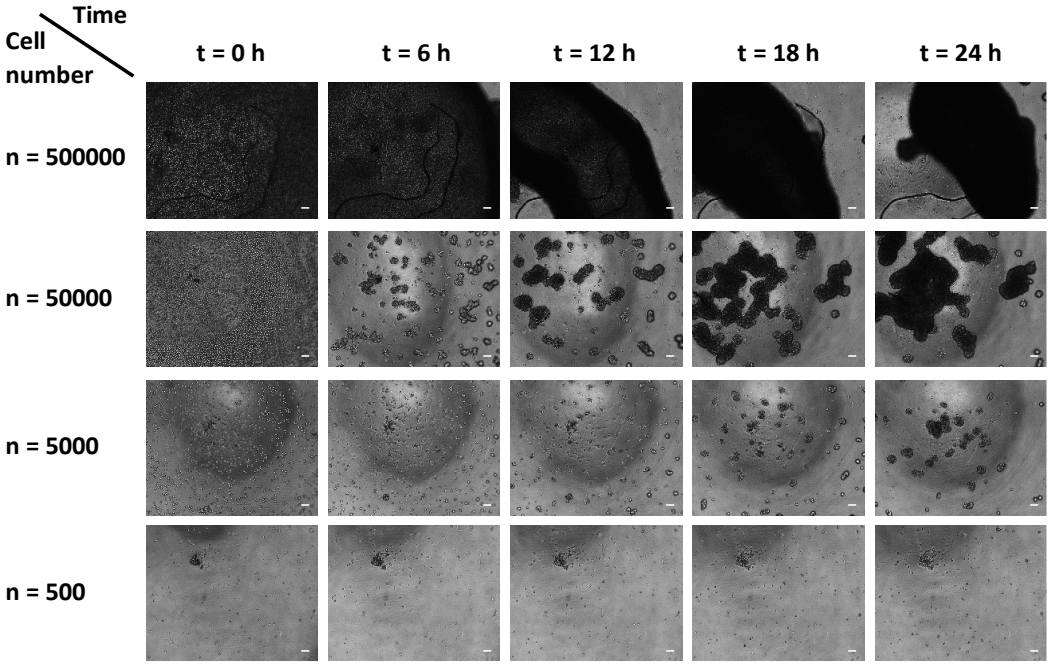

Figure 3.6 Morphological evolution of F78 P1 HAC aggregates from different ten-fold cell densities in 96-well microplates over a period of 24 h. Scale bar = 100 µm.

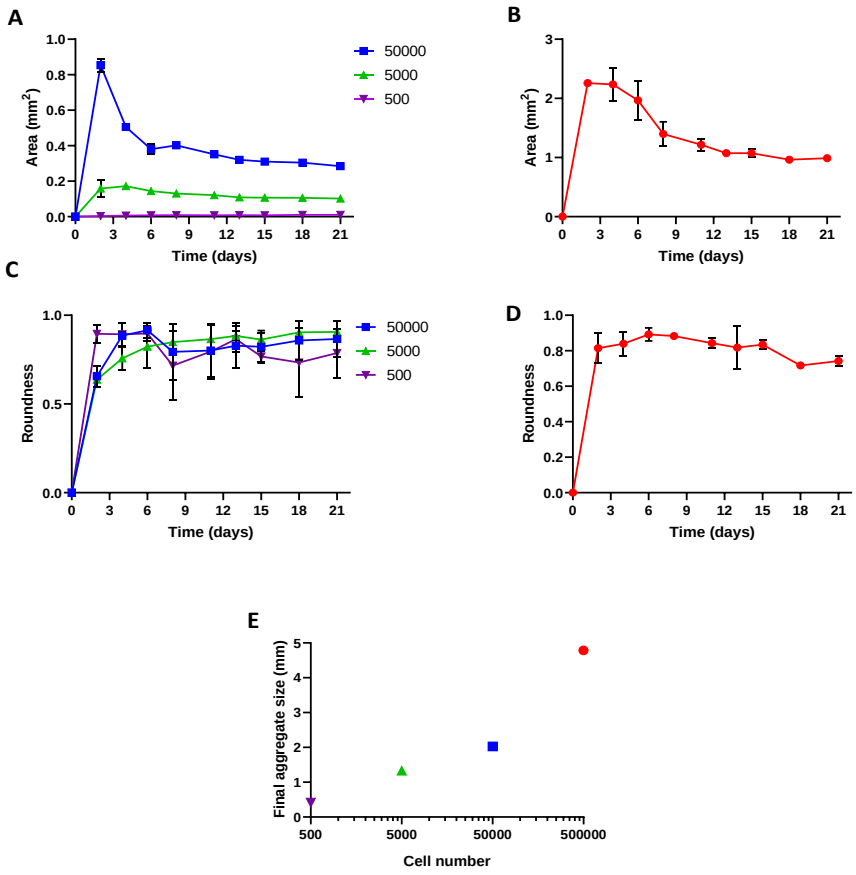

Figure 3.7 Image analysis plots of time-lapse HAC condensation over 21 days of chondrogenic differentiation culture: (A) Maximum aggregate cross sectional area over time for 50000, 5000 and 500 cell spheroids; (B) Maximum aggregate cross sectional area over time for 500000 cell spheroids; (C) Roundness for 50000, 5000 and 500 cell spheroids; (D) Roundness for 500000 cell spheroids; (E) Final aggregate size for all cell numbers (error bars are included within the data). The error bars represent the SD of n = 3 experimental replicates.

3.3.2 Chondrogenesis: characterisation of multicellular spheroids in chondrogenic differentiation culture

3.3.2.1 Multicellular spheroids from human primary cells successfully differentiated after 21 days of culture in round-bottom 96-well microplates

The ultra-low adherence BRAND InertGrade™ round bottom 96-well plates had not been validated as a platform for pellet culture, nor had the appropriate cell number range been established. As a proof of principle, a parallel experiment was designed culturing three cell types and seeding 500000 cells/well. ATDC5 were designated as positive chondroprogenitor control cells that have been reported to serve as a reference model for chondrogenesis (Tare et al., 2005). HACs and unselected HBMSCs primary cells were pelleted at passage 1 (P1). The former were reported in the literature to be a robust *in vitro* model for cartilage structural formation (Li et al., 2015) and the ability of the latter to differentiate into cartilage was evaluated. The three cell types were stained with Alcian

blue/Sirius red and Safranin O histological stainings and the immunolocalisation of SOX9 and type II collagen chondrogenic protein markers examined after 21 days of culture to determine the resulting histological features following chondrogenic differentiation.

The A/S staining on F74 P1 HACs (Figure 3.8A and F) exposed a PG-rich matrix with intense collagen distribution around the periphery and to a lesser extent inside the spheroid. Besides, a cartilage-like extracellular matrix with chondrocytes in lacunae embedded in it and enriched in PGs was observed throughout. SO confirmed abundant sGAG synthesis, mostly localised within the one half of the imaged pellet and appreciable by the strong orange to red staining (Figure 3.8B and G). Immunohistochemical staining for type II collagen again indicated concentrated collagen presence in the peripheral areas of the pellet and more evenly spaced inside. Similarly, SOX9 was generally distributed across the pellet yet more profusely in the lower left region (Figure 3.8D and I). The negative control lacking primary antibody incubation did not show any residual product from the AEC colourimetric reaction (Figure 3.8E and J).

F85 P1 HBMSCs spheroids stained with Alcian blue/Sirius red intensity did not produce the glycosaminoglycan matrix resembling cartilage seen in HACs with an intense blue staining and organised lacunar structures (Figure 3.9A and J). Safranin O staining was also visibly weaker, secluded to a small area with cartilage-like matrix and the remaining areas populated by cells with faint staining and undifferentiated morphologies (Figure 3.9B and G). HBMSCs were positive for type II collagen and SOX9 immunohistochemical stainings with overall expression inside the spheroids and weak Alcian blue counterstain (Figure 3.9C, D, H, E, H, I, J).

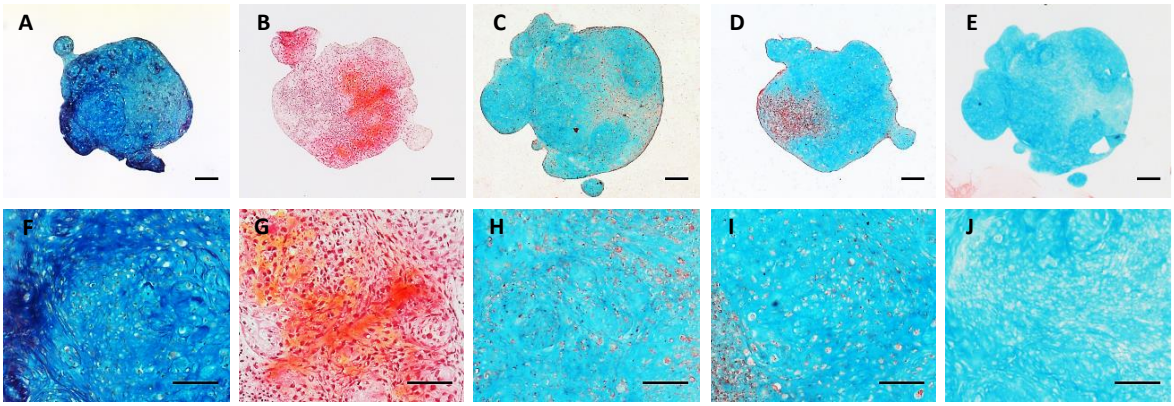

Figure 3.8 Histological and immunohistochemical stainings on positive primary control F74 P1 HAC spheroids after 21 days of chondrogenic differentiation culture with 500000 cells seeded initially in the 96-well culture platform: (A,F) Alcian blue/Sirius red staining; (B,G) Safranin O staining; (C,H) Immunohistochemical distribution of type II collagen; (D,I)Immunohistochemical distribution of SOX9; (E,J) Negative control for immunohistochemical staining. The scale bars for low magnification represent 200 µm, while those corresponding to high magnification are equivalent to 100 µm.

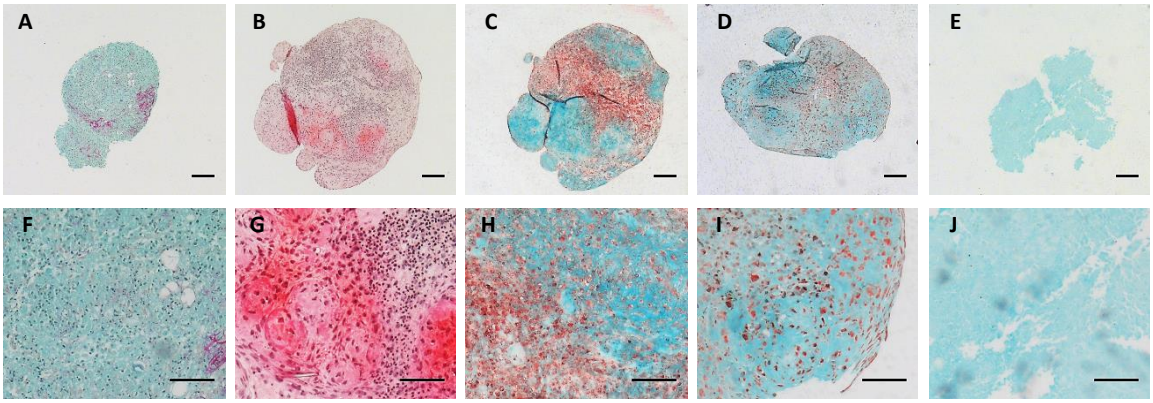

Figure 3.9 Histological and immunohistochemical stainings on F85 P1 HBMSC spheroids after 21 days of chondrogenic differentiation culture with 500000 cells seeded initially in the 96-well culture platform: (A,F) Alcian blue/Sirius red staining; (B,G) Safranin O staining; (C,H) Immunohistochemical distribution of type II collagen; (D,I) Immunohistochemical distribution of SOX9; (E,J) Negative control for immunohistochemical staining. The scale bars for low magnification represent 200 µm, while those corresponding to high magnification are equivalent to 100 µm.

ATDC5 spheroids shared a common trait with HBMSCs: suboptimal glycosaminoglycan and PG synthesis in the extracellular matrix as seen through faint Alcian blue staining in A/S (Figure 3.10A) sections and counterstains for IHC (Figure 3.10C, D and E) along with negligible SO staining at the edge of the samples (Figure 3.10B). In contrast, the size of ATDC5 spheroids increased over chondrogenic differentiation due to FBS supplementation. This might have caused the nutrient demand to rise, thus implying that the volume of media added to the wells might have been insufficient to meet it.

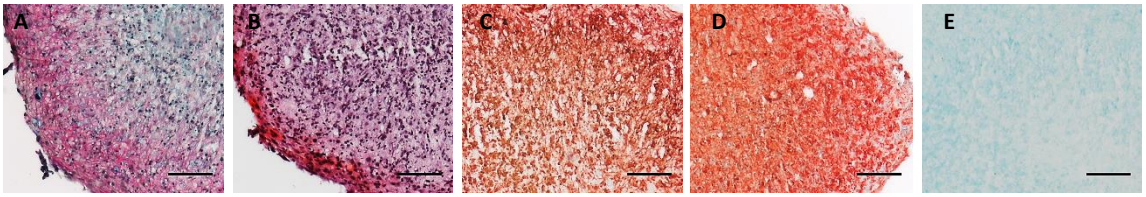

Figure 3.10 Histological and immunohistochemical stainings on ATDC5 spheroids after 21 days of chondrogenic differentiation culture with 500000 cells seeded initially in the 96-well culture platform: (A) Alcian blue/Sirius red staining; (B) Safranin O staining; (C) Immunolocalisation of type II collagen; (D,I) Immunolocalisation of SOX9; (E,J) Negative control for immunohistochemical staining. Scale bar = 100 µm.

3.3.2.2 Histological characterisation of multicellular spheroids over time: comparison of differentiation potential of unselected HBMSCs and HACs

Unselected HBMSCs and HACs were set as experimental controls to determine the differentiation potential of multicellular cell spheroids grown *in vitro* on ultra-low adherence plates, seeking to establish a threshold for analysis with regard to spheroids formed following microfluidic cell encapsulation in droplets. In addition, histological stainings (A/S and SO) served to address the

question of how many cells are optimal to detect favourable chondrogenic differentiation using this culture system.

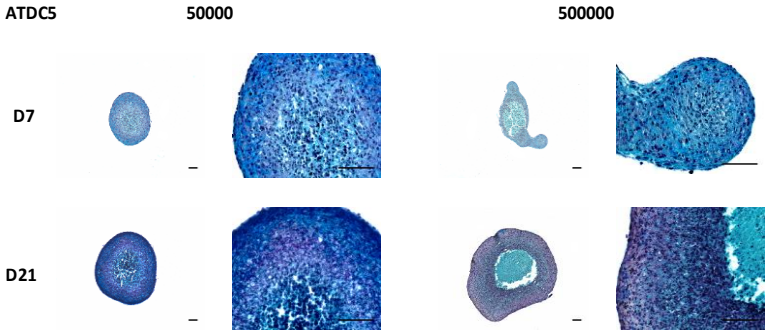

Figure 3.11 A/S stained 50000 and 500000 ATDC5 cell spheroid sections on day 7 (D7) and day 21 (D21) of chondrogenic differentiation culture. Scale bar = 100 µm.

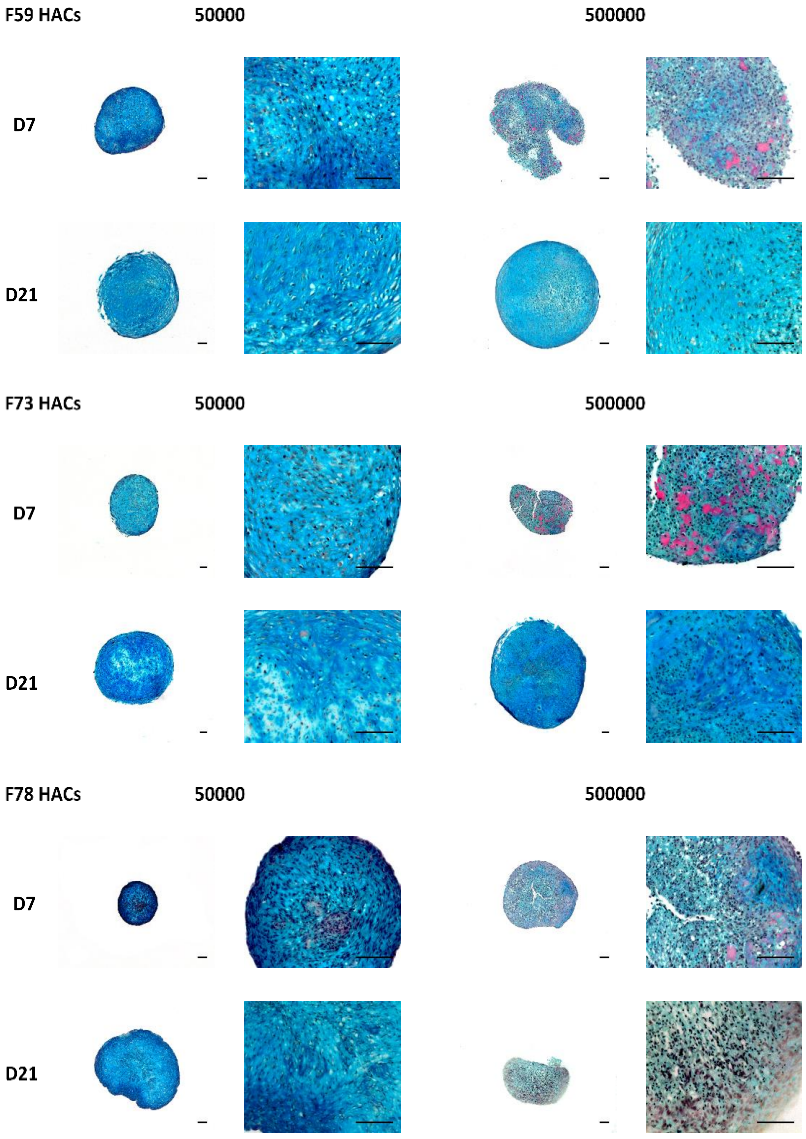

Figure 3.12 A/S stained 50000 and 500000 HAC cell spheroid sections from three human donors (F59, F73 and F78) on day 7 (D7) and day 21 (D21) of chondrogenic differentiation culture. Scale bar = 100 µm.

Given the known heterogeneity of unselected primary cells and for reasons of consistency with earlier studies, 50000 and 500000 spheroids were processed after 7 and 21 days of chondrogenic culture. The cells were sourced from three different patients (n = 3; F59, F73 and F78 P1) and both cell types corresponded to the same patient (i.e. femoral head and bone marrow). ATDC5 cells were again included as chondroprogenitor controls.

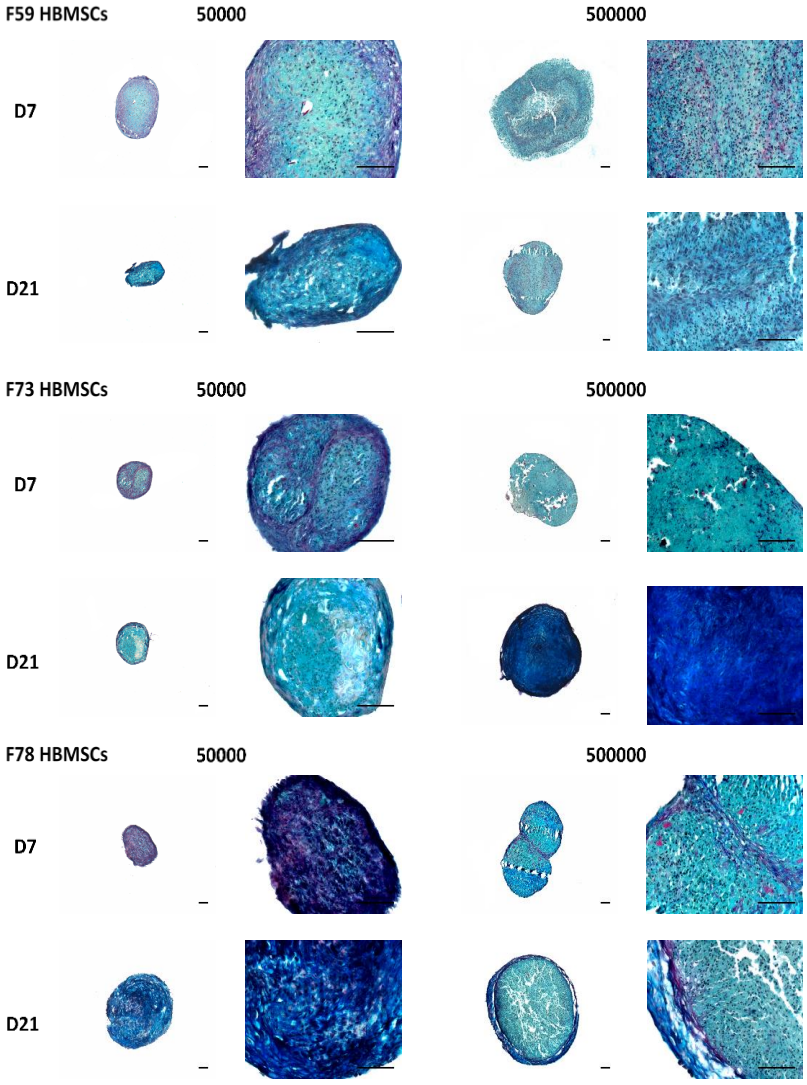

Figure 3.13 A/S stained 50000 and 500000 HBMSC cell spheroid sections from three human donors (F59, F73 and F78) on day 7 (D7) and day 21 (D21) of chondrogenic differentiation culture. Scale bar = 100 µm.

ATDC5, despite being a documented robust chondroprogenitor cell line, failed to display a clear cartilage-like matrix and rather underwent an irregular differentiation, as shown in A/S and SO histological sections (Figure 3.11 and Figure 3.14). 50000 cell spheroids produced a more uniform histological structure compared to 500000 cell samples. An overall differentiation gradient was nevertheless observed that resulted in differentiated cells at the periphery and less differentiation and ultimately necrosis towards the core.

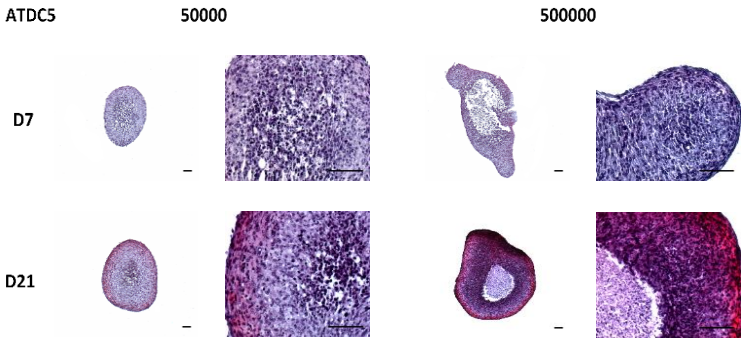

Figure 3.14 SO stained 50000 and 500000 ATDC5 cell spheroid sections on day 7 (D7) and day 21 (D21) of chondrogenic differentiation culture. Scale bar = 100 µm.

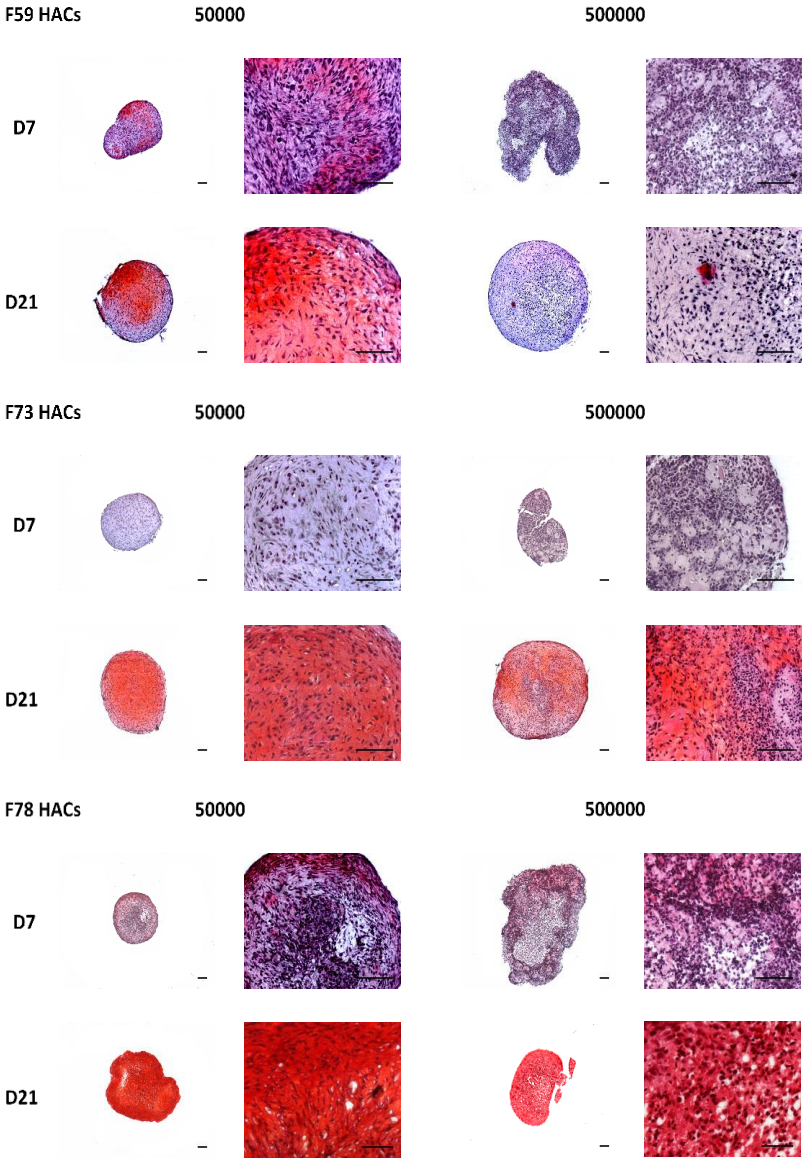

Figure 3.15 SO stained 50000 and 500000 HAC cell spheroid sections from three human donors (F59, F73 and F78) on day 7 (D7) and day 21 (D21) of chondrogenic differentiation culture. Scale bar = 100 µm.

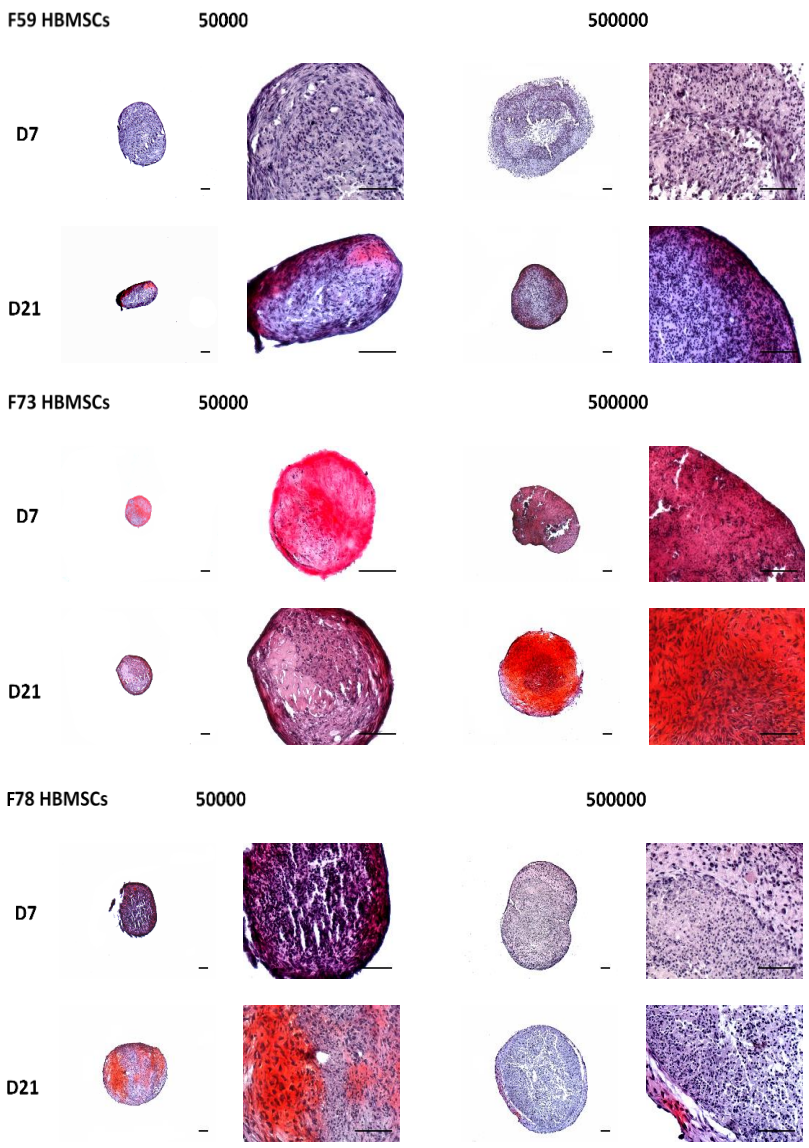

Figure 3.16 SO stained 50000 and 500000 HBMSC cell spheroid sections from three human donors (F59, F73 and F78) on day 7 (D7) and day 21 (D21) of chondrogenic differentiation culture. Scale bar = 100 µm.

The highest degree of patient variability was observed in HBMSCs. A/S and SO stainings revealed a slightly more advanced differentiation for 50000 cell spheroids (Figure 3.13 and Figure 3.16),with a single exception with strong AS and SO stainings for 500000 F73 HBMSCs. 500000 samples comprised a range from fairly incomplete (F59 and F78) to more successful differentiation (F73). F78 HBMSCs, for instance, had a distinct narrow outer layer of differentiated cells with a distinct undifferentiated structure for the rest of the section area.

HACs, however, had a closer histological structure to that of hyaline cartilage yet they faced the effects of variability among patients. A clearer transition was identified from undifferentiated cells on day 7 to some lacunar morphologies resembling cartilage tissue on day 21. HACs consistently showed strong AS and SO staining for all 50000 cell samples, as opposed to highly varying 500000

cell ones. F73 HACs had both strong A/S and SO, F59 AS had strong AS but faint SO staining and F78 AS staining pointed to a remarkable absence of differentiation coupled with a fairly modest SO staining (Figure 3.12 and Figure 3.15).

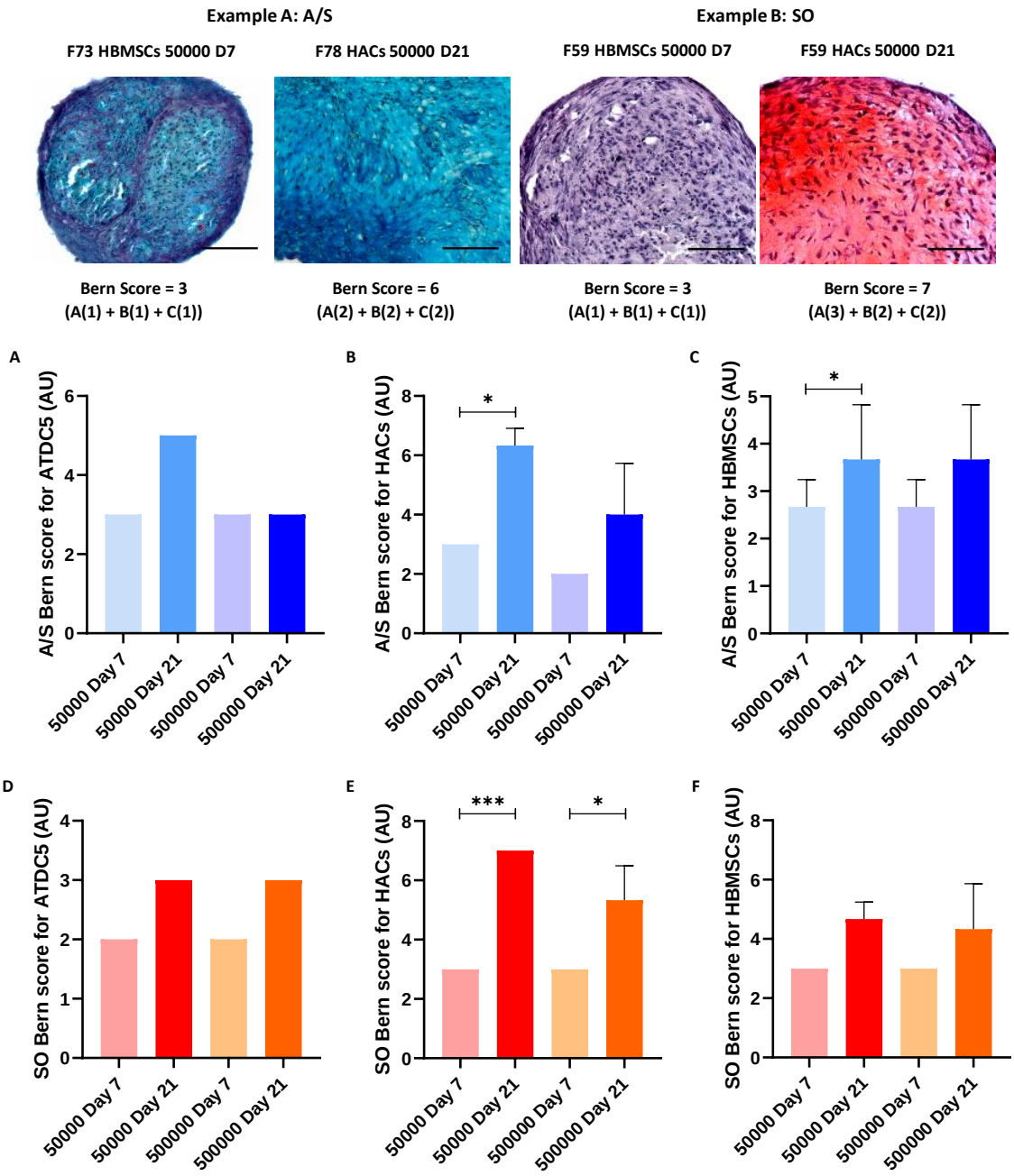

Figure 3.17 Bern scores for A/s stainings of ATDC5 (A), HACs (B), HBMSCs (C) and for SO stainings of ATDC5 (D), HACs (E) and HBMSCs (F). Two-way ANOVA Tukey's multiple comparisons test was used to determine statistical significance: * ($p \leq 0.05$), *** ($p \leq 0.001$). Practical examples A and B of Bern scoring on sample images stained with A/S and SO are illustrated above. Scale bar = 100 µm.

A/S and SO generally revealed complementary matching histological morphology and outlined the expected heterogeneity that was heavily marked in HBMSCs, where the starting population of cells was made up of diverse adherent cell types. 50000 was the most robust cell number for histological

characterisation on spheroids formed using ultra-low adherence 96-well plates, with a minimised risk of necrosis associated with it.

When the sections were evaluated using Bern score categories for all three cell types and both stainings, the analysis outlined significant improvements from day 7 to day 21 for 50000 HAC and HBMSC pellets stained with A/S and a similar trend seen for SO HACs and non-significant increases in the score values for all 500000 cell pellets regardless of AS and SO staining after 21 days of culture and 50000 HBMSC SO-stained sections (Figure 3.17).

3.3.2.3 Effect of cell number on chondrogenesis of small multicellular spheroids

The study of chondrogenesis was expanded and scaled down to lower cell numbers to approach more relevant cell aggregate dimensions for microfluidic encapsulation and adding a time point set on day 7 in agreement with the project hypothesis of early SOX9 expression being predictive of chondrogenesis. The spheroids collected were characterised by immunofluorescence histochemistry on slides for processed and paraffin embedded 50000 and 500000 cell samples and whole mount on 5000 and 500 cells to elucidate any cell number-related impact on chondrogenesis. This distinction between paraffin embedding and whole mount staining was based on the information from time-lapse cell aggregation about spheroid dimensions for all cell types.

3.3.2.3.1 Fluorescent immunohistochemistry for characterisation of SOX9 distribution

SOX9, type II collagen and aggrecan protein expression was the criterion to assess chondrogenesis in ATDC5 and HBMSCs. ATDC5 cells stained positive for SOX9 and type II collagen. Type II collagen was distinctly present from day 7 and developed into a tighter fibrous network by day 21 (Figure 3.18I and J). SOX9 was detected as well, although the morphological structure of the staining was not completely evident owing to non-specific binding and undesired background (Figure 3.18G and H). Similar staining outcomes were observed in M74 P1 HBMSCs. Type II collagen was expressed on day 7 and day 21, seemingly becoming moderately more predominant over time but requiring detailed quantification due to the inferior integrity and resolution of the smaller sample on day 21 (Figure 3.19I and J). SOX9 expression on HBMSCs displayed the same issue as ATDC5 sections, meaning that there existed general background on the sample and a few sparse nuclear-like shapes throughout the pellet impeding conclusive determination (Figure 3.19G and H). The negative control samples did not reveal any major autofluorescence background contributions (Figure 3.18F and Figure 3.19F).

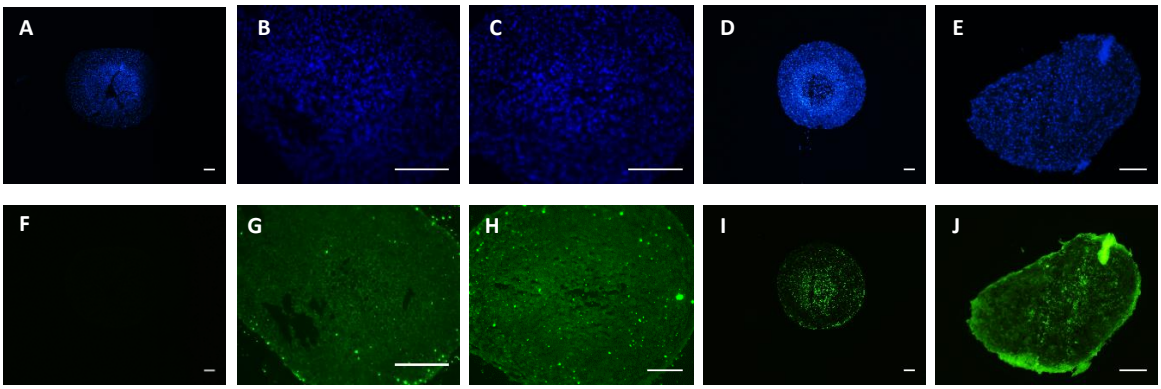

Figure 3.18 Immunofluorescence staining on ATDC5 spheroids after 7 and 21 days of chondrogenic differentiation culture with 50000 cells initial cell-seeding density: (A) Negative control DAPI counterstain; (B) Day 7 spheroid stained for SOX9 counterstained with DAPI; (C) Day 21 spheroid stained for SOX9 counterstained with DAPI (D) Day 7 spheroid stained for type II collagen and DAPI counterstain; (E) Day 21 spheroid stained for type II collagen and DAPI counterstain; (F) Negative control without primary antibody addition; (G) Day 7 spheroid SOX9; (H) Day 21 spheroid SOX9; (I) Day 7 spheroid type II collagen; (J) Day 21 spheroid type II collagen. Scale bar = 100 µm for A, D, E, F, I and J and 200 µm for B, C, G and H.

Aggrecan synthesis was also examined to complete the set of chondrogenic markers on F78 P1 HBMSC sections with 50000 cell spheroids. Localised regions of intense aggrecan expression was apparent on approximately half of the surface of the spheroid section on day 21 (Figure 3.20F), starting from a faint general distribution on day 7 (Figure 3.20E). Again, background autofluorescence was negligible (Figure 3.20D).

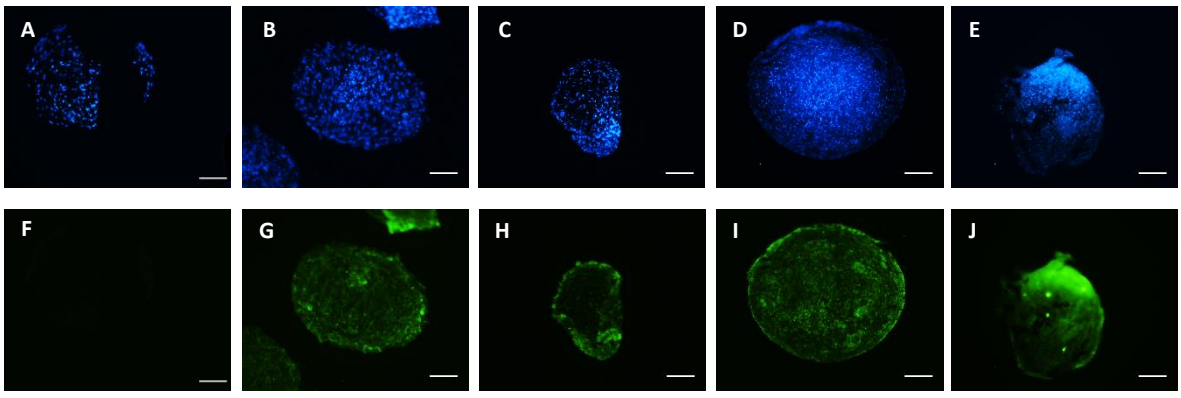

Figure 3.19 Immunofluorescence staining on M74 P1 HBMSC spheroids after 7 and 21 days of chondrogenic differentiation culture with 50000 cells initial cell-seeding density: (A) Negative control DAPI counterstain; (B) Day 7 spheroid stained for SOX9 counterstained with DAPI; (C) Day 21 spheroid stained for SOX9 counterstained with DAPI (D) Day 7 spheroid stained for type II collagen and DAPI counterstain; (E) Day 21 spheroid stained for type II collagen and DAPI counterstain; (F) Negative control without primary antibody addition; (G) Day 7 spheroid SOX9; (H) Day 21 spheroid SOX9; (I) Day 7 spheroid type II collagen; (J) Day 21 spheroid type II collagen. Scale bar = 100 µm.

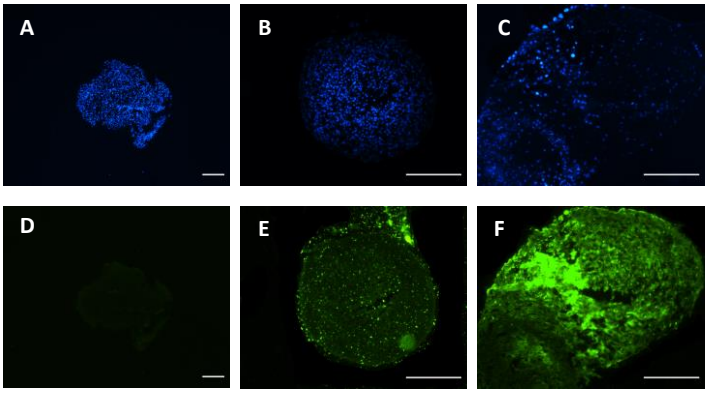

Figure 3.20 Immunofluorescence staining on F78 P1 HBMSC spheroids after 7 and 21 days of chondrogenic differentiation culture with 50000 cells initial cell-seeding density: (A) Negative control DAPI counterstain; (B) Day 7 spheroid stained for SOX9 counterstained with DAPI; (C) Day 21 spheroid counterstained with DAPI; (D) Negative control without primary antibody addition (E) Day 7 spheroid stained for aggrecan and DAPI counterstain; (F) Day 21 spheroid stained for aggrecan and DAPI counterstain. Scale bar = 100 µm.

In an analogous manner to the histological characterisation, SOX9 expression across different cell numbers was a research question to investigate to further verify whether 50000 cell spheroids were indeed optimal for this transcription factor of interest of this research project. The study also targeted the heterogeneity issue of unselected primary cells, as well as the concept of SOX9 suitability for early sorting of robust cell populations for cartilage. The experiment replicated the cell types, numbers and time points selected for A/S and SO stainings and included the minor protocol amendments detailed in section 2.6.

The modifications included improved the quality of the IF detected in tissues, removing part of the non-specific background existing before. ATDC5 cells presented indistinct SOX9 expression regardless of cell number or time point matching nuclear DAPI stain partially coupled with influence from background fluorescence (Figure 3.21). HACs samples varied across patients: very clear, homogeneous and widespread SOX9 nuclear staining for F59 and F73 and less so for F78 (Figure 3.22). SOX9 expression in HBMSCs was good in specific localised regions of the sections and inferior elsewhere, thus showing the highest degree of heterogeneity within separate sections but also across human donors (Figure 3.23). The time point of analysis, early (day 7) or late (day 21), was not found to be critical for any cell type.

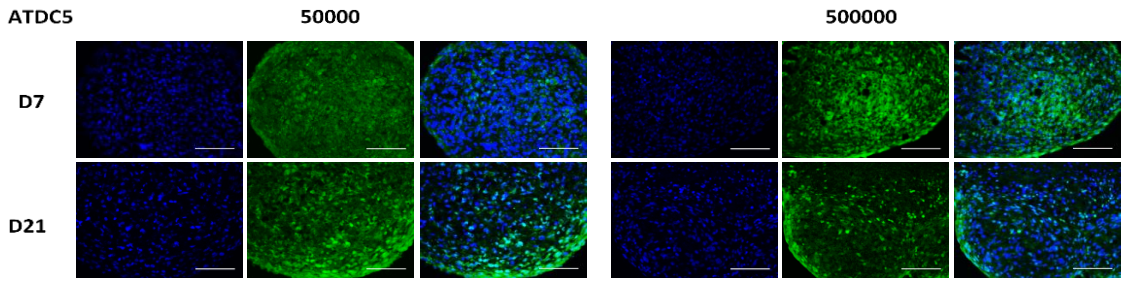

Figure 3.21 SOX9 immunofluorescence distribution in ATDC5 sections on slides for 50000 and 500000 cells on day 7 and day 21. DAPI (left), SOX9 (middle) and merged DAPI/SOX9 are shown for each cell number and time point. Scale bar = 100 µm.

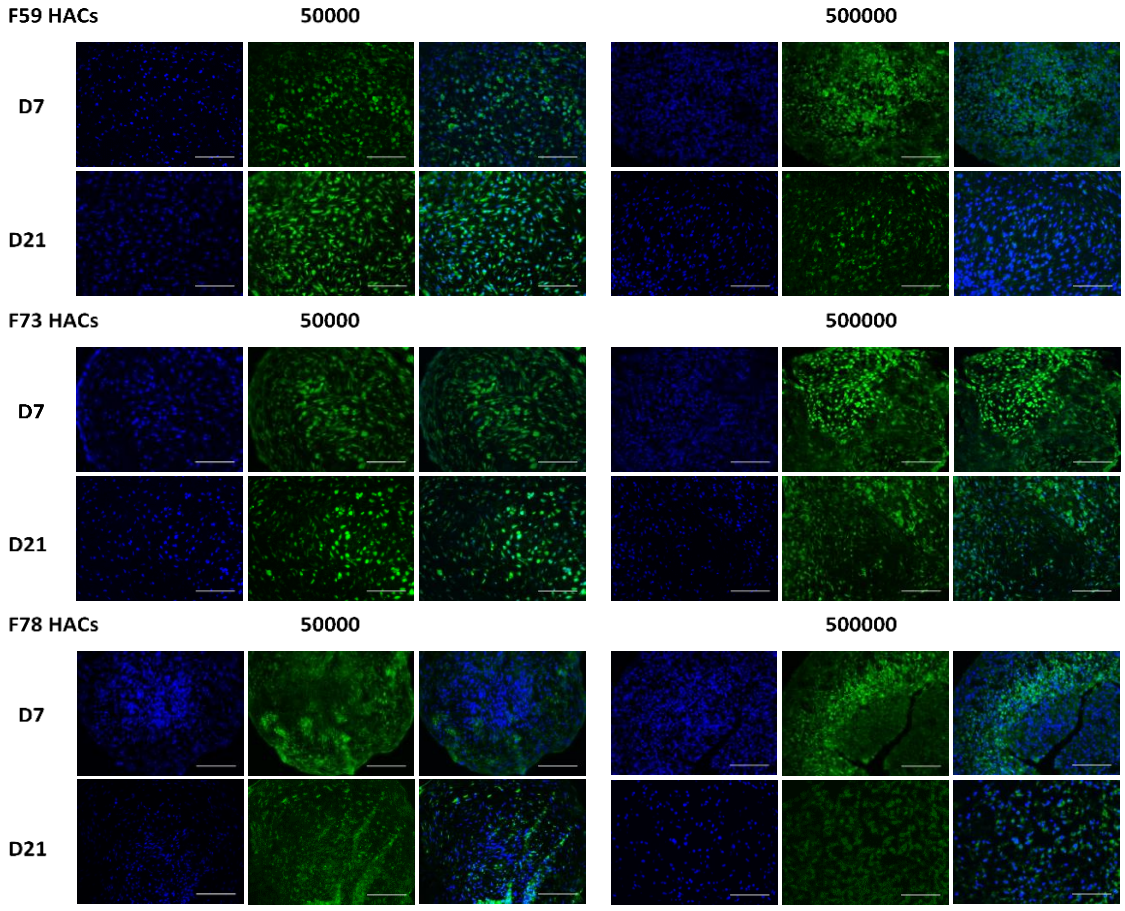

Figure 3.22 SOX9 immunofluorescence distribution in HAC sections from three donors (F59, F73 and F78) on slides for 50000 and 500000 cells on day 7 and day 21. DAPI (left), SOX9 (middle) and merged DAPI/SOX9 are shown for each cell number and time point. Scale bar = 100 µm.

Patient-to-patient variation was the most influential factor on any differences appearing between samples across all cell types regarding SOX9 expression over time point or cell number. SOX9 reflected population heterogeneity as a marker linked to the histological results outlined in the

previous section, implying that a robust and distinctly homogeneous SOX9 distribution correlated with a structure and morphology resembling hyaline cartilage.

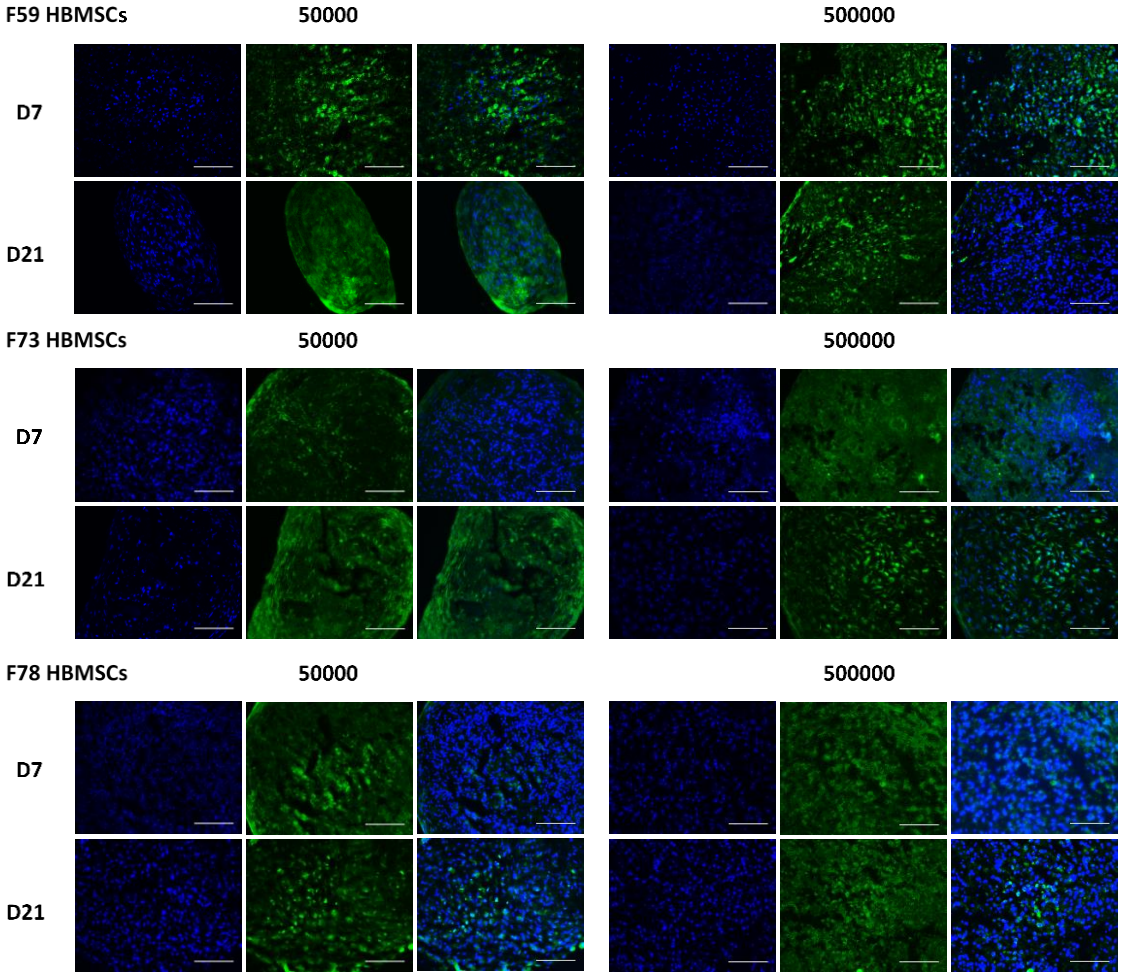

Figure 3.23 SOX9 immunofluorescence distribution in HBMSC sections from three donors (F59, F73 and F78) on slides for 50000 and 500000 cells on day 7 and day 21. DAPI (left), SOX9 (middle) and merged DAPI/SOX9 are shown for each cell number and time point. Scale bar = 100 μm.

3.3.2.3.2 Fluorescent immunohistochemistry on whole mount samples

Whole mount ATDC5 (control) and HBMSC spheroids comprised of 500 and 5000 cells were stained for SOX9 and type II collagen on day 7 and day 21 to examine their expression as early and late chondrogenic markers, respectively (Figure 3.24).

The negative control sample stained with the Alexa Fluor 488 secondary antibody showed minor non-specific background staining. From a morphological perspective, whole mount multicellular spheroids exhibited dense type II collagen fibrous networks and varying densities of SOX9 nuclear staining.

Maximum projections of ATDC5 spheroids suggested sustained SOX9 expression, as expected from their chondroprogenitor ability; and initial localised sparse type II collagen (COL2) expression. Collagen apparently became restricted to the periphery of the spheroid as it expanded during culture (lacking confirmation from confocal microscopy; the fluorescent image shown for day 21 sample was taken using fluorescence microscopy on the Nikon Eclipse Ti microscope).

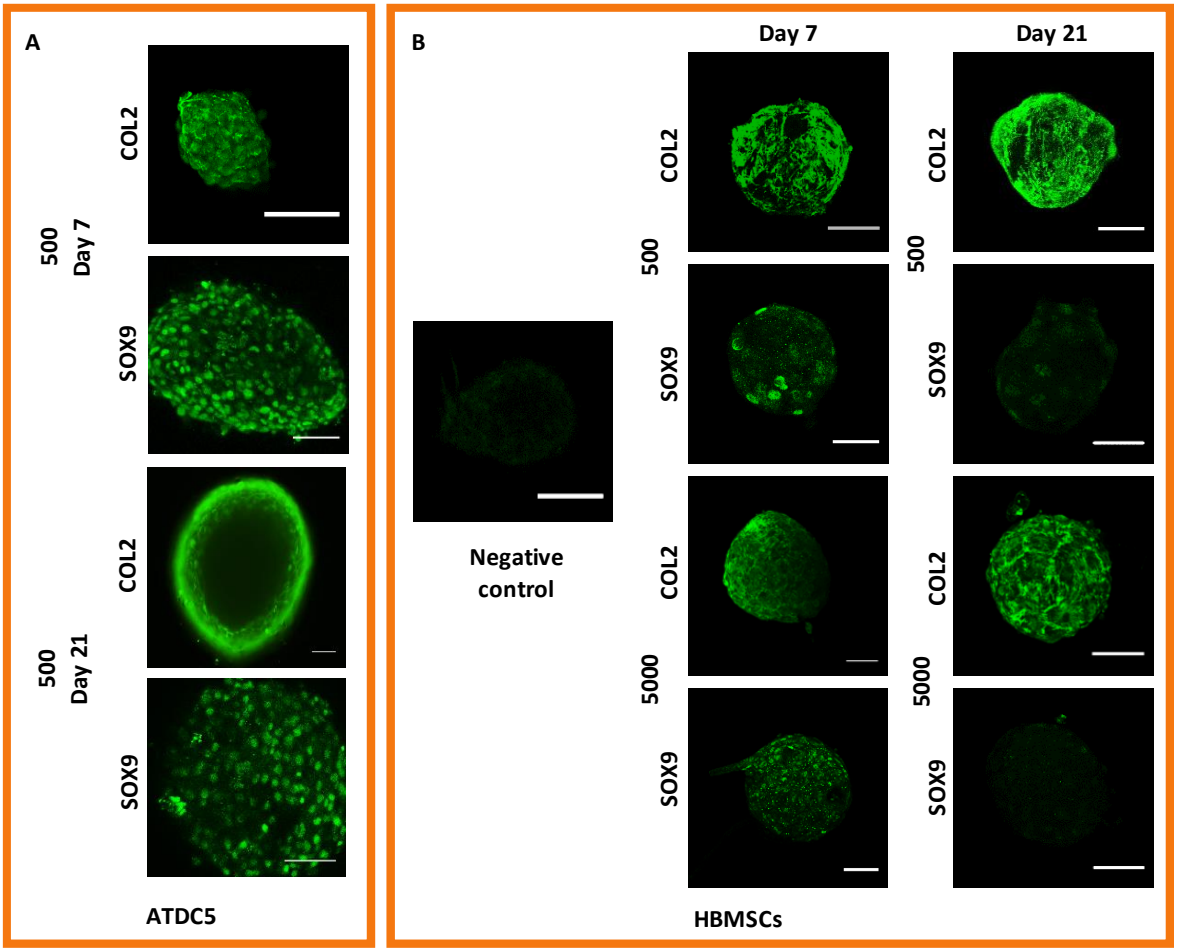

Figure 3.24 Maximum projection of (A) ATDC5 and (B) M74 P1 HBMSC whole mount spheroids stained for SOX9 and Type II collagen after 7 and 21 days of chondrogenic differentiation culture. Scale bar = 100 µm for ATDC5 and 5000 HBMSC spheroids; 50 µm for 500 HBMSC aggregates.

HBMSCs samples followed a different protein expression trend for SOX9 expression: downregulation on day 21 with respect to day 7. Changes in type II collagen expression were harder to assess; the staining extended across the spheroid forming denser networks in 5000 cell sample by day 21 but 500 cell samples could not be clearly distinguished on the basis of their staining distribution or intensity from day 7 to day 21.

Semi-quantitative ROI image analysis to measure antibody penetration in small spheroids

Dye penetration analysis was separated for COL2 and SOX9 antibodies (Figure 3.25 and Figure 3.26). Complete dye diffusion occurred in ATDC5 500 cell day 7 spheroid stained for collagen. DAPI

managed to diffuse entirely into the rest of the 500 cell samples from primary M74 P1 HBMSCs. Collagen antibody penetration was confined to the outer regions of the spheroids with similar values for day 7 and day 21 spheroids: 11% and 8% of the total diameter of the spheroids accessible, respectively. DAPI underwent a drastic reduction in its diffusion across the spheroid in larger 5000 human cell samples, thus accounting for detrimental physical barriers imposed by over three-fold diameter increase from 500 to 5000 cell samples. The resulting computed percentages of dye diffusion for DAPI were close in range, 12-13%, and so were those for COL2, 4-5%.

SOX9 dye antibody diffusion into the spheroid was comparatively inferior to COL2. The modest rise in % diffusion from day 7 to day 21 (10-11%) for ATDC5 aggregates was contrary to the doubling total area (Figure 3.5A) quantified in time-lapse experiment and might merely respond to an abnormally large size as a result of cell seeding-derived inaccuracies when setting up the culture plate (Figure 3.26). SOX9 downregulation in HBMSCs from day 7 to day 21 for both cell numbers agreed with maximum projections in spite of spheroid shrinkage over culture. DAPI adhered to the same trend reported for 500 and 5000 cell spheroids stained for collagen.

The final optimised method detailed in section 2.7.2.1 (and developed through the experiments in Appendix B.5.1) was applied to 500 and 5000 cell spheroids to assess the suitability of SOX9 as an early indicative marker of chondrogenic differentiation and to analyse whether discernible heterogeneity existed among replicate samples or any variations in expression on different time points or related to cell number.

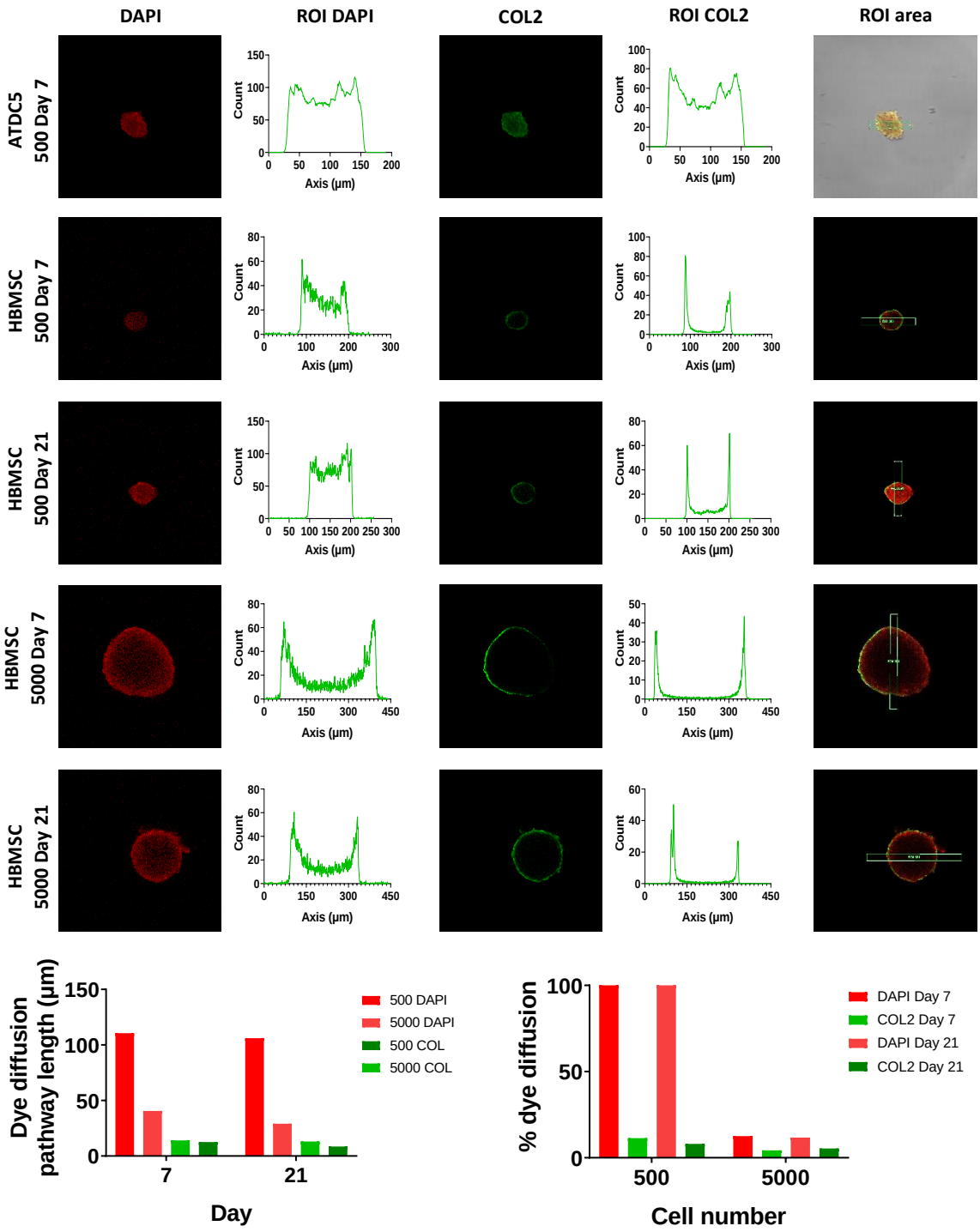

Figure 3.25 Dye diffusion semi-quantitative image analysis relative to DAPI and type II collagen of 500 cell ATDC5 and 500/5000 cell M74 P1 HBMSC whole mount spheroids after 7 and/or 21 days of chondrogenic differentiation culture including separate channels for DAPI and type II collagen, and their ROI peaks from which calculations were extracted. The graphs below depict average dye diffusion length (left) for HBMSCs and the relative % dye diffusion normalised to spheroid diameter (right). ATDC5 spheroid not contained in the graphs displayed complete dye diffusion.

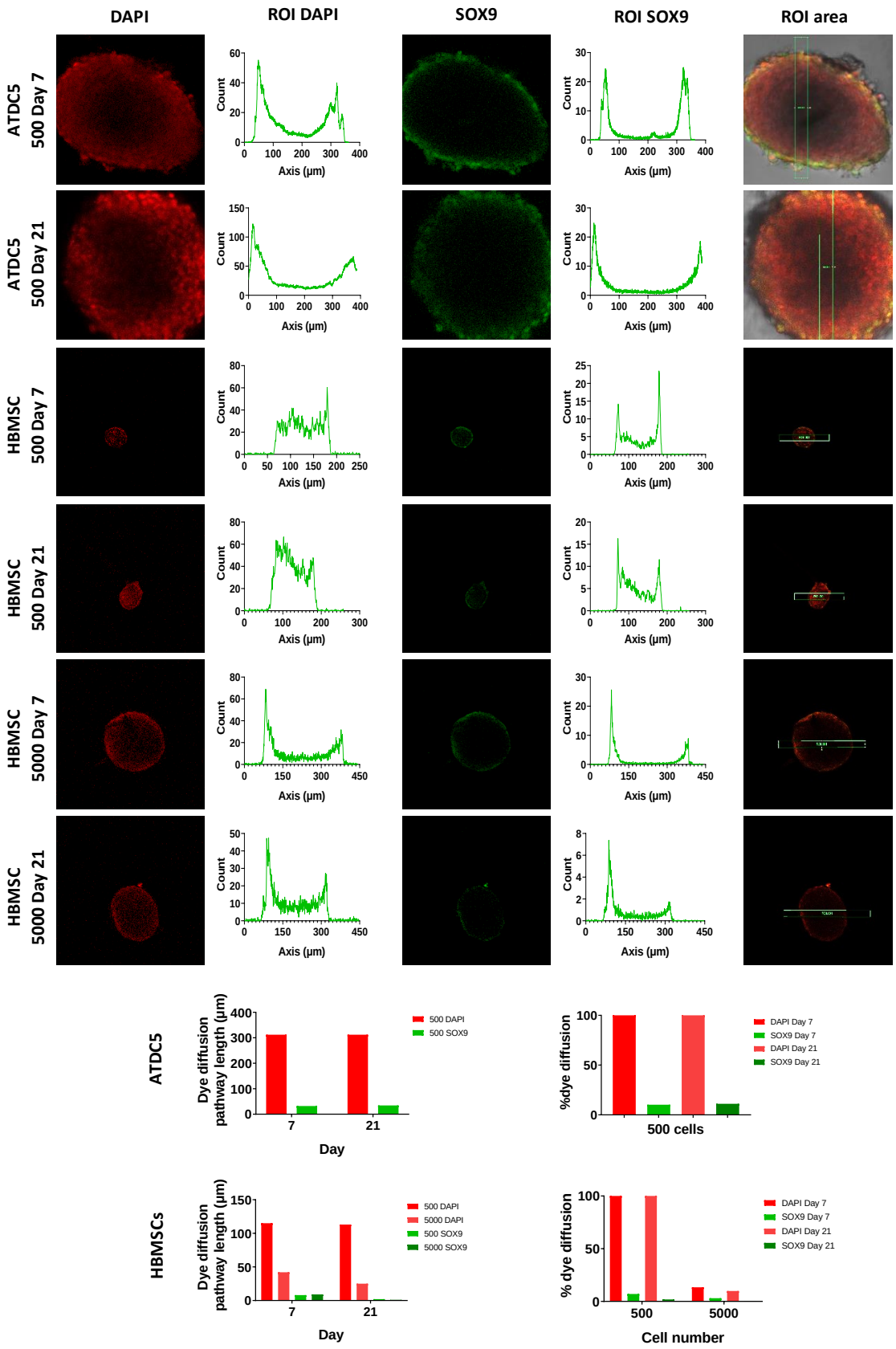

Figure 3.26 Dye diffusion semi-quantitative image analysis relative to DAPI and SOX9 of 500 cell ATDC5 and 500/5000 cell M74 P1 HBMSC whole mount spheroids after 7 and/or 21 days of chondrogenic differentiation culture including separate channels for DAPI and SOX9, and their ROI peaks from which calculations were extracted. The graphs below depict average dye diffusion length (left) for ATDC5 and HBMSCs respectively, and their relative % dye diffusion normalised to spheroid diameter (right).

Early SOX9 expression in whole mount HBMSCs and HACs

Based on the findings in the previous section indicating higher SOX9 expression in HBMSCs for the early time point on day 7, the study was expanded to the first week of chondrogenic differentiation. The aim was to analyse any changes in expression derived from culture time (day 1, 3 and 7) or cell number (500 and 5000) and sources of heterogeneity (i.e. donor, replicate spheroids, cells within spheroids). The negative controls exhibited a minimal non-specific background signal coming from the Alexa Fluor 488 secondary antibody alone. day 1 samples presented a limitation in that spontaneous aggregation, as described in section 3.3.1, failed to lead to a compact spheroid before 2-3 days of chondrogenic differentiation culture and subjected to sample variability. The samples did express SOX9 although their size and observation conditions did not allow a clear level of detail in terms of SOX9 distribution (Figure 3.27).

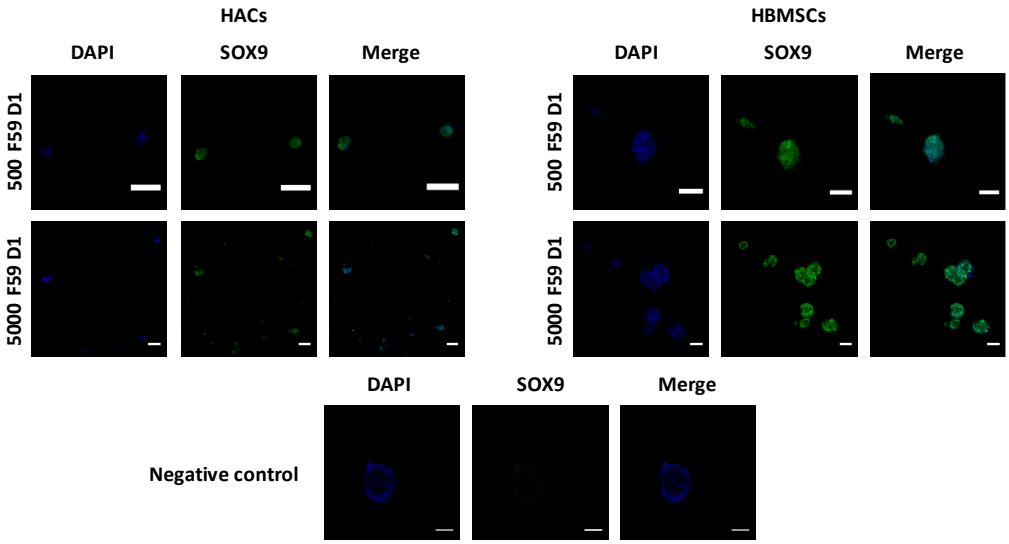

Figure 3.27 Comparative SOX9 immunofluorescence distribution in HACs and HBMSCs from a whole mount sample, F59, on day 1 (top) and negative control (bottom). The results were validated through the biological replicates in Appendix B.5.1 (n = 3). Scale bar = 25 µm (day 1 HAC and HBMSC samples) and 100 µm (negative control).

To give an indication of patient variability, SOX9 expression was compared between cultures from three biological samples (F59, F73 and F78). No appreciable differences in SOX9 expression were observed between donors or as a function of time (i.e. day 3 and day 7) or cell number (i.e. 500 and 5000). In accordance with previous histological staining results and larger immunofluorescent sections, HACs were characterised by an even SOX9 distribution in the surrounding area of cell nuclei counterstained with DAPI across the stained spheroids. HBMSCs showed greater variability with respect to DAPI despite beingam positive for SOX9 expression in all the treatments included in the analysis (Figure 3.28, Figure 3.29 and Appendix B.5.1). Sample replicates adhered to similar SOX9 expression patterns regardless of cell number or days of culture for the two given primary cell types. Cell number was the most important factor for the staining to be discernible at the core of

the spheroid. While 500 cell aggregates displayed complete SOX9 penetration into the core of the spheroid, SOX9 distribution in 5000 cell aggregates was mostly peripheral with decreasing SOX9 fluorescence signal intensity towards the core of the spheroid. The antibody staining was heavily spheroid diameter-dependant and hence affected by cell number.

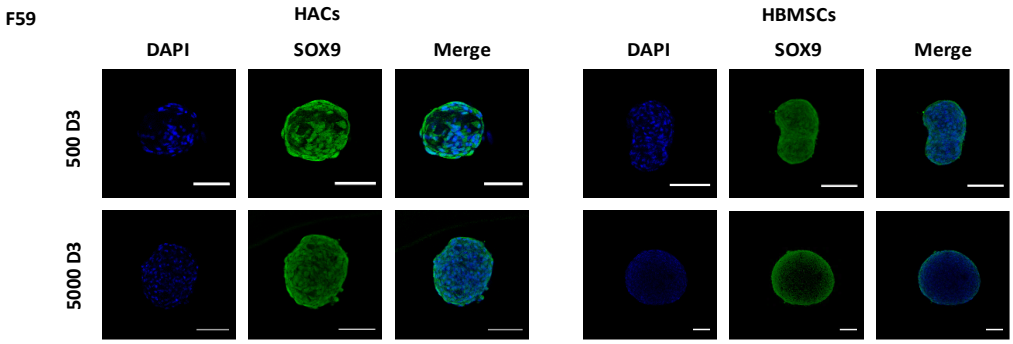

Figure 3.28 Comparative whole mount SOX9 IF distribution in HACs and HBMSCs from F59 sample on day 3. Biological replicates were stained to validate results, all of them presented in Appendix B.5.1 (n = 3). Scale bar = 100 µm.

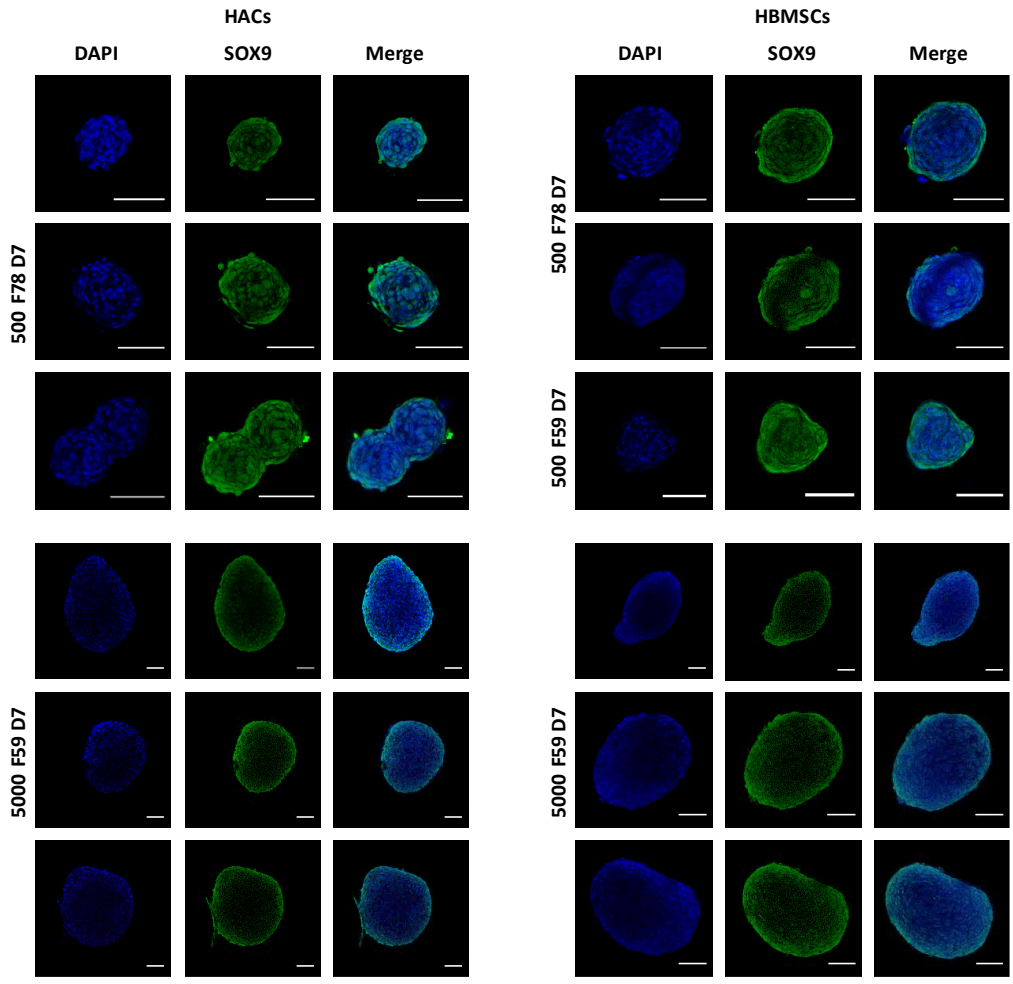

Figure 3.29 Comparative SOX9 IF distribution in 500 (top) and 5000 (bottom) HAC (left) and HBMSC (right) replicates from whole mount samples stained on day 7 of chondrogenic differentiation and displaying heterogeneity across them. The comparison was extended to biological replicates and the complete set of images is shown in the Appendix B.5.1 (n = 3 biological samples). Scale bar = 100 µm.

To test the central hypothesis of the study that SOX9 has a heterogeneous expression pattern among human bone marrow stromal cell subpopulations, differences between spheroid replicates from a single given donor were also characterised. This is important as the existence of such heterogeneity could indicate the possibility of sorting aggregates based on differences in SOX9 expression. To address this question, HACs and HBMSC were stained at larger number of replicates on a specific time point (3 days of chondrogenic stimulation).

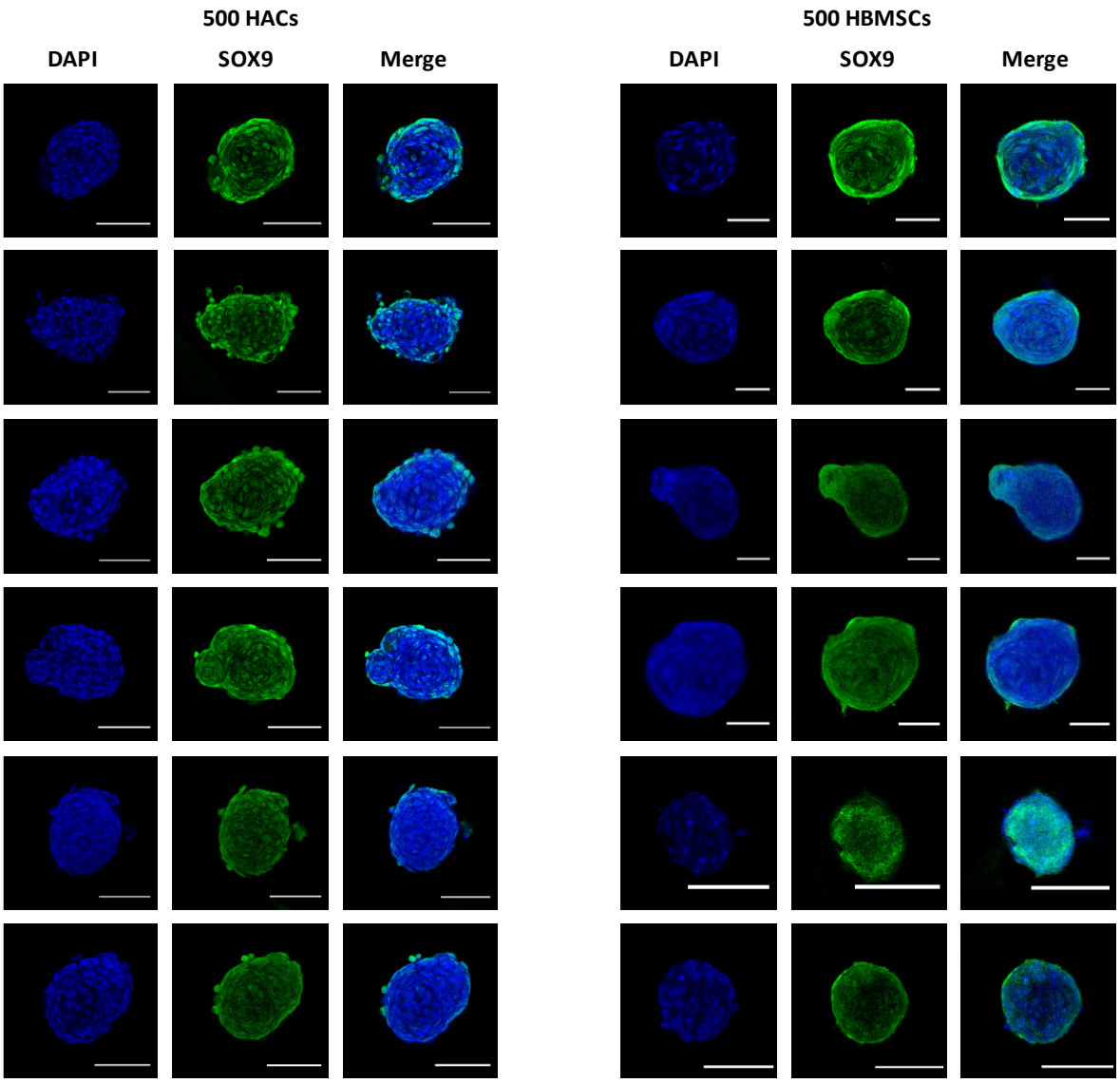

Figure 3.30 Comparative SOX9 immunofluorescence distribution in 500 HAC (left) and HBMSC (right) replicate spheroids stained after 3 days of chondrogenic differentiation on ultra-low adherence well plates (n = 1 biological sample). Scale bar = 100 µm.

500 cell spheroids permitted full antibody diffusion into the spheroid and showed SOX9 distribution in cell nuclei. HACs displayed a homogeneous SOX9 distribution and the cell morphology was for the most part round and resembling cartilage. HBMSCs, in contrast, had localised SOX9 expression and presented small areas composed of groups of round cells and the majority having a variety of different shapes and sizes (e.g. spindle, fibrous). SOX9 did not fully localise to the cell nuclei in

HBMSCs, with variation across replicates (Figure 3.30; i.e. unlike the two 500 HBMSC spheroid replicates at the top showing a higher number of cells that were positive for SOX9 and corresponded to the counterstained DAPI nuclei, the two bottom replicates had a more non-specific expression pattern). Differences in SOX9 distribution were therefore identified between HBMSC spheroid replicates accompanied by intra-spheroid SOX9 heterogeneity which were not observed in HACs.

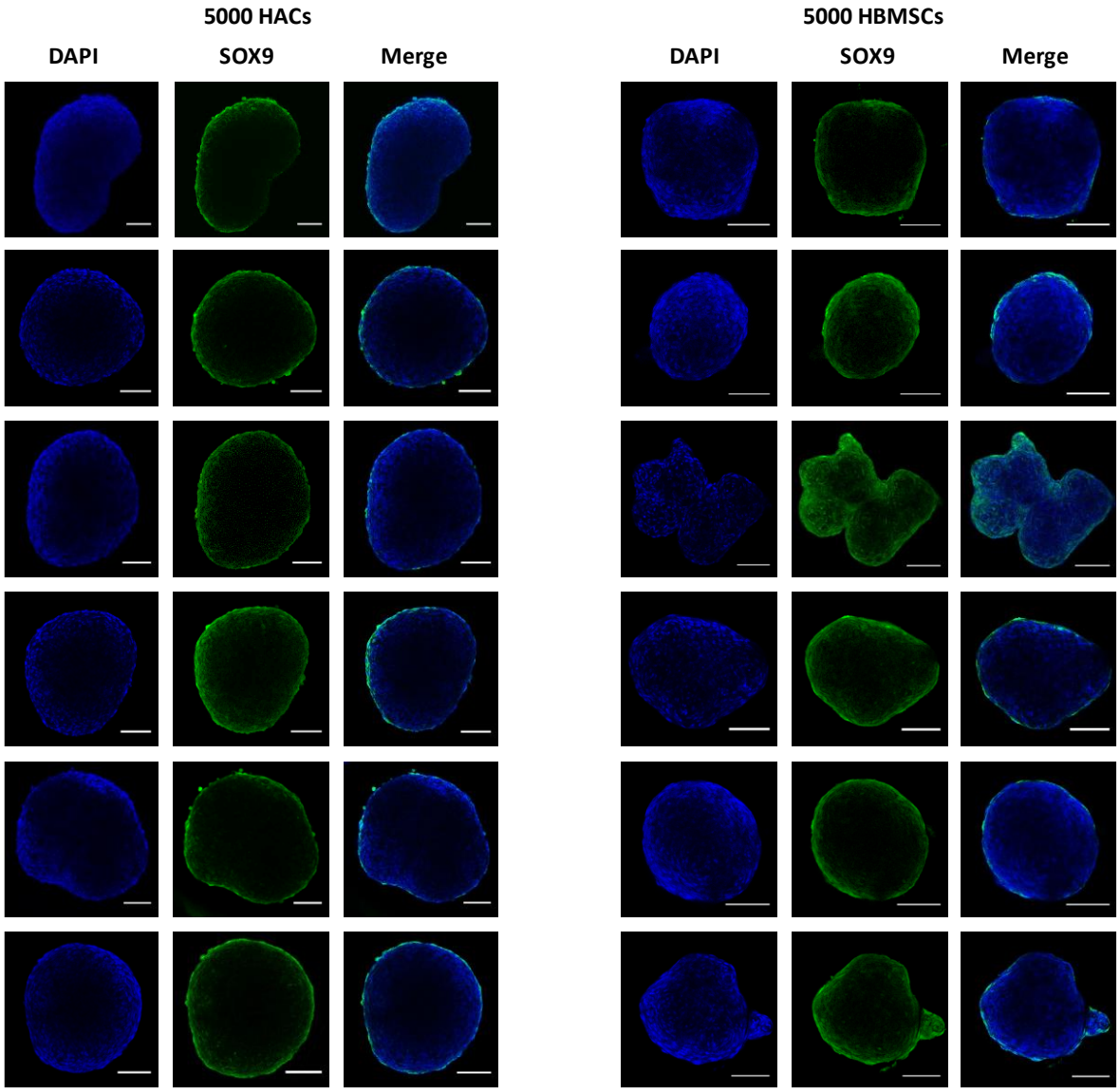

Figure 3.31 Comparative SOX9 immunofluorescence distribution in 5000 HAC (left) and HBMSC (right) replicate spheroids stained 3 days after the onset of chondrogenic differentiation on ultra-low adherence well plates (n = 1 biological sample). Scale bar = 100 µm.

5000 cell spheroids replicated the formerly observed pattern of DAPI and SOX9 positive fluorescence signal that was for the most part isolated at the periphery of the sections. There was a clear effect of size on the staining depth throughout the spheroid and in these scales the differences between cell morphologies were not straightforward to resolve (Figure 3.31). Any

differences for reasons other than size could not be judged and no clear assessment resulted linked to cell heterogeneity. In the cases where SOX9 staining was visible beyond the surface of the spheroid for HBMSCs (e.g. second and third spheroid from the top), small localised regions with distinct SOX9 expression were detected surrounded by non-specific staining. Accordingly, maximum projections of the image stacks acquired were also analysed for SOX9 surface distribution in 5000 cell spheroids. The projections of HBMSC and HAC spheroids agreed with the conclusions from the stained 500 cell spheroids. SOX9 in HACs was uniformly expressed and had the round morphology expected from cartilage chondrocytes in all pellets. SOX9 in HBMSCs, on the other hand, was diversely expressed on various levels in all spheroids with some regions populated by round-like cells (i.e. top left, top right, bottom right), and many others having mixed cell morphologies (i.e. top middle, bottom left, bottom middle) (Figure 3.32).

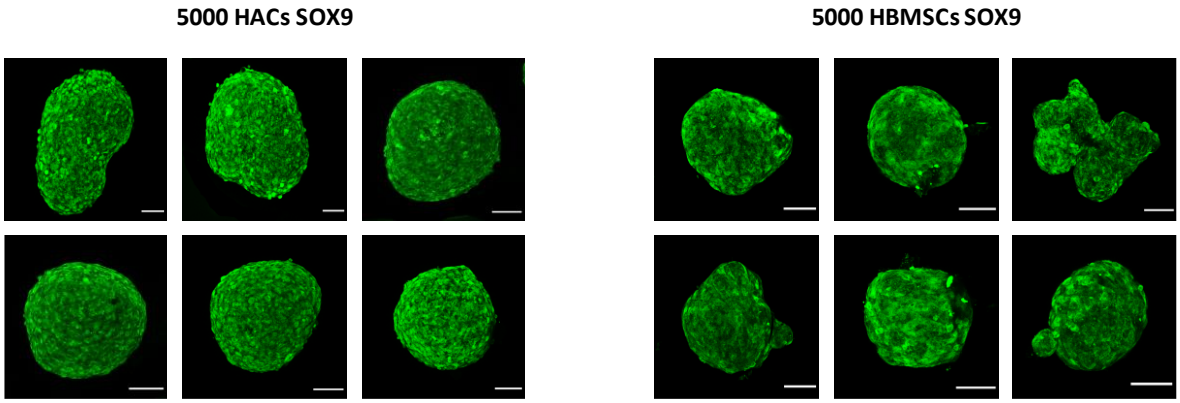

Figure 3.32 Maximum projections of SOX9 immunofluorescence distribution in 5000 HAC (left) and HBMSC (right) replicate spheroids stained 3 days after the onset of chondrogenic differentiation on ultra-low adherence well plates (n = 1 biological sample; n = 6 experimental replicates). Scale bar = 100 µm.

3.3.2.4 Gene expression quantification by RT-qPCR

RT-qPCR was utilised as a complementary quantitative tool to target gene expression patterns of the chondrogenic markers of interest by relating spheroid cell number to early and late stage of chondrogenic differentiation. *SOX9* was studied as an early chondrogenic marker key in this research project and C*OL2A1* was selected as a later marker. *COL10A1* was included as an additional hypertrophy marker to exclude effects of spheroid size (cell number from 500 to 50000 cells) on the outcome of chondrogenic differentiation. The early and late time points were consistent with the previous histological and histochemical characterisations of spheroids and therefore were set on day 7 and day 1, respectively. The technique was progressively optimised by carrying out a series of experiments addressing every stage covering the transition from cell spheroid to cDNA synthesis as a template for PCR (see Appendix B.4).

3.3.2.4.1 Effect of cell number on early and late stages of chondrogenesis of HBMSC spheroids

When assessing the effect of cell number and time, RT-qPCR analysis revealed significant differences regarding the expression of the genes tested for varying cell numbers as well as early and late time points (Figure 3.33). *SOX9* expression decreased with increasing cell numbers but rose on day 21 with respect to day 7 (Figure 3.33A). *COL2A1* expression followed the opposite pattern for 500 and 5000 cells but was downregulated for 50000 cells (Figure 3.33B). *COL10A1* was downregulated for 500 and 50000 cells, and significantly upregulated for 5000 cells (Figure 3.33C). As a general rule, the absolute relative expression of every gene was the lowest for 50000 cell spheroids and the highest for 500 cell samples.

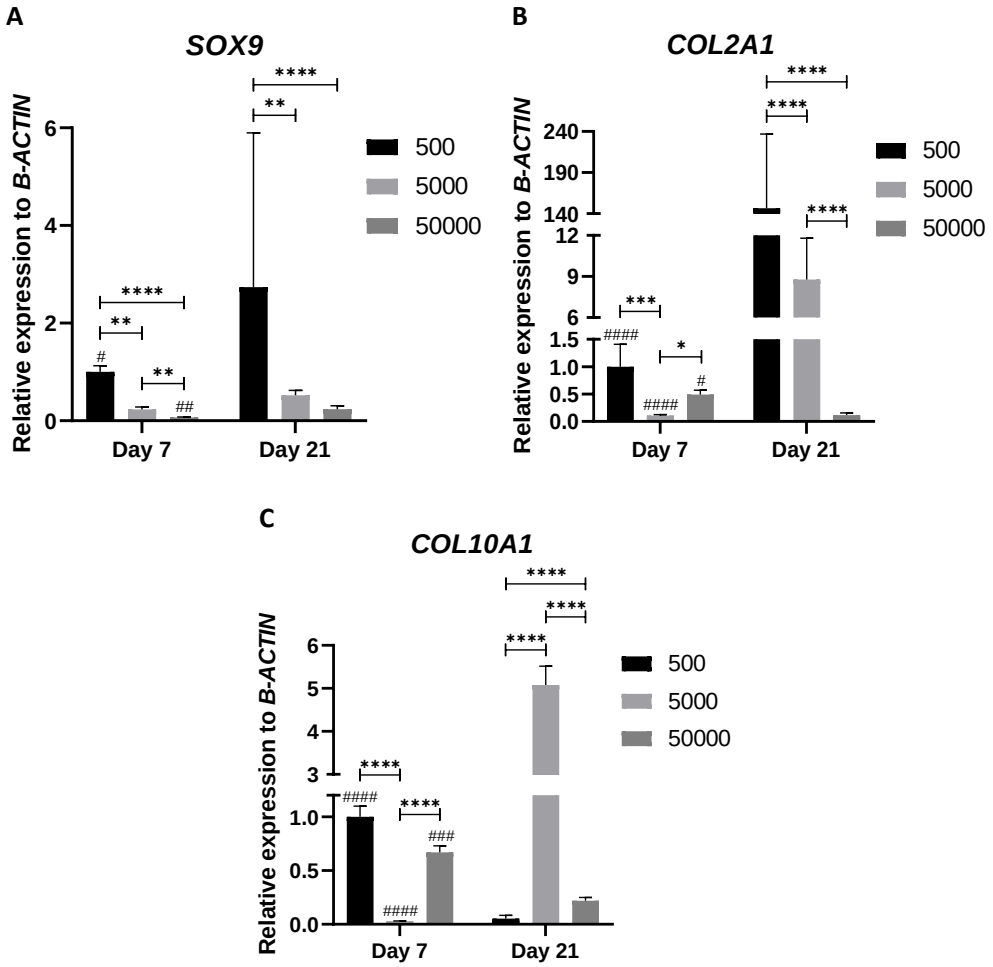

Figure 3.33 M74 P1 HBMSC RT-qPCR relative fold gene expression of (A) *SOX9*, (B) *COL2A1* and (C) *COL10A1* normalised to *B-ACTIN* housekeeping gene plotting the standard error of the mean (SEM). Statistical significance symbols depicted respect GraphPad Prism convention: * ($p \leq 0.05$), ** ($p \leq 0.01$), *** ($p \leq 0.001$), **** ($p \leq 0.0001$) between different cell numbers on a set time point; and # ($p \leq 0.05$), ## ($p \leq 0.01$), ### ($p \leq 0.001$), #### ($p \leq 0.0001$) between time points of a set cell number. The absence of symbols between groups indicates no significance. The statistical analysis was performed using Tukey's multiple comparisons test Two-way ANOVA on ΔC_t values (n = 1 sample per condition; n = 3, technical replicates).

3.3.2.4.2 *SOX9* expression profile in the early stage of chondrogenesis

To answer a more concrete question with relevance for the development of a droplet microfluidic approach for short-term incubation of cell aggregates in microdroplets timelines for *SOX9* expression in early stages of chondrogenic differentiation after spheroid formation were analysed.

Fairly uniform RNA yields from the extraction and isolation were observed for many of the samples (Table 3.4). The samples whose RNA concentrations markedly diverged from those of the other two patients had a smaller purity ratio indicating possible measurement inaccuracies.

Table 3.4 RNA concentrations from M61 P2, M48 P1 and F73 P1 HBMSC spheroids following RNA extraction and isolation with Picopure kit for SOX9 expression timeline.

Patient reference	Sample Reference	RNA (ng/µl)	$A_{260/230}$	$A_{260/280}$
M61 P2	50000 D1	139.6	0.5	2.11
M48 P1		175.5	0.41	2.07
F73 P1		76.3	0.13	1.83
M61 P2	5000 D1	84.6	-3.49	1.7
M48 P1		39	7.36	2.09
F73 P1		38.4	0.17	2.25
M61 P2	500 D1	45.4	-1.13	1.53
M48 P1		8.3	0.03	3
F73 P1		18.5	0.36	2.36
M61 P2	50000 D3	43	-3.05	1.86
M48 P1		104.8	0.9	2.04
F73 P1		85.8	2.12	2.09
M61 P2	5000 D3	28	0.29	1.81
M48 P1		26.9	0.07	2.5
F73 P1		28.8	0.09	2.34
M61 P2	500 D3	7.4	0.02	2.12
M48 P1		18.1	0.29	2.46
F73 P1		18.2	0.35	2.18

M61 P2	50000 D7	21.2	0.52	1.91
M48 P1		32	0.11	2.18
F73 P1		236.6	0.11	2.18
M61 P2	5000 D7	29.3	13.47	1.71
M48 P1		13.9	0.05	2.58
F73 P1		18.2	0.05	2.42
M61 P2	500 D7	1.7	0.02	5.22
M48 P1		3.5	0.01	2.48
F73 P1		3.6	0.05	2.7

No significant differences in SOX9 expression were observed for 500, 5000 or 50000 cell spheroids (Figure 3.34D to F). for two of the patients (M61 P2 and M48 P1), regardless of cell number or day of culture, except for a minor upregulation between 5000 day 3 and 5000 day 7 spheroids. Still, this was not recorded between day 1 and day 7 to ultimately claim that expression increased by day 7 (Figure 3.34A and B).

The third patient, F73 P1, displayed high variability among the samples. 5000 and 500 cell aggregates expressed the highest level of *SOX9* for day 1, whereas 50000 cell spheroid had a stable level throughout the 7-day culture (Figure 3.34C).

The variations that had been highlighted for the F73 patient in Figure 3.34C were not sufficient to conclude that there was a single time point that was more adequate for culture of spheroids through an upregulation in *SOX9* in early chondrogenic differentiation conditions *in vitro*.

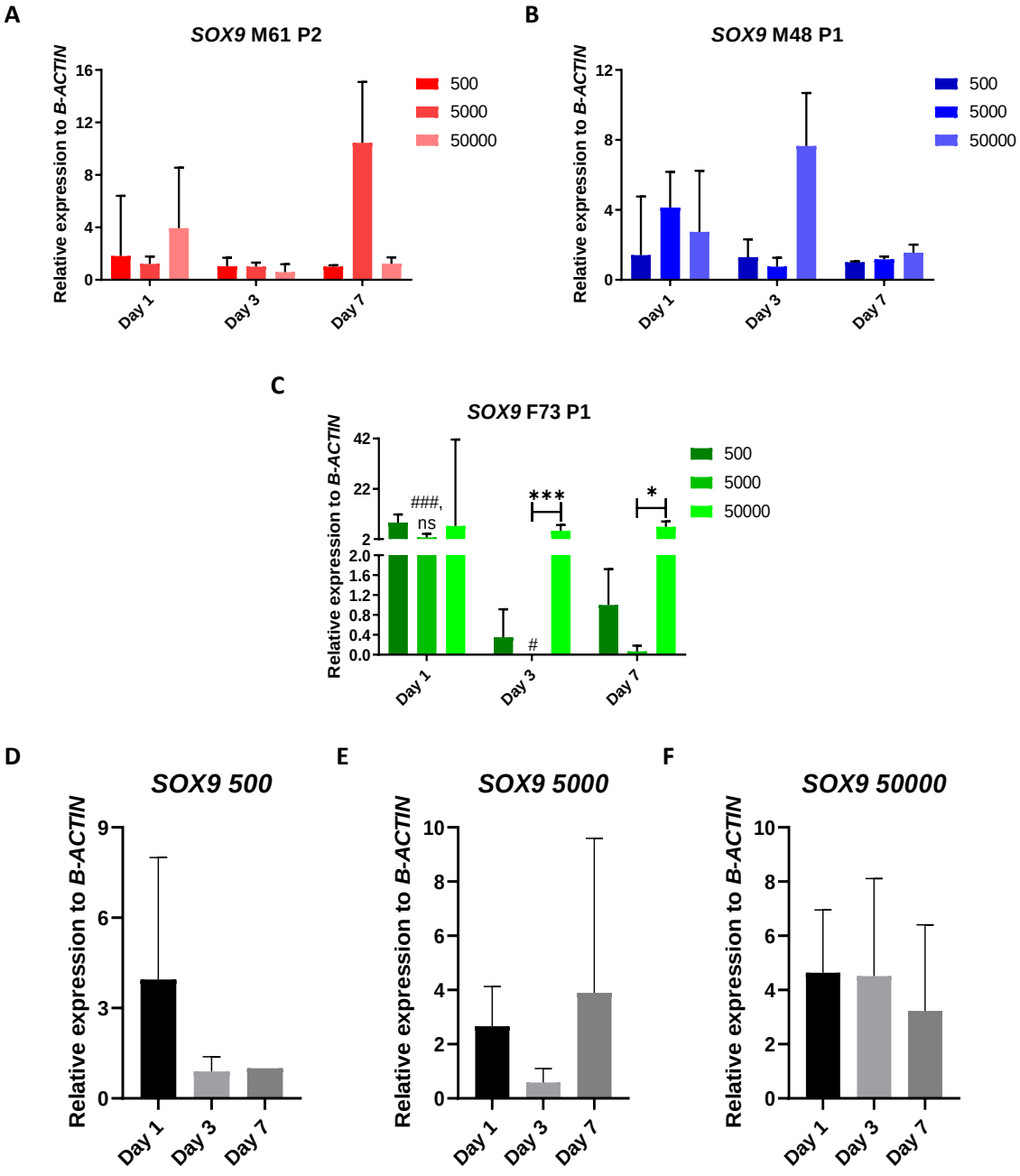

Figure 3.34 *SOX9* early expression multi time point experiment for M61 P2, M48 P1 and F73 P1 HBMSCs (biological replicates). Fold relative gene expression represented for M61 P2 (A), M48 P1 (B) and F73 P1 (C) normalised to *B-ACTIN* housekeeping gene plotting the SEM. Statistical significance symbols depicted respect GraphPad Prism convention: * ($p \leq 0.05$) and *** ($p \leq 0.001$) between cell numbers on a set time point; and # ($p \leq 0.05$) and ### ($p \leq 0.001$) between a set cell number on different time points (i.e. on plot C, ###, ns for 5000 cell spheroids on day 1 means highly significant statistical difference with respect to day 3 and none with day 7; # for 5000 cell spheroids on day 3 relates to statistically significant difference with regard to day 7 only). The absence of symbols between groups and ns indicates no significance. D to F plots represent global relative expression values including the contribution of the three patients through SD for every cell number separately: 500 (D), 5000 (E) and 50000 (F). The statistical analysis was performed using Tukey's multiple comparisons test Two-way ANOVA on ΔC_t values for plots A to C and using Ordinary One-way ANOVA with multiple comparisons on ΔC_t values for plots D to F. 500 cell spheroids on day 7 were set as the control group (n =3, technical replicates).

3.4 Discussion

The aim of the *in vitro* studies presented in the current chapter was to identify the ability of unselected HBMSCs to generate cartilage tissue across different cell numbers (500000 down to 500 cells/spheroid). Throughout these studies, the relationship between cell aggregation and SOX9 was assessed. This was of particular relevance for the development of a microfluidic platform for culture and prospective sorting of cell aggregates. *In vitro* chondrogenic differentiation culture of HBMSCs was characterised on a medium-throughput manual ultra-low adherence round-bottom 96-well microplate platform. Consequently, there was a focus on timelines for cell aggregation and *SOX9* expression, chondrogenic differentiation of microaggregates with small cell numbers evaluated through protein, gene expression and SOX9 heterogeneity across multicellular spheroids.

Cell aggregation experiments on ultra-low adherence plates enabled the simulation of this phenomenon in droplets within a short period of culture, which was expected to occur even earlier for cells encapsulated in spherical droplets. The biological characterisation proved valuable to confirm that unselected bone marrow cells, despite their heterogeneous nature, were able to differentiate into articular cartilage, albeit variably. Histological (A/S and SO) and histochemical (IF) stainings illustrated how large HBSMC spheroids failed to produce robust cartilage in terms of PGs, type II collagen and hyaline structure with the growth factors supplemented and the cell numbers seeded in the microwell plates. The SOX9 expression peak on day 7 in small spheroids raised a research question regarding the timeline for SOX9 expression in the early condensation stage, with a view to translating it to a droplet microfluidic approach. In that regard, the RT-qPCR analysis with HBMSC spheroids from three patients demonstrated no significant variation of SOX9 expression from day 1 to day 7, implying that the moment when the cells start forming a compact aggregate will be the defining point for cell sorting in the microfluidic device. This was validated through confocal microscopy on whole mount samples stained with SOX9 on days 1, 3 and 7 as part of a protocol that achieved nearly complete (for 5000 cell aggregates) to complete (for 500 cell spheroids) antibody penetration into the core of spheroids. The assay also confirmed that HBMSCs displayed notable heterogeneity in SOX9 expression both within and between individual spheroids, although the degree of heterogeneity could not be quantified due to limitations of throughput and staining permeability. However, the observed heterogeneity at both levels justifies the approach of screening and sorting smaller cell numbers for which differences in SOX9 may be critical to enrich chondroprogenitors.

3.4.1 SOX9 expression decreased in late chondrogenic differentiation in small aggregates but no significant variation was observed in early stages

The crucial conclusion extracted from chondrogenic differentiation of small spheroids at an early and a late stage involved SOX9 and was linked to the formulation of a valid criterion for microfluidic cell sorting of cell aggregates in microdroplets. Whole mount immunostaining of small HBMSC spheroids revealed the highest SOX9 expression on day 7 and a reduction by day 21. RT-qPCR analyses on HBMSC spheroids addressed short-term chondrogenic differentiation up to day 7 relevant for cell culture in microdroplets. Higher SOX9 mRNA expression was found on day 1 samples but no significant variations in expression regardless of time point and cell number (500, 5000 and 50000 cells). The parallel whole mount immunostaining assay with the same time frame of analysis matched the RT-qPCR results. These findings reinforced an aspect of the main project hypothesis stating that SOX9 is an early chondrogenic marker for human bone marrow stromal cell populations necessary for mesenchymal cell condensation and chondrogenesis (Foster et al., 1994, Liu and Lefebvre, 2015, Gong et al., 2018, Lefebvre et al., 2019). For the purpose of translation to droplet microfluidic sorting of cell aggregates, a short-term culture of droplets requiring no media changes prior to sorting would additionally remove complications from the system.

SOX9 is a master regulator of chondrogenic differentiation which is expressed prior to the onset of chondrogenesis and its maintained expression is associated with the chondrocyte phenotype (Lorda-Diez et al., 2011, Marín-Llera et al., 2019). SOX9 has been singled out as a transcription factor that is hypothesised to stabilise the chondrocyte phenotype by repressing chondrocyte hypertrophy (Bi et al., 2001, Mueller and Tuan, 2008, Ikegami et al., 2011, Dy et al., 2012). Three potential mechanisms of chondrocyte hypertrophy inhibition have been identified by Li and Dong involving (1) the transcription factor RUNX2 (Zhou et al., 2006, Mackie et al., 2008, Ikegami et al., 2011, Yadav and Yang, 2020); (2) RUNX2 jointly with β-catenin on the Wnt signalling pathway (Topol et al., 2009, Mahmoudifar and Doran, 2012, Chen et al., 2015a) and (3) hypertrophy-related genes such as *COL10A1* and *VEGFA* (Hattori et al., 2010) (Li and Dong, 2016). Nonetheless, there is no reported experimental evidence comparing early and late time points in chondrogenic differentiation for SOX9 expression in small HBMSC spheroids on a protein level. The SOX9 decrease observed in the late stage of chondrogenic differentiation in small spheroids composed of 500 and 5000 cells may be ascribed to pre-hypertrophic chondrocytes in unselected HBMSCs. It is worth noting that such decline in SOX9 expression for whole mount stained small spheroids from day 7 to day 21 was not supported by RT-qPCR analysis of mRNA expression relative to *β-ACTIN*. In fact, the quantitative gene expression data was closer to existing work in the literature for small spheroids (Goude et al., 2014). Similarly, it was in agreeement with the IHC data presented in this chapter for

large spheroids indicating that *SOX9* remained stable over the entire culture period yet with a rising tendency.

The two techniques above presented several limitations that called for a note of caution before drawing a clear conclusion on SOX9 fluctuations during chondrogenesis in small spheroids. On the one hand, the whole mount IF staining was not optimised and the assay was interpreted from maximum projections without replicate samples for confirmation. The maximum projection tool proved graphic to showcase the spatial arrangement of stained proteins and to elucidate trends associated with time for whole mount samples where the staining failed to reach the core. It is critical to note, however, that maximum projection images were not equivalent to a faithful account of the actual stained middle plane at the core of the spheroids. They simply represented an overlay of the stained stacks from the surface and down to the centre. Furthermore, ATDC5 controls had a stable SOX9 expression over time in the study. On the other hand, even if *β-ACTIN* was more appropriate than *TBP* and *RPL13* a housekeeping gene for RT-qPCR, when later screened against GAPDH, it was GAPDH that offered more reliability as a reference gene for HBMSCs (see section 4.2.2.1). Hence, referencing gene expression to *GAPDH* might have aided in reducing global variability of the housekeeping gene for the same cell number on different time points (He et al., 2018). This lack of reliability could also be improved with better purity ratios and higher RNA yields which pose a challenge when conducting experiments with spheroids and low cell numbers. Despite those limitations, both techniques showed that there was in all cases a detectable level of SOX9 expression in small spheroids, thus establishing a rationale for targeting SOX9 as an early marker for chondrogenesis.

Having seen that SOX9 was expressed early in chondrogenic differentiation of small HBMSC spheroids, the biological question was re-focussed on identifying relevant timelines for SOX9 expression for the development of the microfluidic component. Both whole mount small spheroids immunostained for SOX9 and RT-qPCR data on *SOX9* expression demonstrated that there was no specific time point correlating with higher levels of this marker within the first week of chondrogenic differentiation. Kulyk et al. designed an *in vitro* chondrogenic differentiation micromass study along these lines with mesenchymal cells harvested from the distal subridge region of stage 24/25 chick embryo wing buds. Dot-blot hybridisation revealed that *Sox9* RNA levels increased from 2 hours of chondrogenic culture, reached a peak between 20 and 65 hours of culture and dropped before 120 hours (Kulyk et al., 2000). Despite the differences in cell source and chondrogenic differentiation set-up, this study agrees with the *SOX9* mRNA levels measured during the early stages of chondrogenesis and the SOX9 expression and distribution in small spheroids. Notably, both the reference gene and *SOX9* were expressed at cycles closer to the P0 HAC control compared to the preliminary chondrogenesis study with the HBMSC sample. Freshly isolated HAC

P0 pellets were used as positive controls of qPCR data because of their high resemblance to hyaline cartilage human chondrocytes excluding de-differentiation from passaging (Tew and Clegg, 2011). This suggested higher reliability for the early stage *SOX9* expression assay. Furthermore, it encouraged to base the criterion of future characterisation and cell sorting of aggregates in microdroplets on the time required for their formation, thus avoiding long-term culture of metastable droplets.

To summarise, the results obtained in this study are in favour of the hypothesis that SOX9 is an early chondrogenic marker in HBMSCs with expression levels that vary as a function of time in the process of chondrogenic differentiation. Notwithstanding, SOX9 temporal expression pattern in large spheroids differed from that of small spheroids in that there were no apparent differences in expression irrespective of time on day 7 and day 21 samples. This opposing trend raised the possibility that SOX9 might have varying expression patterns for large and for small spheroids and, in consequence, that chondrogenesis might indeed be dependent on cell number.

3.4.2 Chondrogenesis is a cell number-dependent event in HBMSCs

Chondrogenic differentiation of HBMSC spheroids had a different outcome for each of the cell numbers tested. This was observed throughout the multiple characterisation techniques employed to assess several dimensions of chondrogenesis in multicellular spheroids. Cell aggregation was complete for large spheroids (500000 and 50000 cells) within hours and was only partial for small spheroids (5000 and 500 cells) even after one day of culture. For large aggregates, histological A/S and SO stainings over 21 days revealed a slightly inferior PG and collagen matrix for 500000 cells than 50000 cells and differing in both cases from hyaline cartilage and HAC controls. As discussed in the previous section, while SOX9 expression decreased in the later stage of chondrogenic differentiation on Day 21 with respect to day 7 in small spheroids, no major differences were detected in large spheroids.

As reviewed in section 1.6, scaffold-free pellet culture in tubes and microplates is a well-known approach for 3D culture of spheroids for cartilage tissue generation derived from chondrogenic differentiation (Penick et al., 2005, Tare et al., 2005, Welter et al., 2007, Achilli et al., 2012, Schon et al., 2012, Li et al., 2015, Petrenko et al., 2017). For this project, designing an *in vitro* medium-throughput method that illustrated a transition towards the formation of thousands of aggregates on a droplet microfluidic platform was deemed a powerful reason to pursue this approach based on 96-well microplates rather than pellet culture in tubes.

Chondrogenesis in multicellular spheroids was first addressed by monitoring the cell aggregation phenomenon taking place in the initial condensation stage in ultra-low adherence round-bottom

96-well plates. Time-lapse analysis was a useful tool to discern specific real-time development of spheroid self-assembly during the first day of culture. Similar systems such as V-bottom 96-well microplates had already been proposed and validated for culturing HBMSCs (Welter et al., 2007). The microwell plates produced progressive aggregation without external biomechanical stimuli, e.g. centrifuging; proving to be a representative substrate to continue to analyse chondrogenic differentiation in parallel with advances on the microfluidic platform.

ATDC5 cell aggregation within one day of culture for all cell densities became an encouraging finding and anticipated similar effects in microdroplets with a higher curvature to further promote cell aggregate formation. When the time-lapse experiment was translated to HBMSCs, cell aggregation required longer times in a cell number-dependent manner (i.e. 6 h for 500000 cell spheroids and incomplete aggregate formation for cell densities under 50000 cells/well). The optimal range for HBMSC cultures, in this system, was narrowed down to numbers between 500 and 500000 cells, hence excluding 50 cell spheroids because of their excessively small size for accurate image analysis and handling with a view to whole mount immunostaining preparations. That premise was maintained for HAC time-lapse analysis.

ATDC5 cells presented opposite growth patterns with respect to HBMSCs and HACs. ATDC5 spheroids grew in size possibly due to the presence of serum in their chondrogenic differentiation medium encouraging cell proliferation. This trend conformed to previous research on pellets from this chondroprogenitor cell line (Tare et al., 2005, Lewis et al., 2016) at the upper end of the range of cell numbers measured. For HBMSCs and HACs, after the sharp area increase two days following seeding associated with active cell aggregation, the condensation that is expected from chondrogenesis was triggered and cell proliferation was halted in the absence of FBS in the chondrogenic differentiation medium.

From the histological perspective, A/S and SO staining images provided information on the effect of cell number in large HBMSC spheroids (50000 and 500000 cells). 50000 cell spheroids had a tendency towards overall similar or improved differentiation outcomes than 500000 cell aggregates (e.g. 50000 cell samples on day 21 was the most robust treatment). This might have been accentuated due to the constraints imposed by the well dimensions giving rise to a lower culture volume available than demanded by large aggregates for an optimal functionality and a stable development. Synergistically, large cell aggregates might be more prone to undergo cell necrosis in the core as a response to a larger area with defective nutrient supply and limited oxygen diffusion estimated beyond 150-200 μm from the outside to the core. A threshold cell number has been reported for the transition from hypoxic core to compromised cell metabolism and viability above 250000 cells (Cui et al., 2017, Murphy et al., 2017, Tu et al., 2020). This would agree with the

deficiencies observed for 500000 cell spheroids. Moreover, it would endorse the claim that smaller 50000 cell spheroids are preferable for chondrogenic differentiation with the added advantage of lower cell number requirements for the assay. There is nonetheless a limitation to acknowledge regarding the Bern score measurements presented. These were unblinded, which may have induced bias in the scores assigned to the stained sections. A more appropriate interpretation would have stemmed from a blinded approach.

For the purpose of this research project, the central result highlighting differences in chondrogenic differentiation between the cell numbers tested in this chapter was the temporal SOX9 expression pattern in HBMSC spheroids. Whereas SOX9 in small spheroids declined as differentiation progressed, large spheroids did not display any detectable change over time. The higher number of cells in large spheroids might have prompted a synergistic action of cells undergoing differentiation that encouraged other nearby cells to express SOX9. The fact that small spheroids did not exhibit that global SOX9 compensation is of interest for prospective sorting of aggregates formed in microdroplets. In such small scales, the extent of stem cell enrichment might be further intensified for small aggregates made up of considerably fewer cells (below 50) in which individual cell contributions are more decisive.

All in all, these results strongly suggest that cell number is an essential variable to take into account in chondrogenic differentiation of HBMSC aggregates down to relevant scales for microdroplet culture. Although large and small spheroids exhibited independent SOX9 expression patterns, heterogeneity emerged as a common trait for all cell numbers compared to HACs as reflected by IF histochemistry as well as a key element to examine.

3.4.3 Heterogeneity in SOX9 expression was marked in HBMSCs for all cell numbers compared to HAC controls

In this study, the recurring issue of heterogeneity in HBMSCs for their application in cartilage tissue engineering was analysed from multiple levels, i.e. from the macro- to the microscale; variability among donors, clonal subpopulations in replicate spheroids and within single cells in each spheroid (McLeod and Mauck, 2017). The aim was to gain in-depth knowledge of the predominance of each level in HBMSC spheroids for the range of sizes tested. It therefore encompassed large and small spheroids alike, the latter being a more representative model to predict heterogeneity in smaller aggregates cultured in microdroplets. The results presented in this chapter validated the presence

of heterogeneity in HBMSCs across all cell number in contrast with HACs, both structurally and extending to the chondrogenic marker SOX9.

Comparative *in vitro* chondrogenesis studies with 500000 cell spheroids for HACs and HBMSCs as assessed by histological and immunohistochemical stainings functioned as a proof of principle of heterogeneity between cell types. HACs derived from femoral heads from patients yielded tissue closer to hyaline articular cartilage (i.e. abundant glycosaminoglycan matrix with lacunae and regions of strong PG synthesis) and uniform expression of SOX9 and type II collagen proteins. Their application in early passages before irreversible dedifferentiation takes place enables them to retain their chondrogenic epigenetic memory. In addition, it aids in differentiation into hyaline-like cartilage due to SOX9, aggrecan and type II collagen downregulation upon monolayer culture (Lin and Chang, 2008, Li et al., 2015). HBMSCs spheroids displayed a histological structure that diverged from hyaline cartilage with an inferior glycosaminoglycan matrix and areas of incomplete differentiation. The lower chondrogenic differentiation potential of HBMSCs in comparison with HACs was also observed in the three-patient histological assay with A/S and SO stainings. These findings were in agreement with other studies that reported parallel characterisation of both HACs and HBMSCs in pellet culture for a larger patient cohort (Agar et al., 2011, Li et al., 2015).

In accordance with the experimental hypothesis regarding SOX9 heterogeneity in HBMSCs, the focus was shifted to SOX9 protein expression during chondrogenesis. Immunofluorescence results matched the histology when donor-to-donor heterogeneity was assessed in large spheroids. HBMSCs heterogeneity among human donors was evidenced for all treatments regardless of time point and cell number. It was in all scenarios higher than in HAC controls, which had a clear nuclear SOX9 distribution and were affected by patient-to-patient variations to a lesser extent. SOX9 expression analysis was consequently scaled down to small spheroids to account for cell numbers that were more relatable to a droplet microfluidic strategy for cell aggregation in microdroplets. The study was narrowed down to relevant short-term chondrogenic differentiation time points up to day 7, while investigating heterogeneity between spheroid replicates using whole mount immunostaining. The absence of perceptible differences in SOX9 expression and heterogeneity in compact spheroids on day 3 and day 7 for both cell numbers and types did not provide a strong indication that either of those time points might be more adequate for early cell sorting. Patient-to-patient differences were not as relevant in the small spheroids. This is also suggested by the *SOX9* mRNA expression measured by RT-qPCR for spheroids in the first week of chondrogenic culture.

Heterogeneity among replicate spheroids was the next level assayed. Whole mount IF coupled with confocal microscopy did not succeed in conclusively determining heterogeneity across samples

expressing SOX9, even after doubling the number of replicates compared to the previous study on donor-to-donor variability. This was hypothesised to be due to sensitivity and cell number usage limitations. 500 and 5000 cell spheroids might have been too large aggregates that were globally expressing SOX9 fairly uniformly based on a synergistic effect of the most robust chondroprogenitor populations encouraging those that are less so. This hypothesis is supported in the literature where 50 cell aggregates, despite showing inferior stability, were the most responsive to chondrogenic differentiation conditions as reported through their upregulated chondrogenic expression patterns using HACs (Moreira Teixeira et al., 2012) and human periosteum-derived stem cells (HPDSCs) (Leijten et al., 2016). Both studies were conducted under a similar culture principle applied in the present work using low adherence surfaces to prompt cell aggregation. In any event, the observations in the whole mount immunostaining assay indicated that HBMSCs were indeed composed of heterogeneous subpopulations and that this feature led to variability from a replicate spheroid to another. This might imply that a measurable threshold for SOX9 expression could be set that would allow to discriminate between robust and poor aggregates for cartilage. Furthermore, the process of whole mount staining of small spheroids incurred several limitations. It was laborious, the samples that were hard to distinguish and monitor risked being lost throughout the many washing steps and, above all, had a low throughput. Evaluating inter-spheroid SOX9 heterogeneity called for a large number of samples and this technique posed technical challenges to generate them.

The last level of heterogeneity involved cell-to-cell differences within each individual spheroid. Intra-spheroid heterogeneity was identified for all cell numbers and was a common trait of HBMSCs in contrast to HACs. In large spheroids, the sections showed non-specific SOX9 signal in certain regions. Non-specificity may be associated with cells still undergoing differentiation at a slower rate or a lack of complete general SOX9 expression. SOX9 was clearer around the peripherical areas of the spheroids where proliferating cells would be lying. The area stained with SOX9 localised to the nucleus to a great extent, with signs of partial cytoplasmic occurrence. Analogous observations resulted from the analysis of SOX9 distribution in small spheroids on an individual cell basis and for small groups of cells. SOX9 intra-spheroid heterogeneity was distinctly identified for all the replicate small spheroids and appeared to be predominant over the other levels of heterogeneity. The implications of this result emphasise how every individual cell in small spheroids might make a stronger contribution to the fate of differentiation and thus be paramount to enrich HBMSCs.

To conclude, the initial hypothesis that there existed SOX9 heterogeneities among cell subpopulations was expanded to intra-spheroid cell-to-cell heterogeneities that were found to dominate particularly in the small spheroids. These differences potentially set the ground for subsequent development approaches targeting small groups of cells where each individual one may

have a stronger role determining the differentiation prospects of small aggregates. Higher throughput techniques will be essential to resolve heterogeneity issues and the presence of SOX9 heterogeneity on a cell-to-cell level is a promising finding leading to targeting that marker for sorting of aggregates.

3.4.4 Conclusions

The biological characterisation of multicellular spheroids exposed differences in their chondrogenic differentiation outcome with regard to their cell number. SOX9 expression in large spheroids did not change as a function of time. In contrast, SOX9 expression declined in small spheroids in late chondrogenesis and did not vary significantly during the first week, demonstrating that SOX9 could be a potential early marker to predict chondrogenesis in HBMSCs. The degree of heterogeneity among different bone marrow cell populations could not be conclusively quantified. Notwithstanding, a strong component on an intra-spheroid level of SOX9 heterogeneity was observed compared to HACs, which highlighted a potential advantage in harnessing even smaller aggregates for enriching stem cells for cartilage tissue engineering. In anticipation of the development of a microfluidic-based high-throughput sorting strategy for small aggregates in microdroplets, the next objective was to establish an approach to screening viable cells for SOX9. The experience acquired to assess the properties of the cartilage-like tissue being generated is crucial for future characterisation of robust cartilage aggregates once a suitable microfluidic platform combined with a chondrogenic marker cell sorting strategy becomes available.

Chapter 4: Application of nanoflare technology to isolate *SOX9*-enriched HBMSC subpopulations

4.1 Introduction

The previous chapter concluded that SOX9 was expressed heterogeneously in HBMSC spheroids of all sizes compared to a more uniform expression of this chondrogenic marker in spheroids of HACs. SOX9 expression characterised in fixed cells was indicative of chondrogenic differentiation. However, an immunohistochemical approach is not feasible as a cell sorting strategy for a non-cell surface expressed protein such as SOX9.

As discussed in section 1.4.3, SOX9 is considered as one of the gold standard indicators and master regulator of chondrogenesis (Weissenberger et al., 2020). SOX9 could also be a potential candidate functional marker in live cell aggregates for two reasons. First, it is expressed in the initial stage of chondrogenesis during mesenchymal condensation and second, its preserved expression results in improved chondrogenic outcome specific to a stable articular cartilage phenotype. The use of SOX9 as a marker, however, poses challenges in that it requires cell aggregation as well as a screening technique able to reach the cell nucleus for detection (Williams et al., 2010, Jiang et al., 2020). Over the past decade, a potential approach has emerged that offers the possibility to bind SOX9 mRNA transcripts in the cell nucleus and to provide a quantitative read-out in terms of fluorescence intensity. A fluorescence signal is emitted when a probe is supplied to the culture medium which will fluoresce exclusively if mRNA binding takes place.

This technology rests on the principle of hybridisation of fluorophore-labelled reporter sequences such as Cy5 to short DNA sequences (oligonucleotides) called spherical nucleic acids (SNA) gold nanoparticle conjugates. SNAs were introduced by Mirkin et al. along with a method for assembly of gold nanoparticles functionalised with those hybridised SNAs (Mirkin et al., 1996). Years later, the Mirkin group coined the term nanoflare to refer to oligonucleotide gold nanoparticle conjugates that can be internalised by cells to enable mRNA quantification in live cells. They enumerated several advantages with respect to other systems used to detect RNA intracellularly (e.g. probes used for in situ hybridisation and staining, linear oligonucleotide probes, molecular beacons, fluorescent resonance energy transfer pairs) such as high signal intensities, low background fluorescence and sensitivity to variations in the amount of mRNA transcripts in cells and the absence of transfection agents that may be harmful to cells (Seferos et al., 2007, Bao et al., 2009, Prigodich et al., 2009).

A schematic of the structure and the mechanism of action of a nanoflare probe is depicted in Figure 4.1. The nanoflares are composed of a gold nanoparticle of about 13 nm diameter that ensures i) efficient quenching of hybridised fluorescent reporters in the absence of the target mRNA transcript, ii) a high density of functionalised oligonucleotides due to the particle surface area and iii) a minimal interference with visible light. The oligonucleotides of the SNAs constitute the antisense DNA recognition sequence (green) that are functionalised on the surface of the gold nanoparticle through the formation of thiol (-SH) bonds and afterwards hybridised with short cyanine (Cy5, red) reporter sequences. The reporter sequence remains quenched while close to the gold nanoparticle core and is released upon cell uptake and binding of the recognition sequence to the target and complementary mRNA transcript (blue) for a stable duplex generation. The liberation of the reporter Cy5 flare strand leads to the emission of a fluorescent signal that can be measured in live cells relative to abundance of the target mRNA transcript (Seferos et al., 2007, Lahm et al., 2015).

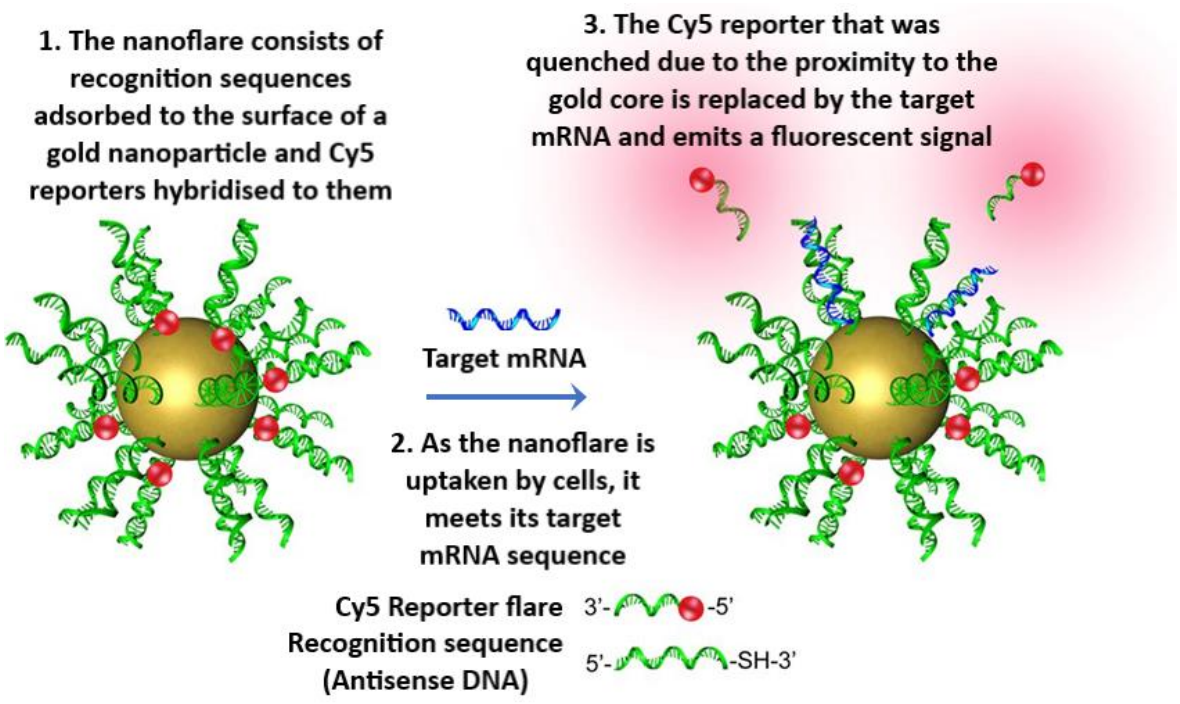

Figure 4.1 Example of the structure and mechanism of action of a nanoflare as it binds the target mRNA sequence once uptaken by cells. Modified from Halo et al. (2014).

Nanoflares became available on the market in 2013 in a commercial version under the name of SmartFlare™ nanoprobes supplied by Merck. Lahm et al. tested Smartflare™ probes targeting *GAPDH* in somatic cells and *NANOG/Nanog* and *GDF3/Gdf3* in ESCs and iPSCs of human, murine and porcine origin and reported reliable mRNA expression of the equivalent genes in subpopulations displaying high fluorescent signals from FACS quantification without any alteration to cell phenotype or growth (Lahm et al., 2015). In relation to HBMSCs and SOX9, Li et al. validated the use of *RUNX2*-Cy5 and *SOX9*-Cy5 mRNA SmartFlare™ probes for sorting of HBMSCs through

matching mean fluorescent intensities measured by FACS and *RUNX2* and *SOX9* expression levels for four subpopulations gated with different *RUNX2/SOX9* ratios (Cleary et al., 2016, Li et al., 2016).

Despite these seemingly promising results, the effectiveness of the Smartflare™ flares has been brought into question in more recent publications such as that of Czarnek et al. In brief, they published their work in which they tested five Smartflare™ probes for *HMOX1*, *IL6*, *PTGS2*, *Nrg1*, and *ERBB4* mRNA targets and could not establish any degree of correlation between the Cy5 fluorescence intensity measured by FACS and the mRNA levels obtained by RT-qPCR analysis. Moreover, they hypothesised that upregulated mRNA levels in highly fluorescent cell subpopulations sorted by FACS after incubation with Smartflare™ probes observed in previous research studies involving cancer stem cells by Seftor et al. and prostate cancer cells by Krönig et al. may simply be due to other coincidental cancer-derived cell features enhancing probe internalisation (Seftor et al., 2014, Krönig et al., 2015, Czarnek et al., 2018). In the context of scientific controversy over the specificity of the probes, their compatibility with stem cells as a whole and permeability issues in other cell types, Merck withdrew Smartflares™ probes from the market in 2018.

In this chapter, a non-commercial nanoflare synthesised by Kanaras group as described in the work of Kyriazi et al. will be explored as a possible *SOX9* nanoprobe (Figure 4.2). The design is a modification of the aforementioned original nanoflare structure created by Mirkin and consists in a nanoparticle dimer with sense strands adsorbed onto the gold nanoparticle surface containing a 5-carboxyfluorescein (FAM) at the 5' end for increased integrity and specificity and a thiol at the 3' end. These were partially hybridised to shorter oligonucleotide complements called flare strands that were chemically modified with Cy5 at the 3' end (Kyriazi et al., 2018).

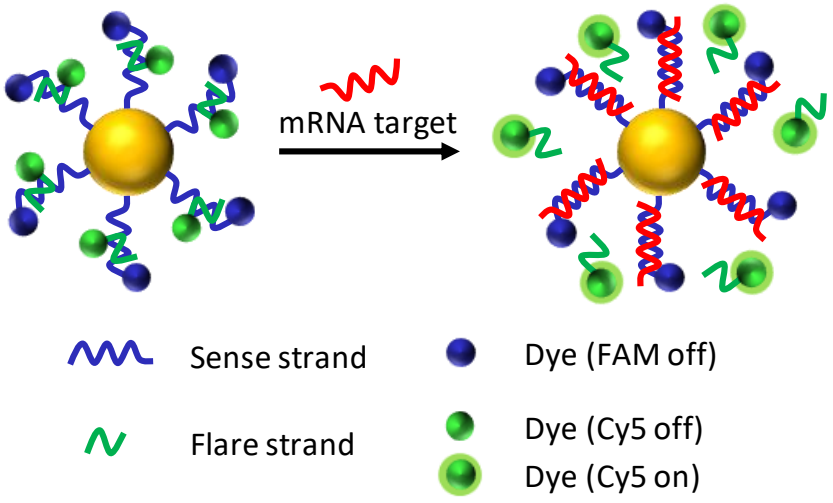

Figure 4.2 Schematic of the structure and mechanism of action of the nanoflare used in this research project to bind SOX9 mRNA target transcripts in HBMSCs. Modified from Kyriazi et al. (2018).

Acknowledging the controversy behind this technology, a series of validation experiments are performed to determine the suitability of this technique to identify HBMSC cell subsets that display higher amounts of *SOX9* mRNA transcripts which could be key to isolate chondroprogenitors for cartilage tissue engineering.

4.1.1 Hypothesis

'*SOX9*-Cy5 nanoflares can be used to identify HBMSC populations with high *SOX9* expression'.

4.1.2 Aims

This chapter intends to assess the suitability and reliability of a nanoflare strategy for detection and quantification of *SOX9* mRNA transcripts in subpopulations of the live HBMSC population with a view to integrating this strategy for the sorting of small aggregates assembled in droplets generated on a microfluidic platform. The specific objectives guiding the experimental design are:

- To confirm *SOX9*-Cy5 nanoflare uptake by HBMSCs through a quantifiable fluorescent Cy5 signal emitted by targeted cells.
- To establish a method for *SOX9*-Cy5 nanoflare incubation for specific binding to *SOX9* mRNA transcripts in HBMSCs.
- To validate that the FACS Cy5-positive fluorescent signal from the cells exposed to *SOX9*-Cy5 nanoflares corresponds to potent chondroprogenitor cells within the HBMSC population.

4.2 Methods

4.2.1 Time-lapse *SOX9*-Cy5 nanoflare uptake assay and FACS quantification

The initial step towards the validation of the use of nanoflares to target SOX9 in live cells was to test the hypothesis that *SOX9*-Cy5 nanoflares are taken up by cells and emit a detectable fluorescence Cy5 signal as a consequence of binding their target, as well as to gauge the incubation time required for this to occur. For that reason, Cy5 signal was first monitored live by time-lapse microscopy from the moment of nanoflare addition to cells and over the course of 24 h. The percentage of Cy5-positive cells at the end of the time-lapse imaging period was then quantified by FACS.

Nanoflares for Cy5 signal detection after binding target SOX9 mRNA transcripts were used as manufactured according to the gold nanoparticle synthesis and flare hybridisation protocols described by Kyriazi et al. (Kyriazi et al., 2018). The sequence of the recognition strands for binding and the Cy5 flare strand for detection are included in Table 4.1.

Table 4.1 Nanoflare mRNA targets used with their respective sense and Cy5 flare strand sequences.

Nanoflare mRNA target	Recognition sense strand sequence	Flare strand sequence
Scrambled	ATGGTATACCGAAAGACTGTTA	AACAGTCTTTCG
SOX9	CCGTCTTGATGTGCGTTCGCTG	CAGCGAACGCA

ATDC5 chondroprogenitor cells were studied as the preliminary positive control for SOX9 and HBMSCs were the target human cell population of interest. The cells were cultured and expanded in their respective culture media detailed in section 2.3 and then harvested and seeded at a density of 10^5 cells/well onto a 24-well plate (Corning, Costar, Sigma-Aldrich, UK) in 500 µl DMEM + 1% P/S (v/v) for ATDC5 and the same volume of αMEM + 1% P/S (v/v) for HBMSCs. Serum-free media were used for nanoflare incubation to avoid any influence from protein content on cell uptake (Choi et al., 2013). Three conditions were tested for imaging (n = 1): cells cultured with no nanoflares as a negative control, cells incubated with *Scrambled*-Cy5 nanoflares (24.4 nM stock concentration) and cells exposed to *SOX9*-Cy5 nanoflares (17.5 nM stock concentration). The nanoprobes were added to culture wells at a 0.2 nM concentration based on previous work by Lanham et al. (Lanham et al., 2019); equivalent to 8.2 µl *Scrambled*-Cy5 nanoflare suspension per ml cell suspension and 11.4 µl/ml for the *SOX9*-Cy5 nanoflare. Time-lapse analysis was run on the Nikon Eclipse Ti inverted

microscope at 37°C and 5% CO_2, capturing images from 3 different regions of the well within an interval of 15 min.

Following time-lapse imaging, the cells from each of three conditions (n = 1) were trypsinised, centrifuged at 272 g for 5 min and resuspended in FACS solution buffer (5 mg/ml BSA, 2 mM EDTA in 1X PBS). The FACS Aria cytometer (BD, Wokingham, UK) was used to acquire cell counts and the data was analysed using the FlowJo software version 10.6.1.

4.2.2 Nanoflare validation for short-term chondrogenic differentiation cultures

A short-term differentiation culture was designed to further assess suitability and specificity of *SOX9*-Cy5 nanoflares to report SOX9 expression in early chondrogenic differentiation cultures that could be reproduced with a microdroplet cell encapsulation system. ATDC5 cells were used as a positive *SOX9*-expressing chondroprogenitor control and HBMSCs were seeded in two groups: basal culture medium and the chondrogenic medium, both described in section 2.3.4 to assess any differences in *SOX9* detection due to chondrogenic induction. Cells were cultured in monolayer at a density of 50000 cells/well on 6-well plates for 7 days at 37°C, 20% O_2 and 5% CO_2 using 3 ml media/well and changing media every 3 days. Three replicate samples of each condition were used at the end of the differentiation culture for FACS quantification after nanoflare incubation in accordance with the method described in section 4.2.1 and three other replicates were employed for gene expression analysis by RT-qPCR. The incubation time was reduced to 1 h for these validation experiments and onwards based on the optimisation protocol established by Lanham et al. concluding that nanoflares were capable of emitting a strong and representative fluorescent signal within that period of contact time with HBMSCs without compromising cell viability (Lanham et al., 2019).

4.2.2.1 RT-qPCR analysis

RNA was extracted from sorted cells using ReliaPrep RNA Cell MiniPrep system kit (Promega, UK) as specified by the manufacturer according to the protocol in section 2.8.2. cDNA conversion from RNA samples was carried out using the Superscript™ VILO™ cDNA Synthesis Kit (Invitrogen, UK) and replicating the protocol detailed in section 2.8.3. RT-qPCR plate preparation and statistical analysis were completed as described in sections 2.8.4 and 2.8.5, respectively. The primers employed are detailed in Table 4.2. Statistical analyses were computed using GraphPad Prism 8.2.1 and selecting Ordinary One-way ANOVA with multiple comparisons on ΔC_t values and the statistical significance was assigned in compliance with the general symbol criteria in section 2.5.

Table 4.2 List of PCR primers used for RT-qPCR and their characteristic sequence and amplicon size in base pairs.

Gene	Primer sequence	Amplicon size (bp)
Mouse		
Gapdh	F: 5' CACCATGGAGAAGGCCGGGG 3'	123
	R: 5' GACGGACACATTGGGGGTAG 3'	
Sox9	F: 5' GAGGCCACGGAACAGACTCA 3'	50
	R: 5' CAGCGCCTTGAAGATAGCATT 3'	
Human		
β-ACTIN	F: 5' GGCATCCTCACCCTGAAGTA 3'	82
	R: 5' AGGTGTGGTGCCAGATTTTC 3'	
GAPDH	F: 5' GACAGTCAGCCGCATCTTCTT 3'	86
	R: 5' TCCGTTGACTCCGACCTTCA 3'	
SOX9	F: 5' CCCTTCAACCTCCCACACTA 3'	74
	R: 5' TGGTGGTCGGTGTAGTCGTA 3'	

4.2.3 Nanoflare validation for sorting of undifferentiated plastic adherent HBMSCs

The final stage of the nanoflare validation process consisted in assessing whether and to what extent the Cy5 fluorescence intensity of different sorted HBMSCs subpopulations incubated with *SOX9*-Cy5 nanoflares correlated with their respective *SOX9* mRNA levels measured by RT-qPCR gene expression.

Plastic adherent cells were split into the same three groups assayed during the preliminary nanoflare uptake study in section 4.2.1 (i.e. nanoflare-free negative control, *Scrambled*-Cy5 specificity control and *SOX9*-Cy5 nanoflare samples) and treated with similar methods regarding cell harvesting, nanoflare incubation and sample preparation for FACS. For the SOX9-Cy5 group, 3×10^6 cells were resuspended in either 500 µl FACS solution buffer. For the two control groups, 10^5 cells were resuspended in 250 µl FACS solution buffer. Cells were injected through the BD FACSAria™ IIIu flow cytometer (BD, Wokingham, UK) and gated for sorting of four subpopulations termed highly negative, negative (i.e. control), positive and highly positive. Sorted cells were collected into three FACS tubes per sample containing 5% FBS (v/v) in 500 µl FACS solution buffer. The cells were centrifuged at 400 g for 5 min in the FACS tubes and the pelleted samples were lysed with BL-TG cell lysis buffer prior to isolating RNA. RNA extraction cDNA synthesis, RT-qPCR plate preparation and statistical analysis were all performed as described in section 4.2.2.1.

4.3 Results

4.3.1 *SOX9*-Cy5 nanoflare uptake by cells and release of Cy5 fluorescence

Time-lapse microscopy on ATDC5 cells and HBMSCs exposed a progressive increase in the red Cy5 fluorescent signal emitted by the sample group that had been in contact only with the *SOX9*-Cy5 nanoflare (Figure 4.3, labelled *SOX9*-Cy5 nanoflare groups for ATDC5s and HBMSCs) over 24 h of incubation. This suggested that the nanoprobes were taken up exclusively when the cells were incubated with the *SOX9*-Cy5 mRNA probe as far as time-lapse microscopy could resolve.

Nanoflare-free negative controls and *Scrambled*-Cy5 control excluded any background originating from the ATDC5 or HBMSCs themselves or non-specific binding (Figure 4.3, corresponding labelled groups), as shown by the absence of any measurable fluorescent signal for 24 h.

Both ATDC5s and HBMSCs displayed detectable signal from 6 h, but in the case of HBMSCs clear signs of cell uptake were not apparent until 12 h and a gradual intensity increase occurred up to 24 h (Figure 4.3, labelled *SOX9*-Cy5 nanoflare group). The fact that the intensity of Cy5 fluorescence at 6 h compared to HBMSCs and the presence of dot-like regions with higher intensity raised the question whether ATDC5 were more permeable to the nanoprobes, they merely exhibited a faster response due to their chondroprogenitor nature or a combination of both. Because the HBMSCs were expanded as opposed to freshly isolated populations, other cell types (e.g. granulocytes, monocytes, lymphocytes) will have failed to grow, died or been removed with media changes.

To obtain a quantitative and comparable measurement of SOX9 fluorescent intensity, cells from the three samples in monolayer culture were harvested after 24 h of time-lapse culture, resuspended in FACS buffer and run through FACS. The Cy5-positive gating threshold in both cell types and the overlay peaks depicted a shift in fluorescence intensity for the distinct Cy5-positive cell subpopulations linked to the incubation with the *SOX9*-Cy5 nanoflare (Figure 4.4).

Similar negligible percentages of Cy5-positive cells were quantified for nanoflare-free negative controls (1.02% for ATDC5 and 0.73% for HBMSCs) and *Scrambled*-Cy5 groups (0.67% and 0.81% for ATDC5 and HBMSCs, respectively). The percentage of Cy5-positive cells corresponding to samples exposed to the *SOX9*-Cy5 nanoflares was close to 100% for both cell types: 97.43% in ATDC5 and 99.78% in HBMSCs; consistent with the Cy5 intensities observed in time-lapse microscopy images. The percentage figure for HBMSCs was excessively high for a heterogeneous cell population. It was attributed to non-specific mRNA binding of the nanoflares because of the long 24-hour incubation. This result indicated the need to reduce the incubation time to obtain a realistic read-out of

nanoflare fluorescence emission. Also, it confirmed that the controls were appropriate to negate the effect of non-specific binding given the low percentages of Cy5-positive cells measured.

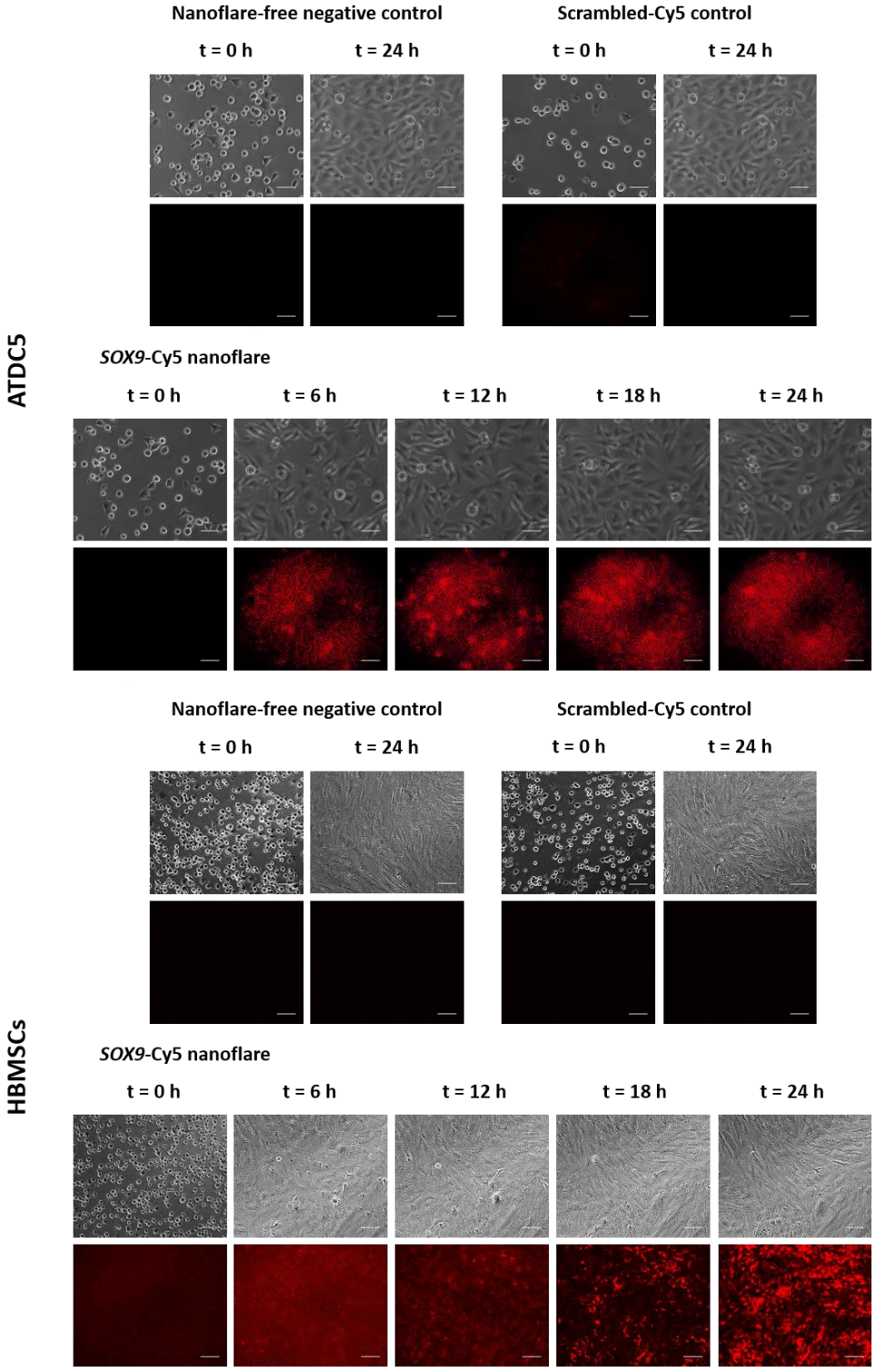

Figure 4.3 Time-lapse nanoflare uptake in ATDC5 (left) and F64 P2 HBMSCs (right) shown for 6 h time intervals up to 24 h with a representative image of nanoflare-free negative control, Scrambled-Cy5 background control and SOX9-Cy5 nanoflare samples. The cells were incubated with nanoflares in serum-free plain medium (i.e. DMEM for ATDC5 and αMEM for HBMSCs + 1% P/S (v/v)). Please note that the poor focus in Figure 4.2 for ATDC5 cells is due to a slight misalignment while fitting the plate holder onto the stage. The time points from 6 h to 18 h were not included for the controls for the sake of simplicity. Scale bar = 100 µm.

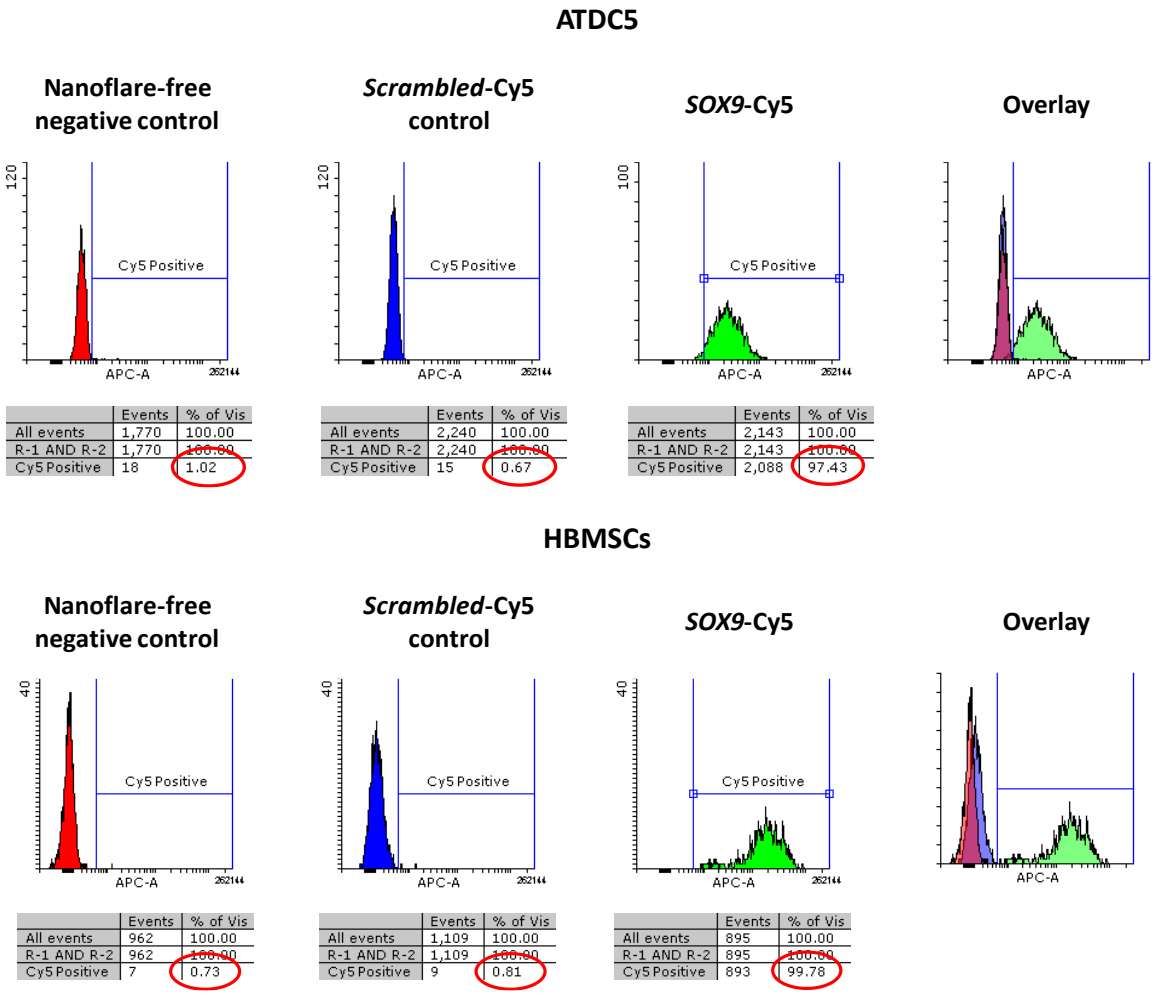

Figure 4.4 FACS quantification of ATDC5 (top) and F64 P2 HBMSCs (bottom) following time-lapse incubation with nanoflares for 24 h. The plots show the fluorescence intensity on the x axis and the event count on the y axis. Nanoflare-free negative control (left), scrambled-Cy5 (middle left), SOX9-Cy5 (middle right) and overlay of the three groups are depicted, all of them with a summary table below where the percentage of Cy5-positive cells is highlighted.

4.3.2 Validation of the *SOX9*-Cy5 nanoflare for short-term chondrogenic differentiation cultures

Time-lapse microscopy and more sensitive FACS quantification verified that ATDC5 and HBMSC monolayer cell cultures that had been in contact with *SOX9*-Cy5 for 24 h exhibited Cy5 fluorescent signals indicative of cell uptake. This assay was conceived as a proof-of-principle of nanoflare uptake by cells and detection of Cy5-positive subpopulations. To ensure high cell viability, the incubation time was restricted to 1 h as previous studies reported reduced cell viability in Saos-2 human osteosarcoma cells after 4-6 hours in contact with nanoflares (Lanham et al., 2019).

Nanoflare validation intended to evaluate the specificity of the nanoprobes to discriminate between cells that have a robust *SOX9* expression and those with poorer *SOX9* expression. This was assessed by quantifying Cy5 fluorescence signal emission using FACS. The hypothesis was that its

intensity was dependent on the abundance of SOX9 mRNA transcripts available for binding. The requirement that had to be met for the purpose of validation was to verify that FACS Cy5 fluorescence signal intensity correlated with mRNA expression of the target by RT-qPCR.

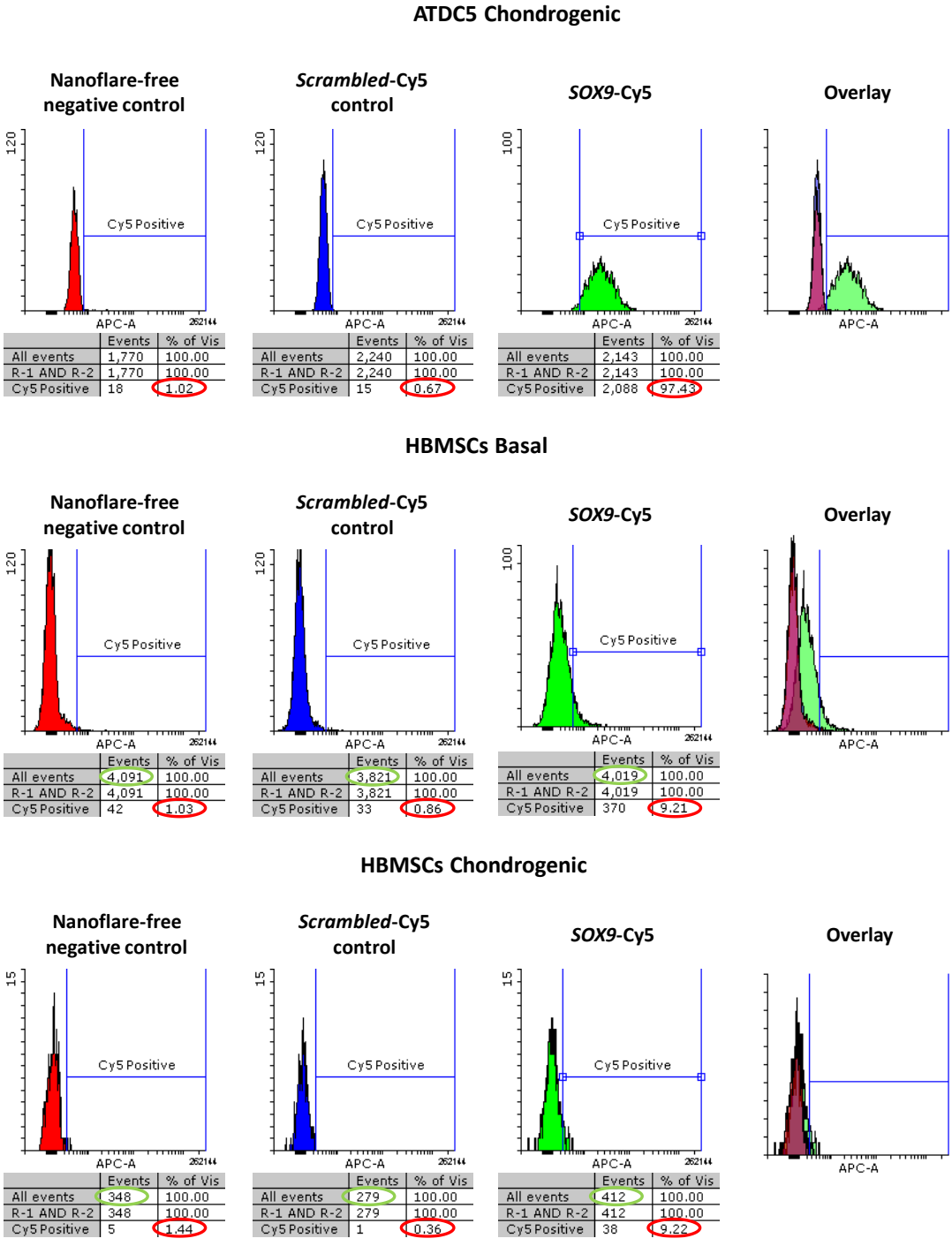

Figure 4.5 FACS quantification of ATDC5 in chondrogenic differentiation medium (top), F60 P2 HBMSCs in basal medium (middle) and F60 P2 HBMSCs in chondrogenic differentiation medium after a week of culture and 1 h exposure to nanoflare probes. The plots show the fluorescence intensity on the x axis and the event count on the y axis. Nanoflare-free negative control (left), scrambled-Cy5 (middle left), SOX9-Cy5 (middle right) and overlay of the three groups are depicted, all of them with a summary table below where the percentage of Cy5-positive cells is highlighted. For the HBMSCs, the number of events measured during the quantification is also highlighted to mark the difference between basal and chondrogenic conditions.

FACS revealed the ability to discern Cy5-positive populations among ATDC5 chondroprogenitor cells exposed to the *SOX9*-Cy5 nanoflare. The percentage of Cy5-positive ATDC5 cells measured was 97.43% after a one-week chondrogenic differentiation culture prior to incubating all the cells in monolayer culture to nanoflare probes for 1 h. For HBMSCs, though, regardless of basal or chondrogenic culture conditions, the percentage of Cy5-positive cells quantified by FACS due to exposure to the *SOX9*-Cy5 mRNA probe was very similar and below 10% (9.21% and 9.22%, respectively). These small percentages indicated that nanoflares were not sufficiently sensitive to detect the smaller effect size of chondrogenic induction on SOX9 expression of HBMSCs. (Figure 4.5).

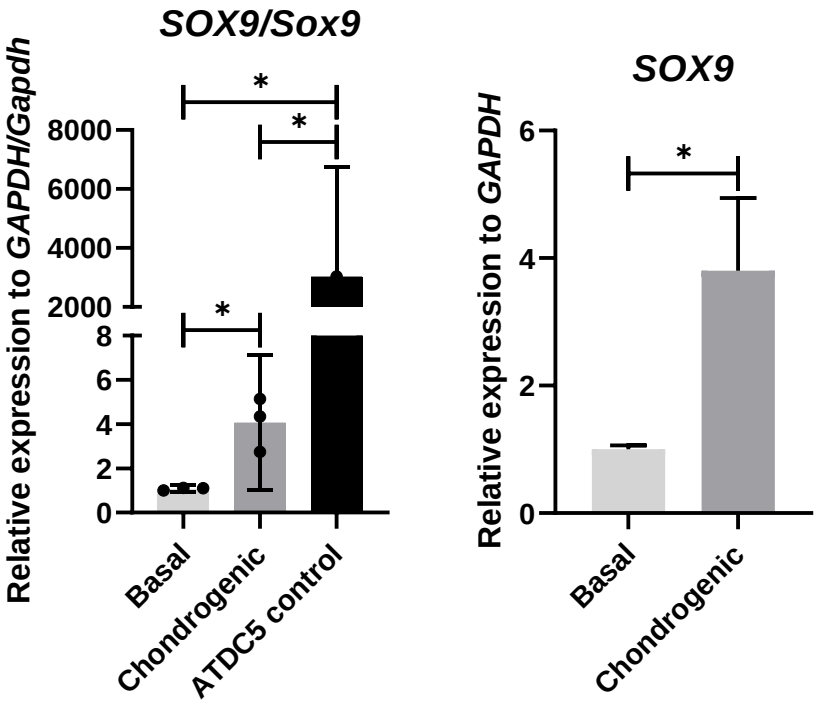

Figure 4.6 Relative *SOX9* and *Sox9* mRNA expression to GAPDH/Gapdh housekeeping gene of F60 P2 HBMSCs grown in basal (reference control) and chondrogenic differentiation medium and ATDC5 mouse chondroprogenitor control cultured in chondrogenic differentiation medium including individual absolute fold values of each replicate (n = 3). ATDC5 and HBMSCs were presented in the same plot for illustrative purposes. The measurements cannot be compared from one species to another because human and mouse primers have different efficiencies of amplification. The plot on the right has comparable groups and displays the overall relative SOX9 expression in the HBMSCs groups presented through their means and SDs (right). The statistical analysis was performed using Ordinary One-way ANOVA with multiple comparisons on ΔC_t values and the statistical significance symbol * refers to $p \leq 0.05$.

RT-qPCR analysis showed high *SOX9* expression matching nanoflare Cy5-positive fluorescent signal from FACS for ATDC5 cells (Figure 4.5 and Figure 4.6, left) and low *SOX9* expression for HBMSCs regardless of culture conditions, which was still significantly higher in the case of the chondrogenic group with respect to basal cultures (Figure 4.6, right). This significant difference measured by RT-qPCR had not been determined during FACS quantification, though it should be noted that the

number of events counted was ten times smaller in the HBMSC chondrogenic group than the basal group which may mean the sample was less statistically representative (Figure 4.5, bottom). Notably, in the case of ATDC5 positive controls where the percentage of FACS Cy5-positive cells was close to 100%, *SOX9* expression normalised to the mRNA levels quantified for HBMSCs in basal culture medium differed by three orders of magnitude (i.e fold difference computed as $2^{-\Delta\Delta C_t}$ relative to *Gapdh*) (Figure 4.6, left).

4.3.3 Validation of the *SOX9*-Cy5 nanoflare for sorting of undifferentiated plastic adherent HBMSCs

In line with the aim of applying nanoflares to sort for the HBMSC chondroprogenitor fraction, the ability of the technique to identify cell subsets expressing *SOX9* more robustly was further validated. HBMSCs were harvested for sorting through FACS according to their Cy5-positive signal and the sorted cells were analysed by RT-qPCR to determine mRNA expression levels.

A preliminary assay was carried out on F69 P1 plastic adherent cells that had been expanded in culture medium (see section 2.3.2) without inducing chondrogenic differentiation. Including the same negative control groups as the previous validation assays (i.e. no nanoflare and *Scrambled*-Cy5), the cells were gated from two distinct fluorescence intensity peaks: one labelled as Neg for Cy5-negative subpopulations with two subgroups termed highly negative (left end) and negative (reference control, right end), and the other labelled as Pos for Cy5-positive subpopulations (Figure 4.7A; each of the black dots at the end of the bars refers to a subgroup of gated cells for sorting) with equivalent positive (left end) and highly positive (right end) subgroups. A detailed schematic of the gating strategy is depicted in Figure 4.7B.

Interestingly, RT-qPCR of sorted cells revealed that only highly positive gated cells correlated with significant upregulation of *SOX9* mRNA expression relative to *GAPDH* housekeeping gene and normalised to the expression of the negative reference control group. In fact, in terms of absolute values, positive gated subpopulations exhibited mRNA expression levels below those of the negative control group. *SOX9* mRNA expression in the highly negative gated group was undetectable (Figure 4.7C).

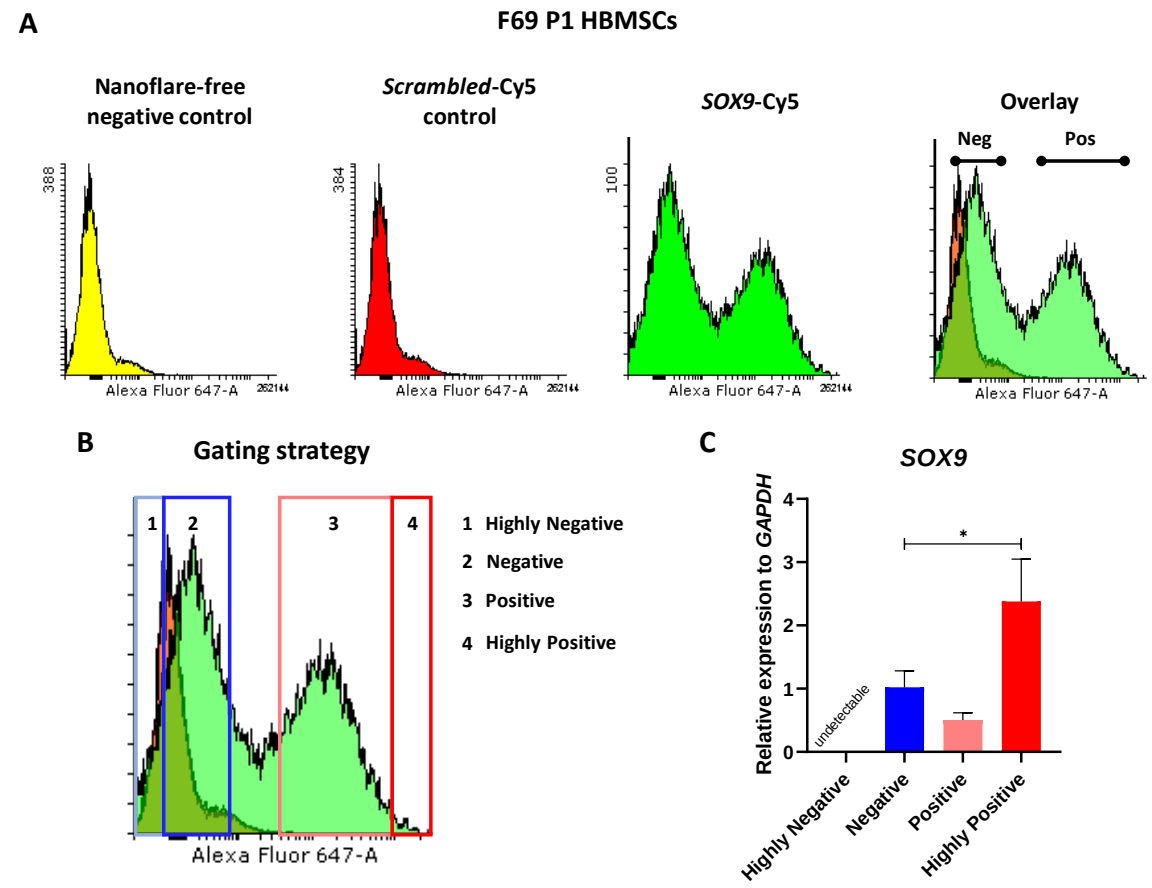

Figure 4.7 Sorting of F69 P1 HBMSCs exposed to *SOX9*-Cy5 nanoflares for 1 h in serum-free αMEM + 1% P/S (v/v): (A) Cy5 fluorescence intensity peaks for the nanoflare-free negative control (left), the scrambled-Cy5 background control (middle left), the samples incubated with the *SOX9*-Cy5 nanoflare (middle right) and overlay (right). The plots display the fluorescence intensity on the x axis and the event count on the y axis. The cells were gated and sorted according to the four groups represented by black dots above the peak overlay (right). The Neg and Pos labels on the peaks stand for ranges assigned to negative and positive, respectively. Hence, the cells were divided into four groups upon sorting: highly negative cell subpopulations at the left end of the Neg bar; negative control cell subpopulations at the right end of the Neg bar; positive cell subpopulations at the left of the Pos bar and highly positive populations at the right end of the Pos bar; (B) Schematic of the gating strategy with the corresponding regions for all the sorted groups in the FACs plot ; (C) qPCR relative SOX9 expression to GAPDH housekeeping gene (fold change) and normalised to the negative group measured for all four cell groups sorted through FACS. The statistical analysis was performed using Ordinary One-way ANOVA with multiple comparisons on ΔC_t values and the statistical significance symbol * refers to $p \leq 0.05$.

These promising findings led to a last validation assay expanding the study to three other human donors and replicating the methodology (Figure 4.8A and B). Unlike the first donor, the second peak that may be attributed to the formerly referred to as Cy5 highly positive subpopulations was considerably flatter for the three donors tested afterwards. Additionally, the cell yield was extremely low in those gating conditions and therefore not deemed valid for comparison by RT-qPCR. This justified a simplification of the gating consisting in exclusively sorting the positive and negative groups for RT-qPCR analysis to ascertain whether there were statistically significant differences in *SOX9* mRNA expression (Figure 4.8C). As a result, only the positive and negative

subpopulations that were gated at the same thresholds established for the preliminary assay in Figure 4.7 were studied in this assay. These were labelled 2 and 3 in both gating strategy plots in Figure 4.7 and Figure 4.8, respectively.

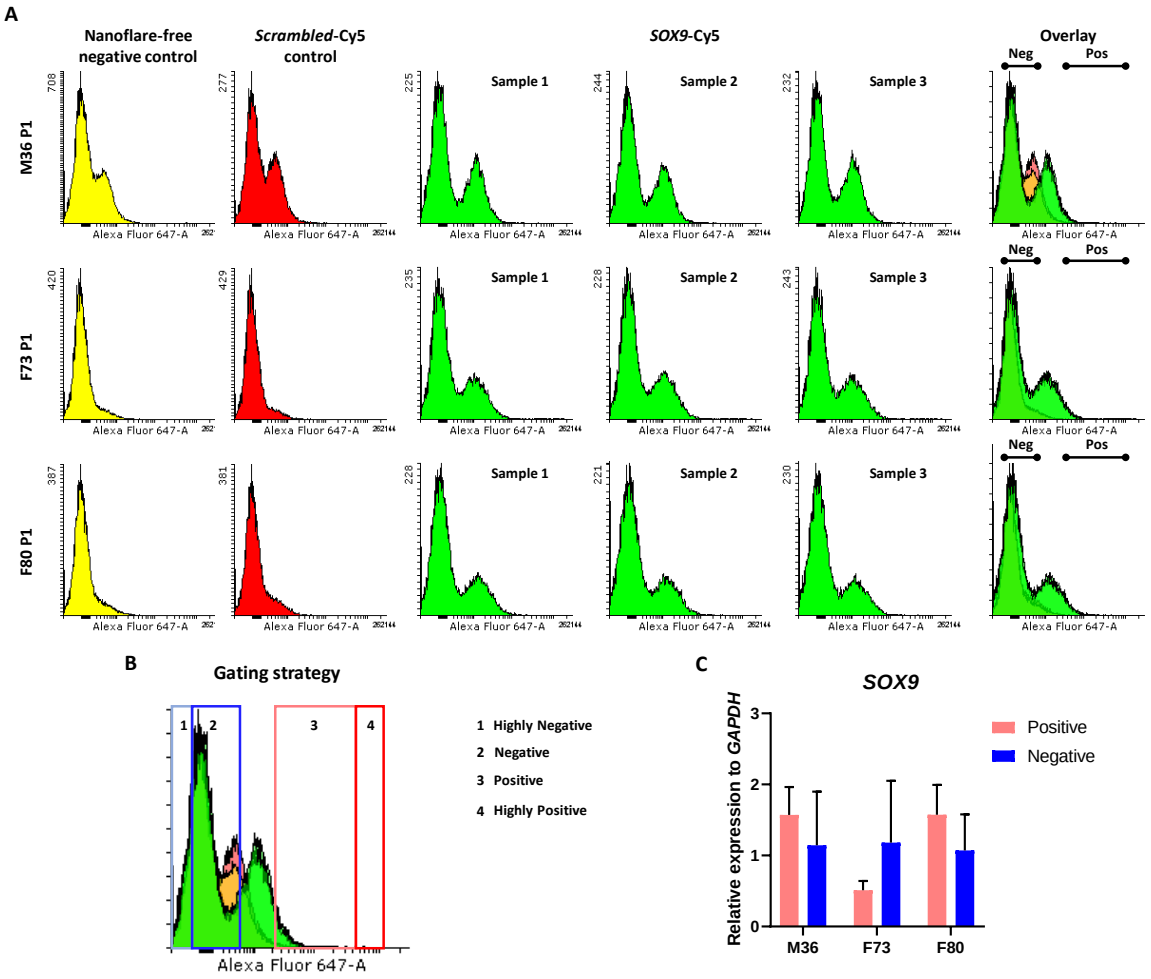

Figure 4.8 Sorting of M36 P1, F73 P1 and F80 P1 HBMSCs incubated with *SOX9*-Cy5 nanoflares for 1 h in serum-free αMEM + 1% P/S (v/v): (A) Cy5 fluorescence intensity peaks for the nanoflare-free negative control (left), the scrambled-Cy5 background control (middle left) and three samples incubated with the *SOX9*-Cy5 nanoflare (middle to right). The plots display the fluorescence intensity on the x axis and the event count on the y axis. The cells were gated according to the four groups represented by black dots above the peak overlay (right). The Neg and Pos labels on the peaks stand for ranges assigned negative and positive subpopulations, respectively. For the purpose of gene expression analysis, two subpopulations were extracted: the negative control cell subpopulations at right end of the Neg bar and the positive test cell subpopulations at the left end of the Pos bar; (B) Schematic of the gating strategy for one of the patients with the regions numbered 2 and 3 corresponding to the negative and positive groups sorted by FACS; (C) qPCR relative SOX9 expression to GAPDH housekeeping gene (fold change) and normalised to the negative group measured for all four cell groups sorted through FACS (right). The statistical analysis was performed using Ordinary One-way ANOVA with multiple comparisons on ΔC_t values and the statistical significance symbol * refers to $p \leq 0.05$.

In agreement with the results for the single donor study, the positive and negative gated cells from the three other human patients failed to exhibit any statistically significant differences. This finding may indicate that the nanoflares may not be sensitive enough within these fluorescent intensity

range. In addition, the highly positive gating where they were specifically correlating with higher *SOX9* mRNA expression that resulted from the single human donor assay may be ascribed to patient-to-patient variability in HBMSCs. Those highly positive cell subgroups may thus correspond to a very rare cell subpopulation in some patients such as the three patients (Figure 4.8) evaluated afterwards and less so in others such as the first donor (Figure 4.7).

4.4 Discussion

The nanoflare validation process undertaken in this chapter was motivated by the ultimate goal of the project of sorting HBMSC subpopulations displaying high chondrogenic potential for cartilage tissue engineering by using the functional marker SOX9. In this context, nanoflares would play the role of mRNA reporters for identification of these chondroprogenitors by targeting *SOX9* mRNA transcripts that could be compatible with small microaggregates formed inside microdroplets. This technology needed an assessment of its suitability and reliability. Validation was performed step by step starting from nanoflare cell uptake verification and followed by evaluation of effectiveness and specificity in chondrogenic differentiation conditions and sorting capabilities in basal conditions.

4.4.1 *SOX9*-Cy5 nanoflares are specifically taken up by cells and emit a Cy5 fluorescence signal

Nanoflare cell uptake was investigated through a combination of time-lapse imaging of ATDC5 chondroprogenitors and HBMSCs as the cells were brought in contact with the nanoflares and FACS quantification after a 24-hour incubation period. For this early study, that long incubation time was selected to see if the critical requirement of cell internalisation was met and to confirm detection of Cy5 fluorescence signal. Fluorescence microscopy had a known limited sensitivity to capture this phenomenon compared to FACS, which implied that a longer contact time to observe uptake was expected (Basiji et al., 2007). Thus, a larger time window for imaging had to be considered for the experimental design in order to obtain visual evidence of the gradual cell uptake and structural information about the cell regions emitting fluorescence. Time-lapse imaging and FACS both coincided in the detection of high Cy5 fluorescence intensity from cell cultures incubated with the *SOX9*-Cy5 nanoflare at 24 h. Additionally, there were signs of binding to mRNA transcripts and uptake happening earlier even in time-lapse imaging before 6 h. Issues with the microscopy imaging set-up during ATDC5 exposure to nanoflares hindered the observation of cell uptake due to a substantial loss in resolution. A clearer and higher resolution visualisation of these samples would have enabled to draw a more accurate conclusion regarding the onset and progression of cell internalisation in these cells.

The parallel time-lapse fluorescence imaging and FACS quantification methodology provided an indication of successful nanoflare cell uptake although a comprehensive cell uptake study was not completed. The mechanism of nanoflare metabolic assimilation by cells has been reported in the literature as a caveolae-mediated endocytosis uptake of nanoprobes and release of gold nanoparticles by exocytosis. The latter is accompanied by nuclease degradation of fluorescent reporter strands that remain non-toxic to cells below a threshold incubation time and nanoflare

concentration (Choi et al., 2013, Briley et al., 2015, Krönig et al., 2015, Lahm et al., 2015, Li et al., 2016). Complementary characterisation techniques could be applied to study nanoflare cell uptake including (i) mass spectrometry to detect gold intracellularly combined with transmission electron microscopy for confirmation to resolve their presence inside cellular structures; (ii) confocal microscopy for higher resolution images, and (iii) biomolecular endocytosis assays (e.g. Western blotting to study endocytosis pathways) (Choi et al., 2013, Li et al., 2018, Lin et al., 2019). For the purpose of the application of this technology to purify heterogeneous HBMSC populations, this was not deemed a central research question to answer. The nanoflare uptake assay merely intended to verify the presence of apparent signs of nanoflare binding to mRNA transcripts in HBMSCs and ATDC5 chondroprogenitor control cell. An interpretation of this biological event was thus made by fluorescent emission from cell structures when imaged under time-lapse fluorescent microscopy and Cy5-positive fluorescent signal quantified by FACS.

The cell uptake assay presented in this chapter comprised a long 24 h incubation period to address the question of nanoflare cell internalisation while allowing a wide enough time window to capture the process by fluorescence time-lapse microscopy and to reference it to more sensitive FACS quantification. That time was purposefully excessive for further culture of these cells as previously tested by Lanham et al. in a comparable Saos-2 human osteosarcoma cell line model. They observed that Saos-2 cells experienced a transition towards necrosis for concentrations from 0.2 to 6.25 nM *Vimentin* nanoflares and contact time of 22 h after incubating cells for 2 and 3 days. Necrotic induction was particularly intense within the first 24 h of incubation for nanoflare concentrations of 1 nM and 6.25 nM concentrations. A reduction in cell viability was also confirmed after 3 days. These results suggest that cytotoxic incubations times may be even shorter in more delicate human primary cells like HBMSCs and endorsed shortening incubation times (Lanham et al., 2019).

4.4.2 Small increases in SOX9 mRNA expression are not detectable by SOX9-Cy5 nanoflares

As a means to determine the utility of *SOX9*-Cy5 nanoflare to report the presence of target *SOX9* mRNA transcripts in HBMSCs for cell sorting, specificity and effectiveness were the two central parameters to assess. The techniques that were commonly applied in the literature were FACS and RT-qPCR by examining the existing correlation between quantified fluorophore intensity from different cell subsets and their relative target mRNA expression (Prigodich et al., 2012, Krönig et al., 2015, Lahm et al., 2015, Li et al., 2016, Czarnek et al., 2018). Even though FACS-sorted cells are usually employed for the gene expression analysis, a preliminary validation of specificity and effectiveness was conducted in this work. Prior to sorting, the ability of nanoflares to selectively detect chondroprogenitor cells (i.e. ATDC5) and primary cells in the process of differentiating along

the chondrogenic lineage (i.e. HBMSCs cultured in chondrogenic differentiation medium) or without chondrogenic induction (i.e. HBMSCs cultured in basal medium) was investigated. A substantial shortening of the exposure time to nanoflares to 1 h was implemented to ensure high cell viability and to maximise specificity (i.e. through the exclusion of non-specific binding to other available mRNA targets). The results underlined that the *SOX9*-Cy5 nanoflare was effective in ATDC5 cells where a percentage of cells near totality were Cy5-positive and the gene expression analysis coincided in a significantly higher expression with respect to reference negative control (i.e. HBMSCs cultured in basal medium). It is worth acknowledging that a reference negative basal condition for ATDC5 cells would have been more adequate for a separate analysis of cells from different species that cannot be compared directly. The fact that analogous and low percentages of Cy5-positive cells were found for HBMSCs culture in both chondrogenic and basal conditions below 10% were measured may respond to two reasons:

1) Very few events and therefore cells counted for the chondrogenic differentiation medium condition, which implies that it would have a lower statistical power.
2) The cells were cultured in monolayer as a proof of principle and for simplicity. As mentioned repeatedly throughout this research work, *SOX9* expression is upregulated when cells form aggregates. Spheroid culture was not carried out because the nanoflare uptake in spheroids would impose an additional variable that would hamper control in a validation stage.

In brief, the short-term differentiation culture in monolayer revealed the expected low *SOX9* expression in HBMSCs relative to ATDC5 chondroprogenitors. Whereas RT-qPCR exposed significant upregulation in HBMSCs cultured in chondrogenic differentiation medium compared to basal conditions, FACS quantification after nanoflare incubation did not outline that difference. This would indicate that the Cy5 nanoprobes lack the sensitivity to detect changes in *SOX9* expression in HBMSCs induced by chondrogenic stimulation when cultured in monolayers.

4.4.3 Evaluation of the application of the SOX9-Cy5 nanoflare for sorting of HBMSCs

To finalise the validation process, the principle mentioned in the former section concerning the scrutiny of the correlation between FACS measurements of Cy5 fluorescent signals from cell subpopulations incubated with nanoflares and their target mRNA levels was explored. The results obtained for the single-donor assay suggested that *SOX9*-Cy5 were effective provided that the cells were sorted by gating at fluorescence intensities over two log10 steps. When that condition was met, the subpopulations sorted according to that gating method termed highly positive reflected higher *SOX9* mRNA expression. For the three-donor assay performed later to verify this behaviour,

however, the gating that had been applied to that first patient only enclosed very few cells at the highly positive end corresponding to a smaller and narrower second peak shifted to the right of negative and *Scrambled*-Cy5 controls. That drawback imposed a limitation to then compare in terms of gene expression and only the positive and negative cell subpopulations were sorted. The ensuing qPCR analysis data were consistent with those found for the first patient. This was reflected in that both showed that when cell subpopulations were analysed from the so-called negative and positive regions, no statistical difference in *SOX9* mRNA expression emerged. The single donor assay justified sample normalisation to the negative subpopulation control since the highly negative group yielded undetectable expression. Taking all these results together, only the highly positive cells located at the right end of the positive gating region yielded significant differences in *SOX9* mRNA expression with respect to the other subpopulations, but the abundance of this population seemed to be heavily patient-specific. In this regard, Li et al. conducted an analogous experiment where they gated for two distinct cell subpopulations, low Cy5 fluorescence intensity and high fluorescence intensity, according to the FACS counts from HBMSCs incubated overnight with *SOX9*-Cy5 Smartflares^{TM} nanoprobes. They noticed an upregulation of the *SOX9* mRNA levels in the high Cy5 intensity cell subpopulation normalised to the low intensity group, although the difference was not statistically significant (Li et al., 2016).

One of the aspects that sparked controversy in relation to the specificity of nanoflares is the correlation of the nanoflare fluorescence signal to mRNA levels. Czarnek and Bereta criticised the effectiveness of Smartflare^{TM} nanoprobes with a series of postulates based on their findings and previous work in the Levy group using the commercial version of nanoflares. In summary, they claimed that the Smartflare^{TM} nanoprobes failed as reporters of the presence or absence of a specific target mRNA transcript and could not differentiate cells expressing a high level of a target mRNA from cells with a low level. They added that the actual existing associations might be between the registered fluorescence intensity and the nanoprobe uptake and the nanoprobe concentration, the latter characterised by a linear pattern. Their Smartflare^{TM} nanoprobe incubation method complied with the manufacturer's recommendations: 0.1 nM final concentration when applied to cells and an overnight incubation (Mason et al., 2016, Czarnek and Bereta, 2017). Very recently and using the same nanoflare design described in this work, Lanham later reported concordant observations upon 15-hour incubation of *RUNX2*-Cy5 and *Osteocalcin*-Cy5 nanoflares at a 0.2 nM concentration with MG63 cells (human bone osteosarcoma-derived cell line) in different cell-seeding densities from 10^5 to 2×10^6 cells/ml. In contrast, their findings exposed that the shorter the contact time with a given nanoflare (e.g. Cy5 signal was detectable by FACS after one-hour contact time) was, the stronger the correlation between the nanoflare fluorescence signal and the measured target mRNA transcript levels. They argued that a single

mRNA transcript could bind to multiple sense strands from different nanoprobes, hence releasing the fluorescent flare strand and increasing the emitted fluorescence signal intensity. Moreover, this phenomenon could be more likely and intense for longer incubation times with nanoflares and lead to a misinterpretation of quantified mRNA expression levels that differ from true mRNA levels (Lanham et al., 2019). This hypothesis would support the approach taken in this research project to shorten the incubation time to 1 h at 0.2 nM nanoflare concentration to additionally ensure that the mRNA level readings from the RT-qPCR analysis were meaningful. Simultaneously, it would question the protocol provided by the manufacturer of the discontinued Smartflare^{TM} nanoprobes and would offer an explanation to findings in previous works in the field. This is the case of the results published by Lahm et al. on pluripotent stem cells incubated with Smartflare^{TM} nanoprobes for 24 h, where RT-qPCR analysis in murine V6.5 ESCs of FACS-sorted cells yielded no statistical differences in the mRNA expression of their genes of interest *Nanog* and *Gdf3* (Lahm et al., 2015). Another example would be Mason et al. criticising the idea of endosomal escape and how that may produce background signals (Mason et al., 2016).

The active debate over the effectiveness of nanoflare technology has not deterred part of the scientific community from investigating further to develop new strategies. For instance, nanoflares have been chemically modified to address new needs in the field. Prigodich et al. synthesised a multiplexed nanoflare probe to detect two mRNA targets simultaneously in HeLa and Jurkat live cells (i.e. survivin and actin) that could serve as a criterion to distinguish between cancerous and non-cancerous cells (Prigodich et al., 2012). The multiplexed nanoprobe structure was later advanced by Kyriazi et al. to integrate up to DNA-intercalating anticancer drugs (i.e. doxorubicin and mitoxantrone) for delivery upon sensing of two mRNA targets at the same time (Kyriazi et al., 2018). Lin et al. designed a novel modification of traditional nanoflares by inserting photoresponsive hairpin DNA and a photocleavable linker that released the fluorescent flares from the gold nanoparticle surface upon time-controlled and tunable UV (ultraviolet) irradiation for an augmented sensitivity and single-cell resolution (Lin et al., 2019). Lastly, Wu and Tseng conjugated molybdenum disulphide nanosheets with dual fluorophore-labelled nanoflares (i.e. FAM and 5-carboxytetramethylrhodamine or TAMRA) to build a ratiometric sensor to detect thymidine kinase 1 (TK1) mRNA in live cells, which is associated with malignancy in cancer (Wu and Tseng, 2020).

4.4.4 Conclusions

Nanoflares failed to provide robust evidence to prove their effectiveness and sensitivity to distinguish *SOX9*-positive populations in HBMSCs in a definitive manner with the aim of isolating chondroprogenitors. The validation assays on short-term ATDC5 chondrogenic cultured revealed that the Cy5-positive cell subpopulations incubated with the *SOX9*-Cy5 nanoflare corresponded

with high *SOX9* mRNA levels and in those instances where there was a clear difference in terms of order of magnitude of Cy5 fluorescence signal in FACS plots between positive and negative gated cells such as the single donor study with unselected plastic adherent HBMSCs in the absence of chondrogenic induction.

Regarding the original hypothesis, there did not seem to be a strong case for using nanoflares in the conditions tested in this work as part of single-cell analysis. Heterogeneous unselected plastic adherent HBMSCs seemed to exhibit lower basal levels of *SOX9* mRNA expression that did not serve to establish marked differences among subpopulations with the purpose of extracting chondroprogenitors. In the patients where these differences were large enough and over two log10 steps of fluorescence (e.g. F69 P1 in Figure 4.7 single donor assay), the data suggested that the nanoflares and the gating method applied were adequate by virtue of *SOX9* upregulation in highly positive subpopulations. For the expanded study to three patients in Figure 4.8, however, the gating that had been applied to that first patient was only covering very few cells at the highly positive end and that restricted the comparability of both assays in terms of gene expression when only the positive and the negative groups were sorted and analysed.

The use of nanoflares as an approach to detect mRNA in live cells still raises doubts within the divided scientific community. There are authors claiming that the appropriate incubation conditions and nanoflare structures need to be optimised to achieve a specific binding to target mRNA transcripts that translates into sensitive readings from the probes. In contrast, other authors argue that their reliability is questionable due to the lack of standardised protocols for their application and subsequent quantification and appraisal of the results.

Nanoflare technology is a promising tool that has potential to be developed to tackle the issues discussed above. In the current state of the approach, it may be beneficial to study the effect of microaggregates as a culture model under the hypothesis that *SOX9* may be upregulated and sensed by the *SOX9*-Cy5 nanoflare. This would require taking into consideration the technical difficulties that may arise from the handling of small aggregates after recovery from microdroplets and with dimensions that may challenge FACS nozzle diameter and may reduce throughput. In the previous chapter, it was concluded that HBMSC aggregates of 500 and 5000 cells might exhibit notably subtle heterogeneity differences between replicates and donors that confocal microscopy of immunohistochemically stained spheroid could not resolve. Droplet microfluidics combined with the integration of a nanoflare-based strategy to detect *SOX9* mRNA in live cells could be a strong candidate to isolate the chondroprogenitor SSC fraction of heterogeneous HBMSCs. Notwithstanding, the current technology and methodology available still needs further optimisation along with more substantial validation before that goal becomes attainable.

Chapter 5: Optimisation of microfluidic devices for droplet generation

5.1 Introduction

The previous chapters have discussed the issue of HBMSC heterogeneity in multicellular spheroids and the possibility of applying the state-of-the-art nanoflare technology to address that challenge. Nanoflares could not detect small differences in *SOX9* mRNA expression in conventional *in vitro* HBMSC cultures either as undifferentiated cell suspensions or chondrogenically stimulated in monolayer. As a consequence, the critical and unique aspect of this research project lies in the translation of *in vitro* chondrogenic differentiation to miniature environments generated via droplet microfluidics. An optimal droplet microfluidic platform enables a simple, rapid and high-throughput method to encapsulate cells that self-assemble into aggregates. Cell microaggregates in droplets could be a more representative model for chondrogenesis. This statement falls under the premise that there is a minimum cell number that provides cell-cell interactions and encourages *SOX9* expression. Droplet microfluidics offers the much needed high-throughput element to amplify the correct pairings for more definitive differentiation.

Prior and simultaneous to developing cell encapsulation in microdroplets, a variety of droplet microfluidic designs were created, tested and optimised. The process of optimisation involved characterising three critical aspects of the droplet populations generated: stability, size and polydispersity. As reviewed in section 1.7.2, droplet stability is mainly affected by the choice of continuous phase: oil and surfactant composition and concentration. For biological applications such as the one described in this project, fluorinated oils are generally preferred and a fixed variable due to their reported biocompatibility and gas permeability (Baret, 2012, Niu and deMello, 2012, Mazutis et al., 2013, Rosenfeld et al., 2014, Mashaghi et al., 2016). The concentration of the surfactant employed can be varied to ensure a compromise between stability understood as prevention of droplet coalescence in the device and cell biocompatibility.

Droplet size and polydispersity were a core object of study as a means to adjust starting cell densities for aggregate formation in the device. Such assessment accounted for the effect of several input parameters (Figure 5.1): liquid choice (or relative viscosity between continuous and aqueous phase), method of generation depending on the action of external forces (active or passive), channel geometry and flow rate (or relative flow rate ratio). For this particular droplet microfluidic system:

- *Liquid choice.* The aqueous phase was composed of cell culture medium containing chondrogenic growth factors (see section 2.3.4). Pursuing droplet stability involved a process of selection of an optimal combination of oil phase and surfactant. FC40 was the fluorinated oil for the continuous phase and the medium for the surfactants tested for optimisation: in-house Soton1 and Soton2; and the commercial Pico-Surf™ 1 (Sphere Fluidics, UK) formulation. All of them were dissolved at a 1.8% mass concentration to promote biocompatibility due to their Krytox®-based surfactant compositions (Holtze et al., 2008). A separate oil and surfactant combination, the Bio-Rad droplet generation oil for EvaGreen, is added to the set for benchmarking droplet stability. This commercial oil has a record of use in QX200™ Droplet Digital™ PCR systems in which droplet stability is essential (McDermott et al., 2013, Yan et al., 2018).
- *Method of generation*. Passive droplet generation dependent on the geometry of the channels is a constant throughout the experimental work.
- *Channel geometry*. Channel dimensions and geometry for droplet generation are variables analysed for their effect on the properties of the droplets (e.g dimensions, morphology) being generated. T-junction and flow-focussing designs were the two channel geometries implemented, varying the pinch junction dimensions and overall channel dimensions. 3D-printing and soft lithography techniques for PDMS chip fabrication with the desired channel geometry are described to compare chip performance and applicability as receptacles for large and small droplets, respectively. The advantages and drawbacks of each method will be discussed as well as the chip characterisation outcomes to define the best-performing devices for cell encapsulation and the surfactant-oil composition that minimises droplet coalescence.
- *Flow rate*. The effect of flow rate and the ratio of continuous to disperse phase is thoroughly quantified in relation to droplet size and polydispersity to select the conditions that produce stable droplet and desired encapsulation efficiency.

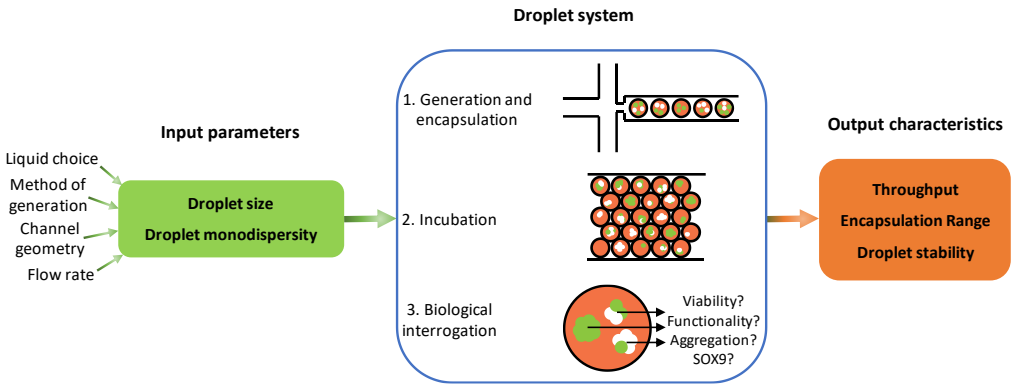

Figure 5.1 Overview of input parameters influencing droplet size and polydispersity, droplet system and output characteristics of the droplet-based assays in this work. Adapted from Rosenfeld et al. (2014).

Three basic steps can summarise the operation principle of the droplet microfluidic system:

1. *Generation and encapsulation*. The process starts with droplet formation and distribution of cells in suspension among them while the pumping system is running.
2. *Incubation*. Next, a stationary phenomenon that can be on-chip or off-chip is triggered consisting in compartmentalised development of individual cells inside the droplets and storage in a humidified atmosphere and normoxia.
3. *Biological interrogation*. Finally, the cells that have been incubated in droplets for a certain period of time are characterised to validate their suitability for cartilage tissue engineering at an early stage. The biological enquiry comprises cell viability, functionality, ability to aggregate and SOX9 expression in a droplet environment.

In this project, droplet size and polydispersity are mainly dependent on channel geometry and flow rates supplied using a syringe pump. Following droplet formation and flow stabilisation, droplet size and the standard deviation of the population confined within an incubation chamber can be measured using image analysis techniques (Basu, 2013). Image analysis produces quantitative data about droplet populations that is linked to throughput. It also shows directly the number of cells per droplet through various droplet frames (i.e encapsulation range). Lastly, it can identify droplet dimensions for droplet stability studies that can be finalised after generation and incubation. Ultimately, all the developmental alterations to the chip designs on the journey towards a final platform for cell encapsulation discussed in this chapter have been summarised in Figure 5.2. It highlights pathways for further characterisation of any existing relationships between cell densities and encapsulation efficiencies for both large and small droplets. Both 3D-printed and soft lithography chips in accordance to their fabrication parameters aim to map a broad tree of possibilities depending on the cell number required per droplet. In this context, coalescence and cell viability may become simutaneously deterred with increasing droplet dimensions and cell numbers. This entails a limited degree of polydispersity in order to potentially generate reproducible and similar-sized cell spheroids for standardisation of cell aggregation across the microfluidic device. Such goal is challenged by the Poisson distribution, which means that there is a probability of having a given number of cells encapsulated in droplets at a particular point and this is event is independent of any other previous or subsequent encapsulation. Altogether, the paramount criterion for an optimised chip design is the generation of stable droplets in the absence of droplet coalescence and exhibiting a controlled and monodisperse droplet size distribution.

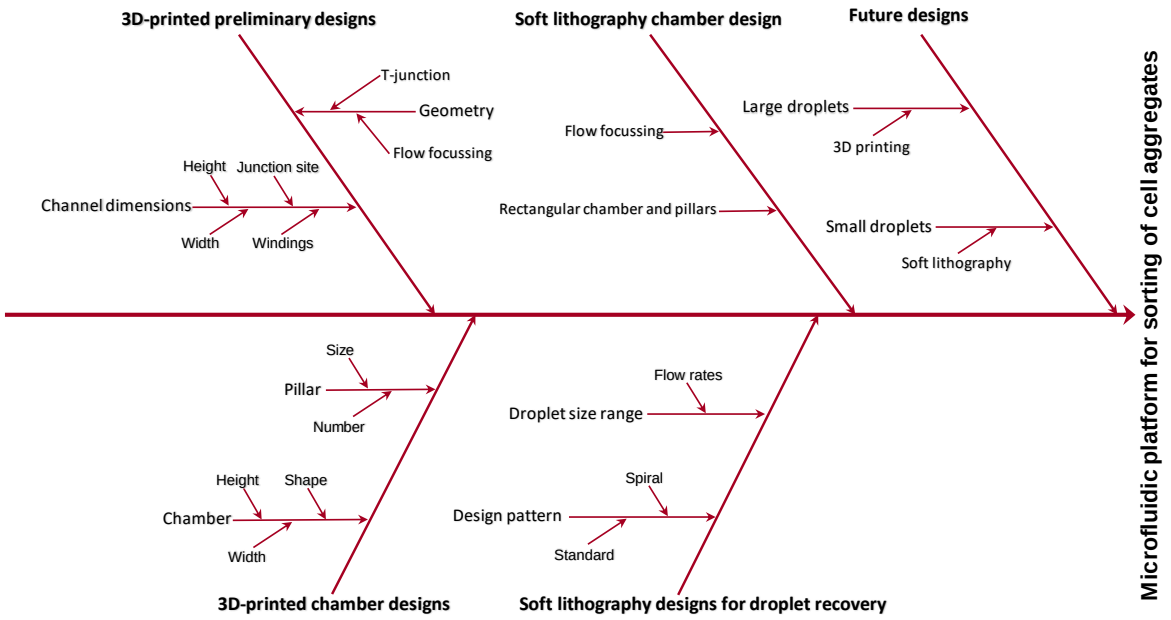

Figure 5.2 Schematic overview of the optimisation steps implemented and discussed throughout this chapter towards the fabrication of a microfluidic platform for sorting of cell aggregates.

5.1.1 Hypothesis

'Droplet microfluidics can provide stable droplet generation within sizes that are relevant for the formation and culture of cell aggregates within microdroplets'.

5.1.2 Aim

This chapter intends to bring together droplet features and generation parameters, outlining the most relevant combinations for the purpose of cell sorting using droplet microfluidics. The main objective is to establish the range of droplet sizes and monodispersity attainable for stable flow in microfluidic devices and encapsulation of cell aggregates in separate compartments as a function of flow rate. The variables delineating the sequence of experiments leading to device optimisation include fabrication method, channel geometry, channel dimensions and channel design.

5.2 Methods

5.2.1 Fabrication of 3D-printed moulds for microfluidic devices

5.2.1.1 Mould design and PDMS chip fabrication

PDMS chip moulds were designed using AutoCAD (AutoDesk) and Solidworks (Dassault Systemes) and printed in a 'VeroClear' material using an Objet500 Connex3 polyjet printer (Stanford Marsh Ltd, UK). The mould was dried overnight at 70°C to evaporate off any remnants from the printing process (e.g. solvents, unreacted monomer) before use.

PDMS silicone elastomer (SYLGARD® 184 BASE, DOWSIL™, Farnell OneCall, UK) was then evenly mixed with curing agent (SYLGARD® 184 silicone elastomer curing agent, DOWSIL™, Farnell Onecall, UK) at a 10:1 mass ratio. The mixture was degassed in a vacuum pump (VE115, Refworld, China) for 10 min with the valve open for 1 min. Once fully degassed, the PDMS and curing agent mixture was poured onto the mould in a Petri dish and degassed again for 20 min to ensure complete bubble removal. The PDMS mould was placed in an oven at 70°C for 1 to 1.5 h until the PDMS layer had cured enough to be peeled off without rupturing it. Simultaneously, the backing layer was prepared with mixture excess and heated for 15-30 min.

A series of 1 mm holes were punched for the inlets and outlets using a 1 mm Miltex biopsy punch (Medisave, UK), the chip was carefully dusted off and then placed on top of backing layer and left to cure overnight again at the same temperature. After checking that both parts were completely bonded together, Aquapel® (PPG Industries, USA) was introduced manually via the inlet/outlet holes into the chip channels to deposit a hydrophobic coating on the surface of the channel. Air was then blown through the punched holes to flush out any Aquapel® excess and the chip was placed on top of a hotplate at 85°C for at least 10 min until excess Aquapel® had evaporated. This hydrophobic coating allowed the oil continuous phase to preferentially wet the channel surface, which is essential for the device performance. Once completed, the chips were ready to be used in microfluidic experiments.

5.2.1.2 Droplet generation set-up and droplet size characterisation

The basic experimental set-up for droplet microfluidics (Figure 5.3) was comprised of a PDMS chip connected to 1 ml syringes containing the aqueous phase/s (e.g. red food dye, cell culture medium) and the oil phase (FC40, 3M, UK), respectively, through PVC tubings (inner diameter 0.5 mm, 0.5 mm wall, Gradko International Ltd., UK) attached to clear polypro hub precision needle tips (0.21 mm ID, 0.41 mm OD, Adhesive Dispensing Ltd, UK). The aqueous and oil phases were distributed in

separate syringe pumps (Harvard Apparatus PHD 2000, Instech Laboratories, Inc., USA; and KDS-100-CE, KD Scientific, USA; respectively) to adjust the incoming flow rates according to the target droplet size and generation rate. The FC40 oil was supplemented with an in-house biocompatible Krytox®-based tri-block PEPE-PEG-PFPE copolymer surfactant, Soton2, to stabilise the droplets and avoid merging (Holtze et al., 2008, Chen et al., 2011, Cho et al., 2013). Droplets were collected in a 25 ml polycarbonate universal via UT3 ultrathin PTFE tubing (0.3 mm ID, 0.10 mm wall, Adtech Polymer Engineering Ltd., UK). Every chip was routinely pre-washed with oil prior to aqueous penetration as a means to expose the channels to the intended continuous phase.

Two syringes were used for droplet generation. Red food dye for imaging purposes was fitted onto in the Harvard PHD 2000 syringe pump filling two different syringes, whereas the FC40 oil with 1.8% Soton2 (w/w) surfactant was loaded onto the KDS-100-CE pump. A DCC1240M CMOS camera (Thorlabs, USA) was attached to a stereo microscope (SZM CTV ½ 0.5X WD165, AM Scope, USA) and videos of the longitudinal section of outlet tubing or the chip channels were recorded and analysed using Droplet Morphometry and Velocimetry (DMV) in MATLAB.

Figure 5.3 Experimental set-up for PDMS chip testing consisting of microscope, chip and tubing, collecting tube, syringes and syringe pumps.

5.2.2 Fabrication of soft lithography moulds for microfluidic devices

As an alternative higher precision approach to design microfluidic devices, soft lithography is a microfabrication technique that produces microstructures employing a patterned SU-8 photoresist with resolutions at the micrometre scale and below on a silicon wafer (Xia and Whitesides, 1998). The mask was designed using a CAD software (e.g. AutoDesk AutoCAD) to transfer the intended pattern to the epoxy-based SU-8 photoresist. To fabricate the master, SU-8 is spin-coated onto a silicon wafer (previously cleaned by rinsing with methanol and prebaking for 10 min at 210°C), avoiding disruptive bubbles that may get trapped in the photoresist. The spin-coating cycle is applied by gradually elevating rotational speeds from 300 rpm to 3000 rpm until a flat layer of

photoresist is created. The spin-coated wafer is then prebaked at 65°C on a hot plate for 1 min and baked at 95°C for 3 min ensuring that all air bubbles have been removed. After cooling down at room temperature, the wafer is irradiated with UV light to crosslink the pattern on the photoresist, with exposure times and energies that vary according to desired channel dimensions. Next, the prebaking and baking step is repeated and the non-exposed photoresist removed by submerging it in propylene glycol monomethyl ether acetate (PGMEA) and shaking gently on an orbital shaker for 4 min for a uniform result. Finally, the liquid excess is left to drain, the wafer is rinsed with isopropanol and dried with nitrogen. PDMS chips can be made via the standard fabrication procedure detailed in section 5.2.1.1 on the wafer moulds stored in a Petri dish (Holtze et al., 2008, Niu et al., 2011, Wu et al., 2011, Mazutis et al., 2013).

5.2.2.1 Microfluidic chip preparation

Two different designs manufactured using soft lithography on a silicon wafer whose mask was ordered from JD-Photo-Tools (UK) were utilised and characterised for the purpose of cell encapsulation in droplets: a *standard* 125x100 µm device and a *spiral* 150x100 µm device (Figure 5.4). The spiral geometry design was driven by secondary flows in curved microchannels that can exert drag forces on cells leading to Dean entrainment. These forces can bring particles to an equilibrium position along the flow streamline. Thus, a periodic spacing can be created for reducing droplet content variations by controlling the radius of curvature of the channels and the flow velocity (Dean, 1927, Ookawara et al., 2004, Bhagat et al., 2010).

5.2.2.1.1 Device cloning from SU-8 silicon wafer designs using castable polyurethane foam

PDMS silicone elastomer and curing agent were thoroughly mixed at the usual 10:1 mass ratio inside a plastic cup using a Pasteur pipette. The mixture was placed in the degassing chamber coupled with a pump to release vacuum until it became fully depleted of bubbles.

Frames of appropriate dimensions were selected to clone the desired structures on the wafer lying on top of a hotplate set at 80°C. The PDMS mixture was poured into the frame area while ensuring the absence of leakages that may prevent the entire frame volume from being preserved, and refilling when necessary. Once PDMS had become firmer after about 30 min to 1h and cured throughout, the frame containing the PDMS pattern was incubated for at least 1 h off the hotplate to cool down.

The frame was carefully removed using a scalpel and the resulting PDMS chip was dusted off on both sides of using 3M adhesive tape. The chip was then placed on top of double-sided red adhesive tape to stick it onto the bottom of a silicone mould for polyurethane curing and degassed in the mould for 2 min. Simultaneously, the Part A and Part B Smooth-Cast® 310 (Smooth-On, Inc, USA)

polyurethane solutions were shaken vigourously to ensure homegeneous distribution of components. Both parts were mixed at a 1:1 ratio and vigorously shaken again for 1 min to achieve a homogeneous solution that was made to cover the mould. Next, the mould was degassed for bubble depletion. The polyurethane foam was left to cure for at least 3 h on the bench.

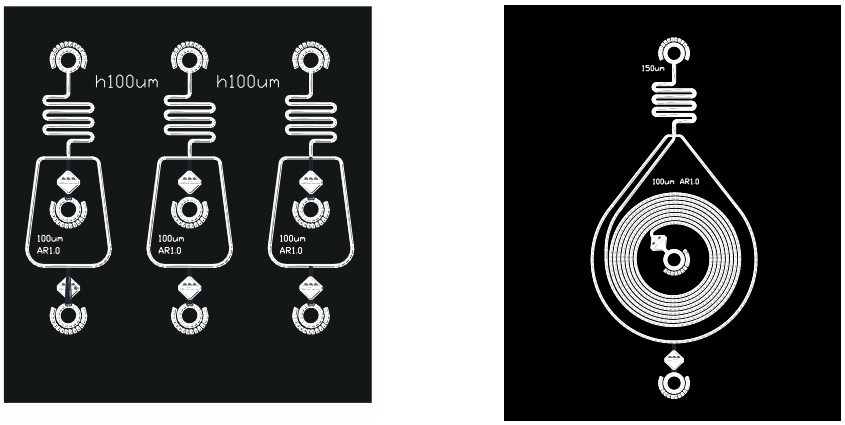

Figure 5.4 Chip designs fabricated for high-throughput droplet generation and characterisation: *standard* (left) and *spiral* (right).

5.2.2.1.2 Chip fabrication from polyurethane moulds, silanisation and bonding to glass slide

The polyurethane block was extracted from the silicone moulds and the required volume of PDMS mixture was prepared as previously described for device cloning. The degassed polyurethane mould was filled with the PDMS mixture up to approximately 90% of the maximum volume and moved to the oven at 60°C for about 1h 30 min. The polyurethane mould was left to cool down in the fridge overnight to ensure fully hardened in advance of removing the PDMS. The PDMS chip was detached from the mould using a fine spatula and sliding it around the edges taking care not to break the chip and avoiding mechanical contact with the microfluidic structures on the reusable polyurethane mould. Adhesive tape was applied to dust off both sides of the chip and holes were introduced for the inlets and outlets of the chip on a Petri dish using a 1 mm disposable biopsy punch (Williams Medical Supplies, UK).

In order to bond the PDMS chip to a glass slide, a 30 s plasma treatment was carried out in a Femto plasma cleaner (Diener Asher, Germany), followed by a brief 5 min incubation in the oven at 60°C prior to silanisation. Silanisation was employed to improve the affinity of immediately post-plasma hydrophilic PDMS channel walls to the oil and surfactant carrier oil by rendering them oleophilic. A 1% Trichloro (1H, 1H, 2H, 2H-perfluorooctyl) silane (Sigma-Aldrich, UK) (v/v) solution in hydrofluoroether (HFE) oil (3M, Belgium NV) was prepared for silanisation (e.g. 10 µl in 1 ml). Using a 10/20 µl pipette, sufficient volume of the solution was flushed into the outlet of the chip to wet

all the channels entirely. Lastly, the chip was allowed to complete bonding by leaving it inside a Petri dish and in the oven at 60°C overnight.

5.2.2.2 Characterisation of soft lithography chips

5.2.2.2.1 Droplet generation set-up

The microfluidic set-up consisted of the PDMS chip connected to a 2.5 ml syringe injecting cell culture medium (DMEM + 1% P/S (v/v) + 1X ITS) and a 5 ml syringe containing QX200™ droplet generation oil for EvaGreen (Bio-Rad, UK) through two 25G Terumo needles fitted tightly into fine bore polyethylene tubing connections (Smiths Medical, OD = 1.09 mm, ID = 0.38 mm) using a 6" forceps (Figure 5.5). Both syringes were mounted on two Fusion 400 syringe pumps (Chemyx, United States). Serum-free cell culture media were employed to prevent any interference with the surfactant that could compromise droplet stability. A collection 1.5 ml Eppendorf was attached to the chip outlets via tubing. A CKX53 Olympus microscope was coupled with a Phantom Miro eX2 (USA) high-speed camera to capture videos via the Phantom Camera Control (PCC) software. Flow rates for both phases were varied in each video to study droplet size after processing in MATLAB DMV. The range of sizes obtained were plotted separately and then compared altogether.

Figure 5.5 Experimental set-up for droplet generation and characterisation of soft lithography chips. Two syringe pumps inject the carrier phase consisting of oil and surfactant and the aqueous phase (i.e. cell suspension), respectively. Cell aggregation in the latter is prevented by continuous stirring of the cell suspension through stir discs that are powered by a magnetic tumble stirrer. The microfluidic device is fitted to the microscope stage using a holder and is connected to the syringes and the collection tube via tubings. Live videos are captured during droplet generation by the high speed camera.

5.2.2.2.2 Particle encapsulation in microdroplets

Microparticles based on polystyrene (Sigma-Aldrich, UK) were used as controls to test the number of cells expected in droplets of different sizes. Their diameter, 10 µm, was selected because the cells to be used were expected to be of a similar scale. The experiment assessed the difference in behaviour between simple and spiral designs as well as the effect of the particle density being injected.

To estimate the dilutions required for these 10 µm particles, the particle number in a suspension made up of theoretically 100% particle stock would be:

$$N_{particles} = \frac{V_{stock\ suspension}}{V_{particle}} \tag{5.1}$$

where $N_{particles}$ is the number of particles in the stock suspension, $V_{stock\ suspension}$ is the volume extracted from the stock suspension and $V_{particle}$ is the volume of each individual particle. The latter, when calculated for 10 µm particles assuming particle sphericity resulted in approximately 0.5 pl. The number of particles estimated through the above equation was multiplied by a factor of 0.02 to account for the actual 2% solid fraction in the stock suspension and the suspension was diluted in deionised water according to the required final particle density (i.e. particles/ml).

Two 5 ml syringes were filled with the aqueous particle suspension and QX200™ droplet generation oil (Bio-Rad, UK), respectively. 25G Terumo needles were fitted tightly into fine bore polyethylene tubing connections (Smiths Medical, OD = 1.09 mm, ID = 0.38 mm) using a 6” forceps. The particles were kept constantly stirring with small magnetic stir discs (PTFE encapsulated Samarium Cobalt, 5 mm diameter, 4 mm thick, V&P Scientific, Inc., USA) subjected by an electromagnetic field stemming from a Magnetic Tumble Stirrer™ (VP 710 Series, V&P Scientific, Inc., USA) to maintain suspension homogeneity. The aqueous phase was pumped at 25 µl/min and the oil phase was supplied at three different flow rates: 25, 50 and 250 µl/min to vary the droplet size generated.

5.2.3 DMV analysis

The microfluidic videos were processed to quantify average droplet size and polydispersity. Droplet size was quantified via the mean equivalent diameter variable in the software, which averaged out droplet dimensions by measuring the mean area of each droplet and correlating it to the diameter of a sphere of equivalent area. The output of the video processing was a histogram with droplet size distributions and a count of the number of droplets for each size shown. Polydispersity was evaluated based on the standard deviation calculated in the size analysis and an estimation given

of the droplet generation stability considering the characteristics of the syringe pump-powered set-up (Basu, 2013).

The mean equivalent diameter of the droplets, $\bar{x}$, and the standard deviation of the population analysed, σ, were the main parameters resulting from image analysis and their ratio was used to calculate the polydispersity index (PDI) as:

$$PDI = \frac{\sigma}{\bar{x}} \tag{5.2}$$

DMV analysis then presented polydispersity data through another variable derived from PDI and called coefficient of variation. This coefficient was computed as $CV(\%) = PDI \times 100$; and it was the conventional term to refer to polydispersity in droplet size distributions employed throughout this chapter. Acceptable values indicating homogeneity were considered for CV < 5% (Liu et al., 2020).

5.2.4 Surfactant stability tests

Surfactant stability is a critical requirement that the microfluidic platform needs to meet to a high extent to succeed during the droplet incubation stage. For that purpose, a preliminary surface tension tensiometer test was first carried out to exclude any merging phenomena derived from a degraded surfactant as well as to test how surfactant efficiency compared among in-house non-ionic Krytox®-based triblock co-polymer Soton1 and Soton2, and commercial Pico-Surf™ 1 (Sphere Fluidics, UK) compositions at a 1.8% (w/w) concentration. Soton1 and Soton2 belonged to different batches of the same surfactant. Soton1 contained some residual unreacted Krytox® groups in addition to the surfactant, whereas Soton2 was an improved version that was only composed of surfactant.

The tensiometer device consisted of a capillary tube that was fitted into a cuvette filled with water and supplied with the oil and surfactant solution of interest infused at 2 µl/min through a clear polypro hub precision needle tip (see section 5.2.1.2). The tip was attached to a 1 ml syringe fitted onto a KDS-100-CE syringe pump and connected to the device via PVC tubings (0.5 mm inner and outer diameter).

The surface tension was assessed by recording oil droplet generation inside the water reservoir using a Digimicro Mobile Portable USB Digital Microscope Camera (dnt, Germany). Afterwards, the width (i.e. diameter w in Figure 5.10, top) of the droplet in the frame was measured before break-off using ImageJ analysis. The value obtained was treated as an arbitrary width, indicating relative surface tension among the different surfactants at the oil-water interface. Greater droplet widths were equivalent to lower surface tensions and inferior surfactant-like performance. Ordinary One-

way ANOVA statistical analysis in GraphPad Prism software was selected establishing significance for $p \leq 0.05$ on droplets from each surfactant (n = 3) and the control surfactant-free FC40 oil (n = 4).

A second functional stability assay was later designed based on the results of the former tensiometer test to evaluate the benefit of replacing the in-house FC40-Soton2 oil and surfactant formulation (and, by extension, Pico-Surf™ 1) by the Bio-Rad QX200™ droplet generation oil for EvaGreen. Droplets were generated at two different flow rate ratios: 25:25 and 25:125 µl/min (aqueous to oil phase) on a microfluidic chip with the standard soft lithography design in Figure 5.3. For the sake of consistency with the ultimate application for cell encapsulation, chondrogenic differentiation medium (see section 2.3.4) was the aqueous phase in this study. Droplets were collected and stored in 2 ml Eppendorf tubes and incubated in a humidified atmosphere at 37°C, 20% O_2 and 5% CO_2.

The stability assay consisted in pipetting a volume of 20-30 µl of the droplet suspension in oil into a Fast-Read 102® (Biosigma, Germany) haemocytometer and imaging droplet arrays under the Carl Zeiss AxioVert 200 inverted microscope over four weeks of incubation. ImageJ analysis was then run to measure droplet diameters and the distributions were plotted to compare droplet dimensions from day 0 to day 28 (chosen as an end point that relates to the duration of *in vitro* chondrogenic differentiation of spheroids). Soton2 and QX200™ were finally compared for the two flow rate values through the droplet diameters measured and the standard deviations in each distribution. Standard deviation was an indicator of higher droplet stability in those distributions presenting the smallest values (i.e. error bars in the plots).

5.3 Results

5.3.1 Microdroplet generation in a 3D-printed culture chamber design

Flow-focussing and T-junction are the most common channel geometries for droplet generation. The primary objective for microfluidic development was therefore to compare the performance of microfluidic devices fabricated with both channel geometries through droplet population parameters: size, monodispersity and stability.

The preliminary 3D-printed flow-focussing device presented a functional drawback at that stage: the oil phase came in contact with the aqueous phase mixture unilaterally due to slight asymmetry derived from printing accuracy limitations at 100 µm. T-junction geometries only requiring a single stream to pinch droplets off the dispersed phase were applied to later stages given their similar resulting sizes and polydispersity stemming from a simple design consisting on three winding segments between the junction site and the outlet (Figure 5.6).

Initial tests were subsequently conducted to optimise a chip design for cell culture in microdroplets within a compartmentalised chamber consisting of evenly distributed pillars. The main function of the pillars was to prevent the top and the bottom parts of the chamber from collapsing. Droplets generated at the T-junction site were accumulated inside the chamber for imaging contemplating prospective prolonged culture of cells at a predefined cell density to form aggregates in microdroplets.

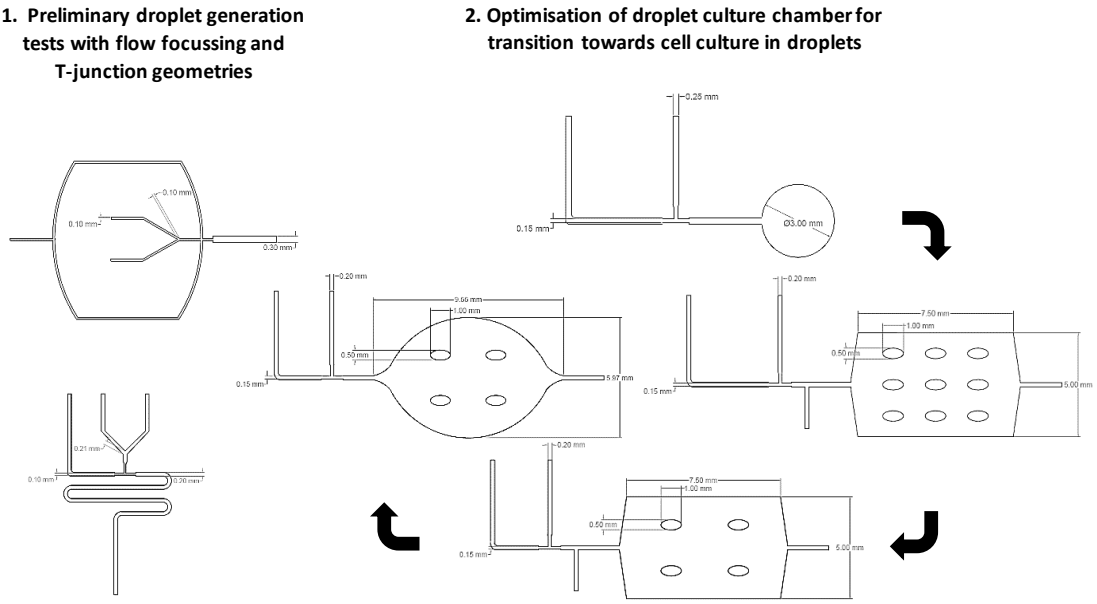

Figure 5.6 Overview of the design optimisation stages leading to microdroplet accumulation in a culture chamber. The first stage on the left refers to preliminary droplet characterisation (size, polydispersity) in flow-focussing (top) and T-junction geometries (bottom). Alongside, the second stage is comprised of four designs portraying changes in culture chamber including enlargement, the addition of pillars and edge smoothening.

The dimensions of the chamber were 7.50×5.00 mm^2 with a height of 200 µm, keeping a 150×150 $µm^2$ junction site. Droplet generation in a chamber with nine 0.50×1.00 mm^2 elliptical pillars filled 1.8% Soton2 (w/w) surfactant in FC40 oil was characterised by an intense droplet merging near the walls of the chamber and around the pillars along with a few polydisperse droplets between them when flow was active. Increasing concentration of surfactant from 1.8% to 3% (w/w) lessened the degree of merging but failed to sufficiently stabilise droplets (Figure 5.7A).

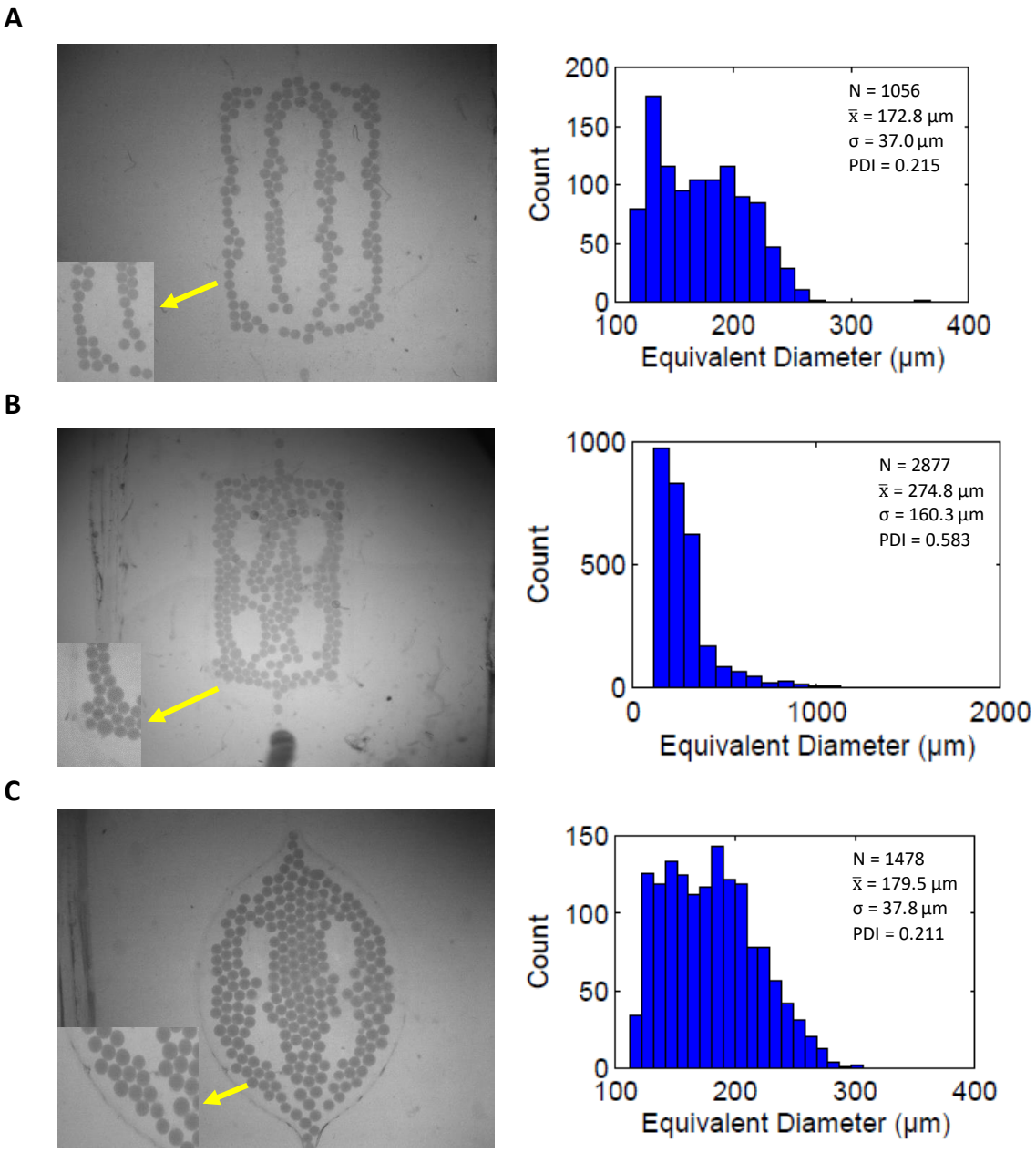

Figure 5.7 Microdroplets produced during active flow using 3D-printed chips with chamber designs: (A) 9-pillar chamber with 150×150 $µm^2$ channels at the T-junction ; (B) 4-pillar chamber with 200×200 $µm^2$ channels at the T-junction;(C) 4-pillar round chamber with 150×150 $µm^2$ channels at the T-junction. Equivalent diameter, droplet count and standard deviation are depicted in DMV generated graphs (right). The flow rates employed were 18 µl/min FC40 oil supplemented with 3% Soton2 surfactant (w/w) and red food dye aqueous phase pumped at 6 µl/min.

Taking into consideration possible pillar oversizing upon printing that could constrain droplets by leaving a smaller space among them than the droplet size, the pillar distribution was altered to contain four more sparsely spaced pillars. The new chamber diminished droplet merging issue during activated flow but remained incapable of preventing droplet merging after flow cut-off (Figure 5.7B). Later design modifications devised involved relieving the straight angles at the walls of the chamber, smoothening the shape into a round container seeking to minimise stagnant areas around the corners and amplifying the height of the chamber (bottom left). This might have imposed additional physical constraints as shown in the histogram in (Figure 5.7B), where droplet size indeed exceeded 200 µm with the 4-pillar rectangular chamberand the higher round chamber had no beneficial effect (Figure 5.7C).

5.3.1.1 Effect of flow rate ratio on droplet size in 3D-printed designs

As an alternative solution for preventing droplet merging observed in enclosed chambers, later designs listed below revolved around the principle of adding multiple windings to hold separate droplets away from each other through oil filling the space between them. In addition, this pattern allowed to reduce the surfactant concentration for the carrier oil and return to the more cell-compatible initial 1.8% (w/w) surfactant concentration in FC40 oil.

The T-junction dimensions employed were:

- 100×100 µm^2 T-junction site with 200×200 µm2 channels (*TJ100*)
- 150×150 µm^2 T-junction site with 250×250 µm2 channels (*TJ150*)
- 200×200 µm^2 T-junction site with 300×300 µm^2 channels (*TJ200*)
- 250×250 µm^2 T-junction site with 350×350 µm^2 channels (*TJ250*)
- 300×300 µm^2 T-junction site with 400×400 µm^2 channels (*TJ300*)

The fabrication conditions consisted of a curing time of 75-90 min for the engraved top layer (10 g elastomer + 1 g curing agent) and 22-25 min for the backing layer (11.0 g elastomer + 1.1 g curing agent) at 65°C for the complete set of chips. Any variations in curing times were due to occasional minor temperature oscillations in the oven (i.e. in the range from 65°C to 70°C).

During chip operation, droplet sizes were altered by fixing the aqueous flow rate at 2 µl/min and sequentially lowering the FC40 oil containing 1.8% Soton2 (w/w) surfactant from 20 µl/min to 2 µl/min (equivalent to flow rate ratio from 10 to 1). Videos were taken after at least 5 min stabilisation for each of the flow rate set values.

The TJ100 chip design failed to reproduce standard one-by-one droplet generation (Figure 5.8A-E) single droplets for high flow rates were only maintained for a few seconds. Otherwise, droplets were pinched off in groups (trains) until an individual large droplet formed once the oil flow rate matched the aqueous phase (lowest flow rate ratio of 1). A closer inspection of the chips from the same batch revealed apparent disruption by PDMS invasion into the channels prior to chip bonding and a deformed T-junction site channel pattern derived from printing accuracy limit reached for those dimensions.

The results of DMV analysis for the rest of T-junction chips (*TJ150-TJ300*) exposed the most drastic size reduction occurred for the devices with the largest channel and junction site dimension between flow rate ratio of 1 and 3.75 (Figure 5.9). For the smaller dimensions, the droplet was smaller and from 3.75 flow rate ratio and upwards the decrease was not very noticeable, reaching a plateau-like condition from there that was most evident for the smallest design. *TJ250* produced the largest droplets at a flow rate ratio of 1, which could be associated with slight flow instability in those conditions as compared to *TJ300*.

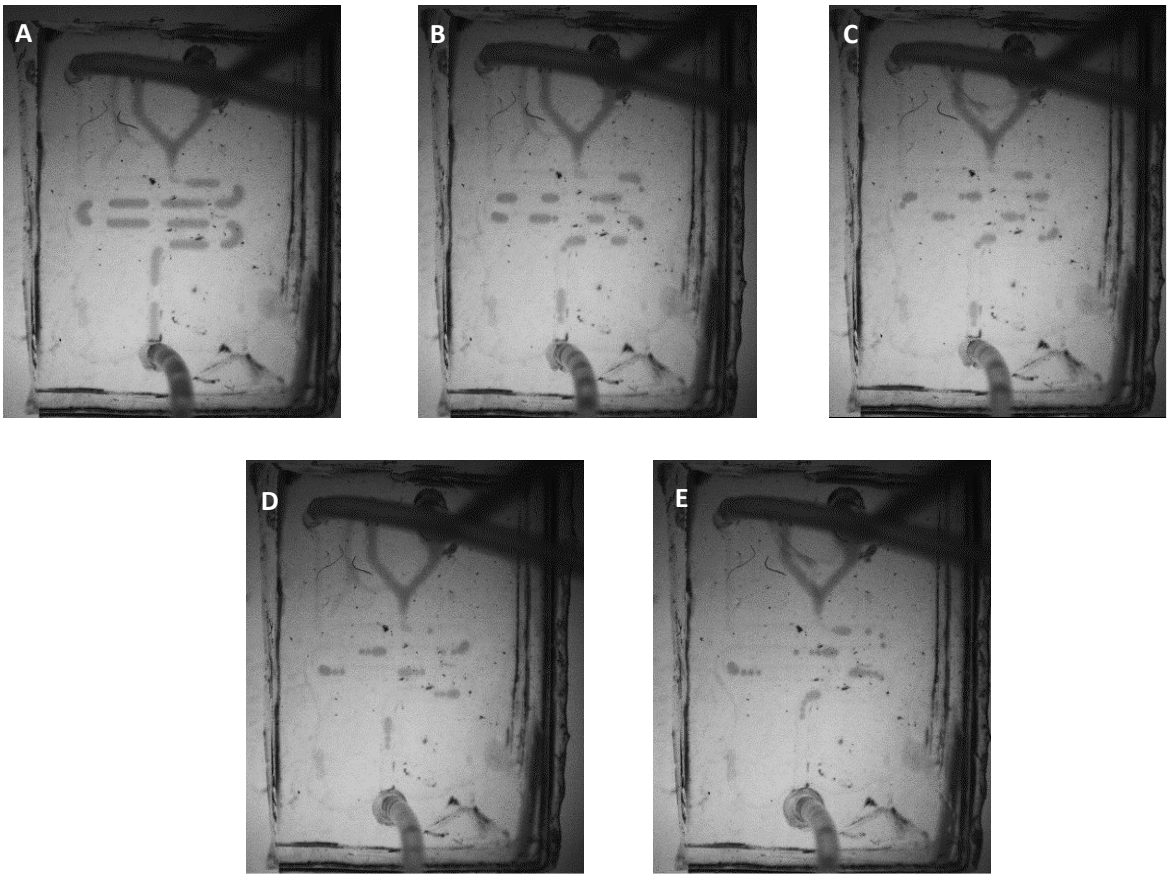

Figure 5.8 Microdroplets produced during active flow in 100x100 µm^2 T-junction PDMS chip with 200x200 µm^2 channels: (A) Flow rate ratio (oil to aqueous, µl/min) of 1(2:2), (B) Flow rate ratio of 2.5 (5:2), (C) Flow rate ratio of 3.75 (7.5:2), (D) Flow rate ratio of 5 (10:2), (E) Flow rate ratio of 10 (20:2). The sequence of images at increasing flow rate ratios display a transition from a single plug-shaped droplet for the lowest ratio in (A) to segmented droplets from (B) to (E) indicating droplet generation instability.

A similar trend was detected for the smaller functional T-junction dimensions, *TJ150 and TJ200,* both undergoing gradual size reduction that was more marked from 1 to 2.5 flow rate ratios and sharp standard deviation decrease for higher flow rate ratios: 3.75 to 10. Size oscillated between 144 and 314 µm for *TJ150*. Considering 250 µm wide and high channels and the respective droplet generation videos, flow rate ratios of 5 and 10 were the only values that completely neglected shear stresses against channel walls and would therefore yield droplets that did not stay static or attached to channel walls. For *TJ200* chips producing sizes from 214 to 368 µm, spherical-like droplets also resulted for the 3.75 flow rate ratio.

The larger dimensions, *TJ250* and *TJ300*, were characterised by an extensive size variability (approximately three-fold as compared to their smaller equivalent designs): mean equivalent diameters of 373 to 1080 µm and 437 to 925 µm, respectively. The mean diameter estimated for an oil to aqueous flow rate ratio of 1 was higher in the smaller *TJ250* chip, which may respond to unstable flow at low ratio values (i.e. lower reliability on quantification in slow droplet generation regime). More monodisperse droplets were predominant at high flow rate ratios, as opposed to *TJ300* slight variations. In those conditions, droplets did not see channel wall movement constrictions, which may affect droplet size and shape at initial and subsequent sections of the chip at equivalent diameter level. Moreover, small standard deviations at small flow rate ratios might be partly ascribed to the low number of droplets analysed (Figure 5.9, bottom).

Two-way ANOVA statistical analysis with Tukey's multiple comparisons ($p \leq 0.05$ confidence level) between means from different TJ dimensions and same flow rate ratio and means from different flow rate ratios for any given TJ dimension revealed significant size changes arising from modifying flow rate ratios for all chip designs except *TJ200* flow rate ratios of 3.75 and 5.

The DMV histograms also included the mean equivalent volume computed in relation to the mean equivalent diameter from DMV analysis as

$$\bar{V} = \frac{4}{3}\pi \bar{R}_{eq}^3 \tag{5.3}$$

where $\bar{R}_{eq}$ is the mean equivalent radius defined as the half of the mean equivalent droplet diameter. The data showed a very wide range of droplet volumes; from the appropriate nanolitre scale volumes generated with the TJ150 design to excessively large volumes in the microlitre scale which were not suitable for a high-throughput microfluidic approach.

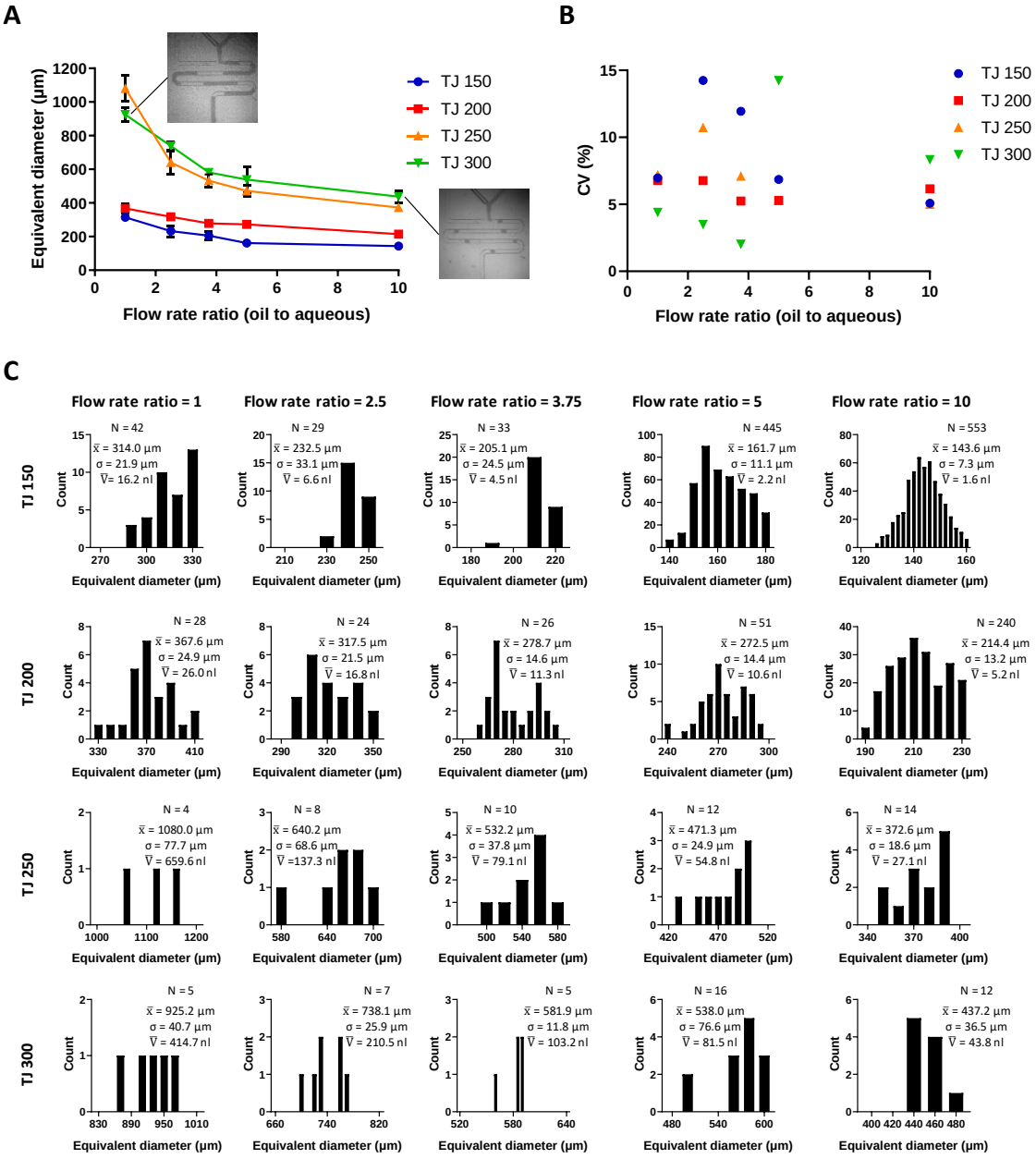

Figure 5.9 Effect of flow rate ratio on the mean diameter of droplets and coefficients of variation for each condition in T-junction 3D-printed chips *TJ150*, *TJ200*, *TJ250* and *TJ300*: (A) Summary of the equivalent droplet diameters measured by DMV analysis for each chip design as a function of flow rate ratio. An example of the droplet shape alteration as the flow rate ratio rises from 1 to 10 is shown through snapshot at minimum and maximum tested ratios. It illustrates how droplets have a heavily elongated morphology at a flow rate ratio of 1 and more spherical-like morphology as flow rate ratio was elevated reaching a value of 10; (B) Coefficient of variation of the droplets measured by DMV analysis for each chip design as a function of flow rate ratio; (C) Droplet size distributions for each flow rate ratio and chip design The scaling of the DMV plots includes the entire range of droplets sizes that were within ± 10% of the mean diameter.

5.3.2 Effect of surfactant formulation on surfactant performance

Given the previous merging issues in 3D-printed designs, surfactant formulations were screened as a criterion for selection of an appropriate oil and surfactant system to ensure droplet stability for prospective short periods of incubation needed for cells to aggregate in microdroplets.

ImageJ analysis on the arbitrary droplet widths measured during the surface tension tensiometer test found that all the surfactant compositions differed significantly from the control surfactant-free FC40 oil. However, there was no significant droplet width increase between Soton1 and Soton2 or between Soton2 and Pico-Surf™ 1, and only a slight improvement from using Soton1 with respect to Soton2 (Figure 5.10, bottom).

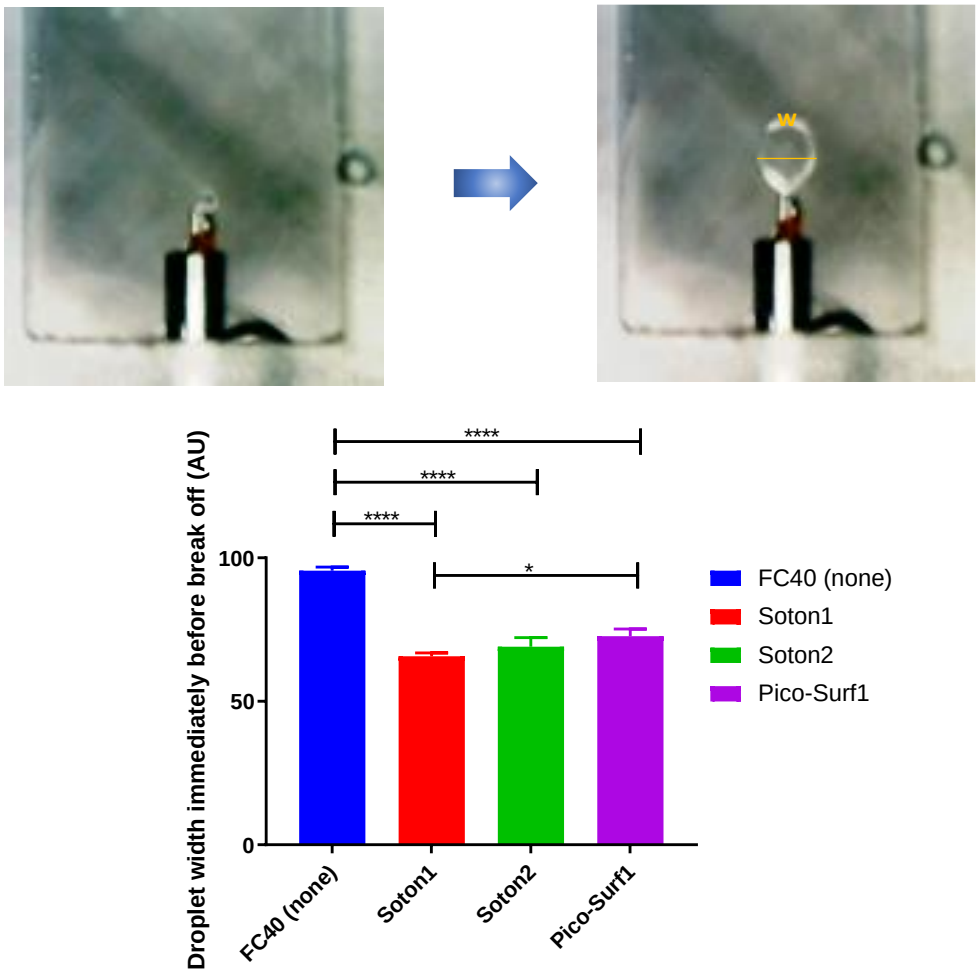

Figure 5.10 Tensiometer test to estimate surface tension and surfactant performance in a semi-quantitative manner. Droplet size at the beginning of the injection is depicted in the top right image, with the final droplet before break-off width highlighted across the droplet and labelled as w in the top right image. The arbitrary droplet width values and the statistical significance analysis are displayed in the bar chart below. Statistical significance symbols depicted respect GraphPad Prism convention: * ($p \leq 0.05$), **** ($p \leq 0.0001$). The absence of symbols between groups indicates no significance. The statistical analysis was performed using Ordinary One-way ANOVA on GraphPad Prism 8.2.1.

These results endorsed the use of more biocompatible Soton2 and Pico-Surf™ 1 surfactants and rejected any major effect from storage-derived surfactant degradation on droplet merging in culture chambers. Soton2 became the preferred surfactant out of the two because it was manufactured in-house, cost-effective and it could be made fresh by mixing the oil and the surfactant. Pico-Surf-™ 1, in contrast, had a shorter shelf-life and was only readily available in a small volume format.

Soton 2 was next screened against commercial Bio-Rad QX200™ droplet generation oil to trial its functional performance in a relevant incubation setting. The considerations for this new assay were that it had to imitate conventional cell culture conditions and to be applicable for cell and spheroid storage in droplets.

Representative examples of droplets inside Fast-Read 102® haemocytometer chambers from day 0 to day 28 for two flow rate values are illustrated in Figure 5.11A and B, respectively. Image J estimations on droplet diameters for both surfactants identified droplet distributions with comparable sizes for both surfactants regardless of the pumping flow rates (Figure 5.11C-E).

On closer inspection, there appeared a few statistical differences that are highlighted in the plots. For instance, Figure 5.11C shows a day 7 droplet distribution for FC40 Soton 2 25x25 that has a significantly smaller size than control day 0 droplets. In this case, some bigger droplets that were present in the images were not captured by the software because they were located at the edges. The other surfactant, QX200™ 25x25, presents a trend of gradual yet controlled increase in droplet size over time. That increase is linked to the expected small contribution of droplet coalescence in a metastable system.

Figure 5.11D again depicts wider error bars for Soton2 across all incubation times than QX200™ for 25x125 flow rates. The latter, however displayed a significantly lower droplet size diameter on day 28 that may be attributed to droplet break-up originated from the emulsion metastability prevalence over coalescence. The most decisive conclusions stem from Figure 5.11E, where the final droplet diameters on day 28 for all the conditions and the standard deviations of their droplet distributions are summarised. Variances and their graphical representation in the form of error bars with standard deviations are the indicators of interest for droplet stability in this assay.

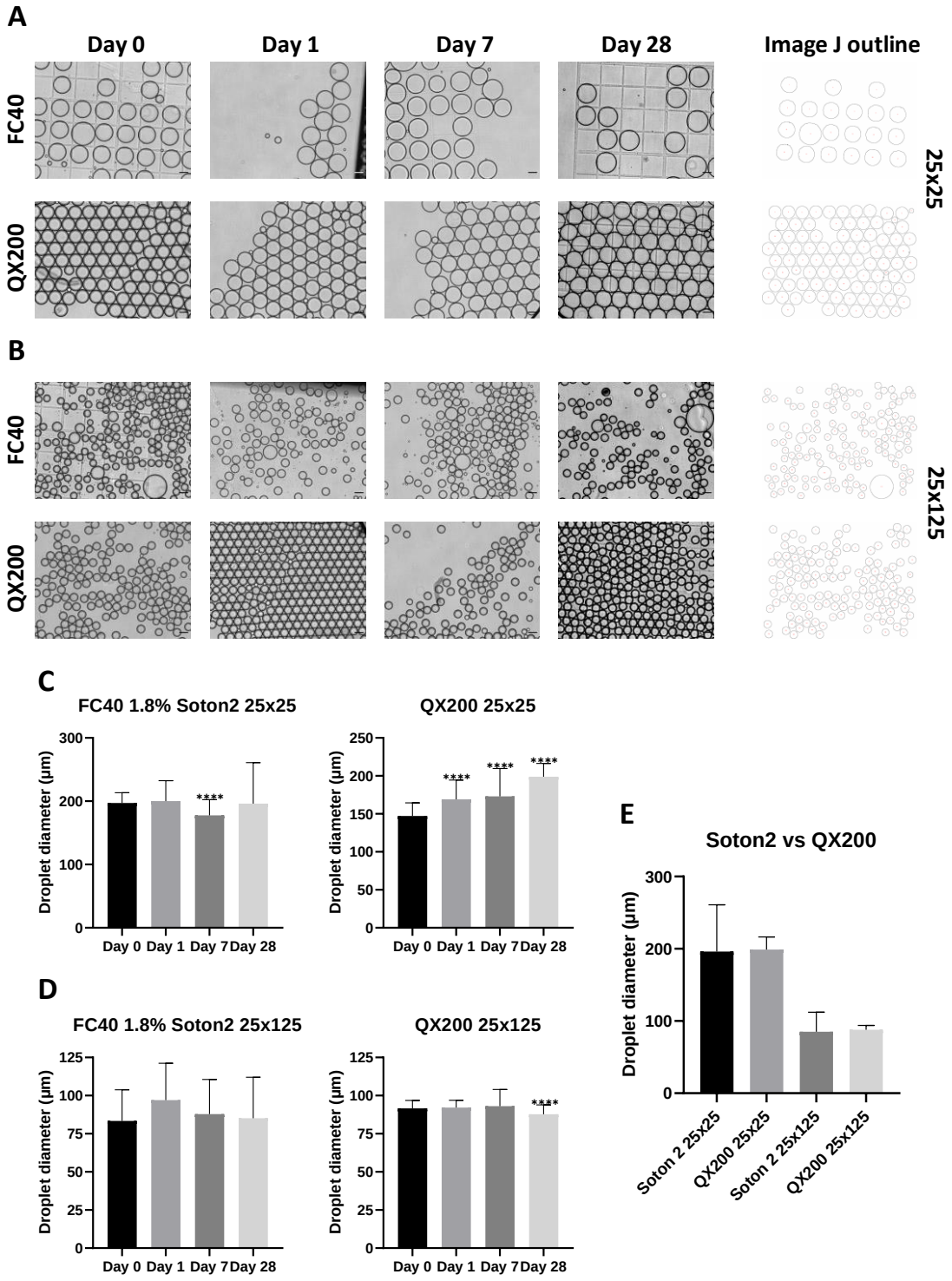

Figure 5.11 Droplet stability assay performed on FC40 oil supplemented with 1.8% (w/w) in-house Soton2 surfactant and QX200™ droplet generation oil: (A) Droplet arrays for both oil and surfactant combinations and flow rates of 25 µl/min for chondrogenic differentiation medium and for the oil phase from day 0 to day 28 along with a sample ImageJ outline demonstrating droplet measurement after thresholding; (B) Analogous experiment to (A) with smaller droplets generated at 25 µl/min for the same aqueous phase and 125 µl/min for the oil phase; (C) Summary of droplet diameters over time for the conditions detailed in (A); (D) Summary of droplet diameters over time for the conditions detailed in (B); (E) Global droplet diameters for the two surfactant and oil formulations and flow rate ratios. The statistical analysis was performed using Brown-Forsythe and Welch's One-way ANOVA on GraphPad Prism 8.2.1. The significance shown on the plots refers to **** ($p \leq 0.0001$) with respect to control day 0 droplets. Bars show mean values and SDs. Scale bar = 100 µm.

Droplet measurements were affected by how the images were taken and how the ImageJ software treated edges (e.g. at different focal planes), which were inevitable because droplet imaging took place on different days and due to the manual character of sample pipetting inside a haemocytometer that was subject to reasonable variability itself. All in all, the Brown-Forsythe and Welch's One-way ANOVA statistical analysis on the results capture in Figure 5.11E detected highly significant difference ($p \leq 0.0001$) between the variances of Soton 2 and QX200™. These findings demonstrated that QX200™ provided superior performance regarding droplet stability over long periods of culture up to 28 days that were better suited to a cell encapsulation platform. Therefore, subsequent studies included the QX200™ oil and surfactant formulation.

5.3.3 Soft lithography flow flow-focussing *standard* and *spiral* designs

Following the finding that QX200™ exhibited the best surfactant performance for droplet stability, two soft lithography chip designs were characterised for the purpose of microfluidic device optimisation towards cell encapsulation and stable aggregate formation. This was a subsequent step to the failed attempt to generate stable and monodisperse droplets inside a chamber using a soft lithography chip (see Appendix C). For these experiments, the chip fabrication protocol was altered. The two soft lithography chips termed *standard* and *spiral* were silanised and plasma-bonded to a glass slide instead of treating the surface of the PDMS channel walls with Aquapel® and bonding PDMS chips to a PDMS backing layer. In addition, QX200™ was employed for droplet generation in these devices.

The *standard* 100x125 µm chip the 125x150 µm *spiral* designs were both tested to characterise potential droplet sizes as an estimation of the average cell number that can be encapsulated using these soft lithography chips. The aqueous and oil phases were supplied at a range of flow rates from 25 to 200 µl/min to register the effect on droplet size. Droplet diameters decreased as flow rate ratio (aqueous to oil) shifted from 1 to 2. The largest droplets corresponded to the lower combinations of flow rate values (i.e. 25x25) and the differences in diameter amplified for flow rate ratios of 2.The *standard* chip encompassed diameters that oscillated between 201.7 µm for the 25x25 condition and 175.0 µm for the 100x100 highest flow rate combination. When the flow rate ratio was changed from 1 to 2, the diameter variation was expanded from 166.6 to 117.1 µm, respectively. The spectrum of droplet diameters spanning the transition from plug flow to more spherical droplets where there was no direct contact with the channel walls was also characterised. The flow rate ratios were altered on the basis of the starting 25x25 condition from 1 to 10 and the diameters dropped down to 97.0 µm (Figure 5.12). The size distributions had an appropriate low polydispersity given by coefficient of variations ($CV(\%)$) that barely exceeded 0.5%.

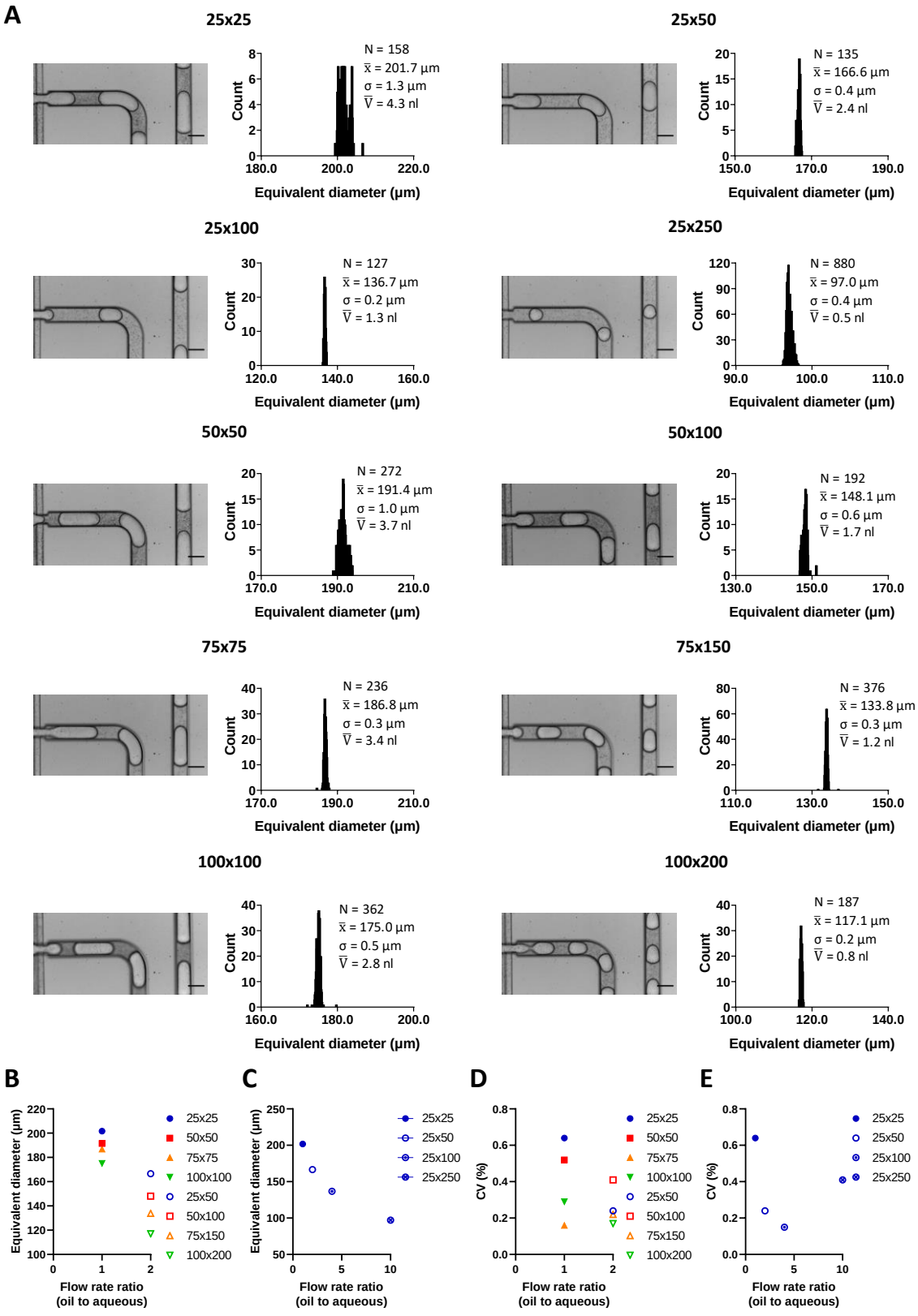

Figure 5.12 Droplet diameter measurements using DMV for the *standard* soft lithography chips: (A) Individual droplet population counts for each flow rate condition tested. The scaling of the plots includes the entire range of droplets sizes that were within ± 10% of the mean diameter; (B) Summary of the effect of flow rate ratio on the droplet diameter for all flow rate values; (C) Summary of the effect of flow rate ratio for droplets generated by injecting the aqueous phase at 25 µl/min; (D) Coefficient of variation for all flow rate combinations; (E) Coefficient of variation for droplets generated by injecting the aqueous phase at 25 µl/min. Scale bar = 100 µm.

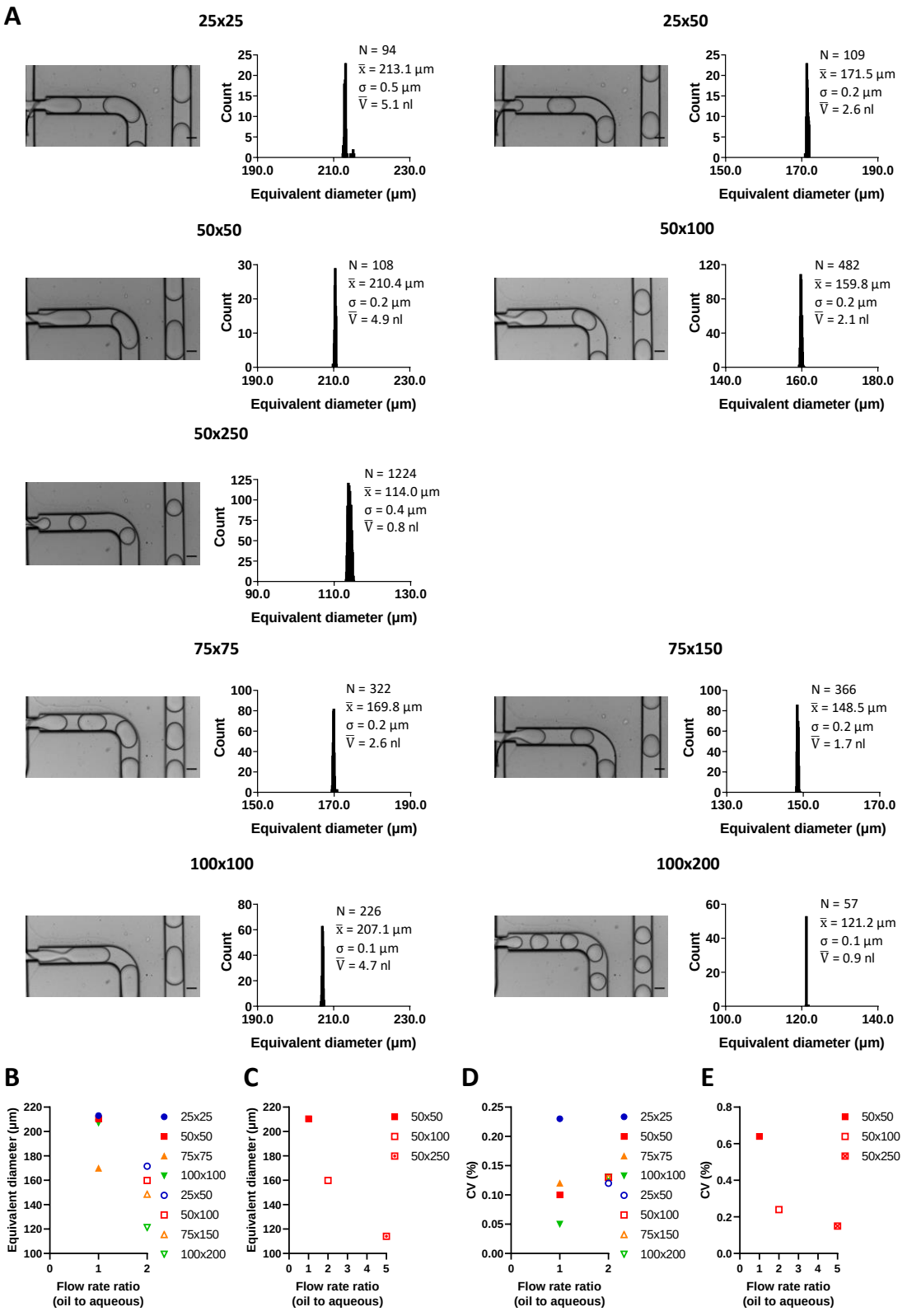

Figure 5.13 Droplet diameter measurements using DMV for the *spiral* soft lithography chips: (A) Individual droplet population counts for each flow rate condition tested. The scaling of the plots includes the entire range of droplets sizes that were within ±10% of the mean diameter; (B) Summary of the effect of flow rate ratio on the droplet diameter for all flow rate values; (C) Summary of the effect of flow rate ratio for droplets generated by injecting the aqueous phase at 25 µl/min; (D) Coefficient of variation for all flow rate combinations; (E) Coefficient of variation for droplets generated by injecting the aqueous phase at 25 µl/min. Scale bar = 100 µm.

A similar phenomenon applied to the *spiral* design, with larger droplets due to its wider channel dimensions. The decline in droplet diameters was much less evident (213.1 to 207.1 μm) with the exception of 75x75 flow rate values, where the diameter measured reached 169.8 μm. The response of droplet diameter to the increase in flow rate ratio from 1 to 5 necessary to abandon plug flow correlated with the results obtained for the standard design (sharp reduction from 210.4 to 114.0 μm) (Figure 5.13). Droplet sizes were therefore more tightly controlled with this particular design, as illustrated by $CV(\%)$ that always remained under 0.25%.

In short, the modified chip fabrication protocol and the surfactant formulation were crucial to achieve a substantial improvement in droplet population monodispersity. Soft lithography devices additionally yielded droplet volumes within a broad range that could create ample opportunities for high-throughput cell encapsulation and formation of small aggregates in microdroplets.

5.3.3.1 Particle encapsulation in soft lithography flow-focussing standard and spiral designs

Particle encapsulation efficiency served as a preliminary indicator of the potential of the soft lithography chips for cell encapsulation. An initial density of 5×10^6 particles/ml was characterised for the *standard* and the *spiral* chips, as well as 2.5 and 1×10^6 particles/ml (Appendix C.3). The aforementioned 25x25 flow rate combination acted as the upper limit point related to the largest droplet diameters and the relationship between flow rate ratios and the number of encapsulated particles was then quantified.

The *standard* chip presented a wide distribution that matched the theoretical Poisson distribution to various extents in all cases: the 25x25 combination had an average number of 6 particles encapsulated per droplet with any number from 2 to 13; 25x50 droplets were empty or contained up to 9 and any number from 0 to 6 was registered for the small 25x250 droplets mirroring Poisson distribution the most closely (Figure 5.14).

No major differences appeared for the *spiral* design: a similar encapsulation efficiency (as measured by number of particles in each droplet) was detected and a particle number distribution that again was close to a Poisson distribution for all flow rate values and ratios. 25x25 droplets encapsulated between 1 and 14 particles, 25x50 and 25x250 replicated the ranges measured for the standard chip and they all had comparable mean and standard deviation values (Figure 5.15).

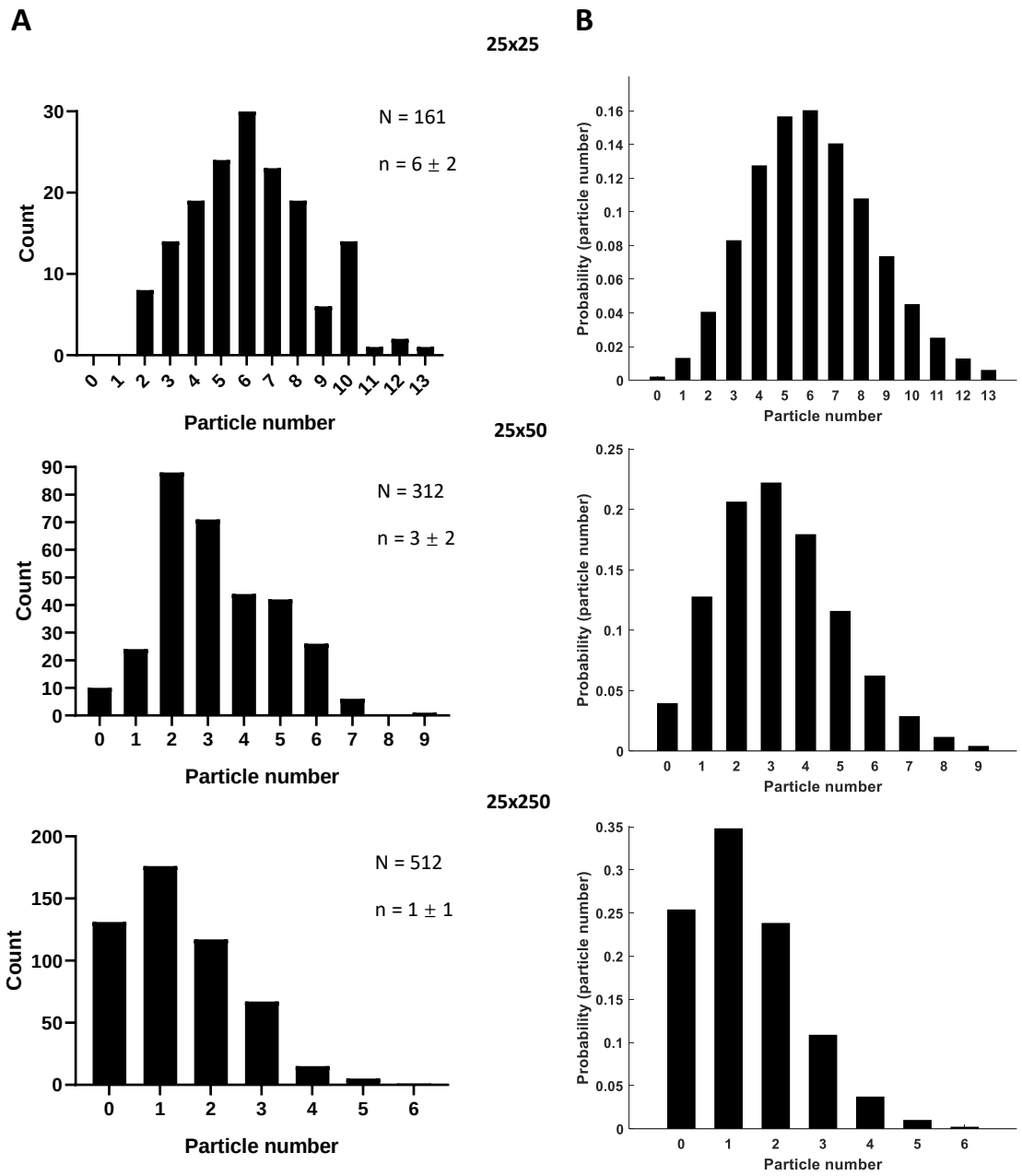

Figure 5.14 Particle encapsulation measurements for a density of 5 million particles/ml and three flow rate combinations using the *standard* chip design: (A) Experimental particle count performed following manual frame-by-frame analysis; (B) Corresponding theoretical Poisson distributions for each of the flow rate conditions tested.

Both chip designs offered comparable encapsulation patterns and mean number of particles per droplet along with a high degree of correlation with the theoretical Poisson distribution. As anticipated by its geometry, the *spiral* design had a larger number of empty droplets. Notwithstanding, the two designs were able to reproduce anything from single particle encapsulation to approximately ten particles per droplet. This was the target range of interest for small aggregate self-assembly from cells, which validated the applicability of these designs for this research project.

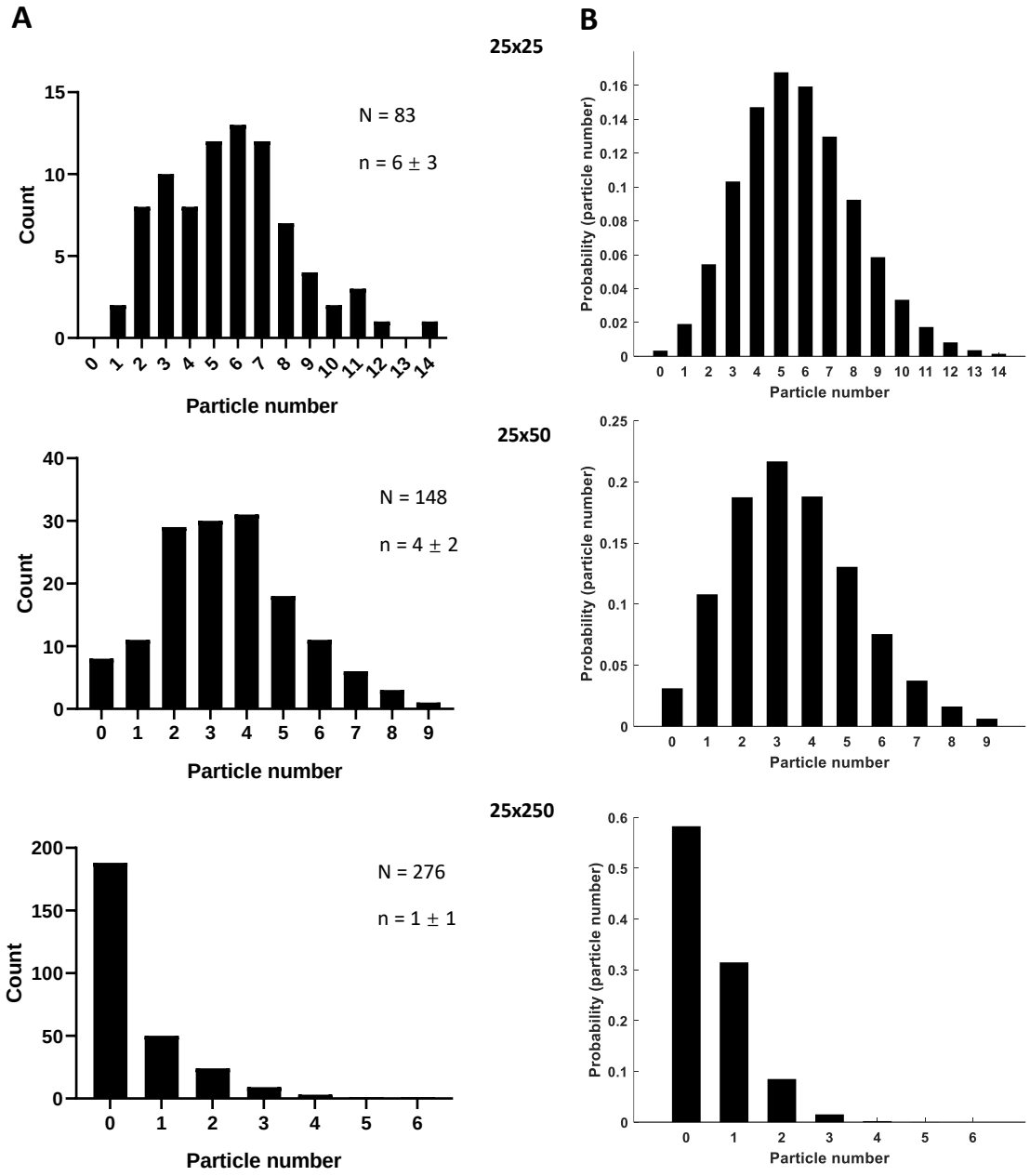

Figure 5.15 Particle encapsulation measurements for a density of 5 million particles/ml and three flow rate combinations using the *spiral* chip design: (A) Experimental particle count performed following manual frame-by-frame analysis; (B) Corresponding theoretical Poisson distributions for each of the flow rate conditions tested.

5.4 Discussion

The project aim of isolating chondroprogenitors from heterogeneous HBMSCs following condensation to enhance SOX9 expression required the development of a microfluidic platform for cell encapsulation. The device optimisation route comprised geometry characterisation, culture chamber refining and systematic analysis with various T-junction winding designs for chips fabricated from 3D-printed moulds and high-throughput droplet generation and culture in soft lithography microfluidic designs. The key microfluidic parameters in the study were surfactant composition; channel geometry and design; droplet stability; flow rate combination; droplet population size and polydispersity.

Droplet microfluidics was conceived for cell culture, aggregation and sorting under the hypothesis that spherical droplets favour cell aggregate formation (Steinbacher et al., 2012). The optimisation study of the microfluidic device for droplet generation presented in this chapter has covered the application of two different techniques for chip fabrication. 3D-printed designs exhibited a droplet merging issue within culture chambers with an array of pillars. This was overcome by introducing a series of windings to replace the chamber at the cost of diminishing the amount of droplets (but yielding broad size ranges) that could be stored and screened at any given time. A relative comparison between surfactants through a tensiometer test found no statistically significant difference between Soton2 and commercial Pico-Surf^{TM} 1 surfactants. The functional stability assay highlighted the benefit of relying on the Bio-Rad QX200^{TM} droplet generation oil commercial variation despite the limitations of the image analysis in droplets inside a haemocytometer chamber. Achieving new soft lithography designs able to produce larger stable droplets became the next step to maximise the output from soft lithography and cell aggregation in microdroplets. Highly monodisperse droplet diameters resulted from the application of new fabrication specifications giving rise to the standard and the spiral chips. Particles were loaded in microdroplets with a variety of numbers in them, indicating Poisson-like distributions that remained applicable and promising for cell encapsulation.

5.4.1 Droplet merging occurred in 3D-printed culture chamber chip designs

The T-junction geometry was selected for 3D-printed chips because of the asymmetry found with preliminary tests on flow-focussing designs, even if both share the ability to generate monodisperse droplets (Frischmuth et al., 2012, Steinbacher et al., 2012, Shi et al., 2014). Shi built a simulation model reconstructing the morphology of droplets generated using both methods and concluded that flow-focussing devices yielded more spherical but smaller droplets and TJ had an elongated configuration fitting the channel dimensions (Shi et al., 2014). Consequently, the first step was to

build a culture chamber for high-throughput droplet storage based on a T-junction channel geometry and to then examine droplet stability.

The development of a culture chamber for high-throughput droplet formation was hampered by an persistent merging issue. Pillars are common elements on microfluidic platforms that can keep structures separated or act as passive agents for controlled merging if arranged within distances below droplet size (Niu et al., 2008). In culture chambers such as the ones relevant for this project, pillars ensure that the chamber remains open and safe from collapse. The fault in the trial 9-pillar chamber chip that yielded rapid merging even when under active flow lied in the design characteristics. With a theoretical total area of the pillars (14.1 mm^2, 1.57 mm^2 each) of over one third of the total chamber area (corresponding to 35 mm^2 in the rectangular region) and regardless of 1 mm spacing (well above droplet size), their abundant distribution may have introduced multiple obstacles that decelerated droplet displacement across the chamber. The interaction between droplets inside the chamber upon contact is the result of a balance between surface tension and viscosity forces represented by the capillary number. At lower speeds, droplets are positioned closer to each other reducing the volume of oil between them and favouring coalescence through the following mechanism (Aarts et al., 2004, Bremond et al., 2008, Gunes et al., 2010, Gu et al., 2011, Feng et al., 2015):

(i) Droplets come in contact through collision, leading to deformation in the form of flattening due to pressure elevation in the contact area.

(ii) The continuous oil phase at the thin lubricating interstitial film drains allowing for interaction between interfaces through van der Waals forces that further contribute to accelerate drainage and film thinning by amplifying thermal capillary wave fluctuations.

(iii) Once the film reaches a critical thickness, attractive van der Waals forces overcome repulsive hydrodynamic forces resulting in breakup of the film and gradual merging until the droplets coalesce.

Among the possible factors that could have an impact on droplet coalescence (e.g. chamber dimensions, especially height; hydrophobicity of channel walls; droplet size; relative flow rate ratio), the next design modification in the chip focused on removing unnecessary pillars to expand the available area for smooth droplet displacement. The 4-pillar chamber managed to elude droplet merging for as long as the syringe pumps were continuously infusing both fluid phases, seeing intense merging starting moments after external pressures ceased to exist with complete coalescence within an hour. The slight improvement did not prove sufficient to solve the issue and

neither did fabricating a higher round-shaped chamber intended to eliminate the contribution of straight angles at the corners of the chamber towards increasing surface tensions among droplets.

After investigating these changes in design features for surfactant concentrations of up to 3% (w/w) Soton2 in FC40 oil, the optimisation process looked at characterising the surfactant-like performance of the compounds available in a qualitative tensiometer test via image analysis from droplet width measurements. The different surfactants were assessed at a 1.8% (w/w) concentration, in accordance with common values used for biological applications around 2% (w/w) for Pico-Surf™ commercial alternatives (Rhee et al., 2014, Kamperman et al., 2017, Terekhov et al., 2017). The lack of obvious statistical difference between Soton1 and Soton2 validated the choice of Soton2 for all previous microfluidic experiments as a surfactant containing fewer impurities that comparatively render it slightly less efficient as a surfactant yet more biocompatible. Similarly, no distinct difference was found for Soton2 and Pico-Surf™ 1, which suggested that Soton2 could be treated as an appropriate control to continue to refine microfluidic devices for droplet generation and then replaced by Pico-Surf™ 1 in the event that it may compromise cell viability. All in all, the tensiometer test enabled confirmation that droplet coalescence in 3D-printed devices was not only a matter of suboptimal surfactant formulations but that there could be other factors in play such as PDMS treatment prior to droplet generation. In fact, in subsequent surfactant performance assays comparing Soton2 and Bio-Rad QX200™ surfactants incorporating relevant cell culture incubation conditions, both formulations succeeded in generating stable droplets. The main variable modified in this case was fabrication method, and more specifically, chip design and PDMS treatment (i.e. silanisation). The droplets generated on silanised microfluidic PDMS chips with soft lithography designs were stable over 28 days and the Bio-Rad QX200™ surfactant provided the most monodisperse droplet distribution.

5.4.2 3D-printed designs with varying T-junction site dimensions achieved a wide range of droplet size distributions that were polydisperse

The lack of success in eradicating droplet merging in culture chambers created the urge to reconsider the entire approach for droplet storage on 3D-printed devices. Stemming from the concept of droplet separation by abundant volumes of oil, new chip batches were fabricated incorporating multiple winding channels. Establishing T-junction site dimensions as the only design variable, a systematic characterisation of the effect of flow rate ratio on droplet size and morphology was completed.

The 100 µm junction site height (*TJ100*) did not attain reproducible chip operation, already evident in PDMS invasion into the deformed rough channels, which matched past results indicating that

these particular dimensions defy the printer resolution limit, rendering them unreliable and heavily divergent from theoretical CAD drawings. That explained the unusual droplet generation pattern: single elongated droplets at the lowest flow rate ratio tested that did not become individual small droplets even at the highest flow rate ratios.

The remaining junction dimensions exhibited consistent general size reduction with increasing flow rate ratios, remarkably more pronounced for the larger ones (i.e. *TJ250* and *TJ300*), in agreement with comparably more unstable large droplet sizes at the lowest flow rate ratios for which higher shear stresses were required to break off droplets. Standard deviations also decreased sharply for higher flow rate ratios, mainly owing to higher numbers of droplets analysed with overall statistical similarities paired with more stable flows. Nonetheless, the majority of the flow conditions yielded droplet size distributions characterised by CV values above 5%. This was a clear indication of polydispersity in the droplet populations generated using that fabrication protocol to make 3D-printed devices. It was only for the low flow rate ratios (below 5) for the largest channel dimensions that the CV did not exceed 5% and this was ascribed to very small sample size (N < 10). Two major limitations on DMV analysis of droplet size thus had to be accounted for:

- The width of the channel was assumed to correspond to designed values but corrections would have to be applied for more accurate dimensions. However, this experiment was a proof of principle of the estimated size range attainable. It showed the trend of the patterns observed in any case and the same analysis procedure was extended to each of the junction site sizes tested.

- For larger dimensions, the software was unable to detect some of the droplets as separate and would treat certain droplets as different droplets from one frame to another, which invalidated the analysis. Therefore, those cases in *TJ250* and *TJ300* chips required analysing droplet population consisting of N < 10, particularly for lower flow rate ratios from 1 up to 3.75.

The detrimental role of chemical solvent residues from 3D printing finish on moulds prompting droplet merging had been acknowledged but could not be excluded. Previous T-junction designs had managed to form consistent droplets. The flow rate ratio range tested in these winding designs failed to yield spherical-like droplets that for the most part adopted an elongated configuration, which diverged from the idea of sphericity as a geometrical enhancer for cell aggregation on-chip. Moving on with the goal of culturing droplets as individual microenvironmental compartments and responding to the need to maximise yield for high-throughput cell sorting, soft lithography designs and a different fabrication methodology were examined to discern whether the benefits justified replacing 3D-printed designs.

5.4.3 Soft lithography standard and spiral designs generated monodisperse droplet distributions

Implementing soft lithography designs pursued two goals in agreement with disadvantages of former 3D-printed strategies: high-throughput generation of stable individual droplets and size monodispersity for a controlled cell encapsulation system. The high-throughput element was given by increased flow rates than those used before for 3D-printed chips while in a stable flow and droplet recovery from Eppendorf tubes for cell culture. Monodispersity was quantified in the new designs and the sharp gain attributed to a revised fabrication protocol that entailed the interaction among the following components:

- *Chip pattern fabrication*. Soft lithography complemented with PU for device cloning contributed to a vast rise in channel resolution in comparison with original CAD files.
- *Tight tube fitting to appropriate gauge needle tips*. Smiths Medical tubings combined with 25G (instead of 23G) needle tips aided in stabilising flow pressures.
- *Silanisation* as a cleaner method than Aquapel® to render PDMS surface of channels hydrophobic and oleophilic for droplet microfluidics.
- *Plasma bonding*. PDMS on glass bonding after a plasma treatment proved more effective for leakage prevention and batch-to-batch reproducibility.
- *Use of disposable 1 mm medical punches* to ensure uniform sized holes for inlet and outlet fittings to tubings.
- *High-speed camera and PCC software* for high-speed video acquisition.
- *A new oil and surfactant system, Bio-Rad QX200™,* that showed the best surfactant performance given by the highest droplet stability upon incubation.

The soft lithography approach was materialised in the fabrication and testing of two designs: *standard* and *spiral* patterns. Whereas the *standard* device was used due to its simplicity, the *spiral* pattern offered a supplementary functionality: inertial ordering. Edd et al. first described the method encompassed by this term and consisting in evenly spacing high-density suspensions of cells or particles travelling rapidly through a longitudinal rectangular channel that is slightly wider than their diameter. Consequently, they consistently loaded single cells in droplets by manipulating the balance of inertial forces. Kemna et al. subsequently elaborated on the inertial ordering mechanism introducing a curved spiral design for single cell encapsulation that incorporated the effect of curvature-dependent Dean flow and forces. Thus, the spiral geometry was selected as a passive method for potential cell entrainment and controlled cell encapsulation (Edd et al., 2008, Kemna et al., 2012).

Standard and *spiral* chips exhibited a similar response to changes in flow rates with comparable droplet size ranges and tendencies. Some irregularities appeared such as the 75 µl/min flow rate combination that were ascribed to microfluidic instabilities during transition from other flow rates prior to stabilisation. Droplet diameters dropped as flow rates were increased while keeping flow rate ratios constant. Hence, the largest droplets were produced at at 25 µl/min bor both aqueous and oil phases. This condition was set for subsequent encapsulation experiments as the central threshold of interest taking into account how further decreasing flow rates would come at the expense of a lower throughput.

Particle experiments were conceived as an intermediate step towards cell encapsulation and a proof of principle of approximation to expected Poisson distribution using electromagnetic stirring for homogenisation. The results showed relatively wide particle count distributions for either of the designs, with the largest 25x25 droplets being the most appropriate for the ensuing cell encapsulations to host multicellular aggregates. Aggregates would require very high cell densities on the order of 3 million cells/ml or above as well as constant and careful mixing rotation. High flow rates for the generation oil while fixing aqueous flow rate led to most droplets having none, 1 or 2 particles per droplet. For all flow rate ratios, except for the higher ones, the particle count closely followed the theoretical Poisson distribution and particle numbers loaded with the *spiral* pattern did not appear to deviate in a measurable manner. This design only displayed reduction in empty droplets for the lowest 25x25 flow rates and certain intervals of particle loadings with similar droplet counts throughout that might have been stochastic. It could not be concluded that the *spiral* design caused inertial ordering to control particle number in each droplet for the flow conditions applied. It is worth considering that the velocity effects were not systematically examined in order to attain a substantial Dean number (i.e. secondary flows for effective ordering). Moreover, on the assumptions that the channel aspect ratio (height to width), $\lambda = \frac{h}{w}$ is designed above 2 and that the particle diameter to hydraulic diameter (defined as $D_h = \frac{2wh}{(w+h)}$) ratio has to be above 0.07, the particles should be approximately 1/7th or ideally much bigger than the channel width for effective ordering (Holloway et al., 2018).

To summarise, the two soft lithography designs together with a more robust chip fabrication protocol proved suitable for particle encapsulation in monodisperse droplets, with similar effects being predicted for cell encapsulation. The throughput achieved with soft lithography designs was notably higher than that of 3D-printed designs, given by their accurate fabrication designs and their superior stability in high flow rate conditions. The combination of these characteristics left these optimised devices in a strong position to pursue the goal of generating and sorting HBMSC aggregates in microdroplets.

5.4.4 Conclusions

Throughout the optimisation journey detailed in this chapter and introduced in Figure 5.3, 3D-printed and soft lithography chips evolved from chambers for on-chip droplet culture to winding designs for off-chip droplet incubation. A global summary of the optimised parameters in the developmental study of microfluidic devices is portrayed in Table 5.1. Whereas T-junctions were more adequate for 3D-printed designs due to the printing resolution creating asymmetries in flow-focussing geometries, the latter were the preferred option for soft lithography chips. 3D-printed designs were more effective at generating larger droplets at the expense of high polydispersities compared to smaller and monodisperse droplets generated in soft lithography designs. This entailed that the two designs provided different opportunities for prospective encapsulation of aggregates of multiple sizes. The flow rate ranges in which devices fabricated operated producing a stable flow of droplets also differed for both fabrication methods. Soft lithography designs performed well at higher flow rates whilst 3D-printed designs experienced unstable droplet generation unless the flow rates employed were one order of magnitude smaller. The surfactant and oil formulation and the most efficient PDMS surface treatment (i.e. Bio-Rad QX200^{TM} and silanisation) that promoted droplet stability were determined in soft lithography designs. Hence, soft lithography chips were employed for subsequent cell encapsulation in microdroplets focussing on the standard design for the reason of simplicity and including both silanisation surface treatment and Bio-Rad QX200^{TM} as the oil and surfactant formulation of choice. A flow rate of 25 µl/min for the aqueous and the oil phases was established as the condition for droplet generation as endorsed by the resulting droplet diameters and the particle encapsulation counts.

Table 5.1 Summary of the optimised parameters for 3D-printed and soft lithography designs established as a result of the study conducted in this chapter.

Optimised parameter	**3D-printed designs**		**Soft lithography designs**
Channel geometry + design	T-junction winding design	Flow-focussing winding design***	Flow-focussing *standard* and *spiral* designs
*Droplet size range (volume)**	*TJ150* Lower limit: 143.6 ± 7.3 µm (1.6 nl) *TJ150* Upper limit: 314.0 ± 21.9 µm (16.2 nl) *TJ300* Lower limit: 437.2 ± 36.5 µm (43.8 nl) *TJ300* Upper limit: 925.2 ± 40.7 µm (0.4 µl)	*FF215* Lower limit: 236.3 ± 1.0 µm (7.0 nl) *FF215* Upper limit: 405.7 ± 2.9 µm (35.4 nl) *FF300* Lower limit: 240.9 ± 0.7 µm (7.3 nl) *FF300* Upper limit: 507.4 ± 0.3 µm (68.4 nl)	*Standard* Lower Limit: 97.0 ± 0.4 µm (1.6 nl) *Standard* Upper limit: 201.7 ± 1.3 µm (4.3 nl) *Spiral* Lower Limit: 114.0 ± 0.4 µm (0.8 nl) Upper limit: 213.1 ± 0.5 µm (5.1 nl)
Polydispersity (CV(%))	*TJ150* Lower limit: 5.1% Upper limit: 7.0% *TJ300* Lower limit: 8.3% Upper limit: 4.4%	*FF215* Lower limit: 0.4% Upper limit: 0.7% *FF300* Lower limit: 0.3% Upper limit: 0.1%	*Standard* Lower Limit: 0.4% Upper limit: 0.6% *Spiral* Lower Limit: 0.3% Upper limit: 0.2%
Flow rate range	Aqueous: 2 µl/min Oil: 2 to 20 µl/min	Aqueous: 25 µl/min Oil: 25 to 250 µl/min	Aqueous: 25 to 100 µl/min Oil: 25 to 250 µl/min
Droplet stability	Limited	High	High
Oil and surfactant combination	FC40 fluorinated oil with 1.8% Soton2 (w/w)**	Bio-Rad QX200™	Bio-Rad QX200™
PDMS surface treatment	Aquapel®**	Silanisation	Silanisation

* Droplet size range is presented as the mean equivalent diameter ± SD with the equivalent volume in brackets. ** The oil and surfactant combination and the PDMS surface treatment included in the table for the left column 3D-printed designs correspond to the parameters used for the droplet characterisation study even though the optimised parameters were later found to be those used for soft lithography and included in the right column. ***The data for the 3D-printed flow-focussing winding designs is detailed in Appendix C.2.

Chapter 6: Establishing a microfluidic platform for cell condensation and analysis

6.1 Introduction

This chapter conveys the originality of this work and the final testing of the project hypothesis of early expression of *SOX9* upregulation in cell aggregates generated in a high-throughput manner within microdroplets. Cell aggregation is required to promote *SOX9* expression during the early condensation stage in chondrogenesis and later on to progress through to differentiation and proliferation of chondrocytes (Akiyama et al., 2002, Glennon-Alty et al., 2013, Jo et al., 2014). By incorporating droplet microfluidics for cell encapsulation, cell aggregation gains a high-throughput component as a microenvironment emerges for culture and monitoring of cell aggregate formation and posterior functional analysis of aggregates.

Examples of cell aggregation in microfluidic devices exist in the literature attempting to achieve 3D culture of viable spheroids that imitate tissue development physiological conditions. In the field of cancer sciences, Hsiao et al. built a 3D model for prostate cancer through a niche consisting of an array of side-microwells onto a bilayer channel system with separate media perfusion and a niche for PC3 cancer cell spheroids to grow via a semi-permeable polycarbon membrane. They observed cell proliferation over 7 days of culture with high viability of spheroids throughout (Hsiao et al., 2009). Along those lines, Zuchowska et al. examined the effect of flow rates spanning between 10 and 20 µl/min on A549 and MRC-5 cancer cell aggregates in microchambers with microwells patterned onto a PDMS chip for 10 days of culture. The spheroids formed after 72 h and reached tridimensional sphericity close to the ideal value, 1. No significant reduction in viability occurred during culture in the microfluidic chip (Zuchowska et al., 2017). These are alternatives to droplet microfluidics that are generated in a parallel, static manner, and therefore with limited throughput.

HBMSC microaggregates have also started to be investigated in a microfluidic setting combining the principles of throughput scalability in microfluidic devices and chondrogenic differentiation in spheroid cultures. Occhetta et al. fabricated microwell patterns on a serial dilution generation microfluidic chip and seeeded HBMSCs for early chondrogenesis characterisation of cell aggregates. They achieved rapid cell spheroid formation within 3 h of microaggregates of 56.2 ± 3.9 µm diameter and 77 ± 15 cells per microaggregate. They then validated cell-cell contact through the expression of neural cadherin (N-cadherin) and cytoskeletal remodelling through positive actin and vinculin staining surrounding DAPI-stained cell nuclei in aggregates cultured for 3 h. In addition,

they investigated the proliferative ability and the chondrogenic differentiation outcome of HBMSC microaggregates cultured on the microfluidic device for 3 days according to three groups: negative control termed Vehicle in serum-free medium, microaggregates supplemented with both 20 ng/ml Wnt3a and 5 ng/ml FGF2, and microaggregates supplemented with 1 ng/ml TGF-β3. Wnt3a FGF2 microaggregates reached the highest degree of proliferation with statistically significant differences compared to TGF-β3 and Vehicle groups. With regard to chondrogenic differentiation studied through type II collagen expression in an immunofluorescence assay, the TGF-β3 group was the only one producing a positive staining (Occhetta et al., 2015). HBMSCs encapsulated in other 3D culture platforms such as gelatin norbornene hydrogel scaffolds generated in a pipette-powered microfluidic device have also shown promising increases in expression of type II collagen and aggrecan cartilage extracellular matrix components compared to pellet culture controls of macroaggregates (Li et al., 2017).

The optimisation process delineated in the previous chapter led to define specific parameter ranges endorsed by experimental operation of microfluidic devices in 3D-printed and soft lithography chip designs that evidenced the wide window of possibilities for cell encapsulation. This chapter follows on those optimisation parameters (i.e. channel dimensions, fabrication technique, choice of surfactant, PDMS treatment and droplet size range) and narrows down the cell encapsulation procedure to reliable soft lithography chip designs where high-throughput and monodisperse droplet populations are achievable.

Consequently, it explores the initial cell-seeding density as a single variable with a direct effect on the number of cells encapsulated per microdroplet and influencing droplet stability and nutrient consumption from available volumes of media in microdroplets. The biological characterisation of HBMSC aggregates composed of different cell numbers as a function of cell-seeding densities becomes a criterion to establish an appropriate setting for sorting of HBMSC cell aggregates to circumvent the heterogeneity issue for cartilage tissue engineering.

Progress towards that end is presented on cell aggregation, cell viability in microdroplets, high-throughput generation of droplets and functional characterisation of cell aggregates. To conclude, the findings of this research project related to chondrogenic differentiation of multicellular spheroids across macroaggregates and microaggregates and microfluidic platform development come together to test the central project hypothesis that aggregation and culture in microdroplets enhances *SOX9* expression and that small cell aggregates can be sorted on the basis of their early *SOX9* expression.

6.1.1 Hypothesis

'HBMSCs self-assemble into aggregates within spherical microdroplets in a PDMS microfluidic device and can be cultured long enough to sort the aggregates on the basis of *SOX9* expression to harness the most robust cartilage-producing populations'.

6.1.2 Aims

The core hypothesis of this chapter entails the use of an oil and surfactant combination that can provide a biocompatible environment inside a microfluidic device for stabilisation of multiple droplets containing cells. Subsequently, this will allow sufficient culture duration to trigger *SOX9* expression with a view to sorting for the most promising populations with chondrogenic prospects. Four aims have been established to test this concept and develop the technology required:

1. To confirm the ability of cells to aggregate indicating chondrogenic condensation and to define time and cell density required for viable cell aggregation in microdroplets.
2. To devise a high-throughput droplet microfluidic generation strategy for efficient monitoring, screening and future sorting of aggregates.
3. To characterise aggregate functionality after incubation in microdroplets.
4. To test the main project hypothesis that aggregates formed inside microdroplets experience *SOX9* upregulation compared to monolayer cultures.

6.2 Methods

6.2.1 Cell encapsulation in microdroplets using optimised soft lithography chips

To ensure droplet stability with the goal of recovering and culturing cells in droplets, two major experimental modifications were introduced: silanisation as opposed to formerly used Aquapel® and a different oil and surfactant system, Bio-Rad QX200™, due to its recent record of use in droplet PCR systems where droplet stability is of the essence (Chen et al., 2017, Sorber et al., 2017, Croset et al., 2018, Valihrach et al., 2018). The microfluidic set-up was analogous to that detailed in section 5.2.2.2.1. For simplicity, the *standard* soft lithography chip design described in the previous chapter was used for droplet generation.

The cells were harvested after trypsinisation in 1X T/E for 5 min, centrifugation at 272 g for 5 min and resuspension in either DMEM (ATDC5) or αMEM (HBMSCs) supplemented with 1% P/S (v/v). The medium was replaced by chondrogenic differentiation medium (see section 2.3.4) prior to cell encapsulation in droplets, keeping the cell suspension in the syringe continuously homogenised using a Magnetic Tumble Stirrer™ (VP 710 Series, V&P Scientific, Inc., USA) on 5 mm diameter PTFE Encapsulated Samarium Cobalt stir discs (V&P Scientific, Inc., USA). The droplets were collected in Eppendorf tubes in which they formed an emulsion on a bed of oil and surfactant. The tubes containing the cells encapsulated in microdroplets were incubated at 37°C, 20% O_2 and 5% CO_2 according to the time points of interest for up to three days.

Videos were recorded to study live cell encapsulation in microdroplets with a focus on the number of cells per droplet. The experimental cell count was performed manually from frame-by-frame analysis was compared to a theoretical Poisson distribution (see equation below) modelled using MATLAB to assess the encapsulation efficiency (see Appendix D.4).

$$P\,(X = k) = \frac{\lambda^k e^{-\lambda}}{k!} \tag{6.1}$$

where $P\,(X = k)$ is the probability of droplets containing a k number of cells and λ is the mean number of cells per droplet obtained from the experimental cell count (Kissell and Posserina, 2017). Similarly, the standard deviation of the droplet population was computed from the experimental cell count. The aggregates in microdroplets were characterised by sampling 20-30 µl in a FastRead® 102 haemocytometer and observing under the CKX53 Olympus, Carl Zeiss AxioVert 200 and Nikon Eclipse Ti inverted microscopes mentioned throughout this work.

6.2.2 Time-lapse cell aggregation in microdroplets

A first approach to observe cell aggregation moments after encapsulation was to collect droplets generated at a flow rate of 25 µl/min for aqueous and oil phases from a starting ATDC5 cell-seeding density of 3 million cells/ml. The droplet suspension was pipetted into a Fast-Read 102® haemocytometer for imaging under an Olympus IX82-UCB microscope. Images were captured at the same haemocytometer chamber every 15 min from 30 min after cell encapsulation in microdroplets until an hour later, which was when the oil evaporated completely. An average of 3 cells was encapsulated in each droplet.

A series of changes in the encapsulation protocol were therefore implemented towards improving droplet stability. These included thorough resuspension of cell pellets in 1 ml chondrogenic differentiation medium prior to syringe loading; centrifugation cycle adjustment; constant uniform stirring of cell suspension while injecting into the microfluidic device; removal of mineral oil for incubation and the use of fresher batches of Bio-Rad QX200™ droplet generation oil. The time-lapse analysis was subsequently performed on ATDC5 and HBMSCs, both injected at 5 million cells/ml. The images of the aggregates were captured using the Carl Zeiss AxioVert 200 following a 60-min, 90-min and overnight incubation of the cells in microdroplets.

6.2.3 Droplet recovery for colony formation functionality assay

As a means to confirm functionality besides viability, the cells and aggregates incubated in droplets in chondrogenic differentiation medium were re-plated on flat bottom 96-well plates at specific time points of interest for early chondrogenesis assessment in microdroplets: day 1 and day 3.

For the purpose of a preliminary assessment, a cell density of approximately 5000 cells/cm^2 for a volume of 200 µl of culture medium per well was the target from starting 2×10^6 cells/ml injected into the *standard* chip. The flow rates for the aqueous and oil phases was kept constant at 25 µl/min. A volume of 50 µl droplet suspension from the collection 1.5 ml Eppendorf tubes was extracted and transferred to a 0.5 ml Eppendorf tube. A similar volume of 1H, 1H, 2H, 2H-Perfluoro-1-octanol (PFO, Sigma-Aldrich, UK) was then added to bring the separate droplets to a single-cell suspension in a matter of minutes. Given 0.32 cm^2 surface area for 96-well plates (Corning, Costar, Sigma-Aldrich, UK), 20 µl of the cell suspension was pipetted into another tube containing 580 µl of DMEM + 5% FBS (v/v) + 1% P/S (v/v) for ATDC5 culture and αMEM + 10% FBS (v/v) + 1% P/S (v/v) for HBMSCs for a final 600 µl volume equally distributed across triplicates (n = 3). Cultures were imaged after 14 days for proliferation and colony formation using the Zeiss AxioVert 200 microscope.

The colony formation assay was then expanded to optimise the aggregate seeding density for cell proliferation once replated. ATDC5 cells and HBMSCs were injected at 3×10^6 cells/ml into the same microfluidic chip design to ensure the formation of cell aggregates over single-cell encapsulation. The droplet break-up protocol described in the preliminary experiment was applied, with a modification in the aggregate seeding process. Aggregate seeding density was the variable examined to determine the threshold density required for colony growth and proliferation. The aggregate seeding densities included in the assay were 1, 3, 10 and 50 aggregates/well and a volume of 200 µl of 5% FBS (v/v) + 1% P/S (v/v) was added to each well of a 96-well plate for ATDC5 culture and αMEM + 10% FBS (v/v) + 1% P/S (v/v) for HBMSCs (n = 5 experimental replicates per condition). Two separate plates were employed for droplets cultured for 1 day and for 3 days. Cultures were inspected after 14 days for proliferation and colony formation. Again, the cells were imaged after 14 days using the Carl Zeiss Axiovert 200 microscope.

The final complete colony formation assay investigated three different cell-seeding densities for unselected HBMSC encapsulation in droplets (10^6 cells/ml, 3×10^6 cells/ml and 5×10^6 cells/ml) and three time points related to droplet incubation time prior to re-plating (day 1, day 2 and day 3). Aggregate seeding density for re-plating was fixed at 30 aggregates/well to adapt the threshold value found in the previous aggregate seeding density optimisation assay to 6-well plates (Corning, Costar, Sigma-Aldrich, UK). These were used in this colony formation assay because of their suitability for distributed colony growth across the surface of the well, imaging and staining for colony counting. Droplets containing aggregates were imaged on each incubation time point (day 1, day 2 and day 3) on the Carl Zeiss Axiovert 200 microscope prior to inducing droplet break-up. Droplet diameters and aggregate diameters were computed using ImageJ analysis from their area measurement and accounting for circularity according to equation 3.1 in section 3.2.2. The droplet break-up protocol conducted in previous assay was maintained and the seeded aggregates were cultured in 2 ml αMEM + 10% FBS (v/v) + 1% P/S (v/v) for 14 days. The cultures were imaged on day 7 and day 14 under the Nikon Eclipse Ti inverted microscope. On day 14, a Crystal violet staining was carried out to discern and count colonies. Cells were washed in DPBS twice and fixed in 95% ethanol (v/v) for 10 min. The wells were air-dried for 10 min and 1 ml 0.05% (w/v) Crystal violet (Sigma-Aldrich, UK) solution was added to each well and incubated for 1 min. The staining solution was then discarded, and the wells were washed twice with distilled water. Colonies were counted by eye using a bright field microscope after allowing the samples to air-dry. The count was presented in absolute values and through the variable called Colony Forming Efficiency ($CE\ (\%)$), defined as

$$CE\ (\%) = \frac{number\ of\ colonies\ counted}{theoretical\ aggregate\ seeding\ density} \times 100 \qquad (6.2)$$

where the $number\ of\ colonies\ counted$ corresponded to visible colonies stained with Crystal violet and the $theoretical\ aggregate\ seeding\ density$ was 30 aggregates/well. The stained colonies were also imaged under the Zeiss AxioVert 200 inverted microscope for detailed morphological observation.

6.2.4 Droplet recovery for RT-qPCR analysis

RT-qPCR analysis was performed to test the core project hypothesis that cell aggregation triggers upregulated expression of *SOX9* that could be used to isolate HBMSC chondroprogenitors. HBMSC microaggregates formed in microdroplets following droplet microfluidic encapsulation were assessed as a function of the time incubated in microdroplets and compared to cells in monolayer culture, all in chondrogenic differentiation conditions.

Unselected HBMSCs were cultured and expanded until confluent. The cells harvested after trypsinising with 1X T/E were split into 3 groups for RT-qPCR analysis. Cells used as a reference control for basal *SOX9* mRNA expression on day 0 were used for normalisation purposes (n = 3 experimental replicates). The monolayer culture group was composed of cells differentiated in chondrogenic induction media on 24-well plates (Corning, Costar, Sigma-Aldrich, UK) and seeded at 5000 cells/well (see section 2.3.4) according to three time points set on day 1, day 2 and day 3 (n = 3 experimental replicates per time point). The last group sampled were cells encapsulated in microdroplets in chondrogenic medium with the same three time points as the monolayer group. An initial seeding density of 3×10^6 cells/ml was selected for encapsulation in microdroplets. A volume of 100 µl aggregate suspension obtained using PFO was aliquoted in a 0.5 ml Eppendorf per sample as detailed in the previous section was centrifuged at 400 g for 5 min and cell-lysed with 100 µl BL-TG buffer for RNA extraction. The RNA extraction, cDNA synthesis and RT-qPCR plate preparation and data analysis were all carried out as described in section 4.2.2.

To summarise, a schematic to visualise the steps leading to functional characterisation of aggregates in microdroplets through colony formation assay and RT-qPCR expression is depicted in Figure 6.1.

6.2.5 Droplet recovery for whole mount fluorescence immunostaining

Whole mount immunostaining of aggregates recovered from microdroplets was conducted as a proof of principle of early SOX9 protein expression and to assess the level of heterogeneity among aggregates compared to the small spheroids cultured *in vitro* as detailed in section 3.3.2.3.2. To this end, cells cultured in monolayer were selected as a control and aggregates were stained in parallel for SOX9. Both were characterised after one day of chondrogenic induction.

Monolayer cells seeded at a density of 50000 cells/well on a 24-well plate (Corning, Costar, Sigma-Aldrich, UK) were fixed in 4% PFA (w/v) solution for 1 h and washed twice with DPBS. The fixed cells were permeabilised in 1% Triton™ X-100 (v/v) in 1X PBS for 5 min, washed in PBST (see section 2.7.1) three times for 5 min and blocked in 0.1% Triton™ X-100 (v/v), 10 mg/ml BSA and 5% goat serum (v/v) in 1X PBS for 5 min. The cells were incubated with the primary SOX9 antibody (1:150 dilution in PBST) for 1 h and washed three times in PBST prior to incubating with the secondary AF488 antibody (1:50 dilution in PBST) for 1 h. The cells were then washed twice with PBST, counterstained with DAPI (25 µg/ml in 1X PBS) for 5 min and washed twice in 1X PBS. The monolayer culture samples (n = 3) were imaged under the Nikon Eclipse Ti microscope.

Aggregates recovered from droplets and generated from an initial seeding density of 3×10^6 cells/ml using PFO as described in section 6.2.3 were fixed for 1 h, washed in 1X PBS, permeabilised for 15 min, washed in PBST for 5 min and blocked for another 15 min. The primary SOX9 antibody and the secondary AF488 antibody were incubated for 1 h each, with a PBST wash in between. A second PBST was performed prior to DAPI counterstaining for 20 min and the aggregates were finally resuspended in 1X PBS for imaging. A centrifugation cycle at 400 g and room temperature for 5 min was applied between each step. Similar reagents and concentrations to those used for monolayer cells were employed. The aggregate suspension was observed under the Leica TCS SP5 confocal microscope for analysis.

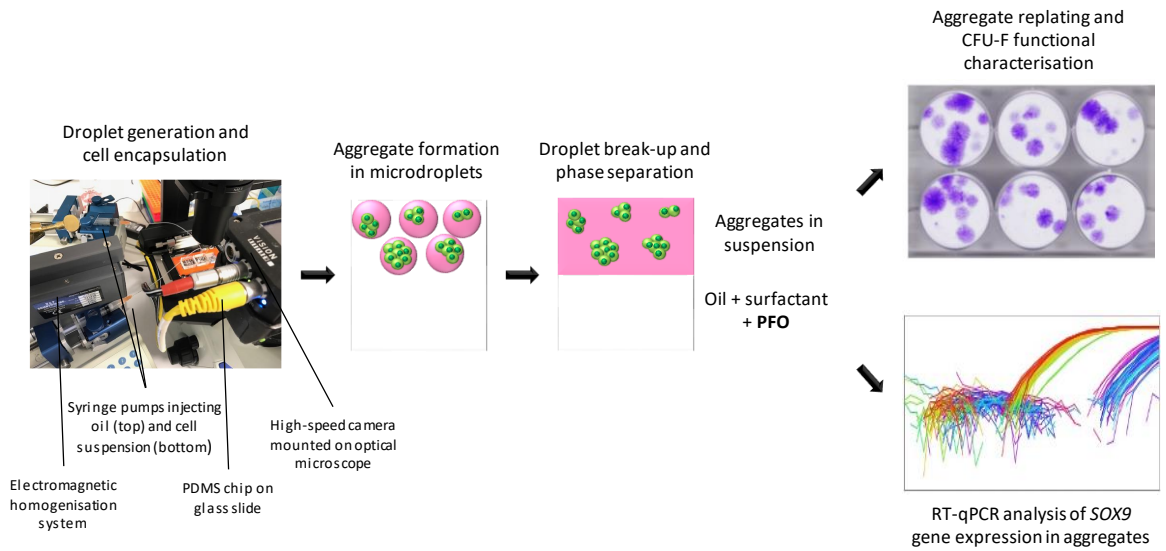

Figure 6.1 Experimental steps taken for functional assessment of cell aggregates self-assembled into microdroplets and analysed by colony formation assay for colony formation ability and RT-qPCR for quantification of *SOX9* mRNA expression.

6.3 Results

6.3.1 Time-lapse study of cell aggregation in microdroplets

Cell sedimentation to the base of the droplets in a confined physical compartment prompts cell-cell contact to trigger aggregation through the combined interaction of cell adhesion molecules (N-CAM and N-cadherin), cell surface receptors (syndecan) and ECM interactions (tenascin, fibronectin) (Hall and Miyake, 2000, Chan et al., 2013, Sart et al., 2014, Sart et al., 2020). To verify that aggregation was a spontaneous event for cells encapsulated in microdroplets and to examine the time required for biological characterisation of compact aggregates, a time-lapse study was designed assessing aggregation moments after encapsulation. The work presented in this chapter was preceded by preliminary experiments using suboptimal 3D-printed chips and a soft lithography chamber design, Soton2 surfactant in FC40 oil and an on-chip incubation strategy. This combination was not successful due to the challenges arising from oil evaporation, droplet coalescence and throughput. In this context, the development and optimisation of soft lithography chips described in the previous chapter prompted the validation of cell aggregation, viability and functionality via an alternative approach to culture chambers for on-chip droplet incubation with an added throughput gain. The simplest *standard* soft lithography chip design incorporating silanisation and plasma bonding to glass slides along with the more stable QX200^{TM} surfactant composition was thus employed in accordance with the flexible droplet sizes, minimal polydispersity and promising particle encapsulation performance. Culture chambers for on-chip droplet incubation were replaced by droplet generation followed by collection in a microcentrifuge tube for off-chip storage in a humidified atmosphere inside an incubator. Droplet observation on set time points was also simplified by adding small volumes of droplet suspension in oil onto a portable haemocytometer.

The encapsulation experiments in Appendix D.2 and D.3 had shown that cell aggregation occurred within hours of encapsulation in microdroplets (i.e. before 6 h, see Figure D.16) although the aggregation phenomenon had not been investigated in detail. This responded to the existing limitations regarding low numbers of cells encapsulated in microdroplets and droplet coalescence. Both posed an obstacle to mitigate before observing live cell aggregation.

Time-lapse analysis of 3×10^6 cells/ml initial cell seeding density imaged minutes after encapsulation in 200 µm droplets showed that cells tended to aggregate over time in a number-dependent fashion. Some aggregates already formed as early as after 30 min of incubation at room temperature and they generally became more visibly round and compact after 90 min (Figure 6.2A). This preliminary time-lapse study, however, was not deemed representative of the actual storage conditions of the cells in the microcentrifuge. During that time when the droplets gradually

coalesced as the oil evaporated, they were not surrounded by oil and the environment lacked the appropriate temperature and humidity conditions for cell culture.

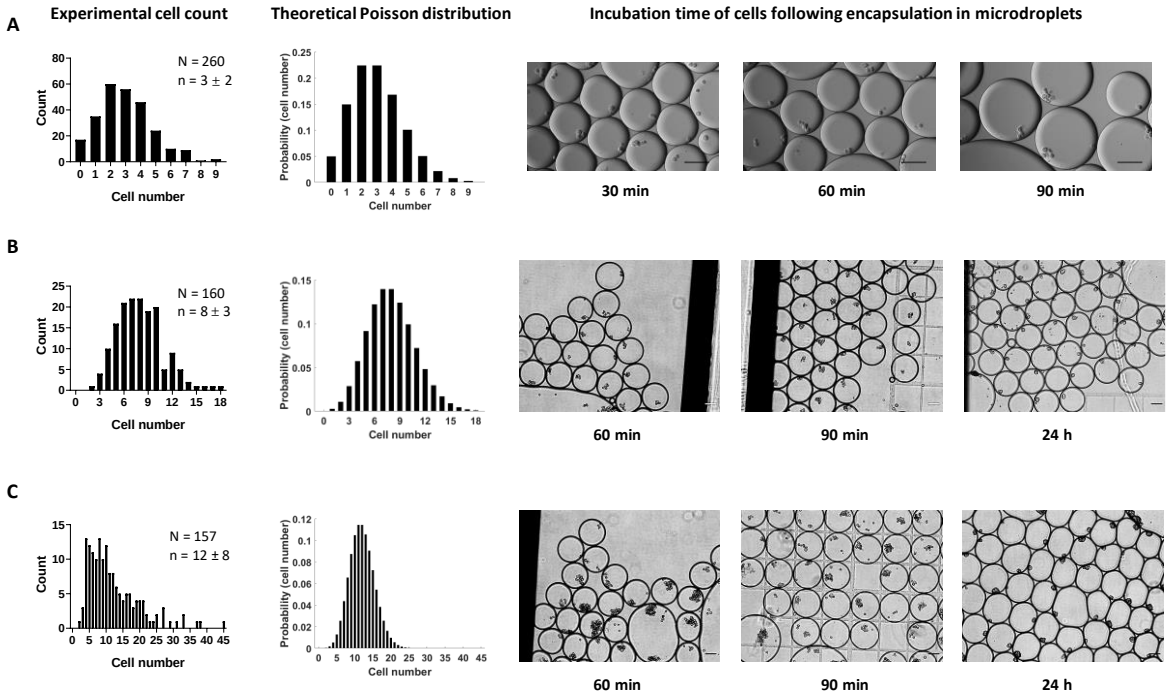

Figure 6.2 Time-lapse cell aggregation study comprising the first two hours following cell aggregation in microdroplets. The experimental cell counts are shown alongside theoretical Poisson distributions: (A) ATDC5 cells encapsulated at a density of 3×10^6 cells/ml in 200 µm microdroplets and injected at 25 µl/min for both phases were imaged on a static haemocytometer chamber for an hour until the oil evaporated (top) as a preliminary study. In subsequent assays, the cell density was increased to $5x10^6$ cells/ml to visualise aggregation while maintaining flow rate conditions and time points (B) and the assay was extended to F51 P2 HBMSCs (C). A time point at 24 h was added to illustrate changes in aggregate compaction owing to incubation (middle and bottom right). Scale bar = 100 µm.

The experiment was refined as a result for similar 200 µm droplets containing ATDC5 cells and HBMSCs were imaged an hour after encapsulation at a seeding density of 5×10^6 cells/ml and then placed in an incubator for 30 min for a second observation. They were finally sampled and imaged overnight to verify aggregate formation and compaction. Compaction was assessed by qualitative inspection of aggregates in droplets. Aggregates were considered to reach compaction when individual cells could not be distinguished within droplets in focus.

ATDC5 cells aggregated after 60 min even if incubated at room temperature. A further 30 min incubation at 37°C and 5% CO_2 revealed a slight increase in aggregate compaction and substantially compact aggregates resulted from overnight incubation (Figure 6.2). HBMSCs adhered to that pattern although the aggregates were less compact in the corresponding early time points. The smaller aggregates were less round, and some aggregates were accompanied by individual cells in some of the microdroplets. Similarly, overnight incubation produced compact HBMSC aggregates (Figure 6.2). This led to conclude that aggregation was a rapid event in microdroplets that occurred

in a matter of minutes and an overnight incubation sufficed to achieve aggregate compaction. When comparing experimental counts of cells encapsulated in droplets to theoretical Poisson distributions, ATDC5 cells displayed a close link for both cell densities and HBMSCs had a broader range for the experimental count distribution with a less pronounced peak. This finding can be explained by an incomplete fragmentation prior to encapsulation of the dense ECM network of HBMSCs in highly confluent cultures, which might cause them to be prone to enter some droplets in small clusters (this was observed during droplet generation and cell encapsulation).

6.3.2 Aggregate stability in short-term chondrogenic differentiation cultures in microdroplets and colony formation functionality assay

To assess cell viability, a method was developed to recover aggregates from microdroplets and to allow their subsequent culture and functional analysis. To achieve this, PFO was added to the layered tube to induce complete droplet coalescence into an aggregate suspension (aqueous phase). Prior to transferring small volumes of the suspension to the flat bottom 96-well plate, cell aggregation was validated for ATDC5 and HBMSCs 3 h following encapsulation (Figure 6.3). ATDC5 repopulated the wells regardless of 1-day or 3-day incubation of aggregates in droplets after 14 d culture on well plates (Figure 6.3A). No clear proliferation was detected for HBMSCs in the 25 µl/min, possibly due to suboptimal seeding densities or sampling errors. In addition, the experimental data indicated a higher number of empty droplets and a lower number of droplets containing cell numbers above the mean in comparison with the theoretical Poisson distribution plot (Figure 6.3B).

The experiment was redesigned to address aggregate seeding density as a relevant variable for cell proliferation upon re-plating. The aim was to determine an appropriate density that could be extended to a more elaborate colony formation assay. ATDC5 cells and HBMSCs were again compared by inspecting droplets that had been incubated for 1 day and 3 days at 37°C, 20% O_2 and 5% CO_2. Differences were observed between the two time points for ATDC5s and HBMSCs. Droplets showed instability-related issues on day 3 (e.g. droplet break-up and coalescence) and accumulation of metabolic products (linked to a cell line that is more metabolically active). With regard to the effect of aggregate seeding density on proliferation after 1-day incubation in microdroplets, the lowest density of 1 aggregate/well did not show signs of proliferation after 14 days. The rest of the aggregate seeding densities all correlated with cell proliferation and 3 aggregates/well was found to be the minimum density to ensure that there was reliable proliferation (Figure 6.4).

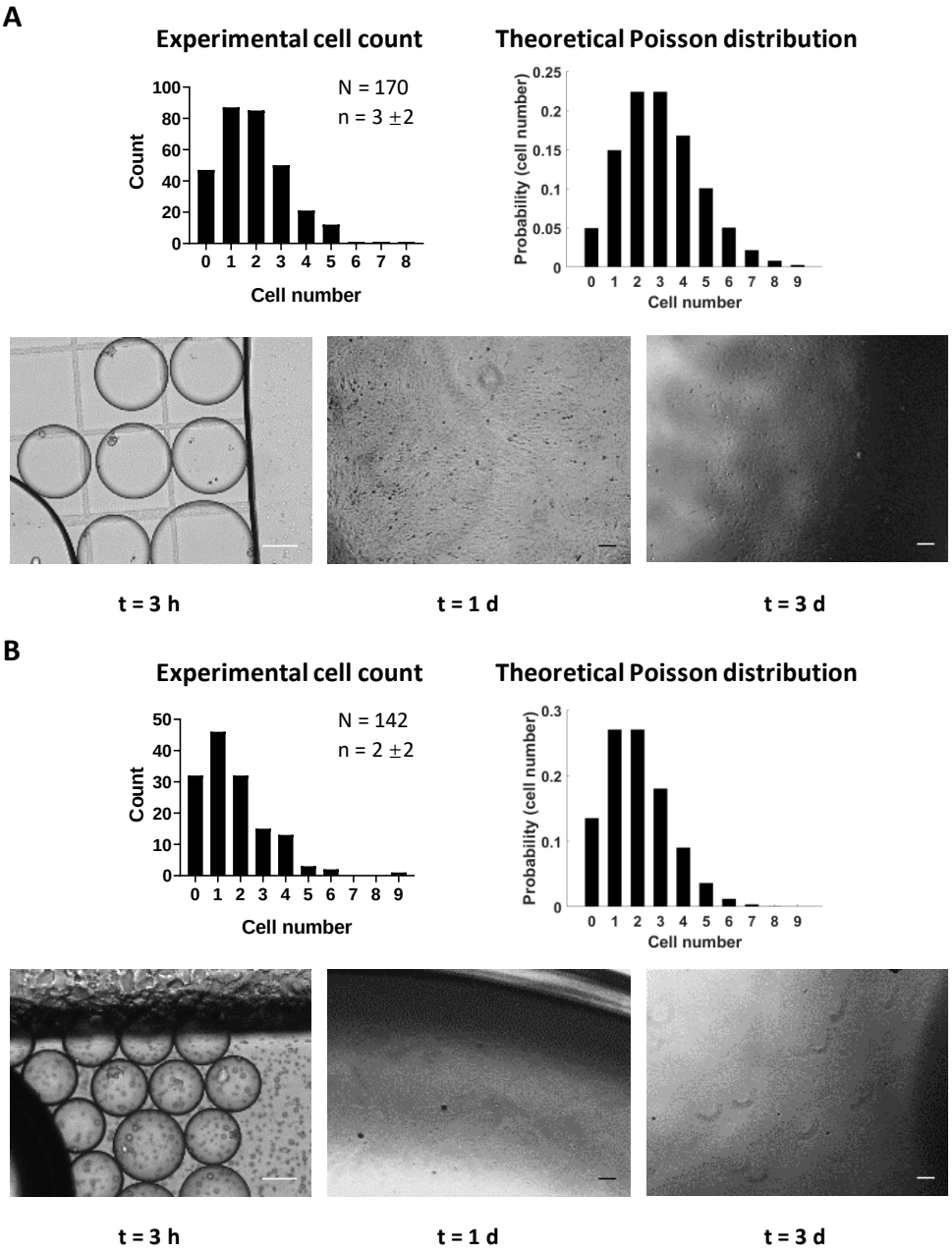

Figure 6.3 Preliminary re-plating experiment with aggregates encapsulated in droplets: (A) ATDC5 cells injected at a density of 2×10^6 cells/ml at flow rates of 25 µl/min (200 µm droplets) and imaged before re-plating after 3 h and at the end of a 14 d culture on well plates for 1 d and 3 d aggregate incubation in microdroplets; (B) Replicate experiment for F78 P1 HBMSCs. Scale bar = 100 µm. Experimental cell encapsulation counts are presented with theoretical Poisson distributions alongside.

A comprehensive colony formation functionality assay for HBMSC aggregates formed in microdroplets was developed using the refined lower threshold of 3 aggregates/well seeding density value as a reference. The assay intended to confirm that the stem cell fraction of the HBMSC aggregates encapsulated in microdroplets retained the ability to form colonies (CFUs) after incubation. Consequently, the assay addressed both cell viability and functionality by means of evaluating cell proliferation from aggregates. 96-well plates were substituted for 6-well plates to

visualise a larger number of colonies for counting. The aggregate seeding density was then adjusted to 30 aggregate/well accounting for larger surface in the new culture plates. Two variables were investigated in the assay: initial cell-seeding density for encapsulation in microdroplets and microdroplet incubation time in chondrogenic differentiation condition. The initial cell-seeding densities comprised 1 million cells/ml (low), 3 million cells/ml (medium) and 5 million cells/ml (high). The usual incubation times (e.g. day 1, day 2 and day 3) were applied for a short-term chondrogenic differentiation assay of aggregates in microdroplets and its impact on each initial cell-seeding density was assessed separately.

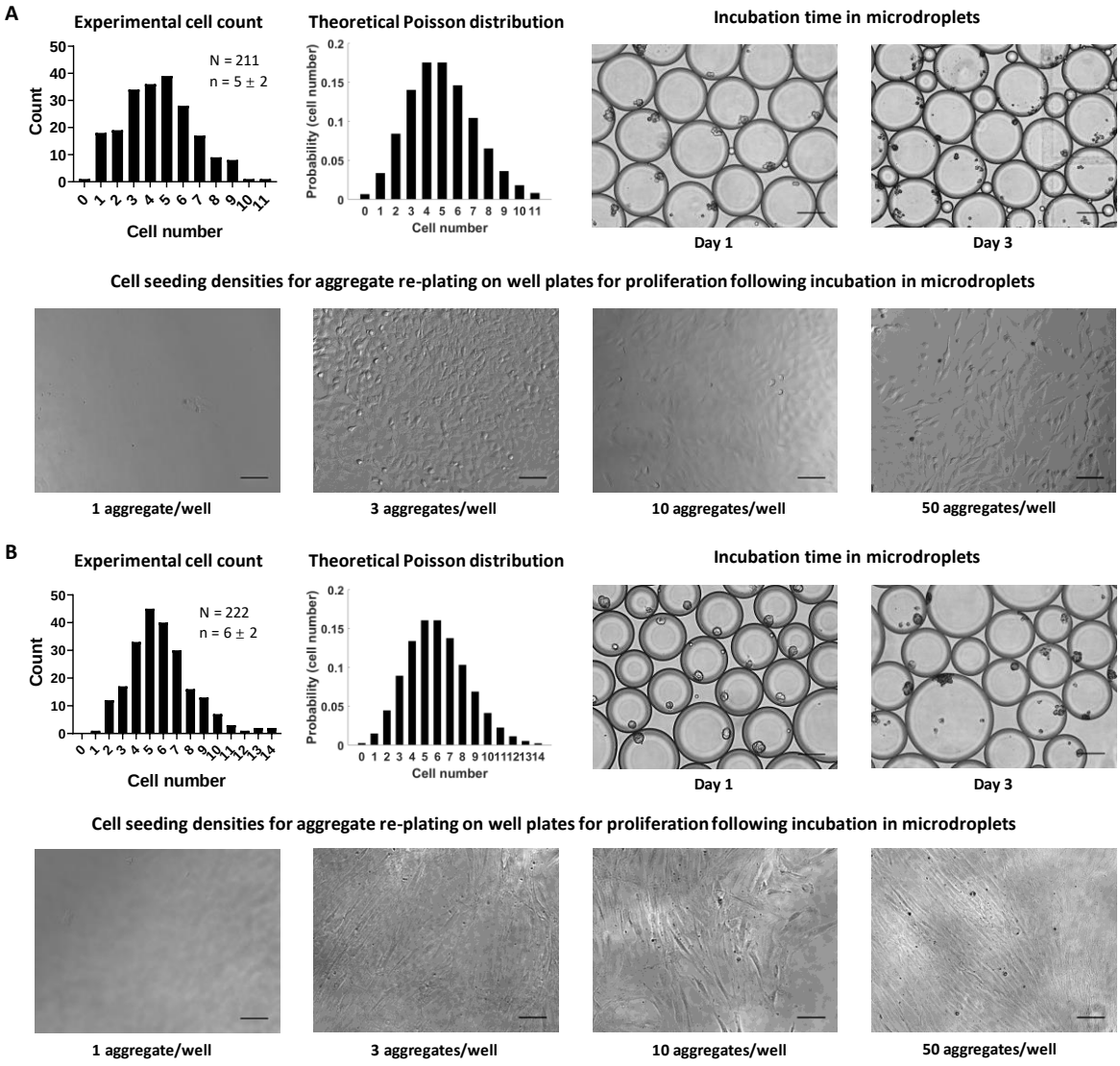

Figure 6.4 Optimisation of aggregate seeding density for re-plating experiment with aggregates encapsulated in microdroplets: (A) ATDC5 cells injected at a density of 3×10^6 cells/ml at a flow rate of 25 µl/min for both aqueous and oil (approximately 200 µm droplet diameter) and imaged in microdroplets following incubation for 1 day and 3 days, respectively. Below are images of cells re-plated after 1 d incubation in microdroplets at different aggregate seeding densities and at the end of a 14-day culture on well plates; (B) Replicate experiment for F78 P1 HBMSCs carried out in parallel and seeded at a density of 5×10^6 cells/ml. Scale bar = 100 µm. Experimental cell encapsulation counts are presented with theoretical Poisson distributions alongside.

The low initial cell-seeding density, 1 million cells/ml, registered an average of 3 cells encapsulated per microdroplets (Figure 6.5). The experimental cell count distribution was close to theoretical Poisson (Figure 6.8) with the exceptions of higher counts measured for droplets containing single cells and for those encapsulating above 8 cells. Small aggregates formed from incubation in microdroplets on day 1.

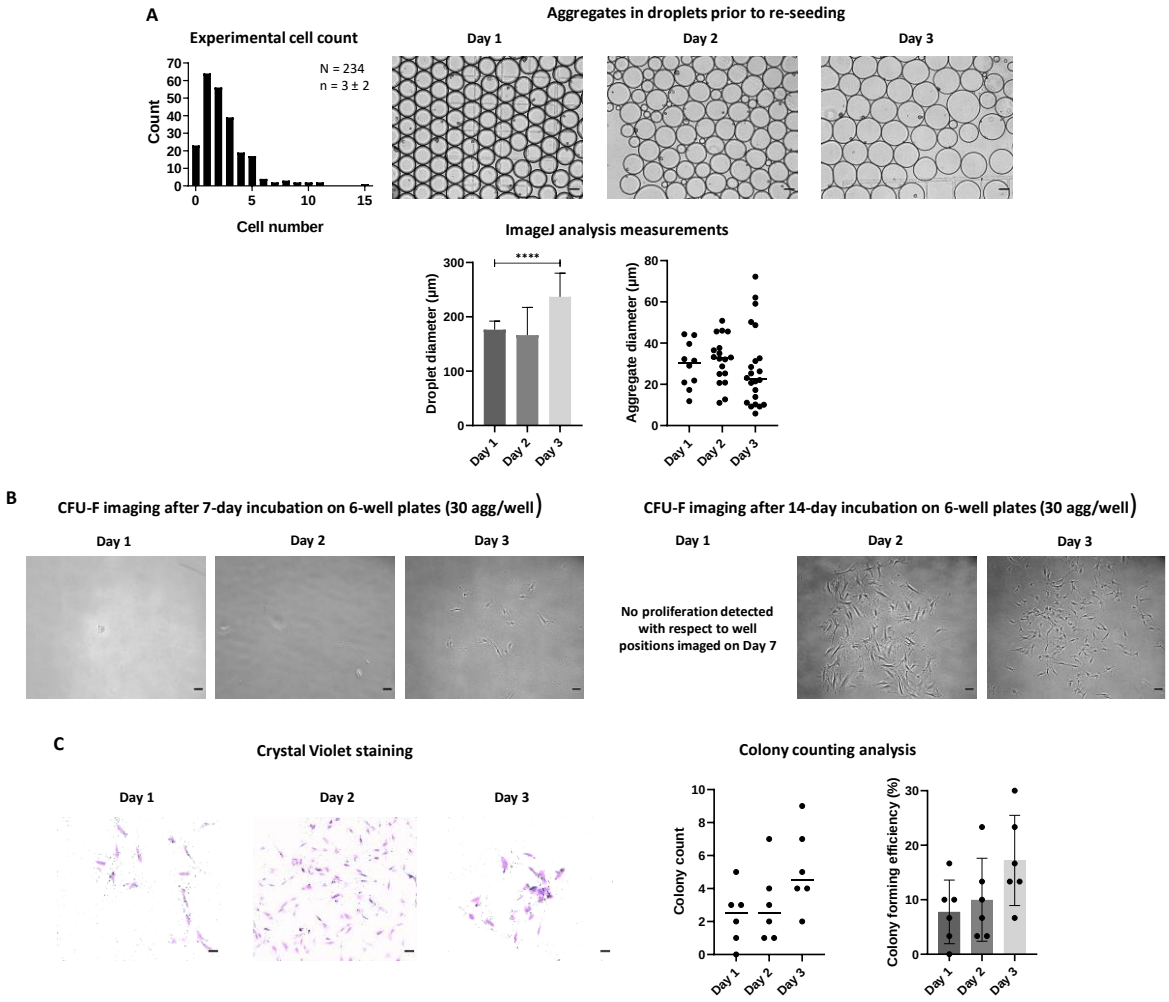

Figure 6.5 Colony formation assay on F69 P2 HBMSCs injected at a cell density of 1 million cells/ml for droplet generation and flow rates of 25 µl/min for both oil and aqueous phases: (A) Aggregates are depicted in microdroplets for the three time points of the study set on day 1, day 2 and day 3 prior to re-plating. Droplet and aggregate diameters were computed using ImageJ analysis; (B) Once re-plated, aggregates were imaged after 7 days and 14 days of culture in basal medium; (C) The colonies were stained with Crystal violet for colony count by eye. Colony forming efficiency was calculated in relation to the theoretical aggregate seeding density (i.e. 30 aggregates/well). Scale bar = 100 µm.

ImageJ measurements on droplets revealed a moderate stability on day 1 (mean droplet diameter of 176.5 µm and a of $CV(\%)$ of 8.8%). Droplet break-up and coalescence were detected from day 2, indicating a decrease in stability over time reflected on higher standard deviation in the droplet diameter plots (mean droplet diameter of 165.5 µm on day 2 and a $CV(\%)$ of 30.7%). Coalescence dominated on day 3, with a statistically significant increase in droplet size (Figure 6.5A,; mean

droplet diameter of 235.8 5 µm on day 3 and a $CV(\%)$ of 18.4%). Mean aggregate diameters remained below 40 µm regardless of incubation time.

When the progress of colony proliferation on day 7 was compared to day 14, no colony growth was detected for day 1 samples imaged after a 14-day incubation with respect to well positions captured seven days earlier. This may respond to an absence of aggregates on the wells captured on day 7 due to difficulties identifying aggregates at this low cell-seeding density. Day 2 and day 3 samples experienced a similar issue although small colonies were visualised on day 14 from the points selected on day 7 (Figure 6.5B). Crystal violet staining of colonies for all three time points showed small colonies grown by day 14. A lower number of colonies resulted on average for day 1 and day 2. It matched the microscopy imaging results where day 3 samples exhibited more noticeable colony proliferation (i.e. colony forming efficiency) (Figure 6.5C). The differences observed may merely be ascribed to sampling during the aggregate re-plating procedure.

The number of cells encapsulated in microdroplets for the intermediate cell-seeding density of 3 million cells/ml increased notably reaching an average of 9 cells (Figure 6.6A). The experimental cell count distribution was slightly skewed to the left compared to the theoretical Poisson distribution (Figure 6.8A). It followed a similar pattern to that observed for the lower cell density resulting in a broader distribution and mentioned in section 6.3.1 (ascribed to higher proneness of HBMSCs to form clusters prior to encapsulation).

Analogous droplet stability kinetics to those described for the lower cell density were observed (mean droplet diameters of 211.1 µm on day 1 and 204.9 µm on day 2; and a $CV(\%)$ of 7.8% and 6.3%, respectively). Droplet break-up was nonetheless predominant on day 3, creating a higher degree of droplet polydispersity derived from metastable incubation and a statistically significant decline in droplet size (Figure 6.6, top; mean droplet diameter of 182.8 µm and a $CV(\%)$ of 28.7%). The average aggregate size measured remained below 40 µm for all incubation times.

The aggregate re-plating experiment showed clear colony formation from aggregates on day 7 and proliferation towards day 14 (Figure 6.6B). The colony counts for all samples based on Crystal Violet staining on day 14 did not expose major differences in terms of colony forming efficiency as a function of aggregate incubation time in microdroplets (Figure 6.6C).

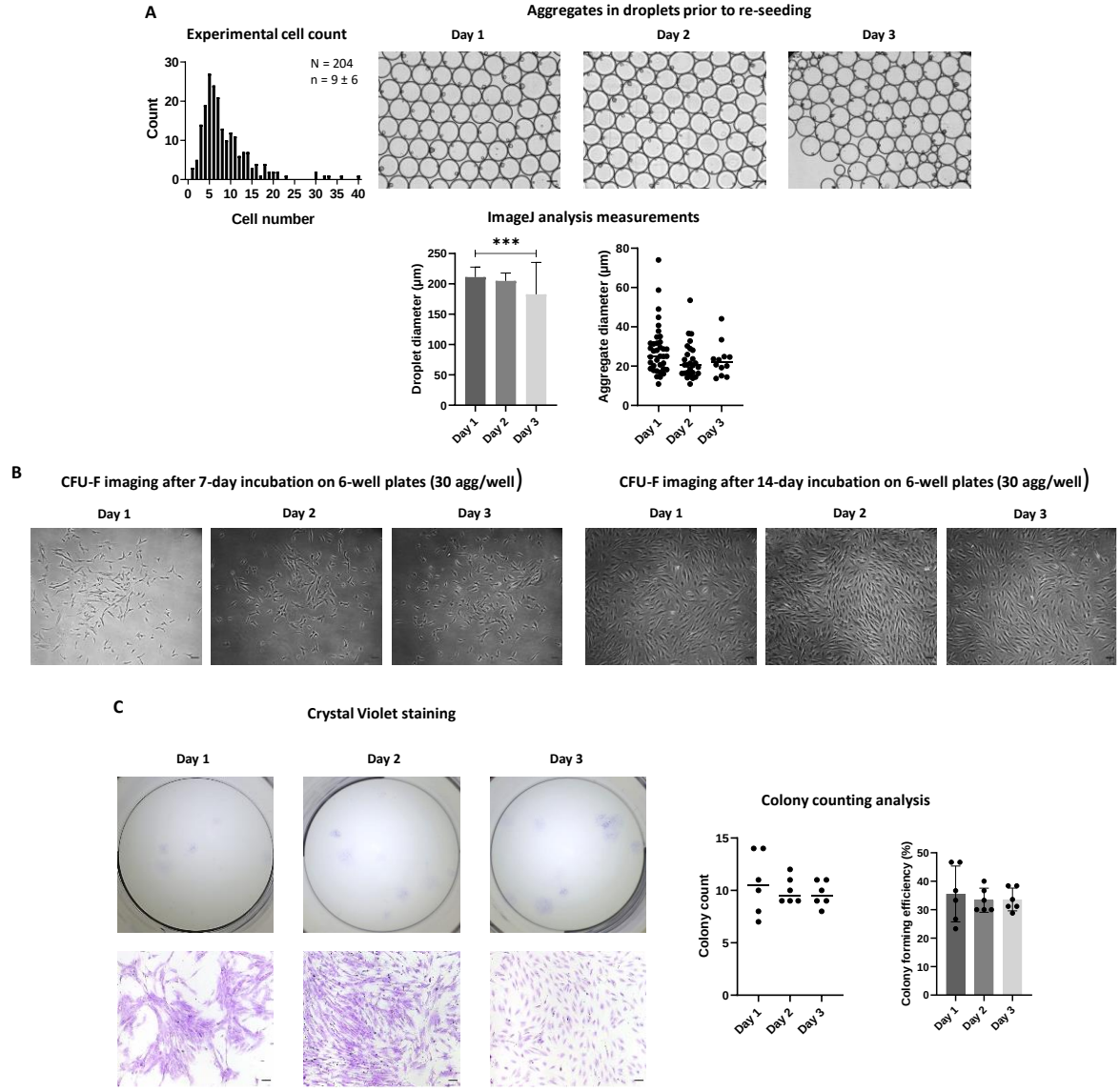

Figure 6.6 Colony formation assay on F51 P1 HBMSCs injected at a cell density of 3 million cells/ml for droplet generation and flow rates of 25 µl/min for both oil and aqueous phases: (A) Aggregates are depicted in microdroplets for the three time points of the study set on day 1, day 2 and day 3 prior to re-plating. Droplet and aggregate diameters were computed using ImageJ analysis; (B) Once re-plated, aggregates were imaged after 7 days and 14 days of culture in basal medium; (C) The colonies were stained with Crystal violet for colony count by eye. Colony forming efficiency was calculated in relation to the theoretical aggregate seeding density (i.e. 30 aggregates/well). Scale bar = 100 µm.

The last and highest cell-seeding density tested was 5 million cells/ml, which achieved the encapsulation of 12 cells per microdroplet on average with a large variation across microdroplets. Again, the experimental cell count distribution matched the previous trends reported for lower cell densities. Similarly, the expected tendency towards slight instability rise over incubation time for aggregates in microdroplets from day 1 to day 3 was perceived through the increase in small droplets originated from droplet break-up and the statistically significant decrease in droplet size by day 3 (Figure 6.7, mean droplet diameters of 277.9 µm on day 1, 259.2 µm on day 2 and 214.18 µm on day 3; with a $CV(\%)$ of 9.1%, 15.2% and 36.1%, respectively). Aggregate sizes were above 40 µm and displayed a wide range. The maximum size registered exceeded 100 µm, which was

slightly above the 80 µm diameter reached for lower cell densities. The colony formation assay and the colony counts displayed similar outcomes to the intermediate 3 million cells/ml density irrespective of incubation time in microdroplets (Figure 6.7).

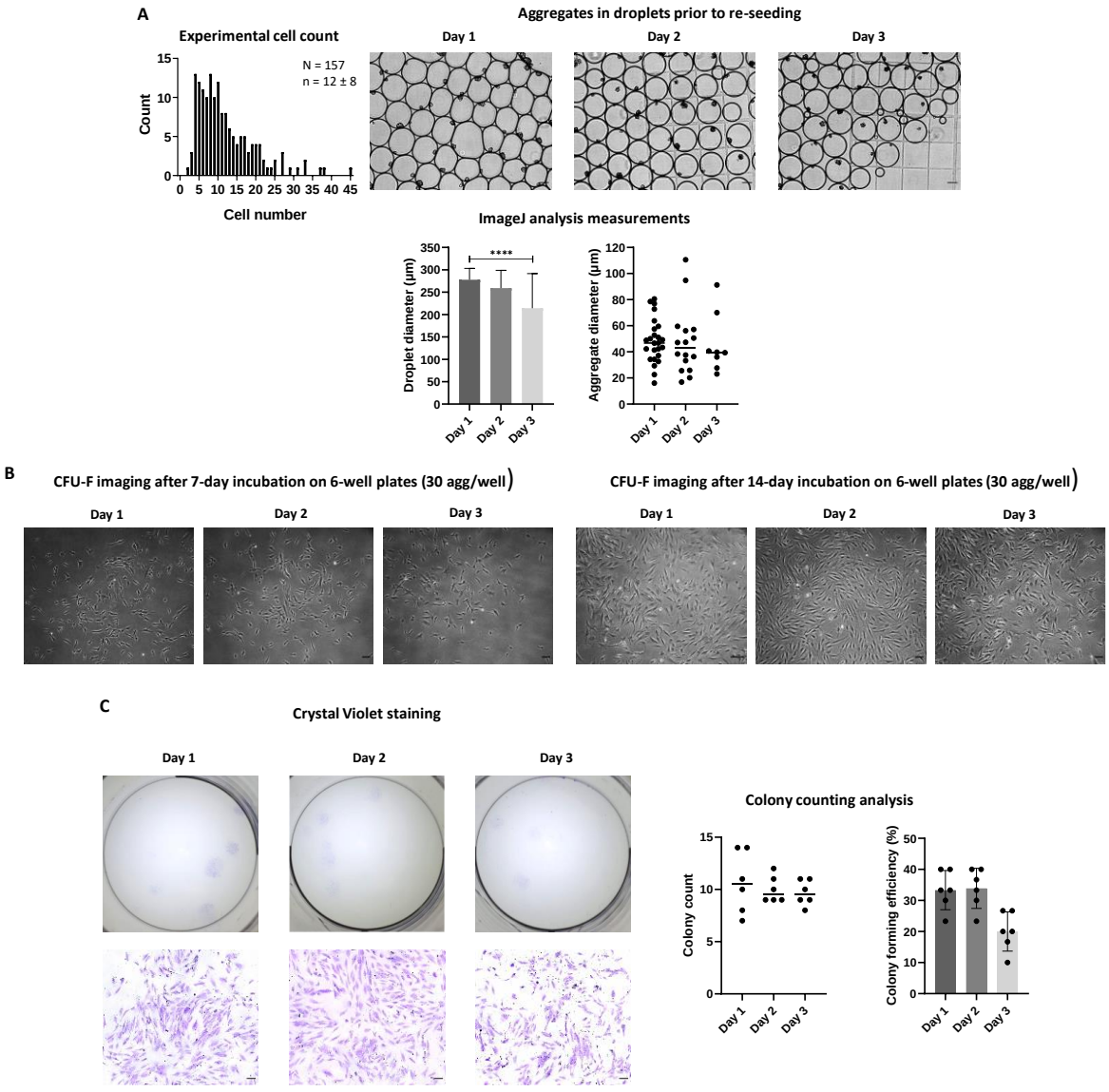

Figure 6.7 Colony formation assay on F51 P2 HBMSCs injected at a cell density of 5 million cells/ml for droplet generation and flow rates of 25 µl/min for both oil and aqueous phases: (A) Aggregates are depicted in microdroplets for the three time points of the study set on day 1, day 2 and day 3 prior to re-plating. Droplet and aggregate diameters were computed using ImageJ analysis; (B) Once re-plated, aggregates were imaged after 7 days and 14 days of culture in basal medium; (C) The colonies were stained with Crystal violet for colony count by eye. Colony forming efficiency was calculated in relation to the theoretical aggregate seeding density (i.e. 30 aggregates/well). Scale bar = 100 µm.

On a general note, an increase in droplet size in connection with higher cell-seeding densities was quantified as concluded from the droplet diameter measurements from day 1 (when incubation-related instabilities had the least effect). Droplet diameters within a day of encapsulation thus changed from 176.5 µm for the low 1 million cells/ml seeding density to 211.1 µm for the intermediate 3 million cells/ml seeding and peaked at 277.9 µm for the high cell-seeding density (i.e. 5 million cells/ml). This observation would agree with what would be expected from cell

suspensions that become more viscous for higher cell-seeding densities (per ml). Aggregate diameters did not undergo substantial changes as a result of incubation time for any of the cell densities assayed, suggesting the exclusion of coalescence as a major issue affecting aggregate development and functionality. Among the cell-seeding densities tested evaluated in these assays, 3 million cells/ml offered a balanced cell encapsulation efficiency (approximately 10 cells per droplet) coupled with droplet stability for the short-term incubation times of interest (up to 3 days) and was the density taken forward for biological characterisation of aggregates.

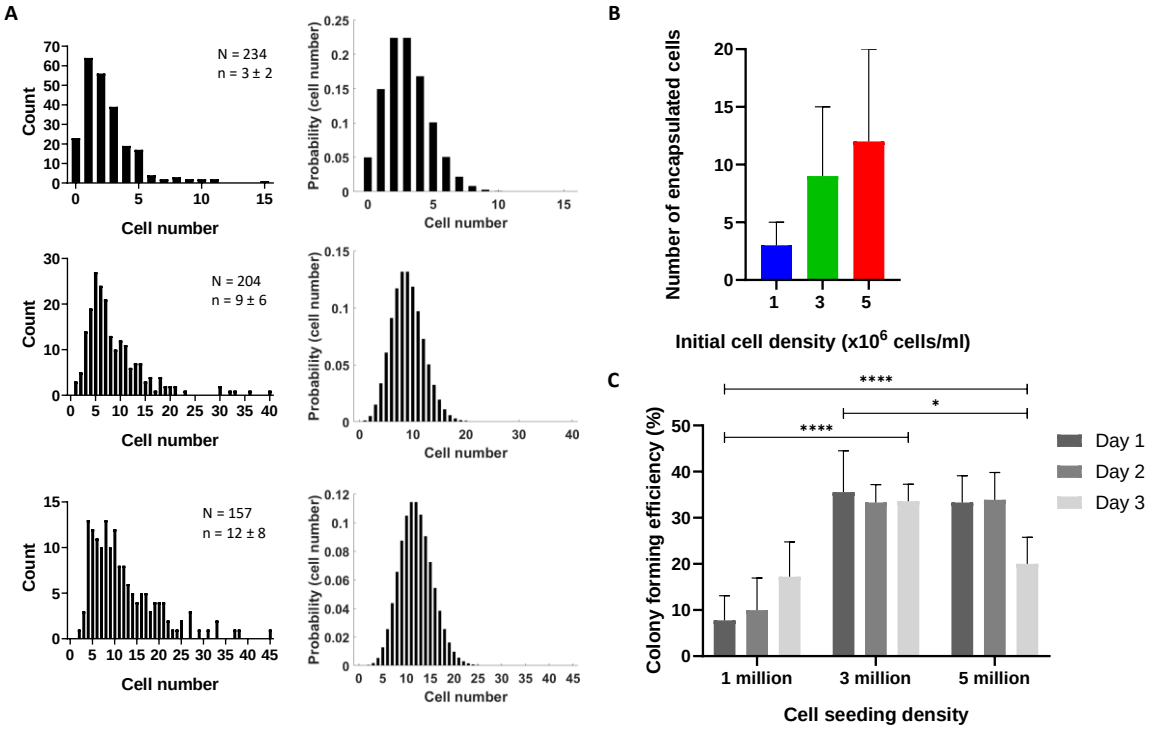

Figure 6.8 Global summary of quantitative findings from colony formation functionality assay: (A) Experimental cell counts for each cell-seeding density (left) and their corresponding theoretical Poisson distribution plots (right); (B) Number of cells encapsulated in 200 µm microdroplets for each of the cell-seeding densities used in the study; (C) CE (%) analysed by including the combined effect of the two variables in the assay, namely cell-seeding density and incubation time in microdroplets.

The series of colony formation assays presented for the three cell-seeding densities tested allowed to draw a series of conclusions about functionality of aggregates formed in microdroplets. The improvements in the microfluidic cell injection protocol facilitated the generation of highly stable microdroplets. They involved a subsequent upgrade of the cell encapsulation capabilities available thus far using the *standard* soft lithography chip design. More promising ranges of cells that could be encapsulated comprised anything from single cells to approximately five cells for the lower cell densities; and up to about 10 and 20 cells for the intermediate and high cell densities, respectively (Figure 6.8A and B). Finally, colony forming efficiency did not vary as a result of longer incubation time in microdroplets up to 3 days of culture (Figure 6.8C). This finding agreed with previous viability

assays and implied that any of the time points employed was a reasonable experimental variable for further biological characterisation without compromising aggregate functionality.

6.3.3 Biological characterisation of aggregates: *SOX9* mRNA expression quantification and whole mount fluorescence immunostaining

The aggregate functionality results in the previous section paved the way to test the hypothesis that *SOX9* expression was upregulated in small cell aggregates self-assembled in microdroplets. The intermediate cell-seeding density (i.e. 3 million cells/ml) was fixed for this assay to exclude the contribution of single cells. In addition, this number restricted the quantification to small aggregates below attainable numbers *in vitro* on well plates.

Frame-by-frame manual analysis of high-speed videos from droplet generation and cell encapsulation distinguished cells encapsulated in microdroplets within a range from 2 to 14 cells and an average of 7 cells per microdroplet (Figure 6.9A).

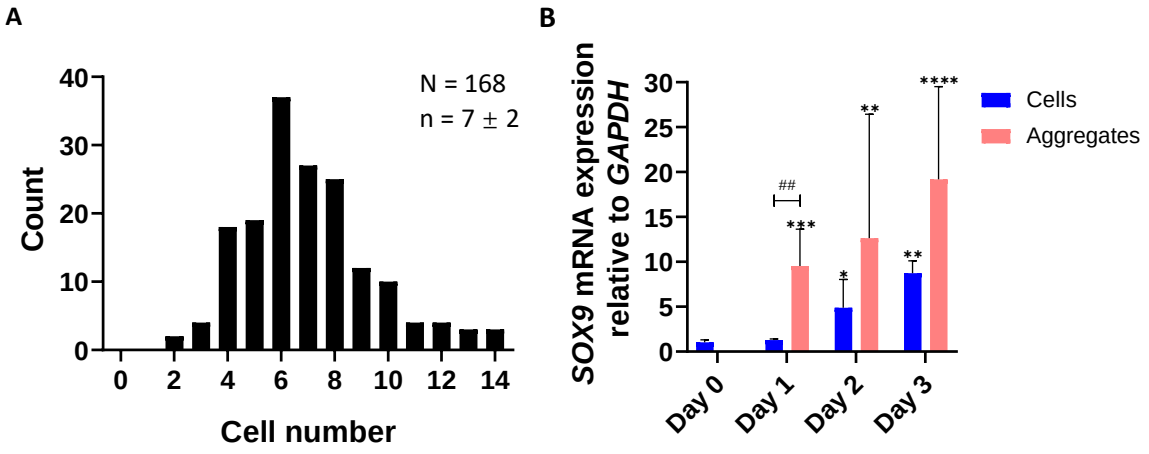

Figure 6.9 SOX9 gene expression quantification in M58 P2 HBMSC aggregates formed in microdroplets: (A) Number of cells encapsulated in microdroplets for a density of 3 million cells/ml; (B) *SOX9* mRNA expression relative to *GAPDH* housekeeping gene in short-term chondrogenic differentiation conditions comprising 3 days of culture. Cells harvested from tissue culture flasks were taken as the day 0 control with no chondrogenic stimulations. Cells cultured in monolayer and cell aggregates incubated in microdroplets were assayed on day 1, day 2 and day 3. Statistical significance symbols depicted respect GraphPad Prism convention: * ($p \leq 0.05$), ** ($p \leq 0.01$), *** ($p \leq 0.001$), **** ($p \leq 0.0001$) between different conditions and the day 0 control; and ## ($p \leq 0.01$) between monolayer cells and aggregates for a set time point. The absence of symbols between groups indicates no significance. The statistical analysis was performed using Tukey's multiple comparisons test Two-way ANOVA on ΔC_t values.

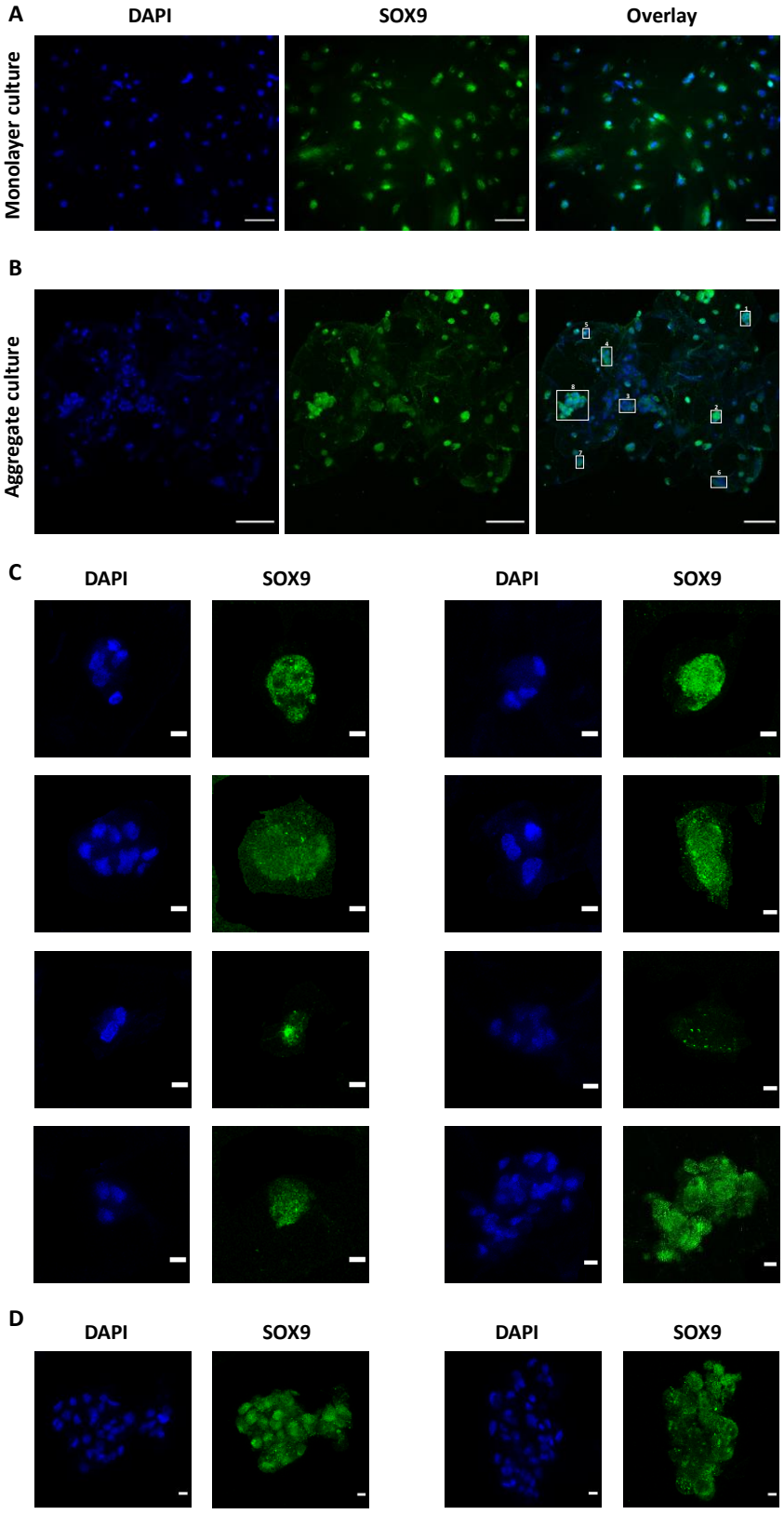

Figure 6.10 SOX9 IF staining of cells cultured in monolayer and aggregates recovered from microdroplets after one day of incubation in chondrogenic differentiation conditions: (A) Cells cultured in monolayer stained for SOX9 and counterstained with DAPI at a seeding density of 50000 cells/well (n = 3); (B) Aggregates generated from an initial seeding density of 3×10^6 cells/ml stained for SOX9 and counterstained with DAPI. Scale bar = 100 µm; (C) Magnified images of eight aggregates highlighted in (B) illustrating SOX9 heterogeneity. Scale bar = 10 µm; (D) Additional magnified images of larger aggregates as part of the aggregate culture staining. Scale bar = 10 µm.

RT-qPCR analysis of those aggregates and cells in monolayer culture in chondrogenic differentiation conditions identified *SOX9* upregulation for aggregates with respect to the control day 0 sample regardless of incubation time in microdroplets. Even if higher SOX9 expression was also measured for aggregates compared to monolayer cells on each incubation time, the difference was only significant on day 1 due to larger variability among replicates on day 2 and day 3 (Figure 6.9B). Importantly, these results supported the central hypothesis of aggregation inducing higher *SOX9* expression in small aggregates formed in microdroplets and the interest of studying chondrogenesis and HBMSC purification in this culture format.

To evaluate SOX9 expression on a protein level and to examine whether SOX9 heterogeneity was discernible in early chondrogenic differentiation of aggregates from microdroplets, aggregates were stained for SOX9 alongside monolayer cells after a day of chondrogenic induction (Figure 6.10). This time point was studied given the significant *SOX9* upregulation measured by RT-qPCR analysis. Fluorescence immunostaining of monolayer cells showed a strong correlation between DAPI-counterstained nuclei and SOX9 (Figure 6.10A). Aggregates cultured in microdroplets were overall expressing SOX9 localised around the cell nuclei (Figure 6.10B). The fluorescence intensity was variable among aggregates regardless of cell number, which may be indicative of existing heterogeneities in SOX9 expression (Figure 6.10C and D). Fluorescence immunostaining of aggregates recovered from microdroplets agreed with RT-qPCR data suggesting that SOX9 is expressed from the onset of chondrogenic differentiation and is detectable within the first day of culture.

On the whole, the droplet microfluidic system developed in this work provided a simple platform to stimulate cell condensation in individual compartments for high-throughput biological characterisation. It enabled examination of SOX9 during the early stage of chondrogenic differentiation and showed that SOX9 could be a candidate marker for sorting of aggregates due to its heterogeneous expression pattern.

6.4 Discussion

This last chapter unified the knowledge acquired in the previous chapters regarding chondrogenic differentiation in multicellular spheroids, SOX9 as a functional marker linked with aggregation and optimisation of a droplet microfluidic platform for high-throughput encapsulation of cells. The first essential requirement was to demonstrate spontaneous cell aggregation in microdroplets as the biological function that could be assessed via *SOX9* quantification. Relevant aspects of these small cell aggregates such as viability and subsequent functionality necessarily had to be validated on set time points in short-term chondrogenic differentiation cultures. The final paramount research question was whether aggregation was indeed accompanied by *SOX9* upregulation compared to other culture methods like monolayer culture. It sought to gauge the benefit of harnessing cell aggregates as units with higher SOX9 expression that could be more useful for sorting of chondroprogenitors with better prospects for robust cartilage generation than single cells.

Cells started to self-assemble into aggregates minutes after encapsulation due to their confinement in a limited space encouraging cell-cell interaction and there was evidence of compact spheroids 3 hours following incubation in normoxic conditions. The *standard* soft lithography designs was effective for cell loading and short-term microdroplet culture as demonstrated in viability assays and more robustly in colony formation and proliferation assays. New modifications in the device fabrication, surfactant system and microfluidic operation steps accomplished droplet stability and homogenisation of cell suspensions in syringes leading to improved cell encapsulation efficiencies. HBMSC encapsulation efficiencies achieved concluded that aggregates in the range from 3-5 cells up to 20-25 cells per droplet could be formed and grown for initial cell-seeding densities of 1 million cells/ml up to 5 million cells/ml. HBMSCs aggregates were successfully recovered from droplets and proliferated following re-seeding on well plates in preliminary studies. HBMSCs later demonstrated maintained colony formationfunctionality when re-plated from aggregates incubated in short-term chondrogenic differentiation cultures for up to 3 days. In addition, HBMSC aggregates self-assembled in microdroplets yielded higher *SOX9* expression than cells cultured in monolayer. This finding could be promising for future sorting of aggregates for chondrogenesis following the development of sensitive techniques for live SOX9 monitoring in cells and cell aggregates.

6.4.1 Cells self-assembled into aggregates within microdroplets following incubation

The process of encapsulating cells in microdroplets for cell aggregation into multicellular spheroids alone has proven technically challenging because of the need to address aspects such as droplet incubation reservoirs, droplet stability and throughput. Evidence of active cell aggregation in microdroplets was obtained subsequent to the modifications in the device fabrication and

treatment protocol covered in section 5.2.2. The changes involved PDMS chips with soft lithography channel designs and silanisation surface treatment along with plasma bonding to glass slides. Soft lithography designs coupled with Bio-Rad QX200^{TM} droplet generation oil were able to generate more monodisperse droplets where aggregates formed before an hour of incubation that were highly compact after three hours.

Aggregation was confirmed for HBMSCs despite underperforming cell encapsulation in microdroplets. This signified that the cell numbers counted in the droplets were below what was expected from the initial cell-seeding densities. The modifications below served to attain higher cell numbers encapsulated and to improve droplet stability:

- Centrifugation cycle adjustment for maximised recovery of pelleted cells before thoroughly resuspending them in 1 ml chondrogenic differentiation medium and loading cells in the syringe.
- Fixed attachment of the microfluidic device onto the microscope plate during operation.
- Homogeneous stirring of cell suspension while injecting into the droplet microfluidic device using 2 PTFE Encapsulated Samarium Cobalt stir discs (5 mm diameter) and a Magnetic Tumble Stirrer at a speed no faster than 30 rpm to exclude damage to cells. This method was analogous to that proposed by Lagus and Edd to prevent and/or delay cell clumping inside syringes during injection (Lagus and Edd, 2012).
- Droplet incubation in closed tubes and removal of the mineral oil layer that had originally been placed above the droplet suspension in oil.
- Use of fresh batches of Bio-Rad QX200^{TM} droplet generation oil less than 3 months to prevent stability loss.

Cell aggregation in microdroplets was assessed at early time points before 2 hours on ATDC5 and HBMSCs. The images on haemocytometers containing sampled droplets showed that aggregation was a cell number-dependent process that can occur minutes after encapsulation and enhanced by droplet sphericity and cell-cell contact in a confined volume. Notwithstanding, cells formed aggregates for all the cell-seeding densities included in the study (from 1 to 5 million cells/ml) and aggregates became compact within 3 hours. A similar timeline for cell aggregation in spherical microdroplets was reported by Chan, who established that compact aggregates formed within 150 min of cell encapsulation (Chan et al., 2013).

Time-lapse analyses of cell aggregation in microdroplets demonstrated that cell confinement in a reduced space within spherical droplets and small volumes prompted cells to self-assemble into aggregates as early as hours after encapsulation, hence confirming the initial hypothesis. This timeline for aggregation was compatible with the aim of incubating aggregates in microdroplets for

short periods of time. It fell under the premise that an accelerated cell aggregation given by an intensified cell-cell interaction may upregulate SOX9 expression in small aggregates at earlier time points. SOX9 would then become quantifiable for sorting provided that the aggregates remained viable and functional during short-term culture in microdroplets.

6.4.2 High-throughput cell encapsulation in soft lithography standard chips and off-chip incubation in microcentrifuge tubes enabled droplet stability and successful recovery for analysis

Cell loading in microdroplets was taken as the gold standard to judge whether the soft lithography chip designs characterised in section 5.3.3 were indeed able to host viable and functional cell aggregates. Prior to performing any analysis on the aggregates, the droplets necessarily had to be stable for the intended period of incubation (e.g avoiding undesired merging) and recovered at sufficient yield for analysis. QX200^{TM} droplet generation oil succeeded in providing a sustained stability for three days of culture with minimal sources of instability. Droplet recovery with PFO was a rapid single emulsion method that allowed to harvest hundreds of aggregates for cell functionality assays and thousands of them for RT-qPCR analysis in aggreement to the microfluidic high-throughput capabilities.

Droplet observation was carried out analogous to conventional cell counting by means of Fast-Read haemocytometers. As an off-the-shelf alternative, they facilitated rapid imaging although the background interference and optical conditions were at times hampering clarity and contrast to focus on identifying cells and aggregates. The experiments and statistics in this work were based on hundreds of droplets/aggregates because multiple time points were assessed from an original single cell suspension, which contained thousands of aggregates. In some of the measurements with Fiji ImageJ analysis, the outlines created due to the optics and the haemocytometer background when capturing images may distort droplet dimensions slightly. The aggregate measurement was partly manual and dependent on thresholds set that were not optimal for every aggregate in the image. Droplets are 3D environments where aggregates can sit on different focal planes and haemocytometer imaging is 2D. Confocal imaging can help to solve this issue yet there is not a strong case for its practicality on a routine basis. In addition, droplet arrays in haemocytometers were constrained by the space available in each chamber; hence outlining a possible route for optimisation in finding more powerful tools to capture thousands of droplets at a time (e.g. by fabricating modified hydrophobic glass slides for droplet imaging in a monolayer over a larger surface than that of haemocytometers) (Bartkova et al., 2019).

The progress made on scrutinising the variables and the merging issues discussed in Appendix D.1 and D.2 was crucial to redirect the droplet microfluidic strategy from on-chip incubation towards off-chip droplet collection and storage. Unlike chamber designs that can anchor droplets and aggregates for on-chip incubation and screening (Occhetta et al., 2015, Sart et al., 2017), off-chip storage in microcentrifuge tubes offered a simpler and higher throughput alternative for short chondrogenic differentiation cultures. For the purpose of studying early *SOX9* expression in aggregates, microdroplet incubation lasted no longer than three days. Moreover, droplet recovery was a straightforward process involving direct contact of the droplet suspension in oil containing surfactant with PFO. Overall, off-chip culture of microdroplets served to increase the throughput from each cell suspension injected beyond the numbers attainable on a microfluidic chamber chip design bonded to a glass slide (thousands compared to hundreds). With these numbers, additional droplet analyses and biological assays became realisable via microfluidic devices.

Cells tendency to self-assemble into aggregates in droplets was the key empirical finding demonstrating the high-throughput capabilities of the microfluidic device. Cell number per microdroplet had an effect on aggregation on the basis that higher cell numbers are expected to encourage aggregation kinetics due to augmented cell-cell interactions. Nevertheless, compact aggregates were routinely visualised after overnight incubation of droplets for all initial cell-seeding densities and cell types analysed in this study.

The *standard* chips complied with the anticipated theoretical Poisson non-deterministic cell encapsulation as a consequence of the passive droplet generation method (i.e. driven by external pressures applied by syringe pumps). This implied that the number of cells per microdroplet was not adjusted. As opposed to the majority of cell encapsulation applications that follow this pattern, other alternatives have been attempted to attain control over the cell number being encapsulated with a focus on ensuring single-cell occupancy in droplets (Kemna et al., 2012, Schoeman et al., 2014, Collins et al., 2015). Inertial cell ordering fits in this context as a strategy that could be delivered by a *spiral* design such as the one characterised in the previous chapter. Higher velocities and flow rates than the ones used in this research work for cell encapsulation would be required for this purpose and it would entail overcoming technical limitations. Such limitations would be related to finding a set of flow parameters that enable inertial cell ordering while encapsulating a sufficient cell number for the formation of aggregates that can trigger a detectable chondrogenic response. This was not deemed a primary objective of this particular project although it could be key if a specific cell number were found to be more adequate for cell sorting in chondrogenesis as part of a future line of research.

Furthermore, the trade-off between droplet size (considering the effect of initial cell-seeding density on the number of cells encapsulated per microdroplets and their viability) and stability must be taken into account. Pressure drops scale inversely with droplet radius and act in favour of droplet merging. According to Young-Laplace equation applicable both in the microscale and the nanoscale (Liu and Cao, 2016):

$$\Delta p = \gamma \left(\frac{1}{R_1} + \frac{1}{R_2} \right) \tag{6.3}$$

where Δp is the pressure difference between the aqueous and oil phase, γ is the liquid surface tension, R_1 is the radius of curvature of the aqueous phase and R_2 corresponds to the radius of curvature of the oil and surfactant mixture.

Biocompatible surfactants are required to preserve individual droplets and cell aggregates within separate culture microenvironments by reducing surface tension. The degree of biocompatibility of a surfactant in fluorinated oils like FC40 relies on the presence of PFPE tail groups that may appear alone or in combination with other groups such as polyethyleneglycol (Baroud et al., 2010, Seemann et al., 2011, Lagus and Edd, 2012). The preliminary application of the in-house Soton2 surfactant exposed limitations in terms of cell viability beyond one day of culture with appreciable loss over time. Pico-Surf™ is a commercial surfactant that has gained recently gained endorsement in cell-based droplet microfluidics by reason of biocompatibility (Shih et al., 2015, Hosokawa et al., 2017, Li et al., 2017). Nevertheless, the high cost of the commercial Pico-Surf™ 1 and the results from the tensiometer surfactant performance test in section 5.3.2 served to exclude it from cell encapsulation studies in microdroplets. QX200™ droplet generation oil which had been proved to display the best stability performance was validated functionality assays for the droplet size and seeding densities in the study. The oil and surfactant system stability of droplets was maximum at the interface with the oil and the droplets on the top layers remained susceptible to coalescence to a small extent owing to prolonged exposure to atmospheric pressures.

Double emulsions (water-in-oil-in-water) have been reported as microenvironments to promote HBMSC aggregation in an aqueous phase for improved droplet stability (Chan et al., 2013). Unlike the simple methodology described in this chapter, aspects such as microfluidic device preparation; droplet generation; encapsulation efficiency and aggregate recovery for analysis would gain extra complexity. Single emulsions were on the whole a straightforward and effective system that facilitated conducting high-throughput biological assays on easily manipulable cell aggregates within an acceptable degree of stability.

The off-chip droplet incubation technique employed to form aggregates in stable microdroplets left droplets readily available for aggregate characterisation on up to thousands of aggregates at a time.

Droplet recovery with PFO took place in a matter of seconds and its effectiveness increased for small volumes by keeping a ratio close to 1:1 with the droplet generation oil. In summary, this rapid and simple droplet incubation system can be expanded to other biological applications that can benefit from large numbers of small replicates such as immunostaining and sorting of aggregates for prospective isolation of subpopulations of interest and subsequent growth of tissue constructs.

6.4.3 Cells encapsulated within microdroplets were viable and retained colony formation functionality in short-term chondrogenic culture conditions

Having optimised the microfluidic chip design, surfactant formulation and fabrication method as detailed in the previous chapter, the *standard* soft lithography design was employed for the purpose of cell encapsulation. The resolution for all dimensions was greatly improved compared to former 3D-printing designs (Sahin et al., 2018). Viability assays (see Appendix D.3.2) were complemented with more robust functionality assays to verify that aggregates maintained their ability to grow in colonies following culture in microdroplets. In that regard, the optimal aggregate seeding density was first established in preliminary studies and then validated after adjusting for the colony formation assays (i.e. 30 aggregates/well on a 6-well plate). Initial cell-seeding density injected into the microfluidic devices was the other variable to investigate. The low value, 1 million cells/ml, was outperformed by the intermediate and high density values (3 and 5 million cells/ml, respectively) in terms of reliable colony proliferation and efficiency counts. Variability found in colony counts for the low cell-seeding density may reflect that low numbers were more prone to be affected by sampling errors. In addition, those small aggregates (and even single cells) might have been composed of other adherent cells that lacked colony formation ability. Colony formation assays had two main advantages over former viability assays. Firstly, they quantified proliferation through the colony counts and the colony forming efficiency calculations derived from them. This provided a more complete piece of information regarding HBMSC aggregate functionality beyond assessing whether or not cells were viable from the detection of the fluorescence signal emitted upon excitation of a viability staining. Secondly, colony formation assays compared the performance of different initial cell-seeding densities injected for encapsulation in microdroplets. That comparison was instrumental to establish that 3 million cells/ml was a promising value for further biological characterisation of cell aggregates.

To the best of the author's knowledge, colony formation assay has not been reported as yet in cell aggregates cultured in microdroplets. There is nonetheless experimental confirmation of viability in HBMSC aggregates for comparable cell-seeding densities, droplet sizes and short periods of incubation (Chan et al., 2013, Occhetta et al., 2015, Sart et al., 2017). These studies detected a gradual yet small reduction of viability over three days of culture, which would be expected from

aggregates confined in small volumes (nanolitre scale). This observation was not directly assessed in this work but the instability-related issues (e.g. droplet coalescence and break-up) in the system, support the claim that this system is appropriate for short-term culture up to three days. The duration of droplet incubation would ideally not exceed this period based on validated aggregation functionality given the absence of a mechanism to change media for simplicity purposes. The results of the colony formation assay went beyond viability assays to confirm that no significant reduction in proliferation occurred during the incubation of 200 µm droplets containing an average of 12 cells and a maximum of approximately 45 cells.

All in all, both viability and functionality assays proved the essential requirement from this microfluidic approach for the purpose of this research project of viable cell aggregates that retained colony formation functionality in microdroplets. Small functional aggregates recovered from microdroplets were a promising substrate for further high-throughput biological characterisation of live HBMSCs.

6.4.4 *SOX9* was upregulated in microaggregates encapsulated in microdroplets compared to cells cultured in monolayer when stimulated in chondrogenic conditions

Throughout this research project, a platform for cell aggregation in microdroplets was developed in parallel with chondrogenic differentiation of multicellular spheroids from large aggregates to the microscale. HBMSCs exhibited heterogeneous chondrogenic differentiation ability across all cell numbers that was reflected on their tissue morphology and more relevantly, SOX9 expression patterns. The aggregation phenomenon was considered a necessary stimulus to drive SOX9 expression early during chondrogenic differentiation and SOX9 was defined as a functional marker for chondrogenesis. The last experiment with aggregates encapsulated in microdroplets pursued the existing relationship between aggregation of a very small number of cells (about 10) and *SOX9* expression. This approach was in line with the characterisation of SOX9 expression across various cells numbers from large spheroids down to small spheroids conducted in Chapter 3. It revealed that the predominant level of heterogeneity for small 500 cell spheroids was cell-cell heterogeneity within each of the spheroids. Simultaneously and as a consequence, it raised a question to explore: i) whether the role of every individual cell within an aggregate gained more importance as the aggregate size decreased, and ii) whether SOX9 could be a predictive marker for chondrogenesis reflecting this phenomenon. If confirmed, it would be a key indication of significant promise for sorting chondroprogenitors as a function of *SOX9* expression by scaling down the cell number while taking advantage of high-throughput from droplet microfluidic generation.

HBMSC aggregates indeed expressed higher *SOX9* mRNA levels compared to reference control cells grown in monolayers over the same time frame. This result agrees with other work in the literature pointing to aggregates expressing more *SOX9* than single cells that are subject to less direct cell-cell interactions (Moreira Teixeira et al., 2012, Leijten et al., 2016). Importantly, it adds a remarkable contribution in that it involves even smaller cell groups that are of particular interest for the ultimate goal of cell sorting. The variabilities observed among replicate samples in the RT-qPCR analysis may indicate that there may be an additional benefit from sorting aggregates with high *SOX9* expression and the whole mount immunofluorescence images of aggregates stained for SOX9 point to the same direction.

In addition, the cell aggregates allowed *SOX9* upregulation to be detected notably earlier than cells grown in monolayer conditions from the first day of culture (with a significant difference quantified at that time point). This provides a strong validation for the main project hypothesis by establishing the necessity of an aggregation-inducing platform for an early functional assessment of a chondrogenic phenotype. Such an early *SOX9* upregulation in aggregates exposes the possibility that HBMSC chondroprogenitors could be detected and isolated after a very short exposure to chondrogenic induction. In fact, SOX9 was also expressed on a protein level at that time point in aggregates recovered from microdroplets, yet not without variability in fluorescence intensity. Early *SOX9* expression kinetics in HBMSC aggregates has not been thoroughly investigated and no evidence has been found of its temporal pattern at the time frame included in this work. SOX9 upregulation has been reported as after 20 h of chondrogenic differentiation of micromasses formed of mesenchymal cells extracted from the distal subridge region of stage 24/25 chick embryo wing buds (Kulyk et al., 2000). Neither this study nor the ones mentioned above, however, describe significant upregulation relative to other conditions (i.e. basal culture) at this early time point, using these small cell numbers and achieving such sample throughput for analysis.

In brief, cell aggregates have the potential to perform as vessels for analysis of differentiation markers in a high-throughput manner as mediated by droplet microfluidic platforms. The findings in this chapter endorsed the main project hypothesis suggesting that a sorting strategy for chondroprogenitors could be developed based on SOX9 as a functional marker on HBMSC aggregates. This sorting strategy would depend on a reliable live imaging and monitoring technique that could be compatible with subsequently enquiring into the cartilage regeneration ability of sorted aggregates.

6.4.5 Conclusions

Cell encapsulation using the *standard* lithography design led to aggregate formation in microdroplets within minutes of incubation resulting in compact aggregates within hours regardless of the initial cell-seeding density. QX200^{TM} droplet generation oil was confirmed to be a suitable oil and surfactant composition for short-term incubation of aggregates up to three days of culture as demonstrated by droplet stability and sustained aggregate colony formation and proliferation ability. Continuous stirring of cell suspensions in syringes for homogenisation prior to injection into the device was essential to reach optimal encapsulation efficiencies. Among the three cell densities employed for encapsulation (i.e. 1, 3 and 5 million cells/ml), the lowest one corresponded to a range of 0 to 5 cells per microdroplet in over 95% of counts, thus falling short of the target to avoid empty droplets and single-cell encapsulation. In contrast, the intermediate and the high cell densities both produced aggregates with average cell numbers in droplets well above the single-cell scenario and comparable colony forming efficiencies. Aggregates generated from the intermediate seeding density selected in order to analyse the contribution of individual cells within small groups rather than collective spheroids attainable *in vitro* displayed higher levels of *SOX9* expression than cells cultured in monolayer. This result agreed with the central project hypothesis, opening a route for enriching HBMSC chondroprogenitors using SOX9 as a differentiation marker in small live aggregates. This project thesis thus paves the way to address the heterogeneity issue in HBMSCs by signalling at potential strategies currently under development such as droplet microfluidics and nanoflare technologies to monitor and to sort cell aggregate in a high-throughput fashion for tissue engineering applications.

Chapter 7: Discussion and Future directions

7.1 Achievements of this study

The aim of this project was to achieve high-throughput cell aggregation simulating early chondrogenic condensation with a view to enriching HBMSC chondroprogenitor subpopulations on the basis of functional, condensation-dependent markers such as SOX9. Droplet microfluidics was incorporated in this stem cell cartilage tissue engineering approach for high-throughput assembly, monitoring and characterisation of HBMSC multicellular spheroids. As a result, the project tested the hypothesis that HBMSC aggregation enhances early SOX9 expression and that small cell aggregates can be cultured using droplet microfluidics and sorted on the basis of their early SOX9 expression.

This research project addressed the above aim by:

- Developing *in vitro* chondrogenic differentiation of multicellular spheroids across a wide spectrum of cell numbers on ultra-low adherence round-bottom well plates.
- Implementing and optimising techniques to characterise multicellular spheroid aggregation and changes in SOX9/*SOX9* expression over time (time-lapse microscopy, histological and histochemical stainings, RT-qPCR).
- Testing a nanoflare-mediated approach to sort HBMSC chondroprogenitors as a function of *SOX9*-Cy5 fluorescence signal measurements
- Optimising droplet microfluidic platforms and achieving droplet monodisperse populations and droplet stability.
- Demonstrating cell aggregation in microdroplets within a short period of time that was suitable for biological characterisation.
- Demonstrating cell viability and functionality of microaggregates in microdroplets
- Analysing *SOX9* expression levels in aggregates formed in microdroplets compared to cells cultured *in vitro* on well plates.

The findings derived from the research carried out in this project were:

- Chondrogenesis was a cell number-dependent process as reflected on differences in timescales for cell aggregation, histological structure and histochemical SOX9 distribution. Spheroids composed of 50000 cells outperformed larger spheroids assembled from 500000 cells.

- *SOX9* expression did not change significantly in time points set during the first week of culture regardless of cell number although higher levels were observed on day 1.
- SOX9 distribution in multicellular spheroids composed of 500 and 5000 cells showed existing heterogeneity in HBMSCs and so did histochemical studies in larger numbers compared to HACs. This implied an inferior chondrogenic efficiency and gave a strong reason pursue detecting heterogeneity across different cell subpopulations.
- *SOX9*-Cy5 nanoflares could only detect correlation between Cy5 fluorescence signal intensity and *SOX9* mRNA expression for a single donor. In that particular case, cells could be sorted from regions under peaks corresponding to at least two orders of magnitude increased fluorescence intensity.
- Soft lithography designs were able to generate monodisperse droplets with stability. QX200^{TM} was the best oil and surfactant formulation. Silanisation and plasma bonding improved device performance.
- Cell aggregation in microdroplets occurred minutes after encapsulation and aggregates became compact within hours.
- HBMSCs remained viable and functional. Aggregates succeeded in proliferating and forming colonies once re-plated onto well plates.
- HBMSC aggregates had higher levels of *SOX9* expression than cells cultured in monolayer in chondrogenic differentiation conditions.

In chapter 3, the biological characterisation of multicellular spheroids exposed differences in their chondrogenic differentiation outcome linked to cell number. SOX9 expression in large spheroids did not change as a function of time. In contrast, SOX9 expression declined in small spheroids in late chondrogenesis and did not vary significantly during the first week, demonstrating that SOX9 could be a potential early marker to predict chondrogenesis in HBMSCs. The degree of heterogeneity among different bone marrow cell populations could not be conclusively quantified. Notwithstanding, a strong component on an intra-spheroid level of SOX9 heterogeneity was observed compared to HACs, which highlighted a potential advantage in harnessing even smaller aggregates for enriching stem cells for cartilage tissue engineering. In anticipation of the development of a microfluidic-based high-throughput sorting strategy for small aggregates in microdroplets, the next objective was to establish an approach to screening viable cells for SOX9. The experience acquired to assess the properties of the cartilage-like tissue being generated is crucial for future characterisation of robust cartilage aggregates once a suitable microfluidic platform combined with a chondrogenic marker cell sorting strategy becomes available.

Chapter 4 evaluated the suitability of *SOX9*-Cy5 nanoflares were assessed for their application for sorting of cell aggregates. Nanoflares failed to provide robust evidence concerning their effectiveness and sensitivity to distinguish *SOX9*-enriched populations in HBMSCs in a definitive manner. The validation assays on short-term ATDC5 chondrogenic cultures showed that the Cy5-positive cell subpopulations incubated with the *SOX9*-Cy5 nanoflare corresponded with high *SOX9* mRNA levels. The same applied to HBMSCs in those instances where there was a clear difference in terms of order of magnitude of Cy5 fluorescence signal in FACS plots between positive and negative gated cells. An example of such was the single donor study with unselected plastic adherent HBMSCs in the absence of chondrogenic induction. The current nanoflare technology and methodology available needed further optimisation along with more substantial validation before tackling the issue of sorting HBMSC aggregates.

Chapter 5 described the optimisation of a microfluidic device for cell encapsulation covered the application of two different techniques for chip fabrication. 3D-printed designs treated with Aquapel® exposed high polydispersity and coalescence in droplets generated with the in-house Soton2 surfactant in FC40 oil. A functional stability assay demonstrated the higher effectiveness of the Bio-Rad QX200™ droplet generation oil commercial variation compared to Soton2. Soft lithography designs were tested with changes in the fabrication procedure such as silanisation and plasma bonding to glass slides. Highly monodisperse droplet diameters resulted in the soft lithography *standard* and *spiral* chip designs. Particles were loaded in microdroplets with a variety of numbers in them. They conformed to Poisson-like distributions that remained applicable and promising for cell encapsulation.

Chapter 6 encompassed the research conducted on cell encapsulation in microdroplets. 3D-printed designs were not compatible with high-throughput droplet generation and culture because of dimensional resolution limits for fabrication. The s*tandard* soft lithography design accomplished droplet stability and were more effective for cell loading and short-term microdroplet culture as demonstrated robustly in colony formation assays. HBMSC aggregates composed of 3-5 cells and up to 20-25 cells per droplet were formed and grown from initial cell-seeding densities of 1 million cells/ml up to 5 million cells/ml. Cells aggregated within 1 h of encapsulation in microdroplets due to their confinement in spherical microdroplets. HBMSCs aggregates were successfully recovered from droplets and displayed maintained colony formation functionality when re-plated from aggregates incubated in short-term chondrogenic differentiation cultures for up to 3 days. In addition, HBMSC aggregates self-assembled in microdroplets expressed higher levels of *SOX9* than cells cultured in monolayer as early as 24 h of chondrogenic induction. This result agreed with the central project hypothesis, opening a route for enriching HBMSC chondroprogenitors using SOX9 as a differentiation marker in small live aggregates.

7.2 A discussion of the main findings and their context

Chondrogenic differentiation has been extensively studied in HBMSCs as the most frequent ASC source for tissue engineering applications. 3D culture systems *in vitro* have been demonstrated to be more representative of physiological events for cartilage formation. Ultra-low adherence plates in particular have offered a higher throughput alternative to pellet culture in tubes. None of them, however, can handle small cell numbers which are decisive for HBMSC subpopulation enrichment. Droplet microfluidics is a technique that specialises in features occurring at a single cell scale and has a record of use for screening and recent application to multicellular spheroids.

SOX9 expression patterns assessed in this study responded to an early chondrogenic marker. Whole mount IF coupled with confocal microscopy revealed heterogeneity across samples expressing SOX9 despite not providing conclusive evidence. This was hypothesised to be due to the cell number usage limitations. 500 and 5000 cell spheroids might have been too large aggregates that were globally expressing SOX9 fairly uniformly based on a synergistic effect of the most robust chondroprogenitor populations encouraging those that were less so. This hypothesis is supported in the literature where 50 cell aggregates, despite showing inferior stability, were the most responsive to chondrogenic differentiation conditions as reported through their upregulated chondrogenic expression patterns (Moreira Teixeira et al., 2012, Leijten et al., 2016). This implied that there may be a measurable degree of uniformity that could allow to discriminate between robust and poor aggregates for cartilage using SOX9 as a marker.

To examine the suitability of nanoflares for cell sorting, the correlation between FACS measurements of Cy5 fluorescent signals from cell subpopulations incubated with nanoflares and their target mRNA levels was explored. The results obtained for the single-donor assay suggested that *SOX9*-Cy5 were effective provided that the cells were sorted by gating at fluorescence intensities over two log10 steps. Only the highly positive cells located at the right end of the positive gating region yielded significant differences in *SOX9* mRNA expression with respect to the other subpopulations, but the abundance of this population seemed to be heavily patient-specific. In this regard, Li et al. conducted an analogous experiment where they gated for two distinct cell subpopulations, low Cy5 fluorescence intensity and high fluorescence intensity, according to the FACS counts from HBMSCs incubated overnight with *SOX9*-Cy5 Smartflares^{TM} nanoprobes. They noticed an upregulation of the *SOX9* mRNA levels in the high Cy5 intensity cell subpopulation normalised to the low intensity group, although the difference was not statistically significant (Li et al., 2016). In contrast, other authors have published data questioning the sensitivity of commercial Smartflare^{TM} nanoprobes by claiming that they failed to conclusively make a distinction between cells expressing a high level of a target mRNA transcript and those with a low level (Mason et al.,

2016, Czarnek and Bereta, 2017). More recently, and using the same nanoflare design described in this work, Lanham reported that a short contact time with nanoflares (e.g. one hour) produced a strong correlation between the nanoflare fluorescence signal and the measured target mRNA transcript levels. They additionally argued that a single mRNA transcript could bind to multiple sense strands from different nanoprobes, hence releasing the fluorescent flare strand and increasing the emitted fluorescence signal intensity. Moreover, this phenomenon could be more likely and intense for longer incubation times with nanoflares and lead to a misinterpretation of quantified mRNA expression levels that differ from true mRNA levels (Lanham et al., 2019). This hypothesis would be in favour of the approach taken in this research project to shorten the incubation time to 1 h at 0.2 nM nanoflare concentration. Taking the results of the nanoflare research work in this thesis, nanoflares lacked sufficient sensitivity to detect *SOX9* in cells cultured in monolayers both in basal conditions and after a week of chondrogenic stimulation. This raised doubts about the abundance of the *SOX9* mRNA transcript required for detection in HBMSCs harvested from monolayer cultures considering the donor variability involved.

In this framework, the novelty of the research presented in this thesis comes with the successful generation of aggregates consisting of tens of cells and even smaller in a high-throughput fashion for analysis. Biological characterisation of aggregates cultured in microdroplets revealed that aggregates expressed higher *SOX9* mRNA levels compared to cells grown in monolayers. Such finding endorsed the main project hypothesis and opened the possibility that a sorting strategy for chondroprogenitors could be developed based on SOX9 as a functional marker on HBMSC aggregates. Recent advances in cell sorting of chondrogenitors are heading in a similar direction. Dicks et al. used two CRISPR-Cas9-edited *COL2A1-GFP* knock-in reporter human iPSC cell lines to identify a set of cell surface markers associated with chondroprogenitor subpopulations with high chondrogenic potential. They distinguished the $CD146^{+}/CD166^{+}/PDGFR\beta^{+}/CD45^{-}$ sorted subpopulation as chondroprogenitors exhibiting a richer sGAG cartilage matrix and significantly higher gene expression of chondrogenic markers (i.e. SOX9, COL2A1, ACAN) along with *COL10A1* indicating progress towards hypertrophy. They argued that *COL2A1*$^{+}$ cells were heterogeneous and they claimed that *COL2A1* was a late chondrogenic marker that could also be encountered signalling the early development of other tissues apart from cartilage (Dicks et al., 2020). *SOX9* could be a better suited specific early chondrogenic marker for sorting and cell aggregates could additionally perform as vessels for analysis of differentiation markers in a high-throughput manner as mediated by droplet microfluidic platforms. To date, the viability of a SOX9-based sorting strategy remains in question and the possibility that SOX9 may be exceedingly inaccessible to serve as a marker for sorting still stands. Other functional markers that could be used that are expressed early during chondrogenesis and are part of the ECM (therefore easier to target) are COMP and fibromodulin

(Barry et al., 2001, Lee et al., 2012). The limited options available for sorting of cell aggregates (e.g. cell surface markers; physical/mechanical properties; intrinsic metabolic markers) do not account for the essential link between a phenotypic trait and the biological function of the tissue to generate. The continuous advancement of nanoflare techniques and other live cell imaging techniques signify promising steps towards sorting of HBMSC aggregates on the basis of a biological function linked with differentiation. This would lead to the realisation of the much sought-after goal of isolating HBMSC subpopulations for tissue engineering.

7.3 Limitations of the study and future directions

Droplet stability was the most recurring issue challenging the incubation of compartmentalised droplet microenvironments for cell aggregation. Chan et al. developed a double emulsion (i.e. water-in-oil-in-water) system to promote stable aggregation of HBMSCs in droplets. The aggregates were later encapsulated in alginate hydrogels for osteogenic differentiation. Despite effective, their approach was more complicated due to the chemistry involved, the high cell densities needed and to the stochastic appearance of empty droplets. Retrieving aggregates from microdroplets is straightforward with the PFO addition technique detailed in this work. Aggregates could then be encapsulated in hydrogel scaffolds to continue the differentiation process or they could be immunostained for SOX9. The two aspects can be integrated into the aggregate characterisation streamline; thereby expanding the versatility of this droplet microfluidic technique beyond sorting of aggregates (Chan et al., 2013).

The *standard* soft lithography design maximised droplet encapsulation efficiency for any cell-seeding density compared to the *spiral* design. An additional limitation characterised the study of these devices, particularly affecting the *spiral* design. Flow rate was the parameter varied and documented but velocity (which is related to flow rate through the cross-sectional area of the channels of known dimensions) was not assessed. Velocity is a crucial factor for inertial ordering and controlled cell encapsulation, scaling directly with Dean drag forces. The interaction between Dean drag forces and inertial forces as well as cell deformability determine the equilibrium position of cells when flowing (Dean, 1927, Ookawara et al., 2004, Gou et al., 2018). In *spiral* designs, achieving control on relevant numbers for cell aggregate formation would demand very high initial cell-seeding densities and thorough homogenisation in syringes prior and during encapsulation to prevent clumping. In fact, low flow rates of 25 µl/min generated instabilities in the droplet generation phase for *spiral* devices. Studying the effect of higher flow rates (and velocities as a result) on cell encapsulation at high initial cell-seeding densities would be a essential step to validate their performance. This avenue of research remains interesting to explore given that the

objective of cell aggregation in stable microdroplets has been accomplished by means of the simpler *standard* design.

Cell encapsulation within microdroplets on optimised soft lithography chips was performed in non-sterile yet clean conditions from the moment that the cells were loaded onto the syringe pump. This was deemed reasonable for short-term cultures such as the ones presented in this research work because cells were encapsulated within microdroplets. Such culture platform would limit the contact with pathogens in the short time that the non-sterile procedures were being undertaken, although it could be adapted to a completely sterile environment.

Sorting of aggregates generated through a droplet microfluidic system on the basis of SOX9 was the ultimate goal of this study. The application of *SOX9*-Cy5 nanoflares to that end could not substantiate an existing correlation between Cy5 fluorescence signal intensities and mRNA expression of the target transcript for HBMSCs sorted as individual cells and in the absence of chondrogenic induction. The results of *SOX9* expression in aggregates formed in microdroplets were promising towards attempting sorting of cell aggregates as a proof of concept. This was not possible due to time constraints and future work could investigate the outcomes of sorting aggregates using *SOX9*-Cy5 nanoflares. These would derive from quantifying *SOX9* gene expression and cross-comparing to histological assessment of combined aggregates after a 21 to 28-day chondrogenic differentiation culture. Sorting of aggregates by means of a FACS strategy is challenged by the nozzle size available on the cell sorter. The aggregate sizes measured with the highest cell numbers employed in this project surpassed 100 μm and may require size filtering prior to sorting. A clumping effect of aggregates incubated for an hour with nanoflares and a certain degree of inhibition of probe internalisation for larger aggregates cannot be excluded and may add to the technical difficulties of this approach.

Lastly, more future work could be carried out to developing a strategy for sorting and targeting markers either for chondrogenesis or for the generation of more tissues. Aggregate formation and screening using droplet microfluidics could be extended to other cell types (e.g. HACs) in conjunction with progress in the nanoflare approach for mRNA binding (i.e. chemical structure modifications, protocol optimisation). SOX9 stands as a marker of interest due to its early expression for chondrogenesis and its role as an enhancer of other cartilage-related genes regulating cartilage ECM generation. The latter has been reported *in vivo* using limb buds in a *Sox9* knock-out mouse model for early chondrocyte marker genes (e.g *Col2a1* and *Sox5*) and cytoskeleton reorganisation in a pre-chondrocyte stage (Liu et al., 2018). Even though transfection-related techniques for sorting cell subpopulations have provided an insight into the expression of cartilage-specific markers and the structure of generated tissues using live cells, they have not

overcome the obstacle of clinical translation (Lee et al., 2012, Dicks et al., 2020). Functional early differentiation markers (SOX9 or other ECM molecules such as COMP and fibromodulin) coupled with high-throughput droplet microfluidics could be the answer to come closer to achieve robust hyaline cartilage generation one drop at a time.

7.4 Concluding remarks

This research work presents the first attempt at evaluating the possibility of using SOX9 as a chondrogenic functional marker to sort multicellular aggregates formed in microdroplets to the best of the author's knowledge. It describes a droplet microfluidics protocol for controlled assembly of small cell aggregates in stable microdroplets and the effect of fabrication techniques and device operation on the overall performance of the platform. The *in vitro* chondrogenic differentiation assays established the differences in chondrogenic response among various cell numbers. They also defined the presence and importance of SOX9 in early chondrogenesis and the existing heterogeneities in unselected HBMSCs. Nanoflares could not provide a robust strategy to sort cells. Cell aggregation and colony formation functionality along with a proof of concept of higher SOX9 mRNA expression encouraged the use of cell aggregates for live characterisation of SOX9 with the aim of finding one route for isolating the chondroprogenitor stem cell fraction in HBMSCs. These findings provide a strong foundation for future high-throughput biological characterisation of aggregates formed in microdroplets which is bound to emerge alongside advances in live cell screening and quantification of differentiation markers.

List of references

(IHME), S. I. F. H. M. A. E. 2017. *Global Burden of Disease Collaborative Network. Global Burden of Disease Study 2016 (GBD 2016) Results.* [Online]. http://ghdx.healthdata.org/gbd-results-tool [Accessed 14 May 2019].

AARTS, D. G., SCHMIDT, M. & LEKKERKERKER, H. N. 2004. Direct visual observation of thermal capillary waves. *Science,* 304**,** 847-850.

ACHILLI, T.-M., MEYER, J. & MORGAN, J. R. 2012. Advances in the formation, use and understanding of multi-cellular spheroids. *Expert opinion on biological therapy,* 12**,** 1347-1360.

AGAR, G., BLUMENSTEIN, S., BAR-ZIV, Y., KARDOSH, R., SCHRIFT-TZADOK, M., GAL-LEVY, R., FISCHLER, T., GOLDSCHMID, R. & YAYON, A. 2011. The chondrogenic potential of mesenchymal cells and chondrocytes from osteoarthritic subjects: a comparative analysis. *Cartilage,* 2**,** 40-49.

AGHAJANIAN, P. & MOHAN, S. 2018. The art of building bone: emerging role of chondrocyte-to-osteoblast transdifferentiation in endochondral ossification. *Bone research,* 6**,** 1-9.

AKIYAMA, H., CHABOISSIER, M.-C., MARTIN, J. F., SCHEDL, A. & DE CROMBRUGGHE, B. 2002. The transcription factor Sox9 has essential roles in successive steps of the chondrocyte differentiation pathway and is required for expression of Sox5 and Sox6. *Genes & development,* 16**,** 2813-2828.

ALBLAWI, A., RANJANI, A. S., YASMIN, H., GUPTA, S., BIT, A. & RAHIMI-GORJI, M. 2020. Scaffold-free: A developing technique in field of tissue engineering. *Computer methods and programs in biomedicine,* 185**,** 105148.

ALLAZETTA, S. & LUTOLF, M. P. 2015. Stem cell niche engineering through droplet microfluidics. *Current Opinion in Biotechnology,* 35**,** 86-93.

AMABLE, P. R., TEIXEIRA, M. V. T., CARIAS, R. B. V., GRANJEIRO, J. M. & BOROJEVIC, R. 2013. Identification of appropriate reference genes for human mesenchymal cells during expansion and differentiation. *PLoS One,* 8**,** e73792.

ARDEN, N. & NEVITT, M. C. 2006. Osteoarthritis: epidemiology. *Best practice & research Clinical rheumatology,* 20**,** 3-25.

BAKSH, D., YAO, R. & TUAN, R. S. 2007. Comparison of proliferative and multilineage differentiation potential of human mesenchymal stem cells derived from umbilical cord and bone marrow. *Stem Cells,* 25**,** 1384-1392.

BAO, G., RHEE, W. J. & TSOURKAS, A. 2009. Fluorescent probes for live-cell RNA detection. *Annual review of biomedical engineering,* 11**,** 25-47.

BARCZYK, M., CARRACEDO, S. & GULLBERG, D. 2010. Integrins. *Cell and tissue research,* 339**,** 269-280.

BARET, J.-C. 2012. Surfactants in droplet-based microfluidics. *Lab on a Chip,* 12**,** 422-433.

BAROUD, C. N., GALLAIRE, F. & DANGLA, R. 2010. Dynamics of microfluidic droplets. *Lab on a Chip,* 10**,** 2032-2045.

BARRY, F., BOYNTON, R. E., LIU, B. & MURPHY, J. M. 2001. Chondrogenic differentiation of mesenchymal stem cells from bone marrow: differentiation-dependent gene expression of matrix components. *Experimental cell research,* 268**,** 189-200.

BARTHES, J., ÖZÇELIK, H., HINDIÉ, M., NDREU-HALILI, A., HASAN, A. & VRANA, N. E. 2014. Cell microenvironment engineering and monitoring for tissue engineering and regenerative medicine: the recent advances. *BioMed research international,* 2014.

BARTKOVA, S., VENDELIN, M., SANKA, I., PATA, P. & SCHELER, O. 2019. CellProfiler: A fit tool for image analysis in droplet microfluidics. *bioRxiv***,** 811869.

BASAD, E., WISSING, F. R., FEHRENBACH, P., RICKERT, M., STEINMEYER, J. & ISHAQUE, B. 2015. Matrix-induced autologous chondrocyte implantation (MACI) in the knee: clinical outcomes and challenges. *Knee Surgery, Sports Traumatology, Arthroscopy,* 23**,** 3729-3735.

BASIJI, D. A., ORTYN, W. E., LIANG, L., VENKATACHALAM, V. & MORRISSEY, P. 2007. Cellular image analysis and imaging by flow cytometry. *Clinics in laboratory medicine,* 27**,** 653-670.

BASOVA, E. Y. & FORET, F. 2015. Droplet microfluidics in (bio) chemical analysis. *Analyst,* 140**,** 22-38.

BASU, A. S. 2013. Droplet morphometry and velocimetry (DMV): a video processing software for time-resolved, label-free tracking of droplet parameters. *Lab on a Chip,* 13**,** 1892-1901.

BATISTA, M. A., NIA, H. T., ÖNNERFJORD, P., COX, K. A., ORTIZ, C., GRODZINSKY, A. J., HEINEGÅRD, D. & HAN, L. 2014. Nanomechanical phenotype of chondroadherin-null murine articular cartilage. *Matrix Biology,* 38**,** 84-90.

BATTULA, V. L., TREML, S., BAREISS, P. M., GIESEKE, F., ROELOFS, H., DE ZWART, P., MULLER, I., SCHEWE, B., SKUTELLA, T., FIBBE, W. E., KANZ, L. & BUHRING, H. J. 2009. Isolation of functionally distinct mesenchymal stem cell subsets using antibodies against CD56, CD271, and mesenchymal stem cell antigen-1. *Haematologica-the Hematology Journal,* 94**,** 173-184.

BAUGÉ, C. & BOUMÉDIENE, K. 2015. Use of adult stem cells for cartilage tissue engineering: current status and future developments. *Stem Cells International,* 2015.

BAYLISS, L. E., CULLIFORD, D., MONK, A. P., GLYN-JONES, S., PRIETO-ALHAMBRA, D., JUDGE, A., COOPER, C., CARR, A. J., ARDEN, N. K. & BEARD, D. J. 2017. The effect of patient age at intervention on risk of implant revision after total replacement of the hip or knee: a population-based cohort study. *The Lancet,* 389**,** 1424-1430.

BEANE, O. S. & DARLING, E. M. 2012. Isolation, characterization, and differentiation of stem cells for cartilage regeneration. *Annals of biomedical engineering,* 40**,** 2079-2097.

BEARD, D. J., DAVIES, L. J., COOK, J. A., MACLENNAN, G., PRICE, A., KENT, S., HUDSON, J., CARR, A., LEAL, J. & CAMPBELL, H. 2019. The clinical and cost-effectiveness of total versus partial knee replacement in patients with medial compartment osteoarthritis (TOPKAT): 5-year outcomes of a randomised controlled trial. *The Lancet,* 394**,** 746-756.

BERGQUIST, P. L., HARDIMAN, E. M., FERRARI, B. C. & WINSLEY, T. 2009. Applications of flow cytometry in environmental microbiology and biotechnology. *Extremophiles,* 13**,** 389-401.

BHAGAT, A. A. S., KUNTAEGOWDANAHALLI, S. S., KAVAL, N., SELISKAR, C. J. & PAPAUTSKY, I. 2010. Inertial microfluidics for sheath-less high-throughput flow cytometry. *Biomedical microdevices,* 12**,** 187-195.

BHOSALE, A. M. & RICHARDSON, J. B. 2008. Articular cartilage: structure, injuries and review of management. *British medical bulletin,* 87**,** 77-95.

BHUMIRATANA, S. & VUNJAK-NOVAKOVIC, G. 2015. Engineering physiologically stiff and stratified human cartilage by fusing condensed mesenchymal stem cells. *Methods,* 84**,** 109-114.

BI, W., HUANG, W., WHITWORTH, D. J., DENG, J. M., ZHANG, Z., BEHRINGER, R. R. & DE CROMBRUGGHE, B. 2001. Haploinsufficiency of Sox9 results in defective cartilage primordia and premature skeletal mineralization. *Proceedings of the National Academy of Sciences,* 98**,** 6698-6703.

BIANCO, P., CAO, X., FRENETTE, P. S., MAO, J. J., ROBEY, P. G., SIMMONS, P. J. & WANG, C. Y. 2013. The meaning, the sense and the significance: translating the science of mesenchymal stem cells into medicine. *Nature Medicine,* 19**,** 35-42.

BIANCO, P., KUZNETSOV, S. A., RIMINUCCI, M. & GEHRON ROBEY, P. 2006. Postnatal skeletal stem cells. *Methods in Enzymology,* 419**,** 117-48.

BIANCO, P., RIMINUCCI, M., GRONTHOS, S. & ROBEY, P. G. 2001. Bone marrow stromal stem cells: nature, biology, and potential applications. *Stem cells,* 19**,** 180-192.

BIANCO, P. & ROBEY, P. G. 2000. Marrow stromal stem cells. *The Journal of clinical investigation,* 105**,** 1663-1668.

BIANCO, P. & ROBEY, P. G. 2015. Skeletal stem cells. *Development,* 142**,** 1023-1027.

BIANCO, P., ROBEY, P. G. & SIMMONS, P. J. 2008. Mesenchymal stem cells: revisiting history, concepts, and assays. *Cell Stem Cell,* 2**,** 313-9.

BIENDARRA-TIEGS, S. M., SECRETO, F. J. & NELSON, T. J. 2019. Addressing variability and heterogeneity of induced pluripotent stem cell-derived cardiomyocytes. *Cell Biology and Translational Medicine, Volume 6.* Springer.

BILGEN, B., ORSINI, E., AARON, R. K. & CIOMBOR, D. M. 2007. FBS suppresses TGF-β1-induced chondrogenesis in synoviocyte pellet cultures while dexamethasone and dynamic stimuli are beneficial. *Journal of tissue engineering and regenerative medicine,* 1**,** 436-442.

BOEUF, S. & RICHTER, W. 2010. Chondrogenesis of mesenchymal stem cells: role of tissue source and inducing factors. *Stem cell research & therapy,* 1**,** 1.

BOMER, N., CORNELIS, F. M., RAMOS, Y. F., DEN HOLLANDER, W., LAKENBERG, N., VAN DER BREGGEN, R., STORMS, L., SLAGBOOM, P. E., LORIES, R. J. & MEULENBELT, I. 2016. Aberrant calreticulin expression in articular cartilage of Dio2 deficient mice. *PloS one,* 11**,** e0154999.

BREMOND, N., THIAM, A. R. & BIBETTE, J. 2008. Decompressing emulsion droplets favors coalescence. *Physical review letters,* 100**,** 024501.

BRIGGS, A. M., CROSS, M. J., HOY, D. G., SANCHEZ-RIERA, L., BLYTH, F. M., WOOLF, A. D. & MARCH, L. 2016. Musculoskeletal health conditions represent a global threat to healthy aging: a report for the 2015 World Health Organization world report on ageing and health. *The Gerontologist,* 56**,** S243-S255.

BRILEY, W. E., BONDY, M. H., RANDERIA, P. S., DUPPER, T. J. & MIRKIN, C. A. 2015. Quantification and real-time tracking of RNA in live cells using Sticky-flares. *Proceedings of the National Academy of Sciences,* 112**,** 9591-9595.

BRITTBERG, M., LINDAHL, A., NILSSON, A., OHLSSON, C., ISAKSSON, O. & PETERSON, L. 1994. Treatment of deep cartilage defects in the knee with autologous chondrocyte transplantation. *New england journal of medicine,* 331**,** 889-895.

BROUZES, E., MEDKOVA, M., SAVENELLI, N., MARRAN, D., TWARDOWSKI, M., HUTCHISON, J. B., ROTHBERG, J. M., LINK, D. R., PERRIMON, N. & SAMUELS, M. L. 2009. Droplet microfluidic technology for single-cell high-throughput screening. *Proceedings of the National Academy of Sciences,* 106**,** 14195-14200.

BYUN, C. K., ABI-SAMRA, K., CHO, Y. K. & TAKAYAMA, S. 2014. Pumps for microfluidic cell culture. *Electrophoresis,* 35**,** 245-257.

BYUN, H., LEE, Y. B., KIM, E. M. & SHIN, H. 2019. Fabrication of size-controllable human mesenchymal stromal cell spheroids from micro-scaled cell sheets. *Biofabrication,* 11**,** 035025.

CAREY-BETH, J. & UHL, T. L. 2001. A review of articular cartilage pathology and the use of glucosamine sulfate. *Journal of athletic training,* 36**,** 413.

CARON, M. M., EMANS, P. J., COOLSEN, M. M., VOSS, L., SURTEL, D. A., CREMERS, A., VAN RHIJN, L. W. & WELTING, T. J. 2012. Redifferentiation of dedifferentiated human articular chondrocytes: comparison of 2D and 3D cultures. *Osteoarthritis and Cartilage,* 20**,** 1170-1178.

CAVALLO, C., CUOMO, C., FANTINI, S., RICCI, F., TAZZARI, P. L., LUCARELLI, E., DONATI, D., FACCHINI, A., LISIGNOLI, G., FORNASARI, P. M., GRIGOLO, B. & MORONI, L. 2011. Comparison of Alternative Mesenchymal Stem Cell Sources for Cell Banking and Musculoskeletal Advanced Therapies. *Journal of Cellular Biochemistry,* 112**,** 1418-1430.

CESCON, M., GATTAZZO, F., CHEN, P. & BONALDO, P. 2015. Collagen VI at a glance. *Journal of cell science,* 128**,** 3525-3531.

CHAN, C. K., GULATI, G. S., SINHA, R., TOMPKINS, J. V., LOPEZ, M., CARTER, A. C., RANSOM, R. C., REINISCH, A., WEARDA, T. & MURPHY, M. 2018. Identification of the human skeletal stem cell. *Cell,* 175**,** 43-56. e21.

CHAN, H. F., ZHANG, Y., HO, Y.-P., CHIU, Y.-L., JUNG, Y. & LEONG, K. W. 2013. Rapid formation of multicellular spheroids in double-emulsion droplets with controllable microenvironment. *Scientific reports,* 3**,** 1-8.

CHAN, K. A., NIU, X., DEMELLO, A. & KAZARIAN, S. 2011. Generation of chemical movies: FT-IR spectroscopic imaging of segmented flows. *Analytical chemistry,* 83**,** 3606-3609.

CHEN, C.-H., SARKAR, A., SONG, Y.-A., MILLER, M. A., KIM, S. J., GRIFFITH, L. G., LAUFFENBURGER, D. A. & HAN, J. 2011. Enhancing protease activity assay in droplet-based microfluidics using a biomolecule concentrator. *Journal of the American Chemical Society,* 133**,** 10368-10371.

CHEN, S., FU, P., CONG, R., WU, H. & PEI, M. 2015a. Strategies to minimize hypertrophy in cartilage engineering and regeneration. *Genes & Diseases,* 2**,** 76-95.

CHEN, S., MIENALTOWSKI, M. J. & BIRK, D. E. 2015b. Regulation of corneal stroma extracellular matrix assembly. *Experimental eye research,* 133**,** 69-80.

CHEN, W. H., LAI, M. T., WU, A. T., WU, C. C., GELOVANI, J. G., LIN, C. T., HUNG, S. C., CHIU, W. T. & DENG, W. P. 2009. In vitro stage-specific chondrogenesis of mesenchymal stem cells committed to chondrocytes. *Arthritis & Rheumatism,* 60**,** 450-459.

CHEN, Z. T., LIAO, P. Y., ZHANG, F. L., JIANG, M. C., ZHU, Y. S. & HUANG, Y. Y. 2017. Centrifugal micro-channel array droplet generation for highly parallel digital PCR. *Lab on a Chip,* 17**,** 235-240.

CHIQUET, M., BIRK, D. E., BÖNNEMANN, C. G. & KOCH, M. 2014. Collagen XII: protecting bone and muscle integrity by organizing collagen fibrils. *The international journal of biochemistry & cell biology,* 53**,** 51-54.

CHO, S., KANG, D.-K., SIM, S., GEIER, F., KIM, J.-Y., NIU, X., EDEL, J. B., CHANG, S.-I., WOOTTON, R. C. & ELVIRA, K. S. 2013. Droplet-based microfluidic platform for high-throughput, multi-parameter screening of photosensitizer activity. *Analytical chemistry,* 85**,** 8866-8872.

CHOI, C. H. J., HAO, L., NARAYAN, S. P., AUYEUNG, E. & MIRKIN, C. A. 2013. Mechanism for the endocytosis of spherical nucleic acid nanoparticle conjugates. *Proceedings of the National Academy of Sciences,* 110**,** 7625-7630.

CHONG, P. P., SELVARATNAM, L., ABBAS, A. A. & KAMARUL, T. 2012. Human peripheral blood derived mesenchymal stem cells demonstrate similar characteristics and chondrogenic differentiation potential to bone marrow derived mesenchymal stem cells. *Journal of Orthopaedic Research,* 30**,** 634-642.

CHOU, W.-L., LEE, P.-Y., YANG, C.-L., HUANG, W.-Y. & LIN, Y.-S. 2015. Recent advances in applications of droplet microfluidics. *Micromachines,* 6**,** 1249-1271.

CHUANG, K. H., HSIEH, Y. C., CHIANG, I. S., CHUANG, C. H., KAO, C. H., CHENG, T. C., WANG, Y. T., LIN, W. W., CHEN, B. M., ROFFLER, S. R., HUANG, M. Y. & CHENG, T. L. 2014. High-throughput sorting of the highest producing cell via a transiently protein-anchored system. *PLoS ONE [Electronic Resource],* 9**,** e102569.

CICIONE, C., MUIÑOS-LÓPEZ, E., HERMIDA-GÓMEZ, T., FUENTES-BOQUETE, I., DÍAZ-PRADO, S. & BLANCO, F. J. 2015. Alternative protocols to induce chondrogenic differentiation: transforming growth factor-β superfamily. *Cell and Tissue Banking,* 16**,** 195-207.

CLEARY, M., NARCISI, R., FOCKE, K., VAN DER LINDEN, R., BRAMA, P. & VAN OSCH, G. 2016. Expression of CD105 on expanded mesenchymal stem cells does not predict their chondrogenic potential. *Osteoarthritis and cartilage,* 24**,** 868-872.

COLLINS, D. J., NEILD, A., DEMELLO, A., LIU, A.-Q. & AI, Y. 2015. The Poisson distribution and beyond: methods for microfluidic droplet production and single cell encapsulation. *Lab on a Chip,* 15**,** 3439-3459.

CROSET, V., TREIBER, C. D. & WADDELL, S. 2018. Cellular diversity in the Drosophila midbrain revealed by single-cell transcriptomics. *Elife,* 7.

CUI, X., HARTANTO, Y. & ZHANG, H. 2017. Advances in multicellular spheroids formation. *Journal of the Royal Society Interface,* 14.

CZARNEK, M. & BERETA, J. 2017. SmartFlares fail to reflect their target transcripts levels. *Scientific reports,* 7**,** 1-10.

CZARNEK, M., MASON, D., HAIMOVICH, G., PUNTES, V. F., BERGESE, P., BERETA, J. & LÉVY, R. 2018. Re-evaluating the spherical-nucleic-acid technology.

DAHER, R. J., CHAHINE, N. O., GREENBERG, A. S., SGAGLIONE, N. A. & GRANDE, D. A. 2009. New methods to diagnose and treat cartilage degeneration. *Nature Reviews Rheumatology,* 5**,** 599-607.

DANIŠOVIČ, Ľ., BOHÁČ, M., ZAMBORSKÝ, R., ORAVCOVÁ, L., PROVAZNÍKOVÁ, Z., CSOEBOENYEIOVA, M. & VARGA, I. 2016. Comparative analysis of mesenchymal stromal cells from different tissue sources in respect to articular cartilage tissue engineering. *General physiology and biophysics,* 35**,** 207-214.

DARLING, E. M. & ATHANASIOU, K. A. 2005. Rapid phenotypic changes in passaged articular chondrocyte subpopulations. *Journal of Orthopaedic Research,* 23**,** 425-432.

DÄSTER, S., AMATRUDA, N., CALABRESE, D., IVANEK, R., TURRINI, E., DROESER, R. A., ZAJAC, P., FIMOGNARI, C., SPAGNOLI, G. C. & IEZZI, G. 2017. Induction of hypoxia and necrosis in multicellular tumor spheroids is associated with resistance to chemotherapy treatment. *Oncotarget,* 8**,** 1725.

DAWSON, J. I., KANCZLER, J., TARE, R., KASSEM, M. & OREFFO, R. O. 2014. Concise review: bridging the gap: bone regeneration using skeletal stem cell-based strategies - where are we now? *Stem Cells,* 32**,** 35-44.

DEAN, W. R. 1927. XVI. Note on the motion of fluid in a curved pipe. *The London, Edinburgh, and Dublin Philosophical Magazine and Journal of Science,* 4**,** 208-223.

DECKER, R. S., KOYAMA, E. & PACIFICI, M. 2014. Genesis and morphogenesis of limb synovial joints and articular cartilage. *Matrix Biology,* 39**,** 5-10.

DELISE, A., FISCHER, L. & TUAN, R. 2000. Cellular interactions and signaling in cartilage development. *Osteoarthritis and cartilage,* 8**,** 309-334.

DELMONTE, O. M. & FLEISHER, T. A. 2019. Flow cytometry: surface markers and beyond. *Journal of Allergy and Clinical Immunology,* 143**,** 528-537.

DEMOOR, M., OLLITRAULT, D., GOMEZ-LEDUC, T., BOUYOUCEF, M., HERVIEU, M., FABRE, H., LAFONT, J., DENOIX, J.-M., AUDIGIÉ, F. & MALLEIN-GERIN, F. 2014. Cartilage tissue engineering: molecular control of chondrocyte differentiation for proper cartilage matrix reconstruction. *Biochimica et Biophysica Acta (BBA)-General Subjects,* 1840**,** 2414-2440.

DESJARDINS, P. & CONKLIN, D. 2010. NanoDrop microvolume quantitation of nucleic acids. *Journal of visualized experiments: JoVE*.

DICKHUT, A., DEXHEIMER, V., MARTIN, K., LAUINGER, R., HEISEL, C. & RICHTER, W. 2009. Chondrogenesis of human mesenchymal stem cells by local transforming growth factor-beta delivery in a biphasic resorbable carrier. *Tissue Engineering Part A,* 16**,** 453-464.

DICKS, A., WU, C.-L., STEWARD, N., ADKAR, S. S., GERSBACH, C. A. & GUILAK, F. 2020. Prospective isolation of chondroprogenitors from human iPSCs based on cell surface markers identified using a CRISPR-Cas9-generated reporter. *Stem cell research & therapy,* 11**,** 1-14.

DOMINICI, M., LE BLANC, K., MUELLER, I., SLAPER-CORTENBACH, I., MARINI, F., KRAUSE, D., DEANS, R., KEATING, A., PROCKOP, D. & HORWITZ, E. 2006. Minimal criteria for defining multipotent mesenchymal stromal cells. The International Society for Cellular Therapy position statement. *Cytotherapy,* 8**,** 315-317.

DY, P., WANG, W., BHATTARAM, P., WANG, Q., WANG, L., BALLOCK, R. T. & LEFEBVRE, V. 2012. Sox9 directs hypertrophic maturation and blocks osteoblast differentiation of growth plate chondrocytes. *Developmental cell,* 22**,** 597-609.

EDD, J. F., DI CARLO, D., HUMPHRY, K. J., KÖSTER, S., IRIMIA, D., WEITZ, D. A. & TONER, M. 2008. Controlled encapsulation of single-cells into monodisperse picolitre drops. *Lab on a chip,* 8**,** 1262-1264.

ELOWITZ, M. B., LEVINE, A. J., SIGGIA, E. D. & SWAIN, P. S. 2002. Stochastic gene expression in a single cell. *Science,* 297**,** 1183-1186.

ERGGELET, C. & VAVKEN, P. 2016. Microfracture for the treatment of cartilage defects in the knee joint–A golden standard? *Journal of clinical orthopaedics and trauma,* 7**,** 145-152.

ESTES, B. T., DIEKMAN, B. O., GIMBLE, J. M. & GUILAK, F. 2010. Isolation of adipose-derived stem cells and their induction to a chondrogenic phenotype. *Nature protocols,* 5**,** 1294.

FABRE, H., DUCRET, M., DEGOUL, O., RODRIGUEZ, J., PERRIER-GROULT, E., AUBERT-FOUCHER, E., PASDELOUP, M., AUXENFANS, C., MCGUCKIN, C. & FORRAZ, N. 2019. Characterization of different sources of human MSCs expanded in serum-free conditions with quantification of chondrogenic induction in 3D. *Stem Cells International,* 2019.

FALANGA, V. 2012. Stem cells in tissue repair and regeneration. *Journal of Investigative Dermatology,* 132**,** 1538-1541.

FARRELL, M. J., FISHER, M. B., HUANG, A. H., SHIN, J. I., FARRELL, K. M. & MAUCK, R. L. 2014. Functional properties of bone marrow-derived MSC-based engineered cartilage are unstable with very long-term in vitro culture. *Journal of biomechanics,* 47**,** 2173-2182.

FENG, S., YI, L., ZHAO-MIAO, L., REN-TUO, C. & GUI-REN, W. 2015. Advances in micro-droplets coalescence using microfluidics. *Chinese Journal of Analytical Chemistry,* 43**,** 1942-1954.

FERNANDES, T. G., DIOGO, M. M. & CABRAL, J. M. 2013. *Stem Cell Bioprocessing: For Cellular Therapy, Diagnostics and Drug Development*, Elsevier.

FOSTER, J. W., DOMINGUEZ-STEGLICH, M. A., GUIOLI, S., KWOK, C., WELLER, P. A., STEVANOVIĆ, M., WEISSENBACH, J., MANSOUR, S., YOUNG, I. D. & GOODFELLOW, P. N. 1994. Campomelic dysplasia and autosomal sex reversal caused by mutations in an SRY-related gene. *Nature,* 372**,** 525-530.

FOX, A. J. S., BEDI, A. & RODEO, S. A. 2009. The basic science of articular cartilage: structure, composition, and function. *Sports Health: A Multidisciplinary Approach,* 1**,** 461-468.

FRIEDENSTEIN, A., CHAILAKHJAN, R. & LALYKINA, K. 1970. The development of fibroblast colonies in monolayer cultures of guinea-pig bone marrow and spleen cells. *Cell Proliferation,* 3**,** 393-403.

FRISBIE, D. D., MCCARTHY, H. E., ARCHER, C. W., BARRETT, M. F. & MCILWRAITH, C. W. 2015. Evaluation of articular cartilage progenitor cells for the repair of articular defects in an equine model. *JBJS,* 97**,** 484-493.

FRISCHMUTH, T., BUCHEGGER, W., KRAFT, M. & VELLEKOOP, M. J. 2012. *Squeezed microfluidic droplet creation with a T-junction and a flow focusing device at very low flow rates*, na.

GADJANSKI, I., SPILLER, K. & VUNJAK-NOVAKOVIC, G. 2012. Time-dependent processes in stem cell-based tissue engineering of articular cartilage. *Stem Cell Reviews and Reports,* 8**,** 863-881.

GAO, Y., LIU, S., HUANG, J., GUO, W., CHEN, J., ZHANG, L., ZHAO, B., PENG, J., WANG, A. & WANG, Y. 2014. The ECM-cell interaction of cartilage extracellular matrix on chondrocytes. *BioMed research international,* 2014.

GARCÍA-CARVAJAL, Z. Y., GARCIADIEGO-CÁZARES, D., PARRA-CID, C., AGUILAR-GAYTÁN, R., VELASQUILLO, C., IBARRA, C. & CARMONA, J. S. C. 2013. Cartilage tissue engineering: the role of extracellular matrix (ECM) and novel strategies. *Regenerative medicine and tissue engineering. Croatia: InTech***,** 365-397.

GELSE, K., PÖSCHL, E. & AIGNER, T. 2003. Collagens—structure, function, and biosynthesis. *Advanced drug delivery reviews,* 55**,** 1531-1546.

GHARAIBEH, B., LU, A., TEBBETS, J., ZHENG, B., FEDUSKA, J., CRISAN, M., PEAULT, B., CUMMINS, J. & HUARD, J. 2008. Isolation of a slowly adhering cell fraction containing stem cells from murine skeletal muscle by the preplate technique. *Nature Protocols,* 3**,** 1501-1509.

GILBERT, S. J. & BLAIN, E. J. 2018. Cartilage mechanobiology: How chondrocytes respond to mechanical load. *Mechanobiology in Health and Disease.* Elsevier.

GILLAM, M., LIE, S., SALTER, A., FURNES, O., GRAVES, S., HAVELIN, L. & RYAN, P. 2013. The progression of end-stage osteoarthritis: analysis of data from the Australian and Norwegian joint replacement registries using a multi-state model. *Osteoarthritis and Cartilage,* 21**,** 405-412.

GIOVANNINI, S., DIAZ-ROMERO, J., AIGNER, T., HEINI, P., MAINIL-VARLET, P. & NESIC, D. 2010. Micromass co-culture of human articular chondrocytes and human bone marrow mesenchymal stem cells to investigate stable neocartilage tissue formation in vitro. *Eur Cell Mater,* 20**,** 59.

GLENNON-ALTY, L., WILLIAMS, R., DIXON, S. & MURRAY, P. 2013. Induction of mesenchymal stem cell chondrogenesis by polyacrylate substrates. *Acta biomaterialia,* 9**,** 6041-6051.

GLYN-JONES, S., PALMER, A., AGRICOLA, R., PRICE, A., VINCENT, T., WEINANS, H. & CARR, A. 2015. Osteoarthritis. *The Lancet,* 386**,** 376-387.

GOLDBERG, A., MITCHELL, K., SOANS, J., KIM, L. & ZAIDI, R. 2017. The use of mesenchymal stem cells for cartilage repair and regeneration: a systematic review. *Journal of orthopaedic surgery and research,* 12**,** 39.

GONG, G., FERRARI, D., DEALY, C. N. & KOSHER, R. A. 2010. Direct and progressive differentiation of human embryonic stem cells into the chondrogenic lineage. *Journal of cellular physiology,* 224**,** 664-671.

GONG, M., LIANG, T., ZHANG, H., CHEN, S., HU, Y., ZHOU, J., ZHANG, X., ZHANG, W., GENG, X. & ZOU, X. 2018. Gene expression profiling: identification of gene expression in human MSC chondrogenic differentiation. *American journal of translational research,* 10**,** 3555.

GORECKA, J., KOSTIUK, V., FEREYDOONI, A., GONZALEZ, L., LUO, J., DASH, B., ISAJI, T., ONO, S., LIU, S. & LEE, S. R. 2019. The potential and limitations of induced pluripotent stem cells to achieve wound healing. *Stem cell research & therapy,* 10**,** 1-10.

GOU, Y., JIA, Y., WANG, P. & SUN, C. 2018. Progress of inertial microfluidics in principle and application. *Sensors,* 18**,** 1762.

GOUDE, M. C., MCDEVITT, T. C. & TEMENOFF, J. S. 2014. Chondroitin sulfate microparticles modulate transforming growth factor-β1-induced chondrogenesis of human mesenchymal stem cell spheroids. *Cells Tissues Organs,* 199**,** 117-130.

GRAF, T. & STADTFELD, M. 2008. Heterogeneity of embryonic and adult stem cells. *Cell stem cell,* 3**,** 480-483.

GRAVES, J. P., GRUZDEV, A., BRADBURY, J. A., DEGRAFF, L. M., LI, H., HOUSE, J. S., HOOPES, S. L., EDIN, M. L. & ZELDIN, D. C. 2015. Quantitative polymerase chain reaction analysis of the mouse Cyp2j subfamily: Tissue distribution and regulation. *Drug Metabolism and Disposition,* 43**,** 1169-1180.

GRIESCHE, N., LUTTMANN, W., LUTTMANN, A., STAMMERMANN, T., GEIGER, H. & BAER, P. C. 2010. A simple modification of the separation method reduces heterogeneity of adipose-derived stem cells. *Cells Tissues Organs,* 192**,** 106-115.

GROGAN, S. P., BARBERO, A., WINKELMANN, V., RIESER, F., FITZSIMMONS, J. S., O'DRISCOLL, S., MARTIN, I. & MAINIL-VARLET, P. 2006. Visual histological grading system for the evaluation of in vitro–generated neocartilage. *Tissue engineering,* 12**,** 2141-2149.

GRONTHOS, S., MCCARTY, R., MROZIK, K., FITTER, S., PATON, S., MENICANIN, D., ITESCU, S., BARTOLD, P. M., XIAN, C. & ZANNETTINO, A. C. 2009. Heat shock protein-90 beta is expressed at the surface of multipotential mesenchymal precursor cells: generation of a novel monoclonal antibody, STRO-4, with specificity for mesenchymal precursor cells from human and ovine tissues. *Stem cells and development,* 18**,** 1253-1262.

GU, H., DUITS, M. H. & MUGELE, F. 2011. Droplets formation and merging in two-phase flow microfluidics. *International journal of molecular sciences,* 12**,** 2572-2597.

GUNDRY, R. L., BURRIDGE, P. W. & BOHELER, K. R. 2011. Pluripotent stem cell heterogeneity and the evolving role of proteomic technologies in stem cell biology. *Proteomics,* 11**,** 3947-3961.

GUNES, D. Z., CLAIN, X., BRETON, O., MAYOR, G. & BURBIDGE, A. S. 2010. Avalanches of coalescence events and local extensional flows–Stabilisation or destabilisation due to surfactant. *Journal of colloid and interface science,* 343**,** 79-86.

GUO, M. T., ROTEM, A., HEYMAN, J. A. & WEITZ, D. A. 2012. Droplet microfluidics for high-throughput biological assays. *Lab on a Chip,* 12**,** 2146-2155.

GUPTA, P. K., DAS, A. K., CHULLIKANA, A. & MAJUMDAR, A. S. 2012. Mesenchymal stem cells for cartilage repair in osteoarthritis. *Stem cell research & therapy,* 3**,** 25.

HAIDER, M., CAPPELLO, J., GHANDEHARI, H. & LEONG, K. W. 2008. In vitro chondrogenesis of mesenchymal stem cells in recombinant silk-elastinlike hydrogels. *Pharmaceutical research,* 25**,** 692-699.

HALL, B. K. & MIYAKE, T. 2000. All for one and one for all: condensations and the initiation of skeletal development. *Bioessays,* 22**,** 138-147.

HALO, T. L., MCMAHON, K. M., ANGELONI, N. L., XU, Y., WANG, W., CHINEN, A. B., MALIN, D., STREKALOVA, E., CRYNS, V. L. & CHENG, C. 2014. NanoFlares for the detection, isolation, and culture of live tumor cells from human blood. *Proceedings of the National Academy of Sciences,* 111**,** 17104-17109.

HAMILTON, G. & RATH, B. 2019. Role of circulating tumor cell spheroids in drug resistance. *Cancer Drug Resist,* 2**,** 762-72.

HAN, H. S., LEE, S., KIM, J. H., SEONG, S. C. & LEE, M. C. 2010. Changes in chondrogenic phenotype and gene expression profiles associated with the in vitro expansion of human synovium-derived cells. *Journal of Orthopaedic Research,* 28**,** 1283-1291.

HAN, L., GRODZINSKY, A. J. & ORTIZ, C. 2011. Nanomechanics of the cartilage extracellular matrix. *Annual review of materials research,* 41**,** 133.

HATTORI, T., MÜLLER, C., GEBHARD, S., BAUER, E., PAUSCH, F., SCHLUND, B., BÖSL, M. R., HESS, A., SURMANN-SCHMITT, C. & VON DER MARK, H. 2010. SOX9 is a major negative regulator of cartilage vascularization, bone marrow formation and endochondral ossification. *Development,* 137**,** 901-911.

HE, B., WU, J. P., CHEN, H. H., KIRK, T. B. & XU, J. 2013. Elastin fibers display a versatile microfibril network in articular cartilage depending on the mechanical microenvironments. *Journal of Orthopaedic Research,* 31**,** 1345-1353.

HE, T., HUANG, Y., CHAK, J. C. & KLAR, R. M. 2018. Recommendations for improving accuracy of gene expression data in bone and cartilage tissue engineering. *Scientific reports,* 8**,** 1-13.

HE, Y., GUDMANN, N. S., BAY-JENSEN, A. C., KARSDAL, M. A., ENGSTROEM, A. & THUDIUM, C. S. 2019. Type II collagen. *Biochemistry of Collagens, Laminins and Elastin: Structure, Function and Biomarkers.*

HE, Y. & KARSDAL, M. 2016. Type IX Collagen. *Biochemistry of Collagens, Laminins and Elastin.* Elsevier.

HE, Y. X., ZHANG, Y., YANG, Q., WANG, C. & SU, G. 2015. Selection of suitable reference genes for reverse transcription-quantitative polymerase chain reaction analysis of neuronal cells differentiated from bone mesenchymal stem cells. *Molecular medicine reports,* 12**,** 2291-2300.

HENDRIX, M., HAY, E. D., VON DER MARK, K. & LINSENMAYER, T. F. 1982. Immunohistochemical localization of collagen types I and II in the developing chick cornea and tibia by electron microscopy. *Investigative ophthalmology & visual science,* 22**,** 359-375.

HERMIDA-GÓMEZ, T., FUENTES-BOQUETE, I., GIMENO-LONGAS, M. J., MUIÑOS-LÓPEZ, E., DÍAZ-PRADO, S., DE TORO, F. J. & BLANCO, F. J. 2011. Bone marrow cells immunomagnetically selected for CD271+ antigen promote in vitro the repair of articular cartilage defects. *Tissue Engineering Part A,* 17**,** 1169-1179.

HOEMANN, C. D., LAFANTAISIE-FAVREAU, C.-H., LASCAU-COMAN, V., CHEN, G. & GUZMÁN-MORALES, J. 2012. The cartilage-bone interface. *Journal of Knee Surgery,* 25**,** 085-098.

HOLLANDER, A. P., DICKINSON, S. C. & KAFIENAH, W. 2010. Stem cells and cartilage development: complexities of a simple tissue. *Stem cells,* 28**,** 1992-1996.

HOLLOWAY, P. M., BUTEMENT, J., HEGDE, M. & WEST, J. 2018. Serial integration of Dean-structured sample cores with linear inertial focussing for enhanced particle and cell sorting. *Biomicrofluidics,* 12**,** 044104.

HOLTZE, C., ROWAT, A., AGRESTI, J., HUTCHISON, J., ANGILE, F., SCHMITZ, C., KÖSTER, S., DUAN, H., HUMPHRY, K. & SCANGA, R. 2008. Biocompatible surfactants for water-in-fluorocarbon emulsions. *Lab on a Chip,* 8**,** 1632-1639.

HOPPER, N., WARDALE, J., BROOKS, R., POWER, J., RUSHTON, N. & HENSON, F. 2015. Peripheral Blood Mononuclear Cells Enhance Cartilage Repair in in vivo Osteochondral Defect Model. *Plos One,* 10.

HOSOKAWA, M., NISHIKAWA, Y., KOGAWA, M. & TAKEYAMA, H. 2017. Massively parallel whole genome amplification for single-cell sequencing using droplet microfluidics. *Scientific reports,* 7**,** 5199.

HSIAO, A. Y., TORISAWA, Y.-S., TUNG, Y.-C., SUD, S., TAICHMAN, R. S., PIENTA, K. J. & TAKAYAMA, S. 2009. Microfluidic system for formation of PC-3 prostate cancer co-culture spheroids. *Biomaterials,* 30**,** 3020-3027.

HUANG, B. J., HU, J. C. & ATHANASIOU, K. A. 2016. Cell-based tissue engineering strategies used in the clinical repair of articular cartilage. *Biomaterials,* 98**,** 1-22.

HUGHES, T. R. 2011. *A handbook of transcription factors*, Springer Science & Business Media.

HUNZIKER, E. B. 2002. Articular cartilage repair: basic science and clinical progress. A review of the current status and prospects. *Osteoarthritis and cartilage,* 10**,** 432-463.

IKEDA, T., KAWAGUCHI, H., KAMEKURA, S., OGATA, N., MORI, Y., NAKAMURA, K., IKEGAWA, S. & CHUNG, U.-I. 2005. Distinct roles of Sox5, Sox6, and Sox9 in different stages of chondrogenic differentiation. *Journal of bone and mineral metabolism,* 23**,** 337-340.

IKEGAMI, D., AKIYAMA, H., SUZUKI, A., NAKAMURA, T., NAKANO, T., YOSHIKAWA, H. & TSUMAKI, N. 2011. Sox9 sustains chondrocyte survival and hypertrophy in part through Pik3ca-Akt pathways. *Development,* 138**,** 1507-1519.

ISLAM, M. A., HANSEN, A. K., MENNAN, C. & MARTINEZ, I. Z. 2016. Mesenchymal stromal cells from human umbilical cords display poor chondrogenic potential in scaffold-free three dimensional cultures.

JAYASURIYA, C. T., CHEN, Y., LIU, W. & CHEN, Q. 2016. The influence of tissue microenvironment on stem cell–based cartilage repair. *Annals of the New York Academy of Sciences,* 1383**,** 21-33.

JEVONS, L. A., HOUGHTON, F. D. & TARE, R. S. 2018. Augmentation of musculoskeletal regeneration: role for pluripotent stem cells. *Regenerative medicine,* 13**,** 189-206.

JIANG, X., HUANG, X., JIANG, T., ZHENG, L., ZHAO, J. & ZHANG, X. 2018. The role of Sox9 in collagen hydrogel-mediated chondrogenic differentiation of adult mesenchymal stem cells (MSCs). *Biomaterials science,* 6**,** 1556-1568.

JIANG, Z., YU, S., LIN, H. & BI, R. 2020. Expression and function of cartilage-derived pluripotent cells in joint development and repair. *Stem Cell Research & Therapy,* 11**,** 1-9.

JO, A., DENDULURI, S., ZHANG, B., WANG, Z., YIN, L., YAN, Z., KANG, R., SHI, L. L., MOK, J. & LEE, M. J. 2014. The versatile functions of Sox9 in development, stem cells, and human diseases. *Genes & Diseases,* 1**,** 149-161.

JOENSSON, H. N. & ANDERSSON SVAHN, H. 2012. Droplet Microfluidics—A Tool for Single-Cell Analysis. *Angewandte Chemie International Edition,* 51**,** 12176-12192.

KABIRAJ, A., GUPTA, J., KHAITAN, T. & BHATTACHARYA, P. T. 2015. Principle and techniques of Immunohistochemistry-a review. *Int J Biol Med Res,* 6**,** 5204-5210.

KAMIL, S., KOJIMA, K., VACANTI, M., ZAPOROJAN, V., VACANTI, C. & EAVEY, R. 2007. Tissue engineered cartilage: utilization of autologous serum and serum-free media for chondrocyte culture. *International journal of pediatric otorhinolaryngology,* 71**,** 71-75.

KAMPERMAN, T., HENKE, S., VISSER, C. W., KARPERIEN, M. & LEIJTEN, J. 2017. Centering Single Cells in Microgels via Delayed Crosslinking Supports Long-Term 3D Culture by Preventing Cell Escape. *small,* 13.

KELC, R., NARANDA, J., KUHTA, M. & VOGRIN, M. 2013. Novel Therapies for the Management of Sports Injuries. *Current Issues in Sports and Exercise Medicine*.

KEMNA, E. W. M., SCHOEMAN, R. M., WOLBERS, F., VERMES, I., WEITZ, D. A. & VAN DEN BERG, A. 2012. High-yield cell ordering and deterministic cell-in-droplet encapsulation using Dean flow in a curved microchannel. *Lab on a Chip,* 12**,** 2881-2887.

KHANG, G., SHIMIZU, T. & NGSERIES, K. W. 2014. *A Manual for Differentiation of Bone Marrow-Derived Stem Cells to Specific Cell Types*, World Scientific Publishing Company.

KIERSZENBAUM, A. L. & TRES, L. 2015. *Histology and cell biology: an introduction to pathology*, Elsevier Health Sciences.

KIM, H. J. & PARK, J.-S. 2017. Usage of human mesenchymal stem cells in cell-based therapy: advantages and disadvantages. *Development & reproduction,* 21**,** 1.

KIM, I. L., MAUCK, R. L. & BURDICK, J. A. 2011a. Hydrogel design for cartilage tissue engineering: a case study with hyaluronic acid. *Biomaterials,* 32**,** 8771-82.

KIM, S.-H., TURNBULL, J. & GUIMOND, S. 2011b. Extracellular matrix and cell signalling: the dynamic cooperation of integrin, proteoglycan and growth factor receptor. *Journal of Endocrinology,* 209**,** 139-151.

KINTSES, B., VAN VLIET, L. D., DEVENISH, S. R. & HOLLFELDER, F. 2010. Microfluidic droplets: new integrated workflows for biological experiments. *Current opinion in chemical biology,* 14**,** 548-555.

KISSELL, R. & POSSERINA, J. 2017. Advanced Math and Statistics. *Optimal Sports Math, Statistics, and Fantasy***,** 103-135.

KNUTH, C., ANDRES SASTRE, E., FAHY, N., WITTE-BOUMA, J., RIDWAN, Y., STRABBING, E., KOUDSTAAL, M., VAN DE PEPPEL, J., WOLVIUS, E. & NARCISI, R. 2019. Collagen type X is essential for successful mesenchymal stem cell-mediated cartilage formation and subsequent endochondral ossification. *European cells & materials,* 38**,** 106-122.

KOAY, E. J., HOBEN, G. M. & ATHANASIOU, K. A. 2007. Tissue engineering with chondrogenically differentiated human embryonic stem cells. *Stem cells,* 25**,** 2183-2190.

KOGA, H., MUNETA, T., NAGASE, T., NIMURA, A., JU, Y. J., MOCHIZUKI, T. & SEKIYA, I. 2008. Comparison of mesenchymal tissues-derived stem cells for in vivo chondrogenesis: suitable conditions for cell therapy of cartilage defects in rabbit. *Cell and Tissue Research,* 333**,** 207-215.

KOLAMBKAR, Y. M., PEISTER, A., SOKER, S., ATALA, A. & GULDBERG, R. E. 2007. Chondrogenic differentiation of amniotic fluid-derived stem cells. *Journal of Molecular Histology,* 38**,** 405-413.

KRAHL, D. & SELLHEYER, K. 2010. Basal cell carcinoma and pilomatrixoma mirror human follicular embryogenesis as reflected by their differential expression patterns of SOX9 and β-catenin. *British Journal of Dermatology,* 162**,** 1294-1301.

KRIEGER, T. & SIMONS, B. D. 2015. Dynamic stem cell heterogeneity. *Development,* 142**,** 1396-1406.

KRÖNIG, M., WALTER, M., DRENDEL, V., WERNER, M., JILG, C. A., RICHTER, A. S., BACKOFEN, R., MCGARRY, D., FOLLO, M. & SCHULTZE-SEEMANN, W. 2015. Cell type specific gene expression analysis of prostate needle biopsies resolves tumor tissue heterogeneity. *Oncotarget,* 6**,** 1302.

KULYK, W. M., FRANKLIN, J. L. & HOFFMAN, L. M. 2000. Sox9 expression during chondrogenesis in micromass cultures of embryonic limb mesenchyme. *Experimental cell research,* 255**,** 327-332.

KURODA, R., USAS, A., KUBO, S., CORSI, K., PENG, H. R., ROSE, T., CUMMINS, J., FU, F. H. & HUARD, J. 2006. Cartilage repair using bone morphogenetic protein 4 and muscle-derived stem cells. *Arthritis and Rheumatism,* 54**,** 433-442.

KYRIAZI, M.-E., GIUST, D., EL-SAGHEER, A. H., LACKIE, P. M., MUSKENS, O. L., BROWN, T. & KANARAS, A. G. 2018. Multiplexed mRNA sensing and combinatorial-targeted drug delivery using DNA-gold nanoparticle dimers. *Acs Nano,* 12**,** 3333-3340.

LACERDA, C., MACLEA, H. B., DUNCAN, C. G., KISIDAY, J. D. & ORTON, E. C. 2013. Human myxomatous mitral valves exhibit focal expression of cartilage-related proteins. *J Hypertens Cardiol,* 1**,** 1-10.

LAGUS, T. P. & EDD, J. F. 2012. High throughput single-cell and multiple-cell micro-encapsulation. *Journal of visualized experiments: JoVE*.

LAHM, H., DOPPLER, S., DREßEN, M., WERNER, A., ADAMCZYK, K., SCHRAMBKE, D., BRADE, T., LAUGWITZ, K.-L., DEUTSCH, M.-A. & SCHIEMANN, M. 2015. Live Fluorescent RNA-Based Detection of Pluripotency Gene Expression in Embryonic and Induced Pluripotent Stem Cells of Different Species. *Stem Cells,* 33**,** 392-402.

LAM, J., LU, S., KASPER, F. K. & MIKOS, A. G. 2015. Strategies for controlled delivery of biologics for cartilage repair. *Advanced Drug Delivery Reviews,* 84**,** 123-34.

LANGER, R. & VACANTI, J. P. 1993. Tissue engineering. *Science (New York, NY),* 260**,** 920-926.

LANHAM, S., XAVIER, M., KYRIAZI, M., ALEXAKI, K., EL-SAGHEER, A., BROWN, T., KANARAS, A. & OREFFO, R. O. 2019. Optimising DNA-Coated Gold Nanoparticles to Enrich Skeletal Stem Cells from Human Bone Marrow Samples. *bioRxiv*.

LASCHKE, M. W. & MENGER, M. D. 2017. Life is 3D: boosting spheroid function for tissue engineering. *Trends in biotechnology,* 35**,** 133-144.

LAWRENCE, T. L. J., FOWLER, V. R. & NOVAKOFSKI, J. E. 2012. *Growth of farm animals*, CABI.

LEE, D., KIM, D., KIM, Y., PARK, K. H., OH, E. J., KIM, Y. & KIM, B. 2014. A negative dielectrophoresis and gravity-driven flow-based high-throughput and high-efficiency cell-sorting system. *Journal of Laboratory Automation,* 19**,** 60-74.

LEE, P., TRAN, K., ZHOU, G., BEDI, A., SHELKE, N. B., YU, X. & KUMBAR, S. G. 2015. Guided differentiation of bone marrow stromal cells on co-cultured cartilage and bone scaffolds. *Soft matter,* 11**,** 7648-7655.

LEE, Z., DENNIS, J., ALSBERG, E., KREBS, M. D., WELTER, J. & CAPLAN, A. 2012. Imaging stem cell differentiation for cell-based tissue repair. *Methods in Enzymology.* Elsevier.

LEFEBVRE, V., ANGELOZZI, M. & HASEEB, A. 2019. SOX9 in cartilage development and disease. *Current Opinion in Cell Biology,* 61**,** 39-47.

LEIJTEN, J., TEIXEIRA, L. M., BOLANDER, J., JI, W., VANSPAUWEN, B., LAMMERTYN, J., SCHROOTEN, J. & LUYTEN, F. 2016. Bioinspired seeding of biomaterials using three dimensional microtissues induces chondrogenic stem cell differentiation and cartilage formation under growth factor free conditions. *Scientific reports,* 6**,** 36011.

LEVENBERG, S., KHADEMHOSSEINI, A. & LANGER, R. 2009. Embryonic stem cells in tissue engineering. *Essentials of Stem Cell Biology.* Elsevier.

LEWIS, M. C., MACARTHUR, B. D., TARE, R. S., OREFFO, R. O. & PLEASE, C. P. 2016. Extracellular matrix deposition in engineered micromass cartilage pellet cultures: measurements and modelling. *PloS one,* 11**,** e0147302.

LI, B., MENZEL, U., LOEBEL, C., SCHMAL, H., ALINI, M. & STODDART, M. J. 2016. Monitoring live human mesenchymal stromal cell differentiation and subsequent selection using fluorescent RNA-based probes. *Scientific reports,* 6.

LI, F., TRUONG, V. X., THISSEN, H., FRITH, J. E. & FORSYTHE, J. S. 2017. Microfluidic encapsulation of human mesenchymal stem cells for articular cartilage tissue regeneration. *ACS applied materials & interfaces,* 9**,** 8589-8601.

LI, J. & DONG, S. 2016. The signaling pathways involved in chondrocyte differentiation and hypertrophic differentiation. *Stem cells international,* 2016.

LI, J., HUANG, J., YANG, X., YANG, Y., QUAN, K., XIE, N., WU, Y., MA, C. & WANG, K. 2018. Two-Color-Based Nanoflares for Multiplexed MicroRNAs Imaging in Live Cells. *Nanotheranostics,* 2**,** 96.

LI, Q., TANG, J., WANG, R., BEI, C., XIN, L., ZENG, Y. & TANG, X. 2011. Comparing the chondrogenic potential in vivo of autogeneic mesenchymal stem cells derived from different tissues. *Artificial Cells, Blood Substitutes, and Biotechnology,* 39**,** 31-38.

LI, S., GLYNNE-JONES, P., ANDRIOTIS, O. G., CHING, K. Y., JONNALAGADDA, U. S., OREFFO, R. O., HILL, M. & TARE, R. S. 2014. Application of an acoustofluidic perfusion bioreactor for cartilage tissue engineering. *Lab on a Chip,* 14**,** 4475-85.

LI, S., SENGERS, B. G., OREFFO, R. O. & TARE, R. S. 2015. Chondrogenic potential of human articular chondrocytes and skeletal stem cells: a comparative study. *Journal of biomaterials applications,* 29**,** 824-836.

LIN, M., YI, X., HUANG, F., MA, X., ZUO, X. & XIA, F. 2019. Photoactivated Nanoflares for mRNA Detection in Single Living Cells. *Analytical chemistry,* 91**,** 2021-2027.

LIN, R. Z. & CHANG, H. Y. 2008. Recent advances in three-dimensional multicellular spheroid culture for biomedical research. *Biotechnol J,* 3**,** 1172-84.

LIN, Z., WILLERS, C., XU, J. & ZHENG, M.-H. 2006. The chondrocyte: biology and clinical application. *Tissue engineering,* 12**,** 1971-1984.

LITWIC, A., EDWARDS, M. H., DENNISON, E. M. & COOPER, C. 2013. Epidemiology and burden of osteoarthritis. *British medical bulletin,* 105**,** 185-199.

LIU, C.-F., ANGELOZZI, M., HASEEB, A. & LEFEBVRE, V. 2018. SOX9 is dispensable for the initiation of epigenetic remodeling and the activation of marker genes at the onset of chondrogenesis. *Development,* 145.

LIU, C.-F. & LEFEBVRE, V. 2015. The transcription factors SOX9 and SOX5/SOX6 cooperate genome-wide through super-enhancers to drive chondrogenesis. *Nucleic acids research,* 43**,** 8183-8203.

LIU, H. & CAO, G. 2016. Effectiveness of the Young-Laplace equation at nanoscale. *Scientific reports,* 6**,** 23936.

LIU, L., XIANG, N., NI, Z., HUANG, X., ZHENG, J., WANG, Y. & ZHANG, X. 2020. Step emulsification: high-throughput production of monodisperse droplets. Future Science.

LIU, Y., XUE, Z.-L., CHEN, S.-P., WANG, Z., ZHANG, Y., GONG, W.-L. & ZHENG, Z.-M. 2016. A high-throughput screening strategy for accurate quantification of menaquinone based on fluorescence-activated cell sorting. *Journal of industrial microbiology & biotechnology***,** 1-10.

LIVAK, K. J. & SCHMITTGEN, T. D. 2001. Analysis of relative gene expression data using real-time quantitative PCR and the 2− ΔΔCT method. *methods,* 25**,** 402-408.

LOEBEL, C., CZEKANSKA, E. M., BRUDERER, M., SALZMANN, G., ALINI, M. & STODDART, M. J. 2015. In vitro osteogenic potential of human mesenchymal stem cells is predicted by Runx2/Sox9 ratio. *Tissue Engineering Part A,* 21**,** 115-123.

LORDA-DIEZ, C. I., MONTERO, J. A., DIAZ-MENDOZA, M. J., GARCIA-PORRERO, J. A. & HURLE, J. M. 2011. Defining the earliest transcriptional steps of chondrogenic progenitor specification during the formation of the digits in the embryonic limb. *PloS one,* 6**,** e24546.

LUND, T. C., TOLAR, J. & ORCHARD, P. J. 2008. Granulocyte colony-stimulating factor mobilized CFU-F can be found in the peripheral blood but have limited expansion potential. *Haematologica-the Hematology Journal,* 93**,** 908-912.

LUO, Y., SINKEVICIUTE, D., HE, Y., KARSDAL, M., HENROTIN, Y., MOBASHERI, A., ÖNNERFJORD, P. & BAY-JENSEN, A. 2017. The minor collagens in articular cartilage. *Protein & cell,* 8**,** 560-572.

LV, F. J., TUAN, R. S., CHEUNG, K. M. C. & LEUNG, V. Y. L. 2014. Concise Review: The Surface Markers and Identity of Human Mesenchymal Stem Cells. *Stem Cells,* 32**,** 1408-1419.

MACKIE, E., AHMED, Y., TATARCZUCH, L., CHEN, K.-S. & MIRAMS, M. 2008. Endochondral ossification: how cartilage is converted into bone in the developing skeleton. *The international journal of biochemistry & cell biology,* 40**,** 46-62.

MADRY, H., LUYTEN, F. P. & FACCHINI, A. 2012. Biological aspects of early osteoarthritis. *Knee Surgery, Sports Traumatology, Arthroscopy,* 20**,** 407-422.

MAHBOUDI, H., KAZEMI, B., HANAEE-AHVAZ, H., ARDESHIRYLAJIMI, A., EFTEKHARY, M. & ENDERAMI, S. E. 2017. Comparison between High Cell-Density Culture Systems for Chondrogenic Differentiation and Articular Cartilage Reconstruction of Human Mesenchymal Stem Cells: A Literature Review. *Regeneration, Reconstruction, & Restoration,* 2**,** 7-15.

MAHMOUDIFAR, N. & DORAN, P. M. 2012. Chondrogenesis and cartilage tissue engineering: the longer road to technology development. *Trends in biotechnology,* 30**,** 166-176.

MAKRIS, E. A., GOMOLL, A. H., MALIZOS, K. N., HU, J. C. & ATHANASIOU, K. A. 2015. Repair and tissue engineering techniques for articular cartilage. *Nature Reviews Rheumatology,* 11**,** 21.

MAN, G. & MOLOGHIANU, G. 2014. Osteoarthritis pathogenesis–a complex process that involves the entire joint. *Journal of medicine and life,* 7**,** 37.

MARÍN-LLERA, J. C., GARCIADIEGO-CÁZARES, D. & CHIMAL-MONROY, J. 2019. Understanding the cellular and molecular mechanisms that control early cell fate decisions during appendicular skeletogenesis. *Frontiers in genetics,* 10**,** 977.

MARKIDES, H., MCLAREN, J. S., TELLING, N. D., ALOM, N., E'ATELAF, A., OREFFO, R. O., ZANNETTINO, A., SCAMMELL, B. E., WHITE, L. J. & EL HAJ, A. J. 2018. Translation of remote control regenerative technologies for bone repair. *NPJ Regenerative medicine,* 3**,** 9.

MARYAM, S., JIANING, S. & WILSON, S. L. 2019. The efficacy of different sources of mesenchymal stem cells for the treatment of knee osteoarthritis. *Cell and tissue research***,** 1-12.

MASHAGHI, S., ABBASPOURRAD, A., WEITZ, D. A. & VAN OIJEN, A. M. 2016. Droplet microfluidics: A tool for biology, chemistry and nanotechnology. *TrAC Trends in Analytical Chemistry,* 82**,** 118-125.

MASON, D., CAROLAN, G., HELD, M., COMENGE, J. & LÉVY, R. 2016. The spherical nucleic acids mRNA detection paradox. *ScienceOpen Research***,** 1-10.

MATTA, C. & MOBASHERI, A. 2014. Regulation of chondrogenesis by protein kinase C: emerging new roles in calcium signalling. *Cellular signalling,* 26**,** 979-1000.

MATTANOVICH, D. & BORTH, N. 2006. Applications of cell sorting in biotechnology. *Microbial cell factories,* 5**,** 1-11.

MAZUTIS, L., GILBERT, J., UNG, W. L., WEITZ, D. A., GRIFFITHS, A. D. & HEYMAN, J. A. 2013. Single-cell analysis and sorting using droplet-based microfluidics. *Nature protocols,* 8**,** 870-891.

MCCALL, M. N., MCMURRAY, H. R., LAND, H. & ALMUDEVAR, A. 2014. On non-detects in qPCR data. *Bioinformatics,* 30**,** 2310-2316.

MCDERMOTT, G. P., DO, D., LITTERST, C. M., MAAR, D., HINDSON, C. M., STEENBLOCK, E. R., LEGLER, T. C., JOUVENOT, Y., MARRS, S. H. & BEMIS, A. 2013. Multiplexed target detection using DNA-binding dye chemistry in droplet digital PCR. *Analytical chemistry,* 85**,** 11619-11627.

MEDVEDEV, S., SHEVCHENKO, A. & ZAKIAN, S. 2010. Induced pluripotent stem cells: problems and advantages when applying them in regenerative medicine. *Acta Naturae (англоязычная версия),* 2.

MEDVEDEVA, E. V., GREBENIK, E. A., GORNOSTAEVA, S. N., TELPUHOV, V. I., LYCHAGIN, A. V., TIMASHEV, P. S. & CHAGIN, A. S. 2018. Repair of damaged articular cartilage: current approaches and future directions. *International journal of molecular sciences,* 19**,** 2366.

MEROLA, M. & AFFATATO, S. 2019. Materials for hip prostheses: A review of wear and loading considerations. *Materials,* 12**,** 495.

MIFUNE, Y., MATSUMOTO, T., TAKAYAMA, K., OTA, S., LI, H., MESZAROS, L. B., USAS, A., NAGAMUNE, K., GHARAIBEH, B. & FU, F. 2013. The effect of platelet-rich plasma on the regenerative therapy of muscle derived stem cells for articular cartilage repair. *Osteoarthritis and Cartilage,* 21**,** 175-185.

MIRKIN, C. A., LETSINGER, R. L., MUCIC, R. C. & STORHOFF, J. J. 1996. A DNA-based method for rationally assembling nanoparticles into macroscopic materials. *Nature,* 382**,** 607-609.

MISTRY, H., CONNOCK, M., PINK, J., SHYANGDAN, D., CLAR, C., ROYLE, P., COURT, R., BIANT, L. C., METCALFE, A. & WAUGH, N. 2017. Autologous chondrocyte implantation in the knee: systematic review and economic evaluation.

MOLLON, B., KANDEL, R., CHAHAL, J. & THEODOROPOULOS, J. 2013. The clinical status of cartilage tissue regeneration in humans. *Osteoarthritis and cartilage,* 21**,** 1824-1833.

MOREIRA TEIXEIRA, L., LEIJTEN, J., SOBRAL, J., JIN, R., APELDOORN, A., FEIJEN, J., BLITTERSWIJK, C., DIJKSTRA, P. & KARPERIEN, H. 2012. High throughput generated micro-aggregates of chondrocytes stimulate cartilage formation in vitro and in vivo. *European cells & materials,* 23**,** 387-399.

MOSNA, F., SENSEBE, L. & KRAMPERA, M. 2010. Human bone marrow and adipose tissue mesenchymal stem cells: a user's guide. *Stem cells and development,* 19**,** 1449-1470.

MUELLER, M. B., FISCHER, M., ZELLNER, J., BERNER, A., DIENSTKNECHT, T., PRANTL, L., KUJAT, R., NERLICH, M., TUAN, R. S. & ANGELE, P. 2010. Hypertrophy in mesenchymal stem cell chondrogenesis: Effect of TGF-β isoforms and chondrogenic conditioning. *Cells Tissues Organs,* 192**,** 158-166.

MUELLER, M. B. & TUAN, R. S. 2008. Functional characterization of hypertrophy in chondrogenesis of human mesenchymal stem cells. *Arthritis & Rheumatism,* 58**,** 1377-1388.

MURPHY, K. C., HUNG, B. P., BROWNE-BOURNE, S., ZHOU, D., YEUNG, J., GENETOS, D. C. & LEACH, J. K. 2017. Measurement of oxygen tension within mesenchymal stem cell spheroids. *Journal of The Royal Society Interface,* 14**,** 20160851.

NAKAGAWA, T., LEE, S. Y. & REDDI, A. H. 2009. Induction of chondrogenesis from human embryonic stem cells without embryoid body formation by bone morphogenetic protein 7 and transforming growth factor β1. *Arthritis & Rheumatism: Official Journal of the American College of Rheumatology,* 60**,** 3686-3692.

NARCISI, R., CLEARY, M. A., BRAMA, P. A., HOOGDUIJN, M. J., TÜYSÜZ, N., TEN BERGE, D. & VAN OSCH, G. J. 2015. Long-term expansion, enhanced chondrogenic potential, and suppression of endochondral ossification of adult human MSCs via WNT signaling modulation. *Stem cell reports,* 4**,** 459-472.

NAWAZ, A. A., CHEN, Y., NAMA, N., NISSLY, R. H., REN, L., OZCELIK, A., WANG, L., MCCOY, J. P., LEVINE, S. J. & HUANG, T. J. 2015. Acoustofluidic Fluorescence Activated Cell Sorter. *Analytical chemistry,* 87**,** 12051-12058.

NG, K. K., THATTE, H. S. & SPECTOR, M. 2011. Chondrogenic differentiation of adult mesenchymal stem cells and embryonic cells in collagen scaffolds. *Journal of Biomedical Materials Research Part A,* 99**,** 275-282.

NIGHTINGALE, A., KRISHNADASAN, S., BERHANU, D., NIU, X., DRURY, C., MCINTYRE, R. & VALSAMI-JONES, E. 2011. A stable droplet reactor for high temperature nanocrystal synthesis. *Lab on a Chip,* 11**,** 1221-1227.

NIU, X. & DEMELLO, A. J. 2012. Building droplet-based microfluidic systems for biological analysis. *Biochemical Society Transactions,* 40**,** 615-23.

NIU, X., GIELEN, F., EDEL, J. B. & DEMELLO, A. J. 2011. A microdroplet dilutor for high-throughput screening. *Nature Chemistry,* 3**,** 437-42.

NIU, X., GULATI, S. & EDEL, J. B. 2008. Pillar-induced droplet merging in microfluidic circuits. *Lab on a Chip,* 8**,** 1837-1841.

NIU, X., PEREIRA, F., EDEL, J. B. & DE MELLO, A. J. 2013. Droplet-interfaced microchip and capillary electrophoretic separations. *Analytical Chemistry,* 85**,** 8654-60.

O'BRIEN, F. J. 2011. Biomaterials & scaffolds for tissue engineering. *Materials today,* 14**,** 88-95.

OCCHETTA, P., CENTOLA, M., TONNARELLI, B., REDAELLI, A., MARTIN, I. & RASPONI, M. 2015. High-throughput microfluidic platform for 3D cultures of mesenchymal stem cells, towards engineering developmental processes. *Scientific reports,* 5**,** 10288.

OCCHETTA, P., PIGEOT, S., RASPONI, M., DASEN, B., MEHRKENS, A., ULLRICH, T., KRAMER, I., GUTH-GUNDEL, S., BARBERO, A. & MARTIN, I. 2018. Developmentally inspired programming of adult human mesenchymal stromal cells toward stable chondrogenesis. *Proceedings of the National Academy of Sciences of the United States of America,* 115**,** 4625-4630.

ONO, N. & KRONENBERG, H. M. 2018. Developmental biology of musculoskeletal tissues for tissue engineers. *Developmental Biology and Musculoskeletal Tissue Engineering.* Elsevier.

OOKAWARA, S., HIGASHI, R., STREET, D. & OGAWA, K. 2004. Feasibility study on concentration of slurry and classification of contained particles by microchannel. *Chemical Engineering Journal,* 101**,** 171-178.

OSHIMORI, N. & FUCHS, E. 2012. The harmonies played by TGF-β in stem cell biology. *Cell Stem Cell,* 11**,** 751-764.

OTERO, M., FAVERO, M., DRAGOMIR, C., EL HACHEM, K., HASHIMOTO, K., PLUMB, D. A. & GOLDRING, M. B. 2012. Human chondrocyte cultures as models of cartilage-specific gene regulation. *Human cell culture protocols.* Springer.

PAN, J.-F., LI, S., GUO, C.-A., XU, D.-L., ZHANG, F., YAN, Z.-Q. & MO, X.-M. 2015. Evaluation of synovium-derived mesenchymal stem cells and 3D printed nanocomposite scaffolds for tissue engineering. *Science and technology of advanced materials,* 16**,** 045001.

PARK, J. S., SHIM, M. S., SHIM, S. H., YANG, H. N., JEON, S. Y., WOO, D. G., LEE, D. R., YOON, T. K. & PARK, K. H. 2011. Chondrogenic potential of stem cells derived from amniotic fluid, adipose tissue, or bone marrow encapsulated in fibrin gels containing TGF-beta 3. *Biomaterials,* 32**,** 8139-8149.

PENICK, K. J., SOLCHAGA, L. A. & WELTER, J. F. 2005. High-throughput aggregate culture system to assess the chondrogenic potential of mesenchymal stem cells. *Biotechniques,* 39**,** 687.

PETERSON, L. 1984. Chondrocyte transplantation. An experimental model in the rabbit. *Trans Orthop Res Soc,* 30**,** 218.

PETRENKO, Y., SYKOVÁ, E. & KUBINOVÁ, Š. 2017. The therapeutic potential of three-dimensional multipotent mesenchymal stromal cell spheroids. *Stem cell research & therapy,* 8**,** 94.

PEVSNER-FISCHER, M., LEVIN, S. & ZIPORI, D. 2011. The origins of mesenchymal stromal cell heterogeneity. *Stem Cell Reviews and Reports,* 7**,** 560-568.

PHULL, A.-R., EO, S.-H., ABBAS, Q., AHMED, M. & KIM, S. J. 2016. Applications of chondrocyte-based cartilage engineering: an overview. *BioMed research international,* 2016.

PITTENGER, M. F., MACKAY, A. M., BECK, S. C., JAISWAL, R. K., DOUGLAS, R., MOSCA, J. D., MOORMAN, M. A., SIMONETTI, D. W., CRAIG, S. & MARSHAK, D. R. 1999. Multilineage potential of adult human mesenchymal stem cells. *science,* 284**,** 143-147.

PONCHEL, F., TOOMES, C., BRANSFIELD, K., LEONG, F. T., DOUGLAS, S. H., FIELD, S. L., BELL, S. M., COMBARET, V., PUISIEUX, A. & MIGHELL, A. J. 2003. Real-time PCR based on SYBR-Green I fluorescence: an alternative to the TaqMan assay for a relative quantification of gene rearrangements, gene amplifications and micro gene deletions. *BMC biotechnology,* 3**,** 18.

PRIGODICH, A. E., RANDERIA, P. S., BRILEY, W. E., KIM, N. J., DANIEL, W. L., GILJOHANN, D. A. & MIRKIN, C. A. 2012. Multiplexed nanoflares: mRNA detection in live cells. *Analytical chemistry,* 84**,** 2062-2066.

PRIGODICH, A. E., SEFEROS, D. S., MASSICH, M. D., GILJOHANN, D. A., LANE, B. C. & MIRKIN, C. A. 2009. Nano-flares for mRNA regulation and detection. *ACS nano,* 3**,** 2147-2152.

RAMOS-VARA, J. A. 2011. Principles and methods of immunohistochemistry. *Drug Safety Evaluation.* Springer.

RANGA, A., GOBAA, S., OKAWA, Y., MOSIEWICZ, K., NEGRO, A. & LUTOLF, M. P. 2014. 3D niche microarrays for systems-level analyses of cell fate. *Nature communications,* 5**,** 4324.

RHEE, M., LIGHT, Y. K., YILMAZ, S., ADAMS, P. D., SAXENA, D., MEAGHER, R. J. & SINGH, A. K. 2014. Pressure stabilizer for reproducible picoinjection in droplet microfluidic systems. *Lab on a Chip,* 14**,** 4533-4539.

RICARD-BLUM, S. 2011. The collagen family. *Cold Spring Harbor perspectives in biology,* 3**,** a004978.

ROBERTS, S., MENAGE, J., SANDELL, L., EVANS, E. & RICHARDSON, J. 2009. Immunohistochemical study of collagen types I and II and procollagen IIA in human cartilage repair tissue following autologous chondrocyte implantation. *The Knee,* 16**,** 398-404.

ROBEY, P. G. 2011. Cell sources for bone regeneration: the good, the bad, and the ugly (but promising). *Tissue Engineering Part B: Reviews,* 17**,** 423-430.

ROMITO, A. & COBELLIS, G. 2016. Pluripotent stem cells: current understanding and future directions. *Stem cells international,* 2016.

ROSENFELD, L., LIN, T., DERDA, R. & TANG, S. K. 2014. Review and analysis of performance metrics of droplet microfluidics systems. *Microfluidics and nanofluidics,* 16**,** 921-939.

ROSS, M. H. & PAWLINA, W. 2006. *Histology*, Lippincott Williams & Wilkins.

ROYCE, P. M. & STEINMANN, B. 2003. *Connective tissue and its heritable disorders: molecular, genetic, and medical aspects*, John Wiley & Sons.

SACCHETTI, B., FUNARI, A., MICHIENZI, S., DI CESARE, S., PIERSANTI, S., SAGGIO, I., TAGLIAFICO, E., FERRARI, S., ROBEY, P. G. & RIMINUCCI, M. 2007. Self-renewing osteoprogenitors in bone marrow sinusoids can organize a hematopoietic microenvironment. *Cell,* 131**,** 324-336.

SAHIN, O., ASHOKKUMAR, M. & AJAYAN, P. M. 2018. Micro-and nanopatterning of biomaterial surfaces. *Fundamental Biomaterials: Metals.* Elsevier.

SAREM, M., OTTO, O., TANAKA, S. & SHASTRI, V. P. 2019. Cell number in mesenchymal stem cell aggregates dictates cell stiffness and chondrogenesis. *Stem cell research & therapy,* 10**,** 10.

SART, S., TOMASI, R. F.-X., AMSELEM, G. & BAROUD, C. N. 2017. Multiscale cytometry and regulation of 3D cell cultures on a chip. *Nature communications,* 8**,** 469.

SART, S., TOMASI, R. F.-X., BARIZIEN, A., AMSELEM, G., CUMANO, A. & BAROUD, C. N. 2020. Mapping the structure and biological functions within mesenchymal bodies using microfluidics. *Science Advances,* 6**,** eaaw7853.

SART, S., TSAI, A.-C., LI, Y. & MA, T. 2014. Three-dimensional aggregates of mesenchymal stem cells: cellular mechanisms, biological properties, and applications. *Tissue Engineering Part B: Reviews,* 20**,** 365-380.

SCHILDBERG, T., RAUH, J., BRETSCHNEIDER, H. & STIEHLER, M. 2013. Identification of suitable reference genes in bone marrow stromal cells from osteoarthritic donors. *Stem cell research,* 11**,** 1288-1298.

SCHOEMAN, R. M., KEMNA, E. W., WOLBERS, F. & VAN DEN BERG, A. 2014. High-throughput deterministic single-cell encapsulation and droplet pairing, fusion, and shrinkage in a single microfluidic device. *Electrophoresis,* 35**,** 385-392.

SCHON, B., SCHROBBACK, K., VAN DER VEN, M., STROEBEL, S., HOOPER, G. & WOODFIELD, T. 2012. Validation of a high-throughput microtissue fabrication process for 3D assembly of tissue engineered cartilage constructs. *Cell and tissue research,* 347**,** 629-642.

SCHRAMM, L. L., STASIUK, E. N. & MARANGONI, D. G. 2003. 2 Surfactants and their applications. *Annual Reports Section" C"(Physical Chemistry),* 99**,** 3-48.

SCHULZE-TANZIL, G., MOBASHERI, A., DE SOUZA, P., JOHN, T. & SHAKIBAEI, M. 2004. Loss of chondrogenic potential in dedifferentiated chondrocytes correlates with deficient Shc–Erk interaction and apoptosis. *Osteoarthritis and cartilage,* 12**,** 448-458.

SCHWAB, M. 2008. *Encyclopedia of cancer*, Springer Science & Business Media.

SEEMANN, R., BRINKMANN, M., PFOHL, T. & HERMINGHAUS, S. 2011. Droplet based microfluidics. *Reports on progress in physics,* 75**,** 016601.

SEFEROS, D. S., GILJOHANN, D. A., HILL, H. D., PRIGODICH, A. E. & MIRKIN, C. A. 2007. Nano-flares: probes for transfection and mRNA detection in living cells. *Journal of the American Chemical Society,* 129**,** 15477-15479.

SEFTOR, E. A., SEFTOR, R. E., WELDON, D. S., KIRSAMMER, G. T., MARGARYAN, N. V., GILGUR, A. & HENDRIX, M. J. Melanoma tumor cell heterogeneity: a molecular approach to study subpopulations expressing the embryonic morphogen nodal. Seminars in oncology, 2014. Elsevier, 259-266.

SEIBEL, M. J., ROBINS, S. P. & BILEZIKIAN, J. P. 2006. *Dynamics of bone and cartilage metabolism: principles and clinical applications*, Academic Press.

SHAW, L. M. & OLSEN, B. R. 1991. FACIT collagens: diverse molecular bridges in extracellular matrices. *Trends in biochemical sciences,* 16**,** 191-194.

SHEN, G. 2005. The role of type X collagen in facilitating and regulating endochondral ossification of articular cartilage. *Orthodontics & craniofacial research,* 8**,** 11-17.

SHENG, G. 2015. The developmental basis of mesenchymal stem/stromal cells (MSCs). *BMC developmental biology,* 15**,** 1.

SHI, Y., TANG, G. & XIA, H. 2014. Lattice Boltzmann simulation of droplet formation in T-junction and flow focusing devices. *Computers & Fluids,* 90**,** 155-163.

SHIH, S. C., GACH, P. C., SUSTARICH, J., SIMMONS, B. A., ADAMS, P. D., SINGH, S. & SINGH, A. K. 2015. A droplet-to-digital (D2D) microfluidic device for single cell assays. *Lab on a Chip,* 15**,** 225-236.

SHIM, J.-U., RANASINGHE, R. T., HOLLFELDER, F., KLENERMAN, D., ABELL, C. & COOPER, J. MEGAHERTZ-GENERATED FEMTOLITER MICROFLUIDIC DROPLETS FOR SINGLE-MOLECULE-COUNTING IMMUNOASSAY. 2013.

SHIRASAWA, S., SEKIYA, I., SAKAGUCHI, Y., YAGISHITA, K., ICHINOSE, S. & MUNETA, T. 2006. In vitro chondrogenesis of human synovium-derived mesenchymal stem cells: Optimal condition and comparison with bone marrow-derived cells. *Journal of cellular biochemistry,* 97**,** 84-97.

SIEBUHR, A. S. & KARSDAL, M. A. 2016. *Type XIII Collagen,* London, Academic Press Ltd-Elsevier Science Ltd.

SMITH, B. D. & GRANDE, D. A. 2015. The current state of scaffolds for musculoskeletal regenerative applications. *Nature Reviews Rheumatology,* 11**,** 213-222.

SMITH, S., ALVAND, A., LOCOCK, L., RYAN, S., SMITH, J., BAYLISS, L., WILSON, H. & PRICE, A. 2019. Partial or total knee replacement? Identifying patients' information needs on knee

replacement surgery: a qualitative study to inform a decision aid. *Quality of Life Research*, 1-13.

SORBER, L., ZWAENEPOEL, K., DESCHOOLMEESTER, V., ROEYEN, G., LARDON, F., ROLFO, C. & PAUWELS, P. 2017. A Comparison of Cell-Free DNA Isolation Kits Isolation and Quantification of Cell-Free DNA in Plasma. *Journal of Molecular Diagnostics,* 19**,** 162-168.

SOTIROPOULOU, P. A., PEREZ, S. A. & PAPAMICHAIL, M. 2007. Clinical grade expansion of human bone marrow mesenchymal stem cells. *Stem Cell Assays.* Springer.

STAPLETON, J. A. & SWARTZ, J. R. 2010. Development of an in vitro compartmentalization screen for high-throughput directed evolution of [FeFe] hydrogenases. *PloS one,* 5**,** e15275.

STEINBACHER, J. L., LUI, Y., MASON, B. P., OLBRICHT, W. L. & MCQUADE, D. T. 2012. Simplified mesofluidic systems for the formation of micron to millimeter droplets and the synthesis of materials. *Journal of Flow Chemistry,* 2**,** 56-62.

TAKAHASHI, K. & YAMANAKA, S. 2006. Induction of pluripotent stem cells from mouse embryonic and adult fibroblast cultures by defined factors. *cell,* 126**,** 663-676.

TARE, R. S., HOWARD, D., POUND, J. C., ROACH, H. I. & OREFFO, R. O. 2005. Tissue engineering strategies for cartilage generation—micromass and three dimensional cultures using human chondrocytes and a continuous cell line. *Biochemical and biophysical research communications,* 333**,** 609-621.

TEMENOFF, J. S. & MIKOS, A. G. 2000. Review: tissue engineering for regeneration of articular cartilage. *Biomaterials,* 21**,** 431-440.

TEREKHOV, S. S., SMIRNOV, I. V., STEPANOVA, A. V., BOBIK, T. V., MOKRUSHINA, Y. A., PONOMARENKO, N. A., BELOGUROV, A. A., RUBTSOVA, M. P., KARTSEVA, O. V. & GOMZIKOVA, M. O. 2017. Microfluidic droplet platform for ultrahigh-throughput single-cell screening of biodiversity. *Proceedings of the National Academy of Sciences*, 201621226.

TEW, S. R. & CLEGG, P. D. 2011. Analysis of post transcriptional regulation of SOX9 mRNA during in vitro chondrogenesis. *Tissue Engineering Part A,* 17**,** 1801-1807.

TEW, S. R. & HARDINGHAM, T. E. 2006. Regulation of SOX9 mRNA in human articular chondrocytes involving p38 MAPK activation and mRNA stabilization. *Journal of Biological Chemistry,* 281**,** 39471-39479.

THOMAS, P. 2019. Intrinsic and extrinsic noise of gene expression in lineage trees. *Scientific reports,* 9**,** 1-16.

THOMSON, J. A., ITSKOVITZ-ELDOR, J., SHAPIRO, S. S., WAKNITZ, M. A., SWIERGIEL, J. J., MARSHALL, V. S. & JONES, J. M. 1998. Embryonic stem cell lines derived from human blastocysts. *science,* 282**,** 1145-1147.

TICE, J. D., SONG, H., LYON, A. D. & ISMAGILOV, R. F. 2003. Formation of droplets and mixing in multiphase microfluidics at low values of the Reynolds and the capillary numbers. *Langmuir,* 19**,** 9127-9133.

TOMASI, R. F.-X., SART, S., CHAMPETIER, T. & BAROUD, C. N. 2018. Studying 3D cell cultures in a microfluidic droplet array under multiple time-resolved conditions. *bioRxiv*, 407759.

TOPOL, L., CHEN, W., SONG, H., DAY, T. F. & YANG, Y. 2009. Sox9 inhibits Wnt signaling by promoting β-catenin phosphorylation in the nucleus. *Journal of Biological Chemistry,* 284**,** 3323-3333.

TU, V. T.-K., LE, H. T.-N., TO, X. H.-V., NGUYEN, P. D.-N., HUYNH, P. D., LE, T. M. & VU, N. B. 2020. Method for in production of cartilage from scaffold-free spheroids composed of human adipose-derived stem cells.

TULI, R., TULI, S., NANDI, S., HUANG, X., MANNER, P. A., HOZACK, W. J., DANIELSON, K. G., HALL, D. J. & TUAN, R. S. 2003. Transforming growth factor-β-mediated chondrogenesis of human mesenchymal progenitor cells involves N-cadherin and mitogen-activated protein kinase and Wnt signaling cross-talk. *Journal of Biological Chemistry,* 278**,** 41227-41236.

TUNG, Y.-C., HSIAO, A. Y., ALLEN, S. G., TORISAWA, Y.-S., HO, M. & TAKAYAMA, S. 2011. High-throughput 3D spheroid culture and drug testing using a 384 hanging drop array. *Analyst,* 136**,** 473-478.

UDE, C. C., SULAIMAN, S. B., MIN-HWEI, N., HUI-CHENG, C., AHMAD, J., YAHAYA, N. M., SAIM, A. B. & IDRUS, R. B. 2014. Cartilage regeneration by chondrogenic induced adult stem cells in osteoarthritic sheep model. *PloS one,* 9**,** e98770.

UK, A. R. 2013. Osteoarthritis in general practice.

VACANTI, J. P. & LANGER, R. 1999. Tissue engineering: the design and fabrication of living replacement devices for surgical reconstruction and transplantation. *The lancet,* 354**,** S32-S34.

VADIVELU, R. K., KAMBLE, H., SHIDDIKY, M. J. & NGUYEN, N.-T. 2017. Microfluidic technology for the generation of cell spheroids and their applications. *Micromachines,* 8**,** 94.

VALIHRACH, L., ANDROVIC, P. & KUBISTA, M. 2018. Platforms for Single-Cell Collection and Analysis. *International Journal of Molecular Sciences,* 19.

VAN DER KRAAN, P., BUMA, P., VAN KUPPEVELT, T. & VAN DEN BERG, W. 2002. Interaction of chondrocytes, extracellular matrix and growth factors: relevance for articular cartilage tissue engineering. *Osteoarthritis and Cartilage,* 10**,** 631-637.

VASILIADIS, H. S., WASIAK, J. & SALANTI, G. 2010. Autologous chondrocyte implantation for the treatment of cartilage lesions of the knee: a systematic review of randomized studies. *Knee surgery, sports traumatology, arthroscopy,* 18**,** 1645-1655.

VON DER MARK, K., GAUSS, V., VON DER MARK, H. & MÜLLER, P. 1977. Relationship between cell shape and type of collagen synthesised as chondrocytes lose their cartilage phenotype in culture. *Nature,* 267**,** 531.

VOS, T., ABAJOBIR, A. A., ABATE, K. H., ABBAFATI, C., ABBAS, K. M., ABD-ALLAH, F., ABDULKADER, R. S., ABDULLE, A. M., ABEBO, T. A. & ABERA, S. F. 2017. Global, regional, and national incidence, prevalence, and years lived with disability for 328 diseases and injuries for 195 countries, 1990–2016: a systematic analysis for the Global Burden of Disease Study 2016. *The Lancet,* 390**,** 1211-1259.

WANG, H. S., HUNG, S. C., PENG, S. T., HUANG, C. C., WEI, H. M., GUO, Y. J., FU, Y. S., LAI, M. C. & CHEN, C. C. 2004. Mesenchymal stem cells in the Wharton's jelly of the human umbilical cord. *Stem Cells,* 22**,** 1330-1337.

WANG, T., NIMKINGRATANA, P., SMITH, C. A., CHENG, A., HARDINGHAM, T. E. & KIMBER, S. J. 2019. Enhanced chondrogenesis from human embryonic stem cells. *Stem cell research,* 39**,** 101497.

WANG, W., RIGUEUR, D. & LYONS, K. M. 2014. TGFβ signaling in cartilage development and maintenance. *Birth Defects Research Part C: Embryo Today: Reviews,* 102**,** 37-51.

WANG, X., LAZORCHAK, A. S., SONG, L., LI, E., ZHANG, Z., JIANG, B. & XU, R. H. 2016. Immune modulatory mesenchymal stem cells derived from human embryonic stem cells through a trophoblast-like stage. *Stem cells,* 34**,** 380-391.

WATSON, J. T., FOO, T., WU, J., MOED, B. R., THORPE, M., SCHON, L. & ZHANG, Z. 2013. CD271 as a marker for mesenchymal stem cells in bone marrow versus umbilical cord blood. *Cells Tissues Organs,* 197**,** 496-504.

WATTS, A. E., ACKERMAN-YOST, J. C. & NIXON, A. J. 2013. A comparison of three-dimensional culture systems to evaluate in vitro chondrogenesis of equine bone marrow-derived mesenchymal stem cells. *Tissue Engineering Part A,* 19**,** 2275-2283.

WEI, Y., ZENG, W., WAN, R., WANG, J., ZHOU, Q., QIU, S. & SINGH, S. R. 2012. Chondrogenic differentiation of induced pluripotent stem cells from osteoarthritic chondrocytes in alginate matrix. *Eur Cell Mater,* 23.

WEISSENBERGER, M., WEISSENBERGER, M., GILBERT, F., GROLL, J., EVANS, C. & STEINERT, A. 2020. Reduced hypertrophy in vitro after chondrogenic differentiation of adult human mesenchymal stem cells following adenoviral SOX9 gene delivery. *BMC Musculoskeletal Disorders,* 21**,** 1-14.

WELTER, J. F., SOLCHAGA, L. A. & PENICK, K. J. 2007. Simplification of aggregate culture of human mesenchymal stem cells as a chondrogenic screening assay. *Biotechniques,* 42**,** 732.

WILLIAMS, R., KHAN, I. M., RICHARDSON, K., NELSON, L., MCCARTHY, H. E., ANALBELSI, T., SINGHRAO, S. K., DOWTHWAITE, G. P., JONES, R. E. & BAIRD, D. M. 2010. Identification and clonal characterisation of a progenitor cell sub-population in normal human articular cartilage. *PloS one,* 5**,** e13246.

WILSON, A., WEBSTER, A. & GENEVER, P. 2019. Nomenclature and heterogeneity: consequences for the use of mesenchymal stem cells in regenerative medicine. *Regenerative Medicine,* 14**,** 595-611.

WOOLF, A. D. & PFLEGER, B. 2003. Burden of major musculoskeletal conditions. *Bulletin of the World Health Organization,* 81**,** 646-656.

WU, H.-W., LIN, C.-C. & LEE, G.-B. 2011. Stem cells in microfluidics. *Biomicrofluidics,* 5**,** 013401.

WU, J.-J., WEIS, M. A., KIM, L. S. & EYRE, D. R. 2010. Type III collagen, a fibril network modifier in articular cartilage. *Journal of Biological Chemistry,* 285**,** 18537-18544.

WU, M.-J. & TSENG, W.-L. 2020. Rapid, facile, reagentless, and room-temperature conjugation of monolayer MoS 2 nanosheets with dual-fluorophore-labeled flares as nanoprobes for ratiometric sensing of TK1 mRNA in living cells. *Journal of Materials Chemistry B,* 8**,** 1692-1698.

WYLES, C. C., HOUDEK, M. T., BEHFAR, A. & SIERRA, R. J. 2015. Mesenchymal stem cell therapy for osteoarthritis: current perspectives. *Stem cells and cloning: advances and applications,* 8**,** 117.

XAVIER, M., HOLM, S. H., BEECH, J. P., SPENCER, D., TEGENFELDT, J. O., OREFFO, R. O. & MORGAN, H. 2019. Label-free enrichment of primary human skeletal progenitor cells using deterministic lateral displacement. *Lab on a Chip,* 19**,** 513-523.

XIA, Y. & WHITESIDES, G. M. 1998. Soft lithography. *Annual review of materials science,* 28**,** 153-184.

XIAO, Y. & ISAACS, S. N. 2012. Enzyme-linked immunosorbent assay (ELISA) and blocking with bovine serum albumin (BSA)—not all BSAs are alike. *Journal of immunological methods,* 384**,** 148-151.

XIE, B., STESSMAN, D., HART, J. H., DONG, H., WANG, Y., WRIGHT, D. A., NIKOLAU, B. J., SPALDING, M. H. & HALVERSON, L. J. 2014. High-throughput fluorescence-activated cell sorting for lipid hyperaccumulating Chlamydomonas reinhardtii mutants. *Plant Biotechnology Journal,* 12**,** 872-82.

YADAV, P. S. & YANG, Y. 2020. Lineage Determination of Chondrocytes and Osteoblasts: From the Perspective of Cellular and Molecular Biology.

YAN, I. K., LOHRAY, R. & PATEL, T. 2018. Droplet Digital PCR for Quantitation of Extracellular RNA. *Extracellular RNA.* Springer.

ZACHWIEJA, E. C., PEREZ, J. & SCHNEIDERBAUER, M. 2017. Hip and Knee Arthroplasty in Osteoarthritis. *Current Treatment Options in Rheumatology,* 3**,** 75-87.

ZARET, K. S. & CARROLL, J. S. 2011. Pioneer transcription factors: establishing competence for gene expression. *Genes & development,* 25**,** 2227-2241.

ZHANG, H., WEN, W. & YAN, J. 2017a. Application of immunohistochemistry technique in hydrobiological studies. *Aquaculture and Fisheries,* 2**,** 140-144.

ZHANG, J., WEI, X., ZENG, R., XU, F. & LI, X. 2017b. Stem cell culture and differentiation in microfluidic devices toward organ-on-a-chip. *Future science OA,* 3**,** FSO187.

ZHANG, L., HU, J. & ATHANASIOU, K. A. 2009a. The role of tissue engineering in articular cartilage repair and regeneration. *Critical Reviews™ in Biomedical Engineering,* 37.

ZHANG, L., SU, P., XU, C., YANG, J., YU, W. & HUANG, D. 2010. Chondrogenic differentiation of human mesenchymal stem cells: a comparison between micromass and pellet culture systems. *Biotechnology letters,* 32**,** 1339-1346.

ZHANG, Q., ZHANG, P., GOU, H., MOU, C., HUANG, W. E., YANG, M., XU, J. & MA, B. 2015a. Towards high-throughput microfluidic Raman-activated cell sorting. *Analyst,* 140**,** 6163-74.

ZHANG, R., LIBERSKI, A., SANCHEZ-MARTIN, R. & BRADLEY, M. 2009b. Microarrays of over 2000 hydrogels–identification of substrates for cellular trapping and thermally triggered release. *Biomaterials,* 30**,** 6193-6201.

ZHANG, X., HIRAI, M., CANTERO, S., CIUBOTARIU, R., DOBRILA, L., HIRSH, A., IGURA, K., SATOH, H., YOKOMI, I., NISHIMURA, T., YAMAGUCHI, S., YOSHIMURA, K., RUBINSTEIN, P. & TAKAHASHI, T. A. 2011. Isolation and Characterization of Mesenchymal Stem Cells From Human Umbilical Cord Blood: Reevaluation of Critical Factors for Successful Isolation and High Ability to Proliferate and Differentiate to Chondrocytes as Compared to Mesenchymal Stem Cells From Bone Marrow and Adipose Tissue. *Journal of Cellular Biochemistry,* 112**,** 1206-1218.

ZHANG, X., XUE, K., ZHOU, J., XU, P., HUANG, H. & LIU, K. 2015b. Chondrogenic differentiation of bone marrow-derived stem cells cultured in the supernatant of elastic cartilage cells. *Molecular medicine reports,* 12**,** 5355-5360.

ZHOU, G., ZHENG, Q., ENGIN, F., MUNIVEZ, E., CHEN, Y., SEBALD, E., KRAKOW, D. & LEE, B. 2006. Dominance of SOX9 function over RUNX2 during skeletogenesis. *Proceedings of the National Academy of Sciences,* 103**,** 19004-19009.

ZUCHOWSKA, A., JASTRZEBSKA, E., ZUKOWSKI, K., CHUDY, M., DYBKO, A. & BRZÓZKA, Z. 2017. A549 and MRC-5 cell aggregation in a microfluidic Lab-on-a-chip system. *Biomicrofluidics,* 11**,** 024110.

Appendix A Materials and equipment

A.1 Materials

Table A.1 Cell culture, chondrogenic differentiation and characterisation of multicellular spheroids.

Material	Supplier	Product code
6-, 12-, 24- and 96-well clear sterile flat-bottom cell culture plates	Costar®, Corning®	3516, 3513, 3524, 3596
8-well glass bottom µ-slide	Ibidi	80826
Acetic acid	Sigma-Aldrich	537020
Alcian Blue 8GX	Sigma-Aldrich	A5268-100G
Aminoethyl carbazole	ACROS Organics™, Thermo Fisher Scientific	AC147870050
Anti-Aggrecan, monoclonal (goat)	R&D Systems	AF1220
Anti-SOX9 antibody, polyclonal (rabbit)	Millipore	AB5535
Anti-Type II Collagen, polyclonal (rabbit)	Calbiochem	234187
Bovine serum albumin reagent graded powder	Thermo Fisher Scientific	BP1600-100
Cell culture flasks with vent cap (T25, T75 and T175)	Corning®	430639, 430641U, 431080
Citric acid	Sigma-Aldrich	251275
Clear polyolefin Starseal (PCR)	Starlab	E2796-9793
Collagenase B from *Clostridrium histolyticum*	Roche	11088815001
Collagenase, type IV from *Clostridrium histolyticum*	Life Technologies, Thermo Fisher Scientific	17104019
DAPI (4',6-Diamidino-2-Phenylindole, Dihydrochloride)	Invitrogen, Thermo Fisher Scientific	D1306
Dexamethasone	Sigma-Aldrich	D4902-25MG
Diaminoethanetetra-acetic acid disodium salt dihydrate (EDTA)	Thermo Fisher Scientific	D/0650/60
Dimethylformamide	VWR	23469.298
DPX (Phthalate Free) Mounting Media	Thermo Fisher Scientific	D/5330/05
Dulbecco's Modified Eagle Medium (DMEM) with 4.5 g/l Glucose with L-Glutamine with sodium pyruvate	Lonza	BE12-604F
Dulbecco's Modified Eagle Medium: Nutrient Mixture F-12, HEPES	Life Technologies, Thermo Fisher Scientific	11330057

Dulbecco's Phosphate Buffered Saline (1X DPBS) without Calcium and Magnesium	Lonza	17-512Q
Ethanol, Absolute ≥99.8%	VWR	20821.467
Ethanol, Molecular Biology Grade	Thermo Fisher Scientific	BP2818-500
ExtrAvidin®-Peroxidase	Sigma-Aldrich	E2886-1ML
Fast-Read 102® haemocytometer	Biosigma	BVS100
Fluoromount	Sigma-Aldrich	F4680
Foetal Bovine Serum	Life Technologies, Thermo Fisher Scientific	42F0461K
Glycerol, 99%	Sigma-Aldrich	G6279
Goat anti-rabbit Immunoglobulins/Biotin	Dako, Agilent	E0432
Goat serum	Sigma-Aldrich	G9023-10ML
GoTaq® qPCR Master Mix	Promega	A6001
Histo-Clear	National Diagnostics™	HS-200
Human primer *COL10A1* F	Sigma-Aldrich	9480 - 008
Human primer *COL10A1* R	Sigma-Aldrich	SY110328219 - 075
Human primer *COL2A1 F*	Sigma-Aldrich	SY130226909 - 051
Human primer *COL2A1* R	Sigma-Aldrich	SY130226909 - 052
Human primer *GAPDH* F	Sigma-Aldrich	SY090603768 - 049
Human primer *GAPDH* R	Sigma-Aldrich	SY090603768 - 050
Human primer *RPL13* F	Sigma-Aldrich	SY161100654 - 058
Human primer *RPL13* R	Sigma-Aldrich	SY161101692 - 073
Human primer *SOX9* F	Sigma-Aldrich	SY171042634 - 093
Human primer *SOX9* R	Sigma-Aldrich	SY171042634 - 094
Human primer *TBP* F	Sigma-Aldrich	SY161100654 - 056
Human primer *TBP* R	Sigma-Aldrich	SY161100654 - 057
Human primer *β-ACTIN* F	Sigma-Aldrich	SY150636973 - 092
Human primer *β-ACTIN* R	Sigma-Aldrich	SY150636973 - 093
Human recombinant TGFβ-3	Peprotech	100-36E
Hyaluronidase from bovine testes (Type I-S, lyophilised powder)	Sigma-Aldrich	H3506-1G
Hydrochloric acid ACS reagent , 37% solution in water	ACROS Organics™, Thermo Fisher Scientific	423795000
Hydrogen peroxide solution, 30% (w/w) in H_2O	Sigma-Aldrich	H1009-100ML
Hydromount	National Diagnostics™	HS-106

IgG (H+L) Alexa Fluor™ 488 Goat Anti-Rabbit	Invitrogen, Thermo Fisher Scientific	A11008
IgG (H+L) Alexa Fluor™ 488 Rabbit Anti-Goat	Invitrogen, Thermo Fisher Scientific	A11078
ImmEDGE™ Hydrophobic Barrier Pen	Vector Laboratories, Cole-Parmer	H-4000
ISOLATE II RNA Mini Kit	Bioline, UK	BIO-52073
Isopropanol, molecular biology reagent	Sigma-Aldrich	I9516
ITS Liquid Media Supplement (100X)	Sigma-Aldrich	I3146-5ML
L-Ascorbic acid 2-phosphate sesquimagnesium salt hydrate	Sigma-Aldrich	A8960-5G
MEM Alpha Eagle (αMEM) with Desoxyribonucleotides, Ribonucleotides and UltraGlutamine 1	Lonza	BE02-002F
Mouse primer *Col10a1* F	Sigma-Aldrich	SY130706851 - 091
Mouse primer *Col10a1* R	Sigma-Aldrich	SY130706851 - 092
Mouse primer *Col2a1* F	Sigma-Aldrich	SY131129410 - 029
Mouse primer *Col2a1* R	Sigma-Aldrich	SY131129410 - 030
Mouse primer *Gapdh* F	Sigma-Aldrich	3664 - 090
Mouse primer *Gapdh* R	Sigma-Aldrich	3664 - 091
Mouse primer *Sox9* F	Sigma-Aldrich	SY130706851 - 090
Mouse primer *Sox9* R	Sigma-Aldrich	SY130706854 - 043
Mouse primer *β-actin* F	Sigma-Aldrich	SY120413680 - 083
Mouse primer *β-actin* R	Sigma-Aldrich	SY120413680 - 083
Nuclease-free water	Promega	P1193
Paraffin multipurpose grade	Thermo Fisher Scientific	P048053
Paraformaldehyde 96% extra pure	ACROS Organics™, Thermo Fisher Scientific	416780010
Penicillin-Streptomycin	Lonza	09-757F
Phosphate Buffered Saline (tablets)	Oxoid	BR0014
Phosphomolybdic acid hydrate 80%	ACROS Organics™, Thermo Fisher Scientific	206381000
PicoPure™ RNA Isolation Kit	Applied Biosystems, Thermo Fisher Scientific	KIT0204
ReliaPrep RNA Cell MiniPrep system kit	Promega	Z6010
Safranin O	Sigma-Aldrich	S2255
Semi-skirted 96-well PCR plates with raised rim	Starlab	E1403-7700

Sirius Red (0.1%) in saturated picric acid	Clin-Tech Limited	640745
Sodium acetate anhydrous	BDH®, VWR	301045M
Sterile cell strainer, 70 µm	Fisherbrand™, Thermo Fisher Scientific	11597522
Sterile syringe filter, Filtropur S 0.2 µm	Starstedt, VWR	103573-246
Superscript™ VILO™ cDNA Synthesis Kit	Invitrogen, Thermo Fisher Scientific	11754050
Triton™ X-100	Sigma-Aldrich	X100
Trizol	Invitrogen, Thermo Fisher Scientific	15596026
Trypan blue solution	Sigma-Aldrich	T8154-100ML
Trypsin-EDTA (1700000 U/l trypsin, 2 g/l EDTA)	Lonza	CC-5012
Tween® 20	Sigma-Aldrich	P1379
Ultra-low adherence 96-well U-bottom inertGrade microplates, PS Standard, transparent	BRAND™, Kinesis	781900
Weigert's Haematoxylin A	Clin-Tech Limited	640494
Weigert's Haematoxylin B	Clin-Tech Limited	640504
β-mercaptoethanol (2-mercaptoethanol)	Sigma-Aldrich	M3148

Table A.2 PDMS chip fabrication, droplet microfluidic generation and characterisation, cell encapsulation.

Material	Supplier	Product code
1 mm Miltex biopsy punch	Medisave	SCH-33-31AA
1 mm Miltex plunger disposable biopsy punch	Williams Medical Supplies	D6345
25G needles x5/8''	Terumo	300600
Aquapel®	PPG Industries	47100
Clean Cut tubing cutter with exchangeable blade	S.C.A.T	900103
Clear polypro hub precision needle tip (0.21 mm ID, 0.41 mm OD)	Adhesive Dispensing Ltd.	TE727050
Fine bore polyethylene tubing connections (ID = 0.38 mm, OD = 1.09 mm)	Smiths Medical	800/100/120
Fluorinert™ FC-40 oil	3M	98-0204-0901-1
Hydrofluoroether (3-Ethoxy-1,1,1,2,3,4,4,5,5,6,6,6-dodecafluoro-2-(trifluoromethyl)-hexane, HFE) oil	3M	HFE-7500 (21148)
Magnetic discs (PTFE encapsulated, 5 mm diameter, 4 mm thick)	V&P Scientific, Inc.	VP779-5

Microparticles based on polystyrene, 10 µm	Sigma-Aldrich	72822-5ML-F
PDMS elastomer and curing agent SYLGARD® 184	DOWSIL™, Farnell Onecall	101967
Pico-Surf™ 1 (5% (w/w) in FC-40)	Sphere Fluidics	C012
PVC tubing (ID = 0.5 mm)	Gradko International	SC0175
QX200™ droplet generation oil for Evagreen	Bio-Rad	1864005
Smooth-Cast® 310	Smooth-On	47740A, 47740B
Syringe, 2.5 ml/5 ml	Terumo/BD	SS*02DE1/309050
Trichloro (1H, 1H, 2H, 2H-perfluorooctyl) silane, 97%	Sigma-Aldrich	448931-10G
Ultrathin PTFE tubing (0.3 mm ID, 0.5 mm OD)	Adtech Polymer Engineering Ltd.	UT3

A.2 Equipment

Table A.3 Equipment.

Equipment	Manufacturer
7500 quantitative RT-PCR system	Applied Biosystems
Centrifuge 5415R	Eppendorf
Centrifuge 5810R	Eppendorf
Centrifuge minispin	technico
CMOS camera DCC1240M	Thorlab
Confocal laser scanning microscope TCS SP5	Leica
Digimicro Mobile Portable USB Digital Microscope Camera	dnt
Digital Camera G10 P1305	Canon
FACS Aria cytometer	BD
FACSAria™ IIIu flow cytometer	BD
Femto plasma cleaner	Diener Asher
High speed camera Phantom Miro eX2	Phantom
Homogeniser ULTRA-TURRAX T8	IKA
Hotplate and stirrer Model 1000	Jenway®
Insulated drying cabinet IWC 200	Genlab
Inverted microscope AxioVert 200	Carl Zeiss
Inverted microscope CKX53	Olympus
Inverted microscope Eclipse Ti	Nikon

Inverted microscope IX82-UCB	Olympus
Magnetic Tumble Stirrer™ VP 710 Series	V&P Scientific, Inc.
Megafuge Heraeus 1.0R	Thermo Fisher Scientific
Microcentrifuge 5424R/5430R	Eppendorf
Microscope IX82-UCB	Olympus
Mini plate spinner MPS 1000	Labnet International, Inc.
Nanodrop™ 1000 Spectrophotometer	Thermo Fisher Scientific
Objet500 Connex3 polyjet printer	Stanford Marsh Ltd
Oven Heraeus T12	Thermo Fisher Scientific
Paraffin embedding station Blockmaster III	Raymond A Lamb
Paraffin section flotation bath Mh8517	Electrothermal
Precision hotplate Model 1000-1	Electronic Micro Systems Ltd.
Refrigerated microcentrifuge Axyspin R	Axygen®
Rotary microtome HM 325 902100	Thermo Fisher Scientific
Rotary vane mechanical vacuum pump D4B	Leybold
Slide drying bench MH6616	Electrothermal
Stereo microscope Stemi 2000-C	Carl Zeiss
Stereo microscope SZM CTV ½ 0.5X WD165	AM Scope
Syringe pump Harvard Apparatus PHD 2000	Instech Laboratories, Inc.
Syringe pump KDS-100-CE	KDS Scientific
Syringe pump NE-1000	New Era
TopMix infrarer vortex mixer FB15013	Thermo Fisher Scientific
Vacuum pump VE115	Refworld
Veriti™ 96-Well Thermal Cycler	Applied Biosystems

Appendix B Optimisation of techniques to analyse chondrogenic differentiation of HBMSC spheroids

This appendix covers a series of methods and techniques that were optimised before conducting the RT-qPCR analyses detailed in sections 3.2.5, 4.2.2.1 and 6.2.4 (Appendix B.1, B.2, B.3, B.4) and the whole mount immufluorescence staining of spheroids in sections 2.7.2 and 6.2.5 (Appendix B.5).

B.1 Method for RNA extraction and isolation with ISOLATE II RNA Mini kit (Bioline BIO-52073, UK)

The cell aggregates had previously been frozen down at -80°C to render them sensitive to disruption. For cell lysis, a 1:100 β-mercaptoethanol (Sigma-Aldrich, UK) in Bioline RLY lysis buffer dilution (v/v) was prepared in a fume hood to add 350 µl RLY lysis buffer along with 3.5 µl per sample. The mixture was vortexed vigorously and crushed mechanically using an IKA® T10 standard ULTRA-TURRAX® PCR kit homogeniser. The lysate was transferred to a gDNA (genomic DNA) eliminator spin column consisting of a 2 ml collection tube with an ISOLATE II filter supplied in the kit. The column was discarded an the flow-through saved after centrifuging for 60 s at 9390 g at 18°C.

An equivalent volume of 70% ethanol (another 350 µl) was added to the flow-through and mixed well by gentle pipetting. Half of the total volume, 350 µl, was pipetted at a time into the spin column in a different collection tube and centrifuged for 60 s at 9390 g. The flow-through was discarded and the column tapped to remove any remaining volume on top of the column. The process was repeated and the spin column was placed in a new 2 ml collection tube.

A volume of 350 µl membrane desalting buffer (MEM) was added to the spin column, followed by centrifugation for 1 min at 9390 g to dry membrane and removing the flow-through. To digest gDNA, 10 µl reconstituted DNase I in the kit was added to 90 µl Reaction Buffer to DNAse I (RDN) and mixed gently by tapping the tube. The DNAse I reaction mixture was applied directly onto the centre of the silica membrane at a volume of 95 µl and incubated at room temperature for 15 min. Afterwards, a series of two washes were performed to dry the membrane:

- First wash with 200 µl Wash buffer 1 (RW1) and 30 s centrifugation at 9390 g changing the collection tube at the end.
- Second wash with 600 µl Wash buffer 2 (RW2) and 30 s centrifugation at 9390 g discarding the flow-through and placing the spin column back in the collection tube.

- Third wash with with 250 µl Wash buffer 1 (RW1) and 2 min centrifugation at 9390 g to dry the membrane completely.

The spin column was then moved to a new 1.5 ml collection tube supplied in the kit and 33 µl RNase-free water (also supplied) were added directly onto the spin column membrane and left to incubate at room temperature for 1 min before proceeding to centrifuge for 1 min at 9390 g. This step was repeated with the elute to maximise RNA concentration. The final RNA elute was stored in ice during quantification measurement in NanoDrop™ 1000 Spectrophotometer.

B.2 Gibco's Trizol method for RNA extraction and isolation

Trizol (Ambion, Life Technologies, UK) was added to spheroids that had been frozen down at -80°C as a part of a four-step procedure:

1) *Phase separation*: the samples were incubated for 5 min at room temperature for the aggregates to defrost. In a fume hood, a 1:5 chloroform (Sigma-Aldrich, UK) in Trizol dilution (v/v) was prepared (60 µl chloroform in 300 µl Trizol for 360 µl final volume) and added to each cell aggregate. The mixture was shaken vigorously for 15 s and incubated for 2-3 min at room temperature. Next, the samples were centrifuged at 13520 g at 4°C for 15 min to separate phases into three layers: RNA aqueous phase sat at the top, DNA interphase stayed in the middle and protein organic phase sank to the bottom.
2) *RNA precipitation*: the aqueous RNA phase was transferred to new 1.5 ml RNase-free tubes, adding 500 µl isopropanol (Fisher Scientific, UK) and vortexing briefly to mix. The samples were incubated at room temperature for 10 min and then centrifuged at 13520 g for 10 min at 4°C ensuring that a pellet had formed wherever possible.
3) *RNA wash*: a volume of 1 ml 75% ethanol was added to the pellets after carefully removing the supernatant. The samples were then centrifuged at 5285 g for 5 min at 4°C and the supernatant was again carefully discarded avoiding complete pellet drying.
4) *RNA re-dissolving*: RNase-free water that had been pre-warmed at 65°C in a water bath was distributed into the tubes, 40 µl each to dissolve RNA by gentle pipetting as the pellets became resuspended.

The final RNA solutions were stored in ice during quantification measurement in NanoDrop™ 1000 Spectrophotometer.

B.3 Reverse transcription cDNA synthesis using Taqman™ Reverse Transcription Reagents

The reverse transcriptase reaction mix employed for cDNA synthesis and 20 µl reaction volume was comprised of:

a) Non-enzymatic components, namely 2 µl of 10x Taqman RT Buffer (PCR Buffer II); 4.4 µl of 25 mM MgCl2; 4 µl of 2.5 mM dNTPs mixture and 1 µl of 50 µM random hexamers.
b) Enzymatic components, i.e. 0.4 µl of RNase Inhibitor (20 U/µl) and 0.5 µl of MultiScribeTM Reverse Transcriptase (50 U/µl).
c) RNA sample volume (7.7 µl).

The non-enzymatic components of the reaction mix were first combined and mixed by gentle pipetting and brief vortexing; after which the enzymatic components were incorporated and mixed by inverting the tubes containing the reaction mix and pipetting up and down. The total volume (12.3 µl) was transferred into new 200 µl microcentrifuge tubes and 7.7 µl RNA sample were added for a 20 µl reaction volume. The samples were then placed in an Eppendorf® Mastercycler Gradient (Sigma-Aldrich, UK) and the reaction cycle sequence programmed: 10 min at 25°C for primer incubation, 30 min at 48°C for reverse transcription, 5 min at 95°C for reverse transcriptase inactivation and cooling down to 4°C. Once the cycle was complete, cDNA was stored at -20°C until used for qPCR.

B.4 Optimisation of RT-qPCR experimental conditions

B.4.1 Early and late chondrogenic differentiation of ATDC5 cell microaggregates

ATDC5 spheroids cultured in chondrogenic differentiation conditions were analysed at 500 and 5000 cell numbers on day 7 and day 21 time points to determine the most suitable RNA extraction method for cell aggregates. Bioline ISOLATE II RNA Mini kit, Trizol and Arcturus® Picopure® RNA Isolation kit were tested and the best isolation method was selected based on the measurements taken by the Nanodrop™ 1000 Spectrophotometer (Table B.1).

The NanoDrop measurements of RNA concentrations and purity ratios showed low RNA purity below ideal $A_{260/280}$ ratios within an acceptable interval of 1.8-2.0 for 500 cell spheroids extracted by either Bioline kit or Trizol. Trizol overall yielded negative values for 500 and 5000 day 7 samples, usually attributed to incorrect measurements or phenol/guanidium thiocyanate residual contamination (Desjardins and Conklin, 2010). The remaining purity ratios for 5000 B7 and day 21

samples were deemed acceptable. The maximum volume of RNA (7.7 µl) was used for Taqman™ cDNA synthesis and all samples were used for qPCR analysis.

Table B.1 RNA concentrations measured following RNA isolation protocols. B stands for Bioline, T refers to Trizol and P corresponds to Picopure kit.

Reference	RNA (ng/µl)	$A_{260/230}$	$A_{260/280}$
500 B7	4.3	0.02	1.67
500 T7	1.6	0.03	-2.22
5000 B7	13.1	0.07	1.94
5000 T7	2.3	0.09	-9.9
500 P21	21.1	0.13	1.81
5000 P21	36.3	0.12	2.02

The two housekeeping genes compared for normalisation of relative expression of the chondrogenic genes of interest were *Gapdh* and *β-actin*. Their melt curves derived from the qPCR amplification curves confirmed that *Gapdh* was the most consistent gene across the samples analysed with the smallest variations among triplicates (Figure B.1), thus concurring with previous work in the literature on the ATDC5 cell line (Tare et al., 2005, Bomer et al., 2016). Day 7 samples whose RNA had been extracted using Bioline isolation kit were dismissed because of the repeated late expression pattern of 500 B7 sample for all genes tested. Trizol samples (500 and 5000 T7) with seemingly inadequate starting RNA purity ratio expressed housekeeping genes (*Gapdh* and *β-actin*) within close C_t intervals with respect to day 21 Picopure samples, and 5000 B7 sample (Table B.1 and Table B.2).

Sox9, *Col2a1* and *Col10a1* were the designated genes of interest to study chondrogenesis on day 7 and day 21 time points (Figure B.2). *Sox9* did not vary significantly between time point or cell numbers and conformed to expected pattern from chondroprogenitor cell line (Figure B.2A). *Col2a1* presented a small upregulation ($p = 0.1941$) for 500 cells from day 7 to day 21 and negligible difference for 5000 cells (Figure B.2B). Hypertrophic *Col10a1* marker was detected in all the cell spheroids. *Col10a1* expression in 500 cell samples saw a marked increase by day 21 and differed from stable gene expression for 5000 cell spheroids (Figure B.2C).

Table B.2 List of mouse PCR primers used and their characteristic sequence and amplicon size in base pairs.

Gene	Primer sequence	Amplicon size (bp)
Mouse		
β-actin	F: 5' TTGCTGACAGGATGCAGAAG 3'	85
	R: 5' GTACTTGCGCTCAGGAGGAG 3'	
Gapdh	F: 5' CACCATGGAGAAGGCCGGGG 3'	123
	R: 5' GACGGACACATTGGGGGTAG 3'	
Sox9	F: 5' GAGGCCACGGAACAGACTCA 3'	50
	R: 5' CAGCGCCTTGAAGATAGCATT 3'	
Col2a1	F: 5' CGAGTGGAAGAGCGGAGACT 3'	66
	R: 5' AACTTTCATGGCGTCCAAGGT 3'	
Col10a1	F: 5' ACGGCACGCCTACGATGT 3'	77
	R: 5' CCATGATTGCACTCCCTGAA 3'	

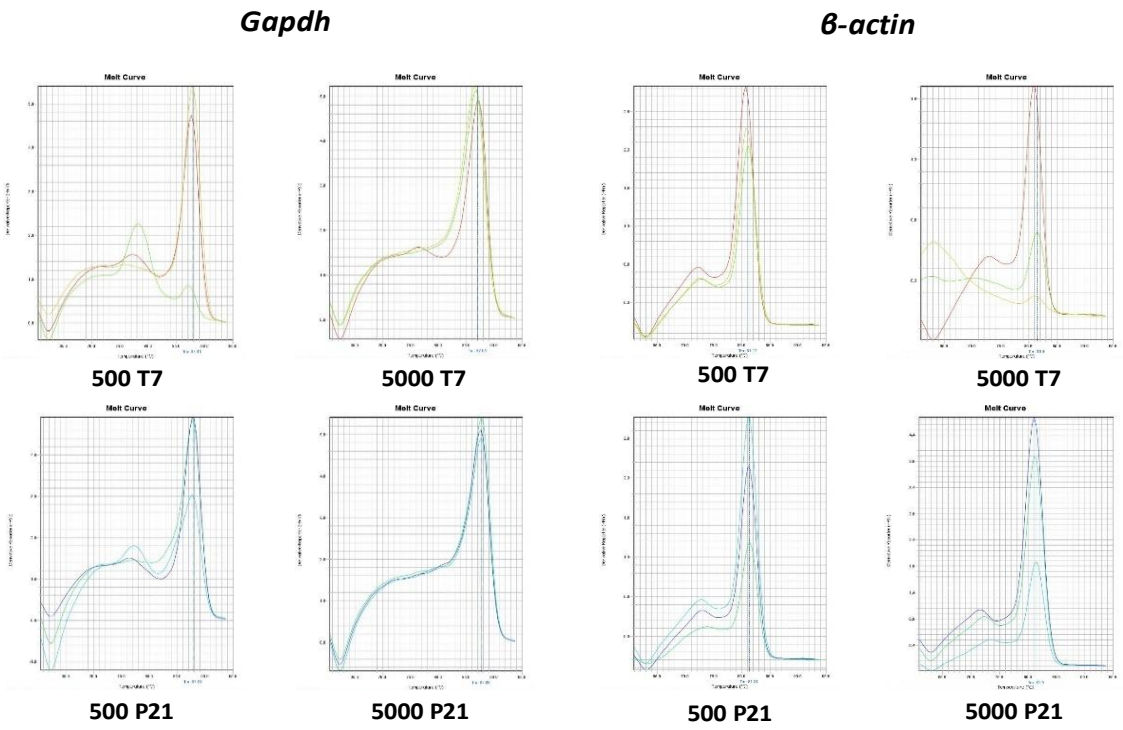

Figure B.1 Melt curves of the housekeeping genes for the ATDC5 spheroids included for the qPCR analysis: *Gapdh* (A) and *β-actin* (B).

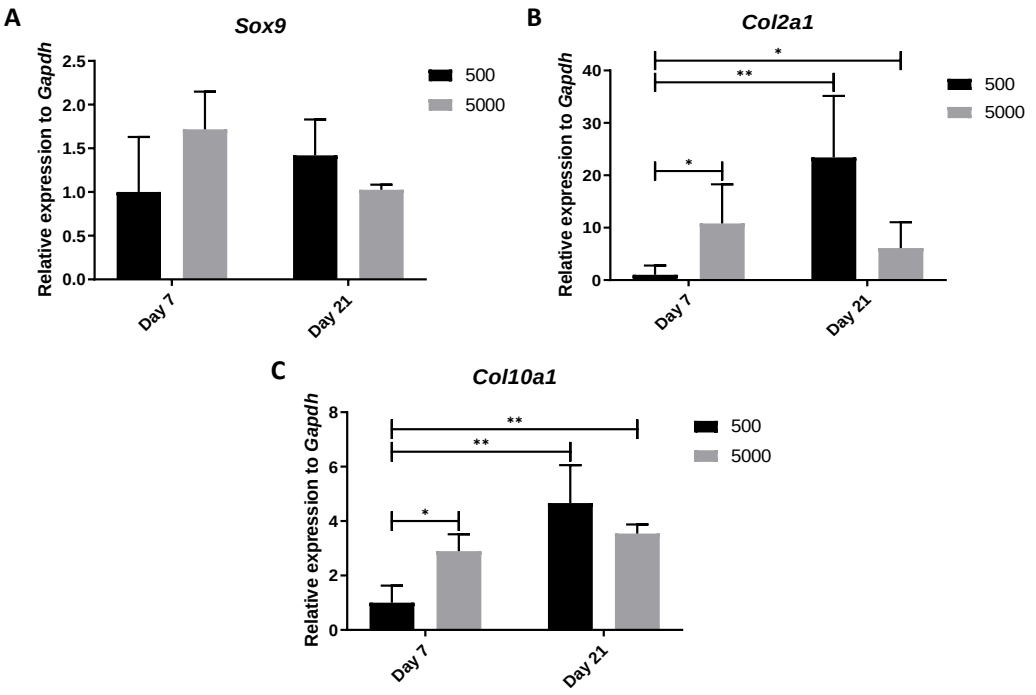

Figure B.2 ATDC5 RT-qPCR relative gene expression of (A) *Sox9*, (B) *Col2a1* and (C) *Col10a1* relative to *Gapdh* housekeeping gene with the error bars depicting SEM. Statistical significance symbols depicted respect GraphPad Prism convention: * ($p \leq 0.05$) and ** ($p \leq 0.01$). The absence of symbols between groups indicates no significance. The statistical analysis was performed using Two-way ANOVA with Tukey's multiple comparisons test on ΔC_t values.

B.4.2 Early and late chondrogenic differentiation of HBMSC microaggregates and effect of cell number

From the RNA extraction optimisation, Picopure was found to be the kit that yielded the best RNA purity ratio. Picopure was applied to isolate RNA from hBMSC spheroids in an experiment that aimed to assess the effect of cell number on chondrogenic differentiation (the scaling-down transition from in vitro to droplet microfluidic aggregates). Spheroids with similar cell numbers to those characterised for protein expression were examined for gene expression. Their RNA concentrations were generally low and the purity ratios were within the 1.8-2.0 interval, except for 500 D7 and 5000 D21 samples (Table B.3). VILO™ cDNA synthesis kit was utilised to maximise the cDNA yield and purity from the human cell spheroids.

Table B.3 RNA concentrations from M74 P1 HBMSC spheroids following RNA extraction and isolation with Picopure kit.

Reference	RNA (ng/µl)	$A_{260/230}$	$A_{260/280}$
50000 D7	18.2	0.18	1.83
5000 D7	8.2	0.02	2.12
500 D7	12.9	0.1	1.65
50000 D21	5.4	0.01	1.91
5000 D21	51.9	-1.43	1.42
500 D21	10.1	0.1	1.86

No definitive set of reliable housekeeping genes has been identified for HBMSCs extracted from human donors (Schildberg et al., 2013, He et al., 2015) and previous validation is therefore essential. The selection of housekeeping genes to normalise the expression of the genes of interest involved commonly used reference genes: *β-ACTIN, RPL13A* and *TBP* (Amable et al., 2013, Schildberg et al., 2013). Again, melt curves plotted during the polymerase chain reaction allowed to compare the consistency of each gene as a housekeeping reference (Figure B.3 and Figure B.4).

TBP was rejected due to an appreciable higher variability among the technical triplicates, together with late relative expression. *β-ACTIN* and *RPL13A* did not differ widely, except for 500 D7 samples (two peaks appeared for *RPL13A*). *β-ACTIN* finally became the reference gene of choice, as a gene with a record of use in HBMSC chondrogenesis (Haider et al., 2008, Dickhut et al., 2009).

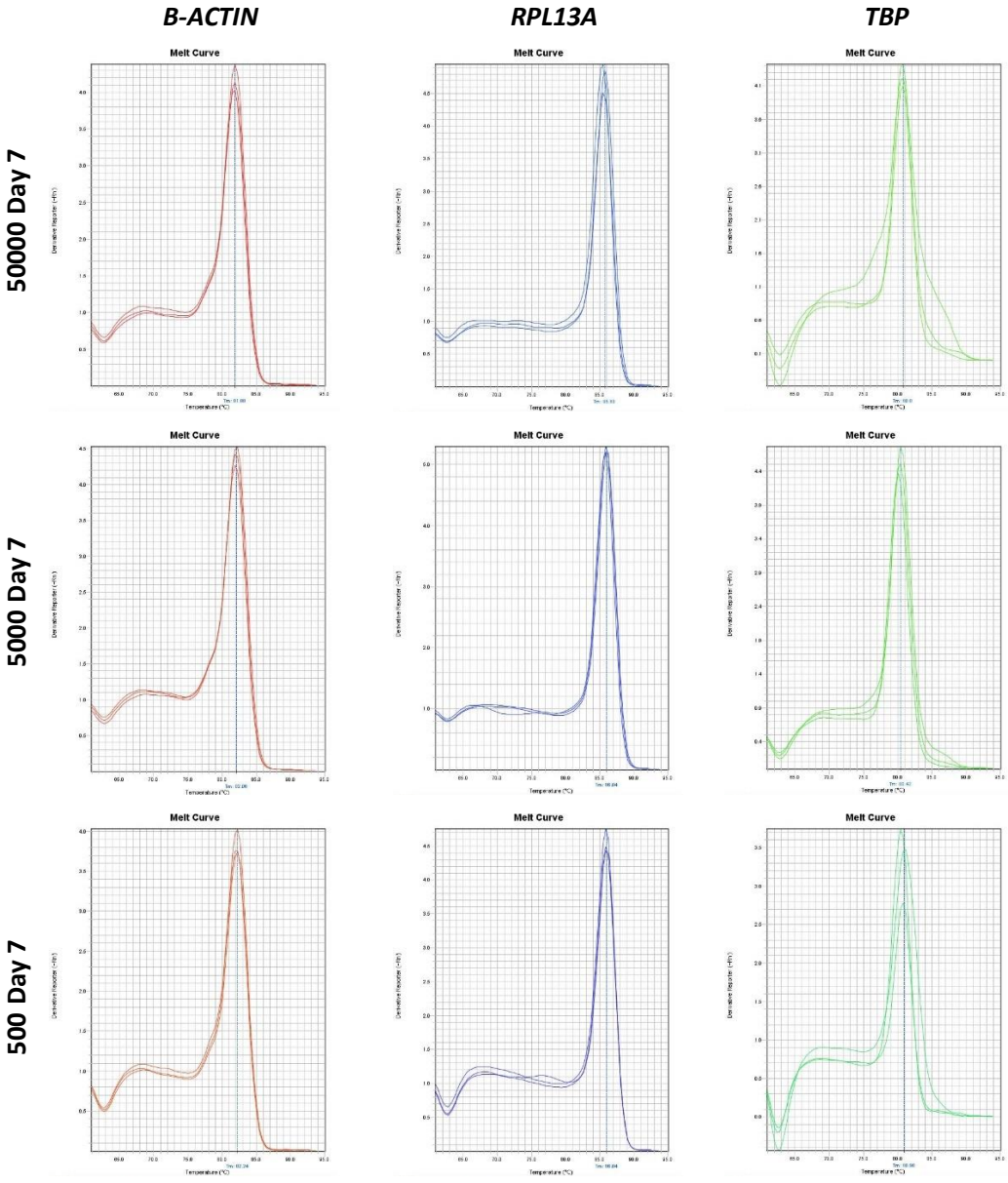

Figure B.3 Melt curves of the housekeeping genes for the M74 P1 HBMSC day 7 spheroids included for the RT-qPCR analysis: and *B-ACTIN* (left), *RPL13A* (middle) and *TBP* (right).

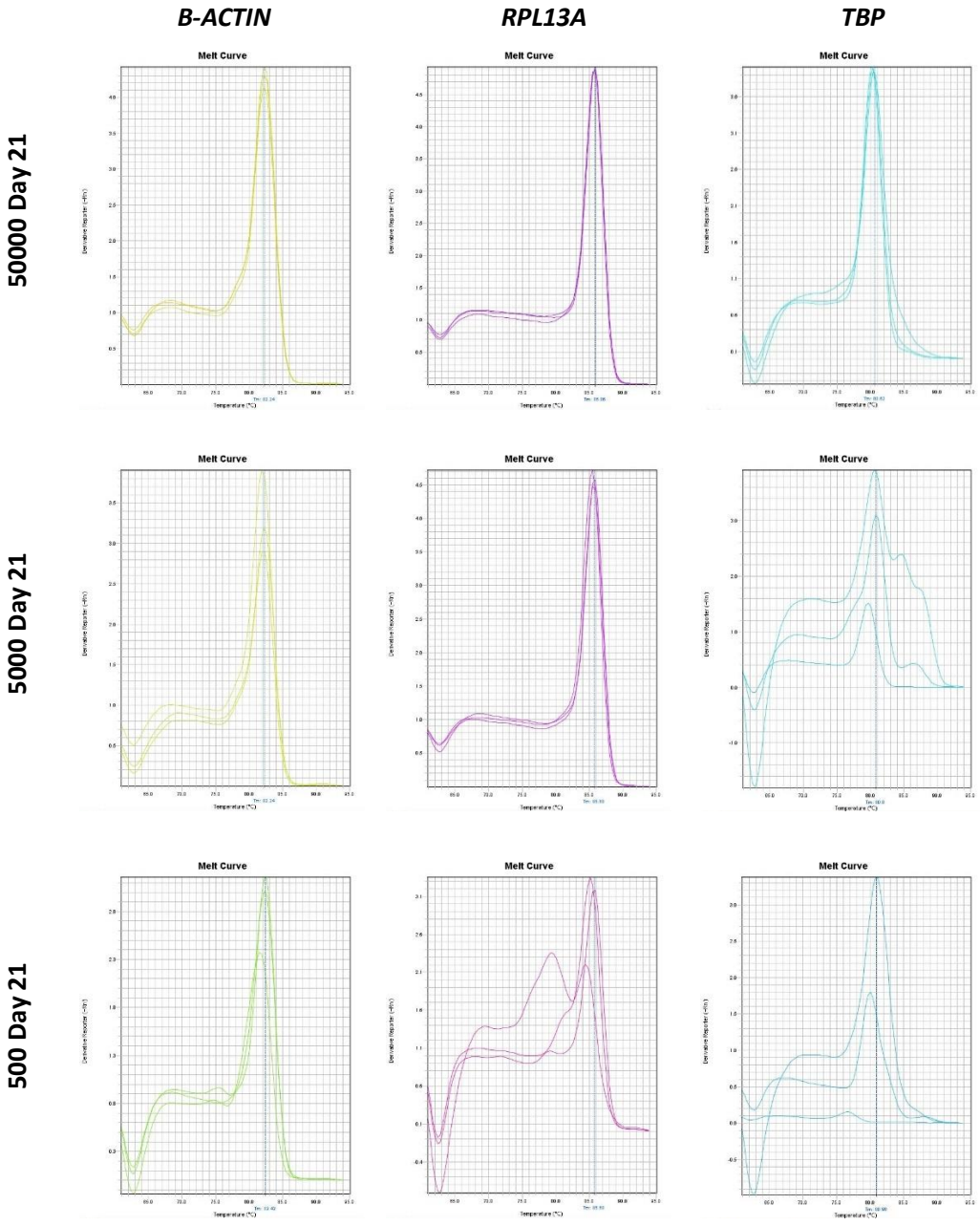

Figure B.4 Melt curves of the housekeeping genes for the M74 P1 HBMSC day 21 spheroids included for the RT-qPCR analysis: and *B-ACTIN* (left), *RPL13A* (middle) and *TBP* (right).

B.4.3 Supplementary information: qPCR

Table B.4 C_t values and standard deviations for all ATDC5 cell aggregates studied for trial qPCR analysis including no template control. Values of 40 indicate undetected expression of the gene of interest.

Sample	C_t *Gapdh*	SD *Gapdh*	C_t *Sox9*	SD *Sox9*	C_t *Col2a1*	SD *Col2a1*	C_t *Col10a1*	SD *Col10a1*
500 B7	33.991	1.330	32.574	0.517	39.287	0.606	40.000	0.000
500 T7	23.729	0.703	25.173	0.078	34.817	2.476	25.034	0.067
5000 B7	21.647	0.586	21.924	0.059	31.347	0.703	19.647	0.054
5000 T7	22.783	0.276	23.446	0.160	31.763	0.706	22.552	0.026
500 P21	23.170	0.348	24.108	0.115	31.035	0.471	22.254	0.148
5000 P21	21.366	0.042	22.773	0.669	31.165	0.851	20.846	0.122
NTC	34.256	1.397	39.604	0.687	40.000	0.000	40.000	0.000

Table B.5 C_t values and standard deviations for all M74 P1 HBMSC cell aggregates studied for trial qPCR analysis including no template control. Values of 40 indicate undetected expression of the gene of interest.

Sample	C_t *B-ACTIN*	SD *B-ACTIN*	C_t *SOX9*	SD *SOX9*	C_t *COL2A1*	SD *COL2A1*	C_t *COL10A1*	SD *COL10A1*
50000 D7	19.644	0.128	31.335	0.005	27.679	0.172	24.190	0.003
5000 D7	17.914	0.026	27.782	0.302	28.106	1.232	26.824	0.016
500 D7	25.597	0.135	33.375	0.112	32.610	0.476	29.565	0.016
50000 D21	21.865	0.081	31.714	0.346	31.990	0.399	28.021	0.137
5000 D21	23.600	0.063	32.310	0.255	27.480	0.422	25.224	0.101
500 D21	30.513	0.101	37.197	0.911	30.690	0.292	39.694	0.530
HACs P0	17.955	0.050	22.841	0.104	17.605	0.149	26.424	0.124
NTC	34.256	1.397	38.394	2.147	34.288	0.149	40.000	0.000

Table B.6 C_t values and standard deviations for M61 P2, M48 P1 and F73 P1 HBMSC cell aggregates studied for *SOX9* expression in early time points including negative no template control. Values of 40 indicate undetected expression of the gene of interest.

Patient reference	Sample reference	C_t *B-ACTIN*	SD *B-ACTIN*	C_t *SOX9*	SD *SOX9*
M61 P2	50000 D1	14.392	0.053	24.372	1.119
M48 P1		15.210	0.152	26.228	1.173
F73 P1		15.940	2.509	25.896	0.284
M61 P2	5000 D1	20.250	0.059	31.928	0.545
M48 P1		17.928	0.207	28.354	0.540
F73 P1		14.003	0.185	25.410	0.609
M61 P2	500 D1	26.936	0.239	38.025	1.795
M48 P1		24.516	0.121	36.491	1.748
F73 P1		24.195	0.335	33.897	0.308
M61 P2	50000 D3	17.487	0.663	30.212	0.761
M48 P1		15.516	0.403	25.056	0.262
F73 P1		16.238	0.695	26.645	0.442
M61 P2	5000 D3	15.196	0.212	27.154	0.494
M48 P1		14.079	0.104	26.968	0.744
F73 P1		6.892	1.644	30.053	1.284
M61 P2	500 D3	16.775	0.133	28.689	0.690
M48 P1		22.973	0.065	35.073	0.836
F73 P1		20.449	0.069	34.761	1.364
M61 P2	50000 D7	13.699	0.142	25.352	0.455
M48 P1		13.777	0.159	25.621	0.338
F73 P1		14.880	0.148	24.905	0.357
M61 P2	5000 D7	17.018	0.192	30.475	0.104
M48 P1		14.753	0.089	27.000	0.162
F73 P1		9.039	1.398	25.768	0.467
M61 P2	500 D7	18.495	0.088	30.453	0.117
M48 P1		18.590	0.038	31.067	0.074
F73 P1		17.730	0.036	30.540	0.781

	HACs P0	16.353	0.159	24.506	0.725
	NTC M61 P2	34.918	1.269	35.622	2.579
	NTC M48 P1	39.290	0.710	39.687	0.313
	NTC F73 P1	40.000	0.000	37.862	0.909

B.5 Fluorescence immunohistochemistry on whole mount samples

B.5.1 Optimisation of whole mount fluorescence immunostaining

The low antibody penetration for all dyes in larger cell numbers and particularly for the antibodies utilised for whole mount immunofluorescence staining exposed the need to optimise the existing staining protocol and adapt it to pursue uniform staining throughout the entire volume of the spheroid to be characterised. The main modifications introduced consisted in extending the blocking incubation in 1% BSA in 1X PBS to 1 h; the primary antibody incubation to at least 24 h at 4°C, setting the secondary antibody incubation at 4°C for an extra 24 h and counterstaining with DAPI for 30 min. Two optimisation protocols were attempted simultaneously as a preliminary step by altering a single parameter: (1) 24 h primary antibody incubation at 4°C and (2) 48 h in the same conditions. A 5000 cell day 7 sample was subjected to optimisation (1) treatment. 500 cell day 21 and 5000 cell day 21 spheroids received optimisation (2) treatment (Figure B.5).

Lengthening permeabilisation, blocking, antibody incubation and DAPI counterstain exposure times improved the effectiveness of the staining process across all tested samples. For 500 cell day 21 and 5000 cell day 7 spheroids of similar dimensions, DAPI staining appeared uniform across the cross section. SOX9 diffusion was also maximum for 5000 cell day 7 sample (Figure B.5). SOX9 antibody diffusion after treated with optimisation (1) method yielded a constant value compared to its counterpart spheroid stained according to the former protocol except for a very small increase in intensity. Diffusion in the large 500 nm diameter 5000 cell day 21 aggregate only reached 8% for DAPI and 3.8% for SOX9.

Adding a step to remove excess water from the small spheroids through dehydration and rehydration to promote staining using graded methanols did not produce any observable improvement in the dye diffusion. Similarly, the use of transwell plates was not effective due to their excessively large pore size and the repeated washing steps in the staining protocol (Figure B.6). Finally, optical clearing resulted in a slight increase in the area of the core of the spheroid that was stained with SOX9 for both cell numbers (500 and 5000) (Figure B.7). Taking all the results together, the best optimisation route for whole mount experiments was adopting the optimised treatment above (i.e. lengthening incubation times in general to facilitate antibody diffusion into the core of the spheroids) and optical clearing prior to confocal microscopy. This staining method is shown in the main text of this thesis and in Figure B.8, Figure B.9, Figure B.10 and Figure B.11.

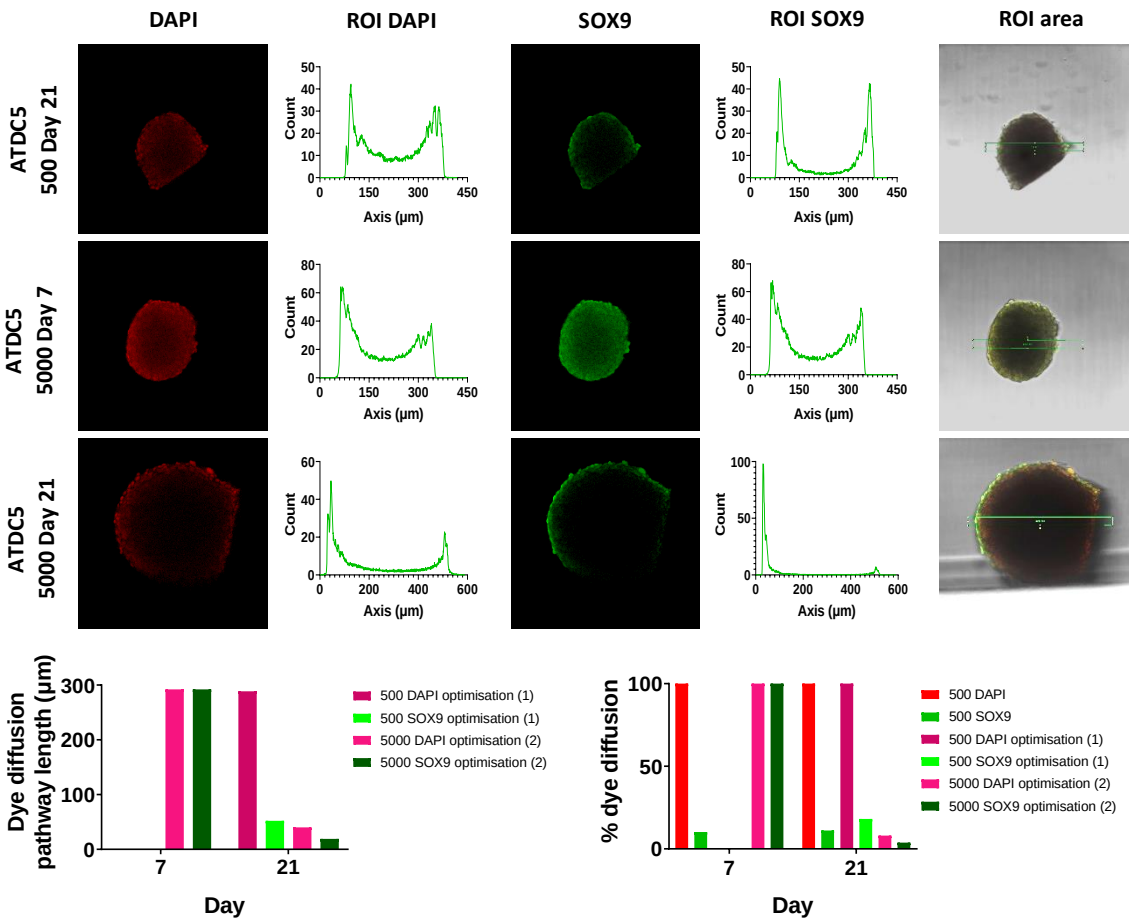

Figure B.5 Optimisation experiment with ATDC5 cells consisting on dye diffusion semi-quantitative image analysis relative to DAPI and SOX9 of 500 and 5000 cell ATDC5 whole mount spheroids after 7 and/or 21 days of chondrogenic differentiation culture subjected to different treatments: optimisation (1) and optimisation (2). Separate channels were included for DAPI and type II collagen, and their ROI peaks from which calculations were extracted. The graphs below depict average dye diffusion length (left) for the three samples tested and their relative % dye diffusion normalised to spheroid diameter (right).

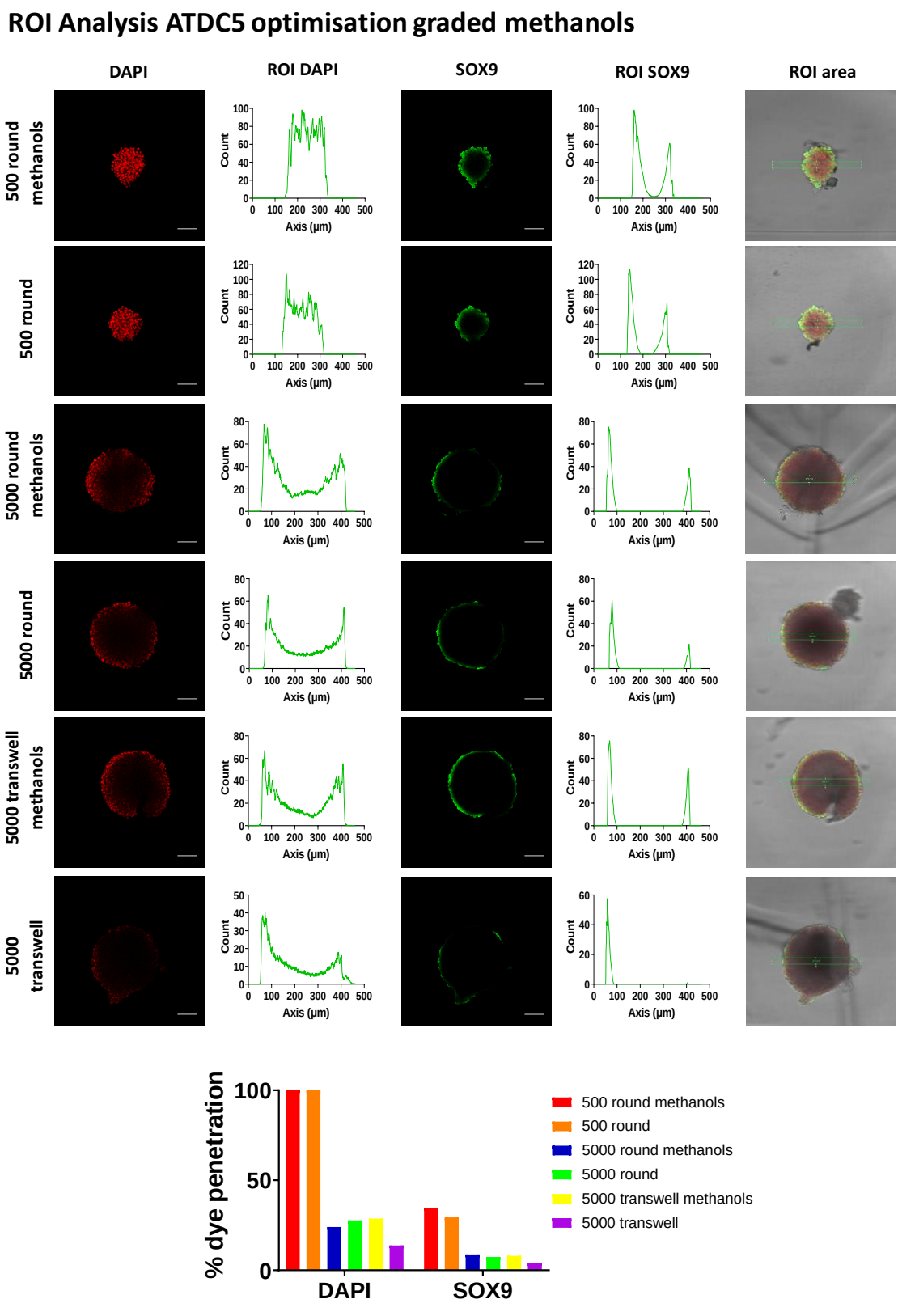

Figure B.6 Optimisation experiment with ATDC5 cells consisting on dye diffusion semi-quantitative image analysis relative to DAPI and SOX9 of 500 and 5000 cell ATDC5 whole mount spheroids after 3 days of chondrogenic differentiation culture subjected to graded methanols or in the absence of them and stained on ultra-low adherence round-bottom well plates or transwell plates. Separate channels were included for DAPI and SOX9, and their ROI peaks from which calculations were extracted. The graph below shows their relative % dye diffusion normalised to spheroid diameter. Scale bar = 100 µm.

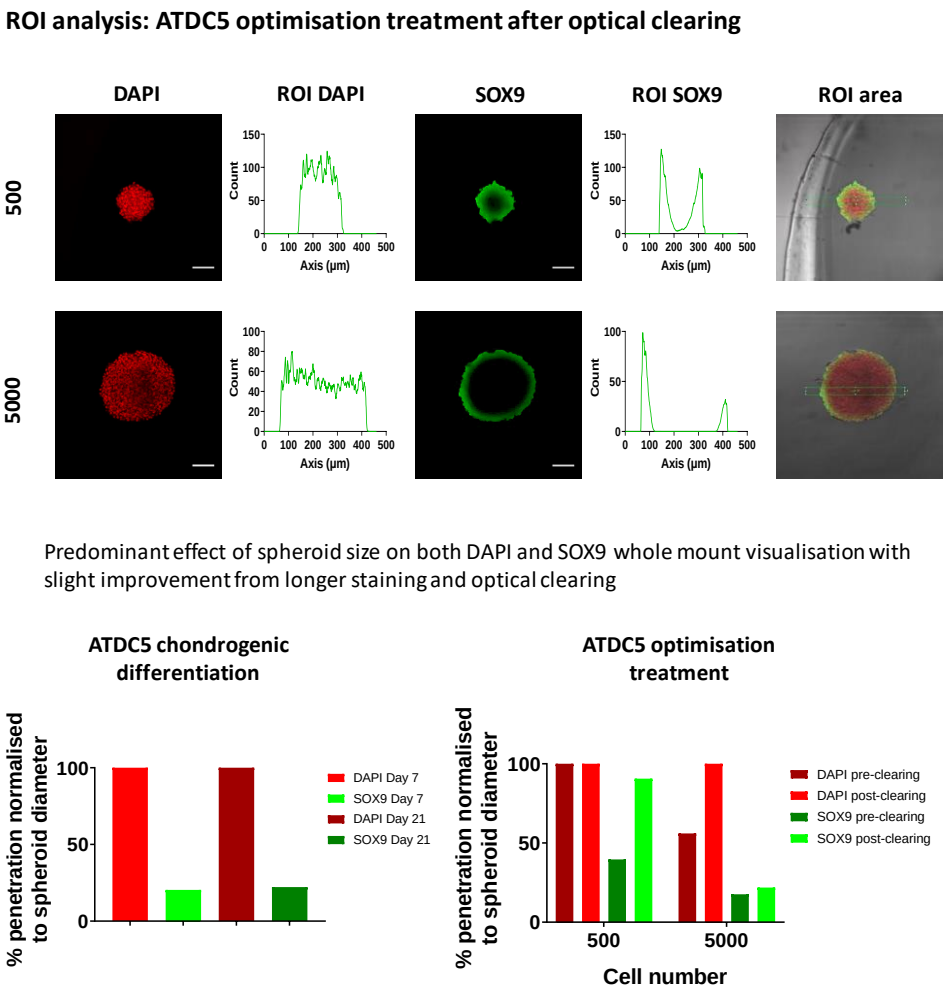

Predominant effect of spheroid size on both DAPI and SOX9 whole mount visualisation with slight improvement from longer staining and optical clearing

Figure B.7 Optimisation of visualisation of SOX9 immunofluorescence distribution on whole mount ATDC5 samples. 500 and 5000 cell spheroids were stained after 2 days of culture in chondrogenic differentiation medium, imaged and analysed measuring on the relevant ROI. Previous data exposed the lack of complete SOX9 imaging throughout the area of the spheroids (bottom left graph). An optical treatment with 80% glycerol/20% 1X PBS enhanced SOX9 visualisation under the Leica SP5 confocal microscope. Scale bar = 100 µm.

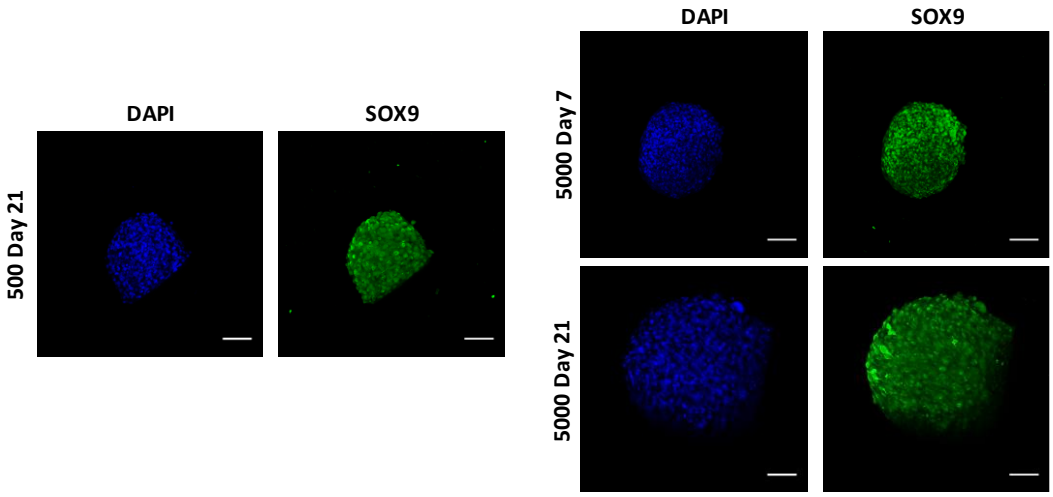

Figure B.8 Whole mount SOX9 immunofluorescent stained 500 (left) and 5000 (right) ATDC5 cell spheroids on day 7 and day 21 according to the modified staining protocol in section 3.3.2.3.2, showing homogeneous SOX9 distribution at the core of the spheroids. Scale bar = 100 µm.

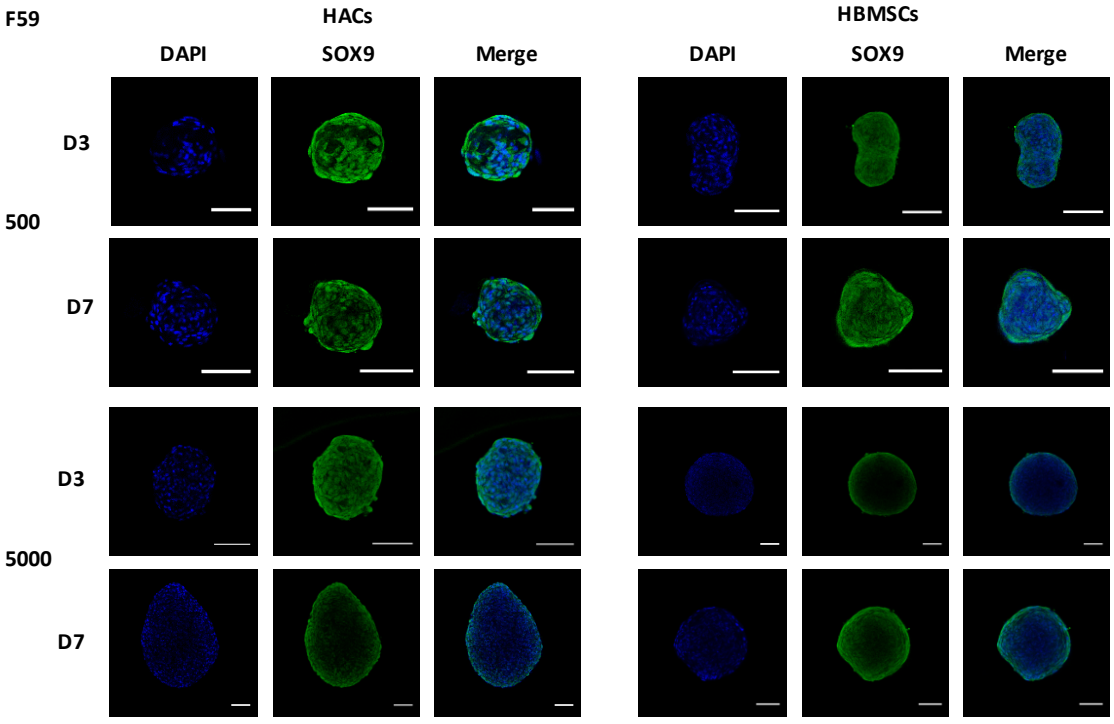

Figure B.9 Comparative of SOX9 immunofluorescent distribution in 500 and 5000 HAC (left) and HBMSC (right) cell spheroids cultured for 3 and 7 days corresponding to F59 donor. Scale bar = 100 µm.

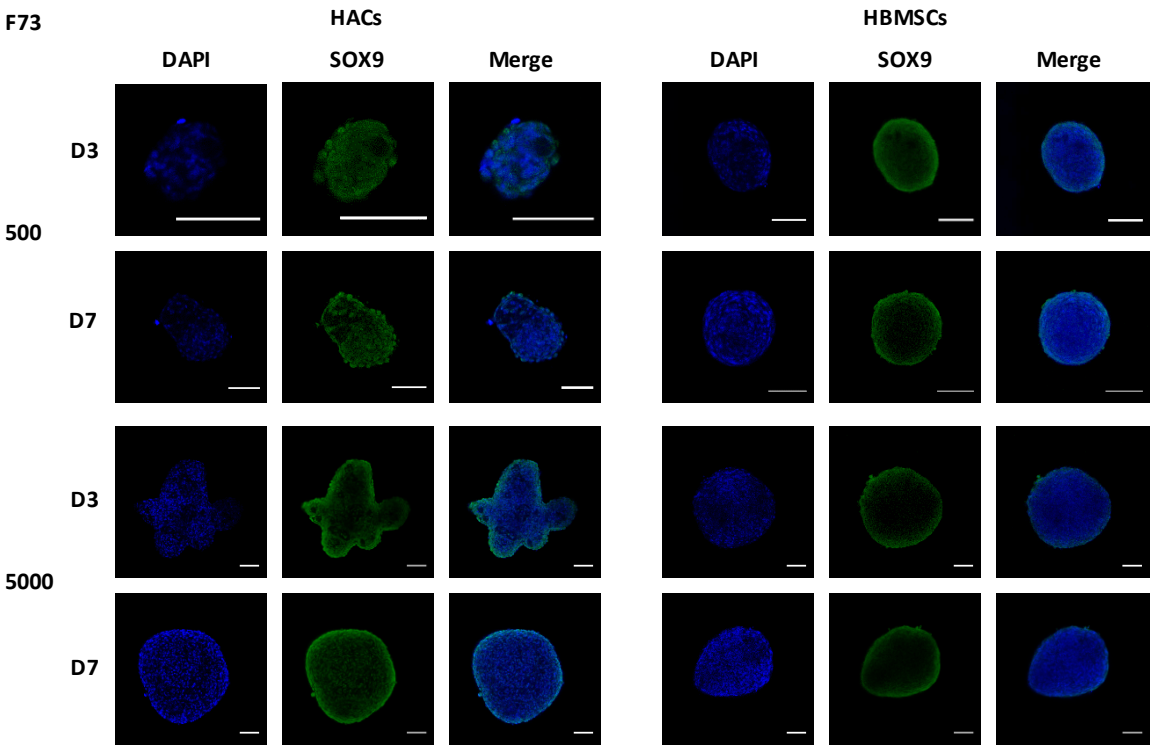

Figure B.10 Comparative of SOX9 immunofluorescent distribution in 500 and 5000 HAC (left) and HBMSC (right) cell spheroids cultured for 3 and 7 days corresponding to F73 donor. Scale bar = 100 µm.

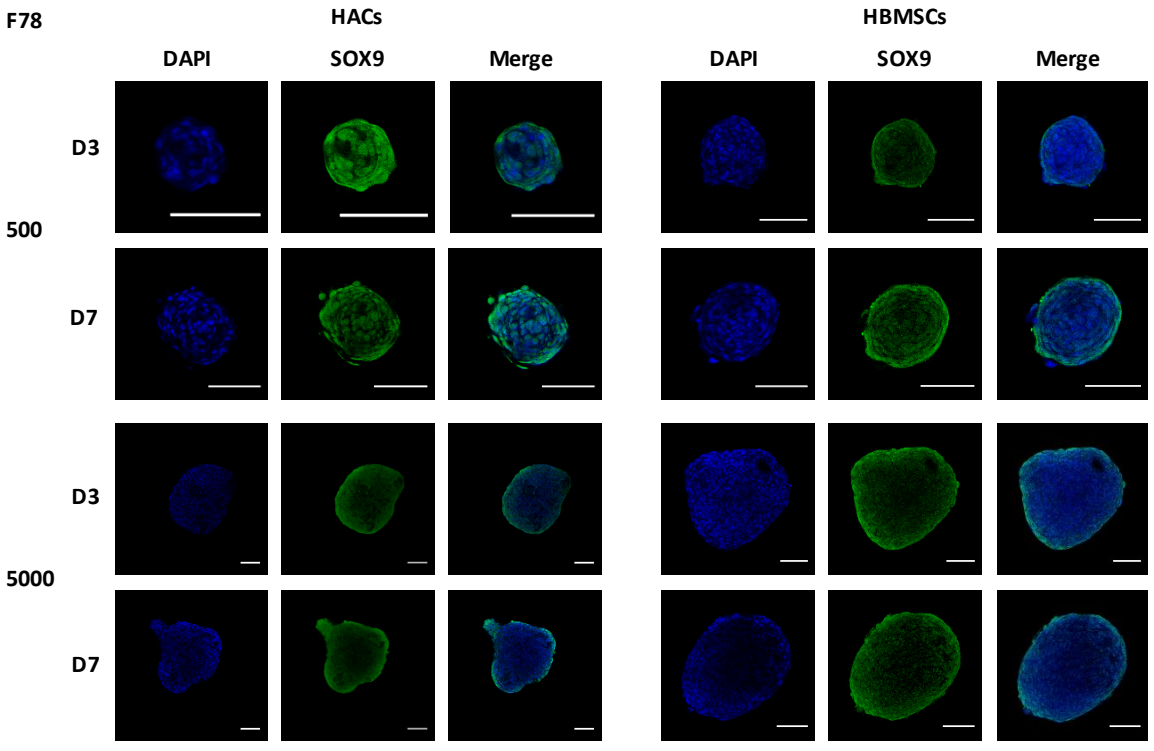

Figure B.11 Comparative of SOX9 immunofluorescent distribution in 500 and 5000 HAC (left) and HBMSC (right) cell spheroids cultured for 3 and 7 days corresponding to F78 donor. Scale bar = 100 µm.

Appendix C Optimisation of microfluidic devices for droplet generation

This appendix includes additional optimisation steps that were taken towards the development of a microfluidic platform for cell encapsulation described in Chapter 5:. Hence, it contains preliminary work using a soft lithography chamber for on-chip droplet incubation (Appendix C.1) and a proof of principle of medium-throughput droplet generation in more recent 3D-printed chip designs for encapsulation of higher cell numbers than those employed in Chapter 6:. In addition, supplementary information is presented of particle encapsulation measurements from other particle numbers (e.g. 1 and 2.5 million particles/ml).

C.1 Soft lithography flow-focussing chamber design

Moving on with the principle of keeping droplets as individual microenvironmental compartments and accounting for the need to maximise yield for high-throughput cell sorting, a specific soft lithography mould available from previous work in our group was examined as part of a preliminary pilot optimisation step to discern whether the benefits justified replacing 3D-printed designs.

The soft lithography design specifications were as follows (Figure C.1A and B):

- Flow-focussing droplet generation geometry.
- A 50 µm high rectangular-shaped cell culture chamber supported by four rectangular pillars.
- In-built Y-junction for aqueous phase mixing/reaction and droplet dilution areas.
- Filters at inlets that were not necessary for this application and punched above to neglect any subsequent interaction with incoming cell suspension.
- Fabrication consisting in a curing time of 1 h 15 min for the engraved top layer and 15-20 min for the backing layer starting from a 17.0 g elastomer and 1.7 g curing agent 10:1 mixture at 70°C depending on layer thickness.

To assess the stability of droplet generation and to quantify droplet dimensions and the degree of polydispersity in this microfluidic device, a series of increasing flow rate ratios (1, 2.5, 5, 7.5, 10; replicating the same value as the systematic study with T-junction 3D-printed chips) were injected and droplets were captured as they flowed through the winding channels and into the culture chamber. Droplets could not be distinguished as separate entities with sufficient resolution using

the stereomicroscope system coupled with a Thorcam camera, even after dyed with rose bengal (Sima-Aldrich, UK). For that reason, the experimental setup was moved and adapted for imaging under an Olympus IX82-UCB microscope attached to an optiMOS™ Scientific CMOS camera (Qimaging) and videos were recorded via the cellSens software package. The continuous phase was 1.8% Soton 2 in FC40 and the dispersed phase corresponded to ATDC5 cell culture medium (see section 2.3.1).

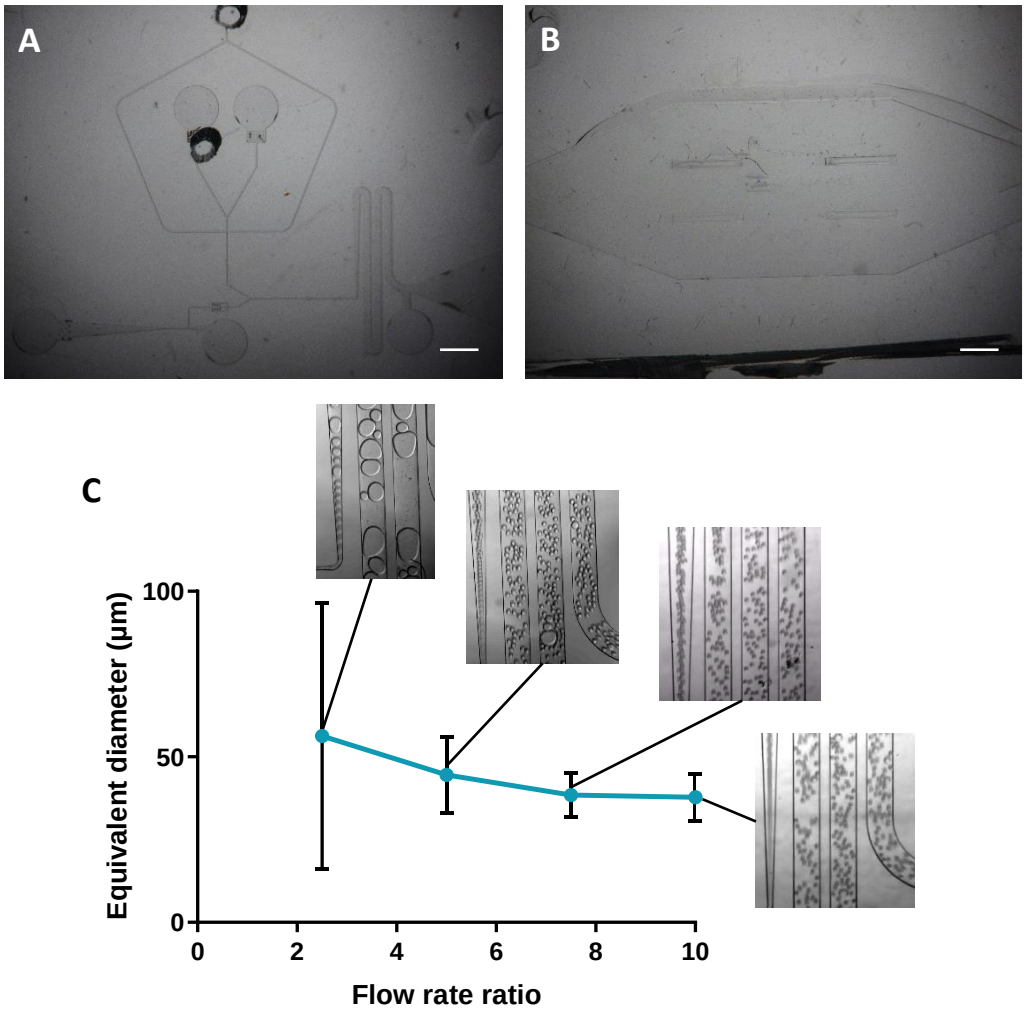

Figure C.1 Characteristics of soft lithography design with culture chamber and flow-focussing geometry: (A) Inlet region and winding channels for access to chamber, (B) Culture chamber region, (C) Effect of flow rate ratio on the mean equivalent diameter of droplets in soft lithography flow-focussing chip and images of winding channels and variations in droplet morphology during device operation. Scale bar for (A) and (B): 1mm.

No droplet break-off occurred for a flow rate ratio of 1 and the cell suspension entered the cell culture chamber as a single stream in the absence of the continuous phase. The flow remained unstable for a flow rate ratio of 2.5, with droplets produced uniformly before the widening region at the winding channels and displaying an extremely polydisperse distribution thereafter; i.e. 56.3 ± 40.2 µm droplets. Flow rate ratios between 5 and 10 underwent drastic reductions in polydispersity yet standard deviations did not fall under 19% of equivalent diameters due to larger

droplets regularly forming (Figure C.1C). Negligible differences were registered between 7.5 and 10 flow rate ratios.

C.2 Implementation of flow-focussing channel geometry, silanisation and Bio-Rad QX200^{TM} droplet generation oil in microfluidic devices made from 3D-printed moulds

Given the substantial improvement in droplet stability and droplet population monodispersity that was obtained after characterising soft lithography microfluidic device performance, the new optimisation parameters were applied to 3D-printed microchips. These implied manufacturing new moulds to include a flow-focussing geometry, treating PDMS surface with silane groups, plasma bonding to glass slides and replacing FC40/Soton2 by Bio-Rad QX200^{TM}. Two chip designs were made with two different channel heights: 215 and 300 µm; called *FF215* and *FF300*, respectively. Chip moulds were designed as detailed in section 5.2.2.1 and the chips were fabricated from the moulds according to the procedure described in section 5.2.2.1.2 (Figure C.2).

Droplets were generated using Bio-Rad QX200^{TM} droplet generation oil for the carrier phase and serum-free DMEM supplemented with 1% P/S and 1X ITS under a series of flow rates within the range of 25 to 250 µl/min for the oil phase and keeping the aqueous phase at a constant 25 µl/min. The droplets were imaged under the CKX53 Olympus microscope at 4x magnification and videos containing 1000 frame were recorded with a Phantom Miro eX2 high-speed camera. Droplet size was computed using MATLAB DMV analysis. The mean equivalent diameter values and the statistical analysis of droplet population for both designs are included in Figure C.3.

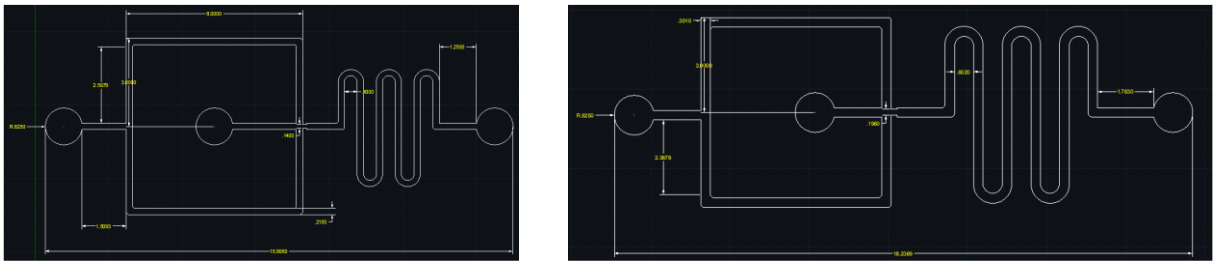

Figure C.2 AutoCAD designs for 3D-printed chip mould designs including channel dimension measurements for *FF215* (left) and *FF300* (right).

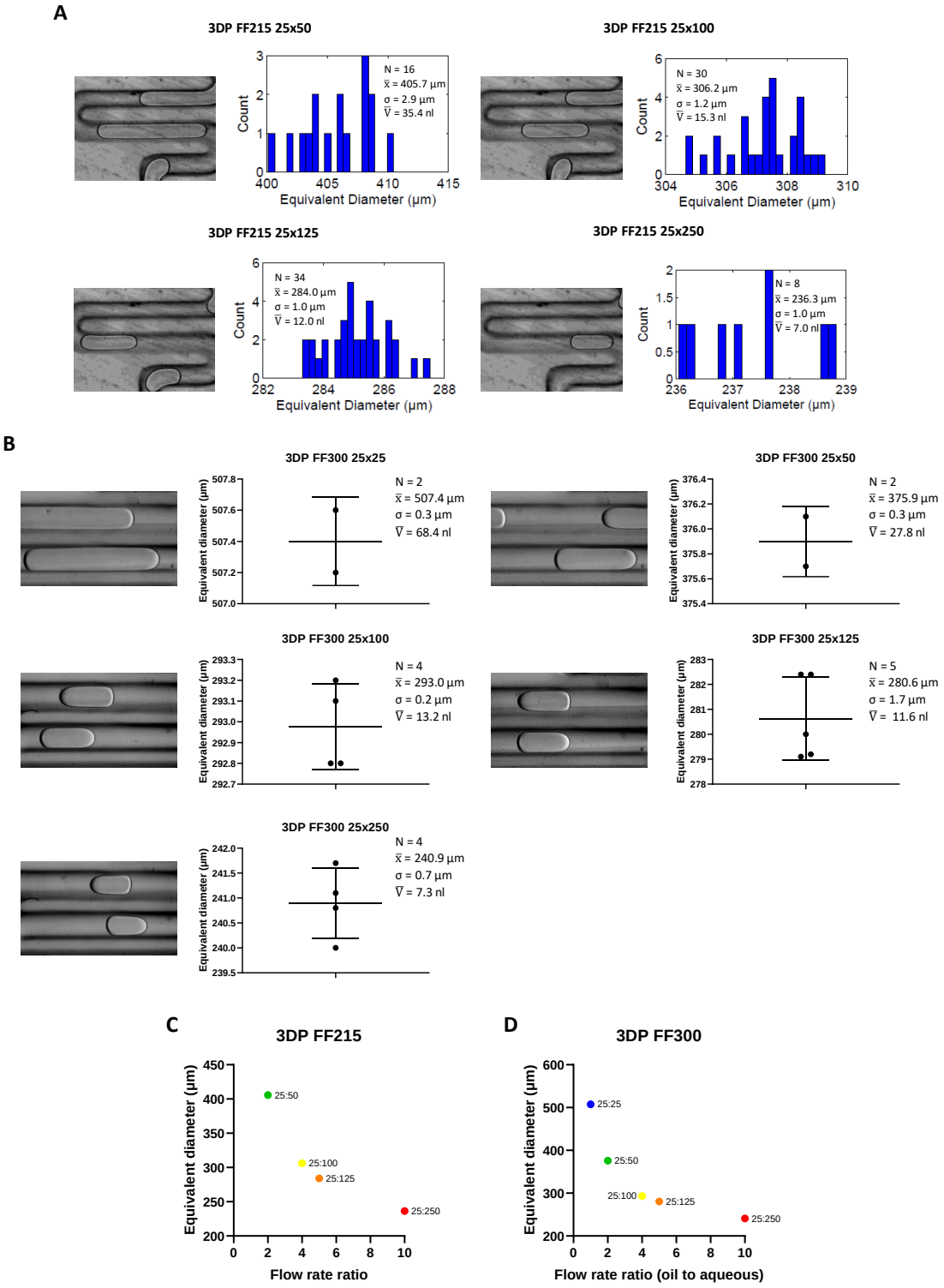

Figure C.3 Droplet diameter measurements using DMV for the *FF215* and *FF300* 3D-printed chip designs: (A) Summary of the individual droplet measurements for all the flow conditions tested using the *FF215* chip design; (B) Summary of the individual droplet measurements for all the flow conditions tested using the *FF300* chip design; (C) Summary of the effect of flow rate ratio on the droplet diameter for all flow rate values tested for the *FF215* chip design; (D) Summary of the effect of flow rate ratio on the droplet diameter for all flow rate values tested for the *FF300* chip design.

The droplet size range (and mean equivalent volume) was notably wide for both flow-focussing 3D-printed designs: 236.3 to 405.7 µm (7.0 to 35.4 nl) in *FF215* microchips and 240.9 to 507.4 µm (7.3 to 68.4 nl) in *FF300* microchips (Figure C.3). The plots showing the equivalent droplet diameter as a function of flow rate ratio showed the expected downward trend of droplet size with increasing flow rates for the oil phase in both cases (Figure C.3, bottom). Channel and droplet dimensions posed a limitation in the number of droplets that could be counted for statistical population analysis. Even though this restriction was more marked in *FF300* chips, where up to 5 droplets were counted in the smaller droplet sizes, the 25:25 slowest flow rate combination in *FF215* generated droplets whose size exceeded the channel length of the straight region of interest for analysis and could not be quantified.

Droplet population monodispersity in *FF215* and *FF300* 3D-printed designs as expressed in the variable formerly defined as $CV\,(\%)$ increased by an order of magnitude and reached similar values to those exhibited by soft lithography designs below 1%. Higher monodispersity in droplet distributions was derived from the change in fabrication parameters with respect to the T-junction winding chips. It suggested that droplet size was equally controllable in 3D-printed designs provided that the oil and surfactant and PDMS fabrication and surface treatment were modified and adapted to the new optimised chip fabrication procedure developed for soft lithography designs.

Finally, droplet stability was assessed macroscopically from visual inspection of droplets collected in a 1.5 ml Eppendorf following microfluidic operation for both *FF215* and *FF300* designs as a proof of principle of tentative application for cell encapsulation. The droplets were kept at room temperature for 28 days and then incubated for 3 days in an incubator at 37°C and 5% CO_2 as conducted in the surfactant stability test in section 5.3.2. Droplets remained separate with no signs of coalescence in all the storage conditions tested and regardless of the 3D-printed chip design.

C.3 Supplementary information: particle encapsulation experiments

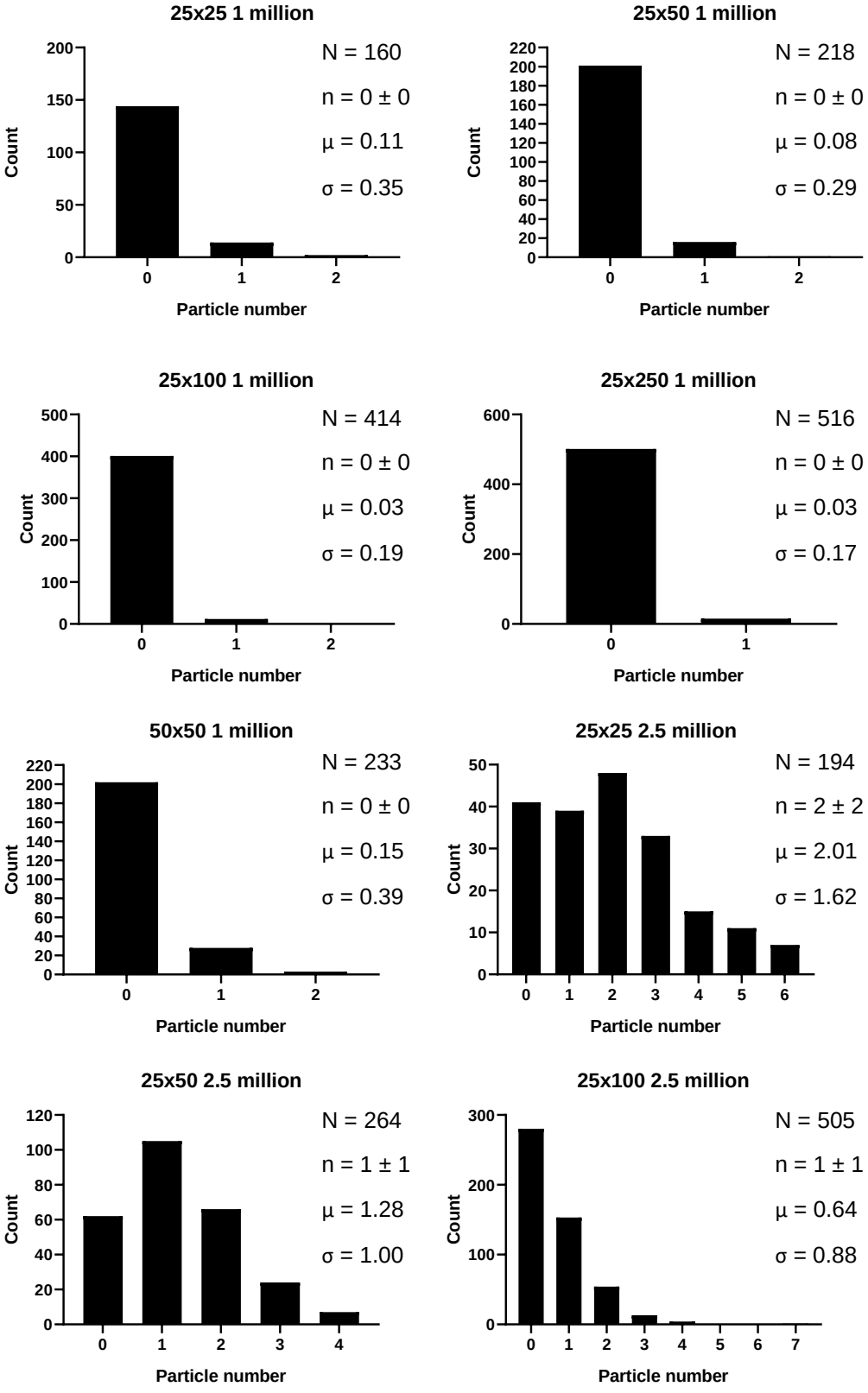

(continues on next page)

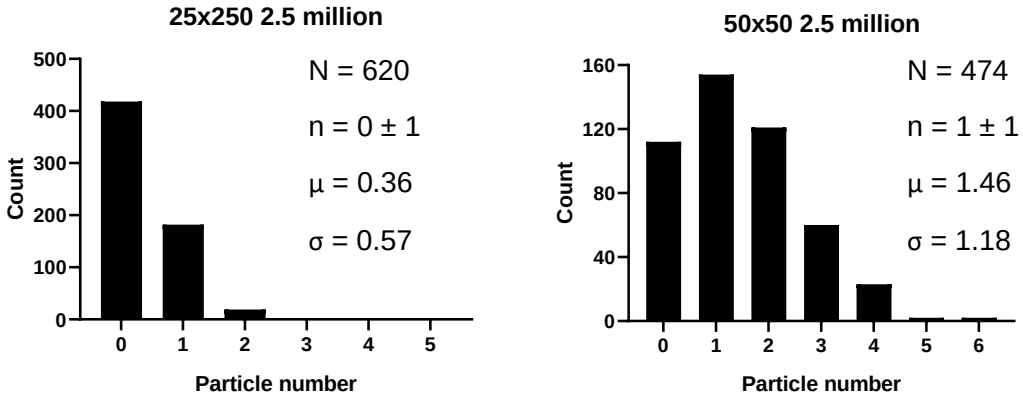

Figure C.4 Particle counts in spiral design for densities of 1 and 2.5×10^6 particles/ml for all flow rate ratios tested.

Appendix D Cell encapsulation in microdroplets: method development

In this appendix, the preliminary cell encapsulation experiments using 3D-printed chip designs, a soft lithography chamber design and both the *standard* and *spiral* soft lithography designs are thoroughly described to illustrate the methodological development preceding the work presented in Chapter 6:.

D.1 Cell encapsulation in microdroplets using 3D-printed designs

D.1.1 Experimental setup

Prior to commencing droplet microfluidic encapsulation, the chips and the pieces of tubing to be inserted into the oil and aqueous inlets and the outlet were UV-sterilised for 20-25 min. A 1 ml syringe was filled with the filter-sterile 1.8% Soton2 (w/v) FC40 oil and surfactant mixture and placed onto a syringe pump (NE-1000, New Era, Farmingdale, US). The oil was made to flow through the Aquapel®-treated chip channels for pre-conditioning by preferentially exposing them to the hydrophobic phase. The cells were harvested after a 5-minute incubation time in 1X T/E and counted to determine the volume of cell suspension to be inserted in the other 1 ml syringe. The cell suspension was centrifuged at 272 g for 5 min and resuspended in basal culture or chondrogenic differentiation medium. The syringe was then loaded onto another syringe pump (KDS-100-CE, KD Scientific, Holliston, US) and both phases were kept running for 5-minute stabilisation. Meanwhile, the chip was continuously monitored using an in-house microscope device for droplet size and characteristics as well as cell encapsulation (Figure D.1). Afterwards, the flow was stopped, the chip tubings detached and the chips moved onto 6-well plates or Petri dishes (according to size) for imaging on Zeiss Axiovert 200 or Nikon ECLIPSE Ti inverted microscope.

In parallel with cell aggregation, the viability of the cells encapsulated in droplets had to be confirmed to dismiss any negative effects coming from the surfactant-oil formulation used to stabilise the droplets in the culture chamber. A modification in the general experimental setup was added consisting in pre-labelling cells with Calcein AM green (Invitrogen, C3099, Fisher Scientific, Loughborough, UK) by incorporating it into the suspension at a 1 µM concentration (e.g. 1 µl Calcein AM in 1 ml DMEM). Off-chip and on-chip studies with Calcein AM and Soton2 were carried out for verification of cell viability upon exposure to the surfactant concentration employed.

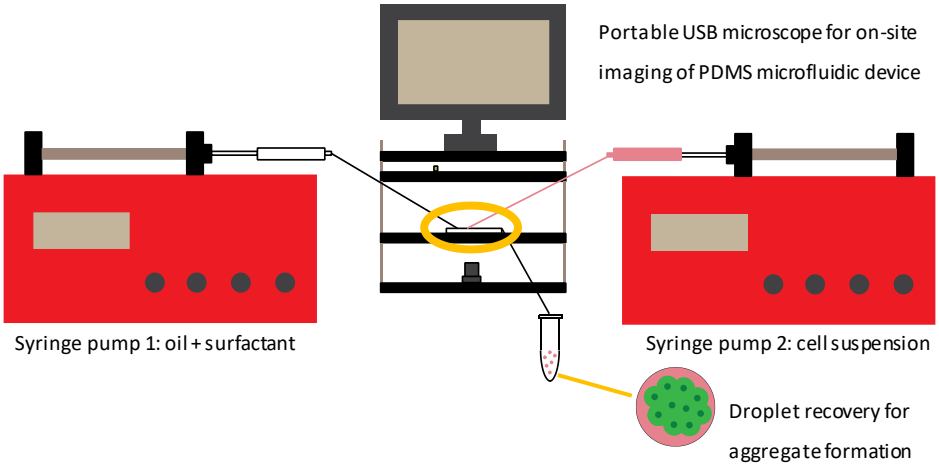

Figure D.1 Experimental set-up designed for cell encapsulation using a droplet microfluidic device consisting of two syringe pumps to inject the oil and aqueous phase, respectively, along with a portable microscope to image cell encapsulation live and a centrifuge tube for droplet collection and retrieval towards off-chip droplet incubation.

D.1.2 Preliminary cell encapsulation and on-chip incubation in microdroplets

Cell encapsulation in droplet microfluidic devices required establishing and testing a combination of the optimisation parameters discussed in the previous chapter to verify their suitability for cell culture in microdroplets. Firstly, cell encapsulation was studied using the experimental set-up in Figure D.1 in 3D-printed chip designs and a soft lithography chamber design. Two aspects derived from cell encapsulation were investigated: cell aggregate formation and cell viability in microdroplets. To that end, two T-junction winding designs characterised in section 5.3.1.1, *TJ250* and *TJ300*, and a soft lithography chamber design described in Appendix C.1 were employed. This approach focussed on initial cell-seeding densities and on-chip incubation time as variables to gauge their effect on cell aggregate formation and cell viability.

D.1.2.1 Cell aggregate formation in microdroplets

In connection with the time lapse cell aggregation analysis on ultra-low adherence 96-well plates, the preliminary microfluidic experiments aimed to ascertain whether and how cells tend to aggregate in microdroplets, starting by using the tested 3D-printed chip designs in section 5.3.1.1 and Table D.1. The ATDC5 cell line was selected as a positive control to identify the extent of cell aggregation in microdroplets.

A first trial experiment consisted in a time-lapse analysis to observe cell encapsulation in microdroplets in basal culture medium. The parameters adjusted for the time lapse study on an individual droplet in one chip from the *TJ250* batch (*TJ250 (1)*) were a cell density of 3×10^6 cells/ml and a flow rate ratio of 5 (10 µl/min 1.8% Soton2 in FC40 oil to 2 µl/min for cell suspension).

Following flow stabilisation for 15 min and interruption, the chip was stored on a 6-well plate (Corning, Costar, Sigma-Aldrich, UK) and inside the microscope chamber at 37°C and 5% CO_2.

Table D.1 Experimental references and parameters for droplet generation in 3D-printed chips.

Experimental reference	Cell density (cells/ml)	Flow rate (µl/min)
TJ250 (1)	3×10^6	10 (oil), 2 (aqueous)
TJ250 (2)	1.5×10^6	10 (oil), 2 (aqueous)
TJ300 (1)	1.5×10^6	90 (oil), 2 (aqueous)
TJ300 (2)	3×10^6	90 (oil), 2 (aqueous)
TJ300 (3)	1.5×10^6	10 (oil), 2 (aqueous)
TJ250 (3)	3×10^6	10 (oil), 2 (aqueous)

The time-lapse study over 38 h revealed an important issue: evaporation inside the chip channel, which had not incorporated any fluid reservoir to maintain hydration as a test. Evaporation hampered any accurate determination of cell proneness towards condensation in microdroplets and established a priority in terms of resolution towards developing a microfluidic platform that can host cell aggregates in microdroplets short-term. Cells in droplets displayed a morphology that diverged from that of cells in suspension (Figure D.2A-C): swollen irregular cells that moved along the pressure gradient caused by evaporation.

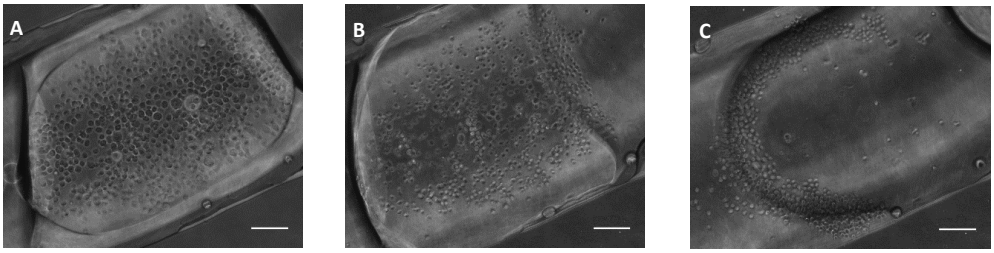

Figure D.2 Time-lapse images of ATDC5 cells encapsulated in *TJ250* chip design (experimental reference *(1)*) over a day of culture: (A) Initial (B) 12 h (C) 24 h. Scale bar = 100 µm.

Subsequent refined experiments prioritised addressing evaporation issues by culturing chips with an array of microdroplets in the channels in a normoxia incubator (37°C, 5% CO_2 and 20% O_2) and imaging them after set time points (e.g. 24 h, 72 h) to assess the degree of evaporation in the channels. Cell culture medium (DMEM +1% P/S) or PBS were deposited as reservoirs surrounding the wells on plates where the chips were stored. The plates were wrapped in parafilm leaving a small opening for gas exchange.

An overnight incubation of a TJ250 chip (*TJ250 (2)*) loaded with 1.5×10^6 cells/ml basal culture medium exposed cells with a suspension-like appearance inside the droplets, albeit in a low density format. The cells remained static during culture with no detectable displacement across the droplets. (Figure D.3A, B). Cell aggregate clusters were observed in a TJ300 chip (*TJ300 (1)*) when the same cell density was pumped through the channels (Figure D.4A): one at the leftmost edge

(Figure D.4B) and another one on the top right-hand side of the droplet (Figure D.4C). The remaining cells that did not form aggregates were floating individually in the suspension. In this experiment, droplet generation differed in the sense that the droplet break-off location shifted towards the serpentine channel instead of at the junction site. The chips were inspected after 24 h, finding that complete drying had occurred and was visibly concentrated at the chip aqueous inlet.

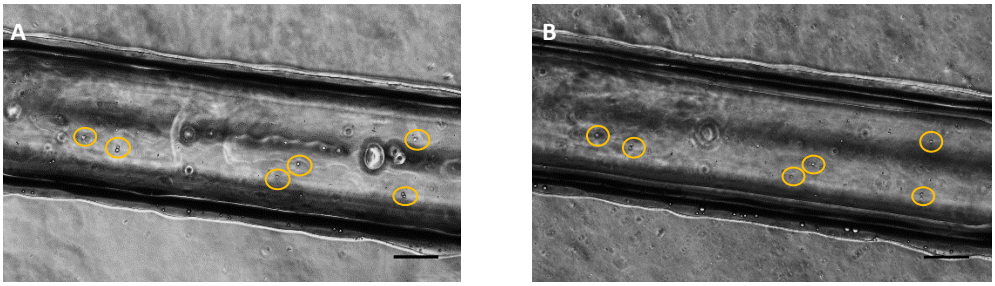

Figure D.3 ATDC5 cells encapsulated in microdroplets in *TJ250* chip (experimental reference *(2)*, cells highlighted inside yellow circles): (A) initial state, (B) microdroplet after overnight incubation. Scale bar = 200 µm.

For further clarification on methods and techniques needed to prevent evaporation while achieving cell aggregation, a repeat experiment was conducted by injecting 3×10^6 cells/ml and introducing chondrogenic differentiation medium to promote cell condensation. A similar issue re-emerged for this *TJ300 (2)* chip from the same batch as *TJ300 (1)*: despite breaking off at the junction site, the droplets were larger than predicted for non-sterile conditions with red food dye in section 5.3.1.

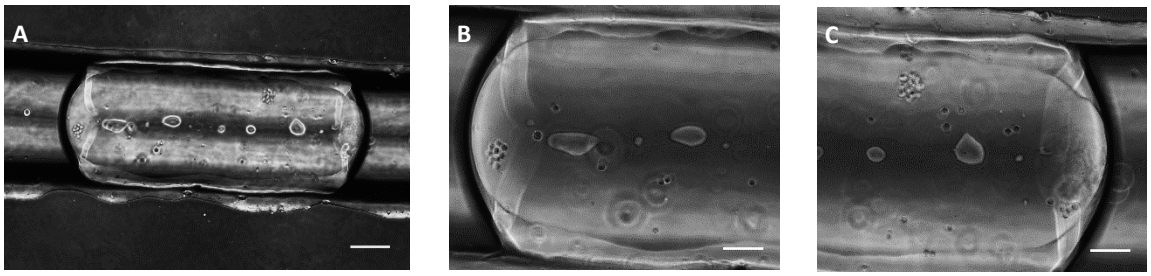

Figure D.4 ATDC5 cells encapsulated in microdroplets in *TJ300* chip (experimental reference *(1)*): (A) initial whole microdroplet, scale bar: 200 µm (B) initial microdroplet (left half), scale bar: 100 µm, (C) initial microdroplet (right half). Scale bar = 100 µm.

Despite higher initial cell density, the droplets imaged after cell encapsulation contained very limited cell numbers in suspension and an absence of cell clusters (Figure D.5). Evaporation caused droplets to migrate towards the chip inlets and to merge into a large droplet around the cell suspension inlet.

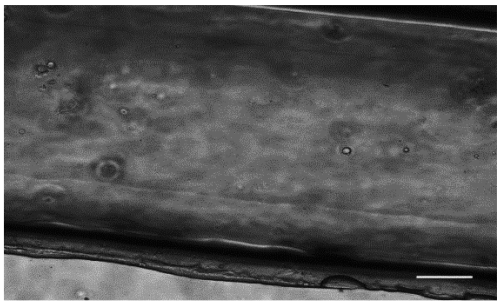

Figure D.5 ATDC5 cells encapsulated in microdroplets in *TJ300* chip (experimental reference *(2)*). Scale bar = 100 µm.

A considerable reduction in evaporation was achieved by means of a different storage approach post encapsulation tested on *TJ300 (3)* batch with a cell density of 1.5×10^6 cells/ml. The microchip was deposited on a PBS bed with the inlet and outlet tubings partly cut off and occluded, and surrounded by wells filled with PBS for storage and imaging on a 6-well plate almost entirely covered with parafilm. The extent of evaporation was studied by imaging overnight and after 3 days (Figure D.6). The cells were not straightforward to image clearly due to small cell numbers per droplet and chip thickness (hindered by PBS layer underneath). Notwithstanding, the droplets retained their static in-channel position after up to 5 days of culture.

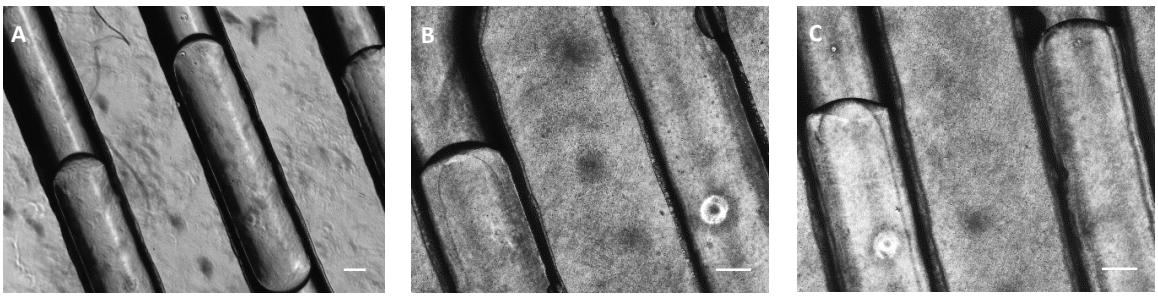

Figure D.6 ATDC5 cells encapsulated in microdroplets in *TJ300* chip (experimental reference *(3)*): (A) initial droplets (B) droplets after 24 h (C) droplets after 72 h. Scale bar = 200 µm.

Multiple cell encapsulation, of approximately 50 cells (Figure D.7A), resulted in *TJ300 (4)* chip design. An unusual phenomenon was registered as droplets were being generated: droplet break-off was decelerated when clusters of cells reached the junction site, causing an effect comparable to higher inertial/viscosity forces. Shear stresses had to overcome this obstacle before the cells rendered successfully encapsulated in droplets. Droplet size varied in consequence, having small stable droplets unless cell groups gathered at the T-junction. In accordance to what might be expected, the medium-sized more spherical-like droplets (Figure D.7A) displayed more intense cell aggregation concentrated in one of the droplet edges than the larger elongated ones, even moments after formation. Applying the same principles for evaporation prevention as in *TJ300 (3)*, appreciable cell encapsulation and aggregation occurred upon one day incubation, although mostly confined to one edge and characterised by slight evaporation (Figure D.7B).

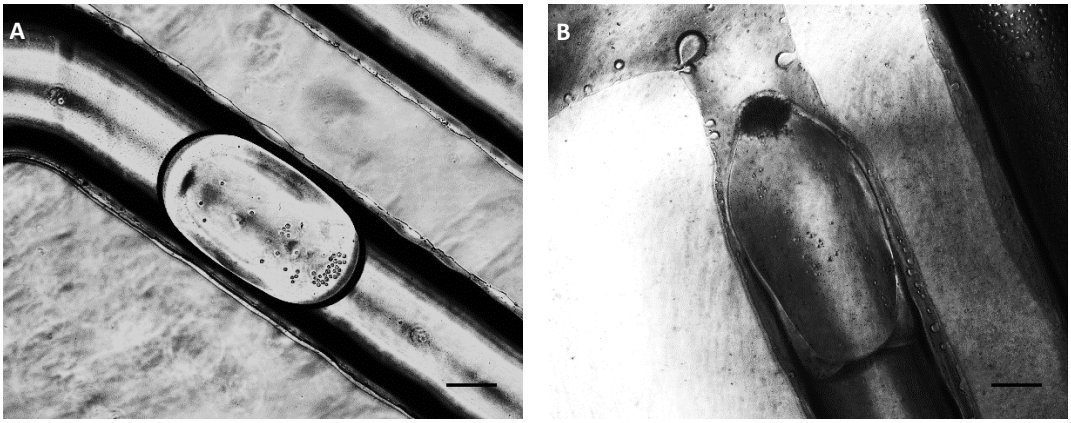

Figure D.7 ATDC5 encapsulated in microdroplets in TJ250 chip (experimental reference *(3)*): (A) initial droplets (B) droplets after 24 h. Scale bar = 200 µm.

D.1.2.2 Cell viability assessment in microdroplets

With the data available from the multiple experiments carried out to study cell aggregation in microdroplets, it became necessary to validate cell viability in the microfluidic device once the range of working cell loading densities had been narrowed down and the flow parameters were controllable.

Prior to starting the on-chip experiments, *in vitro* cell viability was examined on a 96-well plate (Corning, Costar, Sigma-Aldrich, Poole, UK) with droplets containing ATDC5 cells in chondrogenic differentiation medium. A volume of 250 µl was extracted from the original 2×10^6 cells/ml suspension and was topped up to 1 ml in a 1.5 ml Eppendorf tube. Calcein AM was added at 1 µM in serum-free DMEM and incubated at 37°C in normoxia for 30 min. After incubation and centrifugation at 400 g for 5 min, the medium was replaced with chondrogenic differentiation medium and diluted 1:10 (volume ratio) for target 5×10^4 cells/ml. An array of increasing volumes was prepared on a 96-well plate: 1, 2, 5, 10, 25, 50 µl (from 50 to 2500 cells/droplet). The drops were pipetted on top of a 100 µl 1.8% Soton2 FC40 oil and images taken after preparation and after one day for confirmation of viability maintenance.

The cells captured in the same plane were viable on day 0, although less so or not so clearly by day 1 in the sense that higher exposure times were required to visualise cell viability, yielding excessive background and overexposure as viability fluorescent signal was not readily detected (Figure D.8). The droplets characterised by small volumes (i.e. 1, 2 and 5 µl) did not gather sufficient cell density or present an adequate droplet morphology to draw any conclusion from the images. The elongated droplet morphology upon addition to well owing to surface tensions on the walls generally hampered imaging and viability assessment.

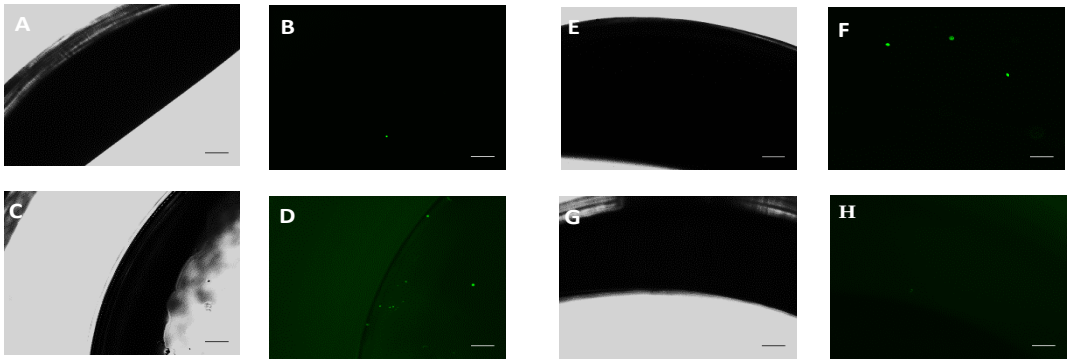

Figure D.8 Off-chip viability assay of ATDC5 cells exposed to FC40 oil with 1.8% Soton2 surfactant: (A) 10 µl droplet, brightfield day 0; (B) 10 µl droplet, calcein day 0; (C) 10 µl droplet, brightfield day 1; (D) 10 µl droplet, calcein day 1; (E) 25 µl droplet, brightfield day 0; (F) 25 µl droplet, calcein day 0; (G) 25 µl droplet, brightfield day 1; (H) 25 µl droplet, calcein day 1. Scale bar = 200 µm.

Seeking to improve cell-imaging possibilities of the *in vitro* transition experiment to on-chip viability in droplets surrounded by oil and surfactant system, a new approach was developed. It built on the failed sequence where the cell suspension drop was pipetted on top of the oil medium with the surfactant, which created strong adhesion on the edge of wells. The reverse order was employed instead, thus depositing a droplet at the bottom of each well covered by oil. Cells were seeded at different drop volumes (1,2,5 and 10 µl) at a 1:1, 1:10 and 1:100 volume dilution of the initial cell suspension. Cell numbers ranged from 10 to 10000 cells/droplet. The cells in the drops were incubated at 37°C, 20% O_2 and 5% CO_2 from day 0 to day 7 for viability assessment through imaging.

The staining became visibly reduced throughout culture for the majority of cell numbers and culture volumes (Figure D.9). The samples analysed on day 1 time point were irradiated with the wrong laser (between DAPI and FITC), which prevented real assessment of cell viability. Considerable background signal was present on cell aggregates from day 1 and onwards, indicating progressive viability loss.

To gain more clarity about the effect of surfactant exposure on cell viability, ATDC5 cells were cultured on 24-well plates at a cell-seeding density of 1000 cells/well on a series of increasing surfactant concentrations ranging from 0.6 to 3.0% Soton2 (w/v) in FC40 oil on 1000 cells/well after incubating the cells with the surfactant for 24 h in monolayer (n = 6). A live-dead assay was performed on cells fixed in 95% ethanol and stained with CellTracker™ Green (excitation at λ_{ex} = 492 nm and emission at λ_{em} = 517 nm; Invitrogen, UK) to identify cells and Ethidium Homodimer-1 (λ_{ex} = 528 nm and λ_{em} = 617 nm; Invitrogen, UK) to detect the extent of cell death. The working concentrations were 10 µg/ml for CellTracker™ Green and and 5 µg/ml for Ethidium Homodimer-1 and each well was incubated with 200 µl of both dyes in plain serum-free DMEM.

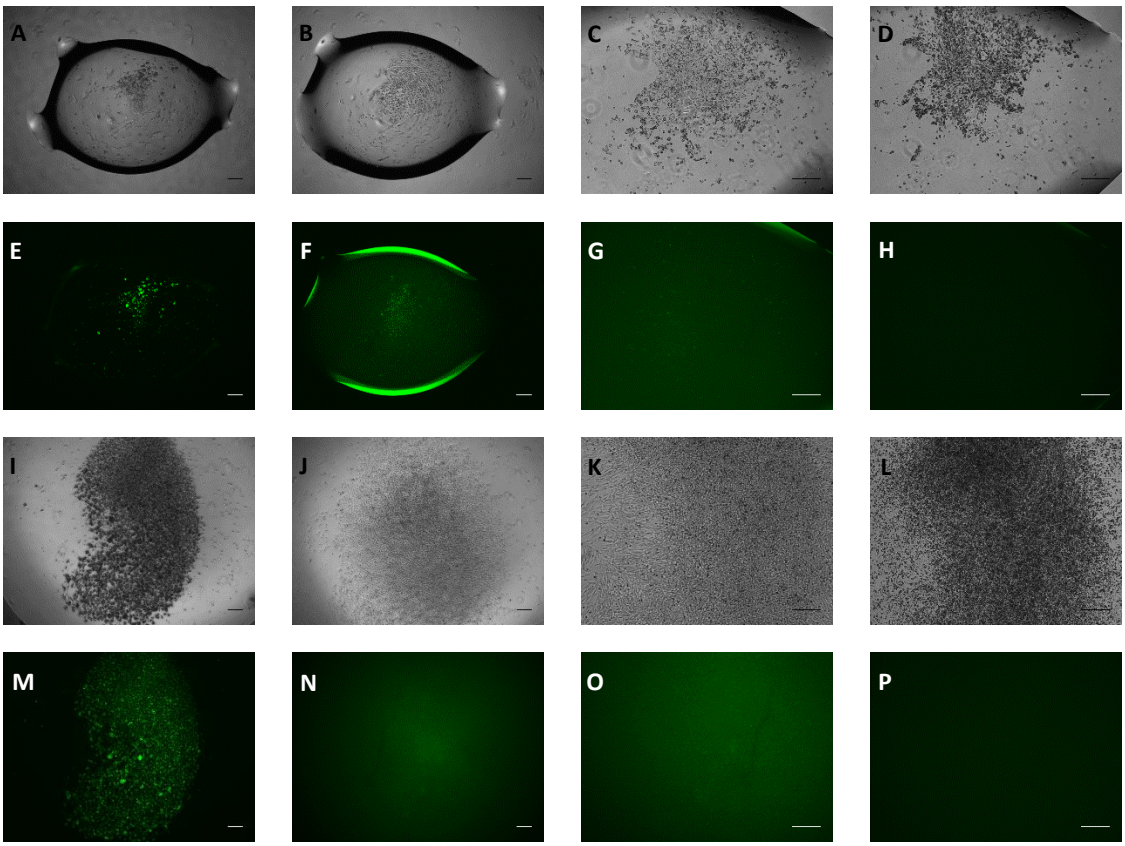

Figure D.9 Off-chip viability assay of ATDC5 cells exposed to FC40 oil with 1.8% Soton2 surfactant and seeded onto 96-well plates: (A) 500 cells, 5 µl, brightfield day 0; (B) 500 cells, 5 µl, brightfield day 1; (C) 500 cells, 5 µl, brightfield day 3; (D) 500 cells, 5 µl, brightfield day 7; (E) 500 cells, 5 µl, calcein day 0; (F) 500 cells, 5 µl, calcein day 1; (G) 500 cells, 5 µl, calcein day 3; (H) 500 cells, 5 µl droplet, calcein day 7; (I) 10000 cells, 10 µl, brightfield day 0; (J) 10000 cells, 10 µl, brightfield day 1; (K) 10000 cells, 10 µl, brightfield day 3; (L) 10000 cells, 10 µl, brightfield day 7; (M) 10000 cells, 10 µl, calcein day 0; (N) 10000 cells, 10 µl, calcein day 1; (O) 10000 cells, 10 µl, calcein day 3; (P) 10000 cells, 10 µl, calcein day 7. Scale bar = 200 µm.

Cells accumulated mainly by the walls of the wells and were easily detected through the CellTracker™ Green fluorescence signal. Ethidium Homodimer-1 (EthD-1) staining was negligible in the control surfactant-free group and cells exhibited a slight increase in fluorescence signal intensity as the Soton2 surfactant concentration was varied from 0.6% to 3% (w/v). There was no strong evidence of cell death in any of the surfactant concentrations after 24 h of direct exposure (Figure D.10).

For translation to the microfluidic platform, the cell harvesting and pre-labelling steps were maintained with no modifications. A suspension of 10^6 cells/ml in chondrogenic differentiation medium was injected into two chip designs: TJ200 and TJ250 with the usual 10:2 oil flow rate ratio and chip storage on PBS bed with occluded clipped tubings. The Calcein AM fluorescence-based assay distinguished viable cells following encapsulation (t = 60-90 min) with consistent viability loss over 1 day in spite of traces of existing viability (Figure D.11).

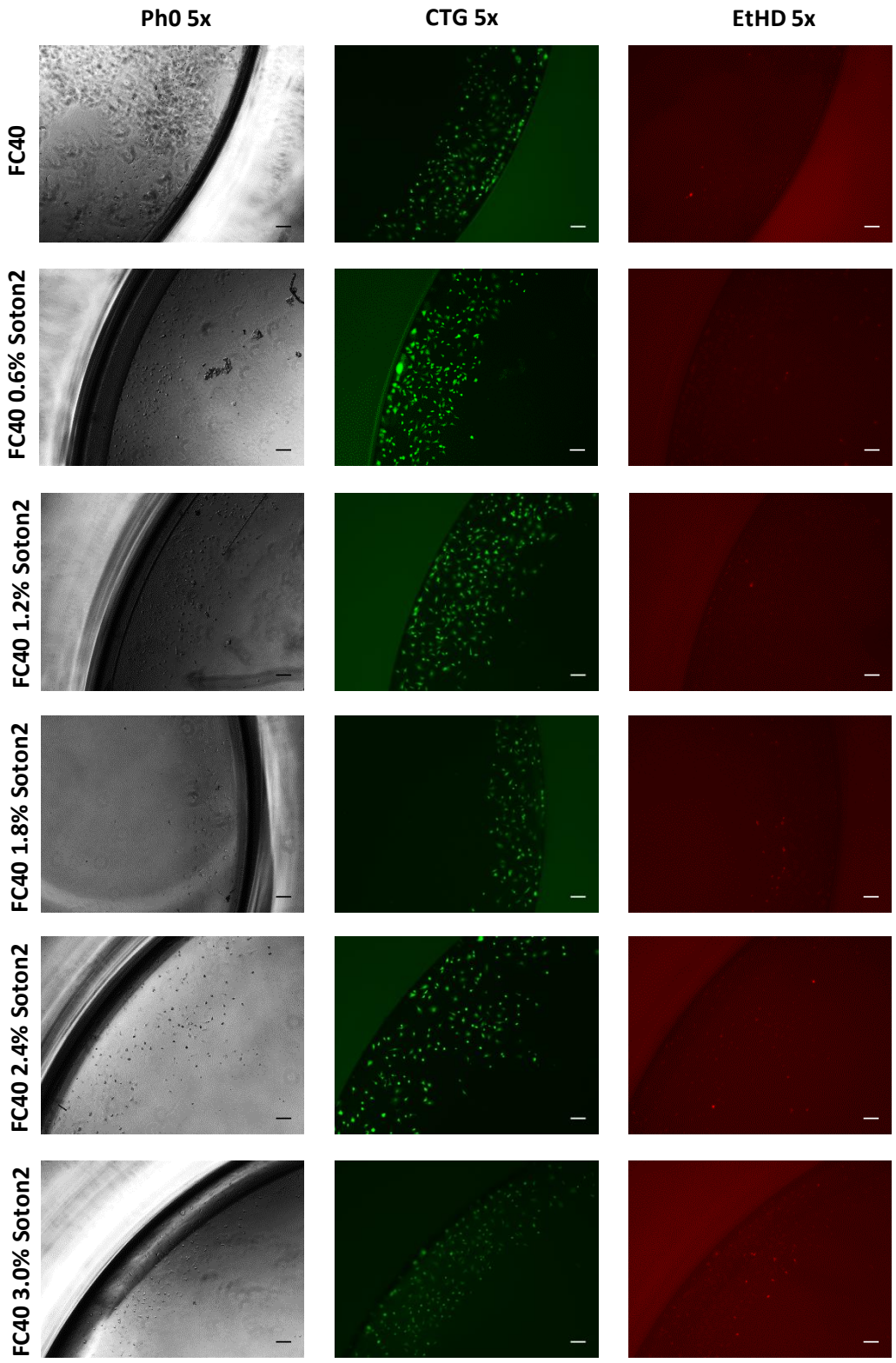

Figure D.10 Off-chip cell viability assay on 1000 ATDC5 cells seeded on 24-well plates and in the presence of FC40 oil with increasing Soton2 surfactant concentrations from top (surfactant-free control) to bottom (3.0% (w/v)). Brightfield images (left), ATDC5 cells stained with cell tracker green (CTG) and ATDC5 cells stained with Ethidium Homodimer-1 (right) are presented in the comparative diagram (n=6). Scale bar = 100 µm.

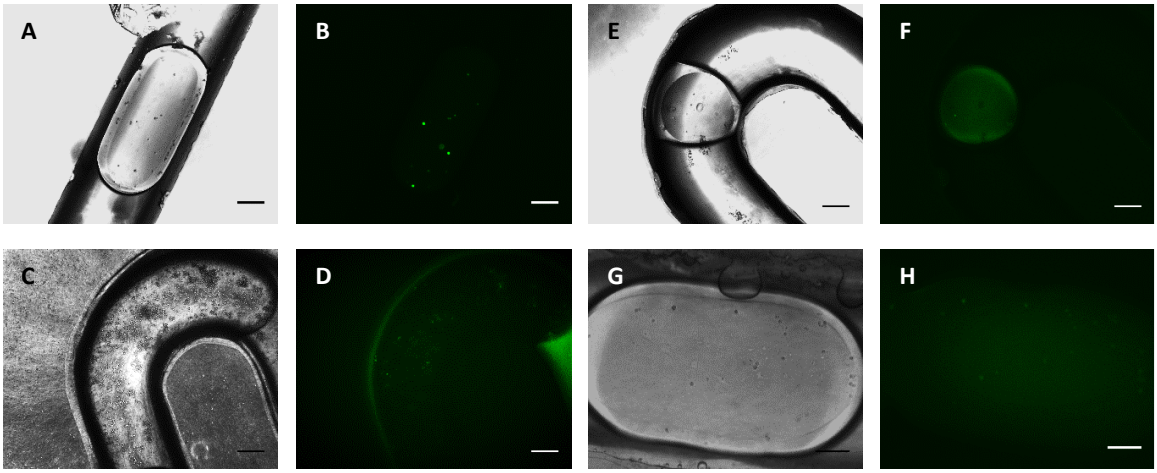

Figure D.11 On-chip cell viability assay of ATDC5 cells injected at an initial density of 10^6 cells/ml into *TJ200* and *TJ250* chips: (A) droplet in TJ200, brightfield day 0; (B) droplet in TJ200, calcein day 0; (C) droplet, brightfield day 1; (D) 10 µl droplet, calcein day 1; (E) 25 µl droplet, brightfield day 0; (F) 25 µl droplet, calcein day 0; (G) 25 µl droplet, brightfield day 1; (H) 25 µl droplet, calcein day 1. Scale bar: 200 µm (A-F) and 100 µm (G,H). Scale bar = 100 µm.

D.2 Cell encapsulation in a soft lithography chamber design for on-chip incubation

Before testing these chips and based on the design presented in section C.1, a brief optimisation procedure was needed to find appropriate curing times for the chips fabricated by soft lithography. Preliminary testings of these chips with cells highlighted the need to re-evaluate the set of tubings used for cell encapsulation in microdroplets, seeing as the designs underwent pressure problems that prevented the cell suspension from entering the chip channels if the oil phase was running simultaneously. The PVC tubings used for 3D-printed devices had enabled correct chip operation yet seldom batch-to-batch reproducibility problems related to this issue had appeared.

The new tubing used was fine bore polyethylene (Smiths Medical, Fisher) with an inner diameter of 0.58 mm and an outer diameter of 0.96 mm, sold as sterile. Terumo AGANI 23G needles (Medisave, UK) for medical applications were selected to replace the 23G 0.5”. Polypro Hub dispensing tips used for 3D-printed designs due to their cost-effectiveness and their characteristic sterility and disposability.

A pilot testing experiment with the soft lithography winding design (150 µm channel height) produced no droplets with a spherical configuration for flow rate ratios between 1 and 5. Droplet diameter exceeded channel width and their arrangement across the winding sections was sparse, which questioned real suitability for high-throughput applications.

The alternate 50 µm chamber height design fabricated by soft lithography succeeded in supplying with high-throughput generated droplets for a flow rate ratio of 3 (oil and aqueous phases infused at 10 and 3.33 µl/min, respectively). After 15 min, flow was halted for imaging with Zeiss Axiovert 200 microscope and the chip was placed in a Petri dish with PBS and clipped tubings. ImageJ analysis of the droplets formed moments after interrupting the flow showed that extensive variability existed in droplet size (Figure D.12), with an average diameter of 81.2 µm and an even higher standard deviation (82.6 µm). The values were calculated from direct circularity and droplet area measurements and applying the equation 3.1 in section 3.2.2. Regarding the cell density among droplets, large droplets often included single cells or small groups of cells, whereas more common smaller droplets seldom included single cells.

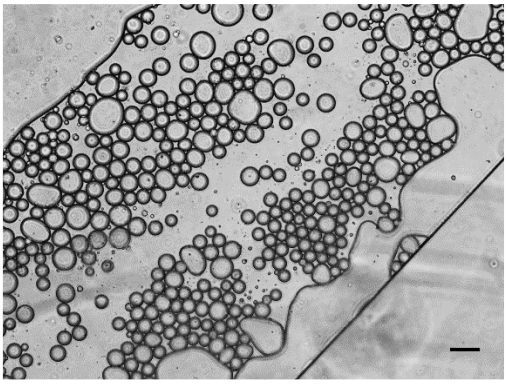

Figure D.12 Droplets generated in pilot experiment using soft lithography design with 50 µm high chamber illustrating size polydispersity. Scale bar = 100 µm

This experiment was repeated to rule out any past batch-to-batch reproducibility issues regarding chip functionality and operation and to set more adequate cell densities for encapsulation in chondrogenic differentiation medium. The fabrication conditions for the PDMS microfluidic device for this specific design were optimised by leaving the top layer to cure for 1 h 15 min and incubating the backing layer for 17-20 min at 70°C.

The droplet generation parameters were 3 µl/min for FC40 oil and 1.8% Soton2 surfactant and 1 µl/min for the cell suspension, which was injected at a 5×10^6 cells/ml density. Once the flow was stable (after 10-15 min), the tubings were clipped off and the chip placed in a Petri dish with DMEM around.

Relevant areas of the culture chamber were imaged on day 0, day 1, day 2 and day 3 (Figure D.13). Temporal evolution of the droplets was evaluated in the context of morphological changes, inspecting for signs of viable cells aggregating and general cell encapsulation assessment. Droplets became more and more prone to merging and coalescing as the oil gradually evaporated and the cell suspension stretched out to cover available free space, therefore increasing surface tensions

(Figure D.13D, H). Cells aggregated at the edges of large cell suspension areas by day 1 (Figure D.13B, F) and that effect intensified by day 2 (Figure D.13C,G).

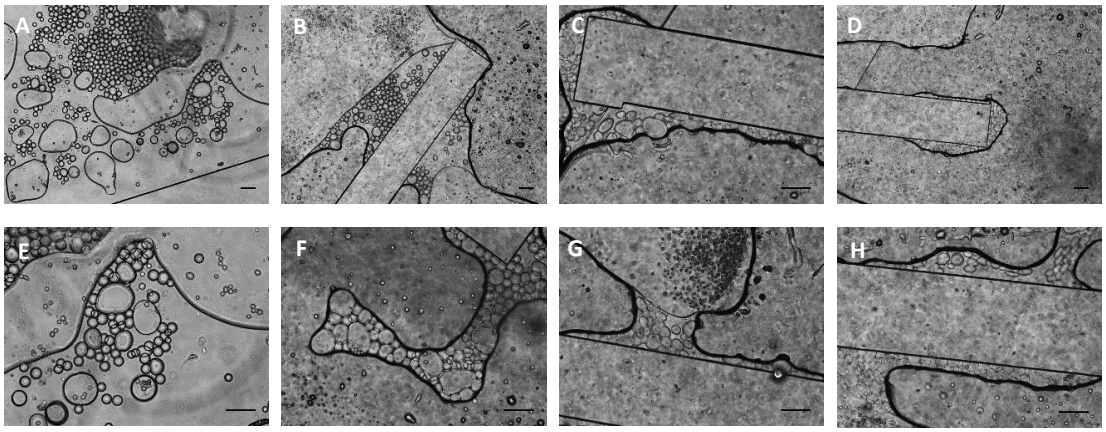

Figure D.13 Droplets generated in cell aggregation experiment using soft lithography design with 50 µm high chamber illustrating size polydispersity and droplet coalescence as a result of oil evaporation: (A) 5x day 0, (B) 5x day 1, (C) 10 x day 2, (D) 5x day 3, (E) 10x day 0, (F) 10x day 1, (G) 10x day 2 from another area inside the chamber, (H) 10x day 3. Scale bar = 100 µm.

Also, even if cells were abundantly concentrated in the cell suspension patches invading the channels, their presence in the droplets was heavily limited. The majority of droplets contained none due to their size and very few droplets had cell groups or individual cells in them. A higher number of stable droplets that had not merged with the big cell suspension were mostly located around the pillars of the chamber, which held the culture chamber in place avoiding collapse (Figure D.13B, C, D, G and H). More robust confirmation was required to draw conclusions on cell aggregation and viability.

A cell viability assay pre-labelling cells with 1 µM Calcein carried out on the soft lithography 50 µm high culture chamber maintaining 5×10^6 cells/ml as initial cell density injected and testing two separate chips for two different flow rate conditions:

- Chip 1: Flow rate ratio 3:1 with FC40/1.8% Soton2 pumped at 10 µl/min and the cell suspension at 3.33 µl/min.
- Chip 2: Flow rate ratio 3:1 with FC40/1.8% Soton2 pumped at 3 µl/min and the cell suspension at 1 µl/min.

Droplet generation was active for 10-15 min and the cells on the chips were imaged after clipping off tubings and laying on a Petri dish with sufficient amount of DMEM + 1% P/S to form a thin layer. Viable cells populated the culture chamber area on day 0 (Figure D.14B, F) in spite of the very reduced number of them encapsulated in microdroplets, whilst (Figure D.14D, H) little to no viability was the dominant trend for most parts of the culture chamber by day 1. Regardless of flow rates,

the average droplet diameter of each of the brightfield images displayed for both chips on day 0 and day 1 was not sufficient to host but a few cells.

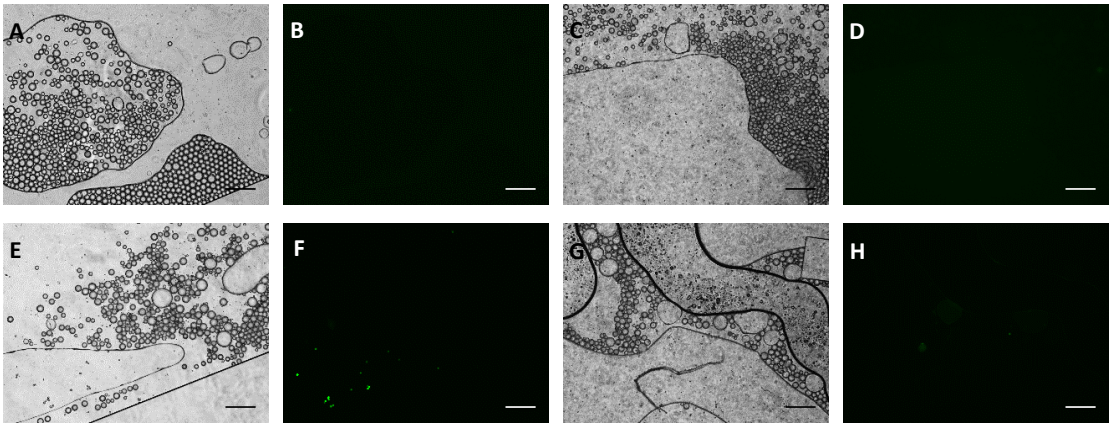

Figure D.14 Droplets generated in cell viability experiment using two chips with a soft lithography design consisting of a 50 µm high chamber: (A) chip 1, brightfield, day 0; (B) chip 1, calcein, day 0; (C) chip 1, brightfield, day 1; (D) chip 1, calcein, day 1; (E) chip 2, brightfield, day 0; (F) chip 2, calcein, day 0; (G) chip 2, brightfield, day 1; (H) chip 2, calcein, day 1. Scale bar = 100 µm.

Despite the limitation regarding comparison given that the images on day 1 did not correspond to the same region in the chip and droplets experienced displacement over time, the sizes were estimated using ImageJ in order to elucidate major droplet sizes which may result from evaporation and/or coalescence. Chip 1, which was subjected to higher flow rates, generated 28.8 ± 23.0 µm droplets on day 0 and slightly smaller droplets, 24.2 ± 23.8 µm by day 1, although the difference may be due to a separate region in the chip. Chip 2, as expected considering lower flow rates yielded larger droplets: 32.8 ± 36.9 µm on day 0 and 36.0 ± 60.4 on day 1.

Another cell viability assay replicated the chip design, pre-labelling method, surfactant concentration and cell density (5×10^6 cells/ml) to explore the effect of a biocompatible surfactant oil, Pico-Surf^{TM} 1 (Dolomite Microfluidics, UK), on droplet merging and cell viability. The flow rate ratio was increased to 10:1 (10 µl/min 1.8% Pico-Surf 1 in FC40 oil, 1 µl/min cell suspension) for the most stable droplet configuration. Keeping the same active operation time and chip storage conditions, the chip imaged on day 0 and day 1 (Figure D.14) faced the recurring challenges from the previous experiments with this chip design. The volume of cell suspension accessing the channel before droplet generation stabilised remained static during operation and opposed displacement across the culture chamber. In consequence, some of the larger droplets moving in the surrounding area coalesced into the predominant cell suspension even during syringe pump operation. The fraction of stable droplets separated by the oil phase continued to adhere to a polydisperse distribution with few droplets hosting functional cell aggregates (Figure D.15A, B). Those cell aggregates within droplets retained viability after 1 day of culture (Figure D.15C, D), exposing a

trade-off between cell viability and droplet merging when compared to in-house Soton2 surfactant formulation.

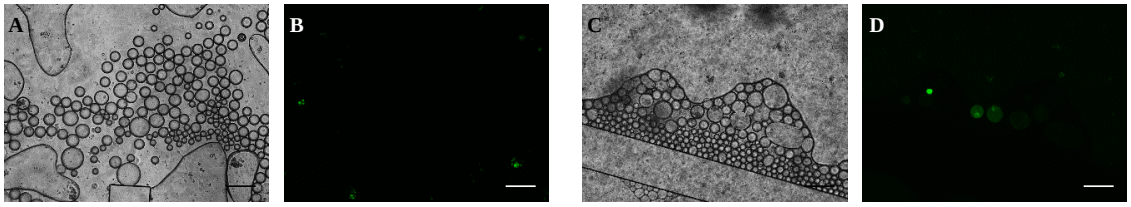

Figure D.15 Droplets generated in cell viability experiment using a soft lithography design consisting of a 50 µm high chamber and 1.8% Pico-Surf1 in FC40 oil: (A) brightfield, day 0; (B) calcein, day 0; (C) brightfield, day 1; (D) calcein, day 1. Scale bar = 100 µm.

D.3 Cell aggregation in microdroplets using optimised soft lithography designs

D.3.1 Preliminary pilot studies with ATDC5

Cell encapsulation was first approached using the *standard* chip design and ATDC5 as a positive control for rapid cell encapsulation and due to the already characterised ease of aggregation in section 3.3.1. In order to investigate how droplet size affected the number of cells encapsulated and analogously to particle experiments in section 5.2.2.2.2 and Appendix C.3, droplets were generated at two different flow rates (25 and 125 µl/min) for the carrier oil phase while keeping the flow rate for the cell suspension fixed at 25 µl/min.

The encapsulation performance of large droplets (25x25) differed greatly from that of the small (125x125) ones: 6 cells on average as opposed to 1 and standard deviations of 3 and 1, respectively. Both distributions resembled Poisson to a certain degree but the large droplets had cell numbers slightly skewed to the left with 4 being the most common result and the small ones were predominantly containing single cells and fewer duplets and triplets than anticipated. No empty droplets were identified during manual counting. The cells that appeared as separate in spherical droplets layered onto a haemocytometer consistently formed aggregates after 6 h in the large droplets that remained intact for 1 d. Aggregation also occurred in the small droplets 1 d following encapsulation (Figure D.16).

Once aggregation was confirmed for ATDC5 cells, they were pre-labelled with Calcein AM and viability was assessed 3 h, 1 d and 3 d after the cells in microdroplets were incubating at 37°C and 5% CO_2. The cells and aggregates that had already self-assembled in droplets after 3 h were positive for Calcein AM for 3 days, which indicated that the system was stable for translation to human

primary cells and potentially for SOX9 expression read-outs over that period of culture (Figure D.17).

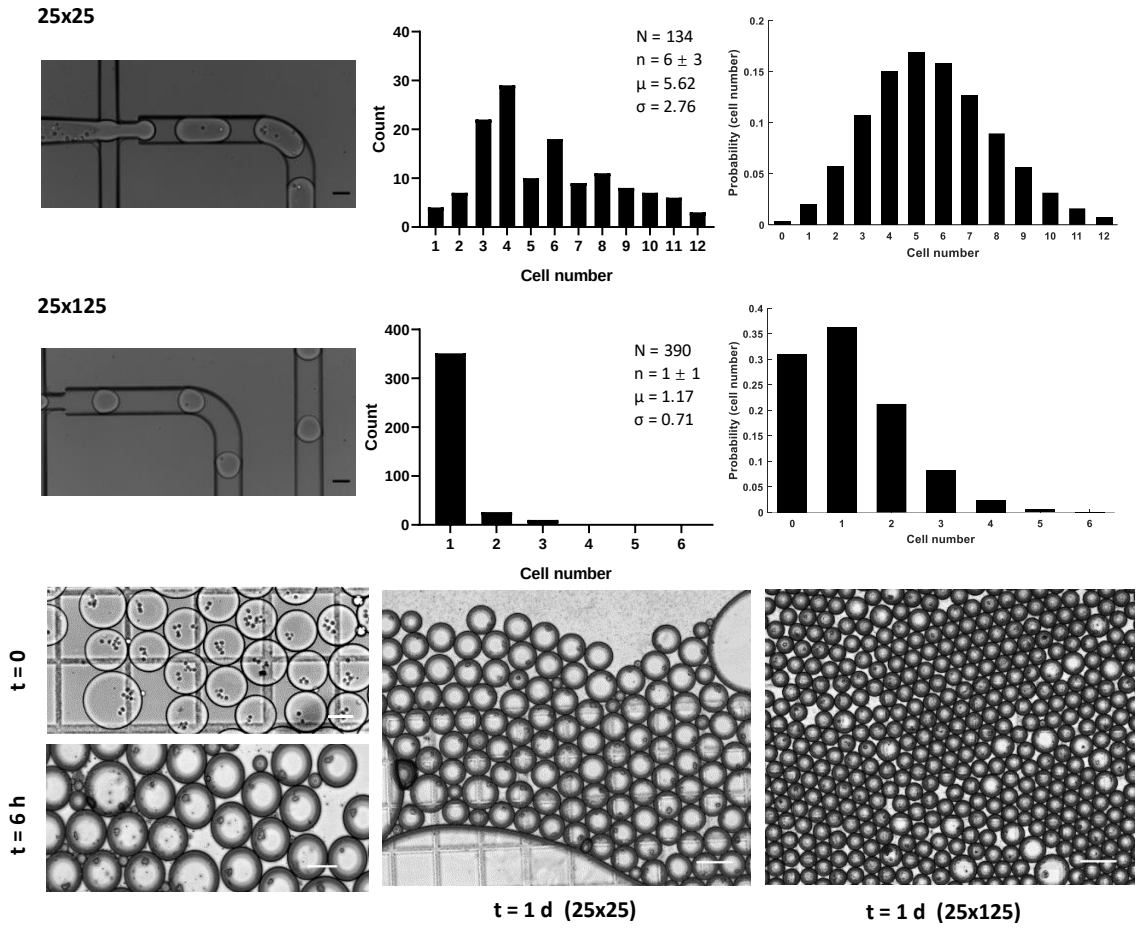

Figure D.16 ATDC5 cell encapsulation in microdroplets for two flow rate conditions (25x25 and 25x125) and injection at a density of 5×10^6 cells/ml: cell count (middle) and theoretical Poisson (right) distribution; and aggregate formation from individual cells at t = 0 to aggregates after 6 h that remained into t = 1 d. Scale bar = 100 μm.

To determine whether the *spiral* design was beneficial to regulate the process of cell encapsulation within droplets, similar flow parameters and cell densities to formerly established for the *standard* design were implemented. For the high cell density, 5 million cells/ml, the oil phase supplied at 25 μl/min did not suffice to produce separate droplets and the minimum flow rate necessary was 75 μl/min. The cell number distributions were significantly skewed to the left (Figure D.18A) of Poisson reference and the standard deviations were close or above the mean values. The same results were recorded for the low density, 3 million cells/ml, as shown through the decreasing counts as cell number moved away from the empty droplet state (Figure D.18B). This allowed to conclude that the *spiral* design alone did not impose any positive constraint (e.g. decline in the number of empty droplets) for the cell densities used and the particular channel dimensions of the microfluidic chips.

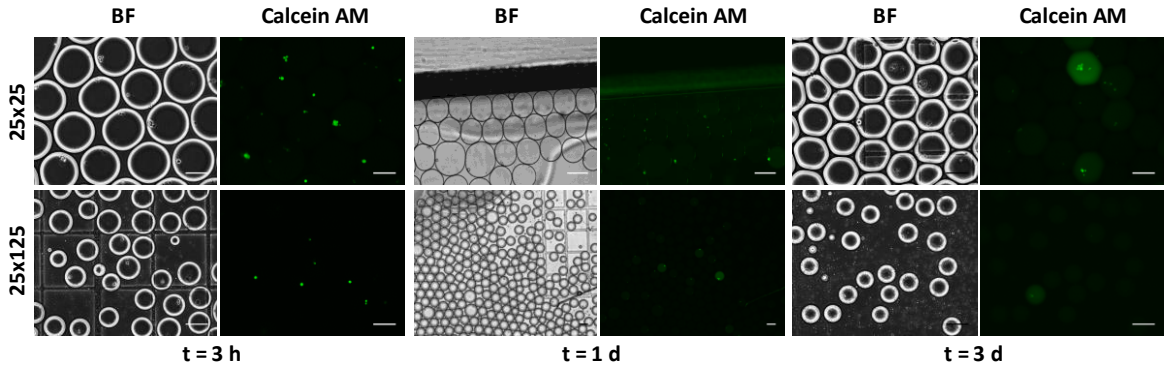

Figure D.17 ATDC5 viability assay on cell aggregates in droplets for two flow rate conditions (25x25 and 25x125) with time points at 3 h (left), 1 d (middle) and 3 d (right). Scale bar = 100 µm.

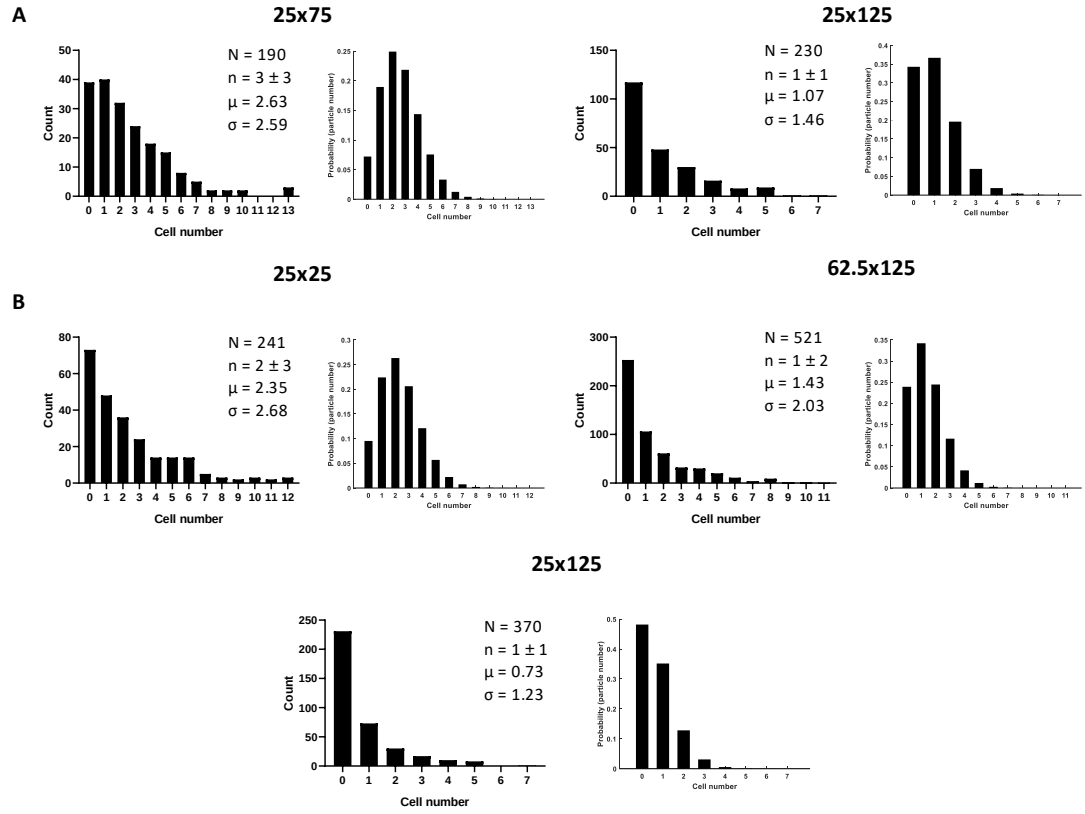

Figure D.18 ATDC5 encapsulation in *spiral* design: (A) 5 million cells/ml for 25x75 and 25x125 flow rates; (B) 3 million cells/ml for 25x25, 62.5x125 and 25x125 flow rates.

D.3.2 HBMSC and HAC encapsulation in microdroplets and cell viability

HBMSC aggregation and viability were assayed reproducing the flow parameters and experimental analysis. Cell aggregation was confirmed 1 day after encapsulation and viability within droplets was sustained for 3 days of cell culture in droplets in spite of the low initial cell density injected: 2 million cells/ml. Accordingly, the encapsulation efficiency was poor, achieving average single cell

encapsulation, a large proportion of empty cells and a small fraction of them containing more than one cells (Figure D.19).

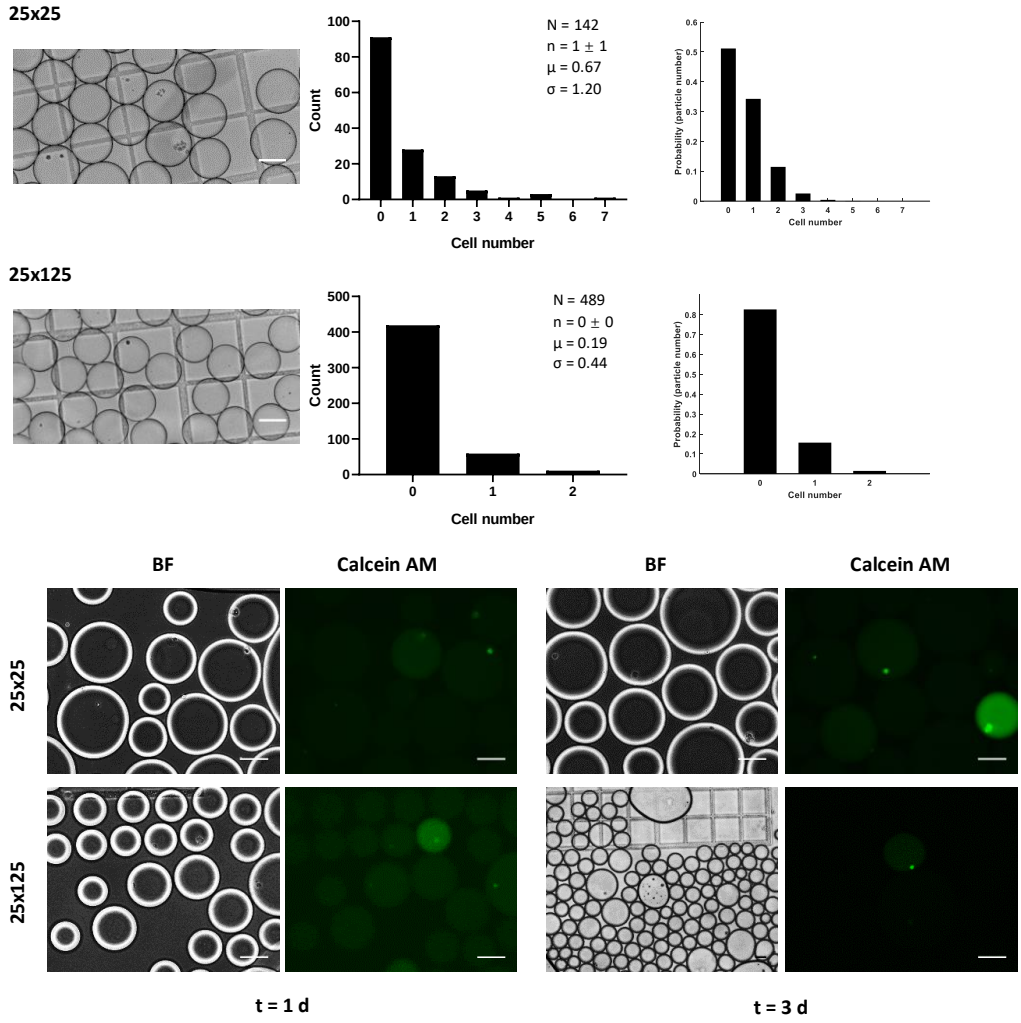

Figure D.19 M48 P2 HBMSC encapsulation at a density of $5x10^6$ cells/ml in microdroplets for two flow rate conditions (25x25 and 25x125): cell count (middle) and theoretical Poisson (right) distribution; and viability assay from cell aggregates at t = 1 d (bottom left) and t = 3 d (bottom right). Scale bar = 100 μm.

HBMSC cell encapsulation efficiency was further investigated by injecting different cell densities (2,3 and 5 million cells/ml). A compromise was observed between the stable 2 and 3 million cell suspensions that yielded 1-2 cells per droplet on average to 5 million cell suspensions undergoing uncontrolled merging over time but had a mean value of 5 cells per droplet. Standard deviation values generally revealed a strong variability in cell number (Figure D.20).

The replicate assay for HACs consisted of a starting density of 3 million cells/ml injected due to limited cell numbers preceding harvesting. Poisson-like distributions were quantified determined by single cell encapsulation for small droplets together with a mean cell number of 3 and a standard deviation of 2 for larger droplets. The cell groups hosted in droplets matched the aggregation

pattern corresponding to HBMSCs one day following encapsulation. Viability was again validated for HACs in droplets cultured for 3 d (Figure D.21).

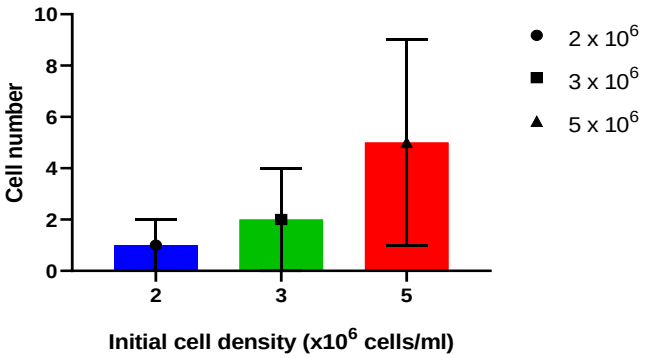

Figure D.20 Cell count per droplet as a function of initial HBMSC density injected using the *standard* chip design prior to optimising microfluidic settings for encapsulation.

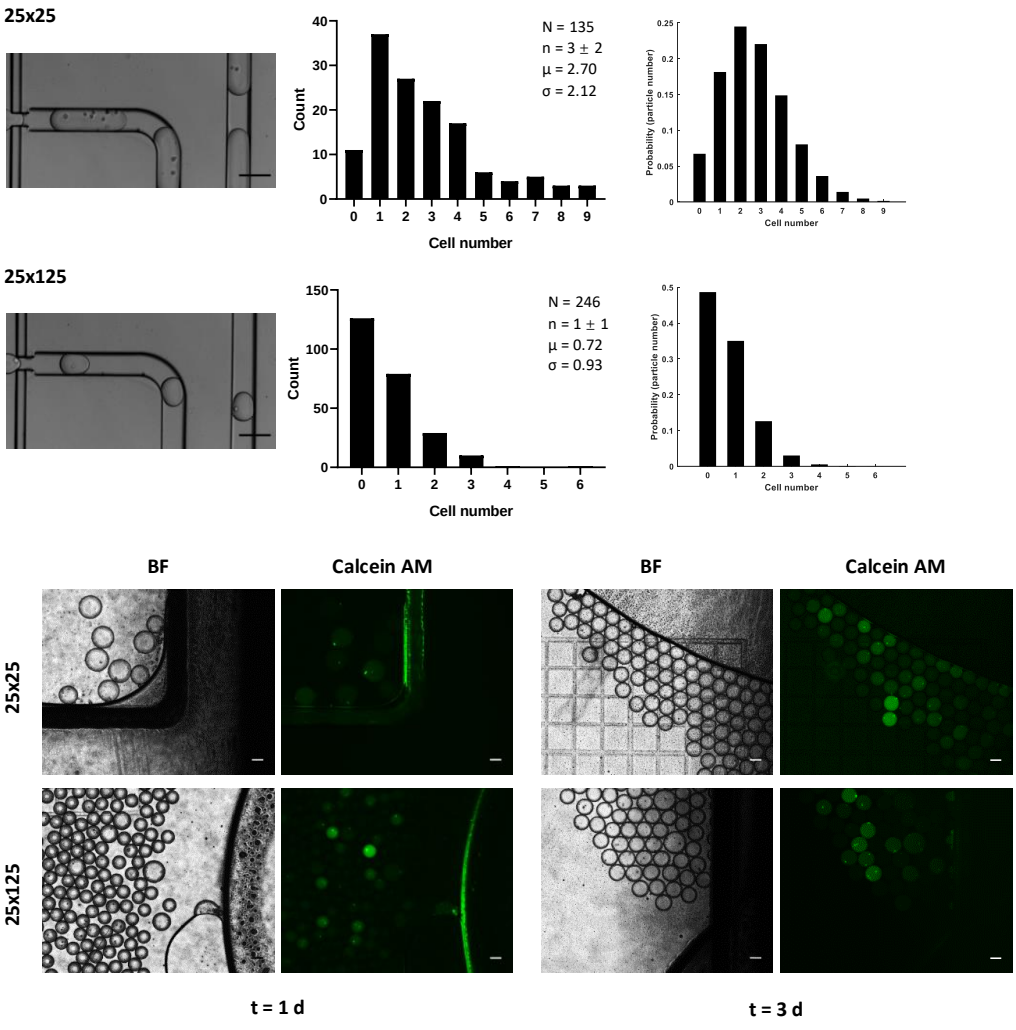

Figure D.21 F78 P2 HAC encapsulation at a density of 3×10^6 cells/ml in microdroplets for two flow rate conditions (25x25 and 25x125): cell count (middle) and theoretical Poisson (right) distribution; and viability assay from cell aggregates at t = 1 d (bottom left) and t = 3 d (bottom right). Scale bar = 100 μm.

D.4 MATLAB code to calculate theoretical Poisson distributions for particle and cell counting

```
% Compute and plot the pdf of a Poisson distribution with parameter |lambda = y| and with x corresponding to cell number range of the experiment

x = 0:n;

y = poisspdf(x,mean cell number of the experiment);

% Create axes: number corresponds to any preferred digit for bar width

axes1 = axes;

hold(axes1,'on');

bar(x,y,'LineWidth',1,'LineStyle',':','FaceColor',[0 0 0], 'EdgeAlpha',0,'BarWidth',number)

% Create label for x axis: number corresponds to any preferred digit for font size

xlabel({'Cell number'},'FontWeight','bold','FontSize',number);

% Create title: number corresponds to any preferred digit for font size

title({'x'},'FontSize', number);

% Create label for y axis: number corresponds to any preferred digit for font size

ylabel({'Probability (cell number)'},'FontWeight','bold','FontSize',number);

box(axes1,'off');

% Set the remaining axes properties: numbers corresponds to any digits that will be displayed on the x axis (e.g. [0 1 2 3 4] produces a graph with ticks at 0, 1, 2, 3 and 4)

set(axes1,'FontSize',12,'FontWeight','bold','XTick',[numbers]);
```